

Advanced Manufacturing Systems

Part 1

Edited by
Daoguo Yang, Tianlong Gu, Huaiying Zhou,
Jianmin Zeng and Zhengyi Jiang



TRANS TECH PUBLICATIONS

Advanced Manufacturing Systems

Edited by
Daoguo Yang
Tianlong Gu
Huaiying Zhou
Jianmin Zeng
Zhengyi Jiang

Advanced Manufacturing Systems

Selected, peer reviewed papers from the
International Conference on
Manufacturing Science and Engineering
(ICMSE 2011),
April 9 - 11, 2011, Guilin, P.R. China

Edited by

**Daoguo Yang, Tianlong Gu, Huaiying Zhou,
Jianmin Zeng, Zhengyi Jiang**



Copyright © 2011 Trans Tech Publications Ltd, Switzerland

All rights reserved. No part of the contents of this publication may be reproduced or transmitted in any form or by any means without the written permission of the publisher.

Trans Tech Publications Ltd
Laubisrutistr. 24
CH-8712 Stafa-Zurich
Switzerland
<http://www.ttp.net>

Volumes 201-203 of 3-vol.-set
Advanced Materials Research
ISSN 1022-6680

Full text available online at <http://www.scientific.net>

Distributed worldwide by

Trans Tech Publications Ltd
Laubisrutistr. 24
CH-8712 Stafa-Zurich
Switzerland

Fax: +41 (44) 922 10 33
e-mail: sales@ttp.net

and in the Americas by

Trans Tech Publications Inc.
PO Box 699, May Street
Enfield, NH 03748
USA

Phone: +1 (603) 632-7377
Fax: +1 (603) 632-5611
e-mail: sales-usa@ttp.net

The 2011 International Conference on
Manufacturing Science and Engineering
(ICMSE 2011)

Sponsored by

Guangxi University, China

Guilin University of Electronic Technology, China

University of Wollongong, Australia

Korea Maritime University, Korea

Hong Kong Industrial Technology Research Centre (ITRC), Hong Kong

Conference Organization

Consultative Committee

Academician Prof. Baixin Liu, Tsinghua University, China

Academician Prof. Bingheng Lu, Xi'an Jiao Tong University, China

Academician Prof. Baicheng Liu, Tsinghua University, China

Academician Prof. Yu Zhou, Harbin Institute of Technology, China

Prof. Shandong Tu, East China University Of Science And Technology, China

Prof. Weidong Huang, Northwestern Polytechnical University, China

Prof. Guoning Qi, Zhe Jiang University, China

Prof. Yushun Fan, Tsinghua University, China

Co-Chairmen

Prof. Jianmin Zeng, Guangxi University, China

Prof. Huaiying Zhou, Guilin University of Electronic Technology, China

Prof. Tianlong Gu, Guilin University of Electronic Technology, China

Prof. Daoguo Yang, Guilin University of Electronic Technology, China

Prof. Zhengyi Jiang, University of Wollongong, AU

Prof. Yun-Hae Kim, Korea Maritime University, Korea

Prof. Shanqing Li, Research Institute, Baosteel, China

Local Organizing Committee

Prof. Deguang Cao, Guangxi University, China

Prof. Taoshen Li, Guangxi University, China

Prof. Fuyun Liu, Guilin University of Electronic Technology, China

Dr. Mark Fong, Hong Kong Industrial Technology Research Centre

Mrs. Min Xu, Guilin University of Electronic Technology, China

Technical and Organizing Committee

Prof. Tianlong Gu, Guilin University of Electronic Technology, China

Prof. Xianghua Liu, Northeastern University, China

Prof. Jingtao Han, University of Sci. and Tech. Beijing, China

Prof. Kaiming Wu, Wuhan University of Science and Technology

Prof. Zhengyi Jiang, University of Wollongong, AU

Prof. AKM Nurul Amin, International Islamic University, Malaysia

Prof. Carlos Caceres, The University of Queensland, Australia

Dr. Chunsheng Lu, Curtin University of Technology, Australia

Prof. Lin He, Guizhou University, China

Prof. Jun Wang, Northeastern University, China

Prof. Qiang Wang, University of Jinan, China

Prof. Shao Hui Yin, Hunan University, China

Prof. Wenlei Sun, Xinjiang University, China

Prof. Chun Liang Zhang, Guangzhou University, China

Prof. Jinglong Bu, Hebei Polytechnic University, China

Prof. Xiaoming Jia, Hebei Polytechnic University, China

Prof. Jianmin Zeng, Guangxi University, China

Prof. Daoguo Yang, Guilin University of Electronic Technology, China

Prof. Huarui Xu, Guilin University of Electronic Technology, China

Prof. Yuan Gao, Guilin University of Electronic Technology, China

Prof. Yun-Hae Kim, Korea Maritime University, Korea

Prof. Junyou Shi, Qingdao University of Science & Technology, China

Prof. Yin Biao Guo, Xiamen University, China

Prof. Ming Dong, Shanghai Jiao Tong University, China

Prof. Wenbo Du, Beijing University of Technology, China

Prof. Hongzhen Guo, Northwestern Polytechnical University, China

Prof. Wenji Xu, Dalian University of Technology, China

Prof. Shiming Ji, Zhejiang University of Technology, China

Dr. Dongbin Wei, University of Wollongong, Australia

Prof. Geun Jo Han, Dong-A University, Korea

Dr. Gui Wang, The University of Queensland, Australia

Prof. Jong Kook Lee, Chosun University, Korea

Prof. Ken-ichi Manabe, Tokyo Metropolitan University, Japan

Prof. Jeng-Haur Horng, National Formosa University, Taiwan

Prof. Jianzhong Zhou, Jiangsu University, China

Prof. Xiaoqin Zhou, Jilin University, China

Prof. Wenjun Meng, Taiyuan University of Science and Technology, China

Prof. Haoran Geng, University of Jinan, China

Prof. Shuguang Gong, Xiangtan University, China

Prof. Yijian Huang, Huaqiao University, China

Prof. Changhe Li, Qingdao Technological University, China

Prof. Cheng Li, Zhengzhou University, China

Prof. Jialu Li, Tianjin Polytechnic University, China

Prof. Zhiyi Liu, Central South University, China

Prof. Yongcheng Lin, Central South University, China

Prof. Xiaoping Liao, Guangxi University, China

Prof. Deping Liu, Zhengzhou University, China

Prof. Jia-Horng Lin, Feng Chia University, Taiwan

Prof. Kyung-Man Moon, Korea Maritime University, Korea

Dr. Mark Fong, Hong Kong Industrial Technology Research Centre

Prof. P. S. Pa, National Taipei University of Education, Taiwan

Prof. Sagar Kamarthi, Northeastern University, USA

Prof. Meihong Liu, Kunming University of Science and Technology, China

Prof. Dehong Lu, Kunming University of Science and Technology, China

Prof. Yongjin Chen, KunMing University of Science and Technology., China

Prof. Shaojian Ma, Guangxi University, China

Prof. Qingsen Meng, Taiyuan University of technology, China

Prof. Furen Xiao, Yanshan University, China

Prof. Kailin Pan, Guilin University of Electronic Technology, China

Prof. Jingang Qi, Liaoning University Of Technology, China

Prof. Pengcheng Wang, Inner Mongol University of Technology, China

Prof. Shoujun Wang, Tianjin University of Technology, China

Prof. Shahrum Abdullah, University Kebangsaan Malaysia, Malaysia

Prof. Toshio Haga, Osaka Institute of Technology, Japan

Prof. Walid Mahmoud Shewakh, Beni Suef university, Egypt

Dr. Yuantong Gu, Queensland University of Technology, Australia

Prof. Yu-Shiang Wu, China University of Sci. and Tech., Taiwan

Prof. Jun Xiao, Wuhan University of Technology, China

Prof. Ligang Yao, Fuzhou University, China

Prof. Zhaohui Zhang, Beijing Jiaotong University, China

Prof. Xiaoping Zhou, Hubei University Of Technology, China

Prof. Jian Gao, Guangdong University of Technology, China

Prof. Changsheng Li, Northeastern University, China

Prof. Xiaoming Sang, Hebei Polytechnic University, China

Prof. Ping Zou, Northeastern University, China

Prof. Zhihai Han, Xi'an Jiao Tong University, China

Preface

The International Conference on Manufacturing Science and Engineering is the premier forum for the presentation of new advances and research results in the fields of Manufacturing Science and Engineering. The conference brings together leading researchers, engineers and scientists in the domain of interest from around the world. The 1st International Conference on Manufacturing Science and Engineering, ICMSE 2009, was successfully held from Dec. 26 -28, 2009 at Zhuhai, China. The 2nd international conference on Manufacturing Science and Engineering, ICMSE 2011, is held in Guilin, China, between 9 and 11 April 2011. Delegates from more than 20 countries or districts attended those conferences.

The present volumes provide up-to-date, comprehensive and worldwide state-of-the-art knowledge of the manufacturing science and engineering, including: manufacturing process technology, advanced engineering materials, new and advanced materials, advances in mechanical design and advanced manufacturing systems. All papers included in those volumes have already passed the strict peer-reviewing by 2-5 expert referees and been accepted for publication.

The editors hope that those volumes will not only provide the readers a broad overview of the latest advances but also provide the researchers a valuable summary and reference in this field.

We would like to express our sincere appreciations to all the authors for their contributions to those books. We are indebted to all the referees for their constructive comments on the papers. Thanks are also given to Trans Tech Publications for producing those volumes.

Prof. Daoguo Yang
Guilin University of Electronic Technology, China

Prof. Tianlong Gu
Guilin University of Electronic Technology, China

Prof. Huaiying Zhou
Guilin University of Electronic Technology, China

Prof. Jianmin Zeng
Guangxi University, China

Prof. Zhengyi Jiang
University of Wollongong, Australia

Table of Contents

Sponsors, Committees and Preface

1. CAD/CAM/CAE

Hot-Stamping Process Simulation and Optimize Research for Collision Beam of Automobile Door	
C. Wang, B. Zhu, Y.S. Zhang, J. Shi and H. Dong	3
The Interpolation Algorithm of Feed Rate Control Based on Trigonometric Acceleration-Deceleration and Machine Dynamics Conditions	
L. Jiang, G.F. Ding, B.B. Xie and J.M. Wang	9
An Approach to Multi-Constrained 3D Modeling for Curtain Wall System Based on Spatial Point-Line Model	
Z.Z. Hu, F.Q. Yu, G.X. Li and Z.L. Wang	15
A Novel Symbolic OBDD Algorithm for Generating Mechanical Assembly Sequences Using Decomposition Approach	
Z.B. Xu, T.L. Gu, L. Chang and F.Y. Li	24
The Analysis of the Temperature Field and Deformation of Cylinder Liner Base on Finite Element Method and Experiment	
K. Li, T.X. Su, X.J. Li and S.X. Xing	30
Problems in the Application of Commercial CAD/CAE Software and Improvement Methods	
C. Wang, X.W. Yang and B.K. Yang	36
A Method of Machining Region Planning for Tyre Tread Mold Machining	
J.S. Liu, H.N. Tu, F.C. Xia and J.X. Xiong	40
Finite Element Analysis of Laminating Press Frame	
X.Z. Zhang, S.B. Wang, K. Wu and Y. Sun	44
Lightweight Design of Electric Scooter Frame by Finite Element Optimization	
H.B. Dong and W. Zhang	49
A Feature-Based CAD-CAE Integrated Approach of Machine Tool and its Implementation	
W.T. Niu, P.F. Wang, Y. Shen, W.G. Gao and L.N. Wang	54
Using Software Engineering to Guide Commercial CAD Software Secondary Development	
C. Wang, B.K. Yang, X.W. Yang and G.R. Yan	59
Research on 3D Non-Destructive Measurement System Based on Homogeneous Entity	
Y. Gan, J.R. Zhong and D.F. Gan	63
Study on the Parallel Rendering Technology Used in Virtual Prototype System	
M.Q. Yin and S.Q. Li	69
Models and Simulations of the UV Lithography Process Based on Thick Photoresists	
Z.F. Zhou, Q.G. Huang and W.H. Li	75
Research on Computer-Aided Conceptual Design of Palletizing Robot	
Z.M. Li and W. Liu	80
Study on the Computer Numerical Control Process of Variable Pitch, Groove Depth and Groove Width Screw	
M. Han, S. Li and L.T. Deng	85
Numerical Simulation on Aerodynamics of Ramjet Projectiles	
J.X. Zhang, Y.N. Wang and R.M. Liu	89
A Parametric Die-Base in SolidWorks	
X.Q. Zhang	93
A Study on the Digital Simulation for Sheet Metal CNC Incremental Forming Based on Z-Map	
H. Zhu, Z.J. Liu and J. Kang	99
The Research and Realization of Efficient DDA Interpolation Algorithm for Multi-Axis Linear Linkage	
X.L. Yan, J.Y. Zhang and W.L. Wang	103

Finite Element Analysis on Structural Stress of 8×8 InSb Infrared Focal Plane Array with Underfill Q.D. Meng, L.G. Sun and J.X. Pu	108
Research on 3D Reconstruction of the Facial Surface Reverse Engineering J. Yang and L. Zhao	113
A Digital Near Net Shape Manufacturing Propeller with Complex Surface Z.F. Jiao, S. Yao, S.M. Zhao, F. Zeng and D. Wu	117
Finite Element Analysis for Analog Modes of SCS Series Truck Scale with Different Loads W.T. Shi, J. Li and J. He	121
Finite Element Analysis of Blanking Process by Superimposing Ultrasonic Vibrations W.C. Yeh, T.S. Chu, S.S. Wang, K.H. Fuh and K.H. Chen	126
Special Purpose Five-Axis Machine Tool for Manufacturing a Precision Cam C.H. She, K.S. Li and Z.H. Zheng	133
Accurate Prediction of Die Face Coloring Rate for Short-Period Manufacturing of Automotive Drawing Dies Q. Yu, D.H. Miao, Y.J. Cai and C.F. Men	138
Automation of Design and Analysis in Simulation System for Rough Rolling Process of H-Beam C.Y. Li, Q.H. Zhang, R.P. Ma and B.T. Dong	143
A Fuzzy C-Means Clustering Method Based for 3D Mechanical Models Retrieval H. Jing, C. Li, B. Kuang, M.F. Huang and F.Y. Liu	147
Tolerance Synthesis Modeling Based on Degree of Freedom of Geometric Variations of Features B.S. Xu, C. Wang and M.F. Huang	151
Development of CAD/CAE Software System for Raw-Soil Structure Z.H. Zhou, J. Hu and Q.L. Zhang	157
The HSM Intelligent Database System Based on Neural Networks L.J. Liu, M. Lv and W.G. Wu	162
Study on Meshing Characteristic and CAM Technology of Limacon Type Gears J.L. Zhao and P.F. Meng	167
Theoretical Model of Wall Heat Transfer in Turbulent Flow W.Z. Zhang, X. Liu and C.H. Xiang	171
Local Gouge Detection Algorithm for 5-Axis Sculptured Surface Machining Using the Toroidal Cutter W.G. Fan, J.Y. Li, Y.L. Cai and Z.H. Huang	176
Virtual Processing Research on Auto Control Valve Cylinder Mold P. Xu, K.P. Ma and S.F. Wang	180
Boom System Kinematic Simulation of Truck-Mounted Concrete Pump X.X. Zhou, N.N. Ren, S.J. Guo, Y.L. Tang and R.L. Tian	185
Research on Assembly Variant Design Based on Complex Network K. Xu, F.Y. Liu and G. Li	189
Line Segment Nearest Neighbor Query of Spatial Database Based on R*S-Tree D.Z. Sun, Y.W. Sun, X.C. Kang and Y.R. Li	194
Study on the Optimum Choice of Cutting-Tools in NC Machining Based on the Polychromatic Sets Theory E.F. Liu, X.Y. Liu, Y.X. Fang and Z.B. Li	198
Analysis and Simulation of the Shear Deformation for Woven Cloth L. Chen, S.G. Zhao, L.J. Zhang, L.Q. Zhang and W.B. Zhang	203
Molding CAE Technology and its Application Research Y.F. Wang	209
Research and Development of UG-Based CAD/ CAM System for Turbine Blade F.J. Ren, S.Q. Zhou, J. Li, Z.Q. Wan, Y. Zhao and Y. Liu	215
Kinematics Analysis and Simulation of a New Type of Mechanical Excavator with Controllable Mechanism G.W. Cai, Z. Zhang, Y.C. Pan, D.C. Wu and X.Y. Xu	220
3D Laser Inner Engraving Path Generation and Simulation for Crystal Glass H. Zhu, N. Li and Z.J. Liu	225

Visualized Equivalent Variational Modeling in Tolerance Analysis of 3D Mechanical Assemblies	
D.Y. Yang and J. Gong	229
Computer Simulation of Uniform Corrosion Process for Carbon Steel	
A.Q. Wu, H.Y. Yu and D.B. Sun	234
The Analysis in the Difficulty of Carrying on the Innovation Based on the TRIZ Theory	
K.S. Wang, H.L. Liu and Y.X. Xu	241
A Nonlinear Tolerance Analysis Method Using Worst-Case and Matlab	
M.Q. Yu, Y. Yan, J. Hao and G.X. Wang	247
Theoretical and Finite Element Analysis of Crosshead of Quintuple Cylinders Fracturing Pump	
Z.P. Lv, S.Z. Zhou and X.H. Ma	253
A Lamp Coating Temperature Field Calculation Method	
K. Lin	257
Numerical Simulation of the Two-Phase Flow in a New Type Cyclone	
N.N. Xing and W.L. Zhao	263
Holonic Engineering Data Management Framework for Allied Concurrent Engineering	
C.C. Wen	267
Simulation Analysis to Shock Strength of Electromechanical Products Using MSC.PATRAN and MSC.DYTRAN	
B.C. Ma and X.K. Tian	272
Design of Vehicle's Controlling System Used a 4WS Control Method Based on BP Neural Network	
Y.P. Liu, Y. Tang and J.B. Bi	276
Parameter Transfer Method of Mixed-Language Programming	
Y.H. Sun, R.S. Lai, J. Zhang and B. Kuang	281
Design and Simulation of the Cleaning Parts of Comb-Type Cotton Picker	
Y.P. Yuan, W.L. Sun, S. Huang and Y.Y. Ni	286
Research on the Installed Position of the Cutting Device of a Small-Scale Sugarcane Harvester Using Virtual Prototype Technology	
J.H. Zhou, S.P. Li and X. Lai	290
Research on Network-Based Intelligent EDM CAPP System	
J.Z. Zhao and Y.T. Liu	298
Thermal Stress Analysis of a Tubesheet with a Welding Clad	
H.F. Li, C.F. Qian and X.D. Yu	302
Application of Experimental Design and MPI Technology in Injection Molding Parameters Optimization	
Y. Hu and W.L. Xie	308
A Study on Durability Enhancement of Band Brake for Mooring Winch	
D.S. Han, G.J. Han and D.H. Choi	314
An Integrated Approach of CAD/CAM for Spatial Cam with Oscillating Cylindrical Rollers	
J.N. Lee, Y.C. Tsai, H.S. Chen and H.K. Kung	318
FEM Analysis of Plug Packer Based on the Model of Mooney-Rivlin	
C. Zhang, S.M. Zhang, D. Geng, J.M. Zheng and W.B. Fan	326
Simulation of End Milling for Weak-Rigidity Structural Parts of Aluminium Alloy in Aviation	
C.L. Fu, C.K. Wang, T.G. Li and W.S. Wang	332
Thermal-Mechanical Couple Analysis for a Piston of Oil Engine Based on ANSYS	
H. Li	337
Manufacture of Custom Contoured Seat Cushions Using Computer-Aided Design Computer-Aided Manufacturing (CAD/CAM) Technique	
S. Sekou	342
Anti-Crashing Energy-Absorbing Simulation and Optimization of Thin-Walled Components	
B.Z. Chen, Z.D. Lv, S.M. Xie and W.Z. Zhao	347
Mixed Loop Scheme and it's Industry Application	
Z. Shi	356

The Numerical Study of Oil Drop Jet from Oil-Air Lubrication Nozzle J.L. Wang, L.Q. Li and L. Cai	361
---	-----

2. Energy Storage and Energy Development

The Optimum Solution to Diameter of the Down Wind Turbine L. Zhang	367
Analysis on the Key Technologies of CBM Surface Well Development in Mining Active Areas of China J.H. Chen	372
Profit-Oriented Decision-Making Model of Manufacturing Systems M.Q. Li and D.Y. Li	378
Practical Optimization of Industrial Gravel Size in Gravel Packed Well J.G. Deng, Y. Chen, L.H. Wang, W.L. Zhao and P. Li	383
Service-Oriented Manufacturing: the Development Trend of Chinese Manufacturing Industry J.L. Lin, R. Miao, Z.B. Jiang and L.Y. Wang	388
A Prediction of Water Breakthrough Time of Horizontal Wells in Gas Reservoirs with Bottom Water W.Y. Zhu, X.H. Huang, H.Q. Song, J. Deng and X. Liu	393
Formation Pressure Analysis of Water-Bearing Tight Gas Reservoirs with Unsteady Low-Velocity Non-Darcy Flow H.Q. Song, M. Yue, W.Y. Zhu, D.B. He and H.J. Yi	399
Behaviour Characteristics of Pressure Bump of Deep Mining in Kailuan Coal Mine and Micro Seismic Monitoring Technology Y. Zhang, L.F. Gao, S.Z. Zhang, J. Sun and P. Zhang	404
Geological Features of Kailuan Coal Mine and the Laws of Pressure Bump for Deep Mining L.F. Gao, Y. Zhang, Y.H. Niu, Y.C. Wang, J. Sun and P. Zhang	408
Mechanism of Frequency Conversion Vibration Stimulating Exploiting Technology with Marine Gas Hydrate and its Numerical Simulation Z.G. Zhang, L.F. Gao, Y. Zhang, Y. Wang, G.Y. Shi and C.S. Liu	413
Key Technology of Safety and Effective Mining in Thick Coal Seams with Dirt Band W.D. Pan, H.B. Zhao and S.L. Yang	417
Spheroidization Modification of Artificial Graphite Applied as Anode Materials for High Rate Lithium Ion Batteries Y.S. Wu, T.S. Yeh, Y.H. Lee and Y.C. Lee	421
Intelligence Mining with Electro-Hydraulic Control Technology M.X. Lu, M.F. Lv, J.G. Wang, M. Li, J. Zhao, Y.Y. Liu, Y. Zhao and J. Wang	425
Design of the Speed Regulating PIG with Butterfly Bypass-Valve G.B. Tan, S.M. Zhang and X.X. Zhu	429
Key Technologies of Sucker Rod Pump Card Diagnosis Based on BP Neural Network X.D. Wu, R.D. Zhao, Z. Hao, T. Zhen and S. Lei	433
Review of Sour Gas Field on Corrosion Factors and Development Progress Y. Han, X.H. Zhao, Z.Q. Bai and B. Wei	438
The Principle and Calculation of Hydraulic Driven Downhole Twin-Screw Pump Z.H. Zhao, Z.L. Li and S.N. Lu	448
Design and Matching Calculation of Hydraulic Helical Axial Multiphase Pump Z.L. Li, S.N. Lu and Z.H. Zhao	454
The Study of the Heat Device in Wind-Magnetic Water Heater X.H. Liu, C.C. Chen, H.D. Yu, G.D. Wei and Z.D. Tian	460

3. Mining Machinery Manufacturing

Resistance Analysis of Belt Conveyor during Horizontal Turning Section X.W. Cheng and H.B. Du	467
SDS Effect on CH₄/N₂/O₂ Hydrate Formation Rate for CMM Separation and Storage Q. Wu, X. Gao and B.Y. Zhang	471

Numerical Simulation of Unsteady Pressure Field for Mammoth Electric Diving Pump C.C. Gao, X.Y. Liu and L.J. Feng	476
Structural Improvement of the Braking System of Electric Locomotive Based on FEM Analysis L.B. Cao, P.G. Yan, Z.G. Ou Yang and C.C. Hu	482
Research on Design and Magnet Assembly Process of Multivariate and Multi-Roll Permanent Magnetic Separator H.G. Jiao, C.L. Shi and R.X. Tian	486
Compensation Experiment Analysis of Adaptive Optical System in Space Laser Communication X.H. Zhai and H.T. Zhang	491
Compensation Effects Analysis of Adaptive Optical System Based on Space Laser Communications H.T. Zhang and X.H. Zhai	495
Simulation Analysis of the Tilted-Jaw Crusher Based on ADAMS P.P. Huang, Q. Lei and K. Wang	499
Design and Research on the New Combining Vibrating Screen N.Q. Guo, H.M. Lou and W.P. Huang	504
Study on XML-Based Apriori Algorithm Applying to Remote Diagnosis System for Hoist J.L. Li and Z.J. Yang	510
Improvement to the Gear Reducer for a 45T Mining Car L.B. Cao, Z.W. Deng and T.G. Xiong	514
Finite Element Analysis of Heavy-Duty Dump Truck Subframe Based on ANSYS H.G. Li, J.P. Si, L. Han and B.W. Zhang	518
Design and Application of Flexible Auxiliary Haulage System for Material Supply in Underground Coal Mine J.C. Chang and Q.H. Chen	524
Study on Optimal Real-Time Feedback Scheduling of Networked Collaborative Design Project under Uncertainty D.T. Liu and D.J. Zhou	529
Study on Topology Optimum Design of Middle Pan Y.H. Qie, B. Liu, X.H. Wang and X.L. Li	534
Coordination and Optimization of Energy Using the Multiple Linear Regression Analysis in a Green Power System X.N. Niu, Y. Sun, C.H. Zhao and S.H. Yu	539
Optimization on Motion Errors of Ultra-Precision Machine Tools Based on Multi-Body System and Monte Carlo Simulation T.J. Li, S.J. Chen and K. Cheng	543
Scroll Profiles Geometric Parameters Optimization Based on CPSO G.F. Xiao and G.P. Liu	550

4. New Energy Equipment and Manufacturing

Design of Non-Contact Balance Head for Grinding Wheel J. Su and B. Gao	557
Design of 4-Axis Reconfigurable CNC Machine Tool for Relief Grinding Sphere Gear Hob Z.Q. Hu and Y.K. Li	561
Multifunction Evaluation System for Coal-Bed Gas Adsorption Isothermal and Pollution of Drilling Fluids W.C. Yu, Q. Hu, X.Q. Lai, X.S. Xiao and W.Q. Liu	565
Study on Degree of Engineering Changes Based on Product Family F.H. Zeng, L.H. Zhou and Z.R. Li	572
Research on the Serialized Design Criterion and Engineering Application Z.H. Lu, Y. Bo and W. Zhang	577
Study of Parameters Optimization of Organic Rankine Cycle (ORC) for Engine Waste Heat Recovery H.G. Zhang, E.H. Wang, M.G. Ouyang and B.Y. Fan	585

Hydraulic Variable Pitch Control and Aerodynamic Load Analysis for Wind Turbine Blades	
Y.G. Kong, H. Gu, J. Wang and Z.X. Wang	590
The Application and the Driver Design of Double Axis Step-Drive Electromotor in the Motorcycle Meter	
S.B. Li	594
Research of Two Stage Single Screw Expander Organic Rankine Cycle System Scheme Based on the Waste Heat Recovery of Diesel Engine's Exhaust Gas	
H.G. Zhang, H. Liang, X. Liu, B. Liu, Y. Chen, Y.T. Wu, W. Wang and K. Yang	600
Design of Adjustment Devices of the Weaving Density for Computerized Knitting Machines	
G.J. Hu, H. Qi and W.Q. Zhao	606
Test Study and Development of High Energy Direct Ignition System for Electronic Control CNG Engine	
Q.P. Chen, H.Y. Shu and C.H. Shi	610
Exploration of Optimizing Processing Technic Based on HS-WEDM	
J.W. Liu and X.Y. Liu	614
CFD Analysis of Evaporator Condition on Ejector Performance in a Solar Energy Air Conditioner	
J.F. Wang, J. Xie, L.R. Tao, Y.H. Wang and X.Y. Yang	618
Study on Mixture Formation of Liquid LPG for a Center Injection DISI Engine	
B.Y. Xu, D.Z. Sun, Y.L. Qi, Y.W. Zheng, H.Y. Tian and S.L. Cai	622
Simulation of Failure Detection Based on Neural Network for No-Ball Mill	
K.S. Li, X.H. Wang and W.M. Wang	627
Study on Characteristics of the Linear Air-Conditioner Compressor at Varied Operating Conditions	
J.F. Xie, X.H. Li and H. Zhang	632
Develop Course of Chinese Laser Fusion	
Z.J. Xie, Q. Liu, X. Xu, L.D. Zhou and H.Y. Chu	637
A System of Selective Non Catalytic Reduction of NO_x for Diesel Engine	
B.Y. Xu, H.Y. Tian, J. Yang, D.Z. Sun and S.L. Cai	643
Research and Modeling for Bi-Directional DC/DC Converter Based on Formation Technology for Lithium Battery	
H.L. Liu and Y.Z. Wang	647
Fabrication of High Concentration Reflected Photovoltaic Module	
C.Y. Hsu, Y.D. Chiang and Y.L. Lin	652
The Design and Application of the Localization Sensor Based on the CCD Image	
J.L. Liu, A.C. Zhang and Y.Y. Yan	656
Finite Element Analysis of the Stress on Cylinder of the Fluidized Bed Reactor for Fast Pyrolysis	
Q.R. Xie, Y. Sun, L.W. Zheng, H.Q. Wang and Z.F. Tong	660

5. Cloud Manufacturing and Extreme Manufacturing

Separate Mapping and Application in Data Share for Network Manufacturing	
J.L. Song	667
Cloud Manufacturing	
F. Tao, Y. Cheng, L. Zhang, Y.L. Luo and L. Ren	672
Study on Fault Tolerance for Virtualization-Based Computer Simulation Systems	
L. Ren, Y.L. Luo and Y.B. Zhang	677
Research of Resource Virtualization Technology Based on Cloud Manufacturing	
C.Q. Li, C.Y. Hu and Y.W. Wang	681
Study on Multi-View Model for Cloud Manufacturing	
Y.L. Luo, L. Zhang, D.J. He, L. Ren and F. Tao	685

6. Bio-Manufacturing

Rapid Preparation of Pure Antibodies against Classical Swine Fever Virus from Pig Serum by Immunoaffinity Chromatography G.Z. Wang, L. Feng, Y. Li and R.Q. Li	691
Surface Roughness Prediction of High Speed Milling Based on Back Propagation Artificial Neural Network J.P. Hu, Y. Li and J.C. Zhang	696
Investigation of Liquid Sensor Using a Dual-Mode Thin Film Bulk Acoustic Resonator (FBAR) Combined with Au/Cr Layers W.T. Chang, Y.C. Chen, R.C. Lin, K.S. Kao, J.M. Jiang, C.H. Yang and C.C. Cheng	700
Study on the SMT Chip Resistor Solder Joint Two-Dimensional Quality of Information Extraction Based on VC++ Y.F. Sun, D.J. Zhou, Q. Zhao and S.H. Zhu	704
Research on CFD of Fluidization of Biomass Waste Fast Pyrolysis Reactor R. Li, L.J. Jing and M.M. He	708
Aviation Equipment Maintenance Job Card Generation Method Based on Lightweight Model J.H. Geng, X.T. Tian and X.L. Jia	714
Shear Mode ZnO Thin Film Applied in FBAR Sensor C.C. Cheng, R.C. Lin, W.T. Chang, Y.C. Chen, K.S. Kao and S.L. Ou	718
Production of Bacterial Cellulose Using Different Carbon Sources by Two-Stage Cultivation Strategy J.H. Lin, Y.J. Lin, J.C. Kuo, T.Y. Chen and W.P. Sung	722
Studying on Auxiliary Gradient Rings for the Collecting Area of Electrospinning D.L. Liu, X.Y. Zhao, H.G. Zhang, Y.Y. Liu and Q.X. Hu	726

7. Enterprise Informationization

Solving the TSP by Simulated Annealing Genetic Algorithm Based on Google Maps JavaScript API X.B. He and Y.W. Mo	733
Dynamic Evaluation Model of Enterprise Informatization Level and its Application W.Y. Qian, Y.G. Dang and C.Y. Lin	738
A Product Structure Management Method Based on Ajax N.Y. Lu, F.Y. Liu and T. Shay	744
Decision Support Technology of Enterprise Production Management Based on Data Mart J.T. Chang, Y.Y. Qiu and S. Li	750
Product Design for PRO/E-Based Master Part F. Feng, G.J. Hu and H. Pan	755
Strategy of the Information Construction in Modern Tourism Enterprise Y.R. Zhang	759
Process-Oriented Software Development Based on HPN Business Process Model G.X. Yun and J. Zhang	763
Parametric Design of Foamed Sheet Die Z.L. Chen, G.J. Si, C.Y. Wang and D.L. Wu	768
Model of Collaborative Knowledge Innovation with Distributor Participation in Supply Chain X.M. Zhang, N.L. Shen and X.P. Mao	773
Research on Knowledge Navigation Supporting Rapid Design of Complex Product Y.J. Ji, K. Long and G.N. Qi	779
PRO/E Based Parametric Design of Spur Gears F. Feng, H. Pan and G.J. Hu	790
The Study of Job Shop Scheduling Based on Genetic Algorithm J.X. Xiong, J.P. Zhao and H.N. Tu	795
Research on Generating Interference-Free Tool Path Based on Triangular Bézier Surface X.C. Kang, D.Z. Sun, Y. Shi and Y.W. Sun	799
VD Vacuum Furnace Shell's Buckling Numerical Analysis Based on Ansys Z. Gao, X.D. Liu and Q.M. Huang	805

Development of Intelligent CAD Design System for Straw Crusher L.Q. Chen, L. Lu, J.Q. Zhang and J.X. Wang	810
Reverse Engineering in the Design of a Plastic Part C.H. Sun, Z. Wei and L.L. Yang	814
Influence of Radial Position of Medium Size High Voltage Asynchronous Motor Stator Ventilation Channel Peri-Axle Terminal on Fluid Flow Pattern J.B. Wen and H.Y. Yan	818
Study on Trustworthy Interaction-Chain of Human-Information System in Distributed Cooperative Manufacturing Environment L. Zhang, S.P. Yi and R. Zhao	824
Study on Crankshaft Design Based on CAD/CAE C.G. Xia, J.K. Su and M.H. Pan	830
Using Logic Synthesis and Circuit Reasoning for Equivalence Checking Q.R. Fan, F. Pan and X.D. Duan	836
Design of a CAM System for End Mills Based on Solid Modeling Z.H. You, F. Tang, S.Z. Li, X.F. Yue and X.H. Wang	841
Registration and Integration of Automobile-Bodies Scattered Point Cloud Based on K-D Tree Y. Zhou, W.B. Zhang and F.R. Du	846
Design of Data Acquisition System in MES Based on RFID X.J. Li, P. Wang and X. Huang	852
Complex Products Remote Collaborative Design and Implementation of its Flexible Flow X.X. Wu and Q.F. Gao	857
Building of Mechanical Components Ontology in the Networked and Collaborative Environment Q.L. Zeng, L. Qin and C.L. Wang	863
Information Collaboration Model for Modular Product Based on SM L.W. Song, Y.J. Ji and G.N. Qi	867
Resource Modeling of Manufacturing Process Optimization under Dynamic Environment M. Lv, X.D. Sun, G. Wang and Y. Che	878

8. Integrated Manufacturing System

Research on the In-Process Model Based on CIMS C.X. Fan and W.Z. Wu	885
Study of Process Planning Based on Machining Feature J.P. Tian, C.H. Fu, A.H. Tang and C.F. Mi	889
A Novel Extremity Balance System-Design and Manufacturing J.W. Chen, H.S. Hsieh, Y.H. Chen, S.J. Wu and L.A. Chiu	895
Study on the Structured Process Operation Language Based-On Predicate Logic S.C. Zeng, R. Wei, X.P. Liao and F.H. Zhou	904
Study of the Knowledge-Based Integrated Equipment Management System for Process Enterprise Y. Yu, X. Ji, D. Wang, F. Zhao and J.H. Tang	912
Domain-Based Trust Evaluation Strategy for Manufacturing Grid Z.H. Ge, T.S. Li and L. Li	920
A System for 3D Digital Assembly Process Planning and Simulation in Airplane Manufacturing Enterprises Y. Li, L. Dong, J.F. Yu and K.F. Zhang	926
Generation, Analysis of Switched Mode Dc to Dc Converters by the Use of Converters Cells H.L. Liu, R.B. Zhang and P. Yang	931
Research on Integration of Rapid Manufacturing Grid J.S. Shan and R.L. Hu	936
Design and Implementation of Machine Vision Automatic Laser Scanning System H.F. Yan, J. Shao and J.M. Chen	940
Research on SVG-Based Web-To-VDP S.W. Yang, Z. Liu and Z.J. Mao	944

9. Quality and Safety of Products

Interface Stress Analysis of the Bending Cylinder Containing Inclusion X.Y. Tang	951
Fault Diagnosis System for Large-Scale Equipments Based on Hybrid Reasoning M. Chen, R. Zhang and Y.L. Li	956
An Assessment Method of Structure Safety for General Overhead Traveling Crane Based on Bayesian Network G.N. Xu and W.X. Guo	962
Research of the Calculation Method Structure System Fuzzy Reliability Based on the Fault Tree N. Li and B.W. Song	968
The Application of Inertial Measurement Unit in Inertia Parameter Identification B. Wang, Z.X. Hou, X.Z. Gao and S.Q. Shan	974
Material Selection of Casing in Gas Well Containing CO₂ and H₂S X.Z. Yan, B. Shao, X.J. Yang and T.T. Wang	982
Statistical Process Control Based on Kalman Filter in Manufacturing Process P. Wang, D.H. Zhang, S. Li, M.W. Wang and B. Chen	986
Coal Mine Safety Monitoring Based on Improved ID3 Algorithm Y.Q. Zhao, Z.C. Wang, C.Z. Jiang, W.L. Hao and G.Q. Wang	990
The Evaluation in Weapon Operational Effectiveness Base on Fuzzy Analytic Hierarchy Process Y.P. Zhao and N. Li	995

10. Products Processing and Storage

Task Scheduling of Product Development Process Based on Complex Features of Web X.J. Li and Y.P. Yuan	1003
The Effect of Ultra-High Pressure on the Functional Property and Conformation of Whey Protein Isolated H.P. Liu, Y.H. Wei and Y.W. Xu	1008
The Hydraulic Jack-Up System Design on the Ocean Petroleum Platform 161 - the First Self-Installing Product Platforms in China D.T. Li, H.Q. Tian, Y.P. Wang and Y.Y. Huang	1015
The Oil Absorption of Soy Protein Isolate in High Temperature and Humidity Storage B.Y. Sun and Y.G. Shi	1019
Effect of Ampicillin as Bacteriostats on the Performance of Phosphate Solubilizing <i>Rhizobium. Meliloti</i> Inoculants J.F. Li, S.Q. Zhang, S.L. Shi, P.H. Huo and L.Y. Chen	1023
Technical Economic Analysis of Remanufacturing of Large-Scale Food Processing Equipments D.Y. Li and W. Li	1033

11. Production and Operation Management

Cost Optimization of Scheduling Based on Simulation J. Li and P.A. Du	1039
Optimization Design of Biscuit Formula Based on the Grey System W. Li and D.Y. Li	1044
Study on Operation Management of Producing Service Company for Manufacturing Enterprise L. Han and R. Du	1050
Single-Machine Scheduling to Minimize Absolute Value in Maximum Lateness with Deteriorating Jobs J.B. Wang, D.L. Yang and C.J. Hsu	1054

Risks and Risk Management in Chinese Iron and Steel Enterprises J.L. Zhang	1061
A Production Planning Model for Make-To-Order Companies with Capacity Constraint H.L. Gao, B. Dan and Y.G. Jing	1066
Using a Hybrid Genetic Algorithm to Minimize the Number of Tardy Jobs in the Flow Shop J.J. Wu	1070
Optimize the Transit Vehicle Routing for the Emergency Evacuation D.A. Chen, W.T. Xu and W. Zhang	1075
Molding and Optimization of Workflow Based on Stochastic Timed Petri Nets in Customized Supply Chain Management W.J. Xu and J. Yao	1082
An Systematic Modeling and Simulation Study on WIP Optimization in Semiconductor Assembly and Test Factory Y.T. Ni, J.M. Li, W. He and J. Yao	1086
Based on Adjacent Cross-Coupling of Multi-Motor Synchronous Drive P. Zhang, J.H. Zhang, D.S. He and B. Zhang	1093
Supply Chain Revenue Coordination Mechanism Based on Game and Lead Time Compression with 3PL Intervention Q. Lv, J.Z. Huo and J.J. Gao	1098
Simulation-Based Genetic Algorithm for Cross-Docking Center Operation Optimization under Supply Disruptions Y.F. Wu	1103
Game Analysis of Selecting Manufacturing Service Modes for Manufacturers X.M. Zhang, J. Tong, M. Zhao and J.R. Guo	1107
Research on Path Optimization of Automated Warehouse Based on Ant Colony Algorithm H.P. Li, Z.F. Fang and Y. Wang	1112
The Empirical Study on Relationship between Design-Manufacturing Integration and Manufacturing Performance of Chinese Manufacturing Enterprises S. Chen and Y.Z. Tian	1116
Research on Resource Optimization of Block Erection Procedure Based on PSO Y.G. Zhong, L.J. Hang and W.M. Shi	1121
Development Simulator for Operation of Kanban System B.S. Oh and J. Park	1127
Balance Analysis and Improvement of Flywheel Production Line Q.H. Jia, Y. Xiao, Y.J. Gong and K.Q. Zhou	1131
Online Due Date Strategy on Mass Customization R.Y. Pang, D.C. Liu and Q. Li	1135

12. Industrial Design

Holistic Design Concept in the Application of Wine Packaging H. Zhao, X.M. Yu and S.F. Bao	1143
A Form Generation System Based on Design Thinking Patterns T.W. Chang and S.W.W. Tseng	1147
Component Variant Design Method Integrating Dimension and Tolerance B. Kuang, L.Z. Xiao, F.Y. Liu and Y.H. Sun	1151
Study on Application of Grey System Theory in Fatigue Span Design of Machine Tool Axles J. Xu and C.X. Wang	1156
Misoperation Study on Samsung VP101 Digital Video Camcorder B. Cheng	1161
Tensegrity Form-Finding Using Finite Particle Method X. Xu, Y. Yu, Y.Z. Luo and Y.B. Shen	1166
Research on Evaluation and Decision-Making Model of Product Design Scheme Based on TFN-AHP-GRA X.A. Yang, Q. Deng, G.L. Sun and B.B. Wang	1170
Form Generation Model of Two Thinking Paths S.W.W. Tseng, T.W. Chang and J.H. Lin	1177

Fault-Tolerant Permanent Magnet Synchronous Linear Motor P. Liao, S.Y. Ma, J.F. Mao, G.Q. Wu and A.D. Jiang	1181
The Design of Automatic Conveying System for Hot Rolling Bearing-Steel-Ball Blanks Y.D. Zhou, Q. Wang and S.Y. Ma	1188
Taking the Pulse of Subsea Trees Design towards Deepwater Application K. Ding, H.W. Zhu, J.Y. Zhang, X.L. Kong and C. Wang	1192
Torque Ripple Suppression of Brushless DC Motors with Non-Ideal Back EMF for EPS Applications X.F. Zhang, X.W. Ji and F. Gao	1198

13. Engineering Optimization

Uncertainty Quantification of a Flapping Airfoil with a Stochastic Velocity Deviation Based on a Surrogate Model L.Y. Zhao and X.Q. Zhang	1209
The Optimal Design of Work Location for a RRR 3-DoF Manipulator S.X. Tian and S.Z. Wang	1213
Optimum Design of Wheeled Loader's Steering Rubber Buffer Seat Based on ANSYS H.Q. Wang, X. Xiao and X.R. Luo	1217
Energy-Based Optimum Pattern Development for Garment Industry J.J. Fang and Y. Ding	1223
Group Decision Making of Naval Ship Principal Dimensions Based on PSO Algorithm Y.H. Hou, S. Huang, Y.L. Hu, X.Y. Meng, W.Q. Wang and C. Wang	1233
The Application of Fuzzy Modeling and PSO in Spaces Allocation of Naval Ship Y.L. Hu, S. Huang, Y.H. Hou, X.Y. Meng, W.Q. Wang and C. Wang	1238
Study on Measurement Method of Spark Energy for Automotive Engine X.H. Liu, D.J. Wang and F.S. Liu	1243
The Elementary Exploration on Teaching Reform of Training Center of Engineering Y.P. Ma, G.F. Yuan and Y.S. Yao	1248
Equipment Selection Optimization System of Draglines and it's Applications in Opencast Coalmine in China X.R. Mei	1253
Multi-Objective Optimization Method Based on WSLs Evolutionary Game Model and its Application in Mechanism Design R. Li, N.G. Xie and R. Meng	1258
Study on the Match of Ignition Coil with Hydrogen Internal Combustion Engine X.H. Liu, Z.Q. Fan and F.J. Lu	1263
The Coal Plough Equipment Gray Connection Decision Model Base on Entropy Value Law Q. Zhang and Q.S. Song	1268
A Closed-Form Approach for Optimum Tolerance Allocation of Assemblies with General Tolerance-Cost Function K.M. Cheng and J.C. Tsai	1272
Frequency Optimal Design Method and Application S.Y. Bi and X.P. Liang	1279
The Aerodynamic Characteristics of a Microbus X.N. Qi, J. Meng and Y.Q. Liu	1284
Improved Genetic Algorithms Based Optimal Design of The Shuangji River Aqueduct X.L. Bai, W. Yu, D.F. Wang and Y.Y. Fan	1288
On Optimal Inventory Model for Obsolescence Perishable Products under Unpermitted-Stockout X.L. Xie	1292
Aerodynamic Analysis of Pickup Truck X.N. Qi, J. Meng and Y.Q. Liu	1296
Influence of Non-Technical Factors on the Construction of Tunnels J.Q. Ma	1300
Study on Lightweight of the Engine Piston Based on Topology Optimization F.R. Du and Z. Tao	1308

Reliability-Based Robust Optimization Design for Lattice Tower Structure X. Jiang, H.J. Li, B.F. Gao and X. Liang	1312
The Gradual Optimization Automatic Mathematic in the Job-Shop Environment J.S. Li, A.M. Wang and C.T. Tang	1317
Study on Reinforcement Scheme of Foundation Underpinning Technology for Accident Buildings in Loess Region Y.D. Hu and Y. Wang	1321

14. Product Design and Development

Investigation into the Cutting Technology of the Interior Helical Surface of Metallic Screw Pump Stator Q.X. Ding, H.Q. Cui, X.Z. Lou, X.Z. Dong, Z. Liu and K.L. Hui	1327
The Research on the Cutting Property and Structural Optimization on Tooth of Oil and Gas Pipeline Tapping Cutter Q.X. Ding, X.M. Liu, X.Z. Lou, Z.M. Han, S.M. Zhang, Y.C. Tian and K.L. Hui	1335
A Hybrid Approach for Part Geometry Optimization through Engineering Simulation L.H. Qiao, A. Zia and N. Cai	1342
Development of Micro-Cutting Force Sensor Based on Principle of Resistance Strain Y.F. Yang, B.S. Kou, H.W. Ma and H. Chen	1348
Structure Analysis of Electron Gun Deflection Coil Based on ProE and ANSYS H.L. Liu, R.B. Zhang and Y.P. Huang	1352
Modular Code, Combination and Database Management of NC Spiral Bevel Gear Machine Tools Q. Li, D.P. Li, T.Y. Wang, M. Hu, X.H. Xiao and B. Geng	1356
Study on Work Form and Architecture of Collaborative Product Development System R.S. Liu, X.S. Wang and Y.X. Qin	1363
Design and Implementation of a Linear IC Based Low Cost Digital Tachometer for Laboratory and Industrial Application S.M. Ferdous, M. Rokonzaman, E.G. Ovy and M.A. Hoque	1368
Design and Development of New Auto-Detecting Platform for Hoists of Suspended Access Platform J. Sun, Y.H. Wu and K. Zhang	1373
Modeling and Solving Product Configuration Problems Using Petri Net D. Yang	1379
Formulation of Dextromethorphan Oral Disintegrating Tablet Using Ion Exchange Resin W. Samprasit, P. Opanasopit, P. Akkaramongkolporn, T. Ngawhirunpat, K. Wongsermsin and S. Panomsuk	1384
The Design of Jumping Robot K.S. Wang, J. Mi, W. Zhang, Y.X. Xu and D. Wang	1388
Re-Creation Process Model of Conceptual Design H.B. Miao	1392
Construction of 7YGS-45 Type Orchard Transport Automatic Control Test Platform S.J. Li, J.J. Xing, Y.L. Zhang, X.J. Li and Q.Z. Fan	1396
The System Model of the Bulldozer Machine Based on the Theory of Design Space Integration and its Experimental Verification A.L. Wang, B.N. Yue, H. Liu, P.J. Zhou and B.F. Gong	1402
Hydraulic Support Development Based on Virtual Prototype Collaborative Development Platform C.L. Wang, Q.L. Zeng, Z.H. Liu and X.W. Wu	1408
A Study on Data Flow Model of Web to Print Z. Liu, C.X. Liu and S.W. Yang	1412
Structure Design of Multi-Purpose Elevation Mechanism K.S. Wang and D. Wang	1416
Research on the Development of High-Quality Hemp Fiber Y.C. Ji and F.Q. Jiang	1420
Analysis Method for Commonality of Module and Part in Modular Product Family S.F. Wang, L. Hou, H.L. Wang and W.G. Lin	1425

Development of Reciprocating Air-Cool Oilless Compressors Series Product Y.F. Zhu	1429
The Design of Movable Landslide Physical Model Testing Frame D.P. Zhao, S.M. Wang, Y.Z. Tan and X.L. Liu	1433
Factors Affecting the Design of Product Innovation T. Wang, F. Zhao and H. Deng	1439
Analysis of Energy Factor Effectiveness in Air-Conditioning Refrigeration System Y. Wang, G.F. Liu, S.X. Song and P. He	1443
Innovative Evolution Process Model of Product Platform Based on Evolutionary Design Q.L. Wang, L. Hou and H.L. Wang	1447
Study on the Intelligent Creel of Advanced Carpet Loom J.Z. Guo, J.W. Sun, F.H. Zhang and X.J. Yang	1451
Fuzzy Comprehensive Evaluation on Battery Electric Vehicle Dynamics and Energy Consumption Economy M. Chen and L.X. Guo	1456
Variant Design Method of Assembly Consisting of Different Types of Parts X.S. Xu, D. Li and M.L. Sun	1460
Pneumatic Press Based on Toggle-Lever Force Amplifier J.E. Wang, Z.L. Cui and K.M. Zhong	1464
The Designing and Manufacture of Rear Mounted Fluid Coupling Transmissions for Deceleration(YOC_{HJ}1000/1500/700) W.Z. Shao, M.Y. Zhang and L. Zhang	1469
Modern Machinery Products Adaptability Vague Comprehensive Evaluation Z.J. Xin and H. Guo	1475
Research and Design of Transmission Rate Adaptive Control in Public Video Monitoring System L.H. Mei and W.B. Jin	1481
Equipment Design of the Ship Sewage Treatment X.C. Zhang and J.P. Xu	1486
Study on Grinding Methods of Different Shape Turning Tool Rake Face H.L. Hou and N. He	1492
Intelligent Mapping of Semi-Structured Customer Needs for Web-Based Product Customization Y.G. Jing, B. Dan, S. Peng and L.F. Guo	1496
Investigation on Slider Structure Deformation and Crowning System of Large-Scale Press Brake H. Li, Q.K. Liu, L.Y. Qian and Y. Han	1500
A Multi-Objective Leverage Planning Method for Flexible Platform Using Quantitative Indices Z.K. Li, X.H. Jiang and Q. Jiao	1504
Study on Technology of Noncircular NC Turning Based on Active Disturbance Rejection Control H. Cao, S.Y. Li and X.P. Yao	1508
Research on New Hybrid Active Power Filter J.J. Peng, X.P. Fan and G. Li	1512
A New Roller Conveyor Driven by Linear Motor H.S. Zhao and Y.Z. Wu	1517
Research and Application of Intelligent CAD Technology in R and D and Management of the Electric Equipment H.G. Zhou, W.C. Tang, X.W. Jing and S. Han	1521

15. Quality Monitoring and Control of Manufacturing Process

Application of Six Sigma Method in Quality Improvement of Hard Alloy Gear Circular Saw Blades H.Z. Zhao, L.L. Meng and C.G. Lu	1529
--	------

The Design Technology of PDC Bit in The High Hardness and Abrasiveness Formation of Xishanyao	
Z.L. Wei, H.P. Lin, J.J. Du and Y.Y. Pan	1535
The Features of the Integrated Multilayer-Wrapped High Pressure Vessel and its Fabrication Quality being Inspected by Hydrostatic Test	
P.Y. Song, Y. Yong, W. Zhong, W. Yu, M.F. Hu and X.Q. Zhu	1539
Constant-Universal Joint of Double Cross-Cross Ring Based on Spatial Linkage	
X. Zhang, Z.L. Chen and H. Gao	1544
A Diehole Arranging Optimization Strategy in Multi-Hole Die Design for Profile Product Extrusion	
J.B. Zhang, J.W. Wang and Z.Y. Duan	1548
Application of Quality Early Warning System Base on Web Form Design	
L.B. Sun, S.S. Guo, Y.B. Li, J. Guo and S.Q. Wu	1553
The Research and Application of Drilling Fluids Technology in Zhoushen Well X1	
Z.L. Wei and L. Ge	1558
Research on Real Tooth Surface Deviation Correction of Spiral Bevel Gear Based on Truncated Singular Value Decomposition	
S.H. Chen, H.Z. Yan and S.H. He	1562
Three Dimensional Parametric Design of the Die Channel for Plastic Extrusion Based on SolidWorks	
H. Gao, Z.L. Chen and X. Zhang	1569
Research on PCB Electroplating Current Monitoring System Based on a Wireless Sensor Network	
X.F. Li and H.X. Xian	1573
Theoretical Calculation of Negative Skin Friction for Pile Foundation in Layered Soil	
S.P. Chen, W.J. Yao and S.Q. Zhu	1577
On-Machine Illumination Technique in Industry Machine Vision	
Z.R. Wang and Y.H. Wu	1582
Design of the Proportional Feeding System of Raw Mill	
B.Y. Luo, F. Du and Y.M. Mo	1586
Study on Polarization Distribution of Polarization Encoder in Oblique Incidence	
M.Z. Zhou, Y.R. Chen, Q. Zhao and Y. Xin	1590
Nonlinear Method for Load Transfer Model of Super-Long Pile in Layered Soil	
S.P. Chen, W.J. Yao and S.Q. Zhu	1596
Nonlinear Finite Element Analysis of Super-Long Pile and Soil Interaction in Soft Soil	
S.P. Chen, W.J. Yao and S.Q. Zhu	1601
Adaptive Fuzzy Control for Ink Key of Offset Printing Machine	
J.S. Kang, H.Y. Chu and L.G. Cai	1606
Morphology and Formation Mechanism of Martensite in Steels with Different Carbon Content	
Y.P. Ji, Z.C. Liu and H.P. Ren	1612
Automated Visual Inspection of Surface Defects on Hot-Rolled Plate	
Q. Song	1619
3D Finite Element Analysis for Magnetic Flux Leakage Testing	
Q. Song	1623
Quality Prediction Model Based on PCA-BP Neural Network for Tobacco Leaves Redrying Process	
J.K. Yin, C.H. Chen, J.M. Li, F. Zhang and J. Yao	1627
Operational and Control Decision Making in Aluminium Smelters	
Y.S. Gao, M.P. Taylor, J.J. Chen and M.J. Hautus	1632
A Calculation Method for Compliance Uncertainty of GPS Standard-Chain	
J.X. Wang, X.Q. Jiang and P. Wang	1642
Effect of Tidal Fences on the Stress and Deformation of Bridge Structure	
Z.D. Zhang, Z.X. Cheng, Z.J. Sun and Z.B. Tang	1649
Thermal Deformation Errors Compensation System of Machine Tools	
S. Li, X.H. Yao and J.Z. Fu	1657
Simulation and Analysis of Natural Ventilation of Residential Building's Arrangement	
F. Tao and J. Li	1662

Process Parameter Experiments on Vacuum Casting Using a Silicone Rubber Mold for ABS Plastic Parts	
D.Y. Chang and C.S. Deng	1668
Multi-Dimensional Vibrating Screen Design and Motion Analysis	
C.J. Wang, L.Z. Ma and Y.M. Li	1672
3D Model Retrieval Based on Fuzzy Weighted Shape Distributions	
Z.Q. Chen, K.S. Zou, W.H. Ip and C.Y. Chan	1678
DEWMA Control Chart for the Coefficient of Variation	
E.P. Hong, H.W. Kang and C.W. Kang	1682

16 Metallurgy Engineering

Recovery of Niobium from Baogang Tailings by Carbochlorination	
T. Zhao, H.T. Lin, B.W. Li and D.Q. Cang	1691
Griffith-II Type Crack Generation and Chip Formation Simulation in Vibration Turning Based on Prandtl-Reuss Flow Principle	
L.Z. Gu, Q. Hong and B. Cheng	1699
Theoretical Analysis and Experiment on Slag Detection System Based on Eddy Current Effect in Continuous Casting	
S.F. Huo, S.S. Cheng and X.P. Song	1704
Kinematics Characteristic Analysis and Structural Parameter Optimization of Twist Beam Rear Suspension	
A.H. Tang, J.P. Tian and X.X. Liu	1710
Kinetics of Reduction Roasting of Hematite to Magnetite in Crude Niobium Concentrate under Microwave Irradiation	
J. Li, L. Wang, B.W. Li and B.W. Zhang	1714
Feedstock Characterization for Micro Powder Injection Molding (μPIM)	
H.P. Li and M. Norhamidi	1721
Leaching Behaviour of Metals from a Sphalerite Concentrate in Sulfuric Acid-Oxygen System	
C.X. Li, C. Wei, H.S. Xu, J.Q. Liao, Z.G. Deng and G. Fan	1725
Study on the Continuous Casting Production of 823 Steel	
C.W. Du, L.Y. Li, D. Wu, H.B. Wang and Q.H. Liang	1732
Study on Preparation Process of Zinc Ferrite	
S.J. Ma, G.F. Wang, J.L. Yang, S.J. Que, L.Q. Tang and J.P. Feng	1736
A NeuroEndocrine-Inspired Manufacturing System Using the Potential Field Concept	
K. Zheng, D.B. Tang and W.B. Gu	1741
Optimal Control for Quality Indices of Heat Furnace	
Y.W. Chen and T.Y. Chai	1748
Study on the Leaching of LiCoO_2 in Low H_2SO_4 Concentration Solutions	
Y.Q. Yang, C.Y. Wang, D.F. Li, F. Yin, Y.Q. Chen and X.W. Jie	1752
Effects of Sintering Temperature on the Properties of Cu-Co-Based Alloys Matrix	
Y. Lu, H.F. Dong and W.S. Li	1757
Experimental Research of New Technology on the Precise Reduction of Micron-Sized Iron Oxide	
S.Q. Li, J.T. Gao, P.Y. Chen, P. Shen, Y.T. Zhang, R.Z. Liu and Y.G. Wang	1763
Study on Indium Leaching from Indium-Poor Zinc Residue Enhanced by Ultrasonic Treatment	
J.H. Yao and X.H. Li	1770
Innovative Process of Leaching of Nickel Supported Activated Carbon in Ammonium Sulfate	
Z.B. Zhang, W.K. Wang and J.H. Peng	1774
Research on High-Temperature Properties of Typical Iron Ores Used in China and its Blending Optimization	
S.L. Wu, O. Dauter, Y.M. Dai, J. Xu and H. Chen	1780
Densification of Vanadium Nitride by Microwave-Assisted Carbothermal Nitridation	
H.J. Pan, Z.B. Zhang, J.H. Peng, L.B. Zhang and W. Li	1787

Research and Application on Burden Movement Model for Bell-Less Top of BF C.L. Fu, S.L. Wu, J. Xu, C.S. Liu and M.Y. Kou	1793
Circumferential Distribution Characteristics of Airflow in Blast Furnace Hot Blast Systems C.S. Liu, S.L. Wu, J. Xu, C.L. Fu and M.Y. Kou	1798
Research on Influence Law of Fuel Structure for Low-FeO Sintering M.L. Bian, S.L. Wu and Q.F. Wang	1802
New Evaluation Index of Blast Furnace Raceway Activity X.Q. Liu, S.L. Wu, C.S. Liu, J. Xu, C.L. Fu and M.Y. Kou	1806
Effect of Mechanical Activation on Extracting Indium from Neutral Leach Residue of Zinc Calcine Y.J. Zhang, X.H. Li, L.P. Pan and Y.S. Wei	1810
Study on Process of Microwave Magnetizing Roast for Low-Grade Hematite J. Li, B.W. Li, B.W. Zhang and L. Wang	1816
Study on the Sorption of Rhenium by Anion Exchange Resin H.Z. Ma, X.Z. Lan and Y.N. Wang	1821
Pattern Search Method and Artificial Neural Network Prediction of Double Ellipsoid Heat Source of Submerged Arc Welding P.L. Li and H. Lu	1825

17. Industrial Robotics and Automation

Analysis and Experiments on Pulse Vibrating Suction Method for Wall Climbing Robot X.Y. Zhao, R. Liu, K. Wang and J.H. He	1837
Flocking Task Research for Multiple Mobile Robots Based on Evolutionary Game Model Y. Ye, N.G. Xie, Y.W. Cen and Q.Y. Liu	1845
Orientation Workspace Analysis of a Novel 3SPS+1PS Symmetrical Parallel Manipulator Based on Unit Quaternion J.L. Yu, G. Cheng, S. Zhang and D.K. Zhang	1849
Consensus Algorithm for Swarm Robotics Cooperative Control B. Lei and L.C. Zeng	1854
Design and Research of a New Portable Barrel-Scrubbing Robot W.J. Tao, K. Liao and H.T. Feng	1858
Analysis, Design and Simulation of the Biomimetically Facial Material on the Humanoid Robot C.K. Wang	1863
Pose Accuracy Analysis of Robot Manipulators Based on Kinematics J.Y. Zhang, C. Zhao and D.W. Zhang	1867
Trajectory Planning of Robotic Orthodontic Wires Bending Based on Finite Point Extension Method Y.D. Zhang and J.X. Jiang	1873
Analysis and Implementation of Coulomb's Frictional Material on the Wheeled Platform of Moving Robots C.K. Wang	1878
The Optimize Design of the Intelligent Electric Mini-Car Y.Z. Zhang and Q.M. Zhao	1882
Research and Design of Range Positioning System Based on Ultrasonic Sensor for Intelligent Mobile Robot J. Han and R.L. Chang	1886
Developing and Research on Motor Driving System of Wheeled Mobile Robot R.L. Chang and J. Han	1891
Force Control of a Distributed-Parameter Flexible Arm via Parallel Compensation L.Y. Liu and H.C. Lin	1898
Analysis and Design of Lower-Mobility Parallel Mechanism of Non-Symmetrical Based on Variable Topology Theory R.J. Cui, Z.H. Guo, Z.X. Yin and S.S. Zhu	1907
Condition of Intelligentize Realization of Robots Y.Y. Liu, X.Y. Zhang and H.Y. Zhang	1913

Design of Automatic Buildup Welding Machine and its Application in Train Hook Repair H.X. Shi, J.H. Zhu, L.M. Song, X.P. Zou and J. Han	1919
Research on Welding Robot Path Planning Using Ant Colony Optimization J.H. Wang, R.H. Xiao and Y.L. Ma	1926
Trajectory Tracking of Omni-Directional Wheeled Opera Robot Based on Wavelet P.Y. Liu, Y.Y. He, J. Li, Q.Y. Meng and S. Guo	1930
Design of the System in Asynchronous Multiplexing at Low Rate Y.Z. Zhang and X.Q. Zhang	1935
Modeling and Analysis of the Steering Resistance Moment in Small Tracked Robot Y. Ou, S.J. Huang, H.T. Feng and W.J. Tao	1939
Research on Control Method of a Novel Type of Excavator Based on Multi Degree-Of-Freedom Controllable Mechanism G.W. Cai, D.C. Wu, Y.C. Pan, X.Y. Xu and Z. Zhang	1949
Based on Least Square Method for Spray Partition of Complex Curved Surface Y. Zeng, J. Gong and T. Sun	1955
A Microcontroller Based Controller Circuit for the Motion Control of an Articulated Robot with Three Degrees of Freedom E.G. Ovy, M. Rokonzaman, S.M. Ferdous and N.A. Chowdhury	1960
Smooth Track-Keeping and Real Time Obstacle Detection Algorithm and its PID Controller Implementation for an Automated Wheeled Line Following Robot M. Rokonzaman, S.M. Ferdous, E.G. Ovy and M.A. Hoque	1966
Design and Implementation of an Articulated Robotic Arm for Precise Positioning E.G. Ovy, S.M. Ferdous, M. Rokonzaman and N.A. Chowdhury	1972
Dynamic Cooperative Manipulating Pattern Generation for Mobile Humanoid Robot Using Waist Moment Compensation T.J. Zhao	1978

18. Measure Control Technologies and Intelligent Systems

The Experimental Study on Wireless Short Distance System for Downhole Data Transmission H.X. Wang, H. Lou, L. Li, N.H. Hou, J. Zhang and Y.X. Liu	1985
Research and Implementation of an Expert System for Fault Diagnosis of Fan Based on Knowledge Rule L. Wang, T.Z. Sui, Y. Song, H.X. Zhao and B.R. Zhuang	1989
The Remote Monitoring System for Fault Diagnosis Using ActiveX Control Technique H.L. Shi, Y.M. Song, J.W. Xiang, W.W. Yue and C. Liao	1993
The Research of Speckle Technique in Deformation Measurement Fields Z.X. Chen, J. Liang and C. Guo	1998
Smith Predictor Based on Predicting Induced-Delay S.D. Li, Y. Chen and C.X. Liu	2003
Design of an Intelligent Vehicle System for Storehouse Management Based on Image Processing and RFID Technologies W.D. Li, G.W. Chen, J. Chen and X.J. Zhang	2007
A Novel Approach for PC-Based Test and Measurement Applications Development with Autonomous Sensors J.B. Zhao, T.L. Shi, X.P. Yan and C.Q. Yuan	2014
Research of the SMT Product Character Segmentation Based on Contour Feature H.H. Zhao, D.J. Zhou and Y.M. Xu	2019
Design of Measure Control System for Thermal Defects Based on ZigBee J.H. Xiong, S.Q. Xu and C. Yun	2023
Researching on Fuzzy Control System of Jigging Discharge Based on PLC Y. Chen	2028
Study on Adaptive Fuzzy-PID Grouting Pressure Stabilization Control System C. Wei and X. Meng	2033
Research on Simulation and Experiment for Piezoelectric Smart Structures R. Yang, X.S. Liu and H.Y. Ren	2039

The Appraisal of Velcro's Surface Quality Based on Machine Vision Systems D.X. Zhao and Q. Lin	2045
A Layer-Driven Trouble Hunting in Satellite-Networks of Cyberspace J. Yin, Q.M. Li and J. Hou	2049
Underwater Intrusion Surveillance System Based on Underwater Sensor Networks: Architecture, System Design and Research Challenge J.J. Zheng, Z.H. Liu, L. Yin, S. Ye and Y. Wang	2053
Research on the Spatial Error Distribution Model of Flexible Coordinate Measuring Machines Based on Support Vector Regression D.T. Zheng, Y.T. Fei, Y.G. Hu and R.C. Yang	2058
Hardware-in-the-Loop Simulation System in the Development of Temperature Controller of Plastic Extruder J.L. Xu, G.K. Zuo and J.H. Chen	2063
Infinite AdaBoost and its Application on Fault Diagnosis for Analog Circuits H.X. Wang, C. Liu and Y.Q. Sun	2070
Performance Analysis of W Phase Detector in Galileo Signal Receiver M. Li	2075
The Research on the Model of a Precision Magnetic Stage System Y. Zhang, H.Z. Sun and H. Zhou	2079
A Fuzzy Control Method in ACC of the Constant Interval Mode L.G. Zhao and D.J. Chen	2083
Study of Predictive Control in Industrial Networked Control System F. He, X. Li and Q. Wang	2087
Construction and Realization of Networked Virtual Test System Based on LabVIEW G.X. Cai	2091
The Application of FPGA and DSP Techniques in Intelligent Wattmeter H.R. Li, L.J. Pang, X.F. Zhang, G. Deng and Y.W. Tong	2096
Analysis and Modeling of the Harmonic Compensation Errors Based on PWM Converters X.D. Wang and B.C. Gao	2101
Optimal Design of the Thickness of the Multi-Layer Homogeneous Absorption Plates Based on the Max Absorption Coefficient of the Automotive Body C.Y. Zhu	2108
Ziegler-Nichols Based Intelligent Fuzzy PID Controller Design of a SPM System with Parameters Variation J.M. Lin and P.K. Chang	2113
Dirty-Face Game Analysis on Mixed Traffic Flow at Unsignalized Intersection L. Wang, N.G. Xie and R. Meng	2119
Research of Channel Dismatch Errors in Parallel AD Acquisition System Based on FPGA X.L. Shao, W. Yang, Z.Y. Wang and W.D. Zhang	2126
Application of Non-Negative Tensor Factorization in Intelligent Fault Diagnosis of Gearboxes S. Peng, F.Y. Xu, M.P. Jia and J.Z. Hu	2132
Energy Saving Control System for Central Air-Conditioning Based on Terminal Temperature Measuring and Frequency Conversion Control Technology H.Y. Zhou, X.J. Chen, Z.H. Chen and M.W. Tong	2144
Research Based on Barycenter Identification about Array Haptic System Pressure and Temperature Information Y. Bai, Y.H. Hou, Z.W. Chen and Y.J. Song	2154
Research on the Absorption Characteristic of Three-Layer Microperforate Plate of the Automotive Body C.Y. Zhu	2160

19. Transmission and Control of Fluid

Research on Automatic Booster Valve of Powered Props of Powered Supports C.Q. Jia, W. Li and L. Yu	2169
Modeling and Simulation of Pneumatic Impactor for Tubing Plugging W. Sun, G.X. Meng, Q. Ye and W.H. Xie	2174

Investigation of the Unsteady Flow for the Supersonic Jet Element Y. Xu, G.Q. Zhang and F. Wang	2178
Intelligent Design of Mechanism Kinematic Chains by Advanced Optimal Methods M. Zhang, N.B. Liao, C. Zhou and X. Tao	2182
New Method of Improving Intake Port Flow Characteristics in a Four-Valve Engine S.Q. Zhang, Z.Q. Li, X.L. Wei and H.G. Wang	2186
The Optimal Design on Connection Order of Network in Hydraulic Manifold Block J.J. Zhang, J.S. Wang, J.Y. Wang, G. Liu and J. Wang	2190
Speed Control of Fluid Coupling Based on Fuzzy Control Theory W.Z. Shao, Y.H. Li, Y. Wu and L. Wang	2195
Study on the Spring-Piston External Mesh Gear Pump with Low Flow Fluctuation J.Z. Zhang, K.K. Li, M. Gao and T.Z. Zhu	2200
Analysis on the Shifting Performance of the Hydraulic System of a Transmission for Construction Machinery Y.M. Li, Z.H. Liu, D. Wang and Y. Zhang	2206
Fluent Based Numerical Analysis of Eliminating Ultra-Limit Gas in Upper Corner by Using Rotary Jet Fan J.Y. Chen, X.Q. Fan and Z. Liu	2212
Symmetrical Beauty: Pneumatic Press Based on Quadratic Orthogonal Force Amplifier Driven by Double-Face Rack-Gear Mechanism K.M. Zhong, X. Li and W.F. Zhang	2216
Two-Point Floating Clamping Device Based on Fixed Cylinder with Double-Piston and Toggle-Lever Force Amplifier G.J. Si, K.M. Zhong and J.P. Jia	2220
The NC Mechanism of Reciprocating Rectilinear Movement at High Frequency Based on Two Symmetrical Cranks M.D. Wang, K.M. Zhong and Z. Chen	2224
Research on Control Strategy for Energy-Saving Optimization Algorithm of the Hydraulic Hybrid Vehicle Y.L. Chen, S.N. Liu, T. Shang, J.L. Liu, Y.K. Zhang and D.T. Xie	2229
Research on a New Type of Device of Laminar Water Draining with No External Force Q. Li, F.B. Li and X.Y. Su	2238
Flow Distribution Prediction of Gas-Solid Two-Phase Flow in Y-Shaped Branch Pipeline G.B. Duan, Z.M. Liu and W.X. Wu	2242
Pressure Drop of Y-Shaped Branch Pipe in Gas-Solids Flow Z.M. Liu, G.B. Duan and G.L. Chen	2246
Symmetric Beauty: Double-Position Numerical Control Press Based on Lever-Toggle Force Amplifying Mechanism Driven by Linear Servo Motor F. Wu, M.D. Wang and K.M. Zhong	2250
Green Manufacturing: a Pumpless Mechanical-Hydraulic Clamping Device Based on Wormgear and Crank-Slider Mechanism Y.Z. Bai, G.J. Si, X. Li and K.M. Zhong	2254
Study on Process Control Characteristics of 22MN Fast Forging Hydraulic Press J. Yao and X.D. Kong	2258
Research on the Flows of Backspin Movement in Table Tennis Y.F. Chen, T.H. Fang, C.C. Huang, C.H. Liu and W.H. Hsieh	2263
Numerical DPM Model for Two-Phase Flow in Aero-Engine Bearing Chamber R.S. Xu, J.J. Wang, W. Xu and L.B. Liu	2267

20. Mechanical Control and Information Processing Technology

Control System of Bellows Welding Equipment Based on Motion Controller Z.W. Ren, Z.Y. Duan, W.H. Zhao and Y. Zhang	2273
A New Time Series Regression Method Based on Support Vector Machine Plus and Genetic Algorithm W. Sun, G.X. Meng, Q. Ye, J.Z. Zhang and L.W. Zhang	2277
Research on Pneumatic Controlling Mechanism of Flying Splicer of Web-Fed Offset Presses C.W. Chai, J.F. Cai and S.Q. Wu	2281

Research and Analysis on the Multi-Point Piezoelectric Vibratory Feeder of Driving Mode W.F. Wu, L.H. Zhang, H.M. Yin, F. Han, G. Wang, S.P. Shi and Y.Q. Zhang	2286
Mechatronic Cooperative Design and Simulation of a Multi-Axis Bar Tacking Machine X.H. Xie, Q. Sun, C.C. Zhao, C. Ma and R.X. Du	2291
A Depth-Setting TUV Control System Based on RS-485 Network G.H. Xu, K. Yu and X. Shen	2295
A Fault Detecting System of Intelligent Detection and Diagnosis R.P. Shao, Y.L. Li and W.T. Hu	2300
Research on the Monitoring Technique of Non-Contact Running Status of Cooling Tower Fan Blades J.P. Chen and W. Dong	2307
Design and Implementation of a Novel Communication Interface for Eddy Current Displacement Sensor H.Y. Tsai, J.S. Chen and Y.Y. Hsu	2312
Study and Design of CAN Bus Node Based on MC912D60A Microcontroller in Automobile J.F. Chen and L.Q. Zhao	2317
Remote Monitoring Technology on Oil of Large Equipment X.S. Zhang and J.H. Cui	2322
SINUMERIK 802D Applied in the Transformation of Profiling Machine P.M. Dong, W.B. Liu, T.Q. Wang and X.L. Dang	2326
Wavelet-Contourlet Retrieval Using Energy and Kurtosis Features X.W. Chen, Z.Q. Ma and L.W. Liu	2330
The Confined Chord Error Algorithm for High Precision Machining Parametric Surface Z.Q. Zhang, W.J. Wang, Z. Jian and T.Y. Wang	2334
Electrical Control System Designing Based on Logic Relation Chart G.Z. Cheng and Y.B. Cheng	2338
Design of DC Motor Control System Based on Clonal Selection Algorithm P.B. Zhao and Y.Y. Shi	2343
The Design of Wireless Communication System in Oil Log Spot P.M. Dong, X.L. Dang, T.Q. Wang, G.Z. Li, J.L. Zhang, D.H. Xu and Z.G. Yao	2349
Design and Realization of Remote Monitoring System for Automatic Forced Fitting Production Line J.H. Cui, X.S. Zhang and J.H. Zhu	2354
Slider Position Servo Control of the Double Toggle Mechanical Press Directly Driven by Transverse Flux Machine J. Xie, S.D. Zhao, Z.H. Sha and J.T. Liang	2360
Concise Robust Control for Ship Roll Motion Using Active Fins W. Guan and X.K. Zhang	2366
Design of GA-Based Control for Electrical Servo Drive K.H. Su and F.H. Hsiao	2375
Research on Heavy Rail Pre-Bending Vehicle Control Technology Based on Fuzzy Neural Network Z.J. Xu and G.F. Yin	2379
Self-Sensing Control Research on a Linear Compressor L.Q. Zhang, G.H. Peng, H.M. Zou and C.Q. Tian	2385

21. Embedded System

Research on the Control and Key Technology for Parallel Operation System of Mobile Generator L.B. Mao, W.J. Wang and J. Yang	2393
Embedded Control Design for Insulin Pump W.G. Ali and G. Nagib	2399
Fuzzy ADRC Controller Design for PMSM Speed Regulation System G. Su	2405
Research of CNC System for Ultrasonic Vibration Internal Grinding Based on Embedded Technology B.F. Wang, Z. Yin and O. Xie	2409

Design of the Control Circuit Based on FPGA for the Underwater Trash Detection System G.K. Zhao and Q. Zhang	2414
Strain Transfer From the Host Structure to Optical Fiber Sensor S.C. Her and C.Y. Tsai	2419
Linear Interpolation Control of Numerical Control Machine Tools and its Realization Based on Multi-Axis Motion Control Card X.M. Shi, Y. Dai and W. Liu	2423
Distributed Battery Management System in Battery Electric Vehicle Y. Liao, J.H. Huang and Q. Zeng	2427
A Study on the Method of Rust Prevention of High-Strength Bolts for the Bridge Parrel L.C. Wang, J. Chen, S.L. Li and X.D. Wang	2431
The Design of Embedded Control System in Knee-Joint Rehabilitation Trainer Based on S3C2440 X. Li, Z.B. Zhang and X. Hong	2435

22. Other Related Topics

An Empirical Study on the Coordinated Development of Chinese Manufacturing and Logistics Industry S.W. Ji, H.L. Xia, J.M. Meng and X.Y. Han	2443
Performance Test and Analysis of Clothing Materials Y. Yu and X.M. Qian	2447
Study on the Mixer Used for the Thermal Flow-Reversal Reactor Y.Q. Liu, X.C. Chen, R.X. Liu, Z.Q. Gao and J.T. Wang	2451
Based on Balance Scorecard to Make Teacher Performance Appraisal in College L.L. Zhao and Z.P. Wu	2456
Analysis on Thermal-Mechanics Coupling of Milling Insert Based on Principle of Cellular Automation B.J. Sun and G.Y. Tan	2460
Building Energy Consumption Prediction of Housing Industry in China Based on Hybrid Models Y. Xie	2466
Fuzzy Synthetic Evaluation of Power Quality Based on Combination Weighting Method Y.S. Huang and L.M. Yuan	2470
Thermal Fatigue and Fracture Mechanics Analysis of Aluminium Alloy W.X. Zhang, G.D. Gao and G.Y. Mu	2476
Short-Term Load Combination Forecast Based on Rough Set and Support Vector Machine Y.S. Huang and L.M. Yuan	2481
The Digital Ink-Jet Printing Properties of Cashmere Treated by Low-Temperature Plasma J.Y. Tian and R.D. Pang	2488
Research on the Ink Penetration Depth into Offset Paper Y.G. Yang and Q.Z. Gao	2492
Application of Neural Network and Particle Swarm Optimization Algorithm in Slope Runoff and Sediment Yield Calculation J. Huang, P.T. Wu, X.N. Zhao and J. Wang	2496
Research on the Rice Leaf Morphological Formation and its Visualization H.W. Liu, Y.Y. Liang and H. Zhang	2504
Inventory Control Policy of Service Parts under the Background of Service-Embedded Manufacturing P.P. Wang, X.G. Ming, D. Zhang, D. Li and Z.Y. Wu	2509
Optimization of Fermentation Process of Pear Vinegar by Response Surface Methodology H. Gao, G.F. Xu, Y.Y. Fan, H.J. Nan and S.F. Fu	2513
A Low Dimensional Embedding Method for Combining Clusterings S. Xu, T. Zhou and H.L. Yu	2517
Study on Expanded Food Quality Improving Based on Six Sigma G.Y. Mu, L. Li, W.X. Zhang and G.D. Gao	2521
Optical Fiber Temperature Sensor Based on Fluorescence Mechanism S.T. Wang, Y.Y. Cui and L. Huang	2526

Digital Simulation of Bridge Wind Fields Based on Wavelet Method T.H. Jiang and J.R. Peng	2532
Some Improvements of Genetic Programming in Data Fitting H. Jie, J.Q. Feng and D.L. Chen	2536
Study on Heavy Metal Adsorption in Coastal Sediment of the Yellow River Estuary Q.Q. Wu and J.G. Ren	2540
Structure Design of a New Kind of Rotary Refrigeration Compressor J. Li, X.P. Ou Yang and L.J. Zhang	2544
Microwave Synthesis of Schiff-Base Complexes and Organic Tin C.Y. Deng, Z.Y. Lin, M.L. Yang and B.J. Xu	2550
Study on Bore Cores Evaluation Systems of Asphalt Pavement Y. Zhao and H. Ma	2554
Research on Oil-Water Interfacial Properties Effect of Polymer / Surfactant Binary Flooding System W.X. Wu and Z.Q. Yu	2558
Study on Physical Simulation Experiments of Different Chemical Displacement Systems W.X. Wu, D.H. Mu and Q.D. Liu	2562
Finite Element Analysis Technique and its Application in Numerical Simulation of Knitted Fabric C.Y. Li and R. Wang	2567
Characteristics of Supersonic Projectile Shock Wave Y.C. Wu, H. Chang and T.T. Tsung	2571
Trend Analysis of the Slow-Speed and Heavy-Load Equipment with Acoustic Emission M. Li, J.H. Yang and J.W. Xu	2578
Ultrasound-Assisted Acceleration of Soybean Oil Epoxidation and the Interfacial Tension Study L.J. Han, L. Li and G.Q. Liu	2583
Study on Soil Consolidation Coefficient on CPTU Model Test Y.C. Tang, G.T. Meng and Q.F. Mao	2587
Geometrical-Optics Approximation for the Simulation of Light Scattering by Single-Nuclear Cell M. Bu and Y.W. Wang	2593
Experimental Research on Superlong Deep-Hole Drilling Processing Technology for Steel of 4145H Drill Collar Z.F. Liu and R.L. Li	2597
The Effect of Coefficient of Thermal Conductivity of Fabric-Layer on Human Body Temperature Fields J. Li	2601
Study on Industrial Waste Sites Monitoring Based on Remote Sensing Technology W.H. Zhao and S. Liu	2607
Corrosion Performance of Hot Dip Galvanized Steel J. Zhang and Z.H. Yu	2611
Effect of Different Packaging Films on Senescence of Pleurotus Nebrodensis Auto MAP X.H. Li, T. Xue, Y.Y. Li and L. Chen	2615
Optimum Conditions of Pretreatment in Producing Bioethanol from Wheat Straw L. Cui, Z. Liu and L.F. Hui	2619
Preparation and Performance of MoB/CoCr Coatings by LPPS on 20G Boiler Steel X. Chen, R.Y. Zhang and F. Li	2623
Preparation and Second Harmonic Generation of CdS Doped Lead Silicate Glasses H. Liu, X.T. Wang, B.G. Zhang, Z.F. Wang and X.J. Zhao	2630
Study on Application and Issues of Bag Dedusters in Coal-Fired Power Plants H.C. Wang, D.H. Jiang and Q. Wang	2634
The Optimum Design of Large-Scale Inner-Tower Truss-Supporting Structure Based on Finite Element Analysis X.J. Wang, D.H. Li and Z.H. Gao	2645
The Regenerative Experiment of Activated Alumina Granules D.J. Wu, D. Li, L.R. Weng, W.J. Zheng and X.Y. Qu	2649

Study on Lateral Pressure of Bulk Materials in Silos C.B. Chen	2653
The Flow Field Analysis and Optimization of Diagonal Flow Fan Based on CFD X.J. Wang, R. Chen and Y. Zhou	2657
Parameter Optimization and System Design of the Welding Power Supply for Resistance-Butt Welding of Nuclear Fuel Rod F.Q. Chen, Z.W. Lin and G.W. Liang	2661
Research and Analysis of the Effects of Building Height on Wind Vibration Sensation in High-Rise Steel Structure H. Zhang, S.G. Chu and Y.H. Liu	2667
Study and Application of Bridge Structure Finite Element Model Updating Based on Static-Load Testing M.Y. Deng and F. Li	2672
Fractal Characteristics of Soil Particle-Size Distributions under Different Landform and Land-Use Types X.Y. Song and H.Y. Li	2679
Daily Load Forecasting Based on Combination Forecasting Techniques C. Gao, H.J. Ma and P.N. Gao	2685
Design and Implementation of Single-Stage Boost Converter in Wind Power System Y.Y. Hsu and C.W. Lai	2690
Synthesis and Properties of Novel Carboxylate Gemini Surfactant J. Li, Q.M. Chen, R.M. Zhang and W. Tong	2695
Experimental Study of Hematite Melting Reduction under High Temperature Y.M. Nie, F.S. Niu and S.X. Liu	2700
Analysis of an Energy-Efficiency Supervision and Diagnostic System for Large Public Buildings in Ji Nan D. Li, Z. Li and Y.M. Cao	2704
Research on Stability of a 2 DOF Articulated Vehicle W. Wei, X.H. Liu and Y.L. Chen	2709
Numerical Simulation of Die Casting for Semi-Solid Aluminium Alloy and its Mould Research Y. Huang, Y. Huang, Q. Wu, X.M. Du and C.Z. Wang	2717
Numeberical Simulation of a New Enhanced Heat Transfer Burener X.F. Lu, D. Liu and Y.Q. Li	2721
Cooling Process after HTST Orange Juice Sterilization Optimization Based on CFD J.F. Wang, J. Xie, L.R. Tao, Y.H. Wang and X.Y. Yang	2727
Biofilms and Safety Design Criteria for Food Equipments Y.J. Li, B. Du, N.W. Li, J. Liang and G.M. Yang	2731
Optimization of Turbine Blade's Cathodes Feeding Routes in Three-Electrode Feeding Electrochemical Machining L. Wang	2737
Cold-Model Study on Fluidized-Bed Photo-Oxidation Reactor for Shenfu Coal Y.T. Zhang, G.H. Wang, W. Zhao and A.N. Zhou	2741
Symmetric Beauty: Multi-Point Press Based on Parallel and Synchronous Toggle Mechanism Driven by Pneumatic Muscle P.L. Qin, M.D. Wang and K.M. Zhong	2745
Process Mineralogy and Concentrating of Hematite-Limonite Ore in Southern China S.X. Liu, L.L. Shen and J.X. Zhang	2749
Study on Monitoring Damage about Material of Blade in Wind Turbine Based on Acoustic Emission X.G. Zhao, C.Z. Chen, B. Zhou and X.H. Liu	2753
Application of Materials on Foil Thrust Bearings for Micro Turbines Q. Zhou, Y. Hou and R.G. Chen	2759
Wind Tunnel Test Investigation on Sectional Models of Chaotianmen Yangtze River Bridge C.Q. Wang, Z.L. Li and Z.T. Yan	2763
Study on the Properties of Boron-Containing Ores/Epoxy Composites for Slow Neutron Shielding Z.F. Li, X.X. Xue, T. Jiang, H. Yang and M. Zhou	2767

Physical and Electrical Properties of Lead-Free (Na_{0.5}K_{0.5})NbO₃-(Bi_{0.5}Na_{0.5})TiO₃ Ceramics C.H. Wang	2772
Study on Order-Flexibility Method H.Y. Song, Z.M. Liu and L.F. Liang	2776
Numerical Analysis of Cavitation Flow during Vertical Water Exit of Underwater Vehicles J.Z. Zhang, T.Q. You, Q.K. He, Y.J. Wei and C. Wang	2780
Research on Flow Mechanism of Materials and Micro-State of Distortion Area in Closed Extruding Fine Blanking Process L. Lv, G.S. Ning and M.M. Chen	2785
The Preliminary Investigation of Low Grade Zinc Oxide Ore J.L. Yang, S.J. Ma, G.F. Wang, J.P. Feng, W. Mo and X.J. Su	2789
Research on TFP of Enterprises in China's Manufacturing Industry Based on Malmquist Index Approach S.C. Li, S. Gai and D. Yuan	2793
Study on Livestock and Poultry Farming Wastewater Treatment Using a Hybrid Baffled Reactor L.J. Shi, L.T. Ban, H.F. Liu, J.C. Hao and W.Y. Zhang	2797
Driving Force Testing of Lift Mechanism for Green Energy Furniture T.L. Chen, T.T. Tsung, L.Y. Yang and H. Chang	2803
Simulation of Wind Effects Embracing a Complex Shape Super High-Rise Steel TV Tower Using CFD Y.Y. Tan and C.X. Li	2807
Catalytic Hydrothermal Depolymerization Technology and Kinetics of DGEBA/EDA Epoxy Resin J.Q. Zhang, W.Y. Deng, J.H. Zu, H.B. Ding and P. Cai	2814
Ultrasound-Enhanced Coagulation Pilot Plant for Micro-Polluted Water of Huaihe River D.J. Wu, C.W. Luo, W.J. Zheng, X.D. Zhai and J.F. Liu	2820
Preparation and Properties of Graft Copolymer of Phenols and Starch with HRP Catalysis S.H. Lv, G. Rui, J.P. Duan, Y.F. Ma and R.J. Gao	2825
Preparation and Properties of Modified Starch Tannage S.H. Lv, X.L. Yan, R.J. Gao and J.P. Duan	2829
Research on Direction of Wet-Chemical Model of Loess Y. Wang and Y.D. Hu	2833
Contract Model of Knowledge Trading between Tourism Enterprises Y.R. Zhang	2837
Two-Position and Highly-Efficient Clamping Device Based on Lever-Toggle Force Amplifier Driven by Pneumatic Muscle L. Lu, M.D. Wang and K.M. Zhong	2841
Novel and Saving Energy Lifting Permanent Magnet Design N. Ding, D.T. Zhang and Y.Z. Pei	2846
Neutral Deinking Process Optimization and Comparison with Alkaline Deinking of Old Newsprint S.J. Wang, F.G. Kong, J.C. Chen and G.H. Yang	2850
Electrochemical Delignification Mediated with Violic Acid and Subsequent Bleaching of Poplar Kraft Pulp F.G. Kong, C.F. Li, S.J. Wang and S.Y. Fu	2854
Carboxylation Modification of Fiber Reclaimed from Old Newspapers and its Effects on Properties of the Reinforced Polylactic Acids Composites Y.Q. Wu, X.G. Li, H. Li and F. Cheng	2858
Texture Profile of Gelatin and Tea Polyphenol Mixed Gels A.N. Wang, L.G. Wu, Y.D. Sun, Y.Y. Zhang, X.Y. Xu, X.L. Li, J. Wang, C. Wang, Q.Q. Fu and L.L. Jia	2862
Study on the Blend Film Prepared by Chitosan and Gelatin A.N. Wang, L.G. Wu, X.L. Li, Y.D. Sun, J. Wang, S.W. Wang, A.X. Jia, C. Wang, Y.Y. Zhang, Q.Q. Fu and X.Y. Xu	2866
Enhancement of Gas Physical Absorption in Gas-Liquid-Liquid System W.X. Li, G.R. Xu, Z.G. Zhang and Z.L. Ji	2870

The Influence of Oolong Tea Polyphenol and Black Tea Polyphenol on Gelatin Gels Texture A.N. Wang, L.G. Wu, X.L. Li, Y.D. Sun, S.W. Wang, A.X. Jia, X.Y. Xu, Y.Y. Zhang, J. Wang, C. Wang and Q.Q. Fu	2875
Study on the Blend Film Prepared by Alginate and Gelatin A.N. Wang, L.G. Wu, Y.D. Sun, X.L. Li, X.Y. Xu, C. Wang, J. Wang, Q.Q. Fu and Y.Y. Zhang	2879
Impermeability of Wet-Sieving Fine Aggregate Concrete Made from Ordinary Concrete X.K. Li, S. Zhao, L. Sun and S.B. Zhao	2883
Experiment of Carbonization for Wet-Sieving Fine Aggregate Concrete Made from Ordinary Concrete S.B. Zhao, N. Liang, X.L. Ma and S. Yang	2887
Research on Pipe-Soil Displacement Transfer Coefficient for Buried Pipeline X.Z. Zhang, A.H. Han and Z.L. Wu	2891
Fluid-Structural Coupling Analysis of Composite Material Blades for the Offshore Wind Power Generator G.C. Tsai, W.S. Li, Y.Y. Chang and J.T. Tseng	2896
Compression Test on Cold-Formed Steel Built-Up Back-to-Back Channels Stub Columns C.H.T. Ting and H.H. Lau	2900
Effect of Electromagnetic Field on the Solidification Structure of HMn084 Brass B.M. Li, H.T. Zhang and J.Z. Cui	2904
Numerical Study on Influence of Joint Characters on Rock Mechanical Parameters Y.F. Feng, T.H. Yang, H. Wei, H.G. Gao and J.H. Wei	2909
Measurement and Evaluation of Angularity Error Based on Coordinate Rotation Y.H. Sun, J. Zhang, J.D. Bao, R.S. Lai and M.F. Huang	2913
Comprehensive Evaluation for Undergraduate Teaching Management Level in Institutions of Higher Education W. Sun and Y. Li	2917
Tolerance Modeling and Optimization of XY-Table for LED Die Bonder Based on Multi-Body Systems M.F. Huang, J.T. Huang, X. Cheng, J. Zhang and H. Jing	2922
A Study on Universal Design Product Development Combined with Value Engineering Approach S. Park and J.I. Park	2927
Research on Fracture of FRP Reinforced Concrete Beams Y.F. Feng, T.H. Yang, H. Wei, Y.F. Gu and H.J. Wang	2931
Study on Steam Extraction Technology Assisted by Microwave of Anise Star Oil from the Fruit of <i>Illicium verum</i> Hook. f. G.E. Yang, G.W. Wang, Z.P. Wu and X.Z. Li	2935
Study of Methods for Minimizing Construction Delays: Evidences from a Developing Country T. Pourrostam and A. Ismail	2939

1. CAD/CAM/CAE

Hot-Stamping Process Simulation and Optimize Research for Collision Beam of Automobile Door

Chao Wang^{1, a}, Bin Zhu^{1, b}, Yisheng Zhang^{1, c}, Jie Shi^{2, d}, Han Dong^{2, e}

¹State Key Laboratory of Material Processing and Die and Mould Technology, Huazhong University of Science and Technology, Wuhan 430074, China

²Central Iron and Steel Research Institute, National Eng. Research Center of Advanced Steel Technology, Beijing, 100081, China

^awangchao8321@163.com, ^bzhubin26@gmail.com, ^czhangys@mail.hust.edu.cn, ^dshijie@nercast.com, ^edonghan@nercast.com

Keywords: Advanced High-Strength Steel; Hot-Stamping; Finite Element; Simulation; Coupled Thermo-Mechanical; Collision Beam

Abstract: Hot-stamping molding for ultra-high-strength steel have some similarities with traditional cold-stamping molding in the aspects of molding process and die design. But due to the effect of temperature variation of blank, hot-stamping have some differences in ultra-high-strength products design, material selection and forming process design. Some special forming defects, such as local thinning, cracking and wrinkling, could appear in hot-stamping process due to these differences. In order to obtain uniform phase structure and get high-quality products, it is very important to be able to predict and control the blank temperature and the consistence of blank cooling rate. The thermo-mechanical characteristics of hot-stamping are studied with the material of ADVANCE1500 (22SiMnTiB). Based on the results of simulations and experiments, conclusion are drawn that the complexity of the product and the blank which contacts with die asynchronously causes the uneven distribution of the blank temperature. This is the key factor that leads to the poor mobility of the blank material and local thinning, cracking, wrinkling and other defects in forming process. Proper clearance between punch and die can reduce the probability of defects which could contribute to the improvement of hot-stamping process.

Introduction

In the modern automotive industry, the use of ultrahigh-strength steels in structural and safety components is rapidly increasing in order to meet the steadily rising requirement for vehicle safety and reducing environmental pollution in the automotive industry^[1]. However, traditional cold stamping process will bring on a large amount of residual stress retaining in shaped component which may result in severe spring-back after cold-stamping. Moreover, in traditional cold stamping process, great forming force is generated and complex shapes can hardly be formed^[2].

In hot stamping process, the blanks are completely austenitized at temperature of between 900°C and 950°C for about four to ten minutes inside a continuous-feed furnace and subsequently transferred to an internally cooled die set via a transfer unit. At high temperature, the material has excellent formability, so that complex shapes can be formed in a single stroke. The blanks are

stamped and cooled down under pressure for a specific amount of time according to the sheet thickness after drawing depth is reached. During this period the shaped part is cooled in the closed die set which is internally cooled at a cooling speed, and completing martensitic transformation. Finally, the part leaves the hot-stamping about 150 °C and with high mechanical properties: an ultimate tensile strength of 1500MPa or much higher and little spring-back ^[3-5]. schematic of hot-stamping process is shown in Fig.1 and finite element model of Collision beam is shown in Fig.2.

In this paper, ADVANCE1500 is selected as AHSS, and the finite element analysis is used to research the result and get the solution which leads to the defects of collision beam during the process of hot-stamping.

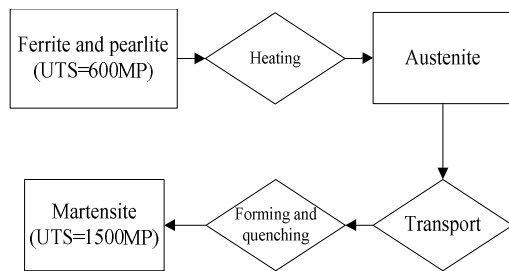


Figure 1 Schematic of hot-stamping process

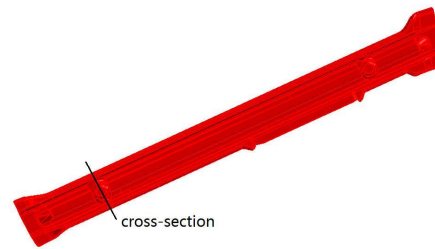


Figure 2 Finite element model of Collision beam

Hot-stamping FE model of collision beam

Definitions of material properties for hot-stamping process. The shaped parts of the collision beam sizing 1300mm × 300mm have low drawing depth which made up of several complex surfaces. This could bring a great deal of difficulty in forming blanks into collision beam components. So hot stamping process is selected which could overcome most difficulty. The thickness of the blank is 1.8mm. The gap between punch and die at the end of quenching is 2mm. The coefficient of friction between mould and blank is 0.3. The drawing depth of experiment and simulation is 35mm.

ADVANCE-1500 is selected as experimental materials. The chemical analysis of the ADVANCE- 1500 steel is given in Table 1. In order to get reliable modeling and numerical simulation of hot-stamping process, the determination of the thermo-mechanical material properties is one consideration. Besides, it is more important to consider the relationship between stress and strain by temperature. This relationship was estimated by hot tensile tests on GLEEBLE mechanical system and the constitution equation has been generated according this relationship. The thermal conductivity between blank and mould change with the pressure and clearance between blank and die^[6]. The other material properties are given in Table1 to Table 4.

$$\sigma = K\varepsilon^m \quad (1)$$

where:

$$m = 0.3515(Z/A)^{0.0434}, K = 353.58(Z/A)^{0.094}, Z = A[\ln \sinh(a\sigma_\varphi)], A = 1.27E20, a = 0.00373$$

Table 1 Chemical analysis of ADVANCE1500

C	Si	Mn	Ti	B	Mo	S	p
0.2	0.85	1.64	0.022	0.001	0.01	0.001	0.005

Table 2 Coefficients of heat conduction at different temperatures

Temperature, °C	20	100	200	400	600	800
Heat conduction, W/(m·K)	50.1	46.1	44.8	39.8	34.3	26.4

Table 3 Young's modulus at different temperature

Temperature, °C	-20	20	100	150	200	300	400	450	475	600	850
Young's modulus, GPa	208	205	203	200	196	186	170	158	151	6.5	5.9

Table 4 Coefficients of thermal expansion at different temperatures^[7]

Temperature, °C	100	200	300	400	850	900	950
Thermal expansion, /°C×10-5	1.93	1.97	2.12	2.17	2.62	2.78	3.08

Table 5 Specific heats at different temperatures

Temperature, °C	50	100	400	850	900
Specific heat, J/(kg·K)	465	471	479	987	1019

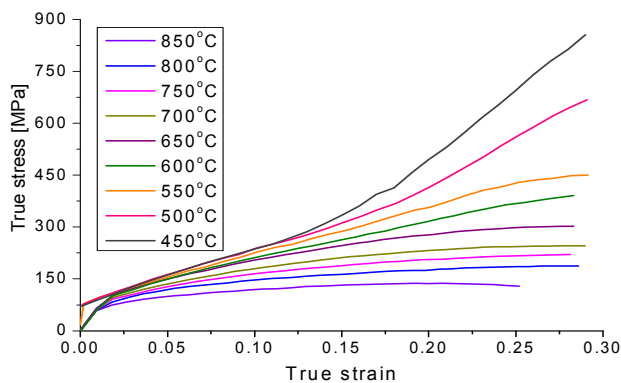


Figure 3 Influence of the temperature on flow curve

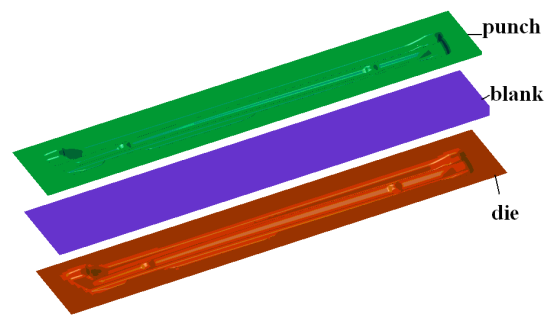


Figure 4 Schematic illustration of tools and blank used within hot-stamping process

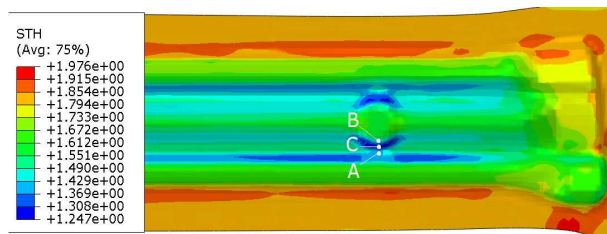


Figure 5 Thickness distribution at the end of holding stage

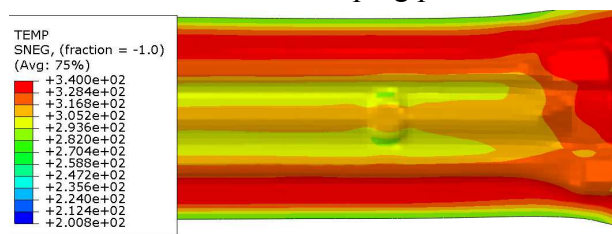


Figure 6 Temperature distribution at the end of holding stage

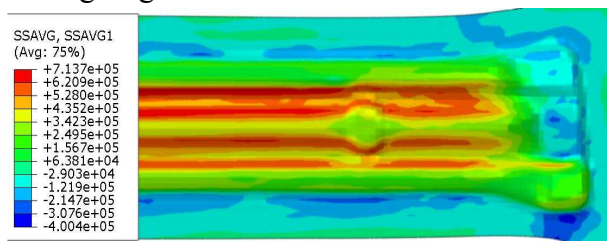


Figure 7 Mises stress distribution at the end of holding stage



Figure 8 Experiment result of hot-stamping of collision beam

Definitions of analysis steps. In hot stamping process, excessive BHF could rapidly cool down the blank and hold back the material flow which would bring on risks of component cracking. So in this hot-stamping experiments and simulations, it is unnecessary to use the model that does not have BHF (Figure 4) though this would acquire a component of severe wrinkling in

some areas. The hot-stamping of collision beam may divide into following three stages: a. Heating and transportation.(at this stage, the blank is heated up to 850°C - 900°C in oven and fully austenitic, and is delivered to the mould by mechanical equipment). b. Forming stage (at this stage, punch move down and the blank is adequately shaped). c. Holding stage (at this stage, the shaped component is hold in the mould for about 6 seconds, cools rapidly and quenches simultaneously). Figure 5 shows the displacement-time curve in direction of punch movement at forming stage and holding stage.

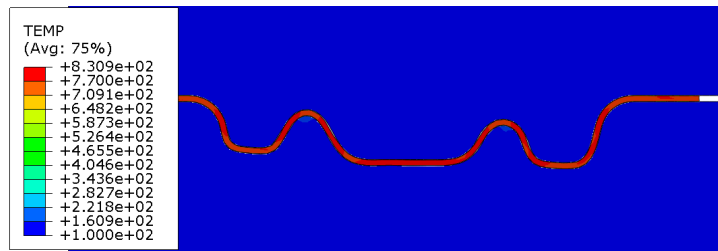
Result and Analysis

Analysis of formability. According to the results of simulation (Figure 6), the shaped component appears obvious thinning areas at the corner of protruding zones (point out in Figure 6), the thickness of the thinnest area has decline 30% and reach 1.247mm. Figure 5 shows the distribution of shaped component temperature at the end of holding stage. It can be seen that the protruding zones (point A and point B in Figure 5) of the shaped component has good contact with mould and cools down more rapidly than other zones. Some of the protruding zones have cooled to 200°C below. Figure 7 shows the distribution of Mises stress. The thinnest area in Figure 5 (point C in Figure 5) also have greatest Mises stress, reaching up to 713.8MPa (Figure6-c). So the places near point C (in Figure 5) have greater possibility of cracking than other places. Figure 8 shows the shaped component in experiment. It can be seen that the component also appears local cracking in the same zone compared with the simulation results.

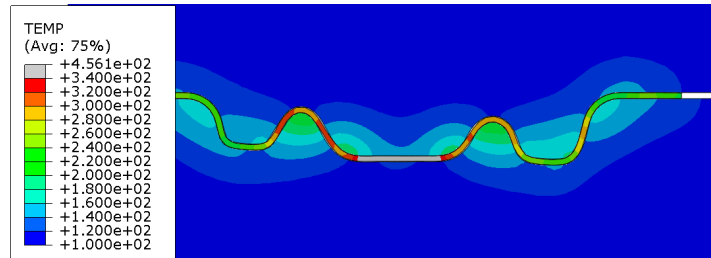
Analysis of Contact. In order to clearly observe the contacts between blank and mould, the internal temperature distribution of the mould and shaped component, stress and strain distribution during the forming stage and holding stage, a cross-section simulation has been performed. The position of the cross-section has been pointed out in Figure 2. This cross-section is across the cracking areas, the results of which can contribute to explaining the reason of cracking.

Figure 9 shows the simulation results of cross-section temperature distribution at the end of forming stage and holding stage (points A, B, C in Figure 9 point out the same spots on the blank compared with the points A, B, C in Figure 6). It can be seen that the protruding zones (point A and B in Figure 9) of the blank which have intimate contact with mould have good thermal conductivity condition and cool down more rapidly than the areas nearby (point C). In addition, point A and point B take priority over point C of contacting with mould first and material near point A and B flow slowly due to the effect of friction. This would result in reducing the thickness of point C. Thus, a gap could occur between blank and mould (shown in Figure 9-c). So the areas near point C would have bad contact with the mould and have higher temperature than the areas nearby. Moreover, the fact that pre-defined gap between blank and mould is larger than the thickness of blank is another key reason for the appearance of local gap between blank and mould after forming.

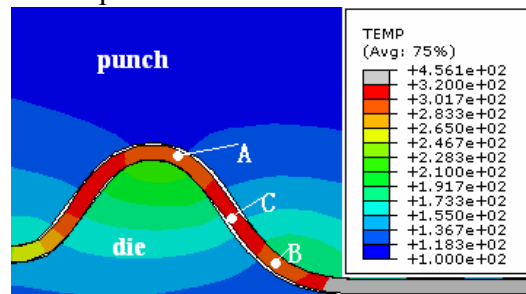
Figure 10 shows the cross-section stress distribution at the end of holding stage. It can be seen that the areas near the point C have great amount of residual stress. As shown in Figure 9-a, at the end of forming stage, the temperature of most part of the blank is still above the recrystallization temperature. So the residual stress can reduce during this period of time. As the temperature drops, thermal expansion coefficients of the blank significantly reduced and the blank shrinks, while protruding zones (like point A and B in Figure 9-c) in good contact with mould would hinder the process of shrinkage. Thus, the part between protruding zones would get a pull force and the residual stress could increase, which would increase the risks of crack at that part.



a. cross-section temperature distribution at the end of forming stage



b. cross-section temperature distribution at the end of holding stage



c. Enlargement of cross-section temperature distribution at the cracking position at the end of holding stage

Figure 9 Cross-section temperature distribution at the end of forming stage and holding stage

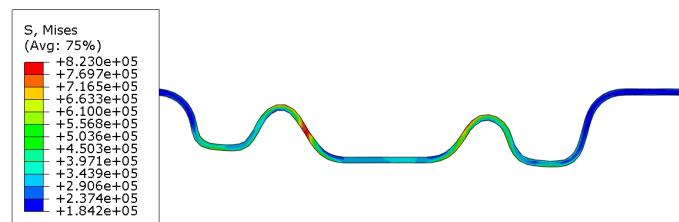


Figure 10 Cross-section stress distribution at the end of holding stage

Analysis of gap between punch and die

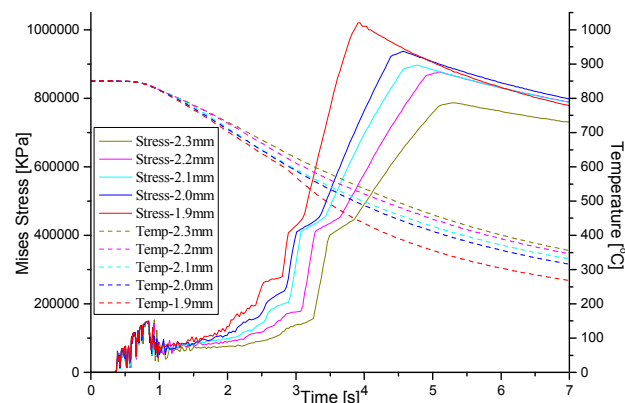


Figure 11 The stress and temperature curves at different time on local cracking areas

In order to ensure the success of hot-stamping, there must be a gap between punch and die which could affect the quality of the shaped component. Figure 11 shows the stress and temperature curves at different time on local crack part (point C in Figure 9-c). The left and right vertical axis represents strain and temperature respectively. The solid line and dotted line represent stress curve and temperature curve. As can be seen from figure, with the gap increasing between punch and die, the cooling rate at point C decreases and the residual stress at the end of holding stage also gradually declines. Moreover, there is a dramatic growth in stress near 600°C at the holding stage. The reason might be that the microstructure of the blank transforms from austenite to martensite near 600°C which leads to the sudden increase of Young's modulus and yield strength. In addition, the shaped component appears spring-back during the cooling period of time, which results in dramatic increasing in stress. The maximum stress is over 1GPa. As shown in Figure 11, with increasing of the clearance between punch and die, the stress at point C decreases. But oversize clearance will make the blank forming incomplete and get unqualified components. So proper gap between punch and die can reduce the residual stress and risks of shaped component cracking after forming and get qualified components.

Conclusion

(1) It is the fact that the different areas of the blank contact with the mould in sequence make the shaped component uneven temperature distribution. Thus the local cracking appears. The first-contact areas on the blank cool down rapidly and have poor mobility. This would make the post-contact areas which are between the first-contact areas greatly thin by the pull force which could leads to the appearance of clearance between punch and die. So the thermal conductivity of post-contact areas decreases. Because of the rapid cooling and uneven temperature distribution, the first-contact areas harden and the microstructure transforms from austenite into martensite. Under the effect of the thermal expansion and contraction, the residual stress of the post-contact areas gradually increases. This would lead to the increase of cracking risks. The experimental results of hot-stamping also prove the conclusion above.

(2) It can reduce the risks of cracking after forming stage to change the clearance size between punch and die. With the reduction of the clearance between punch and die, the cooling rate of blank increase and the residual stress grows at the end of holding stage. Then the risks of cracking increase. But oversize clearance will make the blank forming incomplete and get unqualified components. So it can effectively reduce the risks of the local crack to adjust the clearance size between punch and die. This can provide the reference for the process design of hot-stamping.

Reference

- [1] Merklein, M., Lechler, J., Geiger, M.: CIRP Annals - Manufacturing Technology. 2006, 55(1): 229-232.
- [2] Turetta, A., Bruschi, S., Ghiotti, A.: Journal of Materials Processing Technology. 2006, 177(1-3): 396-400.
- [3] Firat, M.: Materials and Design. 2007, 28(4): 1311-1320.
- [4] Firat, M.: Materials and Design. 2007, 28(4): 1298-1303.
- [5] Firat, M.: Materials and Design. 2007, 28(4): 1304-1310.
- [6] Naderi, M., Uthaisangsuk, V., Prahl, U., Bleck, W.: Steel Research International. 2008, 79(2): 77-84.
- [7] Liu.: Journal of Materials Engineering and Performance. 2010.

The Interpolation Algorithm of Feed Rate Control Based on Trigonometric Acceleration-Deceleration and Machine Dynamics Conditions

Lei Jiang^a, Guofu Ding^b, Binbin Xie^c and Jianmin Wang^d

Southwest Jiaotong University, Chengdu 610031, P.R. China

^ajianglei0506@163.com, ^bdingguofu@163.com, ^cxiebb5688@163.com,

^dwjm_20040812@163.com

Keywords: Feed Rate Control; Trigonometric Acceleration-Deceleration Condition; Machine Dynamics Condition; NURBS Curve; Interpolation

Abstract. According to the requirements of high-speed machining, the feed rate control algorithm based on the acceleration-deceleration control and dynamics conditions is proposed. This algorithm not only satisfies the continuity of displacement, feed rate, acceleration and jerk of the feed movement, but also meets the dynamics condition of high-speed machining. Furthermore, the algorithm is applied to NURBS curve interpolation and optimizes the acceleration-deceleration intervals. At last, the algorithm is verified by simulation. This interpolation algorithm of feed rate control reduces the impact, machine vibration of feed, and improves the surface accuracy and quality of high-speed machining.

Introduction

High-speed machining means cutting with high speed and high feed rate. It has many advantages such as high cutting efficiency, high surface quality, long tool life, small cutting force and so on. High-speed machining has been widely used in aerospace manufacturing. At present, more and more parts with complex surfaces become the cutting object of high-speed machining. NURBS curve can describe geometry characteristics of cutting surface completely. Therefore, the feed path expressed by NURBS interpolation command is the programming development of high-speed machining.

High-speed machining requires machine tools to have high motion precision. And it demands higher requirements of acceleration-deceleration controlling ability for feed rate frequent changes due to the tool path curvature frequent change. How to achieve the control goals of machining smoothly and quickly is the key question of high-speed machining development. Currently, the acceleration-deceleration control has linear, exponential, parabola, S curve, higher functions algorithm and so on[1-5]. Although these algorithms could make feed rate smooth, there still have mutation in acceleration or jerk. And it can not completely avoid the feed impact of high-speed machining.

In this paper, acceleration-deceleration control algorithm based on trigonometric condition and machine dynamics condition is proposed. The control algorithm is used in NURBS interpolation calculation to realize the optimization of acceleration-deceleration intervals. This algorithm can not only guarantee the continuity of feed movement displacement, velocity, acceleration and jerk in high-speed machining, but also meet the dynamics demands of machine tools.

The algorithm of feed rate control

Meeting the acceleration-deceleration conditions of trigonometric function and machine dynamics is the sufficient condition to achieve the continuity of feed movement displacement, velocity, acceleration and jerk, stability of cutting process in high-speed machining.

Trigonometric acceleration-deceleration condition. The goal of acceleration-deceleration control algorithm is to achieve the smoothness of displacement, velocity, acceleration, jerk of the feed path. This goal demands displacement function has third-order derivative at least, which ensures the machine can reach predetermined position at predetermined feed rate shock-free and vibrationless. Trigonometric function has infinite derivatives, so constructing a triangular acceleration-deceleration function can achieve these goals. In this paper, using the monotone increasing characteristic of cosine function in $[\pi, 2\pi]$, we construct the acceleration function as:

$$a(t) = \frac{1}{2} \left[\cos \left(\frac{2t}{t_m} - 1 \right) \pi + 1 \right] a_{\max} \quad (1)$$

where a_{\max} is the maximum acceleration, t is time variable, t_m is the whole time of acceleration process. Acceleration function meets the demands that the acceleration-deceleration interval is monotone and the accelerations at start and end are zero.

Define v_1, v_2 as the feed rates at start and end respectively. Integrating Eq. (1) we can obtain the feed rate function:

$$v(t) = v_1 + \int_0^t a(t) dt = v_1 + \left[\frac{t_m}{2\pi} \sin \left(\frac{2t}{t_m} - 1 \right) \pi + t \right] \frac{a_{\max}}{2} \quad (2)$$

and

$$t_m = \frac{2(v_2 - v_1)}{a_{\max}} \quad (3)$$

Deviating Eq. (2) we obtain feed jerk function:

$$J(t) = -\frac{a_{\max} \pi}{t_m} \sin \left(\frac{2t}{t_m} - 1 \right) \pi \quad (4)$$

Integrating Eq. (2) we obtain the feed displacement function:

$$S(t) = \int_0^t v(t) dt = v_1 t + \frac{a_{\max}}{2} \left[\frac{t^2}{2} + \frac{t_m^2}{4\pi^2} \cos \left(\frac{2t}{t_m} - 1 \right) \pi \right] \quad (5)$$

From Eq. (1), (2), (4), we know that trigonometric acceleration-deceleration condition divides the whole accelerating process into increasing-acceleration section OT_1 and decreasing-acceleration section T_1T_2 , as shown in Fig. 1(a). For the same reason, the whole decelerating process is divided into increasing-deceleration section OT_1 and decreasing-deceleration section T_1T_2 , as shown in Fig. 1(b).

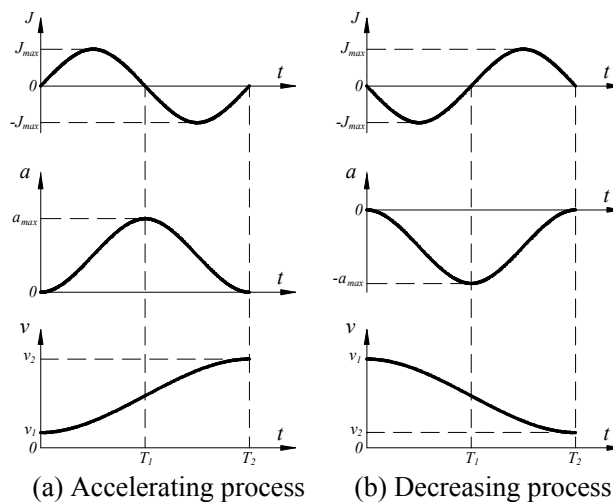


Fig. 1 Kinematic graphics of trigonometric acceleration-deceleration

Machine Dynamics Condition. Machine feed includes rotation of screw and linear motion of table. We define the total mass of the table and workpiece as m , screw lead as l , rotational inertia as I , motor angular velocity as ω , angular acceleration as ε , table linear feed rate as v , linear acceleration as a , axial cutting force as F_c , the servo motor maximum output torque as M_{\max} . The motor shaft torques equivalent to inertia force, cutting force and resistance are defined as M_i , M_c and M_f respectively. We can obtain the following machine dynamics condition function[6]:

$$\begin{cases} M_i = -\text{sgn}(a)I\varepsilon = -\text{sgn}(a)(I + I')\varepsilon = -\text{sgn}(a)\left(I + m\left(\frac{l}{2\pi}\right)^2\right)\frac{2\pi a}{l} = -\text{sgn}(a)\left(\frac{2\pi I}{l} + \frac{ml}{2\pi}\right)a \\ M_c = \frac{F_c l}{2\pi} \\ M_f = \frac{F_f l}{2\pi} \\ |M_i + M_c + M_f| \leq M_{\max} \end{cases} \quad (6)$$

Affected by the depth of cutting, feed rate and cutting speed, F_c could be simplified as

$$F_c(t) = -\text{sgn}(v)K_c |v|^\alpha \quad (7)$$

where K_c is the cutting force factor relatives to the feed rate.

Taking Eq. (7) into (6), we can obtain the machine dynamics constraint function of single axis:

$$\left| -\text{sgn}(a_j)\left(\frac{2\pi I_j}{l_j} + \frac{m_j l_j}{2\pi}\right)a_j + \frac{l_j}{2\pi}\left(-\text{sgn}(v_j)K_c |v_j|^\alpha\right) \right| \leq M_{j\max} \quad (8)$$

where j represents X , Y , Z axis, a_j , v_j represent a , v projection in the axis of j .

NURBS curve interpolation algorithm

NURBS curve could be expressed as a sub-vector rational function, the rational expression is

$$\mathbf{P}(u) = \frac{\sum_{i=0}^n B_{i,k}(u)W_i V_i}{\sum_{i=0}^n B_{i,k}(u)W_i} \quad (9)$$

where V_i is the control points, W_i is the control point weighting factor, and $B_{i,k}(u)$ is the basis function for the k times B-spline.

NURBS curve pre-interpolation. The purpose of NURBS pre-interpolation is to obtain interpolation parameters and initial interval distribution. Based on Taylor series expansion, NURBS pre-interpolation parameter function is[7]:

$$u_{i+1} = u_i + \frac{S_i}{\left\| \frac{dp(u)}{du} \right\|_{u=u_i}} - \frac{\Delta L^2 \left(\frac{dp(u)}{du} \cdot \frac{d^2 p(u)}{du^2} \right)}{2 \left\| \frac{dp(u)}{du} \right\|_{u=u_i}^4} + O(T^3) \quad (10)$$

where S_i is step length of the i interpolation cycle, T is interpolation cycle and v_i is instantaneous feed rate of the i interpolation cycle (default is instructions rate v_c).

Every interpolation points are at NURBS curve, so there is no radial error. However, due to chord substitute curve in each interpolation cycle, there still has approximate error as following:

$$\delta_i = \rho_i - \sqrt{\rho_i^2 - \left(\frac{f_i}{2}\right)^2} \quad (11)$$

where ρ_i is curve radius of the $P(u_i)$ point.

The maximum feed rate, which satisfies the precision of i interpolation cycle could be expressed as:

$$v_{\delta i} = \frac{2\sqrt{2\rho_i\delta - \delta^2}}{T} \quad (12)$$

and normal acceleration is:

$$a_{ni} = \frac{v_{\delta i}^2}{\rho_i} \quad (13)$$

Define a_{ni} , $v_{\delta i}$ represent the projection of a_{ni} , $v_{\delta i}$ in the j axis respectively. Taking them into (4), we can obtain the maximum feed rate satisfies the condition of j axis dynamics. To satisfy the dynamics condition of three feed axes, the feed rate restricted by machine dynamics conditions is:

$$v_{a_i} = \min \{v_{\max a_{ni}}\} \quad (14)$$

Define the instruction feed rate as v_c , the instantaneous feed rate of the i interpolation cycle as $v_i = \min \{v_{\delta i}, v_{a_i}, v_c\}$. If $v_i < v_c$, taking v_i into the Eq. (11), we can obtain the u_{i+1} amended. At the same time, we can obtain feed length sequence of each interpolation cycle. Through pre-interpolation, the feed rate will be changed in the interval where the curvature is large, so the intervals of different feed rate appear.

NURBS curve interpolation. The purpose of NURBS interpolation is to amend the feed rate under trigonometric acceleration-deceleration conditions.

Acceleration-deceleration interval. By analyzing NURBS parameters and feed rate sequence of pre-interpolation, we can obtain the parameters of the acceleration-deceleration intervals. Usually it starts by the constant feed rate v_c to deceleration, then accelerate to v_c . At the maximum curvature point, it reaches minimum feed rate, i.e. the end of deceleration and the start of acceleration.

The a_{\max} of trigonometric acceleration-deceleration. The normal and tangential acceleration of feed motion is interaction achieved by X , Y , Z axes. From Eq. (5), we know that the largest tangential acceleration is at the mid-point of interval. Therefore, we can obtain the a_{\max} of trigonometric acceleration-deceleration algorithm by calculating the minimum of the largest tangential accelerations of 3 axes, i.e. $a_{\max} = \min \{a_{j\tau\max}\}$ at the mid-point of interval. From Eq. (8), we can obtain:

$$a_{j\tau\max} \tau_j + a_n n_j = a_{j\max} = \left| \frac{M_{j\max} - \frac{l_j}{2\pi} \left(-\text{sgn}(v_j) K_c |v_j|^\alpha + u_j N_j + \mu_j v_j \right)}{\left(\frac{2\pi l_j}{l_j} + \frac{m_j l_j}{2\pi} \right)} \right| \quad (15)$$

where a_n , a_τ are the normal and tangential acceleration respectively. n_j , τ_j are the unit normal and tangential vector component of j axis at interval midpoint.

According to the acceleration a_{\max} , we can obtain new feed rate sequence of interpolation cycle in each acceleration-deceleration interval from Eq. (2). According to Eq. (5), (10), we can interpolate from start to end of the intervals by trigonometric function.

The correction of acceleration-deceleration intervals. Through the interpolation of NURBS, we can obtain parameters of interpolation and feed rate that contain a series of acceleration-deceleration intervals. Because the interpolation processes are calculated independently, it may modify intervals

even interfere with adjacent one as the results of the start and end feed rates, acceleration and other limiting factors. It is necessary to correct it.

Define F , B as the forward and backward adjacent acceleration-deceleration intervals, the corresponding parameters of NURBS are $[u_{F_1}, u_{F_2}]$, $[u_{B_1}, u_{B_2}]$, the start and end feed rates are $[v_{F_1}, v_{F_2}]$, $[v_{B_1}, v_{B_2}]$, the maximum accelerations are $a_{\max F}$, $a_{\max B}$ respectively and $v_{F_2} = v_{B_1}$, $u_{F_1} < u_{B_1}$. According to above parameters, the intervals could be divided into two types:

(1) Type 1 $u_{F_2} \leq u_{B_1}$

Type 1 refers the intervals are not interfering, as shown in Fig. 2. In this case, the feed rates meet the actual movement requirements. It needs no correction of the interpolation intervals.

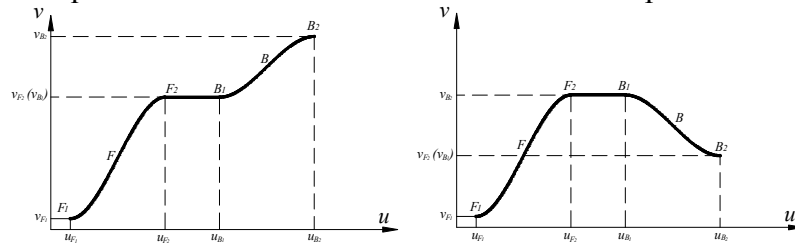


Fig. 2 Type 1

(2) Type 2 $u_{B_1} < u_{F_2}$

Type 2 refers the two adjacent intervals that interfere partly or even complete overlap. The physical meaning is the feed rate cannot attain the predetermination in the interval due to a_{\max} limitation. In this case, interpolation must be corrected to ensure that there is no interference between adjacent intervals. Using iteration method to construct new intervals that combine the original ones, it makes the whole process continuous and smooth.

There are 3 cases of adjacent intervals based on $u_{B_1} < u_{F_2}$.

Case 1 is $a_{\max F} \cdot a_{\max B} < 0$ and $u_{B_1} < u_{F_2} < u_{B_2}$, as shown in Fig. 3. The parameters of new interval are $[u_{F_1}, u_{B_2}]$, the start and end feed rates are $[v_{F_1}, v_{B_2}]$ respectively.

Case 2 is $a_{\max F} \cdot a_{\max B} < 0$ and $u_{B_2} \leq u_{F_1}$, as shown in Fig. 4. The parameters of new interval are $[u_{F_1}, u_{F_2}]$, the start and end feed rates are $[v_{F_1}, v_{B_2}]$ respectively.

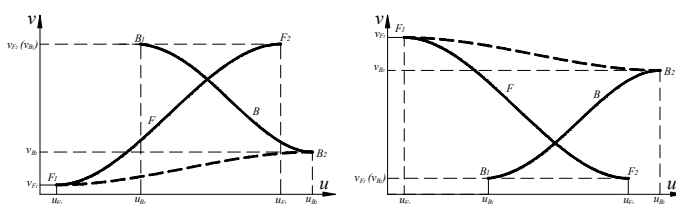


Fig. 3 Case 1 of type 2

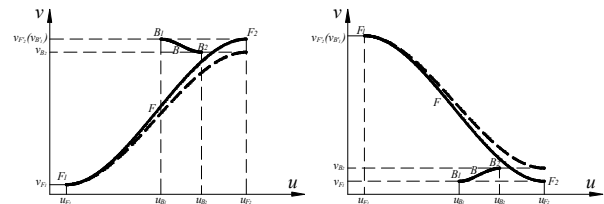


Fig. 4 Case 2 of type 2

The other cases are $a_{\max F} \cdot a_{\max B} > 0$ and $u_{B_1} \leq u_{F_2} \leq u_{B_2}$ or $a_{\max F} \cdot a_{\max B} > 0$ and $u_{B_2} \leq u_{F_2}$, as shown in Fig. 5. The start and end feed rates of new interval are $[v_{F_1}, v_{B_2}]$ respectively, $a_{\max} = \min(a_{\max F}, a_{\max B})$, and the parameter of start is u_{F_1} .

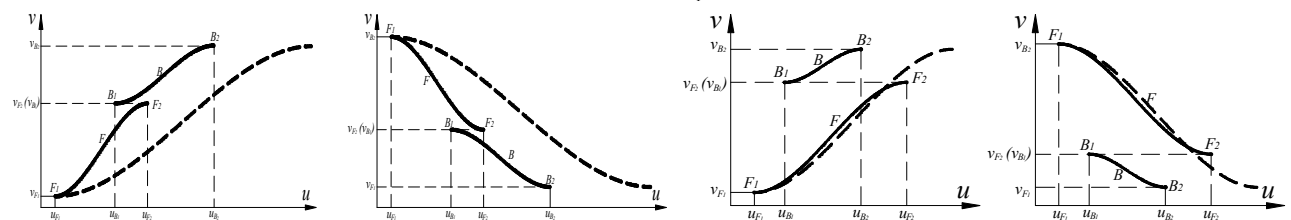


Fig. 5 The other cases of type 2

After constructing new intervals to combine the original ones, the intervals may still intervene with subsequent ones, and it need to continually compare and correct it to ensure all the adjacent interval types are $u_{F_2} \leq u_{B_1}$. At last, we can obtain the new interval parameters by Eq. (2), (5) and (10).

Example

We choose a third-order NURBS curve as the interpolation example, as shown in Fig. 7.

Suppose interpolation cycle as 0.001s, interpolation accuracy as 0.001mm, command feed rate as 300mm/s, each motor power as 400W, the mass of each axis as 50kg, screw lead as 5mm. Fig. 8, Fig. 9 are the contrast charts of normal interpolation and new interpolation algorithm. It shows new control algorithm adjusts feed rate in the large curvature point and makes feed rate, acceleration smooth.

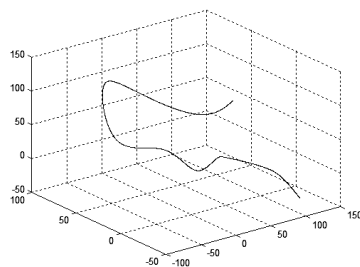


Fig. 7 NURBS curve

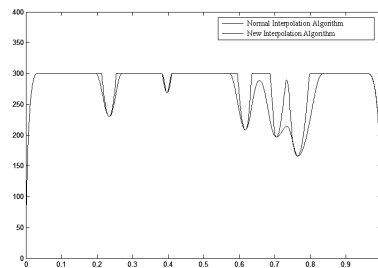


Fig. 8 Feed rate comparison chart

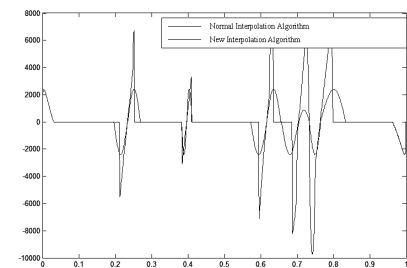


Fig. 9 Acceleration comparison chart

Conclusion

In this paper, the feed rate control algorithm based on trigonometric acceleration-deceleration and machine dynamics conditions is proposed. This algorithm not only satisfies the continuity of displacement, feed rate, acceleration and jerk of the feed motion, but also meets the dynamics condition of the machine. The algorithm can applied to NURBS interpolation calculation using iteration correction technology to achieve the optimization of acceleration-deceleration intervals. The algorithm reduces the impact, machine vibration of feed motion. And it is benefit to improve the surface accuracy and quality of high-speed machining.

Acknowledgements

This work is supported by The Young Teachers Fund of Southwest Jiaotong University, The Fund for New Century Excellent Talents of China, The Special Fund of High-end CNC Machine Tools and Basic Manufacturing Equipment of China (2009ZX04014-051-03) and The Fundamental Research Funds for the Central Universities of China (SWJTU09ZT06).

References

- [1] M C Tsai, C W Cheng, and Cheng M Y: International Journal of Machine Tools and manufacturing. Vol. 43(2003), p. 1217-1227
- [2] S.Bedi, I Ali, N Quan: Transactions of the ASME Journal of Engineering for Industry. Vol. 115(1993), p. 329-336.
- [3] S S Yeh and P L Hsu: Computer Aided Design. Vol. 31(1999), p. 347-359.
- [4] Mi Ching Tsai, Chung Wei Cheng: Transactions of the ASME Journal of Manufacturing Science and Engineering. Vol. 125(2003), p. 449-460.
- [5] Yong T, Narayanaswami R: Computer Aided Design. Vol. 35(2003), p. 1249-1259.
- [6] Peng Fang-yu, He Ying, Luo Zhong-cheng, Li Bin: Huazhong Univ. of Sci. & Tech. (Nature Science Edition). Vol. 33(2005), p. 80-83, In Chinese.
- [7] Du Dao-shan, Yan Cun-liang, Li Cong-xin: Journal of Shanghai JiaoTong University. Vol. 40(2006), p. 843-847, In Chinese.

An Approach to Multi-Constrained 3D Modeling for Curtain Wall System Based on Spatial Point-Line Model

Zhenzhong Hu^{1,a}, Fangqiang Yu^{2,b}, Guoxing Li^{3,c} and Zhongli Wang^{3,d}

¹Graduate School at Shenzhen, Tsinghua University, Shenzhen 518055, China;

²Department of Civil Engineering, Tsinghua University, Beijing 100084, China;

³Zhuhai King Glass Engineering Co. Ltd., Shenzhen 518040, China

^ahu.zhenzhong@sz.tsinghua.edu.cn, ^bfqyu007@163.com,

^clgx@kge-group.com, ^dwzl@kge-group.com

Keywords: CAD; 3D Modeling; Curtain Wall; Multi-Constrained; Shenzhen Airport Terminal 3

Abstract. The accurate spatial 3D models and corresponding coordinates of every key point are needed to determine the sizes, shapes, and locations of installation for all curtain wall elements in the process of production and construction. To solve the transition problems between architectural design and construction design of curtain wall system, four kinds of single-constrained computer-aided 3D modeling algorithm for spatial point-line models were discussed in detail. Then, a multi-constrained iterative 3D modeling process was proposed by considering coupling relationships amongst the various constraints. A 3D modeling system named T3-CW-CAD was developed and applied to the Shenzhen Airport Terminal 3. The application results showed that the presented-algorithm can meet the overall demand for automatically generating multi-layer 3D models according to spatial point-line model, along with sizes and other restraints amongst curtain wall elements, therefore playing a key role in guiding the production and construction of curtain wall system.

Introduction

After the architectural and structural designs of a modern complex building with a curtain wall system have been finished, the design of its curtain wall is needed before the whole construction drawings are printed out. Normally, the architectural design describes the outline of the building, while the structural design is intended to make the result of the architectural design bear its weight and applied loads, whereas the curtain wall design is purposed for detail determination of curtain wall elements and their relations, in order to meet the requirements in the architectural design for the appearance of commercial or large-scale public buildings. Usually, the outline of a building, which is the foundation for curtain wall design, is depicted with 3D point-line models (that is, the construction members of a building such as steel plates and glasses are represented by models made up of points and lines in 3 dimensions, with no thickness, single-layered and simplified) in its architectural design. However, in order to fabricate and install the curtain wall elements, precise 3D models and coordinates of key points are necessary for determination of the size, shape, and location of every element. Therefore, calculations concerning the curtain wall, which shall be performed according to 3D point-line models provided by the architectural designer and the interrelations between the construction elements, are needed.

Task Description

At present, existing CAD systems for curtain wall design are mainly used for site layout of construction elements, formation of checkerwork drawing, material management and structural calculation and analysis^[1, 2]. There are also researches on conceptual design of the architecture and curtain wall by conducting Building Information Model (BIM)^[3, 4]. However, scanty research or application on 3D modeling of curtain wall based on the spatial point-line model, which is the general result form from architectural design. Although, some automatic methods to transform a 2D model

into a 3D one have arisen, they cannot meet most of the requirements because some strict preconditions are need. For instance, some methods depend on not only the existing 2D projection views with assigned layout, but the coordinates and relations of every spatial point as well^[5, 6]. For another method, coordinates transformation of engineering drawings is needed before analyzing the interrelationship among projection systems, in order to support 3D reconstruction from orthographic views^[7]. However, as the result of architectural design is represented by fractals^[8], it is necessary to generate the outline of each layer and coordinates of each key point on the basis of the point-line model and the interrelations among the elements and among different layers, so that detail fabrication drawings of elements and construction blueprints can be produced. In addition, 3D constraints are more complex than 2D constraints and a lot of calculation and analysis are needed for modeling under each kind of constraint. In this particular field, mature CAD systems and corresponding engineering applications are still needed.

On the other hand, there are inevitable interplays among constraints, which means a model which has been modified under one constraint may become ineffective under another constraint. To perform a modeling with more than one constraints, traditionally, Genetic Algorithm or Simulated Annealing Algorithm are used to find an optimized solution^[9, 10]. However, as 3D modeling of a curtain wall calls for colossal computation, these algorithms become unsatisfactory. In this case, iterative modeling, in which the priority of each constraint is determined by discussing the relationship between them so that the constraints can be used in proper order, is applied to work out a complete 3D model.

More and more buildings' outlines become irregular as the buildings become more and more complex and their spans larger and larger, so that it is almost impossible to build up 3D models manually. Therefore, a method for computer to model rapidly is needed to aid the design and construction of curtain wall system.

In the following part of the paper, the modeling methods for four separated constraints that affects on the 3D modeling process from spatial point-line model are firstly summarized. They are intersection constraint, coplanar constraint, constraint on minimum board thickness, and constraint on the inclination. Then by analyzing the interplays among these constraints, an iterative modeling method is proposed and applied to an on-going engineering project. At last, the features of the iterative modeling method are discussed.

3D Modeling Method under Single Constraint

Intersection Constraint. Here we name planes that meet at a single intersecting point as point sharing planes. The deviated planes, which are generated based on the original point sharing planes and their own normal directions and designated displacements, usually cannot meet at one point, as shown in Fig. 1(a). However, the requirement of intersection constraint means that deviated planes based on original point sharing planes are required to be a set of new point sharing planes as shown in Fig. 1(b).

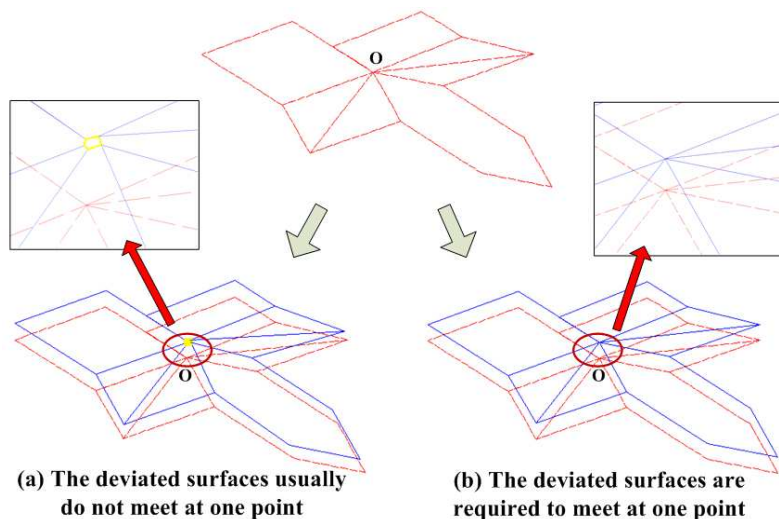


Fig. 1 Intersection constraint of several planes

To be universally known in 3D spaces, three planes that are not paralleled determine a single intersecting point. As a result, in order to meet the requirement of intersection constraint and to determine the point where planes meet, the following steps should be adhered to.

- 1) Choose three reference planes according to the priority of each plane and the relations between the normal vectors of the planes (Algorithm 1);
- 2) Form three deviated planes by allowing the reference planes to deviate designated displacements;
- 3) Work out the intersecting line between two of the deviated planes (Algorithm 2);
- 4) Work out the intersection point between the intersecting line and the third deviated plane (Algorithm 3);
- 5) Set the point as the intersecting point of all the planes; see Fig. 1(b).

Algorithm 1 (For determination of the reference planes).

To determine the reference planes, start from the original intersecting point (See Fig. 1), traverse its adjacent planes according to their priorities, then decide if each plane can be selected as a reference plane according to the relations of plane normals (see Fig. 2(b)). If a plane is selected, it was then added to the reference planes list. The final reference planes list can be determined if the number of the reference planes amounts to 3 or the traversing has been completed.

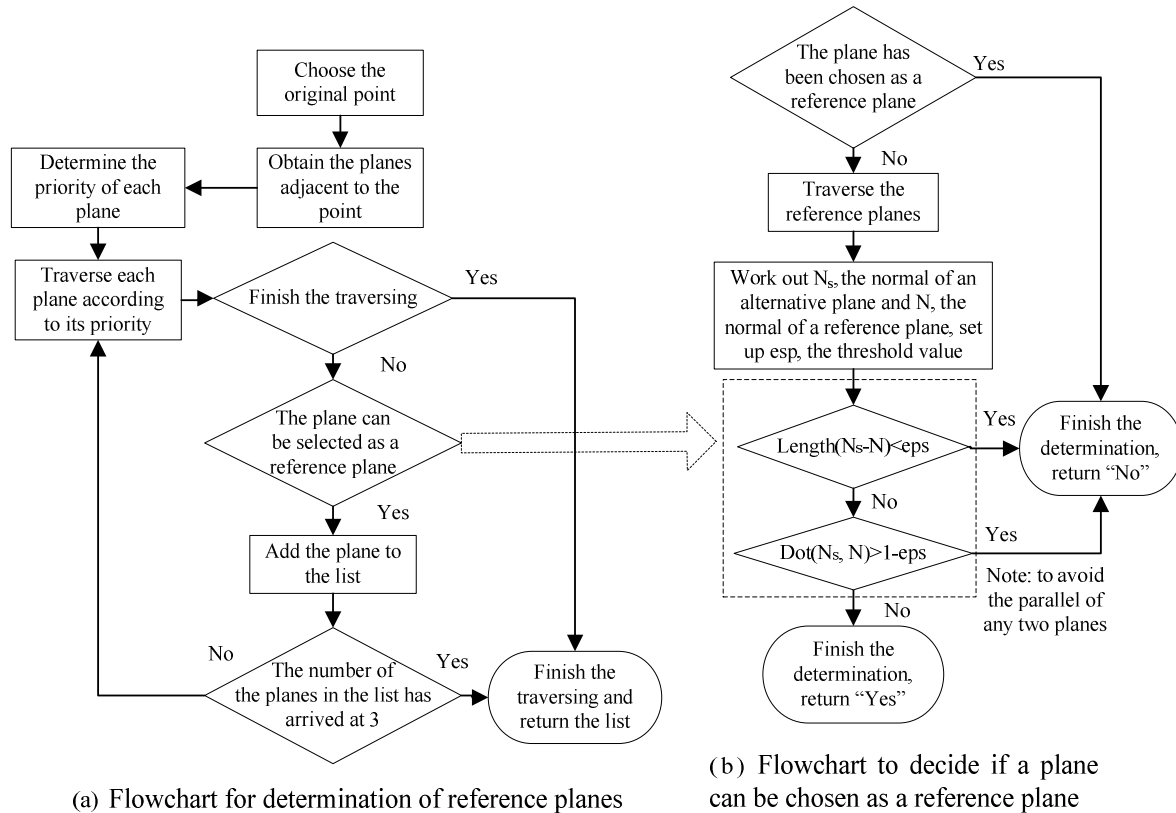


Fig. 2 Flowchart for algorithm of plane selection

Algorithm 2 (For determination of the intersecting line of two planes).

If P_s and P_t are the vertexes of two planes and U , V are their normal vectors, P is a point on the intersecting line and it is possible to set $P_z = 0$, then the following expressions will be concluded by the following Eq. 1.

$$\begin{cases} P_x = (P_s \cdot UV_y - P_t \cdot VU_y) / (U_x V_y - V_x U_y) \\ P_y = (P_s \cdot UV_x - P_t \cdot VU_x) / (U_y V_x - V_y U_x) \\ P_z = 0 \end{cases} \quad (1)$$

Otherwise, it is possible to set $P_x = 0$ or $P_y = 0$, then the coordinates of P can be worked out in the same way.

Having known the coordinates of P, the direction of the intersecting line N can be found as Eq. 2.

$$N = U \times V. \quad (2)$$

Algorithm 3 (For determination of coordinates of the intersecting point).

If N is the normal vector of a plane and P is any point on the plane, P_1, P_2 are two points on a straight line and P_1 is the point where the plane and the straight line meet, then Eq. 3 can be concluded.

$$P_t = P_1 + t(P_2 - P_1). \quad (3)$$

The following expression can be concluded as Eq. 4.

$$t = -(P_1 - P) \cdot N / (P_2 - P_1) \cdot N. \quad (4)$$

If the denominator in the expression is zero, it will be concluded that the straight line parallels the plane. However, if the numerator is zero, it means that P_1 is the intersecting point or the line is on the plane.

Coplanar Constraint. The points in a 3D polygon representing the outline of an element which are not in a plane will make the fabrication difficult. Therefore, it is a must to ensure the coplanarity of these points by fitting a plane and finely adjust the points so that they can meet the requirements of planar constraint.

Algorithm 4 (For planar fitting).

If the plane is represented by the following Eq. 5.

$$z = a_0 + a_1x + a_2y + e. \quad (5)$$

Replace x, y, z with the coordinates of each boundary point to work out the values of a_0, a_1, a_2 [11] as shown in Eq. 6.

$$\begin{bmatrix} n & \sum x_i & \sum y_i \\ \sum x_i & \sum x_i^2 & \sum (x_i \cdot y_i) \\ \sum y_i & \sum (x_i \cdot y_i) & \sum y_i^2 \end{bmatrix} \begin{bmatrix} a_0 \\ a_1 \\ a_2 \end{bmatrix} = \begin{bmatrix} \sum z_i \\ \sum (x_i \cdot z_i) \\ \sum (y_i \cdot z_i) \end{bmatrix}. \quad (6)$$

Finally, form a new plane with these values so that the boundary points of each plane become coplanar in it.

Constraint on Minimum Board Thickness. Normally, the deviated plane formed with the above-mentioned two methods does not parallel the original reference plane. The pipeline and other structures inside the curtain wall requires that the minimum space between the exterior surface of a board and the interior one should not be less than a specific value. Therefore, the minimum space between surfaces should be worked out and if a minimum space is not satisfactory, tiny adjustments of the coordinates shall be done. In the process as shown in Fig. 3, the foot of a perpendicular from a 3D point to a plane and the shortest distance between a point and a polygon should be worked out, which is detailed in the following Algorithm 5 and Algorithm 6.

Algorithm 5 (For the foot of a perpendicular from a 3D point to a plane).

If N is the normal vector of a plane, P_{on} is a point on the plane, P_t is a foot of a perpendicular from a P, a vertex, to the plane, then Eq. 7 can be concluded.

$$P_i = P + t \cdot N. \quad (7)$$

Then the following Eq. 8 can be concluded.

$$t = -(P - P_{on}) \cdot N / N \cdot N. \quad (8)$$

If the numerator equals to zero, it can be concluded that the vector between P and P_{on} is perpendicular to the plane and the vertex is in the plane.

Algorithm 6 (For shortest distance between a 2D point to a polygon).

- 1) Decide if the point is in the plane; if yes, $d_{min}=0$; otherwise go to step 2);
- 2) Work out d_i , the minimum distance between the point and each edge of the polygon ($i=1\dots n$, n equals the number of the edges);
- 3) $d_{min} = \min\{d_i\}$.

Constraint on the Inclination. As the structure at the utmost exterior of a building, the curtain wall has to be suitable for drainage. Therefore, the polygons which do not meet the requirements on drainage must be rotated for a proper angle α (See Algorithm 7 for calculation of α) to adjust its inclination (see Fig. 4 for flowchart of the algorithm).

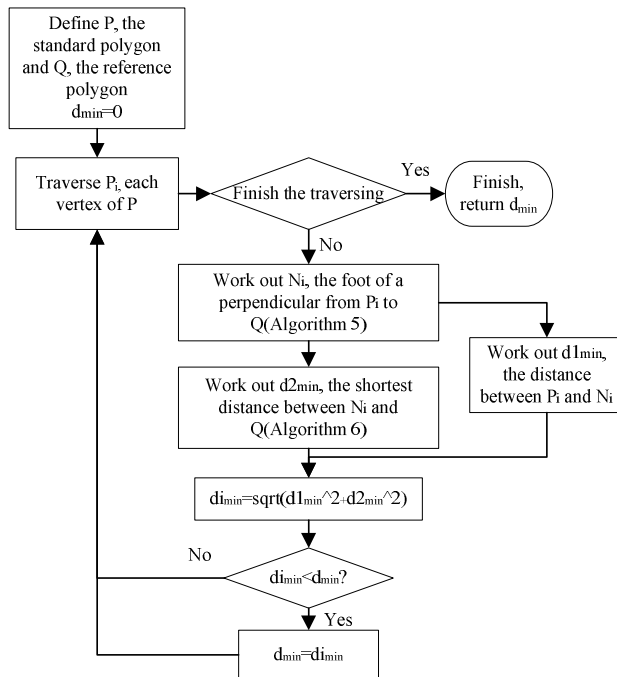


Fig. 3 Flowchart for algorithm of minimum distance calculation between two polygons

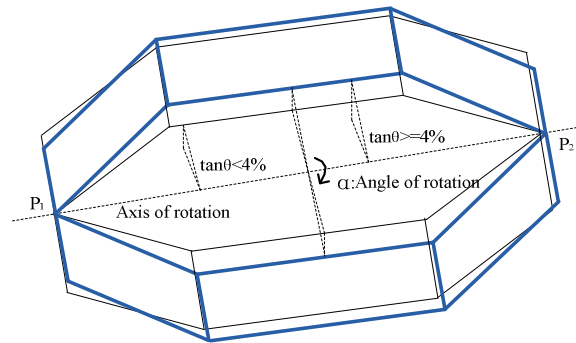


Fig. 4 Shape modification of a curtain wall element

Algorithm 7 (For calculation of the turning angle).

Suppose P is a 3D point whose coordinates are (x, y, z) . It is rotated by α , an angle reference to a rotation axis P_1P_2 to form a new 3D point $P'(x', y', z')$. The coordinates of P_1, P_2 are $(x_1, y_1, z_1), (x_2, y_2, z_2)$. T is defined as a transformation matrix, then Eq. 9 can be concluded:

$$\overline{P'}(x', y', z', 1) = T \cdot \overline{P}(x, y, z, 1). \quad (9)$$

Then the following Eq. 10 can be concluded:

$$T = \begin{bmatrix} 1 & 0 & 0 & -x_1 \\ 0 & 1 & 0 & -y_1 \\ 0 & 0 & 1 & -z_1 \\ 0 & 0 & 0 & 1 \end{bmatrix} R(\alpha) \begin{bmatrix} 1 & 0 & 0 & x_1 \\ 0 & 1 & 0 & y_1 \\ 0 & 0 & 1 & z_1 \\ 0 & 0 & 0 & 1 \end{bmatrix} \quad (10)$$

Where, if $c = \cos(\alpha)$, $s = \sin(\alpha)$, $\vec{u} = \vec{P}_2 - \vec{P}_1$, then $R(\alpha)$ is the transformation matrix ^[12] for a turning around an axle passing the original point whose direction vector is \vec{u} for α radian degree, as shown in Eq. 11.

$$R(\alpha) = \begin{bmatrix} c + (1-c)\vec{u}_x^2 & (1-c)\vec{u}_y\vec{u}_x - s\vec{u}_z & (1-c)\vec{u}_z\vec{u}_x + s\vec{u}_y & 0 \\ (1-c)\vec{u}_x\vec{u}_y + s\vec{u}_z & c + (1-c)\vec{u}_y^2 & (1-c)\vec{u}_z\vec{u}_y - s\vec{u}_x & 0 \\ (1-c)\vec{u}_x\vec{u}_z - s\vec{u}_y & (1-c)\vec{u}_y\vec{u}_z + s\vec{u}_x & c + (1-c)\vec{u}_z^2 & 0 \\ 0 & 0 & 0 & 1 \end{bmatrix} \quad (11)$$

3D Modeling under Multi-Constraints

Analysis of the Interplays among the Constraints. Although the above-mentioned constraints interplay each other, not every pair of constraints have effect on each other. For example, under the coplanar constraint, the fine adjustment of vertex coordinates of a polygon is necessary, which can be done after intersection constraint takes effect, therefore, coplanar constraint doesn't go against the intersection constraint, but it may influence the inclination of an element and finely modify the minimum thickness of an element. See Table 1 for all the interplays.

Table 1 Analysis of the coupling effect amongst the constraints

	Intersection Constraint	Coplanar Constraint	Constraint on Minimum Board Thickness	Constraint on the Inclination
Intersection Constraint			✓	
Coplanar Constraint			✓	✓
Constraint on Minimum Board Thickness	✓	✓		✓
Constraint on the Inclination		✓	✓	

Working Process for the Iterative Modeling Method. Owing to the interplays among the constraints, which vary with the order of action, reasonable working process will greatly improve the efficiency of modeling. On the other hand, every time the model has been constrained, it is necessary to check if the model meet the requirements of the rest constraints; if no, iterative modeling method should be applied until all the requirements are met. Therefore, the working process is the key for 3D modeling of curtain wall system under more than one constraints.

Table 1 indicates that adjustment of the coordinates of the elements' vertexes to meet the requirements on minimum board thickness will lead to the fact that the modeling can not meet other constraints and vice versa. Therefore, the constraint on minimum thickness is the most important one. On the other hand, the plane fitting and plane rotation can be done after the intersection constraint has taken effect so that the fitted and rotated plane can be treated as forced plane to ease the modeling process. Based on these principles, the modeling can be done iteratively according to Fig. 5.

As illustrated in Fig. 5, model checking is done to decide whether the model meet the requirements on minimum board thickness. If yes, finish the modeling; otherwise, firstly decide if the parameters for modeling are convergent in an iterative process as below.

If δ_i is the minimum deviation value of a board thickness from requirement that determined by the following equation

$$\delta_i = \text{the minimum board thickness after } i^{\text{th}} \text{ iteration} - \text{the required minimum thickness} \quad (11)$$

then the parameter is considered to be convergent if $\delta_{i+1} < \delta_i$ ($\delta_{i+1}, \delta_i > 0$).

According to the interplay analysis mentioned above, as the model is under the influence of more than one constraints, the effect of a constraint on the model may be changed after another constraint on the model has been finished. For example, allowance of two surfaces to depart from each other along the normal direction so that the minimum board thickness meet the requirement will lead to unsatisfactory inclination of other board for drainage. For another instance, forced intersection of several plane will influence the distances between the plane and reference plan. Under extreme condition, the requirement on the minimum thickness can not be fulfilled no matter which direct will be taken to move the intersection point, when the parameters become inconvergent. In these cases, parameters including the elements' shape, thickness, drainage inclination and drainage method, have to be modified.

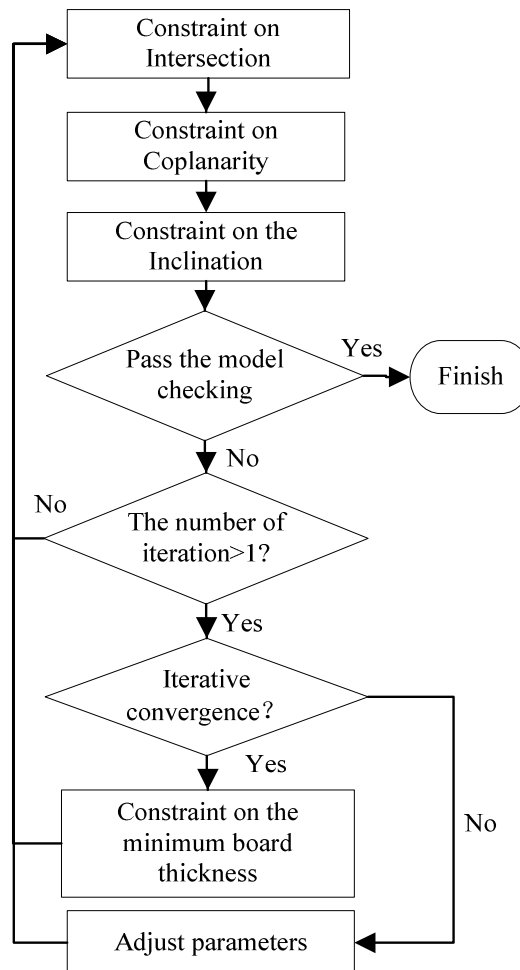


Fig. 5 Flowchart for iterative 3D modeling approach

Engineering Application

The above-mentioned method has been applied to the modeling of the curtain wall system of the T3 terminal of Shenzhen Airport, which is a key project for expansion of the Shenzhen Airport. The curtain wall system is made up of glass panes and metal boards arranged in a way to form a special concavo-convex texture on a free formed surface. The architectural designer has given the point-line model of the curtain wall in the manner of 3D coordinates (See Fig. 6 (a)), which serves as the central line of the steel structure (See Fig. 6 (c), (d)). Multi-constrained, the inner outline and outer one of the

steel boards and the glass panes have to be determined and it is a requisite that the minimum board thickness is 240 mm (See Fig. 6 (b)) and the inclinations of the glass panes be not less than 4%.

The study is based on the platforms of AutoCAD® 2007, Visual studio .NET® and Object ARX .NET® and object-oriented modularize method is used to design and develop a CAD system (T3-CW-CAD) for the modeling of the curtain wall system of the T3 terminal of Shenzhen Airport. Fig. 7 shows the effects of the 3D modeling and iterative process at the corridor of the tower and the huge roof.

The iteration shows that the time needed for every adjustment is longer than that in previous step and the deviation of the minimum thickness from the requirement becomes smaller and smaller, which means it is a convergent process. The application indicates that the method can meet the requirements of modeling of T3 terminal, which is based on point-line model and multi-constrained.

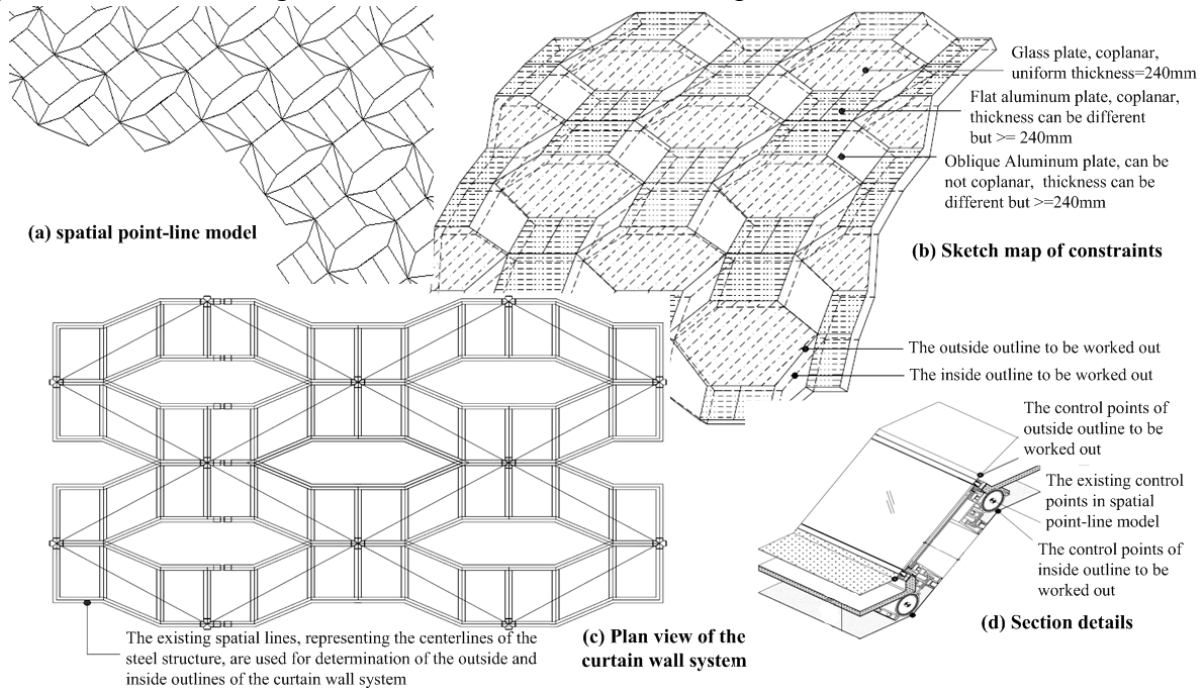


Fig. 6 3D modeling requirements for curtain wall system of Shenzhen Airport Terminal 3

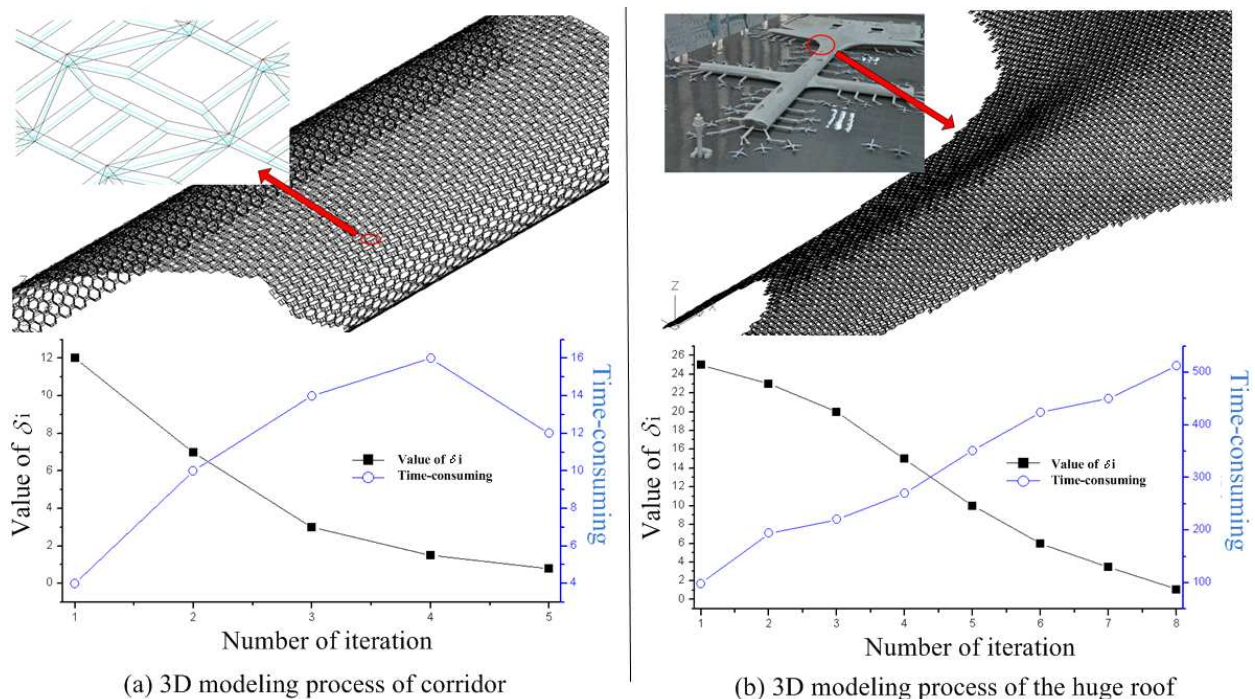


Fig. 7 Application of the iterative 3D modeling approach

Conclusions

The modeling method presented in this paper is mainly featured by:

- 1) Such single constraint as intersection, coplanarity, minimum board thickness and bodily form have been respectively and cooperatively taken into the consideration;
- 2) The iteration will help the realization of automatic modeling and model checking process to greatly improve the efficiencies in description of the fractals of architectural design result and detailed design of the elements;
- 3) The 3D modeling approach can meet the requirements of the curtain wall designer that the integrative multi-layered 3D models must be produced automatically based on the point-line models and the dimensions of elements and interplays determined during the design process. Therefore, the method plays an important role in helping design construction drawing and produce the elements of curtain wall system and their installations.

Acknowledgements

This work was supported by the National Natural Science Foundation of China (No. 51008168) and China Postdoctoral Science Foundation funded project (20090460361).

References

- [1] Jie Wu, Ming Gong, Qilin Zhang: Computer Aided Engineering, Vol. 16 (2007), p. 22-24. (In Chinese)
- [2] Xiaosong Zeng, Qiong Tan: Journal of Yuzhou University (Natural Sciences Edition), Vol. 21 (2004), p. 269-271. (In Chinese)
- [3] Naruo Kano, in: *Proceedings of ISAAC*, Kolkata, India, (2006), p.18-20
- [4] Paola Sanguinetti: Revista del Centro de Investigación, Vol. 8(sup) (2008), p. 49-53
- [5] I. V. Nagendra, U. G. Gujar: Computers & Graphics, Vol. 12 (1988), p. 111-114
- [6] B. Aldefeld: Computer Aided Design, Vol. 15 (1983), p. 59-64
- [7] Aijun Zhang, Changqian Zhu, Zhe Wang: Journal of Southwest Jiaotong University, Vol. 36 (2001), p. 57-61. (In Chinese)
- [8] Oezguer Ediz, Guelen Cagdas: Computer Aided Design, (2007), p. 1-7
- [9] K. L. Mak, Z. G. Guo, in: *IEEE Systems and Information Engineering Design Symposium*, Charlottesville, USA, (2004)
- [10] Jun Lv, Boqin Feng, Bo Li: Journal of Xi'an Jiaotong University. Vol. 39 (2005), p. 1299-1302. (In Chinese)
- [11] P. C. Raymond, C. C. Steve: *Numerical methods for engineers (fifth edition)* (McGraw-Hill Science Engineering publications, 2005)
- [12] Francis S Hill, Jr., Stephen M Kelley: *Computer graphics: using OpenGL (third edition)* (Prentice Hall Press publications, 2009)

A Novel Symbolic OBDD Algorithm for Generating Mechanical Assembly Sequences Using Decomposition Approach

Zhoubo Xu^{1,2,a}, Tianlong Gu^{2,b}, Liang Chang^{2,c} and FengYing Li^{1,2,d}

¹School of Electronic Engineering, Xidian University, Xi'an, 710071, China

²School of Computer Science and Engineering, Guilin University of Electronic Technology, Guilin 541004, China

^axzbli_11@guet.edu.cn, ^bcctlgu@guet.edu.cn, ^cchangl@guet.edu.cn, ^dlyf@guet.edu.cn

Keywords: Ordered Binary Decision Diagram; Assembly Sequence Planning; Cut-Set; Symbolic Algorithm.

Abstract. The compact storage and efficient evaluation of feasible assembly sequences is one crucial concern for assembly sequence planning. The implicitly symbolic ordered binary decision diagram (OBDD) representation and manipulation technique has been a promising way. In this paper, Sharafat's recursive contraction algorithm and cut-set decomposition method are symbolically implemented, and a novel symbolic algorithm for generating mechanical assembly sequences is presented using OBDD formulations of liaison graph and translation function. The algorithm has the following main procedures: choosing any one of vertices in the liaison graph G as seed vertex and scanning all connected subgraphs containing seed vertex by breadth first search; transforming the problem of enumerating all cut-sets in liaison graph into the problem of generating all the partitions: two subsets V_1 and V_2 of a set of vertices V where both the induced graph of vertices V_1 and V_2 are connected; checking the geometrical feasibility for each cut-set. Some applicable experiments show that the novel algorithm can generate feasible assembly sequences correctly and completely.

Introduction

Assembly sequence planning is significant for the design of assembly. It is one of the fundamental research branches of design for product lifecycle. Since 1984, a number of assembly sequence planning systems have been developed; these systems fall into two major categories: those using a direct generation approach and those using disassembly principle. The first approach derives the assembly sequences by putting together separated parts into final assembly; the short coming of this approach is that it may lead to the problem of backtracking when an already assembled part is an obstacle for later assembly operations. The second approach generates the assembly sequences by disassembly principle to decompose the final assembly into separated parts for obtaining the disassembly sequences based on an assumption that the sequence of assembly is the reverse of disassembly sequence, this approach can avoid backtracking. For the most assembly, the assembly sequences can be transformed into the disassembly sequence.

Cut-set decomposition method [1,2] is the most commonly used method for generating disassembly sequence, scanning all cut-sets is the main component of the decomposition method. The traditional algorithms for finding all cut-sets are composed of three steps. First, a spanning tree of the graph is constructed. Second, the fundamental system of cut-sets relative to that spanning tree is found. And third, all the combinations of fundamental cut-sets are computed. The shortcoming of these algorithms is $2^{n-1}-1$ cut-sets (include true cut-set and false cut-set) are generated by them. When the number n is increased, this may lead to the so-called combinatorial explosion.

Homen de Mello and Sanderson presented a more efficient approach to enumerated cut-set [2]. Firstly, all the connected subgraphs having the number of nodes smaller than or equal to a half of the number of nodes in the whole graph is found. For each of these subgraphs, the set of edges of the whole graph that have only one end in the subgraph defines a cut-set if their removal leaves the whole graph with exactly two components. Sharafat and Ma'rouzi proposed a novel algorithm for scanning all

minimal cut-sets of a graph based on the breadth-first search method in conjunction with edge contraction [3]. The experimental results showed that their algorithm was much better than traditional algorithms.

Assembly sequence planning is a typical NP-complete problem under assembly process constraint. It is well known that the number of feasible assembly sequences increases exponentially with the number of parts or components composing the whole products. A practicable strategy to combat or ease combinatorial complexity problem to some extent is using implicitly symbolic representation and manipulation technique. Ordered binary decision diagram (OBDD) or variant thereof can realize implicit representation and search of state space or variable combination, which is one of the most efficient symbolic technique. Efficient symbolic algorithms have been devised for hardware verification, model checking, testing and optimization of circuit [4,5]. Hachtel and Somenzi developed the OBDD-based symbolic algorithm for maximum flow in 0-1 networks that can be applied to very large graph (more than 10^{36} edges) [6]. Recently, there has emerged a class of OBDD-based approaches in mechanical assembly sequence planning. Gu, Xu and Yang proposed symbolic OBDD representations for mechanical assembly sequences[7], the experimental results show that the storage space of OBDD based representation of all the feasible assembly sequences is less than that of AND/OR graph do. Gu and Liu developed an algorithmic procedure using a direct generation approach to generate all feasible assembly sequences by putting together the separated parts into final assembly from the OBDD of liaison graph and translation relation [8], but this procedure leads to the problem of backtracking when an already assembled part is an obstacle for later assembly operations. Xu and Gu presented a novel scheme to integrate constraint satisfaction problem model with the symbolic ordered binary decision diagram for the assembly sequence planning [9], but this procedure also leads to the problem of backtracking.

In this regard, this paper presents a symbolic OBDD algorithm for assembly sequence based on symbolic OBDD assembly model of liaison graph and translation function, the algorithm is developed by integrating the idea of Sharafat's recursive contraction algorithm with cut-set decomposition method, and generates disassembly sequences by decomposing final assembly into separated parts. In this algorithm, assembly sequences are represented by AND/OR graph, the nodes in the AND/OR graph correspond to subassemblies which are represented by OBDD, and the hyperarcs correspond to assembly tasks in which two subassemblies are joined to yield a larger more complex subassembly. The experiment results show that the algorithm can generate geometrically feasible assembly sequences completely and correctly.

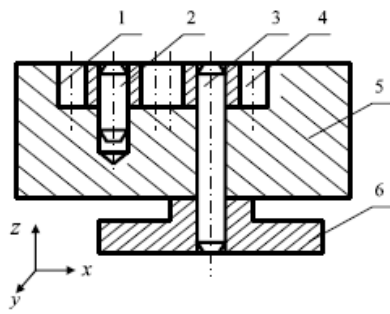
Symbolic formulation of assembly knowledge

Symbolic OBDD representation of liaison graph. Liaison graph is one of the role model for generating assembly sequences. Liaison graph is a undirected connected graph $G=<V,E>$, where V is a set of vertices which corresponding to the parts in the assembly, E is a set of edges, in which one edge for each pair of parts that have at least one contact.

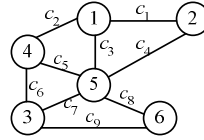
Given an assembly and its liaison graph $G=<V,E>$, we can convert the liaison graph to an OBDD by encoding the parts of the assembly or the elements in V with a length- n binary number, where $n=\lceil \log_2 |V| \rceil$. Each encoded node in V corresponds to a vector of binary variables $X=(x_0, x_1, \dots, x_{n-1})$. For any edge $(u,v) \in E$ can be represented by binary vector $(X,Y)=(x_0, x_1, \dots, x_{n-1}, y_0, y_1, \dots, y_{n-1})$, where $X=(x_0, x_1, \dots, x_{n-1})$ and $Y=(y_0, y_1, \dots, y_{n-1})$ are the binary encodings of node u and node v , respectively. For example, we use an simple assembly shown in Fig.1a, this assembly includes 6 parts, and its liaison graph is presented in Fig.1b. So we need only length-3 binary number to encoding the parts in the assembly. Let part 1, 2, 3, 4, 5 and 6 correspond to binary number 001, 010, 011, 100, 101 and 110 respectively, the characteristic function of E is derived as following:

$$\Phi_C(x_0, x_1, y_0, y_1) = x_0'x_1'x_2y_0'y_1y_2' + x_0'x_1'x_2y_0y_1'y_2' + x_0'x_1'x_2y_0y_1'y_2 + x_0'x_1x_2'y_0y_1'y_2 + x_0x_1'x_2'y_0y_1'y_2 + x_0'x_1x_2y_0y_1'y_2' + x_0'x_1x_2y_0y_1'y_2 + x_0'x_1x_2y_0y_1y_2' + x_0x_1'x_2y_0y_1y_2'$$

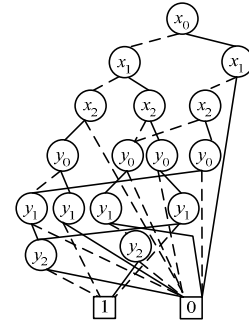
The OBDD for this characteristic function is shown in Fig.1c.



(a) A assembly



(b) Liaison graph G



(c) OBDD for Liaison graph

Fig.1 An simple assembly

Symbolic OBDD representation of translation function. The liaison graph provides only the necessary conditions but not sufficient to assembly two components. To be a feasible assembly operation, it is necessary that there is a collision-free path to assembly parts. Gottipolu and Ghosh defined contact and translational functions to represent the connectivity and the relative motion between parts of the assembly [10]. In fact, contact function can derive from liaison graph and translational function directly. In this regard, we use liaison graph and translational function as assembly model.

Translational function $T: P \times P \rightarrow \{0,1\}^6$, where P is a set of parts, $\{0,1\}^6$ is a 0-1 vector space with six dimension, each dimension correspond to the one of six directions of triorthogonal Cartesian coordinate system. Here, directions 1, 2, 3, 4, 5 and 6 indicate the six directions +X, +Y, +Z, -X, -Y, and -Z of X, Y and Z axes respectively.

Let $(a, b) \in P \times P$, the correspond value of T function is 0-1 vector space with six dimension $(T_1(a,b), T_2(a,b), T_3(a,b), T_4(a,b), T_5(a,b), T_6(a,b))$, where $T_i(a,b)=1$ ($i=1,2,\dots,6$) if the part b has the freedom of translational motion with respect to the part a in the direction i , $T_i(a,b)=0$ if the part b has no freedom of translational motion with respect to the part a in the direction i .

For example, Table 1 shows the translational function T for the assembly shown in Fig.1a.

According to the encoding method introduced in the above section, the i th component of translational function T can be represented by the following characteristic function:

$$\Phi_{T_i}(x_0, x_1, \dots, x_{l-1}, y_0, y_1, \dots, y_{l-1}) = \begin{cases} 1, & \text{if } T_i(a,b) = 1 \\ 0, & \text{otherwise} \end{cases} \quad (1)$$

So, for the assembly shown in Fig.1, the shared binary decision diagram (SBDD) [11] for translation function is shown in Fig.2. For clearly, the edge point to sink node 0 is omitted in SBDD shown in Fig.2.

Table1 T function for the assembly shown in Fig.1

Pair	T_1	T_2	T_3	T_4	T_5	T_6	Pair	T_1	T_2	T_3	T_4	T_5	T_6	Pair	T_1	T_2	T_3	T_4	T_5	T_6
(1,2)	0	0	1	0	0	1	(3,1)	0	1	1	1	1	1	(5,1)	0	0	1	0	0	0
(1,3)	1	1	1	0	1	1	(3,2)	0	1	1	1	1	1	(5,2)	0	0	1	0	0	0
(1,4)	1	0	1	0	0	1	(3,4)	0	0	1	0	0	1	(5,3)	0	0	1	0	0	1
(1,5)	0	0	0	0	0	1	(3,5)	0	0	1	0	0	1	(5,4)	0	0	1	0	0	0
(1,6)	1	1	0	1	1	1	(3,6)	0	0	1	0	0	1	(5,6)	1	1	0	1	1	1
(2,1)	0	0	1	0	0	1	(4,1)	0	0	1	1	0	1	(6,1)	1	1	1	1	1	0
(2,3)	1	1	1	0	1	1	(4,2)	0	1	1	1	1	1	(6,2)	1	1	1	1	1	0
(2,4)	1	1	1	0	1	1	(4,3)	0	0	1	0	0	1	(6,3)	0	0	1	0	1	1
(2,5)	0	0	0	0	0	1	(4,5)	0	0	0	0	0	1	(6,4)	1	1	1	1	1	0
(2,6)	1	1	0	1	1	1	(4,6)	1	1	0	1	1	1	(6,5)	1	1	1	1	1	0

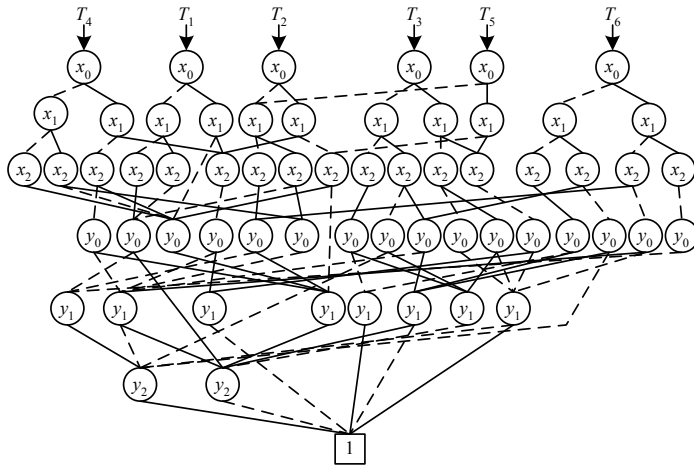


Fig.2 SBDD for translation function

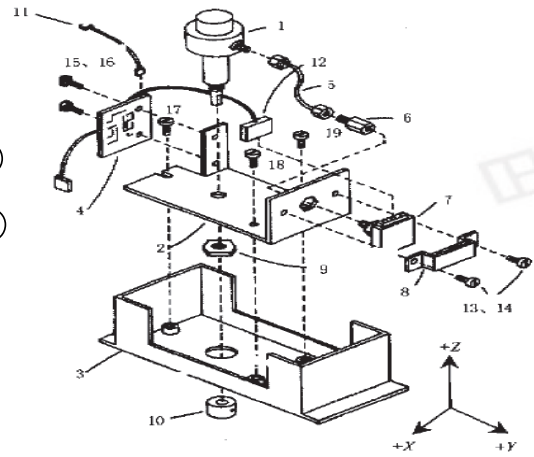


Fig.4 An electrical controller

The algorithm for generating all assembly sequences

Based on an assumption that the sequence of assembly is the reverse of that of disassembly, we applying the assembly by disassembly principle to decompose the final assembly into separated parts for obtaining the disassembly sequences. The decompositions are enumerated by enumerating the cut-sets of the assembly's liaison graph, and each cutset corresponds to a decomposition. For two disjoint sets V_1 and V_2 of vertices in a graph $G=\langle V, E \rangle$, a graph consisting of vertex set V_1 and edge set $E_1=\{\langle v, w \rangle \in E | v, w \in V_1\}$ is designated as a induced subgraph for vertex set V_1 of G and is denoted by $G[V_1]=\langle V_1, E_1 \rangle$. As is well known, a necessary and sufficient condition for a cut $\omega=\{\langle v, w \rangle \in E | v \in V_1, w \in V_2\}$ to be an cut-set in graph G is that the induced subgraphs $G[V_1]$ and $G[V_2]$ of G are both connected, Thus the problem of enumerating all the cut sets in G is reduced to that of generating all the partitions of V into two subsets V_1 and V_2 such that $V_1 \cup V_2 = V$, $V_1 \cap V_2 = \emptyset$, and both $G[V_1]$ and $G[V_2]$ are connected.

The algorithm for generating all assembly sequences is shown in Fig.3, which takes the OBDDs of the assembly's liaison graph $C(x,y)$, translation function $T(x,y)$, a set of parts of the assembly $PSet(x)$ as input. In the procedure, assembly sequences are represented by AND/OR graph, the nodes in the AND/OR graph correspond to subassemblies which are represented by OBDD, and the hyperarcs correspond to assembly tasks in which two subassemblies are joined to yield a larger more complex subassembly.

<pre> GAAS($C(x,y)$, $T(x,y)$, $PSet(x)$) { 1 $open=PSet(x)$; 2 $closed=\emptyset$; 3 while ($open$ is not empty) { 4 $V_1(x)=Pop(open)$; 5 $Push(closed, V_1(x))$; 6 $L(x,y)=Generate_Vertex_Induced_Subgraph($ $V_1(x), C(x,y))$; 7 $seed(x)=Pick_One_Minterm(V_1(x))$; 8 $clist=Find_Connected_Subgraphs_Include_Seed$ $(seed(x), L(x,y))$; 9 while($clist$ is not empty) { 10 $s_1(x)=Pop(clist)$; 11 $s_2(x)=V_1(x)-s_1(x)$; 12 $G_2(x,y)=Generate_Vertex_Induced_Subgraph$ $(s_2(x), L(x,y))$; </pre>	<pre> 13 $CFlag=Check_Connection(G_2(x,y))$; 14 if($CFlag$) { 15 $GFlag=Check_Geometrical_Feasible($ $s_1(x), s_2(x), T(x,y))$; 16 if($GFlag$) { 17 $Insert_Assemble_Task(s_1(x), s_2(x), V_1(x),$ $and_or_graph)$; 18 $Insert_Subassembly(s_1(x), s_2(x), open,$ $closed)$; } } } } return(and_or_graph); } </pre>
---	---

Fig.3 Pesudo-code for generating all assembly sequence

Procedure GAAS uses the lists *closed* and *open* to store the pointers to OBDD of the subassembly whose decompositions into smaller subassemblies, respectively, have and have not been generated. The procedure takes one subassembly from *open* at a time, moves it to *closed*, and calls procedure `Generate_Vertex_Induced_Subgraph()` in line 6 to generate the induced subgraph of vertex set which corresponding to the set of parts in subassembly. Given graph $C(x,y)$ and vertex set $v_1(x)$, the induced subgraph $L(x,y)$ of vertex set $v_1(x)$ is computed as follows:

$$L(x,y)=V_1(x) \wedge C(x,y) \wedge V_1(y). \quad (2)$$

After that, procedure `Pick_One_Minterm()` in line 7 is called to pick one minterm from the OBDD $V_1(x)$, and then the procedure `Find_Connected_Subgraphs_Include_Seed()` in line 8 is called to find all connected subgraphs which include vertex $seed(x)$ in the subgraph $L(x,y)$, and all connected subgraphs's vertex sets are stored in the list *clist*. In the procedure, subgraph $L(x,y)+L(y,x)$ is visited in a breadth-first search (BFS) manner which starts from the seed vertex $seed(x)$, the vertices reached for the first time and not in $seed(x)$ is store in BDD $t(x)$. For each minterm $m(x)$ of $t(x)$, let $r(x)=seed(x)+m(x)$, so the induced subgraph for $r(x)$ is a connected graph, vertices $r(x)$ is inserted into connected subgraph list *clist*. After that, let $r(x)$ is a seed vertex, and repeats the above method until BFS is performed $n-1$ times (n is the number of parts in the assembly). Thus, we get all connected subgraphs with $1,2,3,\dots,n-1$ vertices (there may be no such subgraph with i vertices, $2 \leq i \leq n-1$) respectively, and all of these include vertices $seed(x)$.

For the liaison graph shown in Fig.1b, we suppose initial value of the $seed(x)$ is 1 (for convenience, we use part's number to represent its OBDD), all connected subgraphs with $seed(x)$ are found as follows: Starting from $seed$, the liaison graph is traversed in a BFS manner, we will get the set of vertices $t=\{2,4,5\}$ reachable from the $seed$ in 1 step, thus all the connected graphs with 2 vertices which include $seed$ are found, namely the induced subgraph of vertex set $\{1,2\}$, $\{1,4\}$ and $\{1,5\}$ are connected graphs. After that, we set the above vertex sets to $seed$ one by one, suppose we first set $seed=\{1,2\}$, then starting from $\{1,2\}$, the liaison graph is traversed in a BFS manner, we will get the set of vertices t reachable from the $\{1,2\}$ in 1 step, where $t=\{4,5\}$ in which the vertices in $seed$ is already removed. Thus we will get all the connected graphs with 3 vertices which include $seed$ $\{1,2\}$, namely the induced connected graph of vertices $\{1,2,4\}$ and $\{1,2,5\}$. For the same reason, when we choose $seed=\{1,4\}$, we will get the induced connected graph of vertices $\{1,4,5\}$ and $\{1,3,4\}$, and so on, at last we get all connected subgraphs of liaison graph which induced by vertices $\{1\}$, $\{1,2\}$, $\{1,4\}$, $\{1,5\}$, $\{1,2,4\}$, $\{1,2,5\}$, $\{1,4,5\}$, $\{1,3,4\}$, $\{1,3,5\}$, $\{1,5,6\}$, $\{1,2,4,5\}$, $\{1,2,3,4\}$, $\{1,2,3,5\}$, $\{1,2,5,6\}$, $\{1,3,4,5\}$, $\{1,4,5,6\}$, $\{1,3,4,6\}$, $\{1,3,5,6\}$, $\{1,2,3,4,5\}$, $\{1,2,4,5,6\}$, $\{1,2,3,4,6\}$, $\{1,2,3,5,6\}$ and $\{1,3,4,5,6\}$, and all of these are inserted into *clist*.

For each vertices set in *clist*, it need to check the feasibility of decompositions, which include two step, one step is check connectivity, the other step is check geometrical feasibility. If the decomposition is feasible, then insert the assembly task into AND/OR graph *and_or_graph*, and if the subassembly is not in the list *open* or *closed*, then put subassembly on the list *open*.

For example, for induced connected subgraph of vertices $\{1\}$, compute another subgraph with vertices $\{1,2,3,4,5,6\}-\{1\}=\{2,3,4,5,6\}$, and then check whether or not the decomposition of $\{1,2,3,4,5,6\}$ into $\{1\}$ and $\{2,3,4,5,6\}$ is feasible. Firstly, procedure `Check_Connection()` in line 13 is used to check the connectivity of the induced graph of $\{2,3,4,5,6\}$. If the result is connected then return *true*, else return *false*. Because the procedure returns true, the induced graph of $\{2,3,4,5,6\}$ is a connected graph. The decomposition of an assembly into $s_1(x)=\{1\}$ and $s_2(x)=\{2,3,4,5,6\}$ is corresponding to a cut-set of liaison graph. Secondly, the procedure `Check_Geometrical_Feasible()` in line 15 is used to check geometrical feasibility for subassembly $s_1(x)$ and subassembly $s_2(x)$. If subassemblies $s_1(x)$ and $s_2(x)$ are geometrically feasible, insert the assembly task into AND/OR graph *and_or_graph*, i.e., $\{1\}$ and $\{2,3,4,5,6\}$ are geometrically feasible. If the geometrically feasible subassembly is not in the list *open* or *closed*, insert subassembly into *open*, so subassemblies $\{1\}$ and $\{2,3,4,5,6\}$ are both inserted into *open*.

Experiments

The symbolic algorithms proposed in this paper have been implemented in windows XP and the software package CUDD [12]. Geometrically feasible assembly sequences of some applicable assemblies, such as assembly shown in Fig.1 and electrical controller (Fig.4), were generated by the prototype tool GAAS using Microsoft Visual C++. In both cases, GAAS are run on a P4 3GHz with 512MB of memory. For the assembly shown in Fig.1, the AND/OR graph for that product contains 44 nodes and 133 hyperarcs, and the CPU time is 0.031 seconds for generating all assembly sequences. In electrical controller case, the AND/OR graph for the product contains 1530 nodes and 9659 hyperarcs, and the CPU time is 871.359 seconds for generating all assembly sequences.

Conclusions

A symbolic OBDD algorithm for generating mechanical assembly sequence is presented based on Sharafat's recursive contraction algorithm and cut-set decomposition method. The geometrically feasible assembly sequences are verified and generated symbolically and implicitly using efficient OBDD structures and manipulations. Some applicable experiments show that the novel algorithm can generate feasible assembly sequences correctly and completely.

Acknowledgments

This work has been supported by National Natural Science Foundation of China (60963010, 60903079, 61063002) and Key Natural Science Foundation of Guangxi Province (0832006Z).

References

- [1] D.F. Baldwin, T.E. Abell, M.M.Lui, et al.: IEEE transactions on Robotics and Automation. Vol. 7(1991), p.78
- [2] L.S. Homen de Mello, A.C.Sanderson: IEEE Transaction on Robotics and Automation. Vol. 7(1991), p.228
- [3] A.R. Sharafat, O.R. Ma'rouzi: A novel and efficient algorithm for scanning all minimal cutsets of a graph. ArXiv preprint math. CO/0211436 (2002).
- [4] R. Drechsler, D. Sieling: International Journal on Software Tools for Technology Transfer. Vol. 3(2001), p. 112
- [5] R.E. Bryant: ACM Computing Surveys.Vol. 24(1992), p. 293
- [6] G.D. Hachtel, F.Somenzi: Formal Methods in System Design. Vol. 10(1997), p.207
- [7] T.Gu, Z. Xu , Z.Yang: Computer-Aided Design, Vol. 40(2008), p.411
- [8] T.Gu, H.Liu: Formal Methods in System Design, Vol. 33(2008), p.29
- [9] Z.Xu, T.Gu: Journal of Computer-Aided Design & Computer Graphics, Vol. 22(2010), p.803(In Chinese)
- [10] R.B. Gottipolu, K. Ghosh: Computers in Industry. Vol. 50(2003), p.251
- [11] S. Minato, N.Ishiu, S. Yajima: Proceedings of the 27th ACM/IEEE Design Automation Conference, New York, 1990, p.52
- [12] F. Somenzi. CUDD:CU Decision Diagram Package Release 2.3.1. <http://vlsi.Colorado.edu/>.

The Analysis of the Temperature Field and Deformation of Cylinder Liner Base on Finite Element Method and Experiment

Kun Li^a, Tiexiong Su^b, Xiaojie Li, Shixin Xing

School of Mechanical and Electronic Engineering, North University of China, Taiyuan 030051 China

^a fendou1981@tom.com, ^b sutiexiong@nuc.edu.cn

Keywords: Cylinder Liner; Temperature Field; Deformation; Finite Element Method; Experiment

Abstract. The distortion of the cylinder liners of internal combustion engines has a significant affect on engine operation. It can affect the oil consumption, the blow-by, the wear behavior and, due to friction, the fuel consumption. In order to achieve future requirements regarding exhaust emissions and fuel consumption, the development of low distortion engine blocks will play a significant role. Finite element method with experimental data were used to calculate and analysis the temperature field and machine assembly of a 150 engine cylinder liner in this paper. It can provide a theoretical basis for the controlling of the cylinder liner deformation.

Introduction

The internal combustion engine combustion chamber is formed by the cylinder head, piston, cylinder liner and piston rings. Modern passenger car engines are designed to operate increasingly higher rated engine speeds with higher thermal loads. To reduce engine weight and length, the heat load of the engine will become more and more baptismally. This leads to high temperatures in the siamesed area and to an increase in liner deformation. The deformation of the cylinder liner could damage the piston rings seal, and further affects the engine's economy, power and emissions characteristics [1-2]. To reduce the cylinder liner deformation can reduced radial clearance between piston and cylinder bore. This can reduce the impact of the piston to the cylinder liner and reduce the vibration and noise of the engine. The method of cylinder deformation measurement be combined with the FEM calculations for the crankcase is an effective and cost-reducing tool.

Three-Dimensional solid model and Fem-Calculations model

The finite element calculation method is based on the three-dimensional solid models. The three-dimensional solid models are concluded by the bearing caps, crankshaft, main bearings, cylinder head, cylinder liner, cylinder head gasket, cylinder head bolts, bearing cap bolts and so on. The three-dimensional solid models are shown as figure1 and figure2. The Combined model is shown as figure3. The component materials are shown as Table 1.

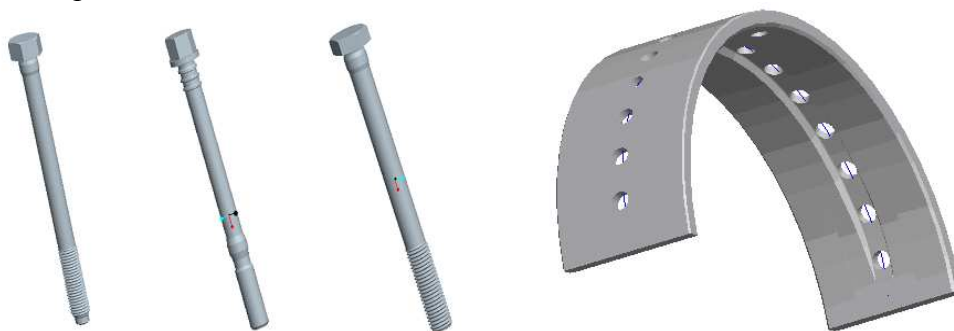


Figure1. The cylinder head bolts model and Main bearing model

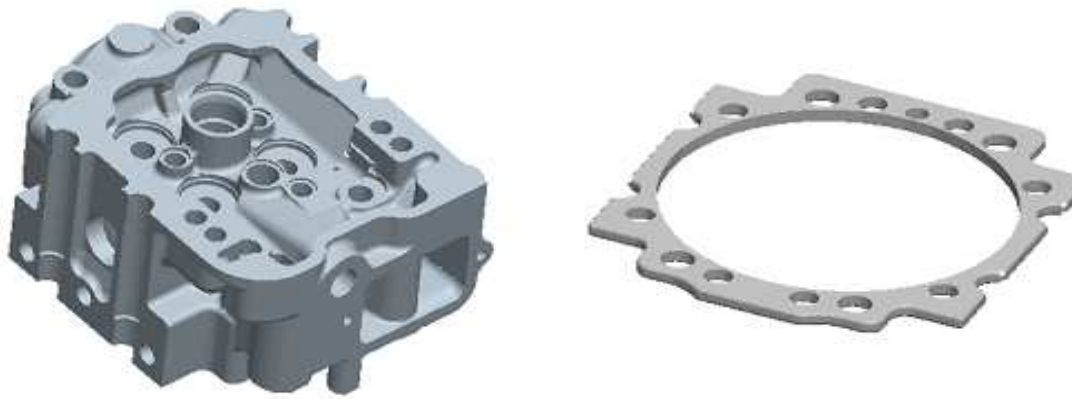


Figure2. The cylinder Head model and cylinder head gasket model

The finite element analysis boundary conditions

It is important to provide accurate boundary conditions for a bore distortion calculation. Some simplifications are made to reduce the calculation time.

2.1 The displacement boundary conditions

The rigid body displacement constraints; body, cylinder, cylinder head, crankshaft, cylinder gasket, main bearing caps the cut surface of symmetry displacement constraints.

2.2 The contact boundary conditions

The model established the contact boundary conditions between the cylinder head and cylinder gasket, cylinder and cylinder gasket, cylinder liner and the body, the body with the main bearing caps, crank and block, crankshaft and main bearing caps and bolts and the body, cylinder head and main bearing caps.

2.3 The force boundary conditions

The loads acting on the liner come from a variety of conditions, for example: Assembly of the cylinder head and cylinder head gasket (assembly loads); Thermal expansion variations between the cylinder block and cylinder head; Gas pressure during fired operation Temperature gradients during fired operation. All of them are stated as Table 2 and Table 3.

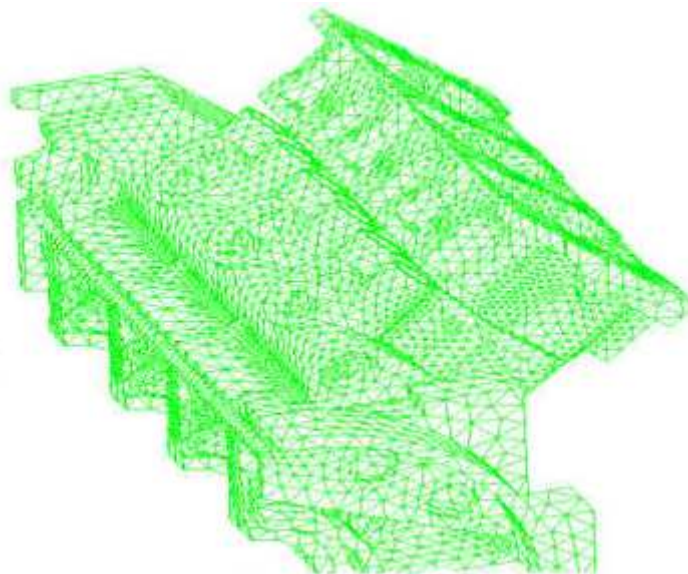


Figure 3. The combined finite element model of half-body

Table1. The material of the solid models

The part	The material
Engine block	QT500-7
Main bearing cap	42CrMo
Bolts	42CrMo
Cylinder liner	Cr-Mo cast iron copper
Rubber sealing ring	Viton
Cylinder head	Special cast iron
Cylinder head gasket	ZL301

Table 2 The size of the bolt preload (unit: N)

The preload of the inside main bearing cap bolt	63269N
The preload of the outside main bearing cap bolt	44815N
Cylinder head bolt tightening force	134464N

Table 3 The forces of the left second cylinder when the engine outbreak (unit: N)

	The first cylinder	The second cylinder	The third cylinder
Gas pressure	2424	2.223e5	207.8
Connecting rod force	19671.8	186078.2	20417.2
Connecting rod force	-4863.8	6905.9	4290.4

The calculation of the cylinder temperature distribution

The temperature distribution along the height of the cylinder liner has regular. It is shown as formula 1 and formula 2.

$$\alpha_m(h) = \alpha_m(0) \cdot (1 + k_1\beta) \cdot e^{-\sqrt[3]{\beta}}; T_{res}(h) = T_{res}(0) \cdot (1 + k_2\beta) \cdot e^{-\sqrt{\beta}} \quad (1)$$

$$\text{Which: } \beta = h/s (0 \leq \beta \leq 1), k_1 = 0.573(S/D)^{0.24}, k_2 = 1.45k_1 \quad (2)$$

where is the average heat transfer coefficient of gas working cycle, is the average temperature of the gas work cycle, β is the ratio of the axial position h to the stroke S , k_1 is the average temperature of gas equivalent, k_2 is the average heat transfer coefficient of gas equivalent.

All of the significant aspects of thermal heat flux and material behavior must be considered. The flux from the piston and gas to the liner—a combustion simulation program, that is based on the Woschni equations shown as formula 1 and formula 2, calculates the piston thermal load. The average gas temperatures shown as Figure4, and the heat transfer coefficients (HTC) from the gas to the liner as a function of cylinder height shown as Figure 5 [3-4]. These boundary conditions are applied to the gas side. The input data to the combustion simulation program are improved by the experience from measured and calculated temperatures. The assumed wall temperatures have a great influence on the resulting thermal heat flow. An iterative procedure is necessary. The temperature nephogram of the cylinder liner by simulating is shown as Figure6. The temperature distribution along the wall of the cylinder as shown as Figure7.

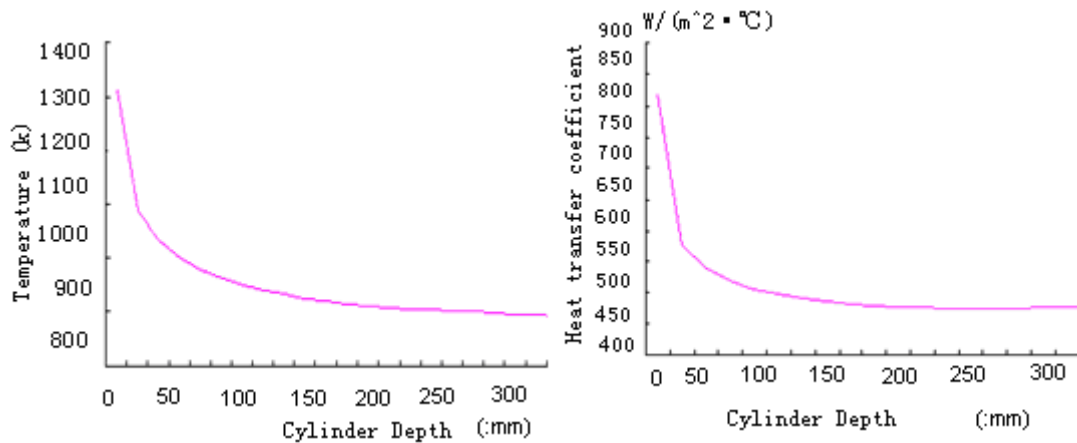


Figure 4. The average temperature of the gas along the cylinder height. Figure 5. The average heat transfer coefficient along the cylinder height .

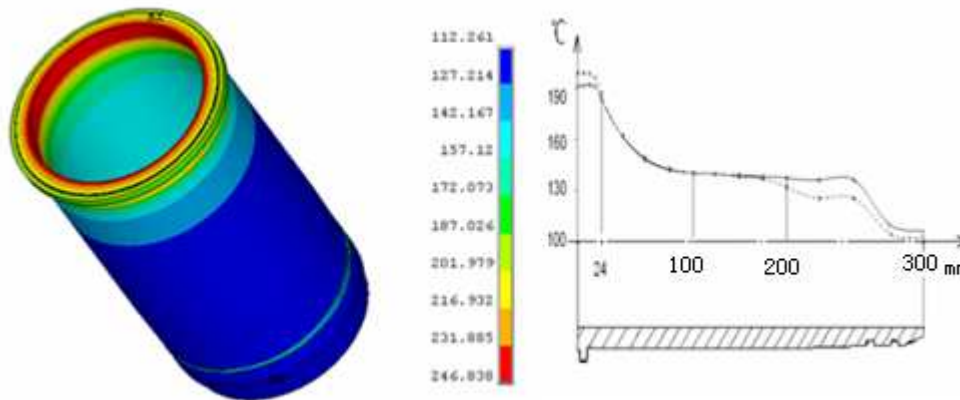


Figure 6. The temperature cloud of the cylinder liner . Figure 7. The temperature distribution along the wall of the cylinder .

The calculation and analysis of the cylinder deformation under thermo-mechanical coupling

The deformations of the engine body and cylinder liner under Thermo-mechanical coupling are calculated by finite element methods. Based on the Large-scale commercial software ANSYS .Take the temperature filed Calculated by the 3 as the boundary conditions in the computing environment. Set the relevant boundary conditions, such as 2.1-2.3 above. The deformation and stress of the engine body and cylinder liner are shown as Figure 8- Figure 11.

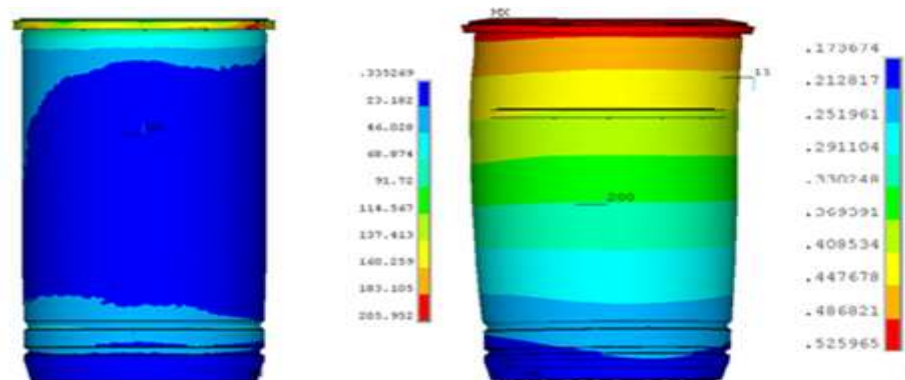


Figure 8. The equivalent stress contour of cylinder. Figure 9. The overall deformation cloud of cylinder

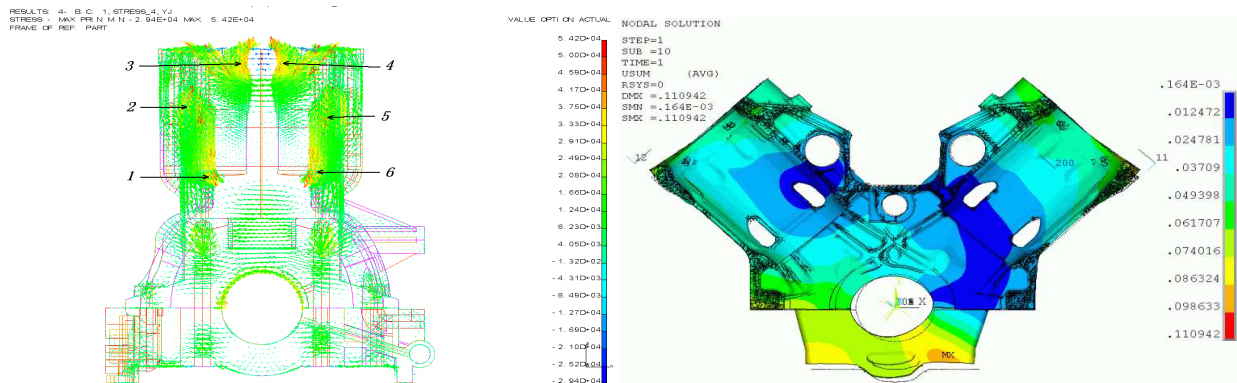


Figure10. The maximum principal stress under thermo-mechanical coupling. Figure11. The deformation of the engine body under thermo-mechanical coupling.

Experiments arrangement and the results compared

The validation of Finite Element Analysis results by measurement is important with respect to the reliability of predictive thermo-mechanical analysis; therefore, verifications are indispensable. In the following text, the measurements are carried out on a 12V150 diesel engine. Strain gauges are attached to the corresponding position of the cylinder and the engine body. The strain gauges can measure the deformation, when the engine cold-static, tensioned. The measurement of the liner geometry is performed after assembling the cylinder head and the cylinder head gasket. This gives reference to the tension after engine assembly and enables one to evaluate the influence of the bolt forces on the liner distortion. They also can measure the deformation when the engine fired. The cylinder contour will be scanned, corresponding to the stroke movement of the piston. This requires the installation of up to 8 eddy current sensors in the production piston of the engine. The arranged of the strain gauges as shown in Figure12.

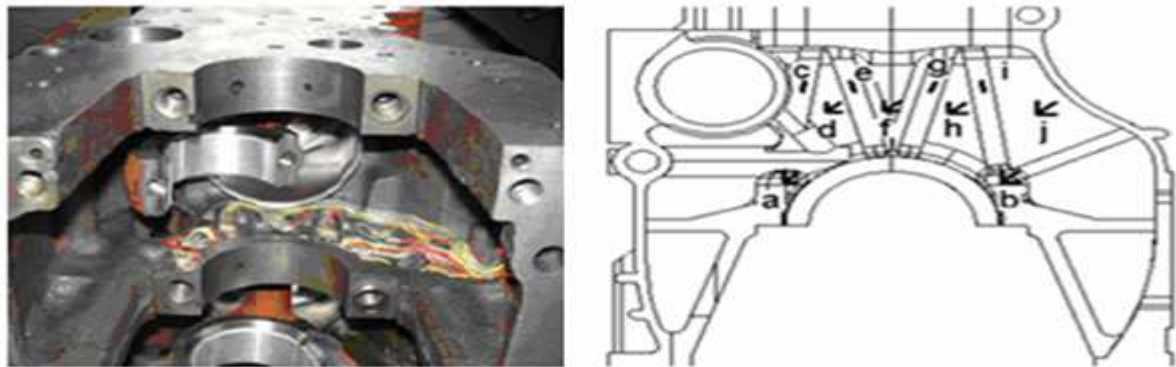


Figure12. The arrangement of the strain gauges

The method presented here for measuring cylinder deformation in operational fired engines represents a suitable tool for adapting the tribological system piston/piston ring/cylinder liner to future requirements [5]. These measurements are also of significant value in calibrating analytical models, enhancing the accuracy and reliability of subsequent analysis. The comparison of the Measurement results and FEA results are shown in Figure 13 and Figure 14.

The FEA results and experimental results show good agreement. In other words, the finite element model and boundary condition settings are correct. The trend that the results of the cylinder liner deformation performance are reliable. Analysis conclusion based on the results obtained by the finite element method is credible.

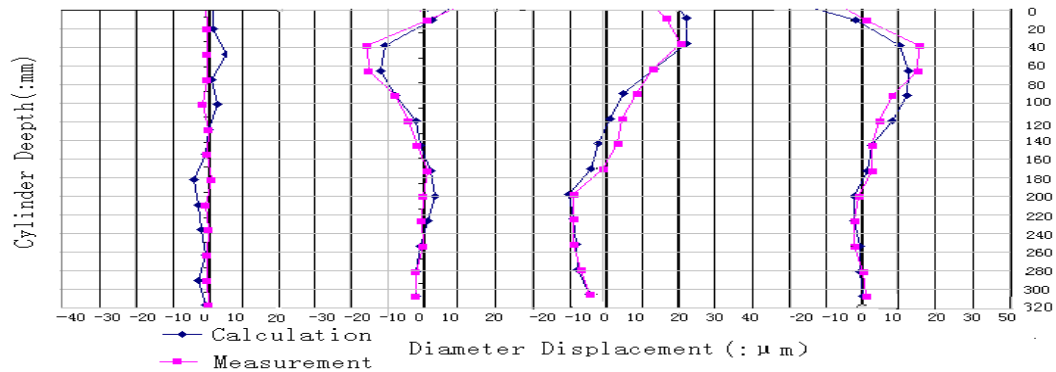


Figure13. Calculated and Measured Bore Distortion, Cold Assembly

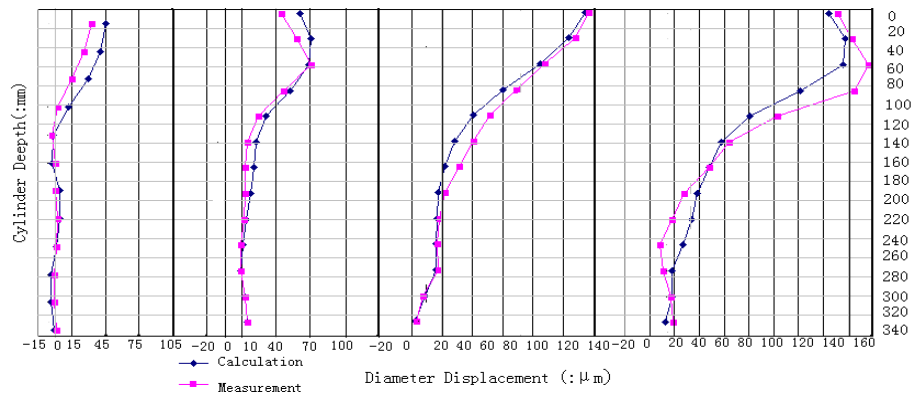


Figure14. Calculated and Measured Bore Distortion, Loads at 5000 rpm, WOT

Conclusions

1. Cylinder temperature decreased gradually from top to bottom, the maximum temperature of 200 °C, the internal wall temperature is higher than outside. Heat transfer coefficient has important implications on the cylinder temperature distribution.
2. Cold-static, and after assembling the cylinder head and the cylinder head gasket. The bolt forces depth has some influence on the deformation of the cylinder liner.
3. Cylinder radial deformation increases, the coupling effect in the heat, when the engine fired under thermo-mechanical coupling. The deformation of the piston thrust side significantly higher than the other side.
4. Control the deformation of the engine block can reduce the deformation of the cylinder liner.

References

- [1] Grogeneweg M.A. Current Application of Finite Element Analysis to Diesel Engine Component Design [J].SAE Paper 870813.
- [2] Gilson A.Vicentini, Jan Vatauvuk. Study of Sea Transportation Effects on Corrosion of Cast Iron Cylinder Liners [J].SAE Paper 2001-01-3978.
- [3] Pranz Koch, Poul Decker. Cylinder Liner Deformation Analysis-measurements And Calculation [J] .SAE Paper 980567.
- [4] J.Abraham, D.R Amoth,J.Mannisto.3D Steady-State Wall Heat Fluxes and Thermal Analysis of a Stratified-Charge Rotary Engine [J].SAE Paper 910706.
- [5] Yang Shiwen , Zhang Yi , Su Tiexiong , et al. Distortion analysis and structural parameters optimization of cylinder liner of heavy duty diesel engines[J] . Chinese Internal Combustion Engine Engineering, 2003, 24 (2) : 252 29. (in Chinese).

Problems in the Application of Commercial CAD/CAE Software and Improvement Methods

Cheng Wang ^a, Xiongwei Yang ^b and Baokun Yang ^c

Key Laboratory for Strength and Vibration of Mechanical Structures, Xi'an Jiaotong University, Xi'an 710049 China

^awc071@163.com, ^b xiongwei@stu.xjtu.edu.cn, ^cyang.bk@stu.xjtu.edu.cn

Keywords: CAD/CAE; Commercial Software; Problems; Software engineer; Improvement Methods.

Abstract. CAD / CAE technology has led traditional product design and analysis to digital. However, commercial CAD / CAE software also has its problems. Problems in the application of commercial CAD / CAE software are summarized in these this paper. From perspective development of software engineer, new technology such as integrated design, design reuse, intelligence and automation, workflow customization, application development, experimental and simulation complement each other are introduced to overcome these problems in this paper.

Introduction

With the development and application of computer, CAD / CAE technology has led a revolution in product design and analysis. Traditional design-prototype performance testing- manufacturing techniques process is difficult to adapt modern production requirements. Using computer systems, CAD / CAE technology provides a reliable guarantee for enterprise to improve product design capabilities, shorten product research and development cycles, and improve product performance. It is an integrated environment oriented to product design, analysis and management, and also a new measure to reconstruct traditional industry and improve technological innovation as well as technical strength. From global R&D, simulation accounts for a significant large proportion and plays a more and more important role. Design and analysis of a great number of foreign companies rely on simulation. For example, Boeing has realized the digital design of Boeing aircraft.

From the perspective of CAD / CAE users, many problems exist in the application of commercial CAD/CAE software for digital design at present. Problems in the application of commercial CAD / CAE software are summarized in these this paper.

From perspective development of software engineer, new technology such as integrated design[1], design reuse[2], intelligence and automation[3], workflow customization, application development [4], experimental and simulation complement each other are introduced to overcome these problems in the application of commercial CAD / CAE software in this paper.

Problems in the Application of CAD/CAE Commercial Software

Difficulties of Information Transmission among Software. The process of CAD / CAE is divided into several steps, and each different step uses different commercial software. In order to achieve efficient and fast access, most commercial software adopt private and incompatible binary file format to achieve efficient and fast access, which results in information transmission difficulty among different software. However, the same model needs to be modified in the application of different software, which brings forward heavy workload and is highly fallible.

Difficulties in Guarantee Accuracy of Simulation Results Page. The core principles and algorithm of commercial software are trade secrets, and are not open to the public. The accuracy of simulation results depend on familiarity with software kernel. At the same time, in pursuit of general-utility, a lot of parameters need to be set in commercial software, but any parameter setting

mistake may greatly affect the simulation results, which is a too high starting point for an engineer who has rare experience.

Difficulties in Fulfilling the Individuation Requirements of Enterprises. Commercial CAD/CAE Software pursues general-utility, while the actual situations of each enterprise and application requirements vary. It is very difficult to establish a unified platform to meet the application under various conditions. And the situations that commercial software does not meet demand of the enterprise frequently emerge. Because of the limitations of algorithm adopted by commercial software, there exists computing capability and suitable application bound limit in dealing with engineering practice issues; It is also very difficult to debug when error emerge. The situation of commercial software does not meet the enterprise demand must Emerge.

Improvement Methods

Integrated Design. CAD/CAE integrated design can realize the share of information and model, maintain the unity of data and improve the efficiency of information transformation. A CAD / CAE integrated software platform with unified file format standard and use style, groupware and modular design and sales mode, user-friendly, will be suitable for the working habits of the technical personnel. And it will also reduce the time to learn and get familiar with machinery construction and minimize the difficulty in training. The framework of CAD / CAE integrated software platform is shown as in Figure 1.

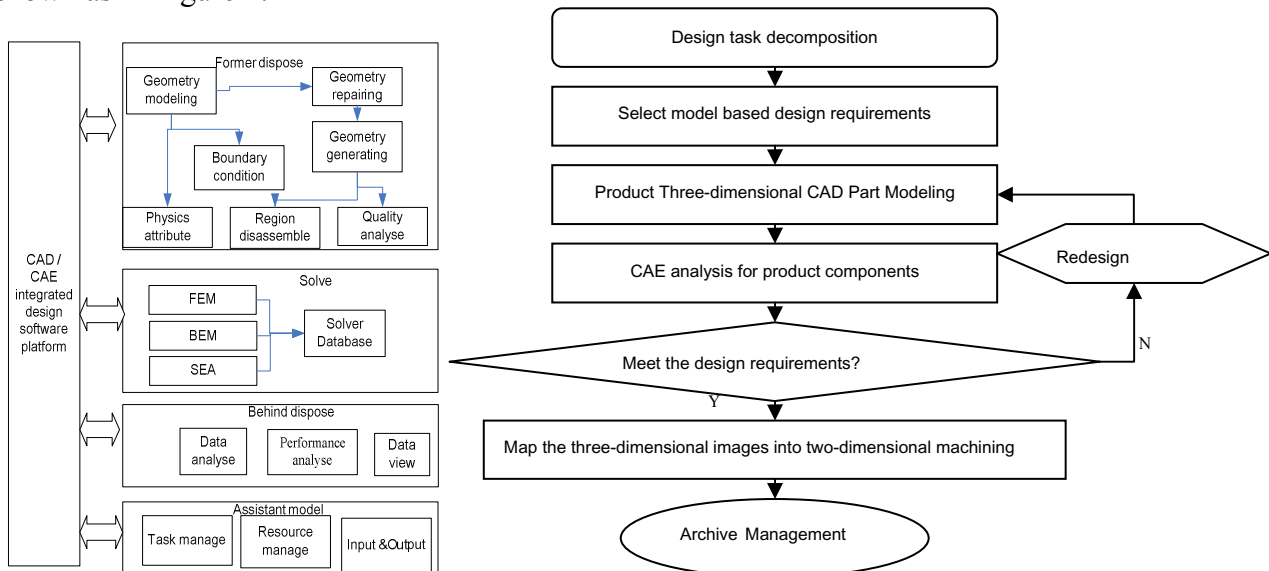


Figure 1: CAD / CAE integrated design software platform Figure 2: Integrated design flow of CAD / CAE

CAD / CAE integrated design process is shown in Figure 2. Various performance, strength, reliability and durability of mechanical equipment can be calculated and analyzed as early as in product development stage. Possible problems can be discovered and solved in product research and development stage. This will shorten product design cycles, save development costs, improve product design quality and ensure product reliability.

Cultivating Compound Talents. Elements of simulation design activities are shown in Figure 3. CAD / CAE software are used by engineers and researchers finally. So the integrated design idea also needs to be implemented by them. Thus, the key factor of digital design is cultivating compound talents with plenty of relative knowledge and experience.

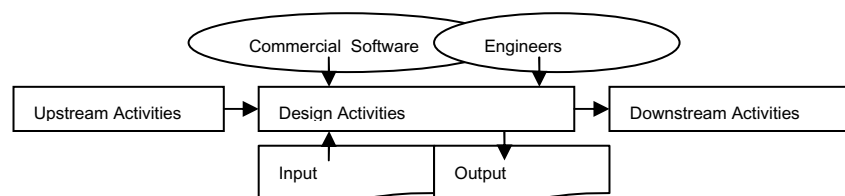


Figure 3: Elements of simulation design activities

Integrated design requests engineers to perfect knowledge systems and accumulate experience. Take the servo valve CAD/CAE integrate design with computational fluid dynamics method for example. The designers are required to be familiar with operating performance and internal flow of hydraulic valve in the hydraulic system.

Experimental and Simulation Complement Each Other. Known from figure 3, digital design cannot carry through without experimental support, which is determined by the problem itself completely. Because digital design is the process of accumulation of user's knowledge gradually, all-digital design is impractical and unnecessary. For example, input parameters of finite element model, such as damping coefficient, damping ratio must come from experimental or engineering experience.

Experiment and simulation are complementary relationship: simulation can replace some experiments to some extent. Simulation could provide the basis for design and improvement of experiment. This will reduce costs and shorten the cycle of research and development. On the other hand, experiment provides input parameters and validates the results for simulation. In the future, experiments are not independent behavior but vital factor that will promote the whole R&D process.

Design Reuse. In new product development process, design reuse technology should be used to make full use of existing business design resources and reduce duplication of development work. For example, the designers could establish standard parts warehouse and the user model base, standard material library and user material library to avoid design duplication, such as: the establishment of bolted parts library, experiment shaking table model base and fixture warehouse. Engineering design and processing graphs should be managed on file. And it is also necessary to establish the user knowledge base. These activities will provide documentation for use restraint and guide the engineering experience.

Intelligence and Automation. The aim of digital is to improve the design efficiency and release human from the heavy repeat work. Therefore, users should make full use of design approach supplied by intelligent, automatic and "fool-style" software. The design approaches include automatic optimization design, structure optimization, parameter optimization design, mesh generation optimization and dynamic stiffness optimization, and so on. With the assistance of these methods, the users will reduce the settings and operations and finally the possibility of making errors. Commercial software generally provides users with two different modes of common operations, as shown in Table 1. The common users firstly complete initial design through a GUI operation. Then experts execute professional optimization with the high-level commands.

Table 1: Two different operation modes supported by commercial software

operation mode	GUI	advanced command stream
user features	weak professional knowledge, less engineering experience, not familiar with software	rich of professional knowledge and engineering experience, familiar with software
operation features	imagery, intuitive, easy to operate, fool-based GUI interface, little user settings and operation, user actions limited	command-line operation, powerful, multi-user settings and operation, user actions unlimited, error-prone
application scope	simple engineering problems, suitable for beginners	specific problems, professional design,, optimization

Workflow Customization and Application development. Open Workflow Architecture of Commercial Software allows user to execute "individual customization" of process accordance with requirements. Enterprises can solidify engineering design, experimental results and parameter settings, and form a clear workflow.

According to characteristics and industrial application requirements, enterprise should make application development based on a full absorption of the introduced business software. It is known from table 2, as long as the choice and application of development method is proper, application development could not only absorb the latest achievements of engineering practice and scientific

research, but can also inherit the advantages ,while avoiding the disadvantages of complete independent software development.

Table 2: Compared between application development and complete independent software development form

development approach	implementation method	scope	advantage	disadvantage
application development	1)using the application development interface, tool and language, built based on commercial software ; 2)according to user's needs, customizing new module, and achieving new algorithm	1)software localize and customization; 2)applications extended, engineering practice experience formal; 3)implement and integrate new algorithms	1)seamless integration with business software and exchange; 2)operation stable; 3)short development cycle, less technical and resource devotion	functionality and performance largely depend on capabilities and openness of the commercial platform
complete independent software development	beginning from zero, completely building all modules with high-level language	bringing the latest scientific research algorithms into application software	1) suitable for highly complicated and exceptions 2) complete intellectual property rights; 3)professional, efficient; 4)customizable output, debugging	1)difficult comprehensive investigation;; 2)difficult with commercial software, with weak market competitiveness; 3)difficult realization of programming, 4)poor stability

Conclusions

The problems in use of commercial CAD / CAE software are summarized in this paper generally. Digitalization is a long and complex process which needs experience accumulation and perpetual improvement. Only with hard exploration and the aforementioned way of unremitting improvement according to actual circumstances, can CAD / CAE software meet individual requirements of enterprise and maximize its efficiency.

Future research directions include a wider range of process integration and collaboration, development direction and technical difficulties of commercial CAD / CAE software.

References

- [1] Bor-Tsuen Lin and Chun-Chih Kuo. The International Journal of Advanced Manufacturing Technology. Volume 35, Numbers 9-10, 1000-1013, 2008.
- [2] Xiao-xia LIN, Shu-you ZHANG, Jing CHEN, Zhen ZHAO. Computer Integrated Manufacturing Systems. 2296-2302,2009 -12(In Chinese).
- [3]Terzic, I., Zoitl, A., Favre, B., Strasser, T.. A survey of distributed intelligence in automation in European industry, research and market. Emerging Technologies and Factory Automation, 2008. ETFA 2008. IEEE International Conference on.
- [4] AJ Albrecht, JE Gaffney Jr.Software Function, Source Lines of Code, and Development Effort Prediction: A Software Science Validation Software Engineering, IEEE Transactions on 2006 - ieeexplore.ieee.org.

A Method of Machining Region Planning for Tyre Tread Mold Machining

Jiansheng Liu^a, Haining Tu^b, Fangchen Xia^c, Junxing Xiong^d

School of Mechanical and Electronic Engineering, Nanchang University, Nanchang
,Jiangxi,330031,China

^avictorljs@163.com, ^bcthn@163.com, ^ccxfc@163.com, ^djx811217@163.com

Keywords: Tyre Mold; Machining Region Planning; Inner and Outer Contour Recognition

Abstract. To satisfy the manufacturing requirement of tyre tread pattern mold, the problem of machining region planning in the computer aided manufacturing of tyre mold is introduced. And it is analyzed that the core technology is the definition of inner and outer contours for machining region planning and tool-path planning. According to the defect of traditional constructed way of machining region, an auto recognition method of inner and outer contour is studied based on the inclusive test method. The detail step of the method is illustrated. Thinking about the special condition of the method, corresponding strategy is given. This method is applied in the computer aided manufacturing of tyre tread mold, by which machining region planning can be solved effectively.

Introduction

Automobile tyre enterprises progresses with each passing day, and new product emerges one after another. Tyre mold is one important process equipment for tyre manufacturing, which plays very role for product quality. The manufacturing tendency of tyre mold is NC manufacturing, so only by the CAD/CAM can tyre mold succeed in improving the quality and cycle-time reduction. Relative paper, for examples, Cavity surface construction of tyre tread pattern mold and its finish machining[1], Application of CAD/CAM Technology in Engraving Letter on Tire Mold Sidewall[2]. In the current CAM software, machining region planning is done by the way of selecting the contour boundary one by one. Efficiency is low for this method, and it is easy to do wrong. In this paper, taking the case of tyre tread mold, a method of machining region planning is provided for tool-path planning.

Tyre Tread Types and Its Machining Method

Tyre tread types include letters, Chinese character, arabic number and company logo. There are two sorts of tread pattern in tyre mold, which include solid pattern and hollow pattern. According to the character of machining region, solid pattern can divided into single-line solid pattern and wide solid pattern. The same as solid pattern, hollow pattern can also divided into single-line hollow pattern and wide hollow pattern. The detail explain is as following.

Single-line Solid Pattern. It consists of arabic number and letter. The pattern whose line-width is less than 1mm can be defined as single-line solid pattern. In CAD model, patten geometry model contains contour line and center line. Center line is basis of machining-path, and that contour line is only to check. The left part in the fig.1 is CAD model of letter “A”, in which the black line is contour line, and the red line is center line. The right part in the fig.1 is machining result(following is the same as).

Wide Solid Pattern. The pattern whose line-width is more than 1mm belongs to wide solid pattern. Its geometry model includes inner contour and outer contour. In generally, tool-path planning of this pattern is by the way of inner contour offset and outer contour offset. Its CAD model and machining result are shown as fig.2.

Single-line Hollow Pattern. The width of machining region is less than 1mm in this pattern. And its machining method is to finish machining along with center line of pattern contour only once. Center line is basis of machining-path, and that contour line is only to check. Its CAD model and machining result are shown as fig 3.

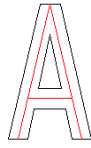


Fig.1 Single-line solid pattern



Fig.2 Wide solid Pattern



Fig.3 Single-line hollow pattern



Fig.4 Wide hollow pattern

Wwide Hollow Pattern. Its geometry model consists of inner contour and outer contour. Inner contour and outer contour offset based on fix width. Inner contour offsets toward outer, and out contour offsets toward inner. Then new contour is got. Its CAD model and machining result are shown as fig 4.

Description of Machining Region

The machining way can be divided into the surface machining and the single-line machining, in accordance with the different machining methods. For example, number pattern belongs to single-line machining, that is to finish machining along with the contour only once. Otherwise, most solid patterns and wide hollow patterns adapt to the surface machining. Tool path planning can be satisfied for the single-line machining as long as the structure of contour is known. And for the surface machining, we should get the cutter location points and its step at first, then the tool path of outer contour offset inward and inner contour offset outward step by step. Therefore the core problem for tyre pattern machining is tool-path planning by offset of inner and outer contour.

Machining Region Recognition Algorithm

In the field of computer graphics, contour is defined as surface boundary, and surface is the region enclosed by contour. A specific region is mostly enclosed by inner contours and outer contours or a single outline. In the fact process of mechanical machining, it aims at the machining region. The inner contour is the internal boundary of the machining region, the outer contour is the external boundary. So that, the identification of inner and outer contours is the basis of determining machining region.

A contour is an closed loop, which consists of segments or curves connected one by one. Maybe it exists inclusion relationship or intersection relationship between contours, so it is not good to judge the location relationship among contours. In this paper, strategy is to select one point on one contour. Then, the mutual position relationship between contours is obtained by determining the inclusion relation of this point in another contour. There are many algorithm about point in polygon testing, such as point in polygon testing [3], Orientation and Point Inclusion Test for Planar Polygon[4], A New Method Deciding Whether a Point is in a Polygon or a Polyhedron[5]. Line cross-point method is presented in this paper to decide whether a point is in one contour. Steps of the algorithm are as follows:

Step 1. Taking some points

A contour is an closed loop, which consists of lines or curves connected one by one. So, the first step is to take one point from some line of two contours.

Step 2. Getting a line from two points

Let one point as testing point getting from step 1. Then it is regard as starting point, and a line will get by connecting these two points

Step 3. Counting the number of intersection points

After calculating the intersection points between the line and the contour in which another point is in. the number of intersection points can be gotten.

Step 4. Determining the parity of the number;

Step 5. Determining whether the two related contours intersect or not;

Step 6. Judgement .

If the number of intersection points is the even, then the contour with the line starting point and this contour doesn't contain each other; if the number of intersection points is the odd number and the two contours don't intersect each other, then the contour with the starting point is the inner contour, the other related contour is the outer contour; If the number of intersection points is the odd number and the two contours intersect each other, then we define that the contour with the starting point and this contour doesn't contain each other.

In this line cross-point method, there are two special conditions. One is the line go through the vertices of another contour, such as point D in the fig.5. Another hand is the line coincide with some edge of another contour, such as point C in the fig.5. It is hard to judge parity.

For these two special conditions, in order to ensure the intersection between rays and contours, and avoid line through vertices or line coincide with some edge of contour polygon, points were selected the middle point of the No.1 line on each contours as test points, then auxiliary line for discrimination are made from one point as starting point to another one, the location relations are determined between every two contours. Another general strategy is to get another auxiliary line, connected by the middle points of No.2 line on each contour. Then the algorithm goes on from the step 3.

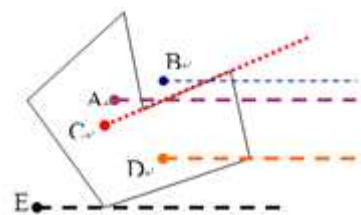


Fig.5 Special conditions about point in polygon testing



Fig.6 one machining region consisting of one outer contour and two inner contour

Application Example

Machining region of some numbers and logo patterns are composed by a outer contour and some inner contours. As shown in figure.6. Aiming at these conditions, it is to view all groups' outer contours after the information of machining groups is obtained. If a contour is many groups' outer contour, at the same time these groups' inner contours don't compose groups each other, then all of these related groups are defined as a machining region. Marking the machining region and recording its information, the single outer contour is the machining region outer boundary and the related inner contours compose its inner boundary.

Conclusions

It is tendency to apply CAD/CAM in the process of mold manufacturing. The description of machining region recognition is explained, and it points out that the basis is the definition algorithm of inner contour and outer contour. Based on point in polygon testing, a line cross-point method is given. For avoiding two special conditions in this method, some effective strategies are provided. The method is applied into fact mold manufacturing. The result shows that it does well in recognizing inclusion relationship between contours, and it can judge among any complex contour.

References

- [1] WANG Qian-ting, LIU Qiong, LIANG Xi-kun. Journal of Zhejiang University (Engineering Science). Vol. 40(2006), p309.
- [2] LI Shu, LI Ye. Contemporary Chemical Industry. Vol, 38(2009), p129.
- [3] YAO Xue-ying and CAI Ying-ji. Computer-aided Design and Manufacturing. Higher Education Publishing House, 2002.
- [4] LI Wei-Shi, LI Jiang-Xiong, KE Ying-Lin. Journal of Computer Aided Design and Computer Graphics, Vol 12(2000), p405.
- [5] WANG Wen-cheng¹, WU En-hua¹. Journal of Software, Vol, 11(2000), p114.

Finite Element Analysis of Laminating Press Frame

Xinzhou Zhang^a, Shangbin Wang^b, Kai Wu^c, Yu Sun^d

School of Mechanical Engineering, Nanjing University of Science & Technology,
Nanjing 210094, China

^azhangxinzhou1984@126.com, ^bwsbin@hotmail.com, ^cwukai@mail.njust.edu.cn,
^dsunyu@mail.njust.edu.cn

Keywords: Laminating Press; FEM; Static Analysis.

Abstract. The structural characteristics of a laminating press were analyzed, and the corresponding finite element model was built with some essential simplification. By structural analysis, the distributions of stress and strain were obtained, based on which the rationality of the frame design can be verified. According to the complex structure and loading conditions of the laminating press, four analytical schemes with different models and boundary conditions were adopted, then the results of different analytical schemes were compared, and the causes resulting in the calculation differences were analyzed. The result shows that in analyzing different parts of the laminating press frame, different models and boundary conditions were required.

Introduction

China is one of the countries with deficiency of forest resources. In recent years, as the architectural decoration and furniture industry grow fast, the domestic demand for lignum is increasing rapidly; as a result, the supply shortage of lignum becomes more and more serious. One of the effective ways to relieve such shortage is to depend on wood-based panel industry, which at the same time can save the lignum resources. With several years of rapid development, the domestic output of wood-based panel has been No.1 in the world for years.

Although China has become a country with great productive capacity of wood-based panel, there still exists some problems, such as structural irrationalities, lower technology, shortage of resources, low industrial centralization etc.. Especially in the innovations of product, technique, equipment and process technology, there are big gaps compared with some foreign countries [1].

The laminating press has a major application in secondary working for surface decoration (paper & veneer) of OSB & MDF/HDF, and the panels treated with the press can be used on furniture, interior finishes, laminate flooring and building. The press is the last actuator of the forming process of the wood-based panel and the rigidity and accuracy of the parts of the press affect directly the quality of the products. Therefore, the frame, one of the most important parts of the press, is the focus of the design in the entire assembly line.

Structural analysis of laminating press frame

The laminating press which bears the major load consists mainly of a frame, cylinders, a moving beam and hot pressboards. It has two types of structures: the combined structure and the integral structure. The combined structure, including upper beam, lower beam and upright column in the middle, is connected by bolts to form a rigid frame, or called column frame. The integral structure is to use a block of steel plate, or to weld together some pieces of steel into an integral frame, or called frame structure [2].

The structure of laminating press frame is shown in Fig.1. The laminating press frame consists of six frame plates or three frame groups (each frame group is formed with two frame plates). The three frame groups, which are fixed to the base, are also joined together with some bolts, and this kind of installation brings the structure a higher lateral rigidity [3].

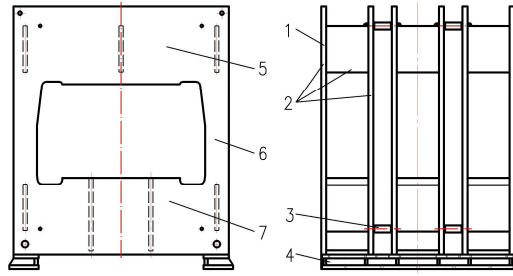


Fig. 1 Schematic diagram of the laminating press frame

- 1—Frame plate 2—A group of frame
3—Connecting bolt 4—The foundation
5—The upper beam of frame 6—Column of frame 7—The lower beam of frame

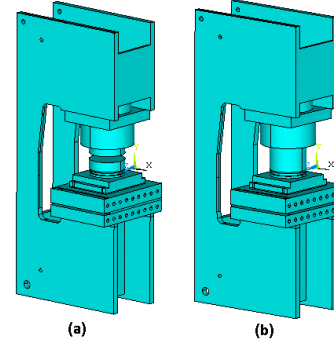


Fig. 2 The finite element model of the laminating press frame

- (a) Model of analytical scheme 1 and 2
(b) Model of analytical scheme 3 and 4

Working parameter of laminating press frame is shown in Table 1. Some parts (such as hydraulic cylinder, hot pressing board, etc) are included to get good results corresponding to the actual solution smoothly in this paper.

Table 1 Parameters of the laminating press frame

Parameter	Numerical Value
Total pressure of the press/KN	14000
Size of hot pressing board/mm	1400×2600
Size of panel/mm	1220×2440
Ram diameter of main hydraulic cylinder/mm	360
Closing speed of the press/mm/s	120
Opening speed of the press/mm/s	100

Finite element analysis of laminating press frame

Finite element model of laminating press frame. Due to the complicated structure and large size of the press, some simplifications are adopted in order to make the analysis more convenient [4-7]: firstly, ignore all screw holes, small holes and fillets, which will not affect the calculation results, and consider all welds in the actual model as an integral part; secondly, displacement constraints are imposed on some small areas of the frame bottom; thirdly, considering the performance of computer, the symmetries of structure, constraints and load, a half of the single group model is used for analysis, and symmetry constraints are imposed on the symmetry plane; fourthly, ignore the thermal radiation of the hot pressboard.

Four analytical schemes are taken in this paper and the comparisons of the analytical schemes are shown in Table 2. The differences of the different schemes depend on whether the contact analysis is taken and where the loads are imposed.

Table 2 Comparison of the analytical scheme

Scheme	Scheme one	Scheme two	Scheme three	Scheme four
Contact analysis	Yes	No	Yes	No
Breaking cylinder	Yes	Yes	No	No
Panel included	Yes	Yes	No	No
Load applied/ MPa	25	25	5.215	5.215

The finite element model of the laminating press frame is shown in Fig. 2. Fig. 2(a) shows the model of Scheme one and two. The model of Scheme three and four is shown in Fig. 2(b).

Material property. Material property of frame, cylinder, hot pressing board and so on: Young's modulus is 206GPa and Poisson's ratio is 0.3. Material property of cushion plate which is made of bakelite: Young's modulus is 2.5GPa and Poisson's ratio is 0.35.

Element. Solid95 element is adopted for the complex stress and strain condition. Solid95 is a higher order version of the 3-D 8-node solid element Solid45. It can tolerate irregular shapes without much loss of accuracy. Solid95 elements have compatible displacement shapes and are well suited to model curved boundaries [8].

Boundary Conditions. The horizontal displacement of the press is zero, symmetry constraints imposed by the symmetry plane. All displacements of the small area of the lower surface of the lower beam are zero.

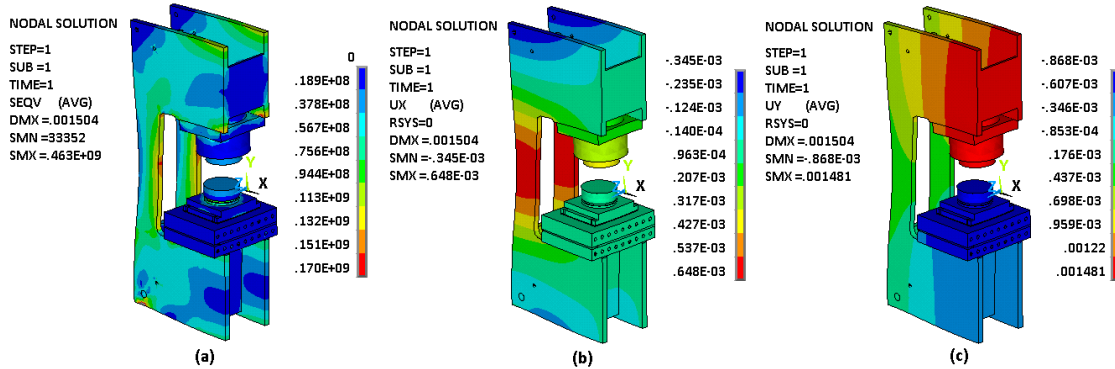


Fig. 3 Stress and displacement of analytical scheme 1
(a) Distribution of Stress (b) Distribution of X direction displacement
(c) Distribution of Y direction displacement

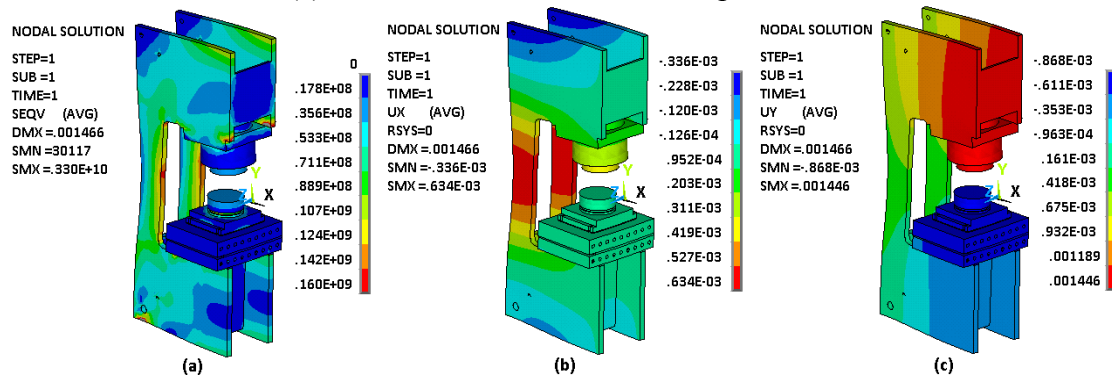


Fig. 4 Stress and displacement of analytical scheme 2
(a) Distribution of Stress (b) Distribution of X direction displacement
(c) Distribution of Y direction displacement

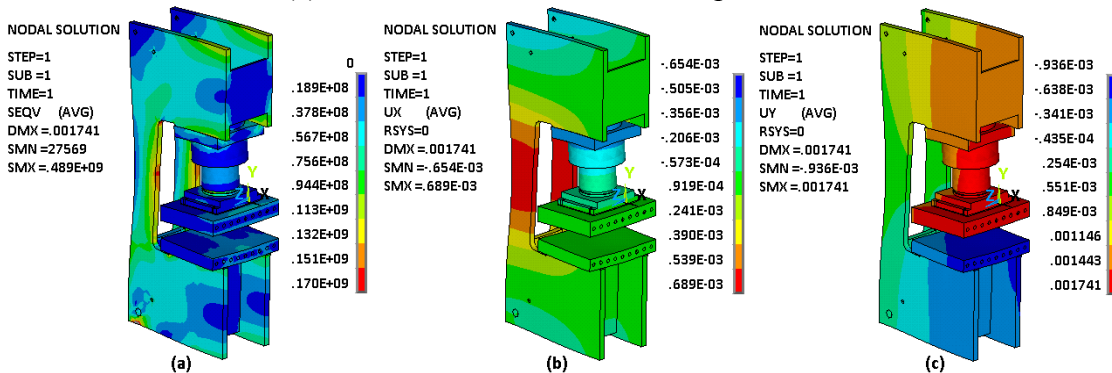


Fig. 5 Stress and displacement of analytical scheme 3
(a) Distribution of Stress (b) Distribution of X direction displacement
(c) Distribution of Y direction displacement

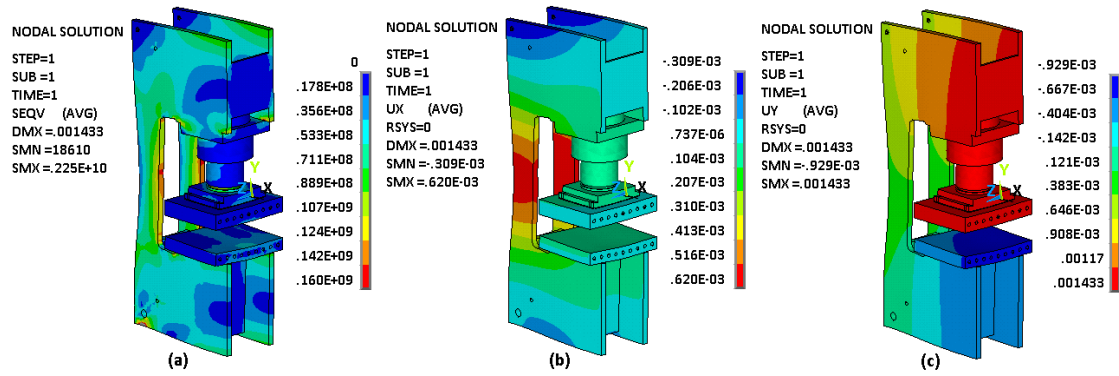


Fig. 6 Stress and displacement of analytical scheme 4
 (a) Distribution of Stress (b) Distribution of X direction displacement
 (c) Distribution of Y direction displacement

Result of the calculation. X direction lies along the width direction of the press, Y direction lies along the vertical direction and Z direction lies along the perpendicular direction of the press plane. The stress distributions and deformation of the press are shown in Fig. 3-6. From the figures one can see that each member has lower stresses regardless of local stress. As shown in Table 3, the maximum stress of the upper and lower hot pressing board is less than the counterparts of the frame, and the global analysis results are bigger than those in the contact analysis.

Table 3 Maximum stress of each member (MPa)

Scheme	Scheme one	Scheme two	Scheme three	Scheme four
Frame	178	183	170	203
The upper hot pressing board	25	26	44	30
The lower hot pressing board	31	31	42	43

The frame is made of A3 steel with yield stress 235MPa. The maximum stress of the frame, which is around filleted corner, is in a small area and the stress of the rest is lower. But in general, the frame can meet the requirements of use.

Table 4 Maximum displacement of frame (mm)

Scheme	Scheme one	Scheme two	Scheme three	Scheme four
The upper beam of frame	1.399	1.373	1.445	1.246
The lower beam of frame	0.534	0.533	0.525	0.518
Column of frame	0.641	0.627	0.687	0.612

Rigidity analysis of the frame includes two parts: the deflection of the upper and lower beam along vertical direction and the maximum displacement of column along X direction. As shown in Table.4, the maximum displacement of upper and lower beam and the column by contact analysis is bigger than that by global analysis; for the reason that the rigidity of the frame with contact analysis is smaller.

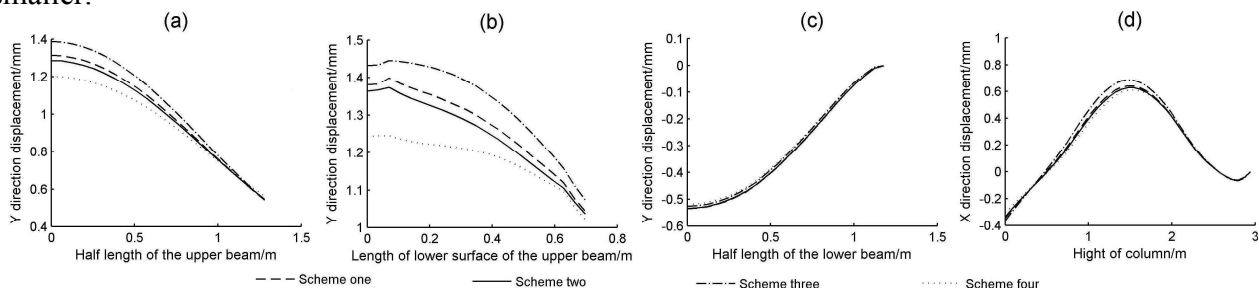


Fig. 7 The curve diagram of the frame deformation

- (a) The upper surface of the upper beam (b) The lower surface of the upper beam
 (c) The lower surface of the lower beam (d) The lateral surface of the frame column

In Fig.7 (a) and (c), the displacement curves of the top surface of upper beam and the bottom surface of lower beam are plot by half due to their symmetry respect to Y-axis, which represent their symmetry plane. The displacement at the edge between the interface and non-interface of the cylinder on its installation plane, the bottom surface of upper beam, does not change consecutively, as a result, a inflexion point can be found in each displacement curve, see in Fig.7(b). From Fig.7 (d), one can see that the maximum displacement of column is in the symmetry plane of the inner window.

The calculating results of lower beam and the column obtained in different schemes have no big difference, while the calculating differences of the top and bottom surfaces of upper beam in different schemes are obvious.

For the deformation analysis of upper beam, the rigidity results of the third scheme are closest to the actual situation, and it is regarded as the optimum scheme. For other analysis, the differences of the results in different schemes are negligible, so the second or the fourth scheme can be regarded as the optimum one in consideration of improving efficiency.

Conclusions

The intensity and rigidity of the laminating press frame were analyzed based on four finite element analysis schemes. The following conclusions can be drawn:

(1) According to the intensity and rigidity analysis of the press frame based on ANSYS, some optimizations can be made for reducing costs.

(2) Though contact analysis was more accurate, the differences between contact analysis and global analysis were negligible. Therefore, in the perspective of efficiency enhancement and qualitative analysis, the global analysis was favored. The contact analysis will be used for better accuracy.

(3) Due to the complexities of the structure and working conditions of the press, detailed analysis is needed instead of a general one. The result shows that different models and boundary conditions were required to analyze different parts of the laminating press frame.

References

- [1] YU Wen-ji, GUAN Li-li, Wu Da-wei. China Wood-Based Panels, Vol. 1-5(2009), In Chinese.
- [2] WU Xin-quan, LUO Yu-ming, QI Sheng-tian: Wood-based Panel Multiplaten Press (China Forestry Publishing House, China 1985), In Chinese.
- [3] Wang Ye-ping, Wu Zhan-wei. Mechanical Research & Application, Vol. 86-87(2005), In Chinese.
- [4] LI Yue-xian, Qi Xiu-mei. Mechanical Engineering & Automation, Vol. 70-71(2008), In Chinese.
- [5] LV Lin, DENG Ming, LI Yan-xia, WANG Zheng-li. Forging & Stamping Technology, Vol. 102-105(2010), In Chinese.
- [6] GAO Xiang, HU Miao. Journal of Machine Design, Vol. 62-64(2009), In Chinese.
- [7] WANG Shang-bin, SUN Yu, ZHANG Qing-fei. Forging & Stamping Technology, Vol. 83-86(2009), In Chinese.
- [8] Information on Release 10.0 Documentation for ANSYS.

Lightweight Design of Electric Scooter Frame by Finite Element Optimization

Hongbo Dong^a, Wei Zhang^b

School of Aeronautical Manufacturing Engineering, Nanchang Hangkong University, Nanchang, Jiangxi, 330063, China

^adonghbo@gmail.com, ^bnihaowoshiwei@sina.com

Keywords: Electric Scooter Frame; Structure Optimization; Finite Element Analysis

Abstract. To reduce the weight of the electric scooter frame, magnesium alloy is used to replace the steel. At the same time, the frame structure and tube thickness are redesigned by using topology optimization and size optimization respectively. In addition, static analysis and mode analysis of the frame are carried out to realize the application capability and dynamic capability. Compared with the original steel frame, mass of the magnesium alloy frame after optimization has been reduced by 60%, and the natural frequency has been improved greatly. The results show that the strength and the rigidity of the new structure can meet the designed demand.

Introduction

Recently, how to develop a structure with high strength and light weight has become one of the important duties of vehicle design. However, lightweight structure has a great impact on strength and rigidity of vehicles, so the structural strength and weight need to be coordinately handled. So far, optimization techniques have been applied in the initial stage of structural design. Compared with the method of trial and error, they have the advantages of high-efficiency and low cost. The traditional methods for optimum structural design include topology optimization, shape optimization and size optimization [1-4]. In addition, the high-strength light metal can be used to greatly reduce the structural weight. Magnesium alloy has been widely used in fields of aerospace, automobile, electronic communication due to its advantages of light weight and high specific strength[5,6]. In recent years, magnesium alloy components have been more and more widely used in electric scooter, with satisfactory results [7].

At present, large weight and short mileage are common problems in the electric scooter market. Lightweight design on a certain type of electric scooter can be carried out for developing high-end market. Although using magnesium alloy instead of the original steel frame that can reduce weight, redesigning the original structure to enhance the comprehensive performance of products is necessary. In this paper, the optimization module of finite element analysis software Hyperworks is used for carrying out topology optimization and size optimization to frame. At the same time, strength analysis and modal analysis are both achieved to get the structural sizes that could meet the designed demand.

Analysis of the original frame structure

General drawing of the original frame of electric scooter is shown in Fig.1. The load bearing structure namely the main frame is welded by 1.5-mm-thick steel tube, and diameter of the riser is 40 mm and the others are 32 mm. Material is 45 steel, yield strength is 355 MPa, density is 7.85

g/cm^3 , elastic modulus is 210 GPa, Poisson's ratio is 0.3. The main frame whose weight is 4.5 kg is in charge of loading the crew and the battery under the seat, the maximum designed load is 2000 N. Finite element model of the main frame of the electric scooter is shown in Fig.2. Static analysis shows that the maximum equivalent pressure in the joint between riser and the chassis U-tube is 274MPa(as shown in Fig.3), the maximum displacement of load position is 5.2 mm. Lanczos method is used to solve unconstrained model, which results show that the first-order natural frequency is 489 Hz , the first-order vibration mode is shown in Fig. 4.

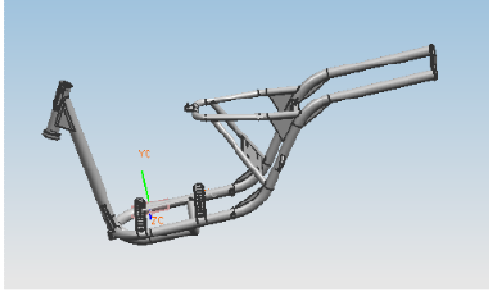


Fig.1 General drawing of the frame

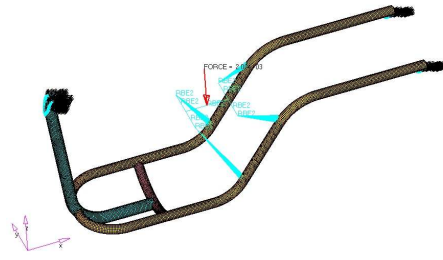


Fig.2 Finite element model of the main frame

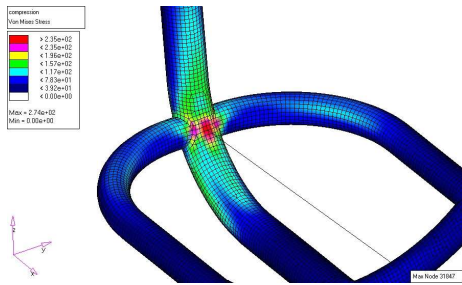


Fig.3 Equivalent stress in the joint area

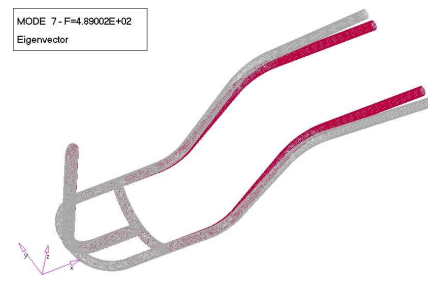


Fig.4 The first-order vibration mode of the frame

Optimal design

Topology optimization. The strength analysis shows that stress in the joint between riser and the chassis U-tube cannot reach yield strength, much higher than other parts. The main frame structure should be redesigned by topology optimization to reduce the stress concentration. The part surrounded by the chassis tube is the optimal design domain, shell elements are used to construct the models and the load and boundary conditions are applied to the main frame (as shown in Fig.5). The maximum structural rigidity is the design objective; the volume that is smaller than 0.25 times of the original volume is constraint after the optimization. Optimization technique of continuum structures is applied based on density method, and the optimization objective function and constraint function are:

$$\begin{aligned} \text{objective function} & \min C(x) \\ \text{constraint function} & \text{s.t. } V(x) - V^U \leq 0 \end{aligned}$$

Among the formula, objective function $C(x)$ is structural flexibility; constraint function $V(x)$ is structural volume, V^U is upper limit of total volume that is 0.25 times of the original volume; and design variable x is unit density which represents the presence or deletion of the unit in microstructure, where density value of each unit should be taken as 0 or 1, so the lower limit is 0 and upper limit is 1.0[8,9]. In this paper, using the density method, unit density is continuously changed between 0 and 1.

Optimization results are shown in Fig.6, where the optimal material distribution of the structure can be seen in setting conditions. According to the results of topology optimization and considering

the processing conditions, the structure is shown in Fig.7 can be got. The frame is still welded by 1.5-mm-thick 45 steel tubes, and its mass is 4.4 kg which is slightly smaller than that of the original structure. The load and boundary conditions is the same as the original frame when the new designed frame is carried on with finite element analysis. The maximum equivalent stress is still in the joint between riser and the chassis U-tube, however, the position has transferred from the inside to the outside in the riser(as shown in Fig.8), the maximum equivalent stress value decreases to 212 MPa which is only 77.4% of that in the original structure and the maximum displacement of the position of the applied load is 5.4 mm. Compared with the original structure, the results show that the first-order natural frequency of the new structure is 1138 Hz which increases by 133%, the first-order vibration mode also changes from the original transverse swing into longitudinal buckle.

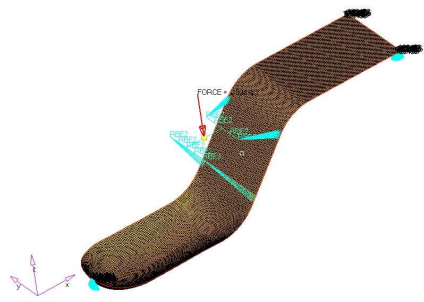


Fig.5 Design domain for topology optimization

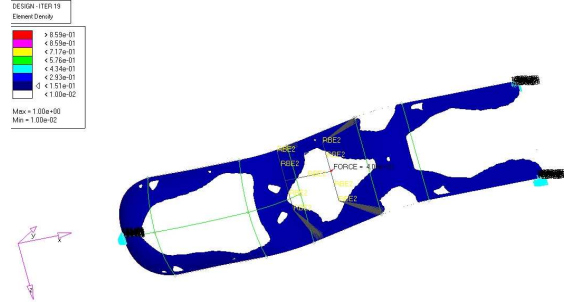


Fig.6 Distribution of material density

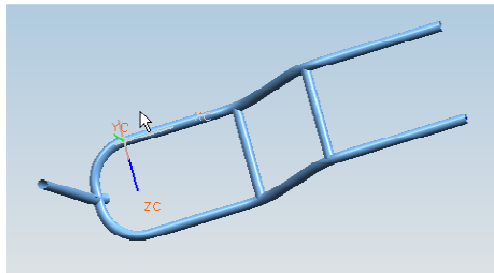


Fig.7 Main frame after topology optimization

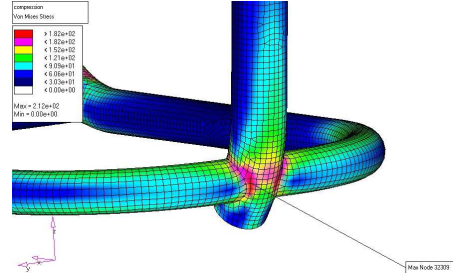


Fig.8 Equivalent stress in the joint area

Size optimization. Strength and natural frequency of frame have been greatly improved after the topology optimization. The steel material is replaced by magnesium alloy AZ91 to reduce the weight significantly. Its density is 1.80 g/cm^3 , elastic modulus is 45 GPa, Poisson's ratio is 0.35, and yield strength is 180MPa. The weight of the main frame is 4.5 kg, and all the thickness of the tube is still 1.5 mm. Static analysis shows that the maximum equivalent stress is 209 MPa and the maximum displacement is 25.4 mm, which means that strength and rigidity of the frame are both worsened. Size optimization analysis is carried out to quickly identify various sizes of the appropriate thickness of various parts of tube. Design objective is the smallest volume; constraint is the maximum equivalent stress and the maximum displacement is less than the set value. Objective function and constraint function of size optimization are:

$$\begin{aligned} \text{objective function} & \quad \min \quad V(x) \\ \text{constraint condition} & \quad \text{s.t.} \quad g(x) - g^U \leq 0 \\ \text{design variables} & \quad x^L \leq x_i \leq x^U \end{aligned}$$

Among the formula, objective function $V(x)$ is structural total volume, constraint function $g(x)$ is the response which is obtained from the structural analysis, where the constraint functions are defined as the equivalent stress and loading- point displacement, and g^U is the maximum equivalent stress and the upper limit of maximum displacement, respectively. Design variable x is the thickness of tube, and x^L and x^U are respectively the lower and upper limits.

For security reasons, the allowable stress of material is 144 MPa that is 80% of the yield stress of magnesium alloy, and the maximum displacement of position of the applied load is not more than 10 mm. Optimized objects are the riser, U-tube and two horizontal tubes respectively. The optimized tube thickness is 1.9mm for riser, 3.3 mm for U-tube and 1.0 mm for two horizontal tubes, respectively. The maximum equivalent stress is 131 MPa and the maximum displacement is 9.7mm.

Table.1 Results of finite element analysis

Design scheme	Materials	Mass m / kg	Maximum displacement d / mm	Maximum equivalent stress σ / MPa	The first-order frequency f / Hz
Original structure	steel	4.5	5.2	274	489
Topology optimization	steel	4.4	5.4	212	1 138
Size Optimization	magnesium	1.0	25.4	209	1 103
	magnesium	1.8	9.7	131	1 302

The results of each analysis are summarized in Table 1. The weight of the main frame reduces from 4.5 kg to 1.8 kg, with losses of 60%.The maximum equivalent stress decreases to 131 MPa from 274 MPa, and natural frequency increases from 489 Hz to 1302 Hz. Although the weight has a significant decrease, the structural strength can still meet designed demand. The maximum displacement increases to 9.7 mm from 5.2 mm, which shows structural rigidity has a slight decrease.

Supporting structure based on main frame is designed, and weak areas are increased stiffener plate by welding in order to further enhance its rigidity and strength. Frame of trial production is compact structure and light-weight. Products after assembly are carried out driving test. Finally, test results show that strength, rigidity and reliability of drive are good performance which can prove that the finite element optimization technique is an effective method for vehicle structural design.

Conclusion

Original steel materials are replaced by magnesium alloy, and the weight of main frame of electric scooter is only 1.8 kg and reduces by 60%, which achieves a substantial decrease. While replacing material, the main frame has been redesigned by using finite element analysis. Compared with the original steel structure, first-order natural frequency of the redesigned magnesium alloy main frame is increased by 166%, so structural strength and rigidity can meet the designed demand absolutely.

A more reasonable mechanical bearing structure is attained by topology optimization, which can enhance the structure strength. On the premise of meeting the design demand of rigidity and strength, size of the minimum thickness of each component can be quickly obtained by size optimization, which improves the design efficiency. The design method may be applied to mechanical structure and design of lightweight components.

Acknowledgment

This work is financially supported by the National Natural Science Foundation of China (Grant No. 50964012).

References

- [1] Yunkai GAO, Dekan MENG and Xi JIANG: China Mechanical Engineering, Vol.17(2006), p.2522 (In Chinese)
- [2] F.Navarrina, I.Muinos, I.Colominas and M.Casteleiro: Advances in Engineering Software, Vol. 36(2005), p.599
- [3] S.L.Lee, D.C.Lee, J.I.Lee, C.S.Han and K.Hedrick: Finite Elements in Analysis and Design, Vol. 43(2007), p620
- [4] B.Torstenfelt and A.Klarbring: Finite Elements in Analysis and Design, Vol. 43(2007), p.1050
- [5] Qichi LE, Xinjian ZHANG and Jianzhong CUI: Materials Review, Vol. 16(2002), p.12 (In Chinese)
- [6] A.Tharumarajah and P.Koltun: Journal of Cleaner Production, Vol. 15(2007), p.1007
- [7] Shu WANG, Chunsheng SHI, Naiqin ZHAO and Zhongxia XIANG: Materials Review, Vol. 20(2006), p.87 (In Chinese)
- [8] Yuanfang FU, Dafeng JIN and Weiwei QIAO: Journal of Mechanical Engineering, Vol. 45(2009), p.210 (In Chinese)
- [9] Weihong ZHANG, Jungang YANG and Jihong ZHU: Acta Aeronautica Et Astronautica Sinica, Vol. 30(2009), p.2335 (In Chinese)

A Feature-Based CAD-CAE Integrated Approach of Machine Tool and Its Implementation

Wentie Niu^a, Pengfei Wang^b, Yu Shen^c, Weiguo Gao^d and Lina Wang^e

¹School of Mechanical Engineering, Tianjin University, Tianjin, China, 300072

^aniuwentie@tju.edu.cn, ^bpfwang1987@126.com

Keywords: Machine Tool; Analysis Feature; CAD-CAE; APDL

Abstract. An analysis feature-based CAD-CAE integrated approach was proposed to solve the problems of rapidly CAE modeling for static and dynamic analysis process of machine tool. Firstly, analysis features were defined in CAD system and analysis feature library was constructed for machine tool and its structural components. Secondly, analysis feature model was constructed by attaching analysis feature to CAD model interactively. Finally, ANSYS parametric design language (APDL) file was generated automatically by mapping analysis features to APDL codes, which realized the integration of CAD system and ANSYS system. Based on application programming interface (API) of SolidWorks, a parametric CAD-CAE tool oriented to static and dynamic analysis of machine tool was developed, which realized parametric modeling and automatic analysis of machine tool and improved design efficiency and quality of machine tool.

Introduction

The tight integration of CAD-CAE is widely adopted for modern product development. In the digital development process of product, CAD is applied to produce digital model, while CAE focuses on the analysis and simulation of product properties. For complex product design, the meaning of CAD-CAE integration includes: (1) product design model is reused in the process of CAE modeling, furthermore, the structure and function information of product included in CAD model will be reused, which realizes the integration of product information [1-3]; (2) the integration of analysis process, analysis knowledge and function is realized in the typical analysis process, which improves the efficiency and quality of CAD modeling and analysis [4, 5].

An analysis feature-based CAD-CAE integrated approach is proposed in this paper. The structure design of machine tool is completed in CAD system, then analysis feature model is established by defining analysis feature interactively. At last based on the type and specific parameters of analysis feature predefined, the APDL file will be generated automatically by mapping the analysis features to APDL codes, which finally implements the integration of CAD and CAE.

Feature-based CAD-CAE integrated process of machine tool

The CAD-CAE integrated process based on analysis feature can be seen in Fig.1. The main processes are as follows: (1) CAD model of machine tool is rapidly constructed with the aids of modular and parametric design tools; (2) analysis features are added interactively to CAD model; (3) analysis features are extracted and the APDL file is generated automatically by mapping analysis features to APDL codes; (4) the CAD model is simplified and converted into CAE geometric model; (5) the CAE geometric model is imported into ANSYS and the APDL file is run, finally the CAD-CAE integration is implemented.

Compared with others, this approach has the following advantages: (1) analysis features are added interactively, which makes the CAE modeling has greater flexibility; (2) APDL codes are mapped directly from analysis features, which make the model simplification, element generation, boundary constraint and load addition knowledgeable and intelligent. In addition, the CAE analysis automation is also implemented.

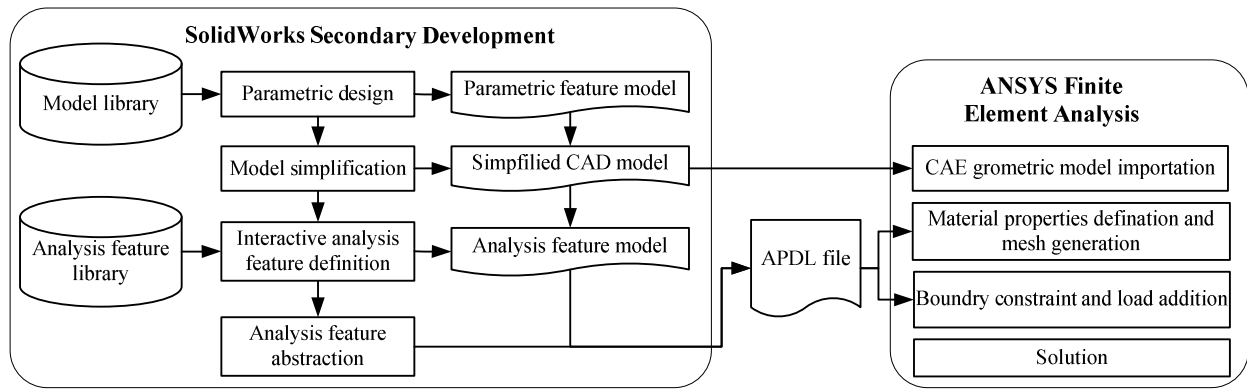


Fig.1 CAD-CAE integrated process

Analysis feature modeling for static and dynamic property analysis of machine tool

As it is difficult to extract analysis parameter from the design feature directly, the analysis feature model is constructed interactively, which is used for static and dynamic analysis of machine tool. The key issue of this approach is to construct the analysis feature library and define analysis model interactively for typical analysis process.

Analysis feature model. The static and dynamic analysis of machine tool include: (1) strength and stiffness analysis of machine tool and its main structural components, which belongs to the static analysis; (2) modal analysis of machine tool and its main structural components, which belongs to the dynamic analysis. According to static and dynamic analysis requirements of machine tool, analysis feature is constructed with five such classes: *Overall Analysis Feature*, *Material Feature*, *Boundary Constraint Feature*, *Load Feature* and *Interface Feature*. The structure of analysis feature classifications can be seen in Fig.2.

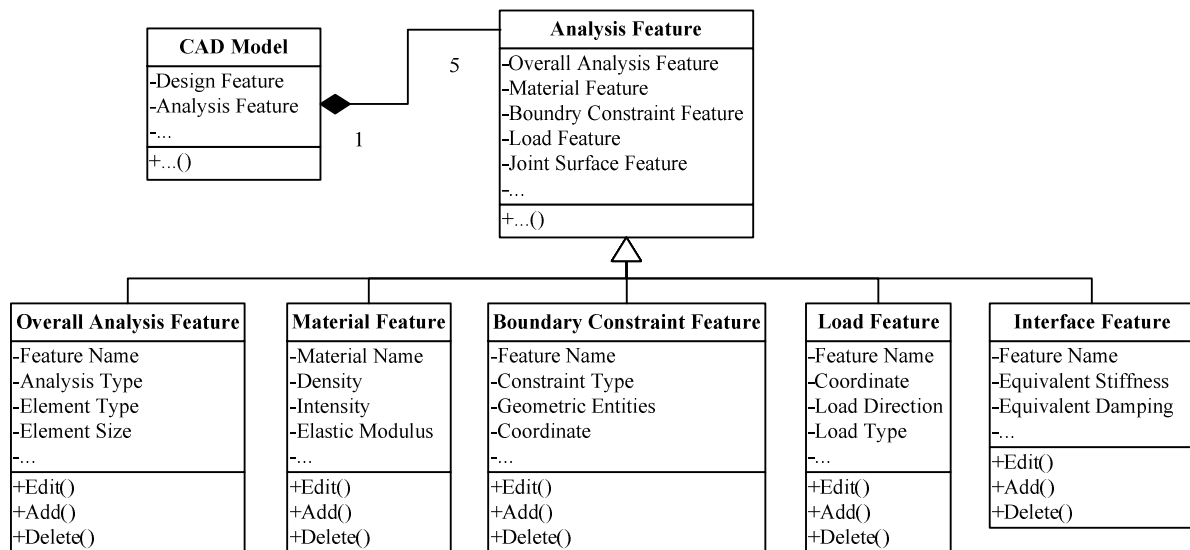
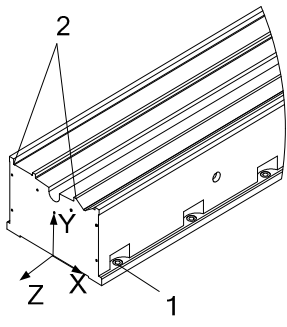


Fig.2 Structure of analysis feature class

With the aids of SolidWorks API, the parameters of analysis feature are attached to geometric entities (point, line, face and feature) and other geometric entity through SolidWorks attribute. Attribute is a container of user-defined variables. With the help of it, user-defined variable can be stored in CAD model. After adding attribute to design feature, the specific information of analysis feature can be obtained rapidly by traveling instances of attribute, which is associated with analysis feature. The essence of analysis feature addition is the attribute addition for the design feature of CAD model, which is the binding of analysis feature and design feature [5]. For static analysis of the bed, Table 1 shows the major analysis features.

Table 1 Analysis feature of the bed

Graphic Sample	Feature Type	Location Of Analysis Feature	Feature Parameter
	Boundary Constraint Feature	1. Cylinder of bolt hole	Coordinate: (0.45, 0.03, -0.2)
	Load Feature	2. Endpoints of guide ridge	Coordinate: (-0.42, 0.53, 0) Load Direction: -Y Load Type: uniform
	Material Feature	Attribute abstract of functional module	Material Name: HT200 Poisson Ratio: 0.25
	Overall Analysis Feature	Attribute abstract of functional module	Analysis Type: static Element Size: 0.3

Interactive defining and modeling approach of analysis feature. To construct analysis feature model, the definition of analysis feature is accomplished by the way of interactive defining. The main processes are as follows: (1) selecting the type of analysis feature to be added; (2) selecting the geometric entities (point, line, surface and feature) according to the type of analysis feature; (3) inputting parameters of analysis feature; (4) attaching analysis feature to geometric entities and files so that the information of analysis feature can be stored in CAD model.

In the interactive defining process, on the one hand, analysis feature can be added interactively; on the other hand, parameters of the analysis feature can be modified if it is necessary. For example, if the length of the bed needs to be increased when it can not meet the requirement after CAE analysis, after parameters of the CAD model is modified, the number of bolts is also changed, so it is necessary to attach analysis feature to those new added bolts.

Mapping of analysis feature to APDL codes

Document structure of APDL file. APDL is a scripting language for parametric design by ANSYS, which can be interpreted line by line. Inputting APDL codes of the model in a parametric way, ANSYS can accomplish the Finite Element Analysis (FEA) process automatically. There are three stages in the FEA process, including pre-processing, solution and post-processing. Pre-processing includes geometric model importation, material properties definition, boundary constraints addition, load addition, solution type definition and other universal processing modules. After combining these universal processing modules together according to the process of FEA, APDL file is generated.

Automatic generation of APDL file. Based on the structure of APDL file, APDL codes can be generated automatically by establishing the mapping relationship between analysis features and APDL codes. For example, the mapping process of the boundary constraint features of the bed is shown in Fig.3.

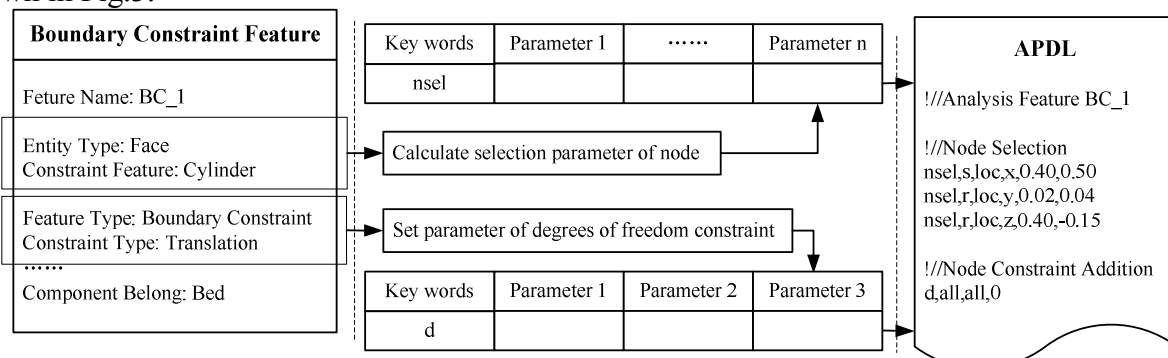


Fig.3 Mapping of boundary constraint features and APDL codes

The automatic generating process of APDL file is detailed in Fig.4. The main processes are as follows: (1) travelling the attribute information stored in CAD model and constructing the analysis feature model based on the type and specific parameters of analysis feature; (2) extracting parameters of analysis feature and determining key words and parameters of the APDL sentence related; (3) combining these APDL modules together according to the document structure of APDL file. Finally, the APDL file is generated.

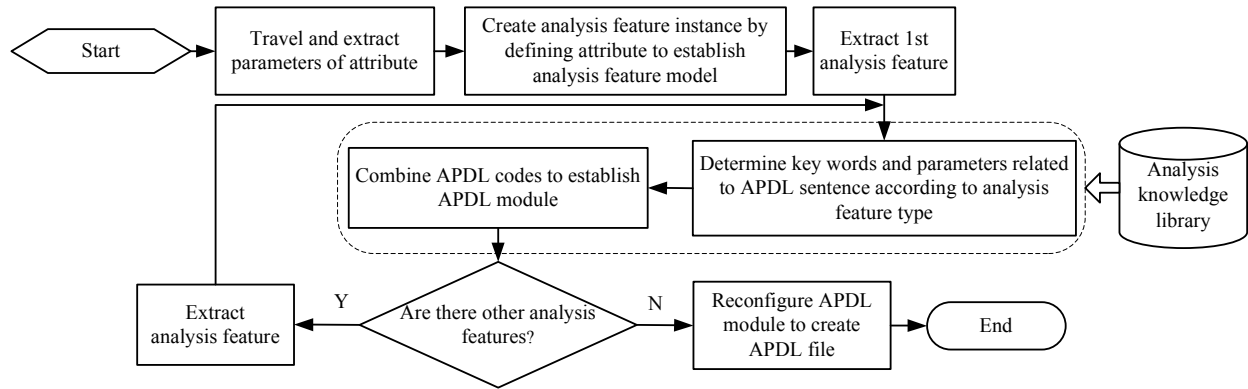


Fig.4 Generating process of APDL file

Case Studies

A modular rapid design system of machine tool was developed, based on the methods above-mentioned, with SolidWorks and ANSYS as the development platform, by means of development tool of VB.NET. It includes parametric design module, static and dynamic analysis module for machine tool and its structural components and automatic engineering formulation of drawing module, which is embeded in SolidWorks as an add-in. For example, the processes of parametric design and FEA for one type of milling planner are as follows: (1) searching for a suitable machine tool according to the requirement of customers; (2) by means of parametric design, product model satisfied with the requirements is generated, which is shown in Fig.5(a); (3) adding analysis feature; (4) simplifying and converting the CAD model, the simplifying process is illustrated in Fig.5(b); (5) mapping analysis features to APDL codes so that APDL file can be generated; (6) running the APDL file to implement the static and dynamic analysis of the milling planner and its structural components. The results of general deformation and modal analysis of the milling planner and its bed components are shown in Fig.6. The maximum deformation of the milling planner is $78.5\mu\text{m}$, the first order modal frequency of the milling planner is 38.4Hz; the maximum deformation of the bed is $1.55\mu\text{m}$, the first order modal frequency of the bed is 336.7Hz.

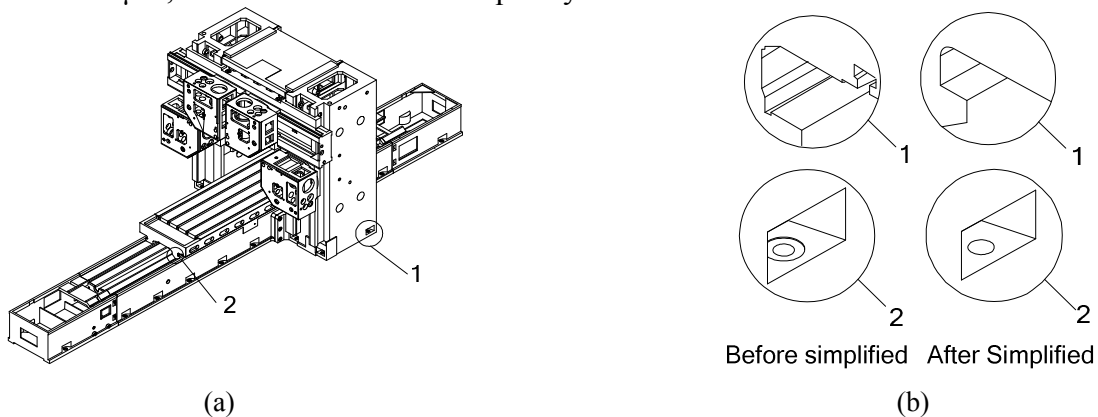


Fig.5 CAD model of the milling planner and model simplification: (a) the model of milling planner (b) the process of model simplification

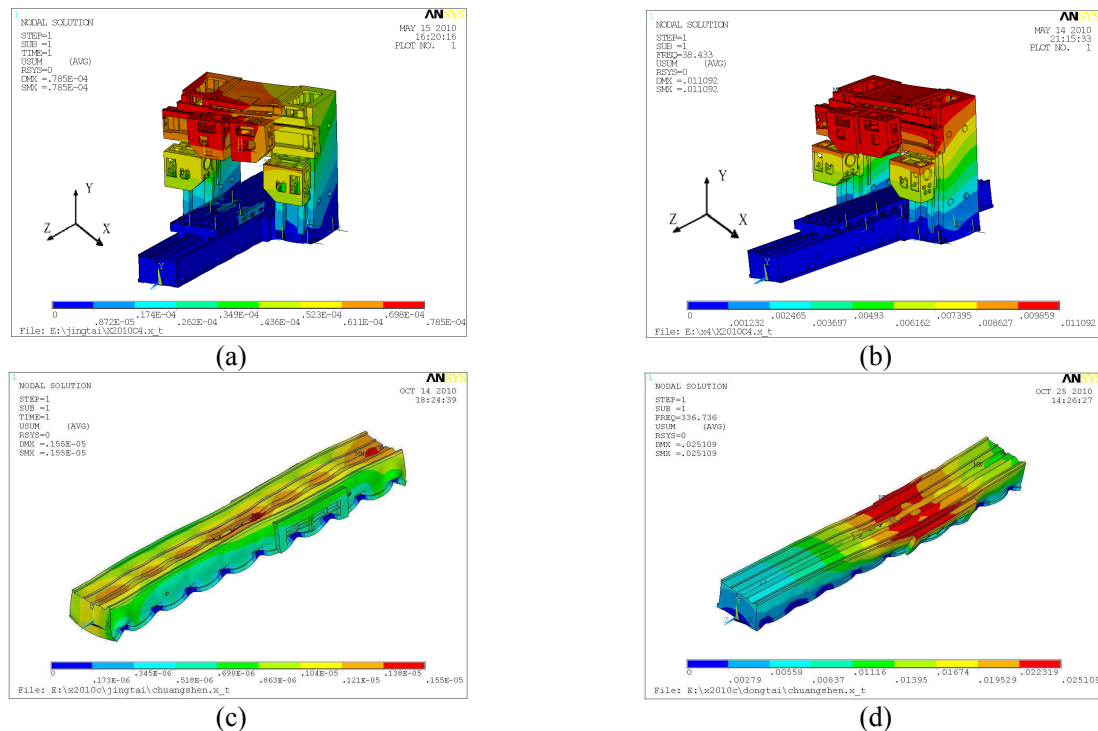


Fig.6 Analysis results of milling planner and its bed component: (a) general deformation of the milling planner (b) the first order modal analysis of the milling planner (c) general deformation of the bed (d) the first order modal analysis of the bed

Conclusions

In this paper, a feature-based CAD-CAE integrated approach was proposed, which can realize rapid modeling and FEA analysis of machine tool. By adding analysis feature interactively, CAE modeling and analysis are more flexible. Furthermore, by the mapping of analysis features and APDL codes, static and dynamic analysis of machine tool and its structural components is more knowledgeable and automatic, and the overlabored and time expended problem in the design and analysis process of machine tool is solved. Finally, the efficiency and quality of machine tool design is improved.

Acknowledgements

The paper is supported by the state high-tech R&D programs of China -- 863 program. (No.: 2008AA042406) and the state S&T project for upmarket NC machine and fundamental manufacturing equipments of China (No.: 2009ZX04014-021, 2009ZX04001-043).

References

- [1] Libin Shen, Aimin Ji and Quansheng Huang: Machine Tool & Hydraulics Vol. 37 (2009), p. 202-205. (In Chinese).
- [2] Sang Hun Lee: Computer-Aided Design Vol. 37 (2005), p.941-955.
- [3] Lijuan Sun, Aihua Wang: Application Research of Computers Vol. 26 (2009), p.917-919. (In Chinese).
- [4] Hong-Seok Park, Xuan-Phuong Dang: Computer-Aided Design Vol. 42 (2010), p.889-902.
- [5] Xiaodong. Shao, Shen Li, Huangling Liu and Gaowen Huang: Computer Integrated Manufacturing Systems Vol. 13 (2007), p.1914-1920. (In Chinese).

Using Software Engineering to Guide Commercial CAD Software Secondary Development

Cheng Wang^a, Baokun Yang^b, Xiongwei Yang^c and Guirong Yan^d

Key Laboratory for Strength and Vibration of Mechanical Structures, Xi'an Jiaotong University,
Xi'an, China 710049

^awc071@163.com, ^b yang.bk@stu.xjtu.edu.cn,

^c xiongwei@stu.xjtu.edu.cn, ^d yangr@mail.xjtu.edu.cn

Keywords: Commercial Software; CAD; Application Development; Software Engineer.

Abstract. Effective secondary development is the key process for CAD application. But as a cross-disciplinary problem and new software development mode, secondary development based on commercial CAD software has new features compared with complete independent software development. From angle of software engineering, this paper summarizes demand of software engineering, standards to observe, software development flow, configuration of development team in the process of commercial CAD software secondary development. Finally, this paper presents the case of secondary development of AutoCAD standard base parametric system to illustrate the specific application of software engineering in detail.

Introduction

A complete CAD process includes: introduction of CAD hardware and software, secondary development of CAD software, application in product design, extension applied to CAM. Although well-known international commercial CAD software basically covers the entire manufacturing industry, they are not aimed at any specific and dedicated requirements that exist in practical and specific industry [1]. For an enterprise that needs to introduce CAD comprehensively and effectively, different levels of secondary development should be carried out according to its industry characteristics and application requirements after it digested and absorbed commercial CAD software completely.

However, main problems exist in current commercial CAD software secondary development, such as lack of unified organization and management in development process, no uniform standards or accepted norms to observe and guide, programs are often "written" according to software developers' experience.

Current research of commercial CAD software secondary development focuses on the realization technology of secondary development, such as COM [2], grid [3], object-oriented technology, database, interface [4] and parameter [5] technology. However, most of the formal researches are limited to technical details, and ignore that the entire secondary development of commercial CAD software is a new software development model and system engineering. Application the idea of software engineering to organize the process of secondary development is a new way to overcome the current problems in commercial CAD software secondary development[6].

Application of Software Engineering

Necessity of Application of Software Engineering into Secondary Development of Commercial CAD Software. (1) The second development project of commercial CAD software need the staff form different divisions to collaborate and to go through several stages of development phases during the developing process. And there are close contact among various parts of software and interface problems always come about to solve with urgency. A rule is highly required to coordinate the complex relationships and problems. (2) At all stages of CAD software development process, the software being developed needs reviewing, inspecting and testing. The problems encountered in

maintenance phase are also closely related to development work. And the management work of software is infiltrated into every stage of the survival cycle of the software.

Therefore, the second development project of commercial CAD software requires consistent and measurable criterion to coordinate the complex relationship. And the idea and methodology of software engineering with systemic logic will be helpful for resolving the problems resulting from different parts of software and various development phases.

Secondary Development Process of Commercial CAD Software. After setting purposes, development method, commercial CAD Software platform, programming language, tool, and mode of secondary development should be selected firstly. And a detailed development plan, including design objectives, design philosophy, and development process should be work out then. Detailed specific implementation technologies, such as front GUI research, back-end database and other enabling technologies should be assessed then. At last, secondary development process should follow the development process of demand research, demand analysis, system analyst and software architecture design, detailed design, programming implement, test (module test, unit test, system test) and modification according to the users' feedback. Second development process of commercial CAD software should adopt human-computer interaction and rapid prototyping law to improve the system through constant communication based on the users' feedback.

Role Configuration of Development Team. Secondary developers do not only understand the machinery industry expertise, but also have capabilities of software development. Therefore, the scientific development team in secondary development process of commercial CAD software should include both professional and technical personnel and software developers, shown in Table 1. However, if the secondary development project is very small, a person may play more than one roles at the same time.

Table 1: Role configuration of development team

Role configuration	Job description	Professional skills required
Requirement analyst	With a mechanical fields of knowledge, understanding of commercial software platform	With a mechanical fields of knowledge, understanding of commercial software platform
System analyst and software architecture designer	Overall system design, system decomposition is determined based on the framework of the whole system to form a "system framework and module design specification"	Have knowledge not only in software but also development technology, have the capability of comprehensive analysis
Programmer	Turning the framework of the system and module specifications into software program with commercial CAD development tools	Familiar with the commercial CAD software secondary development tools and APIs, have experiences and skills of programming
Data processing editor	Mainly engaging in the data processing and data files input work	Patient
Software tester	Module testing, comprehensive integration testing, performance testing, stability testing, found the problem program	Extensive experience in software testing
Experiencing member of new system	Acceptance test, functional inspection, user simulation, experiencing feedback, consistency and integrity verification	Extensive experience in the use of commercial CAD software platform

Application Examples: Secondary Development of AutoCAD Standard library Parametric System

During the mechanical drawing with AutoCAD[7], part drawings and assembly drawings of assembly and standard parts with a lot of nuts, bolts, screws, gears, springs, bearings are often need to draw. These parts have the same shape in view and the only difference is the size. Therefore, establishing a scientific standard parts library system or providing development tools for standard parts development is an integral part of the CAD system.

Design Objectives. (1)System can output calculation results directly, generate scale drawings and output generated products map. (2)System can query design of standard accordance with the basic

shape of the given parameters or models. (3)System can check design and finish calculation of non-standard bearing. (4)With database management function, system can maintain parameters of standard and all non-standard bearing.

Design Philosophy Only when the composition of products is built based on combination-based general components, may CAD system achieve the goal of improving the design quality of new products and shorten the design and development cycle. Based on the modular design idea, the standard library parametric system is divided into three modules: database module, main parameters design and calculation module, parametric drawing module (as shown in Fig 1).

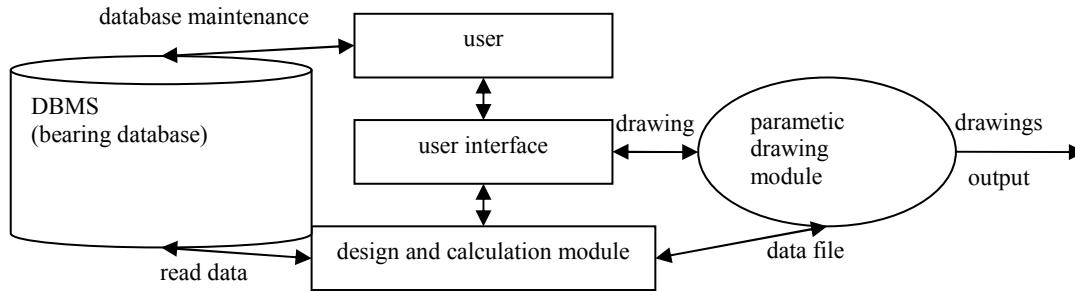


Fig. 1 Standard library parametric system module diagram

(1)Database module: These database tables store indicators related information about standard parts, types, models, geometry, performance and others in mechanical design handbook. And corresponding database maintenance is established to facilitate various operations on the database.

(2)Design calculation module: This module performs the optimization design and calculation based on parameters from the bearing database, and then selects the tolerances of corresponding size and shape, and other auxiliary parameters according to the new gained optimized parameters.

(3)Parametric drawing module: This module reads the main parameters of bearings from parameters optimization calculation module, and draws part drawings and assembly drawings using drawing development tools of AutoCAD ObjectARX.

Process of Design. According to basic standardization and process of rolling design, ball bearing CAD system is made up of two modules: module selection and module check, shown in Fig 2.

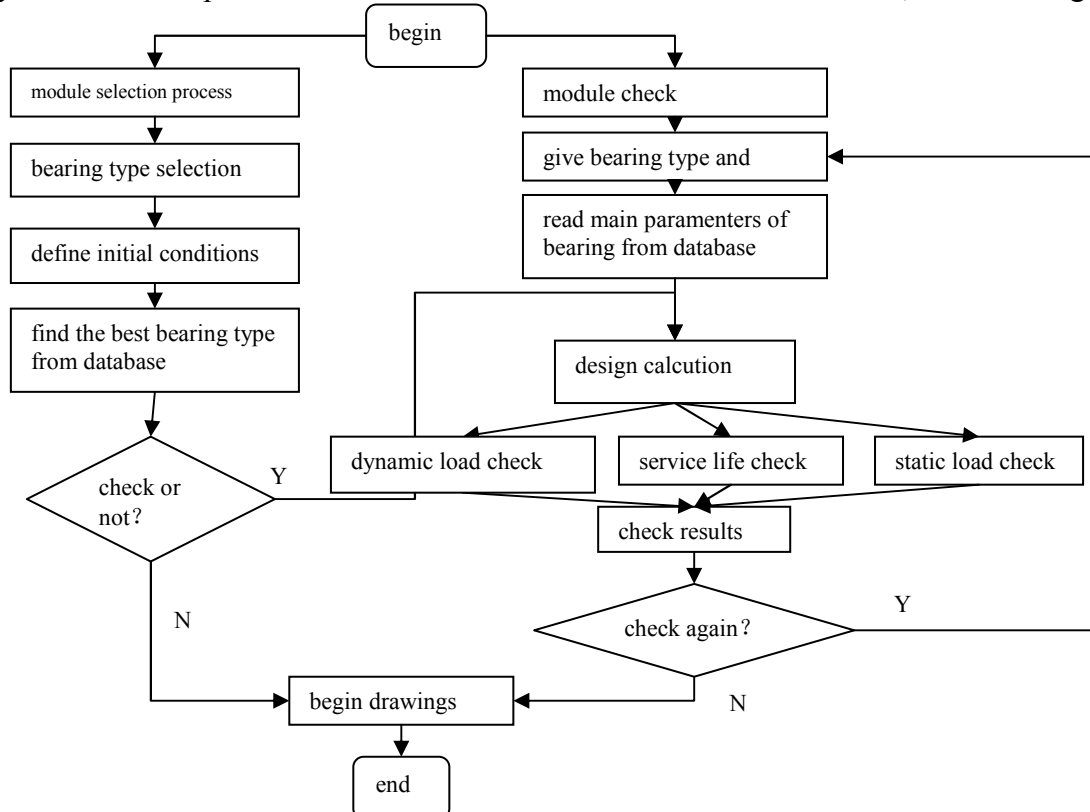


Fig.2 System architecture flow chart of ball bearing CAD system

Specific implementation technologies include: SML, GUI, database management, selection and check of rolling bearings, parametric and so on.

Using software engineering to guide secondary development process of AutoCAD standardized library parametric system will lead to targeted development, clear and reasonable staff division and standard development process. With the guide of software engineering, the planning of development processes is long-term, the role configuration of development team is clear; the collaboration is close, and the exchange is smooth. So application of software engineering into secondary development of commercial CAD software greatly improves the success rate of software development, and assures the software quality of secondary development system.

Conclusions

Current research of secondary development of commercial CAD software focuses on realization technology of secondary development. This paper treats the entire secondary development process of commercial CAD software as a new software development model and system engineering. Secondary development based on commercial CAD software is a cross-disciplinary problem which covers the two fields of mechanical design and software development, and is of high technical complexity. Application of software engineering to commercial software secondary development can improve software quality and accelerate software development speed, reduce development costs and accelerate CAD technology application.

Moreover, the example of secondary development of AutoCAD standard library parametric system is presented to illustrate the process of secondary development with the guide of software engineering. This process can also be applied to parametric drawing and designing, information extraction off-line application form drawings, hydraulic machine design and other secondary development processes. However, as software engineering is a common and universal science, it can be used to guide secondary development processes of general commercial software platform.

Acknowledgements

The author would like to thank his collaborators from MOE Key Laboratory for Strength and Vibration of Mechanical Structures, Xi'an Jiaotong University and the financial support of National Natural Science Foundation of China (10776026).

References

- [1] Shizhong Tong, Ping Li. Secondary development is key points of obtaining actual effect for CAD[J]. Electronic Machinery Engineering, 1999(4): 34~38 (in Chinese).
- [2] Rongqiao Wang, Bo Li, Jiang Fan. Component-Oriented Distributed Part Optimization Design and Data Management System. Journal of Computer-Aided Design & Computer Graphics, 2005, 17(4):789-794 (In Chinese).
- [3] Shengyou Shi, Rong Mo, Haicheng Yang, Chuanshun Zhang. Grid Service Oriented Integration of Standard Part Libraries. Journal of Computer-Aided Design & Computer Graphics, 2006, 18(4):551-555 (In Chinese).
- [4] Weidong Zhao, Xianhui Liu, Gang Wei. Realization Technology of Application Development Toolkit for CAD Software. Journal of Computer-Aided Design & Computer Graphics, 2003, 15(4): 512-516 (In Chinese).
- [5] Dunbing Tang, Dongbo Li, Shiqi Zhang. The Second Development for CAD Applied Software. Digital Manufacturing Industry. 1998,1(In Chinese).
- [6] Aihua Cheng. Integrated Research of Scheme Design and Technical Design of Passenger Train[M]. DaLian JiaoTong University,2005, 05(In Chinese).
- [7] Feng Zhang, Aiping Chen. Study of AutoCAD development environment. Machinery Design& Manufacture, 2005(9):125-127 (In Chinese).

Research on 3D Non-destructive Measurement System Based on Homogeneous Entity

Yong Gan^{1,a}, Jingru Zhong^{2,b}, Dufen Gan^{3,c}

^{1,2,3}College of Mechanical & Electrical Engineering, Guilin University of Electronic Technology, Guilin 541004, China

^aganyong@guet.edu.cn , ^byjw2zjr@yahoo.cn , ^c306280903@qq.com

Keywords: Homogeneous Entity; Digitized; 3D Non-Destructive Measurement; Profile.

Abstract: A new non-destructive measurement system of the homogeneous entity profiles was designed; it included the digitized minute entity cells and the delaminated measuring method for product profiles based on liquid. It is based on Archimedes' principle and lever principle and gravity moment, used optic system to collect images and calculated the verge profiles, combined the equations of the gravity moment and the equations of the center of gravity to reckon the 3D coordinate values of every minute entity cell in different layers by computer. By inputting the 3D coordinate values of the product into the related CAD software system, the 3D model could be obtained. The principles, hardware and software of the system were introduced in details about the measurement system of the homogeneous entity profiles.

Introduction

The earliest method of reverse engineering technology was the probe measure with contact, its typical representative was called Coordinate Measuring Machine (CMM), which was mainly used in the digitization process of the entity's basic geometric shapes, suitable for measuring the external geometry of the entity. This method had high accuracy, but it was easy to fray the probe and mar the entity's surface, it needs manual intervention, and it had high cost, slow measurement speed, the use environment had exacting requirements. The 3D optical non-contact measurement method, such as raster, holography and 2D images, came forth after 1980s. The projection raster method was usually used to measure the external geometry form of the entity, its measurement range was wide, the measure precision was low, the measure velocity was fast and the cost was low, but it can not measure entity that its surface transformation is very steep. The laser trigonometry measurement method, its measure precision is high, the measure velocity was fast, but the cost was high and the surface of measured entity could not be too smooth^[1]. The precision of 2D image method was low and its processing arithmetic of the measured data was very complex. The above methods had the same limitation that they could not measure the interior figure. The current existing methods in international that can measure the interior of the entity are magnetic resonance imaging and CT scanning. But both of the two methods have high cost, the size of the entity is limited, the measure precision is low, particularly the material of tested entity is limited ,they can not measure metal materials used in the engineering field. The other method of measuring the interior of the entity is Automatic CT scan technology, although the precision of the method is high, but it has slow measurement velocity, high cost and long measurement time, and the method may undermine the tested components, so the application of it has been limited^[2].

With the deep development of reverse engineering technology, the research of 3D entity non-destructive measurement and reconstruction has more practical significance. The study not only for the general homogeneous entity but also some homogeneous entities with interior contour, can achieve non-destructive measurement and reconstruction. There are not successful measurement methods at home and abroad for the non-destructive measurement and reconstruction of the entities with interior contours. The paper studies the non-destructive measurement method for 3D entities with internal contour by using the Archimedes' principle, the lever principle and the gravity moment,

through them they are worked out for the 3D coordinate values of the minute entity cells^[3]. The method surpasses the traditional non-destructive measurement and reconstruction methods. This article describes the basic principle, hardware and software system of reverse engineering of homogeneous-entity product profiles.

The basic measurement principle and the system constitution

The basic principle of the measuring system. The basic principle of the measuring system in this program is shown in fig.1. According to the Archimedes' principle, the object immersed in liquid objects upward by the buoyancy, which equals to the liquid weight discharged of. That is to say, The Buoyancy has something to do with the density and volume of the liquid discharged of by the measured entity, but not the shape of the measured entity. This measurement supposes that the measured entity is an equal density and made up of very small square cube-unit entity, the liquid-selected density is known, according to connectors principle, the measured entity will immerge into the liquid completely in initial state, small pipe of the connectors will be in downward movement driven by the precise motion platform, the liquid surface will decrease every isometric piece layer (usually adopts a small cube module entity length, that is, a small cube module entity length). The measured entity will expose the liquid level every piece layer isometric. Without considering the effect of the dampening and the surface tension and other factors, the volume of liquid discharged from each layer should be equal to the volume of the measured entity layer. The 3D entity can be dispersed into the small discrete cube assembly with the expression method of the 3D entity in the space unit. The square unit is fixed up alignment along the direction of the coordinate, if it is the real unit, its quality regards as 1 and 1 is expressed as that the square body unit is filled, the entity exists in the corresponding position of every piece layer of the measured entity, on the contrary, the empty unit expressed as 0^[4]. The weight of every piece layer can be measured by the electronic scales and calculated the buoyancy changing value changed of the corresponding thin layers. Through surveying the three directions of X, Y, Z, combining parameters such as the liquid density, the torques of every thin layer, its quality and barycentre of the orderly every storey can be calculated. Changing the state of measuring, through data processing, utilize the algorithm of reconstructing to extrapolate the position of the small entity's unit in the three-dimensional coordinate system, obtain the three-dimensional information of the examined entity, and reconstruct its outline through CAD three-dimensional graphics processing software.

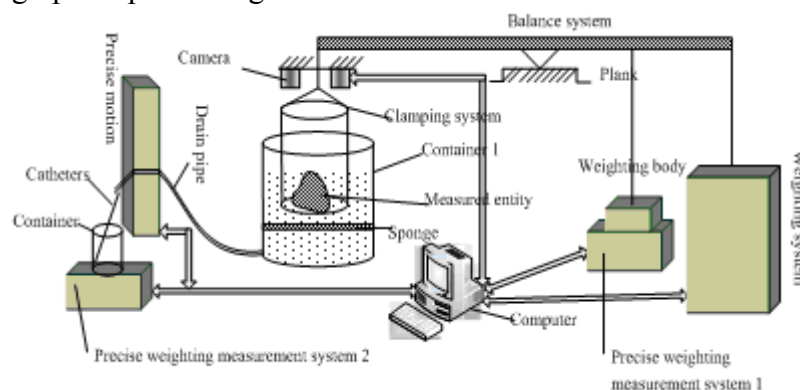


Fig.1 The sketch map of the basic principle of reverse engineering

The composition of the measure control system and the working process. The system constructed is a integration system that contains optical system, mechanical system, electrical system, hydraulic system, information system. It mainly includes the hardware composes of the balance system, the precise motion control system, the liquid level control system, the image acquisition system and the weight system and the software composes of the image acquisition control, the image processing and the data processing. Fig.2 shows the flow chart of the hardware system.

According to Archimedes' law, the object immersed in liquid objects upward by the buoyancy, which equals to the liquid weight discharged of, the formula as follows:

$$F_1 = G_1 = \rho_1 g V_1 \quad (1)$$

Where F_1 is the buoyancy objected by the measured entity immersed in liquid, ρ_1 is defined as the liquid density, V_1 is the liquid volume discharged of by the measured entity immersed in liquid.

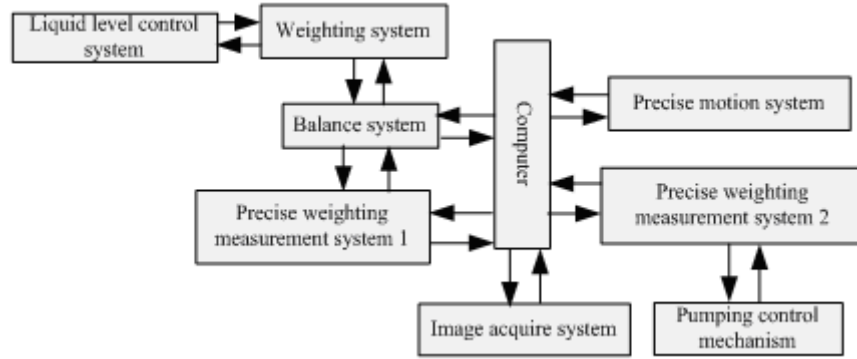


Fig.2 The flow chart of the hardware system

To achieve the measurement of the volume in each layer of the measured entity, use the precise measuring weight system 2(fig.1) directly to measure the weight of the liquid discharged of, and then calculate the volume of the liquid by Eq.1. In order to make compensation and correction for the effects of dampening and surface tension, the balance system is designed, then use the lever principle to measure the weight of the liquid discharged of and utilize the precise measuring weight system 1(fig.1) to measure the changes of buoyancy after each layer liquid discharged, and calculate the volume of the liquid discharged of, combine the precise measuring weight system 1 and 2, give the compensation and correction to the measured entity. Meanwhile, the gravity moment of each layer can be measured by building the space coordinate system and using the balance system, then the center of the gravity in each layer can be calculated. According to the volume of each layer, the quantity of the entities' unit cell can be calculated. Combine each layer's information about the gravity moment and the center of the gravity and the verge profile, the space coordinates of each unit cell can be calculated. When measuring, the measured entity will be immersed into the liquid completely, the mixed configuration liquid with color and small surface tension coefficient should be used, the balance of the balance system should be adjust through the weighting system. Meanwhile, make sure the measuring force of the measuring weight system 1 is small, the computer software will record the above results automatically. Precise motion control system guarantees the top liquid level of the drainage tube and container 1 at the same level in initial state, precise measurement weight system 2 records the initial values with the computer, the camera prepares for working. When the precise motion control system drives drainage tube down a small displacement (e.g.0.05 mm), the liquid level of container 1 descends the same distance, discharged liquid inflows to the container 2, precise measuring weight system 2 sends the weight value of the liquid discharged of to the computer, and then computer calculates the volume of this layer and records it. Meanwhile, the liquid level changes, in order to maintain the balance of the balance system, the force on the precise measuring weight system 1 will be changed, the computer records the value while balance. According to the relationship between the force and the distance on each fulcrum, we can calculate this layer's barcenter coordinate and volume. With the descend of the liquid level, when the precise measuring weight system is closing to its maximum measuring range, the system starts the injecting and pumping control mechanism respectively to balance weight, and record the various state values after balance, then repeat the measurement. In order to ensure the accuracy of measurement, the measured entity in three directions of X, Y, Z can be measured.

The software System design

The software system includes the initialization processing system, the measurement control system, the image acquisition and processing and verge detection system, the measuring and calculating system and the three-dimensional model reconstruction system.

The initialization processing system mainly used to determine, adjust and calculate the various control parameters, then use these parameters to initialize the parameters of the software, the initialization processing system diagram shown in Fig.3. It mainly includes the drain pipe and tank level position and the balance system level adjustment, the run distance and the run times of the movement control system each time, calculate the drain interval, determine the time of image acquisition and the image acquisition parameters and sizes. The balance system level could be adjusted through the weighting system. According to the measured entity dimensions and measurement precision, each time the run distance and run times of the movement control system can be calculated. The drain interval and the time of the image acquisition can be estimated by the distance of the liquid level suck down, the size of the container 1 and the time of the liquid discharged from the drain pipe.

The times of the image acquisition equal to the times of the motion control system operates. When the distance between the camera and the measured entity increasing during the acquisition process, the images are also changing. By setting acquisition four signs to deal with the captured images, the images achieve the same size through the image scaling processing. Then it is easy to deal with the contour tracing later.

The measurement control system is mainly to ensure the system operate concordant, isometric and stability and control the image acquisition system acquire images synchronously (Fig.4). Meanwhile, to achieve the precise measurement instrument overload protection, when the system reaches set conditions, drive the weight system work, then record the values of the equipments before and after. The accuracy of the precise motion control system has great impact on the measurement results. This experiment uses the BAYSIDELM motion platform series made in America^[5]. The repetitive positioning accuracy can reach $\pm 5 \mu m$. Tilt the table a certain installation angle to achieve the precise positioning. The measurement instruments uses the Swiss Metter-Toledo AB203-S Electronic Analytical Balance 1, the maximum weighing value is 220g, the precision arrives at 0.1mg, it is directly connected to the computer through the parallel interface and used to measure the changing force in the system.

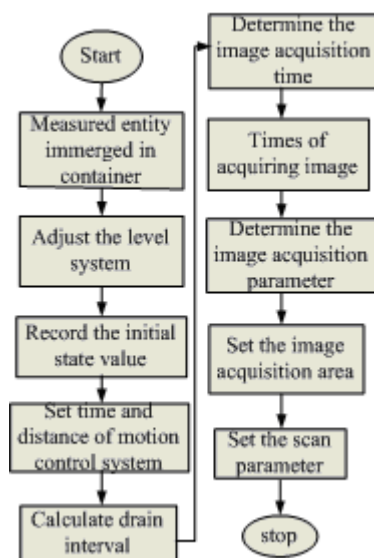


Fig.3 The flow chart of the initialization processing system

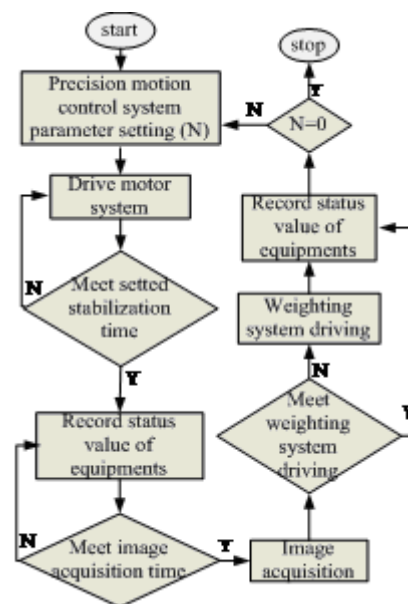


Fig.4 The flow chart of the measurement control system

The image acquisition system is mainly used to control the image real-time and accurate acquisition coordinates all aspects of the computer, shown in Fig.5. During the measurement processing, the camera is arranged with a certain angle, the liquid color is black. The acquisition images are calibrated through the image scaling, so as to facilitate the calculation of every unit cell. The acquisition image does not require higher precision.

The verge extraction processing and the measurement calculation system are used for the calculation of the position of the entities' cells in spatial coordinates, that is, calculating all the spatial coordinates of the tested entities. The verge extraction processing system is to simplify the measuring and calculating system, the part calculation of the unit cells can be estimated by the verge extraction processing. The measurement calculating system combines the equations and the center of gravity coordinates equation of the every layer, the associated nature of the measured entity between two layers, and all the minute entity cells only can be regarded as 0 or 1. Through intelligent calculation, we can get the coordinate values of the minute entity cells in space coordination.

Because the measurement system and the software system above have got all the coordinates of the points of the measured entities' cells and processed the corresponding error points, the point cloud figure of the measured entities have been completed. Three-dimensional model reconstruction system only should analyze the point cloud data and reconstruct models from point to line, from line to plane. The usual commercial CAD software can be used as the reconstruction software of the measurement system.

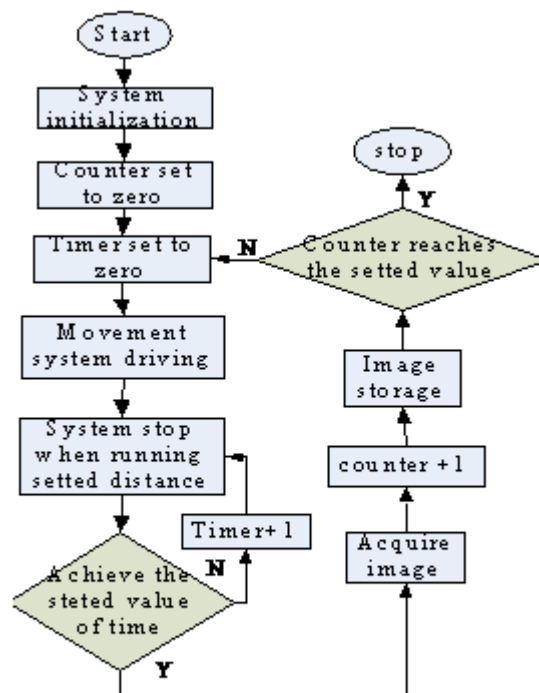


Fig.5 the flow chart of the image acquisition system

Conclusions

To demonstrate the accuracy and the feasibility of the measurement method and the measurement system designed, take the thickness of 1mm measured entity as a example. The contour of the measured entity can be reconstructed and amended through the point cloud of the center coordinates of each entity cell and the images of very layer maps. During the measurement processing, in order to ensure the boundary accuracy of the subdivided cells and improve the reconstruction accuracy, when calculate the number of the entity's cells, if a cell's volume is smaller than a whole cell but larger than its 1/2, then recorded as a whole cell; if it is smaller than its 1/2, then give it up. Take the length of 1mm cell, the reconstruction accuracy of the measured entity is 0.5mm. Due to the effect of the

mechanical friction, the fluid stability, the environmental temperature and other effect, the measurement time of the length of $50\text{mm} \times 50\text{mm} \times 50\text{mm}$ entity is about 3 hours. The experimental system costs less than ¥ 50,000. To further reduce the impact of the above factors, the sensors and the mechanical property can be further improved, through theoretical analysis and the preliminary measurements of the complicated entity, the reconstruction accuracy is expected to reach 0.1mm, and the three-dimensional entity with some through-hole internal contour can be measured.

Acknowledgements

This work was financially supported by the National Natural Science Foundation (50965005) and Scientific Research Project of Guangxi Education office (200911MS81).

References

- [1] Jin Tao, Chen Jianliang, Tong Shuiguang, reverse engineering research[J]. China Mechanical Engineering, 2002, 13(16): 1430~1436. In china.
- [2] Sang Xinzhu, LV Naiguang, Three-dimensional shape measurement method and its development trend[J]. Beijing Institute of Machinery Industry Journal, Vol16, No.2, 2001.6:32~36. In china.
- [3] Sun Ning, A 3D contour measurement of the equipment and methods[P]. China, applications for invention patents statements 03108989.5, 2003.9.16. In china.
- [4] Gan Yong, Sun Ning, Kong Qinghua, Buoyancy-based non-destructive measurement of 3D entity experiment system research[J], Shanghai Mechanical and Electrical Integration, 2007.1:28~30. In china.
- [5] BAYSIDE precision positioning platform[Z]. Beijing Yuan Mao control equipment technology companies with limited liability.

Study on the Parallel Rendering Technology used in Virtual Prototype System

Mingqiang Yin^{1,a}, Shiqi Li^{2,b}

^{1,2}School of Mechanical Science & Engineering, Huazhong University of Science & Technology, Wuhan 430074, China

^ayeml@163.com, ^bsqli@mail.hust.edu.cn

Keywords: Virtual Prototype; Parallel Rendering; PC Cluster; Model Transformation; Huge Dataset.

Abstract. With continuous expansion of manufacturing scale, the scene data that virtual prototype system has to deal with is far beyond a single computer's processing power. To meet the requirements of large-scale simulation, this study designs a virtual prototype system based on PC cluster. The problems including software architecture of virtual prototype system, transformation of CAD model, scene graph management, real-time rendering of huge dataset, and so on are investigated in detail in this paper. Finally a prototype system has been implemented. The system is constructed by PC cluster and gigabit LAN. The aim of the system is to build a large-scale, high resolution, immersive virtual environment supporting users' virtual design and manufacture.

Introduction

Virtual Prototype is a technology that uses computer models to do some experiments instead of real physical prototype. It is a computer-aided engineering, which developed rapidly with the development of computer technology in 1980s^[1]. The purpose of virtual prototype is to verify designing, to assist product selection, to test manufacturing and to display products ahead of time in digital method^[2]. Finally, it may replace the role of physical prototypes. Virtual prototype can significantly shorten the product design and manufacturing cycles, reduce the costs of product development and improve product design quality.

With the further promotion and application of the virtual prototype technology, simulation scene has extended from the small and simple object to the large-scale and complex product^[3]. Due to increasing 3D scene data, the data need to be dealt with is far beyond the power of a single computer. Image generation speed becomes a bottleneck of real-time simulating. Apparently, advanced hardware is helpful to solve the problem of large scene rendering. It should be noted that there are conflicts between infinite data and limited processing power that current hardware has. So it requires the virtual prototype system to use a variety of new technologies to solve this problem.

In this paper, we describe a virtual prototype system based on parallel computing, and then give the architecture of this virtual prototype system. At last we show some techniques used in the system, such as CAD model transformation, mesh model segmentation, parallel rendering based on PC-cluster. With high performance 3D graphics card and high-speed gigabit Ethernet, we developed a prototype system based on parallel computing.

Related work

It's relatively simple to realize the single-PC-based virtual prototype system, which has been extensively studied at home and abroad. With the quality of 3D scene data increasing, if not decrease the graph quality and complexity of 3D scene, parallel computing under cluster can be the only way to solve the problems in virtual prototype system.

Parallel computing in large-scene rendering has been extensively studied at home and abroad. Some general concepts applicable to cluster parallel rendering have been presented in[4-5] (sort-first architecture). Some generic APIs parallel rendering systems exist which include VR Juggler^[6](and its derivatives), Chromium^[7], OpenGL Multi-pipe SDK^[8] and Equalizer^[9]. VR

Juggler is a graphics framework for virtual reality applications which shield the application developer from the underlying hardware architecture, devices and operating system. Chromium provides a powerful and transparent abstraction of the OpenGL API, which allows a flexible configuration of display resources. OpenGL Multi-pipe SDK (MPK) implements an effective parallel rendering API for a shared memory multi-CPU/GPU system. The Equalizer parallel rendering framework differs in that it supports a fully distributed parallel rendering paradigm and features an extremely flexible task decomposition approach.

However, the targets for these approaches above are different for ours. Instead of parallel rendering only, we should like to devise a more scalable and affordable approach to support large-size scene simulation in virtual prototype system.

Architecture of virtual prototype system

The main features of the system are as follows:

Parallel and distributed computing: This virtual prototype system using the C/S architecture, all modules can be run on the remote server. It provides high-performance parallel numerical libraries, parallel program debugging, trace, and performance analysis tools. All the compute-intensive modules are implemented in parallel computing. MPI (message passing interface) is used as a basic interface for parallel communication.

Scalability: The system only implements the core modules and data management, and all other specific modules can interact with the core modules through TCP/IP dynamically. Problems could be solved collaboratively. All modules can be executed stand-alone. In the system four communication methods are supported, including shared memory, pipes, socket and documents. According to the location of module running, the amount of data to be exchanged and the feature of the problem, the system can choose different methods to communicate between different modules.

Wealth of computing technology support: According to current needs, our system has implemented some function modules such as geometric modelings, geometry repairing, mesh model generation, mesh model segmentation, scientific data visualization and remote job submission, task submission, resource management and so on.

Visualized manipulation: The virtual prototype system provides a friendly graphic interface, all the modules provide graphic interface. Users can control the whole process of calculation interactively. The calculation or manipulation result can be rendered by parallel rendering and displayed in 3D display-wall.

Cross-platform: The core and main modules of the system can run on the most common operating system such as Linux (IA32/IA64), Windows, Unix family platforms (SGI Irix, IBM AIX, etc.); It should support all major hardware platforms, such as shared memory architecture SMP and distributed memory architecture MPP, cluster and so on. Figure 1 shows the architecture of virtual prototype system.

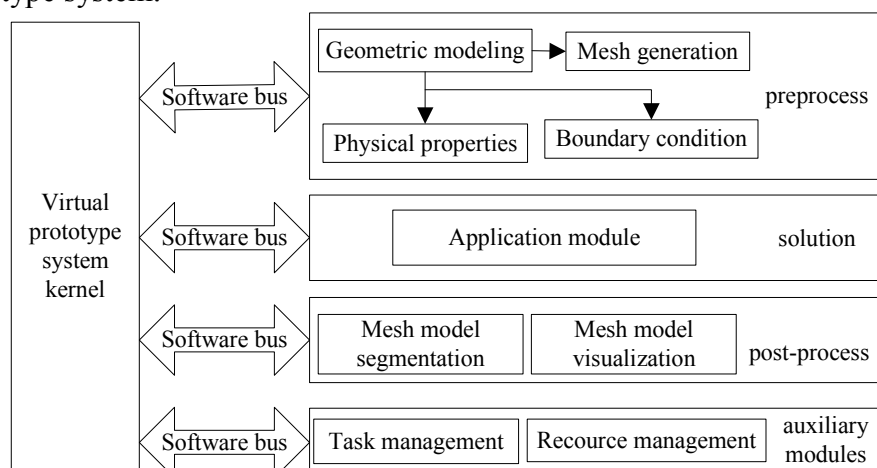


Fig. 1 Software architecture of high virtual prototype system

Important technologies in the system

4.1 CAD model transformation

Virtual prototype system uses triangle or polygon to represent product, whereas CAD systems use accuracy math method such as B-Rep and CSG to represent product. Therefore it is necessary to transform data information from CAD model to mesh model. Because most of CAD systems could save the product information as STEP (Standard for the Exchange of Product model data) format. Therefore, we could realize the data transformation from STEP format. A method based on STEP neutral file is proposed in this paper.

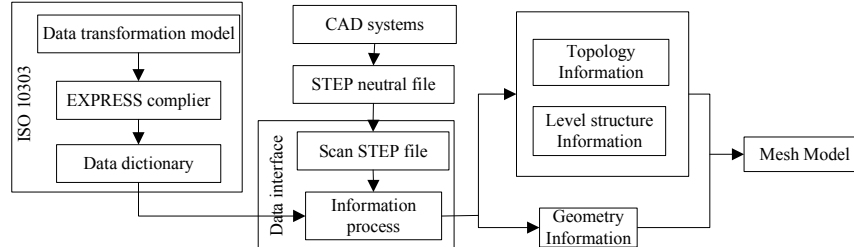


Fig. 2 CAD model transformation flowchart

The transformation flowchart is shown in Figure 2. First, we build the product model in any CAD systems, and export it with STEP format. Then we analyze the file with data interface which includes file scanning and information translation two parts. The data interface is constructed based on the ISO 10303. And the data dictionary is produced based on the analysis of the definition of entities which are defined with EXPRESS language. At last we get the geometry information, hierarchical structure information, and useful information which are necessary in simulation environment.

4.2 Mesh Model Segmentation

In parallel rendering module, if the size of the geometric model is so large, that it will cross several screen areas. The model will be rendered repeatedly in differently rendering nodes. Therefore, these large models will cause serious loss of efficiency. In order to solve this problem, we need to pre-segment the model and divide the whole model containing large facets into several sub-models which contains smaller facets. With the help of frustum cutting, only the sub-model within corresponding screen could be rendered. Thus the number of facets been rendered repeatedly could be reduced. The detail algorithm flow is shown in figure 3.

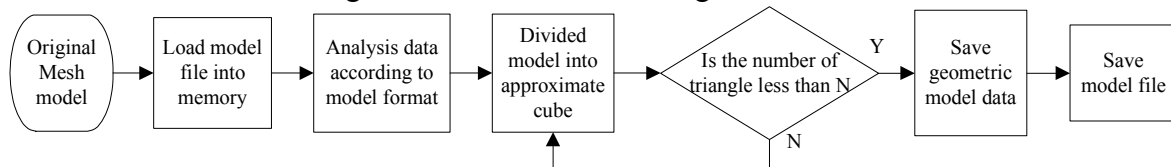


Fig. 3 Flow of mesh model segmentation

4.3 Scene graph management

This virtual prototype system runs in retained model. User node and compute nodes within the system store the entire 3D mesh model. These mesh models can be organized as a scene tree. The scene tree is also stored in distributing compute nodes. In logic, these scene trees can be looked as global scene tree. Any change in the global scene tree should be broadcast to all nodes in the system real-time to ensure the consistency of the rendering result. Global scene tree management focused on model loading, distributing information of the models, updating of the scene tree properties and deleting nodes of scene tree, etc.. In this system, all the model loading function is executed in every parallel computing node in the system, and it saves filename and pointer of the model in the global model library, and then takes a global identification for the mesh model. According to the identification, the address of model in the memory could be found out.

After system initializing, user node will broadcast information of models being loaded to all rendering nodes, then a copy of global model library will be generated according to the information received in every rendering node. With the global model library, mesh model can be loaded dynamically. During process of simulating, user nodes collect information of scene tree in every

frame, and send the information to other nodes, so as to keep content consistency of the scene tree property. Adding or deleting a mesh model in any parallel computing node will be broadcast to the other nodes, and the structure of global scene tree will be updated.

4.4 Parallel rendering

4.4.1 Architecture of parallel rendering

Figure 4 illustrates the principle of parallel rendering. The parallel rendering architecture is based on a master-slave model. It has an event loop which redraws the scene; update data based on received events, and eventually redraw a new frame. The master is responsible for managing the visualization system. It controls and launches the application's rendering clients. The render client implements the rendering part of an application. Its execution is passive. It has no main loop and is completely driven by the master. It executes the tasks received from the server by calling the appropriate task methods in the correct thread and context. The application either implements with application-specific code.

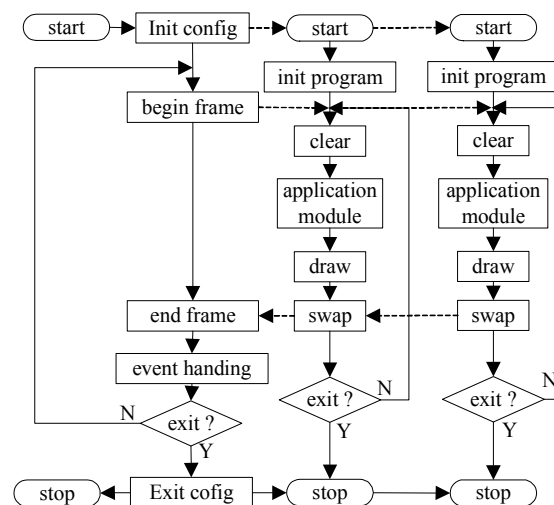


Fig. 4 Architecture of parallel rendering

4.4.2 Load balance

Load balancing is important for parallel rendering. In generally, the smaller the task is divided, the easier the system is to obtain load balancing. However, too smaller task dividing will bring huge information communicating. Therefore, for a parallel computing system, we must make a choice between task dividing and amount of communication data.

With respect to the principle of load balance, there are two methods in frustum division. The first one is to divide frustum statically. It means that when the program starts, dividing strategies and methods have been determined, and no longer changed during program execution. This algorithm is simple, and can reach a certain balance effect. In our system, we divide frustum dynamically. Our algorithm compares the number of triangular in each rendering node, and then take load balancing algorithm for the task dividing, to make sure that the task of each rendering node is relatively equal, and the performance of the system is better. Thus, the system could avoid the problem that a large number of geometric data be processed on a certain rendering node.

4.4.3 Off-screen rendering

Our virtual prototype system is based on parallel rendering. If we adopt the traditional CPU rendering pipeline without modification, there will be some problems. Firstly, each rendering node must render online, which means rendered image must be displayed, and can not be covered. Due to the reason of the operating system, the covered part may not be updated. Secondly, MPI process in slave can not be started in standard windows service mode. So in this MPI environment, the started windows programs will not appear on the screen. We use the latest OpenGL extension technology. It provides off-screen rendering function. In 2005, the OpenGL added a new expansion `GL_EXT_framebuffer_object`. Using this extension, you can create a Frame Buffer Object (FBO) and Render Buffer Object (RBO). This technical performance is greatly improved compared with the original PBuffer. Through this extension, we achieve off-screen rendering. If we simply use

FBO objects for off-screen rendering, the rendering process will not support anti-aliasing function, and the serrated phenomenon on the edge of rendering image will be serious. In order to achieve high-quality rendering of FBO, in 2007, OpenGL added two new extensions, GL_EXT_framebuffer_multisample and GL_EXT_framebuffer_blit. By using these two extensions, we can achieve smooth edges.

Experiment result and analysis

We have tested the virtual prototype system on a cluster composed of 5 computers. All computers are connected by gigabit LAN, and each computer is equipped with one core2 CPU, 2G DDR1 system memory and one graphic card of NVIDIA GeForce 7900 GS.

5.1 Communication Proficiency Test

This test is carried out between two nodes to test the transmission speed. We send the amount of data ranging from 100 Byte~ 5×10^6 Byte in one time. Result shows that the maximum transmission capacity is about 900Mb/s. Consider that we use resolution 1024×768 , then each frame size will be $1024 \times 768 \times 3 = 2\,359\,296$ Byte. Suppose that the efficiency of network transmission is 83%, and the transmission capacity will be about 740MB/s, and it will take 26ms to transmit on frame data.

5.2 Analysis of parallel rendering

In this test, we use one computer as user node and other 4 computers as render nodes. Each render node works as a projection channel and outputs frame images separately. All the system works as a sort-first rendering cluster. Projection channels setup their view frustum as their corresponding display portals and perform frustum clipping. Figure 5 shows the displayed image on the screen, and figure 6 shows the performances of the cluster comparing with single workstation. Figure 6 indicates that with lower triangle number, time consumed by rendering nodes swap-sync can't be neglected so that clusters run at a speed lower than single workstation; but as triangle number increased, swap-sync latency become negligible and the clusters become more efficient than single workstation. The speedup doesn't increase linearly, which is due to the subsistent latencies and the load imbalance of sort-first rendering structure.

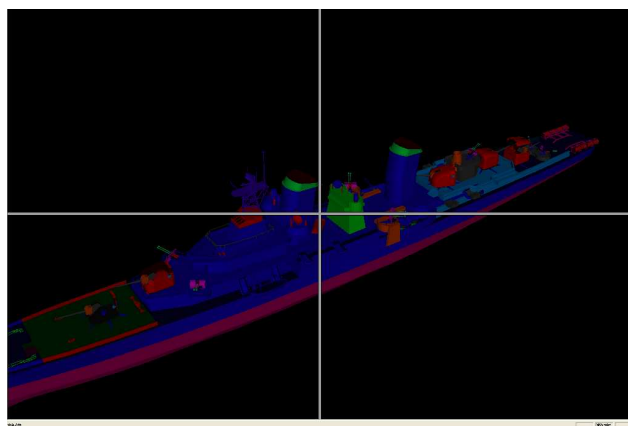


Fig.5 Sample image of virtual prototype system

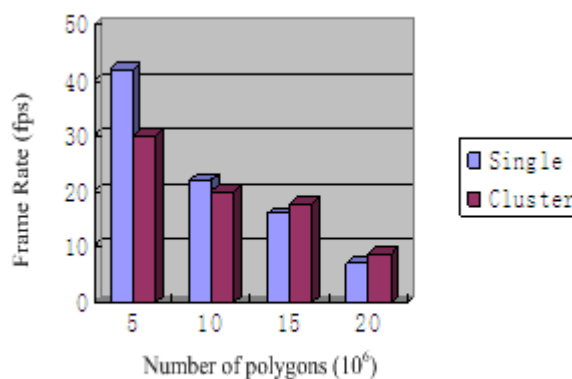


Fig.6 Rendering performance diagram

Conclusions

Virtual prototype is a comprehensive technology. It has been used to achieve optimal design and manufacturing. With the expansion of manufacturing, the object is simulated from simple scene to massive complex one. This paper presented a parallel computing method for interactive rendering of massive complex scene on PCs cluster. The proposed method include: CAD model transformation, mesh model segmentation, management of mesh model, and parallel rendering. CAD model transformation implements conversion method from CAD system to integrated virtual simulation environment. Mesh model segmentation cut the mesh model into smaller one to avoid rendering repeat. Scene graph management ensures the consistency of the scene tree in every

calculating node of the system. Parallel rendering performs the drawing of the whole scene. Experimental results have shown that our prototype system can achieve good performance for rendering massive complex scenes.

Acknowledgements

This research work has been partially supported by National High-tech Research & Development Program of China under Grant NO.2005AA804022.

References

- [1] Yan, X. and Gu, P. (1996). A review of rapid prototyping technologies and systems, *Computer Aided Design*, 28(4), 307318
- [2] Alik, S.M., Lin, J., and Goldenberg, A.A., "Virtual prototyping for conceptual design of a tracked mobile robot", *Canadian Conference on Electrical and Computer Engineering*, Ottawa, Ontario, Canada, May 2006.
- [3] Malik, S.M., "Virtual prototyping for conceptual design of tracked mobile robots," M.S. thesis, Dept. Mech. and Indust. Eng., Univ. of Toronto, Ontario, Canada, 2006.
- [4] MUELLER, C. 1995. The sort-first rendering architecture for highperformance graphics. In *Proceedings Symposium on Interactive 3D Graphics*, 75–84.
- [5] MUELLER, C. 1997. Hierarchical graphics databases in sort-first. In *Proceedings IEEE Symposium on Parallel Rendering*, Computer Society Press, 49–60.
- [6] BIERBAUM, A., JUST, C., HARTLING, P., MEINERT, K., BAKER, A., AND CRUZ-NEIRA, C. 2001. VR Juggler: A virtual platform for virtual reality application development. In *Proceedings IEEE Virtual Reality*, 89–96.
- [7] HUMPHREYS, G., HOUSTON, M., NG, R., FRANK, R., AHERN, S., KIRCHNER, P. D., AND KLOSOWSKI, J. T. 2002. Chromium: A stream-processing framework for interactive rendering on clusters. *ACM Transactions on Graphics* 21, 3, 693–702.
- [8] HUMPHREYS, G., ELDRIDGE, M., BUCK, I., STOLL, G., EVERETT, M., AND HANRAHAN, P. 2001. WireGL: A scalable graphics system for clusters. In *Proceedings ACM SIGGRAPH*, ACM Press, 129–140.
- [9] EILEMANN, S., MAKHINYA, M., AND PAJAROLA, R. 2008. Equalizer: A scalable parallel rendering framework. *IEEE Transactions on Visualization and Computer Graphics*, VOL. 15, NO. 3, MAY/JUNE 2009.

Models and Simulations of the UV lithography Process Based on Thick Photoresists

Zaifa Zhou^a, Qing'an Huang^b and Weihua Li^c

Key Laboratory of MEMS of the Ministry of Education, Southeast University, Nanjing 210096, China

^azfmzhou@seu.edu.cn, ^bhqa@seu.edu.cn, ^cliwh@seu.edu.cn

Keywords: Thick Photoresist; Lithography Simulation; Diffraction; Light Distribution; MEMS

Abstract: This paper presents the models for the ultraviolet (UV) lithography of thick photoresists such as thick SU-8. Simulations for various lithography conditions have been conducted using these models based on the improved dynamical cellular automata method. Some experiments on SU-8 2075 layers under UV source with 365nm wavelength have been implemented to verify the simulation results. The results confirm the validity of the proposed models.

Introduction

Ultraviolet (UV) lithography of thick photoresists such as SU-8 photoresists is increasingly adopted to manufacture novel and complex high aspect-ratio Micro-Electro-Mechanical Systems (MEMS) elements [1-3], since relatively simple and inexpensive lithography equipments are utilized compared to X-ray or laser systems. The UV lithography process of the SU-8 consists of several steps. The SU-8 is firstly spin coated onto a substrate and soft baked to evaporate the solvent. Then the SU-8 is exposed to the UV light, the photoacid generator (PAG) decomposes and generates photoacid within the SU-8. During the subsequent post-exposure bake (PEB) process, the photoacid catalyzes the reaction between the resin and the cross-linking agent to afford a highly cross-linked polymer network which is significantly less soluble than the polymer resin without cross-linking reaction. At last, the unexposed SU-8 is dissolved by an organic solvent, leaving only the cross-linked SU-8 microstructures on the substrate. Many factors affect the final development profiles of the SU-8. It is not practical to determine the best fabrication parameters for the UV lithography process of thick SU-8 using the traditional repeated experiment method. Simulation is acknowledged to be efficient for predicting and optimizing the lithography process.

In this paper, the models for the UV lithography of thick photoresists such as thick SU-8 are presented. A series of simulations for various lithography conditions have been conducted using these models, based on the improved dynamical cellular automata method [4]. Some experiments on SU-8 2075 layers under UV source with 365nm wavelength have been implemented to verify the simulation results. The results confirm the validity of the proposed models.

Simulation models

Ideal contact exposure without any gap between the mask and the SU-8 is not practical for inevitable errors such as surface flatness, surface roughness, etc.. Air gaps from 10 μ m to over 100 μ m are very common for UV lithography process of thick SU-8. The thicker the SU-8 layer is, the larger the gap may be. Because of the high viscosity of the SU-8, it is difficult to obtain uniform spin-coat. For thick SU-8 layer, the UV light diffraction effect of the mask pattern will lead to severe profile distortions. To reduce the diffraction effects, different index matching materials such as water and glycerol have been adopted as index matching materials to fill the air gap [3, 5].

To simulate the light intensity distributions for the UV lithography of thick SU-8 with index matching materials, we define some parameters associated with the calculations of the UV light intensity distribution. n_1 , n_2 , n_3 and n_4 are defined as the refractive indices of air, index matching materials, SU-8 photoresists and wafer, respectively. λ_1 , λ_2 , λ_3 and λ_4 stand for the UV light

wavelength in air, index matching materials, SU-8 photoresists and wafer, respectively. R_1, R_2 and R_3 are the reflection coefficients at air/index matching materials, index matching materials/SU-8 and SU-8/substrate interfaces, defined by $R_1 = ((n_2 - n_1)/(n_2 + n_1))^2$, $R_2 = ((n_3 - n_2)/(n_3 + n_2))^2$ and $R_3 = ((n_4 - n_3)/(n_4 + n_3))^2$, respectively.

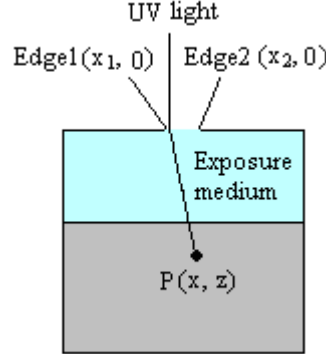


Fig. 1 Schematic of the UV light transmission in a single long slit

For the UV light from S reaching P through a hole, as shown in Fig.1, the Fresnel-Kirchhoff diffraction integral formula has the following form utilizing paraxial approximation technique [5]

$$U_P = -\frac{iA}{2(r+s)} e^{ik(r+s)} \{ [c(u_2) - c(u_1)] + i[s(u_2) - s(u_1)] \} \cdot (1+i) \quad (1)$$

where A is the incident light wave amplitude. r and s stand for the distances of a point on the aperture relative to the observation point and the source, respectively. $k = 2\pi/\lambda$ is the incident wave number,

where λ is the wavelength of incident UV light in the exposure medium. $c(u) = \int_0^u \cos(\pi y^2 / 2) dy$

and $s(u) = \int_0^u \sin(\pi y^2 / 2) dy$ are the Fresnel integrals, where u (u_1 and u_2) is the Fresnel number written as

$$u_i^2 = \frac{2}{\lambda z} (x_i - x)^2, \quad i=1,2 \quad (2)$$

where z is the vertical distance from the mask plane to the calculation point in the SU-8, x_1 and x_2 represent the horizontal coordinates of the left and right edges of the mask, respectively.

Thus the light intensity distribution equation considering the reflection at the air/index matching materials and index matching materials/SU-8 interfaces can be expressed as

$$I_P = U_P^* \times U_P = |U_P|^2 = \frac{(1-R_1)(1-R_2)I_{lamp}}{2} \{ [c(u_2) - c(u_1)]^2 + [s(u_2) - s(u_1)]^2 \} \quad (3)$$

where I_{lamp} is the original intensity of the UV light from the UV source.

During the propagation of the incident UV light, the UV light will be refracted on the index matching materials/SU-8 interface. When the UV light transmits into the SU-8 from the index matching materials, the wavelength, phase, and other relevant information will be changed. The effect of light refraction effect on the final development profiles can not be neglected for soft contact lithography because of the gap between the mask and the SU-8, as shown in Fig.2. However, it is difficult to deal with this refraction in Fresnel integral equation, so the refraction effect has not been considered in current SU-8 UV lithography simulation. This paper presents a method to incorporate the refraction effect into the Fresnel diffraction integral for the UV lithography processes of the SU-8 in two steps.

Fig.2 shows the UV refraction modeling at the index matching materials/SU-8 interface. Firstly, p_1 represents the gap thickness between the mask and the SU-8. Secondly, the mask plane is vertically shifted in such a way that the same field distribution results at the interface between the index matching materials and the SU-8. The gap between the mask and the SU-8 is assumed to be

homogeneously filled with SU-8, and the propagation of the field inside the original SU-8 is now treated as if there were no step in the refraction index behind the mask. In this way, diffraction and refraction effects can be handled simultaneously. p_2 represents the gap thickness after shifting the mask.

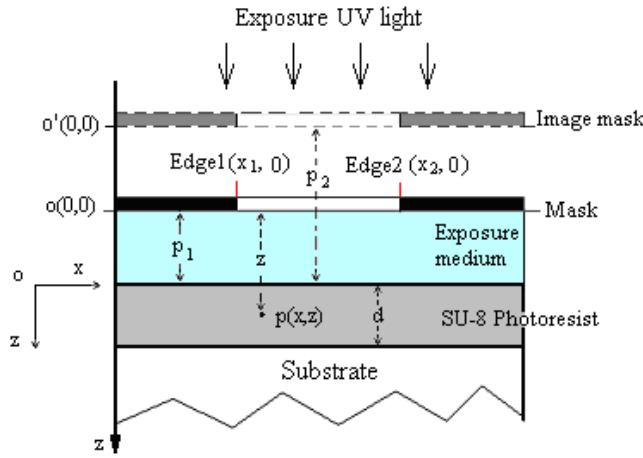


Fig. 2 The aerial image modeling for the UV lithography of the SU-8

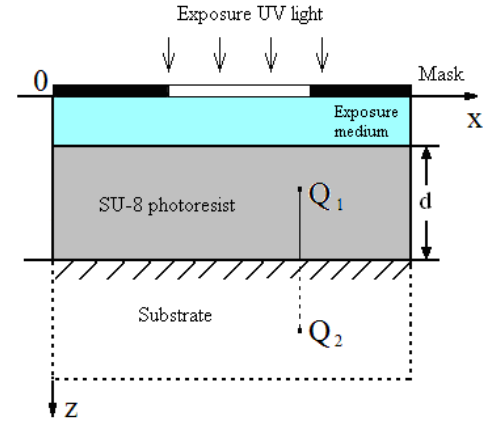


Fig. 3 Schematic of the UV reflection at the SU-8/substrate interface

Before shifting the mask, for the observation point $P(x, z)$ at the index matching materials/SU-8 interface, the scalar field is

$$U_p(x, z) = B' \{ [c(u_2') - c(u_1')] + i[s(u_2') - s(u_1')] \} \cdot (1 + i) \quad (4)$$

where $B' = -\frac{iA}{2(r+s)} e^{ik_1(r+s)}$, and the Fresnel number $u_i' = \sqrt{\frac{2}{\lambda_2 p_1}} (x_i - x)$, $i=1,2$. k_1 stands for the wave number in the index matching materials.

After shifting the mask, for the same observation point, the scalar field is

$$U_p(x, z) = B'' \{ [c(u_2'') - c(u_1'')] + i[s(u_2'') - s(u_1'')] \} \cdot (1 + i) \quad (5)$$

where $B'' = -\frac{iA}{2(r+s)} e^{ik_2(r+s)}$, and the Fresnel number $u_i'' = \sqrt{\frac{2}{\lambda_3(z-p_1+p_2)}} (x_i - x)$, $i=1,2$. k_2 stands for the wave number in the SU-8.

For $r \ll s$ during the UV lithography process of SU-8, the modulus of B' is approximate to B'' . When computing the intensity of the UV light, we only need the modulus of B' and B'' . In order to insure that the field distribution at the index matching materials/SU-8 interface after shifting the mask is the same as the original one, u_i' should be equate to u_i'' . So we can obtain $p_2 = p_1 \cdot n_3 / n_2$. Therefore, the propagation of the light field inside original SU-8 can be treated as if there were no step in the refraction index behind the mask

$$I_p' = \frac{(1-R_1)(1-R_2)I_{lamp}}{2} \{ [c(u_2') - c(u_1')]^2 + [s(u_2') - s(u_1')]^2 \} \quad (6)$$

$$u_i'^2 = \frac{2(n_3/n_2)}{\lambda_3(z-p_1+p_2)} (x_i - x)^2, \quad i=1,2 \quad (7)$$

Generally, the incident UV light will be reflected by the SU-8/substrate interface, and the reflected UV light will pass through the SU-8. Thus besides the diffraction and refraction effects, it is important to incorporate the effects from the reflected UV light on the light intensity distribution into the SU-8. To understand the reflection effect, we mirror the SU-8 at the SU-8/substrate interface. As shown in Fig.3, the reflected intensity at point Q_1 can be calculated out by the Fresnel reflectance at the SU-8/substrate interface and the incident intensity at point Q_2 (the symmetric point of Q_1).

Based on above analysis, the final equation with diffraction, refraction and reflection effects for the intensity distribution pattern calculation at point p, can be finally expressed as

$$I''_p = \frac{(1-R_1)(1-R_2)I_{lamp}}{2} \{ [c(u'_2) - c(u'_1)]^2 + [s(u'_2) - s(u'_1)]^2 \} + R_3 \{ [c(u'_4) - c(u'_3)]^2 + [s(u'_4) - s(u'_3)]^2 \} \quad (8)$$

$$u'^2_i = \frac{2(n_3/n_2)}{\lambda_3(z - p_1 + p_2)}(x_i - x)^2, \quad i = 1, 2 \quad (9)$$

$$u'^2_i = \frac{2(n_3/n_2)}{\lambda_3(2d + p_1 - z + p_2)}(x_i - x)^2, \quad i = 3, 4 \quad (10)$$

where d represents the thickness of the SU-8 layer.

After the light intensity distribution into the SU-8 is obtained using aerial image simulation, the exposure simulation model is used to express the exposure kinetics in the SU-8. Now the problem is that the *Dill* model [6] originally developed for thin photoresist lithography is insufficient to describe the nonlinear effects in the thick SU-8 layers. Unlike the thin photoresists, the nonlinear effects in the thick photoresists, such as the concentration distribution of photoresist components, will significantly affect the exposure processes. To solve the problem, an improved *Dill* model [4] is developed to describe the exposure kinetics in thick SU-8 exposure processes.

During the PEB process, the photoacid induces chemical reactions in the SU-8, resulting in cross-linking of epoxy resin. Since the photoacid concentration is not uniform in the SU-8, there is a photoacid diffusion process while the catalytic conversion is undergoing. The chemical reactions and diffusion of species happen simultaneously and couple with each other. The coupled reaction-diffusion kinetics [7] can be employed to describe the PEB process for the SU-8.

For the development process simulation, the *Notch* model [8] is employed to describe the relationship between the etching rate and cross-linked site concentration. Furthermore, the photoresist etching rate will be significantly increased, because agitation methods are usually adopted for high aspect ratio and/or thick film microstructures during the development processes. Since the etching processes of the SU-8 are depth dependent, and the swelling effect will significantly affect the development profiles of the SU-8. The above *Notch* model, however, should be modified to incorporate the depth-dependent dissolution rate effect, and the swelling model should be adopted to obtain the final development profiles [4].

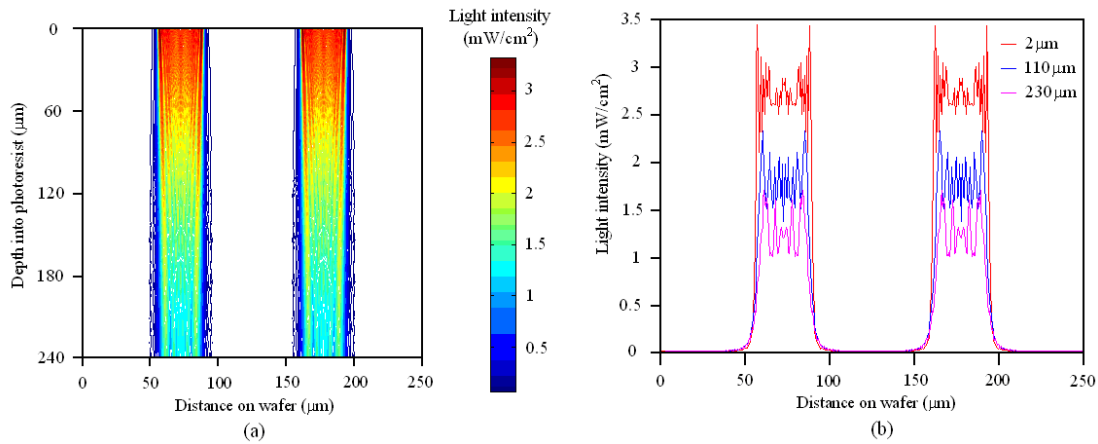


Fig. 4 Simulated light intensity distribution into the SU-8 at the beginning of the exposure process under 280s exposure for 35μm/70μm line/space: (a) the light intensity distribution at the beginning, (b) Fresnel diffraction pattern, for different depth in the SU-8 at the beginning

Simulations and Discussions

Combining the above models and the surface movement algorithms for etching simulation, the UV lithography process simulations of the SU-8 can be implemented. Based on the improved 2D dynamic cellular automata method [4], developed from the original 2D dynamic cellular automata method [9], above mentioned aerial image simulation model, exposure simulation model, PEB simulation model and development simulation model can be used for the simulation of the UV lithography of thick

SU-8. To verify the simulation results, some experiments have been performed using SU-8 2075 under UV source with 365nm ($2.6\text{mW}/\text{cm}^2$) radiation.

Fig.4 shows the simulated light intensity distribution into the SU-8 at the beginning of the exposure process for $35\mu\text{m}/70\mu\text{m}$ line/space microstructure. Here the thickness of the SU-8 layer is $240\mu\text{m}$ and the SU-8 is exposed for 280s using the contact exposure method (assuming the air gap between the mask and the SU-8 is about $15\mu\text{m}$). Fig.5 shows the simulation and experimental profiles of the UV lithography of thick SU-8 for 13min development. The line width at different depth of the SU-8 microstructure was measured, and the variation from the top to the bottom is less than $2.01\mu\text{m}$, and the largest line width variation between the simulation result and experimental result is less than $1.49\mu\text{m}$.

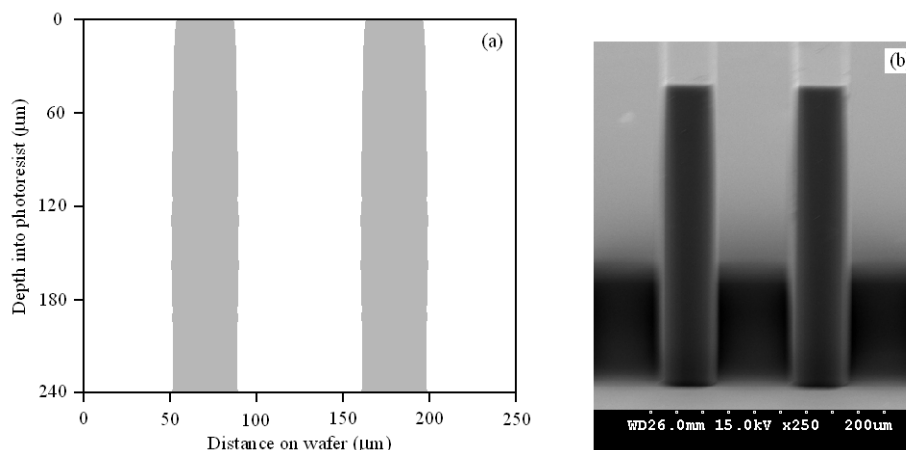


Fig. 5 Simulation result (a) and experimental result (b) for the UV lithography of the SU-8: exposure time=280s, development time=13min, line/space= $35/70\mu\text{m}$.

Conclusions

The models for the UV lithography of thick photoresists have been presented. Combining the models and the improved dynamical cellular automata method, the UV lithography process simulations of the SU-8 have been implemented. The simulations have been verified by the experiments on SU-8 2075 layers under UV source with 365nm wavelength. The results confirm the validity of the proposed models.

Acknowledgements

The authors thank Prof. Chen Di, Zhu Jun, and Ni Zhi-Ping from Shanghai Jiao Tong University, China for some experiments. The project is supported by the Foundation of Southeast University of China under Contract KJ2010409 and 3206000501.

References

- [1] A. Campo and C. Greiner: J. Micromech. Microeng. Vol. 17 (2007), p. R81
- [2] A. Llobera, V. Seidemann, J. A. Plaza, V. J. Cadarso and S. Buttgenbach: J. Microelectromech. Syst. Vol. 16 (2007), p. 111
- [3] R. Yang and W. J. Wang: Sens. Actuators Vol. B110 (2005), p. 279
- [4] Z. F. Zhou, Q. A. Huang, W. H. Li, M. Feng, W. Lu and Z. Zhu: J. Micromech. Microeng. Vol. 17 (2007), p. 2538
- [5] Y. J. Chuang, F. G. Tseng and W. K. Lin: Microsyst.. Technol. Vol. 8 (2002), p. 308
- [6] F. H. Dill, A. R. Neureuther and J. A. Tuttle: IEEE Trans. Electron Devices Vol. ED-22 (1975), p. 456
- [7] M. Zuniga, G. Wallraff and E. Tomacruz: J. Vac. Sci. Technol. Vol. B11 (1993), p. 2862
- [8] A. Mack and G. Arthur: Electrochem. Solid-State Lett. Vol. 1 (1998), p. 86
- [9] Z. F. Zhou, Q. A. Huang, W. H. Li and W. Lu: J. Micromech. Microeng. Vol. 15 (2005), p. 652

Research on Computer-Aided Conceptual Design of Palletizing Robot

Zhongming Li^a, Wei Liu^b

¹School of Automation, Beijing University of Posts and Telecommunications, 100876, China

^abuptlzm@163.com, ^btwlhw@163.com

Keywords: Conceptual Design; Palletizing Robot; Computer-Aided Design

Abstract. The method of computer-aided design oriented to requirement configuration is present for the palletizing robot. Index of design requirement is quantified hierarchically. The whole function of palletizing robot is decomposed according to the working plane. The various kinds of attributes of function carriers are digitized and the consistency is kept with the index of design requirement. Optimal design scheme can be gotten by the computation of evaluation function constructed in this paper. The software of computer-aided conceptual design for palletizing robot is developed.

Introduction

Conceptual design is very important stage in the whole design process of product and innovation, fuzziness and diversity are its features. Computer aided technology of conceptual design is a important research field at present. For mechatronic product, for example, the palletizing robot, the market requirements are diversified and there is an intense competition. The design scheme should be provided agilely according to the individual requirements. Such theories as Theory of the Solution of Inventive Problems (TRIZ) and Quality Function Deployment (QFD) support the process of conceptual design effectively and many papers about these research fields can be found [1]. Some researchers also do lots of works on the automatic generation of design scheme. For example, genetic algorithm, evolution strategy and ant algorithm are applied to the solution of conceptual design scheme [2] [3]. The solution of design scheme should be connected with design requirements from the market with individual requirements.

To meet the costumer requirements as much as possible, computer technology should be used to support fully the process of conceptual design and efficiency will be improved. For the studying object of palletizing robot's conceptual design, a method of digitized design is present in this paper. The requirements index and the attributes of function carriers are quantified, and evaluation method is constructed to select the optimal design scheme of palletizing robot meeting the customer requirement.

Analysis of conceptual design of palletizing robot

The general model of conceptual design. The process of conceptual design of mechatronic products includes several steps as requirement analysis, function decomposition, scheming solving and evaluation [4]. The process model of conceptual design is shown in Fig.1. Firstly the design requirements of product are analyzed and the whole function is defined. Then the whole function can be decomposed into several sub functions. Feasible structure will be found out to realize every subfunction. Finally all function carriers are synthesized and evaluated and the optimal design scheme is obtained. Conceptual design of palletizing robot is based on the model shown in Fig.1 and computer-aided design process is realized in this paper.

Function decomposition of palletizing robot. The task of palletizing robot is transportation of goods from some position to another position and generation of regular stack in accordance with a certain pattern, and goods has no rotation around horizontal axis in process of motion. The whole function can be decomposed by working plane, as shown in Fig.2, after analyzing various kinds of structures and working characteristics of palletizing robot. Palletizing robot implements the elevation

and lowering motion in YZ-plane and movement to the position of stack in XY-plane. Solving of scheme are done separately in these two motion plane. Function carriers meeting the requirement of movement in single working plane is very much, and structure form are various, so computer-aided technology is needed to assistant the rapid searching of optimal solution.

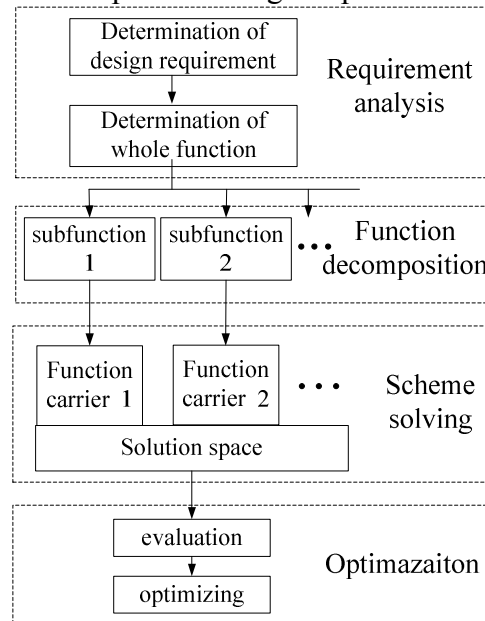


Fig.1. Process model of conceptual design

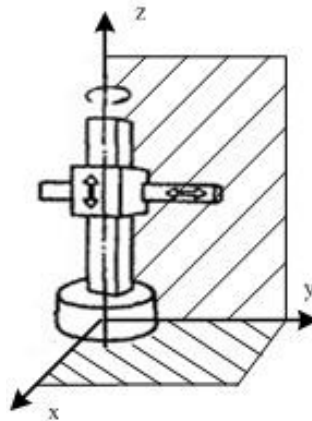


Fig.2. Function decomposition by working plane

Application of computer- aided technology oriented requirement

To support the computer-aided conceptual design, digitization of design process is need to be realized which includes the digitization of design requirement, field knowledge and so on.

Index of customer requirement. Because of different environment and working object, there is a great difference in performance requirements of palletizing robot. For example, the palletizing object may be box with 5 kg medicine, or bucket with 100 kg liquid, but the demand for size and efficiency of palletizing robot are very different. So the optimal design scheme must be based on the analysis of individual customer requirement. Five main indexes of requirement are considered on the basis of analysis of working environment for many kinds of palletizing robot. The indexes are cost, size, load, efficiency and mass and they constitute the synthetic requirement index vector R

$$R = \{R_1, R_2, R_3, R_4, R_5\} \quad (1)$$

where, R_1 is index of cost, R_2 is index of load, R_3 is index of efficiency, R_4 is index of size, R_5 is index of mass.

Consideration degree of these five requirement indexes are varied in different working environment, and the weight of requirement index is digitalized necessarily to support the application of computer-aided design. The numerical value on interval [0, 1] is used to define the consideration degree of every requirement index. If the value is 0, it indicates that there is no consideration on this requirement index. The value is bigger, this index is more important and the value 1 indicates that this index is the most important one compared with other indexes. Requirement weight vector W is composed of all weights of requirement index.

$$W = \{W_1, W_2, W_3, W_4, W_5\} \quad (2)$$

where, W_i ($0 \leq W_i \leq 1$, $i=1,2,3,4,5$) is the weight of corresponding R_i .

Digitalization of function carrier attributes. To fully realize the computer-aided conceptual design for palletizing robot, the related field knowledge also needs to be digitalized. The whole function of palletizing robot is decomposed into subfunctions in XY-plane and YZ-plane, and function solutions in two planes are combined into the whole design scheme of palletizing robot. Solutions in every plane have various kinds of principles and structures and these function carriers constitute solution space.

To support the application of computer aided technology, attribute vector is constructed in which elements corresponding to requirement index are included. The attribute vector P is defined as follow.

$$P = \{P_1, P_2, P_3, P_4, P_5, P_6, P_7, P_8\} \quad (3)$$

where, the meaning of every element is shown in Tab.1.

The value of attribute is quantified as five grades so that difference in attribute of individual function carriers can be specified. The value of five grades is defined as 1, 2, 3, 4, 5 and the meanings of quantified value for elements in attribute vector are shown in Tab.1.

Table.1. Meaning of function carrier attributes

symbol	element	meaning of attribute value
P_1	cost	1-very high, 2-higher, 3-general, 4-lower, 5-very low
P_2	load capacity	1-very strong, 2-stronger, 3-genera, 4-weaker, 5-very weak
P_3	efficiency	1-very high, 2-higher, 3-general, 4-lower, 5-very low
P_4	size	1-very big, 2-bigger, 3-general, 4-smaller, 5-very small
P_5	mass	1-very heavy, 2-heavier, 3-general, 4-lighter, 5-very light
P_6	input power	1-electric, 2-mechanical, 3-hydraulic, 4-phneumatic, 5-other
P_7	output power	1-electric, 2-mechanical, 3-hydraulic, 4-pneumatic, 5-other
P_8	movement type	1-rotation, 2-translation, 3-other

Attributes from P_1 to P_5 are consistent with elements in requirement index vector. Attributes P_6 and P_7 indicate power type of input and output port. They ensure the matching of upstream or downstream function carrier's port so that the combined function solution is feasible. The power types include electric, mechanical, hydraulic, pneumatic power and so on. P_8 indicates type of output motion which includes rotation and translation.

Scheme generation based on evaluation function

Definition of evaluation function. Function carrier library is composed of lots of carriers and their attribute vector. It is the solution space for subfunctions of palletizing robot. For a specific design requirement, many feasible solutions can be found. The evaluation function is needed to determine every design scheme good or bad. Comprehensive evaluation is suitable for conceptual design.

Combined with requirement index stated in previous part, the evaluation function is defined as follow.

$$E = \sum_{i=1}^n \left(\sum_{j=1}^5 W_j \cdot |R_j - P_{ij}| \right) \quad (4)$$

where, n is total number of function carriers in whole design scheme.

R_j is element of requirement index vector in Eq. 1, where R_j should be the quantified value corresponding to requirement index. It indicates the different demand for individual index, and its value is 1, 2, 3, 4 or 5, where its meaning is consistent with the value in Tab.1. W_j is element of weight in equation (2). P_{ij} is element of attribute vector and it indicates the j th attribute value of i th function carrier. This evaluation measures the consistency between design requirements and attribute vectors of all carriers in whole design scheme. The value of E is smaller, the design scheme is more consistent with design requirement.

Searching of optimal scheme. The generation process of design scheme is shown in Fig.3. The computer-aided conceptual design is a process of man-computer interaction, and design procedures are based on function decomposition of palletizing robot. In XY-plane or YZ-plane, basic motion is further divided into rotation and translation and so on according to movement type. These parameters can be configured in man-computer interaction module. Every motion type can be mapped into many kinds of specific function carriers. For example, translation motion can be mapped into rack-and-pinion, lead screw and hydraulic cylinder and so on. According as parameters set in man-computer interaction module, computer searches the solution in function carrier library for single plane motion. Then the function solutions are combined and port matching of upstream and downstream carriers is ensured. All feasible combined solutions are found out and evaluated by evaluation function respectively. The design scheme whose value of evaluation function is the smallest is the optimal solution.

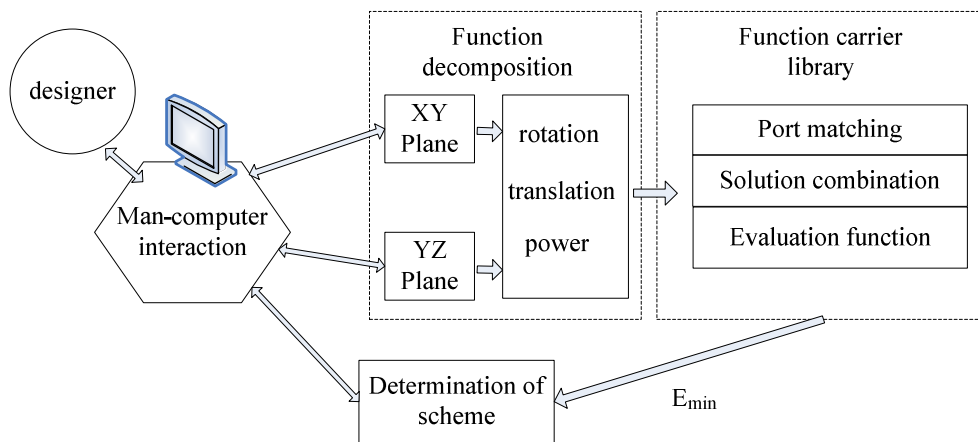


Fig.3. Process of scheme generation

Software prototype

Software system of computer-aided conceptual design for palletizing robot - PRCAD is developed. Java program language and database management system MYSQL are used as development tools. Several modules are included in PRCAD, such as requirement design module, database management module, scheme solving module, result display module and so on.

Up to now tens of carriers is collected into the function carrier library. The library keep to be open and carriers can be added, edited or deleted. Optimal solution set can be provided by PRCAD according to the parameters in requirement design module. The solution set is composed of several optimal solutions whose value of E is minimum or second minimum.

Conclusions

Palletizing robot is complex mechatronic product and scheme of conceptual design has the feature of multiplicity of solutions. Technology of computer-aided conceptual design can be applied to find out optimal scheme quickly. The method of computer-aided conceptual design for palletizing robot is present in this paper and is oriented to requirement configuration. Requirement index and attribute of function carrier are digitalized, and the optimal solution can be found out in lots of feasible solutions by evaluation function. Software system of is developed based on this method proposed in this paper. The software is used for conceptual design of palletizing robot and the method is reasonable and feasible.

Acknowledgements

This work is supported by the Fundamental Research Funds for the Central Universities.

References

- [1] CUI Yong, SUN Feng: Computer Integrated Manufacturing Systems Vol.12 No.2 220-224 (2006). (In Chinese)
- [2] QIU SL, KORK SC, CHEN CH: The international Journal of Advanced Manufacturing Technology, 20 (9) 683-691 (2002).
- [3] Bo Ruifeng, Huang Hongzhong, Wu Weidong: Journal of XI'AN JIAOTONG University Vol.39 No.11 1236-1240 (2005). (In Chinese)
- [4] ZHAO Hong, HUANG Hongzhong: Chinese Journal of Mechanical Engineering Vol.42 No.10 190-196 (2006). (In Chinese)

Study on the Computer Numerical Control Process of Variable Pitch, Groove Depth and Groove Width Screw

Min Han^{1a*}, Shan Li^{2b}, Lutao Deng^{3c}

¹ Department of Mechanical Engineering, Xiamen University of Technology, Xiamen, 361024,

² Department of Mechanical and Electric Engineering, Xiamen University, Xiamen, 361005, China

³ Huaxia College, Xiamen, 361024, China

¹hanw20032004@163.com, ^{2,3}mhan@xmut.edu.cn

Keywords: Variable Pitch; Groove Depth; Groove Width Screw; Mathematical Analysis; CNC Machining.

Abstract: The article introduces three design techniques of variable pitch & groove depth & groove width screw. We found parameterized mathematical model of the type of heterotypic screw by analyzing and computing. Then it can realize to CNC machining of variable pitch & groove depth & groove width screw on lathe.

Introduction

Molding screw is the essential part in the nylon zipper molding machine. In the waterproof of nylon zipper molding machine, the temperature is changing constantly and leading to change nylon diameter and elongation constantly during molding process of sprocket. So the type of heterotypic screw should have groove with variable pitch & groove depth & groove width. Besides, this type of heterotypic screw is providing device of various extruding machine. It was widely used for the processing of raw material and delivery process in petroleum, chemical industry, steel rolling, oak plastic, light industry, and machine industry and so on ^[1]. Therefore, we have found the corresponding mathematic model by researching on the relationship between basic theory and parameters of the heterotypic screw. It can offer theoretical basis for optimized design and CNC machining of the heterotypic pitch screw. Then we developed special CNC machining program of variable pitch & groove depth & groove width screw.

Design of heterotypic screw

A whole heterotypic screw is composed by export segment, middle segment and import segment. Then export segment and import segment usually are isometric spiral line. However, middle segment is variable spiral line which can be used variety of ways, such as steady accelerated spiral curve, sine or cosine accelerated spiral curve, polynomial accelerated spiral curve and so on. The distance from arbitrary point on spiral curve to initial point on screw is supposed as L . In the export segment, initial pitch is R_0 , groove depth is H_0 and groove width is d_0 . In the middle segment, variable pitch length is L_m , pitch variation is ΔR , groove width variation is Δd , groove depth variation is ΔH and circle number of screw thread is i . If total circle number of variable pitch in middle segment is i_m , then in the import segment, pitch should be R_m , groove depth should be H_m and groove width should be d_m . If rotational speed of screw is n , axial velocity of spiral curve can be expressed as $V=R*n$. After derivation calculus to velocity V , we can get acceleration equation as $a=V'$. Therefore, we can deduce mathematic equations of steady accelerated spiral curve, sine accelerated spiral curve and polynomial accelerated spiral curve respectively, as shown in Eq.1, Eq.2 and Eq.3^[2].

$$\begin{cases} L = i * R_0 + i^2 * \Delta R \\ R = R_0 + (2i - 1) * \Delta R \\ H = H_0 + \frac{i}{i_m} \Delta H \\ d = d_0 + \frac{i}{i_m} \Delta d \end{cases} \quad (1)$$

$$\begin{cases} L = \frac{R_m + R_0}{2} i - \frac{i_m}{\pi} * \frac{R_m - R_0}{2} \sin(\frac{i}{i_m} \pi) \\ R = \frac{R_m + R_0}{2} - \frac{R_m - R_0}{2} \cos(\frac{i}{i_m} \pi) \\ H = H_0 + \frac{i}{i_m} \Delta H \\ d = d_0 + \frac{i}{i_m} \Delta d \end{cases} \quad (2)$$

$$\begin{cases} L = R_0 i + (4L_m - R_m i_m - 3R_0 i_m) i^3 / i_m^3 + (\frac{1}{2} R_m i_m + \frac{3}{2} R_0 i_m - 2L_m) i^4 / i_m^4 \\ R = R_0 + (12L_m - 3R_m i_m - 9R_0 i_m) i^2 / i_m^3 + (2R_m i_m + 6R_0 i_m - 8L_m) i^3 / i_m^4 \\ H = H_0 + \frac{i}{i_m} \Delta H \\ d = d_0 + \frac{i}{i_m} \Delta d \end{cases} \quad (3)$$

We take blank for example, which is roughing column with diameter $\Phi 10\text{mm}$. Then the total length of screw thread is 151mm, variable pitch length is 18mm. In the export segment, the length is 60.5mm, initial pitch R_0 is 1.70mm, initial root diameter D_0 is $\Phi 8.84\text{mm}$ and initial groove width d_0 is 0.75mm. And then from export segment to import segment, screw thread pitch gradually increases to R_m . In the import segment, the pitch R_m is 1.88mm, root diameter D_m is $\Phi 8.30\text{mm}$ and groove width d_m is 0.83mm. The above-mentioned screw parameters were respectively substituted into Eq.1, Eq.2 and Eq.3. We have found that the minimum theoretical error was Eq.1 of steady accelerated spiral curve model. The absolute error of screw pitch was -0.00007mm and relative error was 0.03889%.

Mathematic analysis of variable pitch & groove depth & groove width screw

1) For Eq.1 of steady accelerated spiral curve model, axial velocity of spiral curve can be expressed as $V = R * n = R_0 * n + \Delta R * n(2i - 1)$. After derivation calculus to velocity V , we can get acceleration equation as $a = V' = 2\Delta R * n$. So axial displacement of arbitrary point on spiral curve is uniformly accelerated rectilinear motion. The velocity is increasing along with a sloping line. However, acceleration is constant, which has a finite value mutation only at starting and ending point. It will come into being flexible impact. In the product line of high speed, flexible impact will lead to material running over by shaking. But if the device speed is not high, flexible impact will not affect the transmission stationarity. So this method is more applicable in low or middle speed motion control^[3]. While using steady accelerated spiral curve model in the CNC machining control of variable pitch & groove depth & groove width screw, the transition of variable screw pitch is rather smooth and the cumulative error is minimal.

2) For Eq.2 of sine accelerated spiral curve model, acceleration equation can be expressed as $a = \frac{\pi n}{i_m} \frac{R_m - R_0}{2} \sin(\frac{i}{i_m} \pi)$. The acceleration line is a smooth and continuous sine curve in the accelerated segment, which is zero at starting and ending point. By using motion law of sine accelerated spiral curve, acceleration changes continuously during the whole process of screw transmission and it won't bring any impact even in high speed. It can satisfy the request of stationarity in high speed screw. So this method is suitable for high speed motion^[4]. However, it requires a higher processing. Besides, the displacement changes slowly in the starting and ending segment, so the cumulative error is relatively large.

3) For Eq.3 of polynomial accelerated spiral curve model, acceleration equation can be expressed as $a = V' = (\frac{(24L_m - 6R_m i_m - 18R_0 i_m)i}{i_m^3} + \frac{(6R_m i_m + 18R_0 i_m - 24L_m)i^2}{i_m^4}) * n$. The acceleration changes continuously in the accelerated segment, which is zero at starting and ending point. This method can design different spiral curves according to different boundary conditions. And it can fulfill the requirement of displacement, velocity and acceleration to make material transmission steadily and accurately. However, there is some reasonless that it may occur interference when speed is too high or too low.

Therefore, we adopt steady accelerated spiral curve model to control screw machining.

CNC program development of variable pitch & groove depth & groove width screw

In CNC lathe, we take single stroke thread cutting instructions G32 to machining variable pitch & groove depth & groove width screw. The instruction format is G32 X (U)___Z (W)___F___, in which X (U) and Z (W) is screw thread terminal point coordinate, F is pitch of screw thread^[5]. We use Visual Basic6.0 to develop CNC program. In Visual Basic6.0, we add program codes about mathematic equations of variable pitch & groove depth & groove width screw, and then run program VB to acquire CNC machining codes of heterotypic screw^[6]. By CutViewer Turn V3.0 of CNC lathe simulation software, we input NC codes and simulated. Then we measured the simulated machining screw. The result shows that in the export segment, initial pitch R_0 is 1.70mm, initial root diameter D_0 is $\Phi 8.846$ mm and initial groove width d_0 is 0.752mm; in the import segment, the pitch R_m is 1.88mm, root diameter D_m is $\Phi 8.34$ mm and groove width d_m is 0.828mm; and then in the middle segment, the changes of pitch, groove depth and groove width were according with Eq.1. The simulation result indicates that the CNC machining program of variable pitch & groove depth & groove width screw is reasonable and feasible.

Conclusions

This article has deduced and analyzed three parameterized mathematic model of variable pitch & groove depth & groove width screw. It can provide theoretical basis for machining control system about this type of heterotypic screw. And it will also offer a feasibility method to design or machining variable pitch screw. However, it still needs further research about practicing on CNC lathe to machining variable pitch & groove depth & groove width screw which tallies with size precision. What's more, as pledging machining precision, it also need perfect machining parameters by different machine to achieve more high efficiency machining. And that it can carry out to machining various heterotypic screws with complex structure and high precision.

Acknowledgements

Fujian Provincial Natural Science Foundation (2008J04020) funded

References

- [1] Ren Xuejun, Lin Xiaojun, Shi Yaoyao. "The Research of Mathematics Model and NC Processing technique of Profiled Screw", *Machine Tool & Hydraulics*, 2004, 1:56-58
- [2] Li Shan, Han Min, Deng Lutao. "Mathematics Model Analysis of Variable Pitch Screw", *Mechanical & Electrical Engineering Technology*, 1009-9492 (2009) 05-0029- 02
- [3] Wu Guiquan. "Design and Manufacture of Simple Screw Curve with Variable Pitch", *Packaging and Food Machinery*, 1005-1295(2004) 02-0053- 02
- [4] Lin Shuang. "A General Program for Pitch-varying Spiral Design Using UG", *Packaging and Food Machinery*. 1998, 4 (16) : 8-15
- [5] Liu Xiongwei. "CNC Machining Theory and Program Technology", Beijing: *Machine Industry Press*, 2000.01
- [6] Chen Wenjie, Zhang Hui, Zhao Zhishui. "Mathematical Modeling Heterotypic Screw NC Programming", *Machine Design & Research*, 1006-2343 (2008) 03-110-03

Numerical Simulation on Aerodynamics of Ramjet Projectiles

Jiaxian Zhang^a, Yanna Wang, Ruimin Liu

Beijing Institute of Aerospace Testing Technology, Beijing 100074, China

^acallingxh@gmail.com

Keywords: Projectile; Ramjet; Aerodynamics; CFD; TVD

Abstract: Three-dimensional Reynolds-averaged Navier-Stokes simulations have been performed to explore the aerodynamic characteristics of ramjet projectiles. The turbulence model used is the RNG k-ε model. The numerical algorithms termed total variational diminishing (TVD) was adopted. The complex wave structures of ramjet projectiles with different architecture at different inflow Mach number were achieved by numerical simulation. The influence of inflow Mach number on aerodynamic characteristics and pressure center of ramjet projectiles were analyzed. Results show that lift coefficient and pressure center increase with the argument of inflow Mach number. Ramjet projectiles with different architecture have different drag coefficient trend.

Introduction

Due to predominant performance of simpler structure, lower cost, higher assisted range efficiency, and smaller decreasing of warhead mass, various ramjet projectiles have been developed all around the world, including USA, South Africa and et al. One typical product is American TGTR for the 105-mm M68 tank cannon. Nowadays, by using ramjet to assisted range, the effective range of projectiles can be doubled.

Lots of researches have been done on ramjet projectiles. Chen Xiong has done investigations of ramjet inlet [1]. Ronald revealed the working on solid fuel ramjet propulsion for gun launched projectiles in the Netherlands Organization [2]. Guo Jian has studied flight performance of solid fuel ramjet [3]. Xiao Yinli et al. has done investigations of scramjet isolator [4]. Wang Yufeng has researched the inner flow of ramjet engine [5]. The TNO Defence, Security and Safety and DRDC-Valcartier have worked on the improvement of modeling and simulation tools for the functioning of supersonic air intake for realistic ramjet engines of tactical missiles [6].

As a key segment of research on ramjet projectiles, numerical simulation on aerodynamic characteristics are very important. The second-order implicit TVD scheme was adopted in this paper. And the RNG k-ε model was used to represent turbulence. Finally, the influences of Mach number on aerodynamic characteristics of ramjet projectiles were revealed.

Computational Approach

With decades of development, present CFD approaches can predict the aerodynamic characteristics of vehicles accurately. Still, it is very hard to build a mathematical model which contains all kinds of factors. In this paper, gas-solid two-phase, multi-component and chemical reactions were neglected.

Governing Equations. Governing equations used here are the compressible, Reynolds-averaged Navier-Stokes equations in generalized coordinates. These equations are written in the following conservative form:

$$\frac{\partial U}{\partial t} + \frac{\partial F_1(U)}{\partial x} + \frac{\partial F_2(U)}{\partial y} + \frac{\partial F_3(U)}{\partial z} = \frac{\partial G_1}{\partial x} + \frac{\partial G_2}{\partial y} + \frac{\partial G_3}{\partial z} \quad (1)$$

Detailed formulation form could be found in [1].

Turbulence Model. According to the former experience, computational results verify with changes of turbulence model. An appropriate turbulence model helps to improve computing

accuracy. The standard $k-\varepsilon$ model was very popular in the past. The RNG $k-\varepsilon$ model is brought forward by modifying the standard $k-\varepsilon$ model. The model comes from the strict statistic method. It is very similar with standard $k-\varepsilon$ model, but it has been ameliorated. These characters make the RNG $k-\varepsilon$ model more accurate and reliable than the standard $k-\varepsilon$ model in more complex flow.

The RNG $k-\varepsilon$ model is adopted as turbulence model in this paper. Neglecting influence of buoyancy, dissipation rating and turbulence energy are described as follow:

$$\rho \frac{Dk}{Dt} = \frac{\partial}{\partial x_i} \left[(\alpha_k \mu_{eff}) \frac{\partial k}{\partial x_i} \right] + G_k - \rho \varepsilon - Y_M \quad (2)$$

$$\rho \frac{D\varepsilon}{Dt} = \frac{\partial}{\partial x_i} \left[(\alpha_\varepsilon \mu_{eff}) \frac{\partial \varepsilon}{\partial x_i} \right] + C_{1\varepsilon} \frac{\varepsilon}{k} G_k - C_{2\varepsilon} \rho \frac{\varepsilon^2}{k} - R \quad (3)$$

where, G_k stands for turbulence energy caused by mean velocity gradient. Y_M is the influence on total dissipation rating by pulse expansion of compressible turbulence. α_k is reciprocal of valid turbulent Prandtl number of turbulence energy k . α_ε is reciprocal of valid turbulent Prandtl number of dissipation rating ε . For high Reynolds number, $\mu_t = \rho C_\mu k^2 / \varepsilon$ and $C_\mu = 0.0845$ are suitable for the above equations.

Numerical Algorithm. By using implicit second-order TVD scheme, the discrete form of governing Eq. 1 could be transferred as follow:

$$V_{i,j,k} \frac{dU_{i,j,k}}{dt} = \left(\begin{array}{c} \tilde{R}_{v,i+\frac{1}{2}} - \tilde{R}_{v,i-\frac{1}{2}} + \tilde{R}_{v,j+\frac{1}{2}} - \\ \tilde{R}_{v,j-\frac{1}{2}} + \tilde{R}_{v,k+\frac{1}{2}} - \tilde{R}_{v,k-\frac{1}{2}} \end{array} \right) - \left(\begin{array}{c} \tilde{R}_{i+\frac{1}{2}} - \tilde{R}_{i-\frac{1}{2}} + \tilde{R}_{j+\frac{1}{2}} - \\ \tilde{R}_{j-\frac{1}{2}} + \tilde{R}_{k+\frac{1}{2}} - \tilde{R}_{k-\frac{1}{2}} \end{array} \right) \quad (4)$$

where, $V_{i,j,k}$ is cell volume, $\tilde{R}_{i+1/2}$ is the convective fluxes of $\tilde{R}_{i+1/2,j,k}$, $\tilde{R}_{v,i+1/2}$ is the viscous fluxes of $\tilde{R}_{v,i+1/2,j,k}$, and so on. Considered face $i+1/2$, by updating the convective fluxes, the second-order TVD scheme is achieved as follow:

$$\left\{ \begin{array}{l} \tilde{R}_{i+1/2} = \tilde{H}_i^+ + \tilde{H}_{i+1}^+ + \frac{1}{2} R_{i+1/2} (\phi_{i+1/2}^+ + \phi_{i+1/2}^-) \\ \phi_{i+1/2}^+ = \min \text{mod}(\Lambda_{i+1/2}^+ R_{i+1/2}^{-1} \Delta_{i-1/2} U, \Lambda_{i+1/2}^+ R_{i+1/2}^{-1} \Delta_{i+1/2} U) \\ \phi_{i+1/2}^- = \min \text{mod}(\Lambda_{i+1/2}^- R_{i+1/2}^{-1} \Delta_{i+1/2} U, \Lambda_{i+1/2}^- R_{i+1/2}^{-1} \Delta_{i+3/2} U) \\ \min \text{mod}(x, y) = \text{sgn}(x) \max\{0, \min[|x|, y \text{sgn}(x)]\} \end{array} \right. \quad (5)$$

After linearization and splitting by ADI method, the final numerical scheme is shown as Eq. 6.

$$\left\{ \begin{array}{l} -\Delta \tau \bar{C}_{i-1/2}^{+,n} \cdot \delta U_{i-1,j,k}^{**} + [I + \Delta \tau (\bar{C}_{i-1/2}^{+,n} - \bar{C}_{i+1/2}^{+,n})] \cdot \delta U_{i,j,k}^{**} + \Delta \tau \bar{C}_{i+1/2}^{-,n} \cdot \delta U_{i+1,j,k}^{**} = -\Delta \tau RHS \\ -\Delta \tau \bar{C}_{j-1/2}^{+,n} \cdot \delta U_{i,j-1,k}^{**} + [I + \Delta \tau (\bar{C}_{j-1/2}^{+,n} - \bar{C}_{j+1/2}^{+,n})] \cdot \delta U_{i,j,k}^{**} + \Delta \tau \bar{C}_{j+1/2}^{-,n} \cdot \delta U_{i,j+1,k}^{**} = \delta U_{i,j,k}^{**} \\ -\Delta \tau \bar{C}_{k-1/2}^{+,n} \cdot \delta U_{i,j,k-1}^{**} + [I + \Delta \tau (\bar{C}_{k-1/2}^{+,n} - \bar{C}_{k+1/2}^{+,n})] \cdot \delta U_{i,j,k}^{**} + \Delta \tau \bar{C}_{k+1/2}^{-,n} \cdot \delta U_{i,j,k+1}^{**} = \delta U_{i,j,k}^{**} \\ U_{i,j,k}^{n+1} = U_{i,j,k}^n + \delta U_{i,j,k} \\ RHS = \tilde{R}_{i,j,k}^n - \tilde{R}_{v,i,j,k}^n - \tilde{R}_{s,i,j,k}^n \\ \Delta \tau = \Delta t / V_{i,j,k} \end{array} \right. \quad (6)$$

Modeling and Boundary Conditions

Four kinds of ramjet projectiles analyzed in this paper are shown in Fig. 1. I type and III type of ramjet projectile each have a centre wimble. II type and IV type of ramjet projectile get ride of the centre wimble based on I type and III type, respectively. There are a few differences between I type and III type, such as structure of inlet and exterior structure of projectile. For the I type projectile, cylindrical part is connected with arc part by tangent, so its head is fat in some sort. For the III type projectile, cylindrical part is connected with arc part by secant, so its head is a little thin. In addition, some small holes are dig on stern parts of I type and II type.

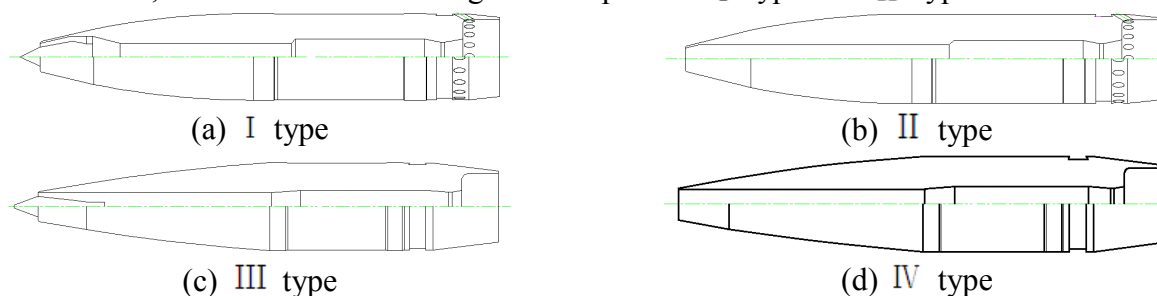


Fig. 1 Structures of each kind of ramjet projectile

Three-dimensional models were built for the aerodynamics analysis, with 6° angle of attack for lift coefficient analysis and no angle of attack for drag coefficient analysis. Inlet boundary and far field boundary use the conditions of far field of pressure. The temperature and static pressure of far field of pressure boundary is 288K and 101325Pa. Mach numbers of inflow are respectively 2.13, 2, 1.6, 1.4, 1.1 and 0.9.

Results and Discussion

The typical character of flow field of ramjet projectile is the wave structure at base. Owing to the structure similarity, external flow structures of I type and III type of ramjet projectile are similar with II type and IV type of ramjet projectile, respectively. Wave structures of these four kinds of ramjet projectile at $M=2.13$ without angle of attack are shown in Fig. 2.

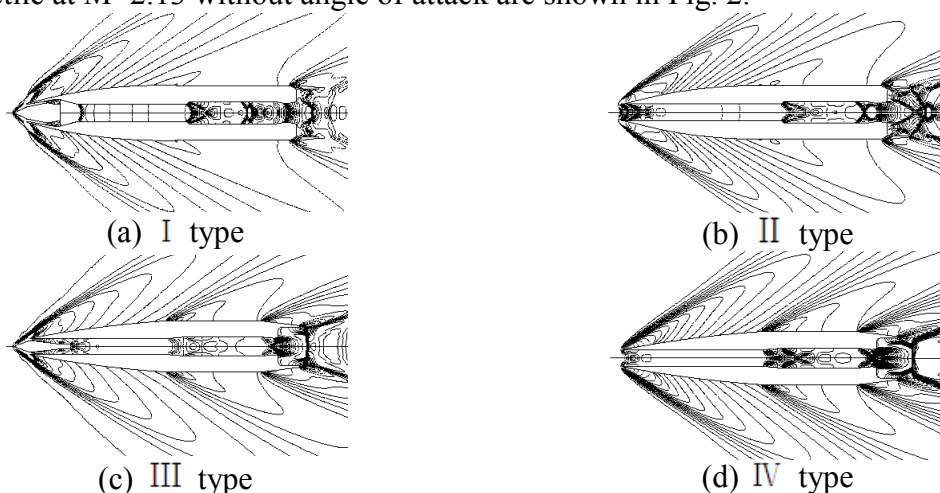


Fig. 2 Wave structures of ramjet projectiles at $M=2.13$ without angle of attack

At $M=2.13$, due to the center pipe of ramjet projectile, jet flow structure appears at the base of I type, Arch bridge type of shock waves form at the exit of nozzle, intersect shock waves appear at the base of II type. Two titled shock waves will emerge in the combustion chambers of these two types of ramjet projectile. Comparing to the I type, due to the thin head, titled shock wave at outboard of inlet of III type became weaken obviously. Internal flow field of III type and IV type is obviously different. The reason is their different inlet structures.

Influences of Mach number on these kinds of ramjet projectile are shown in Fig. 3. For the lift coefficient, all kinds of ramjet projectile show the same trend that the coefficient rises with the increasing of Mach number. As shown in Fig. 3, lift coefficients of ramjet projectiles without centre

wimble are bigger than those with centre wimble. For the drag coefficient, the trends are conversely different with lift coefficient. And drag coefficients of ramjet projectiles without centre wimble are smaller than those with centre wimble. As increasing of Mach number, these gaps become obscure, especially between III type and IV type of ramjet projectile.

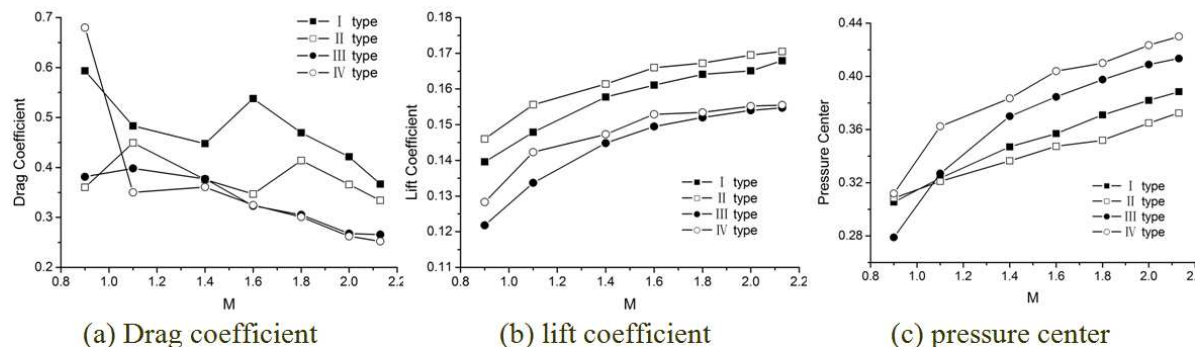


Fig. 3 Influences of Mach number on aerodynamics

In this paper, definition of pressure center is relative to the head of projectile. As shown in Fig.3, the faster inflow is, the bigger pressure center is. Pressure centers of ramjet projectiles without holes at the stern part are bigger than those with holes. That means base wave structures have great influence on the pressure center.

Conclusions

Aerodynamic characteristics of ramjet projectiles were numerically analyzed. Drag coefficient characteristics were achieved with no angle of attack. Lift coefficient and pressure center characteristics were achieved with angle of attack equaling to 6 degree. Results show that lift coefficient and pressure center increase with the argument of Mach number. In fact, lift coefficients of ramjet projectiles without centre wimble are bigger than those with centre wimble. Owing to the great influence of wave structures at base, pressure centers of ramjet projectiles without holes at the stern part are bigger than those with holes. Meanwhile, drag coefficients decrease with the argument of Mach number.

References

- [1] CHEN XIONG, ZHENG YA, ZHOU CHANGSHENG, JU YUTAO. Numerical simulation on ramjet inlet with different cowl leading edge, AIAA 2005-5288.
- [2] Ronald G. Veraar and Alfons E. H. J. Mayer. The Role of the TNO Free Jet Test Facility in Solid Fuel Ramjet Projectile Development. AIAA 2005-3828.
- [3] Jian GUO, Weihua ZHANG, Zhixun XIA. Flight performance analysis of the solid fuel ramjet. Journal of national university of defence technology. 2007, Vol.29, No.2: 10-14. (in Chinese)
- [4] Yinli XIAO, Liang CHEN, Wenyan SONG. Study on flow characteristics of scramjet isolator. ACTA AERODYNAMICA SINICA. 2007, Vol.25, No.1: 75-79.
- [5] Yufeng WANG, Xiaolong DUAN. Numerical study of the ramjet engine inner flow before ignition. Journal of rocket propulsion. 2006, Vol.32, No.6: 20-22.
- [6] J. -L. Moerel, R. G. Veraar, and et al. Internal flow characteristics of a rectangular ramjet air intake. AIAA 2009-5076.
- [7] Chakravarthy, S. R., Szema, K. Y., and et al. Application of a New Class of High Accuracy TVD Schemes to the Navier-Stokes Equations. AIAA paper 85-0165, Jan. 1985.

A Parametric Die-Base in SolidWorks

Xinqun Zhang

64 South Fengle Road, Chuzhou, Anhui, China

winston4380@yahoo.com.cn

Keywords: Solidworks; Re-Development; Die-Base; Parametric Design; Mold Handle

Abstract: The study of parametric die-base developed on SolidWorks is presented in this paper. Here Visual Basic 6.0 is selected as the development tool, and the handle of a die is taken as an example to describe the design process with dimension driving. Users may create a series of standard-parts automatically by inputting different parameters through the application interface developed with VB.

Introduction

Currently, a great variety of CAD software is used in the three-dimensional design in our country's mold enterprises. SolidWorks is quite widely used.

The standard-parts of ramming molds include guide pillars, guide sleeves, mold bases, mold handles, throwout levers, roof bars, educing material pins, blocking material pins, discharging bolts, bolts, positioning pins, compression springs and so on, which are transferred repeatedly in the mold design process. Since there is no standard-parts base meeting China's GB codes in SolidWorks, some designers have to consult GB codes frequently and revise some specific sizes repeatedly when they transfer standard parts of different specifications in order to renew the entire accessory model. This revision process is extremely tedious and requires massive duplication work, resulting in a long design cycle and low efficiency. Therefore, in order to enhance the application effect of SolidWorks in China's mold enterprises, we must localize and specialize our re-development of SolidWorks to establish a new ramming mold standard-part base.

SolidWorks re-development methods

The model created by SolidWorks is an entirely parametric three-dimensional model, and the re-development of SolidWorks is based on the parametric design to the accessory model.

The concept of parametric design. The parametric design is a highly effective design method which realizes the shape control of the accessory through geometric constraints.

The parametric design process first carries on the parameterization modeling, namely establishing the initial geometry model of the accessory, defines the size of the controlled model shape structure as the variable parameter, and then actuates the parametric model by assigning different values to the variable parameter using the data in the parameter base to restructure the model. This size of the controlled accessory model shape structure is called the characteristic size.

The parametric design process of die-base is as shown in Fig. 1.

SolidWorks re-development methods. At present, SolidWorks re-development methods used by enterprises include programming method and size actuation method.

a. Programming method

The programming method means transcribing the entire modeling process while modeling the

initial accessory, revising the transcribed macrocode, changing the constants to variables, and finally playing the modeling process back.

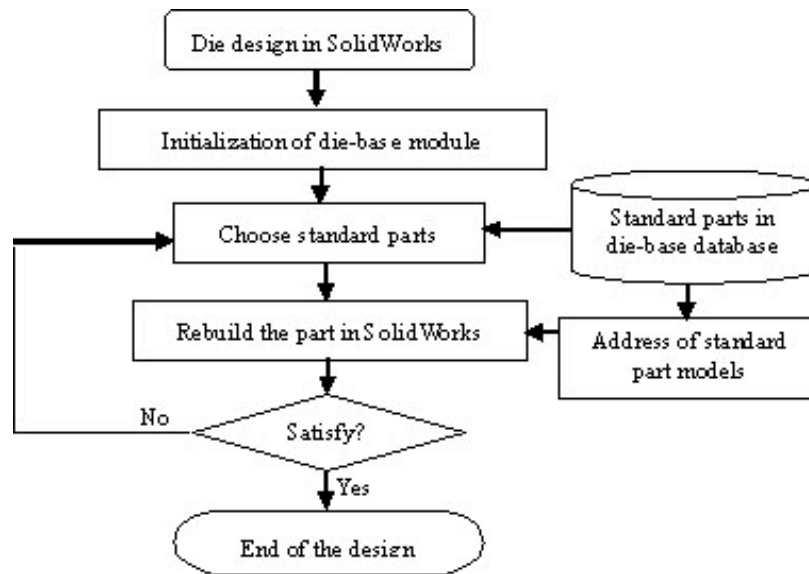


Fig. 1. The parametric design process of die-base

Although the programming method principle is relatively simple, and the macro-tool can be very conveniently transferred, it requests designers to be familiar with C++, VB, VC and other high-level programming languages, and also grasp a great deal of SolidWorks API functions. Because some functions may be left out when transcribing accessory models with macro-tools, the developer has to intentionally compile procedure codes using SolidWorks API function to make it up, thus result in additional difficulty in its realization.

Moreover, the model creation process needs to be executed from beginning to end when the accessory model is renewed, resulting in the long design time and low efficiency.

b. Dimension driving method

The dimension driving method maintains the accessory model structure unchanged, assigns different values to the characteristic size parameters by compiling procedure codes, and then renews the entire model according to the new size values.

The model recreating process in the programming method can be omitted by using the dimension driving method. It only needs to control the changes of the characteristic size based on the original accessory model and renew it.

Therefore the compiled program codes customizable and their total quantity is limited, with a high speed of graph renewal and high efficiency. It is more advantageous that designers can be freed from numerous massive SolidWorks API functions and may even complete the re-development without knowledge of SolidWorks API. Dimension driving method may be the application direction in die-base development, and a very high potential application value in mold and die industry.

Developing the die-base with dimension driving method

This paper introduces the development process of die-base with Visual Basic 6.0 as the development tool and the rimmed mold handle accessory as an example.

Establishing the initial accessory model of the rimmed mold handle. Taking A30×75 JB27646.3-1994 rimmed mold handle Type A as an example, we'll establish an accessory model on SolidWorks interface, as shown in Fig.2, preserved as "rimmed mold handle Type A. sldprt". There are five characteristic size controlling this accessory model, namely the mold handle diameter $\phi 30$,

the rimmed diameter $\phi 75$, the rimmed height 16, the hitting pole aperture 11, the total height 64 (note: the size unit is mm). The mold handle accessory structure will change along with their different values.

Editing size names. When the model of rimmed mold handle Type A is established, SolidWorks system can assign a default size name for the labeled sizes: D1, D2, D3, D4, D5, D6, as shown in Fig.2. But this kind of size naming is extremely irregular without explicit significance, and may be shared by many characteristic sizes. In the parametric design, there is no special request for size naming, but in order to avoid confusion in transferring variable parameter values when the program is compiled, the labeled sizes should be renamed according to its need.

For example, double-click “sketch 1” in the characteristic manager and then click the right key on the size $\phi 30$ (size name is “D1”), choose “attribute” from the pop-up shortcut menu. When the “size attribute” dialog box appears, change the size name to “d”, and then confirm. Likewise, change the other specification size names to D2, h, HH, and DD respectively, as shown in Fig.3.

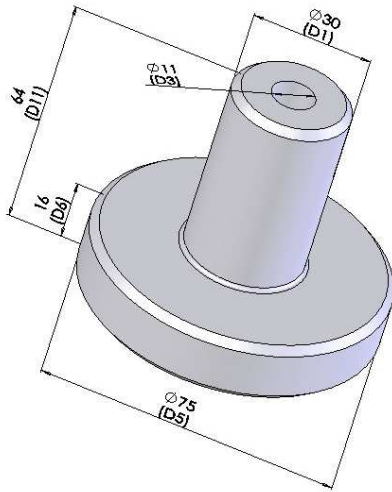


Fig.2. Accessory model of rimmed mold handle Type A

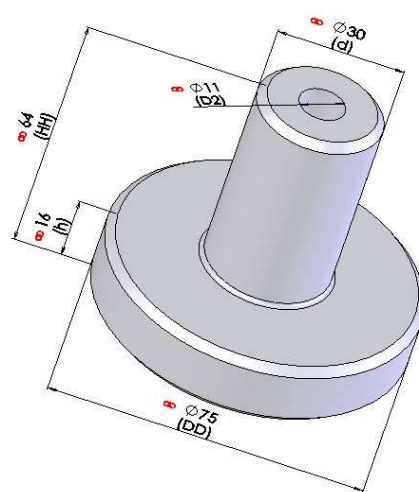


Fig.3. Size names of rimmed mold handle Type A

Designing the window interface for VB documents. Establish a VB project document, then open the menu item “project”→ “part”, and then append an outside control: Microsoft FlexGrid Control 6.0.

Append an image control on the VB window, a Data control, an MSFlexGrid1 control, and two Command controls. The VB window's interface design is as shown in Fig.4.

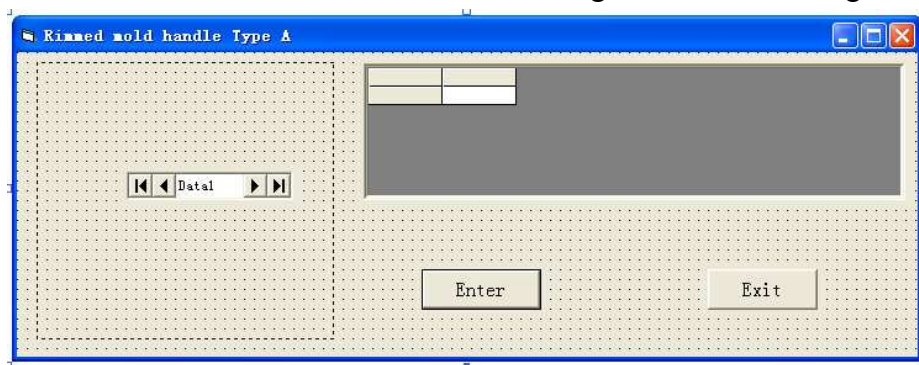


Fig.4. The VB program window interface design of rimmed mold handle Type A

Establishing the database file of variable parameters for the accessory model. Because rimmed mold handle Type A is a standard-part, its characteristic sizes are bundled with some serial of the mold standards. Here the database technology might be used, storing the characteristic size values in the database according to certain data structure forms to be managed by the database system in unification.

This paper adopts Microsoft Access 2003 as the database management system, taking the mold handle diameter d , the rimmed diameter DD , the rimmed height HH , the hitting pole aperture $D2$, the total height HH as the variables, and establishes the data sheet as shown in Fig.5.

mold handle code	d	DD	HH	h	D2
A30×75	30	75	64	16	11
A40×85	40	85	78	18	13
A50×100	50	100	78	18	17
A60×115	60	115	90	20	17
A76×136	76	136	98	22	21
*	0	0	0	0	0

Fig.5. Datasheet of A rimmed mold handle

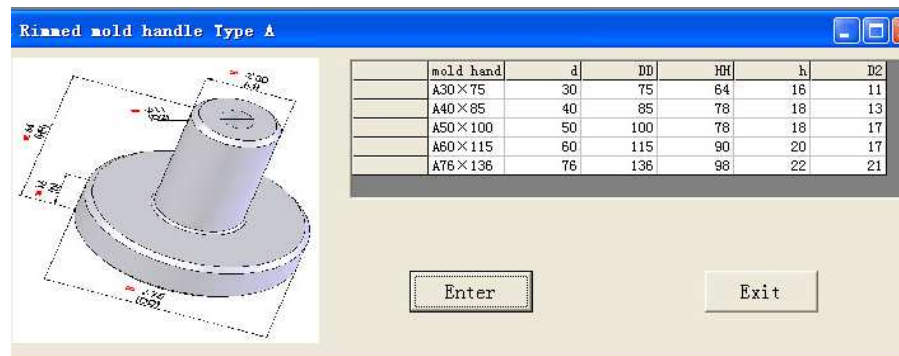


Fig.6. File “rimmed mold handle Type A. exe”

Compiling VB program codes. The main VB program segments are as follows:

Private Sub Command1_Click()

```
Set swApp = GetObject( "SldWorks.Application" )
Set swPart = swApp.OpenDoc(App.Path & "\ A rimmed mold handle. sldprt", 1)
swPart.Parameter("d@ sketch 1").SystemValue = d / 1000
swPart.Parameter("DD@ sketch 1").SystemValue = DD / 1000
swPart.Parameter("HH@ sketch 1").SystemValue = HH / 1000
swPart.Parameter("h@ sketch 1").SystemValue = h / 1000
swPart.Parameter("D2@ sketch 2").SystemValue = D2 / 1000
swPart.EditRebuild
swPart.ViewZoomtofit2
```

End Sub

Private Sub Form_Load()

```
Image1.Picture = LoadPicture(App.Path & "\ rimmed mold handle Type A. jpg ")
Data1.DatabaseName = App.Path & "\ rimmed mold handle Type A.mdb"
Data1.RecordSource = " table1"
```

End Sub

Private Sub MSFlexGrid1_SelChange()

```
MSFlexGrid1.Col = 2: d = Cdbl(MSFlexGrid1.Text)
MSFlexGrid1.Col = 3: DD = Cdbl(MSFlexGrid1.Text)
MSFlexGrid1.Col = 4: HH = Cdbl(MSFlexGrid1.Text)
MSFlexGrid1.Col = 5: h = Cdbl(MSFlexGrid1.Text)
MSFlexGrid1.Col = 6: D2 = Cdbl(MSFlexGrid1.Text)
```

End Sub

Creating file “rimmed mold handle Type A.exe”. File “rimmed mold handle Type A.exe” is as shown in Fig.6.

The EXE file in fact provides a man-machine conversation window which may be conveniently

run right in Windows.

When the EXE file is executed, the different specification standard code numbers and the characteristic size values of rimmed mold handle Type A set by JB27646.3 can be shown in the window, and users may choose different standard-part code numbers directly and specifically to obtain the corresponding model of rimmed mold handle Type A.

Expanding standard-part base of the rimmed mold handle. The rimmed mold handle falls into three types in JB27646.3, Type A, B, and C, types B and C with 3~4 countersunk head screw holes on the rimmed end face bare based on Type A. When accessories are modeled, the screw hole needs to be driven by five characteristic sizes. Therefore, more size variables are needed to control rimmed mold handles Type B and Type C, as shown in Fig.7.

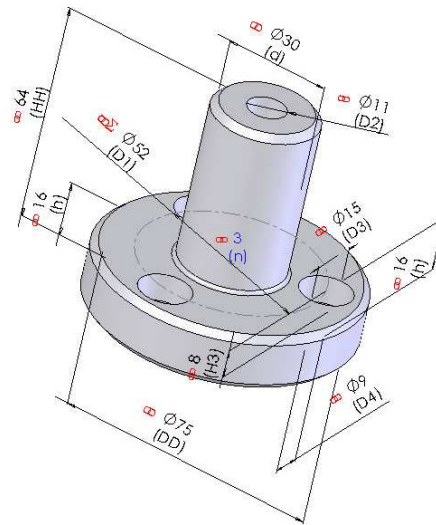


Fig.7. Size names of B rimmed mold handle

Firstly increase a screw hole based on the model of rimmed mold handle Type A, and distribute equally it to three. Then standard-part bases for rimmed mold handles Type B or C may be developed with the same method as A, only increasing some sentences in the original procedures.

The main VB program segments developing rimmed mold handle standard-part base are as follows:

```
Private Sub Command1_Click()
```

```
.....
```

```
swPart.Parameter("hole diameter @ sketch 6").SystemValue = D4 / 1000
```

```
swPart.Parameter("pillar countersunk head hole diameter @ sketch6").SystemValue = D3 / 1000
```

```
swPart.Parameter("D1@ sketch3").SystemValue = D1 / 1000
```

```
swPart.Parameter("pillar countersunk head hole depth@ sketch6").SystemValue = H1 / 1000
```

```
swPart.Parameter("n@ array (circle)1").SystemValue = Text1.Text
```

```
.....
```

```
Private Sub MSFlexGrid1_SelChange()
```

```
.....
```

```
MSFlexGrid1.Col = 7: D4 = Cdbl(MSFlexGrid1.Text)
```

```
MSFlexGrid1.Col = 8: D3 = Cdbl(MSFlexGrid1.Text)
```

```
MSFlexGrid1.Col = 9: D1 = Cdbl(MSFlexGrid1.Text)
```

```
MSFlexGrid1.Col = 10: H1 = Cdbl(MSFlexGrid1.Text)
```

```
End Sub
```

Problems may appear in this program development. The unit controlling characteristic sizes of this accessory model is length unit, and therefore the parameter values corresponding to GB can be directly put into database files, while the parameter n showing the number of the screw holes is not measured by the length unit, so it should be distinguished from the other characteristic size parameter set.

This paper adopts an extremely simple method. It does not list the parameter n showing the number of the screw hole into the database, but sets another sentence for users to choose the number of the screw freely.

swPart.Parameter("n@ array (circle)1").SystemValue = Text1.Text

Meanwhile a Label control and a Text control are appended on the VB window. Users may choose the number of screw flexibly according to their needs when running the program, breaking through the 3 or 4 number limit in GB code.

The created file “rimmed mold handle .exe” is as shown in Fig.8. When executing the customized module, first choose the code number of the rimmed mold handle to be found in the data sheet, then manually input the screw hole number, and then click the “modeling” button; the corresponding rimmed mold handle accessory model can be obtained.

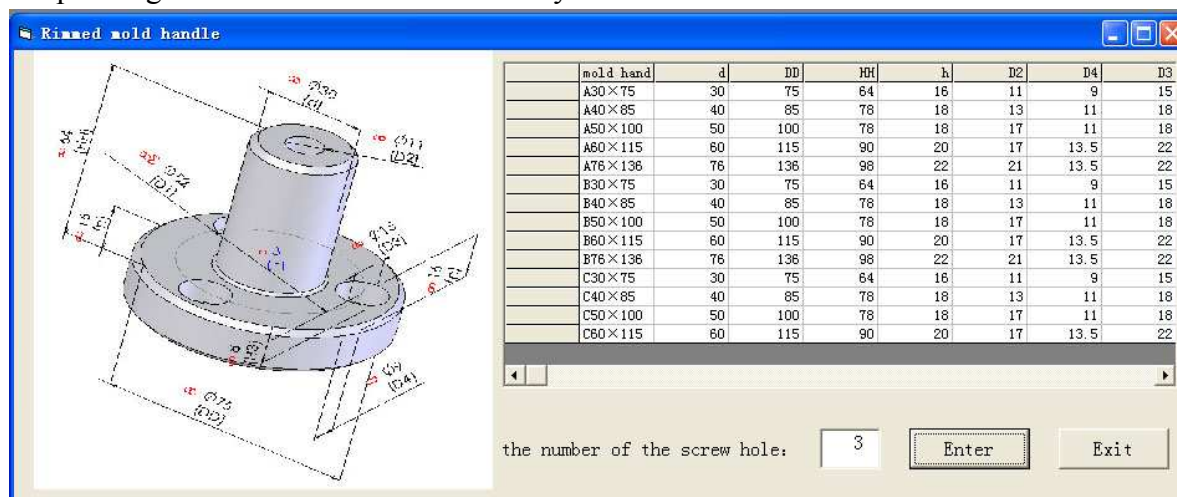


Fig.8. File “Rimmed mold handle. exe”

Conclusions

The application of re-development on SolidWorks to creat die-base can thoroughly save users time in manually revising the size value repeatedly in the SolidWorks interface, effectively reduc redundant work in the mold and die design, and enhanc the design automation.

Meanwhile, the created die-base conforms to China’s project charting standard and three-dimensional modeling provides a friendly man-machine communication interface, which can meet the needs of mold designers, and therefore is especially valuable in middle and small mold enterprises.

References

- [1] Zhong Ji, Xiaoli Wang, and Ren Liu: *Die Mold Design Automation - SolidWorks Application* (Chemical Industry Publications, China 2007). (In Chinese)
- [2] Xinqun Zhang: submitted to Mold industry (2009).(In Chinese)
- [3] Zheng Wei, Lin Mou: *SolidWorks2004.Cold-punched.Die.Design.Training.Tutorial* (Electronics Industry Publications, 2005). (In Chinese)

A Study on the Digital Simulation for Sheet Metal CNC Incremental Forming Based on Z-Map

Hu Zhu^{1,a}, Zhijun Liu^{1,b} and Jaegwan Kang^{2,c}

College of Mechanical and Electrical Engineering, Shenyang Aerospace University, Shenyang, Liaoning 110136,

ChinaSchool of Mechanical Engineering, Kyungnam University, Masan 631701, South Korea

^azhuhu100@yahoo.com.cn, ^bdongfangshenglong1@163.com, ^cjkang@kyungnam.ac.kr

Keywords: Incremental Forming; Digital Simulation; Z-Map; CAD/CAM

Abstract: A method of the digital simulation for the sheet metal CNC incremental forming was proposed based on the Z-map model. The tool extrusion movements were divided into two types according to the principle of sheet metal CNC incremental forming, i.e. vertical movement and horizontal movement. The vertical and horizontal swept volumes of the tool were built to intersect with the Z-map model of sheet metal respectively and the simulation models were generated. The thickness of deformed sheet metal was predicted and the thickness distribution chart was generated. The case studies show that the method can be applied to NC code verification, forming parameters optimization and formability prediction, moreover the system runs stably and reliably in the whole simulation process.

Introduction

Sheet metal CNC incremental forming is an innovative flexible forming technology developed recently[1]. In this technology, the forming is realized by the extruding of tool along the outline of the part[2], so the toolpath and forming parameters that are used for controlling the tool movements have enormous effects on the forming accuracy and time[3]. The simulation technology is a powerful tool for the optimization of forming parameters and reasonable toolpath planning for CNC incremental forming. However, the researches on the simulation for CNC incremental forming are not fully done. There has not been special simulation software developed for CNC incremental forming by now. Most of researches adopts the commercial FEM(finite element method) software such as ANSYS, ABAQUS etc[4,5,6,7]. Since the FEM software cannot directly describe 3D curve, they cannot be suitable for the simulation of the tool movements whose path is complicated 3D curves[8].

CNC incremental forming technology is mainly to face the forming of sheet metal parts with complicated surfaces whose forming paths are complicated curves. Due to its complexity, there must be some errors in the NC code and forming parameters. Therefore, it is necessary to check the NC code, optimize the forming parameters and predict the forming results through simulation before the actual forming process. Thus, the research on the method of simulation for CNC incremental forming is very imperative.

Digital Simulation of CNC Incremental Forming

The sheet metal CNC incremental forming adopts the layered manufacturing technology of the rapid prototyping. The sheet metal is fixed on the backing plate which can slide up and down freely along the guide, and a support is put under the sheet metal to hold up the sheet metal. The sheet metal and tool have a longitudinal feed under the control of the computer, and then the tool extrudes the sheet metal along the contour path. After that, the tool has a longitudinal feed and extrudes the sheet metal along the next contour repeatedly.

In the developed simulation system, support, sheet metal and tool are represented by using STL, Z-map and spherical equation respectively so as to calculate the deformation of the sheet metal expediently. Z-map is a lattice vector model that represents surface with the height values at grid points on the XY plane. The Z-map model can be represented as $\bar{Z}_i(x_i, y_i)$, where (x_i, y_i) represent the positions of grid points on the XY plane. \bar{Z}_i are the vectors along z axis at grid points. $|\bar{Z}_i|$ are the height values along z axis at the grid points, i.e. Z-map values, where $i = 0, 1, 2, \dots, n$. The simulation for the forming process is divided into two parts: one is the simulation for the downward moving process of sheet metal under the control of clamping plate and backing plate; the other is the simulation for the forming process of the sheet metal by the extruding of the tool.

Simulation on the Downward Moving Process of Sheet Metal. In the process of sheet metal CNC incremental forming, the sheet metal moves down a longitudinal feed depth under the drag of clamping plate, which coincides with the downwards movement of the tool. Simulation of the process is realized by the intersection between the Z-map model of sheet metal and the STL model of support. The upper surface of the sheet metal is used in the intersection calculation. The detailed process is as follows: ① Extracting the upper surface of the support. The extracting algorithm is first to find the signs of the z coordinate of the normal vectors of the triangular facets, then extract the facets whose z coordinate of the normal vectors are not negative. ② Building the model of sheet moved down. The model of sheet moved down can be built by modifying the values $|\bar{Z}_i|$ at grid points of the Z-map model of sheet metal. ③ Intersecting between sheet metal and support. In order to construct the model of the upper surface of the sheet metal after moving down, the intersection between sheet metal and the upper surface of support should be done. Then the Z-map values of sheet metal are updated to the sum of z values of intersection points and the thickness of sheet metal.

Simulation on the Extruding Process of Tool. This paper adopted the concept of tool swept volume which is used in the CNC milling simulation. The real-time simulation for the incremental forming process is carried out by updating the deformed shape through calculating the intersection between the tool swept volume and Z-map model of sheet metal. The structure of tool swept volume is related to the tool type and the toolpath. As mentioned above, the movements of the tool have two types: longitudinal feed along the vertical direction and lateral feed along the contours. Therefore, the tool swept volume referred in this paper can be divided into longitudinal feed swept volume and lateral feed swept volume according to the styles of toolpath, as shown in Fig. 1(a), where v_0, v_1 indicates the toolpath. According to the feed styles of tool, there are two cases about the intersection between the Z-map model of sheet metal and the tool swept volume: ① When the tool extrudes the sheet metal along the contour on a layer, if the grid points Z_i are in the XY plane projection area of the tool swept volume, they must be the points extruded by tool. Computing the intersection between Z_i and the tool swept volume, and comparing the z values of intersection points with the z values of grid points. If the z values of

intersection points are less than that of grid points, this means the sheet metal is extruded by the tool, and then z values of $\bar{Z}_i(x_i, y_i)$ are updated to the z values of intersection points. As shown in Fig. 1(b), the projection area of the tool swept volume on XY plane is divided into A , B and C three portions. Where, $v_0(x_0, y_0, z_0)$ and $v_1(x_1, y_1, z_0)$ are two adjacent points of the contour on a layer, r is the radius of the ball-end tool, $p'_i(x'_i, y'_i, z_0)$ is the projection of Z_i on the line v_0v_1 , d is the distance from Z_i to the line v_0v_1 . If $|Z_iv_0| \leq r$ and p'_i isn't on the line segment v_0v_1 , then Z_i is in the area A , and the intersection between the vectors \bar{Z}_i and the tool swept volume can be calculated by using Eq. 1. ② When the tool moves down from one layer to the next layer, as shown in Fig. 1(a), the effective tool swept volume is its ball-end. Ascertaining whether Z_i is in the projection area of the effective tool swept volume by judging if they satisfy the condition $|Z_iv_1| \leq r$. For the grid points in the projection area, Eq. 2 is used for computing the intersecting points and the z values of Z_i are updated using the method mentioned above.

$$\begin{cases} (x-x_0)^2 + (y-y_0)^2 + (z-z_0)^2 = r^2 \\ z \leq z_0 \end{cases} \quad (1)$$

$$\begin{cases} (x-x_1)^2 + (y-y_1)^2 + (z-z_1)^2 = r^2 \\ z \leq z_1 \end{cases} \quad (2)$$

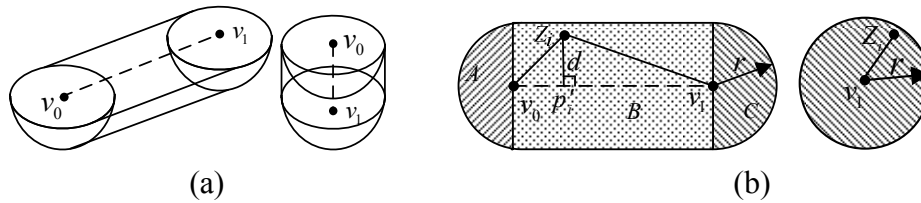


Fig. 1 (a) Tool swept volume (b) The projection of tool swept volume

Deformed Sheet Metal Thickness Prediction and Its Distribution Chart Visualization. The deformed sheet metal thickness is predicted according to the sine's law of thickness change in CNC incremental forming[9]. The sine's law can be described as $t = t_0 \sin \theta$, where t is the deformed sheet metal thickness, t_0 is the initial sheet metal thickness, θ indicates the angle between the forming plate and vertical direction. In order to observe the change of sheet metal thickness, thickness change of sheet metal is needed to be represented by using different colors. Therefore, the Z-map model was converted into STL model and was visualized by OpenGL.

Case Studies

The simulation platform was established using VC++ and OpenGL graphics library on the Windows XP. The user interface of the simulation software, the sheet metal, support, tool and the inputted NC code are shown in Fig. 2, in which the initial thickness of sheet metal is 2 mm, the radius of ball-end tool is 5 mm, the longitudinal feed depth is 0.4 mm. The simulation of the sheet metal CNC incremental forming process is shown in Fig. 3(a). The distribution of sheet metal thickness and the value of sheet metal thickness acquired from simulation are shown in Fig. 3(b).

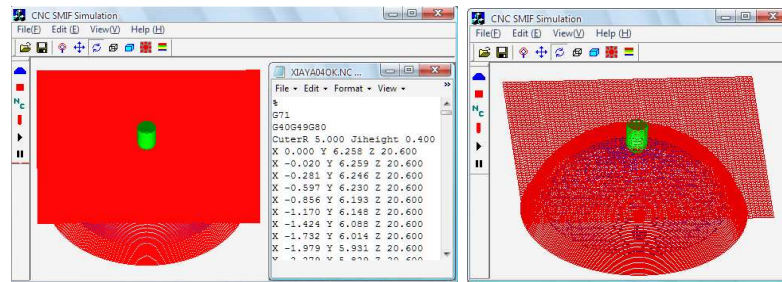


Fig. 2 Simulation software system

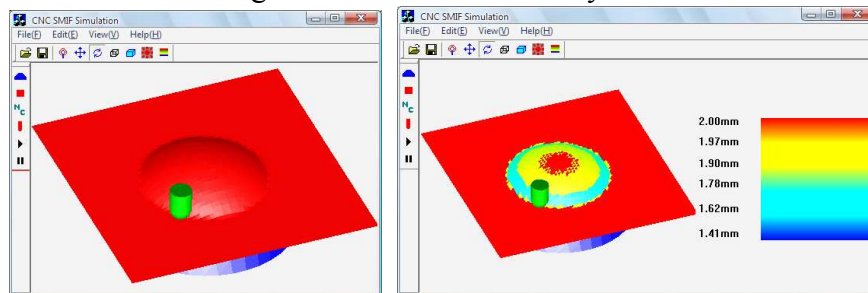


Fig. 3 (a)Simulation process (b)Sheet metal thickness chart

Conclusions

The method of simulation for the CNC incremental forming was studied based on the Z-map model, and the related software system was developed. The system can realize the real-time simulation on CNC incremental forming according to the NC code inputted and runs stably and reliably, which can be used not only to verify the forming NC code and optimize the forming parameters, but also to predict the thickness of formed parts and then estimating the formability, thus can save the cost and time than the actual trial forming.

Acknowledgements

The author gratefully acknowledges the financial support from the Natural Science Foundation of Liaoning (No. 20082012) and the Aerospace Science Foundation of China (No. 2009ZA54005).

References

- [1] A. Kochan: Assembly Automation Vol. 21(2001), p. 321.
- [2] J.J. Park and Y.H. Kim: J. of Materials Processing Technology Vol. 140(2003), p. 447.
- [3] M. Rauch, J.Y. Hascoet and J.C. Hamann: Int. J. of Material Forming Vol. 11(2008), p. 1191.
- [4] C. Henrard, A.M. Habraken and A. Szekeres: Advanced Materials Research Vol. 6(2005), p. 533.
- [5] Y. Minoru, G. Manabu and S.Y. Atsumi: J. of Materials Processing Technology Vol. 199(2008), p.163.
- [6] G. Ambrogio, I. Costantino, L. Filice and M. Muzzupappa: J. of Materials Processing Technology Vol. 153(2004), p. 501.
- [7] H. Iseki: J. of Materials Processing Technology Vol. 111(2001), p. 150.
- [8] J.H. Mo and F. Han: China Mechanical Engineering Vol. 19(2008), p. 491.(In Chinese)
- [9] G. Hirt, J. Ames, M. Bambach, and R. Kopp: Annals of the CIRP Vol. 53(2004), p. 203.

The Research and Realization of Efficient DDA Interpolation Algorithm for Multi-Axis Linear Linkage

Xiaoling Yan^{1,a}, Jiaying Zhang^{2,b} and Wanglong Wang^{2,c}

¹College of Mechanical Engineering, Beijing Technology and Business University, Beijing, China
 102488

²Department of Equipment Remanufacturing, Academy of Armored Force Engineering, Beijing,
 China 100072

^ayanxl@th.btbu.edu.cn ^bjy Zhang0218@sohu.com ^cwwlwyd2002@sina.com.cn

Keywords: Efficient DDA Interpolation; Multi-Axis Linear Linkage; Left Normalized; The Maximum Amount of Movement

Abstract. A new efficient interpolation algorithm for multi-axis linear linkage is proposed in this paper, which uses the principle of DDA algorithm, its function be extended and improved. the left normalized data is used in this algorithm, the maximum amount of movement is used as the basis for the calculation of speed, the efficiency of the interpolation is improved and the uniformity of speed is ensured. At last machining result are presented, which shows that this algorithm is powerful to machine spherical surfaces and planes.

Introduction

The interpolation principle is a very important component of CNC technology, there are a variety of interpolation methods, such as data sampling interpolation method, point by point comparison, the digital integration method (e.g. DDA interpolation) and other interpolation methods, each interpolation method has its advantages and disadvantages.

DDA interpolation method is characterized by its function can be expanded easily, is very convenient to achieve the second curve and multi-axis linear interpolation[1], so the DDA interpolation get widely applied in CNC contouring control, but the drawback is that the feed rate fluctuations, the error is large also. A new efficient interpolation algorithm for multi-axis linear linkage is proposed in this paper, which uses the principle of DDA algorithm, its function be extended and improved, so the uniformity of machine speed can be ensured and the efficiency of interpolation, the machining accuracy of work piece increased.

Efficient DDA interpolation algorithm for spatial line

Mathematical model. Without loss of generality, set the intersecting line L of any two space planes, as shown in Fig. 1.

Set the equation of plane Π_1 is:

$$A_1 x + B_1 y + C_1 z = 0 \quad (1)$$

Set the equation of plane Π_2 is:

$$A_2 x + B_2 y + C_2 z = 0 \quad (2)$$

Therefore, the general form equation of line L is:

$$\begin{cases} A_1 x + B_1 y + C_1 z = 0 \\ A_2 x + B_2 y + C_2 z = 0 \end{cases} \quad (3)$$

If the starting point of spatial line doesn't coincide with the origin of coordinate system, we can translate the xyz axes[2], so that the spatial line become a line through the origin in the new coordinate system $X'Y'Z'$, as shown in Fig. 2, this form of spatial line is called the desired standard form.

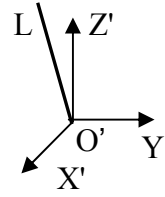
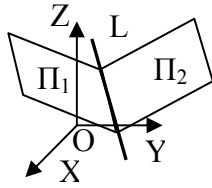


Fig. 1 Description of the spatial line Fig. 2 The standard form of spatial line

Interpolation algorithm for spatial line in standard form. We have gotten the standard form of spatial line which discussed above, suppose that we want to make pulse distribution along a line in the $X'Y'Z'$ coordinate system, the starting point of the line is the coordinate origin O , end point is $E(x_e, y_e, z_e)$, as shown in Fig. 3.

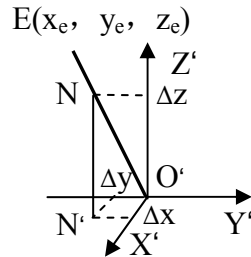


Fig. 3 The interpolation process of spatial line

Assume that v_x , v_y and v_z represent the speed of dynamic point N in X , Y and Z direction respectively, therefore the small increment of moving distance Δx , Δy , Δz in the X , Y and Z direction should be:

$$\begin{cases} \Delta x = v_x \Delta t \\ \Delta y = v_y \Delta t \\ \Delta z = v_z \Delta t \end{cases} \quad (4)$$

$$\frac{v_x}{X_e} = \frac{v_y}{Y_e} = \frac{v_z}{Z_e} = K \quad (5)$$

Where, K is proportional coefficient, in the time Δt , Parametric equation of displacement increment in x , y and z direction is :

$$\begin{cases} \Delta x = kx_e \Delta t \\ \Delta y = ky_e \Delta t \\ \Delta z = kz_e \Delta t \end{cases} \quad (6)$$

The process of the dynamic point N moving from the origin to the end point E can be considered as the cumulative results of each coordinate with increment of kx_e , ky_e and kz_e every Δt time interval, after summing up m times, x , y , z reach the terminal $E(x_e, y_e, z_e)$ respectively, the following equations established:

$$\begin{cases} X = k \sum_{i=1}^m X_e \Delta t = kX_e m = X_e \\ Y = k \sum_{i=1}^m Y_e \Delta t = kY_e m = Y_e \\ Z = k \sum_{i=1}^m Z_e \Delta t = kZ_e m = Z_e \end{cases} \quad (7)$$

Therefore $mk = 1$, Eq. 7 shows that the proportion coefficient k and the time of accumulation m is a reciprocal relationship. Because m must be an integer, so k must be a decimal. The main consideration in selecting k is that increments Δx or Δy , Δz is less than 1, in order to ensure that the feed pulse distributed to each axis every time does not exceed one unit step, e.g.

$$\begin{cases} \Delta x = kX_e < 1 \\ \Delta y = kY_e < 1 \\ \Delta z = kZ_e < 1 \end{cases} \quad (8)$$

Where, the maximum allowable value of x_e , y_e and z_e are limited by bits of controller and bytes in which coordinate values are stored. In general, if we suppose the register is n -bits, the maximum allowable value of x_e , y_e and z_e shall be $2^n - 1$ (bits are all 1), if we take:

$$k = \frac{1}{2^n} \quad (9)$$

This will meet the requirements of Eq. 8, so that, not only the coefficient K can be determined, but also the requirement of Δx , Δy and Δz is less than 1 can be ensured. Therefore, the time of accumulation m which the tool from the origin to the end point will be:

$$m = \frac{1}{k} = 2^n \quad (10)$$

The key components of DDA interpolator are accumulator and integrated function register. An accumulator and a integrated function register are required in each coordinate direction. In general, before the start of interpolation, the accumulator is cleared, x_e , y_e , z_e are stored in the registers respectively; after the start of interpolation, the contents stored in the integrated function registers will be added once in the corresponding accumulator with the arrival of each pulse Δt , the overflow after adding be regarded as feed pulse Δx (or Δy , Δz) that driving the corresponding axis, while the remainder are still stored in the accumulator; when the cumulative number of pulses m sent by the pulse source is just equal to the integrated function register's capacity of 2^n , the overflow pulses is equal to the end coordinate value measured by pulse equivalent (the smallest unit), the tool run to the end point.

Discussions

During the process of DDA linear interpolation, the time interval of each program segment is fixed, This is because the accumulate operations ($m=2^n$) must be finished, regardless of the length of Processing travel, so when the stroke is long, the tool run quickly, when the stroke is short, the tool run slowly, the feed rate of each program segment is inconsistent, this will affect the quality of machining surface, the productivity of program segment which has short stroke is very low especially, in order to overcome this drawback, make the overflow pulse uniform, improve the overflow rate, the following two measures are taken in the efficient DDA interpolation algorithm.

Left normalized data. When the value of the integrated function is small, there are i zeroes before the decimal point, these zeroes should be removed from the integrated function register, this is the process of left normalized data stored in the register.

The definition of normalized data: the MSB (Most Significant Bit) of number stored in register is 1;

The definition of non-normalized data: the MSB of number stored in register is 0.

When the value of the integrated function along X , Y or Z axis is small, shift these data left, when one of the coordinate values becoming normalized data, stop shifting left, when one bit of the data be shifted left, the value of the data will be doubled, p -bits be shifted left, the value will be 2^p times. Because $\Delta x = kx_e$, $k = 1/2^n$, when p -bits have been shifted left, $\Delta x = kx_e 2^p = x_e / 2^{n-p} = k'x_e$, $k' = 1/2^{n-p}$, so

the time of accumulation $m=2^{n-p}$, the integrated function be shift left p -bits, the time of accumulation be reduced p times[3]. In order to ensure the integrated function which has been shifted left can reach the end point, the counter determining the end should be shift right at the same time. After the process of left normalized data, not only the overflow rate has been improved, but also the overflow pulse has become more uniform.

The maximum amount of movement is used as the basis for calculation of speed. During the process of conventional DDA interpolation, the synthesis feed rate fluctuations often, even if the data is normalized left, the speed fluctuations still exist. This is mainly due to there are some NULL operations during the process of interpolation operation, that is, in some interpolation cycle, the accumulator does not overflow, there is no feed axis, there is big variation in axis's speed, the efficiency of interpolation is low.

During the process of efficient DDA interpolation, the maximum amount of movement is used as the basis for calculation of speed, in each interpolation cycle, the axis having the maximum amount of movement has a pulse output, there is no phenomenon of NULL operations, so the interpolation efficiency is improved, the uniformity of speed is ensured.

If there are three movement axes, the amount of movement were Δx , Δy , Δz respectively. Write $M = \max(\Delta x, \Delta y, \Delta z)$, $M = M + 1$. The accumulators were assigned initial value of $u = \Delta x$, $v = \Delta y$, $w = \Delta z$ respectively.

The contents stored in the integrated function registers will be added once in the corresponding accumulator with the arrival of each pulse Δt , then compared these values with M , if they are greater than or equal to M , the corresponding shaft output a pulse, while minus M from the data stored in the accumulator, to prepare for the next operation. At the same time, the interpolation pulse count minus 1, while the interpolation is not completed, this process is repeated until the interpolation complete. When the interpolation pulse count is reduced to 0, the interpolation complete.

If there is a line OE, it's starting point is the origin O (0,0,0), end point is E (4,3,4). Assuming the number of bits for the accumulator and registers is 3, the maximum storage value is 7 ($J \geq 8$ overflow). If using the conventional DDA linear interpolation, it will requires 8 cycles, of which three cycles is NULL operations, there is no pulse output, interpolation calculation process is shown in Table 1, J_E represents the counter determining the end, J_{VX} , J_{VY} , J_{VZ} represents the integrated function register of x , y , z direction respectively, J_{RX} , J_{RY} , J_{RZ} represents the accumulator of the x , y , z directions respectively.

While using the high efficient DDA linear interpolation algorithm, it requires only four cycles and each cycle has pulse output, so that a smooth tool movement can be obtained. Interpolation calculation process is shown in Table 2.

Table 1 Conventional DDA linear interpolation calculation process

X Integrator			Y Integrator			Z Integrator			J_E
J_{VX}	J_{RX}	ΔX	J_{VY}	J_{RY}	ΔY	J_{VZ}	J_{RZ}	ΔZ	
4	0		3	0			0		8
4	0+4		3	0+3		4	0+4		7
4	4+4	1	3	3+3		4	4+4	1	6
4	0+4		3	6+3	1	4	0+4		5
4	4+4	1	3	1+3		4	4+4	1	4
4	0+4		3	4+3		4	0+4		3
4	4+4	1	3	7+3	1	4	4+4	1	2
4	0+4		3	2+3		4	0+4		1
4	4+4	1	3	5+3	1	4	4+4	1	0

Table 2 Efficient DDA linear interpolation calculation process ($M=5$)

X Integrator			Y Integrator			Z Integrator			J_E
J_{VX}	J_{RX}	ΔX	J_{VY}	J_{RY}	ΔY	J_{VZ}	J_{RZ}	ΔZ	
4	4		3	3		4	4		11
4	4+4	1	3	3+3	1	4	4+4	1	8
4	3+4	1	3	1+3		4	3+4	1	6
4	2+4	1	3	4+3	1	4	2+4	1	3
4	1+4	1	3	2+3	1	4	1+4	1	0

When using high efficient DDA interpolation method, before the interpolation operations, firstly determining the movement direction of each axis according to the tool's current position and the end position of interpolation, then the result is delivered to the motor driver of the corresponding shaft ;

secondly comparing the distance of each axis interpolation with the pulse equivalent, make a conversion, that is to say converting the distance to the corresponding number of pulses, then all movement axes' numbers of pulse involved in interpolation are added, their sum is regarded as an input parameters of the interpolation calculation (initial value of J_E). By comparing table 1 and table 2, we can see that using efficient DDA interpolation not only the interpolation speed is improved, but also the machine run smoothly, at the same time the interpolation accuracy is improved.

Features of the hardware for realization of efficient DDA interpolation algorithm

Dual-CPU system has been used in the hardware system[4,5], the main CPU (MB90F346RSA) calculate the pulse period and the maximum amount of movement M , then The amount of movement of each axis and the value of M are transmitted from the main CPU to the Subordinate CPU (STC12C5404). The main CPU output fixed pulses which doesn't take up the resources of the main CPU, the Subordinate CPU make the interpolation calculation in each pulse cycle.

Conclusion

The algorithm above has been realized by C programming language, we machining planes and spherical surfaces in vertical lift axis CNC milling machine(KRN XK5025), achieved good results. Machining results show that the efficient DDA algorithm for multi-axis linear linkages proposed in this paper is very effective, it has high efficiency of interpolation, smooth running during the process of machining, high precision of machining work piece, it is a interpolation algorithm that suitable for implementation in the NC system.

Acknowledgement

The financial support of Beijing Natural Science Foundation (4062011) and Foundation for Young Teachers of Beijing Technology and Business University are gratefully acknowledged.

References

- [1] Information on <http://www.busnc.com/ly/DDA/zhixian.htm> (In Chinese) .
- [2] dehua He, hongzan Bin, J.China Mechanical Engineering vol.5(4)(1994), p.11 (In Chinese) .
- [3] Ferrari M, Lemaitre G. Active optics methods for highly aspheric mirrors. In: Proceedings of SPIE the International Society for optical Engineering, 2000, 4003(5):34~42.
- [4] X.Ai. Development and Application of High Speed Machining Technology. In: Proceedings of the International Conference on High Speed Machining, 2004:21~28.
- [5] H.Schulz. Why High Speed Cutting. In: Proceeding of the International Conference on High Speed Machining, 2004:1~8.

Finite Element Analysis on Structural Stress of 8×8 InSb Infrared Focal Plane Array with Underfill

Qingduan Meng^a, Ligong Sun and Jiexin Pu

School of Electronic Information Engineering, Henan University of Science and Technology, 471003, Luoyang, China

^aqdmengly@mail.haust.edu.cn

Keywords: Finite Element Analysis; Focal Plane Array; Insb; Stress Concentration

Abstract. Based on viscoplastic Anand's model, the structural stress of 8×8 InSb infrared focal plane array (IRFPA) detector is systemically analyzed by finite element method, and the impacts of design parameters including indium bump diameters, heights and InSb chip thicknesses on both Von Mises stress and its distribution are discussed in this manuscript. Simulation results show that the maximum stress existing in InSb chip reaches minimum with indium bump diameter 32μm. Under this condition, for the fixed indium height, as the InSb chip thickness reduces from 21μm to 9μm in step of 3μm, Von Mises stress maximum values of InSb chip seems increases gradually, and when the indium bump height reduces from 21μm to 9μm in step of 3μm, its maximum Von Mises stress increase at random increment, do not show certain rules, and indium bump height seems to have a comparable effect on stress value with InSb chip thickness. When indium diameter, height and InSb chip thickness are set to 32μm, 15μm, and 12μm, respectively, the maximal Von Mises value existing in InSb chip reaches minimal value 628MPa, simultaneously the stress distribution at the contacts areas is uniform and concentrated, and this structure is promising to avoid device invalidation.

Introduction

Indium antimonide (InSb) pn junctions are widely used as infrared photovoltaic detectors and imaging sensors for the 3-5μm spectral range [1,2]. To increase sensitivity and spatial resolution, photovoltaic diodes are usually placed in rectangular array or square array, then via indium bumps, assembled to a silicon readout integrated circuits (ROIC), after that underfill is dispensed between InSb die and Si ROIC substrate for increasing the reliability of flip-chip packaging. To obtain the lowest level of electronic noise possible to approach the photon noise limit, it is necessary to cryogenically cool the infrared focal plane array (IRFPA) to liquid nitrogen temperature (77K). Therefore, fracture in InSb chip usually occurs with the rapid temperature dropping process, due to the mismatch in the coefficients of thermal expansion between the silicon multiplexer and the InSb detector array, which will cause shearing mechanical strain on the bumps as the array is cooled to cryogenic temperatures. In order to reduce the InSb chip fracture possibility and improve the producibility, it is necessary to analyze the induced thermal strain and stress values and its distribution in InSb chip. At present time, the thermo-mechanical reliability of flip-chip assemblies is usually assessed by finite element simulations in conjunction with experimental verification, that is, basing on the strain and stress analysis, the structure reliability is assessed [3,4].

In 2009, Rui Wu Chang research group delivers the constitutive relations of indium in extreme-temperature in Anand's model [5], a rate and temperature dependent constitutive model, applied to represent the inelastic deformation behavior of indium at low temperatures down to -150°C. Based on the above research results, the structural stress of 8×8 InSb array detector with underfill dependent on both indium bump sizes and InSb thickness is systemically researched by finite element method, all these for finding the optimal structural sizes to avoid thermal stress concentration in InSb chip.

Model Creation and Parameters Selection

When creating the finite element analysis model of InSb IRFPA detector, indium bumps are assumed to be octagonal prisms, and no defects existing in the whole device. InSb IRPFA is composed of InSb photodiode arrays, indium bumps array, Si ROIC and underfill encapsulant materials, just as shown in Fig. 1. InSb chip dimensions are $400\mu\text{m} \times 400\mu\text{m} \times (9 \sim 21)\mu\text{m}$, and attached to Si ROIC substrate with 8×8 indium bumps array, Si ROIC substrate dimensions are $500\mu\text{m} \times 500\mu\text{m} \times 300\mu\text{m}$, indium bumps diameter has fixed at $32\mu\text{m}$ with $50\mu\text{m}$ pitch, and its height increases from $9\mu\text{m}$ to $21\mu\text{m}$ in step of $3\mu\text{m}$. When the diameter of indium bump height is set at $32\mu\text{m}$, the maximal Von Mises value existing in InSb chip reaches minimal values and its stress distribution is uniform at contacting areas between InSb chip and indium bump [6]. Here underfill encapsulant is dispensed between InSb die and Si ROIC substrate for increasing the reliability of flip-chip packaging. In order to describe the mesa structure locating between neighboring detectors elements, a triangular prisms, whose cross section area sides length are $2.83\mu\text{m}$, $2.83\mu\text{m}$ and $4\mu\text{m}$, respectively, are employed. Just as shown in Fig.1. Using the geometrical symmetry, only one eighth of the overall package is modeled. One eighth models contain 6 full and 4 half indium bumps.

InSb IFFPA finite element analysis model is created by top down method, that is, model is made up of block volume, then Booleans operation is used to divide the block, after than the glue command realizes the contacts between any neighboring components.

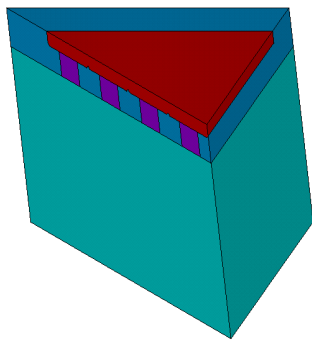


Fig. 1. Three dimensional model of infrared focal plane array device.

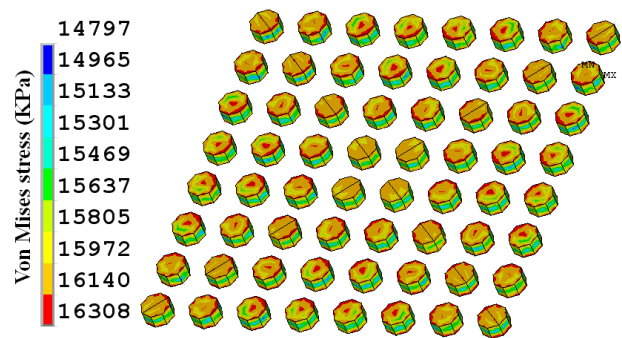


Fig. 2. Von Mises stress distribution of 3-D indium bumps.

Table 1 Liner elastic material parameters

Materials	Elastic modulus [E/Mpa]	Poison's ratio $[\mu]$	CTE [α_1 ppm/K]
Si ROIC	163000	0.28	2.50
InSb chip	409000	0.35	5.04
Indium bump	10600	0.45	33.00
underfill	9000	0.3	26.00

InSb chip, Si ROIC substrate and underfill are all considered to be linear elastic materials. All the employed parameters listed in table 1, E is the Young's modulus, μ is the Poisson's ratio, and CTE is the coefficient of thermal expansion (CTE). Flip chip process is completed at 370K, at this temperature, no residual stress is assumed to exist within the package. In the simulation, the temperature is gradually reduced from 370K to 77K, which causes thermal stresses to develop. Throughout the temperature drop, no transient heat transfer is considered and the temperature within the model is assumed to be uniform. About 71 seconds increments are taken to lower the temperature to ensure the accuracy. Horizontal displacements normal to the symmetrical surfaces are set to zero, at the same time, the displacement of Si ROIC substrate bottom surface center point remains zero.

Indium bump deformation is strongly temperature and time dependent, and associated with the irreversible, temperature and rate dependent inelastic characteristics, which are known to be viscoplastic [7-9]. Here Anand's viscoplastic constitutive model has been used to describe mechanics of constitutive relationship of indium bump [10, 11].

Simulation Results Analysis

When temperature of InSb IRFPA is gradually reduced from 370K to 77K in 71 seconds, Von Mises stress distribution of indium bumps is illustrated in Fig. 2. The maximal Von Mises stress difference (1.6MPa) among indium arrays is so small that the Von Mises stress distribution is assumed to be uniform. The maximal Von Mises stress locating on the indium bump bottom surface locating at the second row and eighth column intersection, which neighbors on the indium bump with the longest distance to neutral point on the chip, so has almost the largest induced thermal stress.

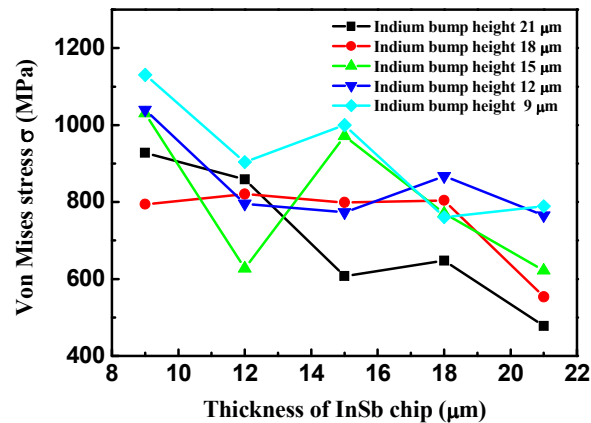


Fig. 3. Von Mises stress maximum values of InSb chip as a function of InSb thickness with varied indium bump standoff height.

In order to learn the effects from both indium bump height and InSb chip thickness on Von Mises stress value and its distribution in InSb chip, here the height of indium bump reduces from 21μm to 9μm in step of 3μm, and InSb chip thickness also decreases from 21μm to 9μm in step of 3μm. For any structure, model meshing, constraints, loading are identical for comparison of simulation results, just as shown in Fig. 3. For a fixed indium height, as the InSb chip thickness reduces from 21μm to 9μm, Von Mises stress maximum values of InSb chip seems increases gradually for indium bump height with 21μm, 15μm and 9μm, yet for indium bump height with 12μm, when the InSb chip thickness reduces from 12μm to 9μm, the Von Mises stress increases sharply, besides, the stress seems to have nothing to do with InSb chip thickness, and fluctuates at 800MPa, for indium bump height with 18μm, when the InSb chip thickness reduces from 21μm to 18μm, the Von Mises stress also increases sharply, besides, the stress also seems to have nothing to do with InSb chip thickness, and also fluctuates at 800MPa. When the indium bump height reduces from 21μm to 9μm in step of 3μm, the maximum Von Mises stress values increase at random increment, do not show certain rules, and indium bump height seems to have a comparable effect on maximal stress value with InSb chip thickness. To take account of the absorption coefficient for InSb material in middle wavelength infrared changes between $2 \times 10^3 \text{ cm}^{-1}$ and $3 \times 10^3 \text{ cm}^{-1}$, thus the corresponding light penetration depth is about 5μm and 3.3μm [12], according to absorption rule, once light transmits in the media for three penetration depths, it will be completely absorbed, so in this paper, we focus on InSb chip thickness from 9μm to 15μm. Apparently when indium diameter, height and InSb chip thickness are set to 32μm, 15μm, and 12 μm, respectively, the maximal Von Mises value existing in InSb chip reaches minimal value 628MPa. And now Von Mises stress distribution of InSb chip, underfill and Si ROIC are shown in Fig. 4 to Fig. 6, respectively.

Apparently, Von Mises stress existing on contact areas between InSb chip and indium bumps is concentrated and uniform, its stress value is about 300MPa, larger than that of its surrounding areas. The maximal stress value about 610MPa situates at the edge far away from neutral point, where the InSb chip is confined by its surrounding underfill encapsulant and does not shrink freely. The minimal stress value about 23MPa locates on the trough intersection zones. There is an obvious stress gradient from contact section center to non-contact region.

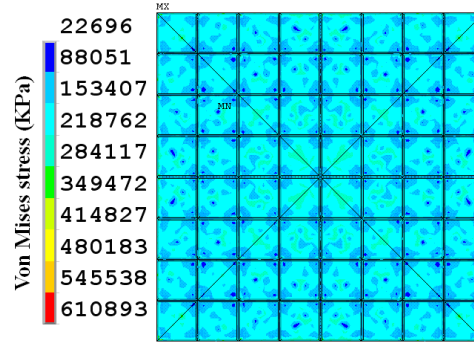


Fig. 4. Von Mises stress distribution of InSb chip bottom surface.

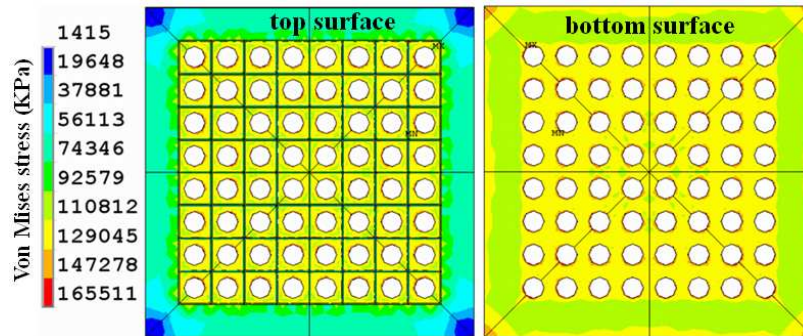


Fig. 5. Von Mises stress distribution of underfill.

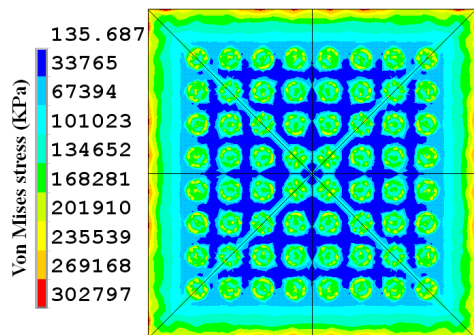


Fig. 6. Von Mises stress distribution of Si-CMOS readout integrated circuit.

Underfill encapsulant is usually dispensed in the gap between InSb chip and Si ROIC to provide mechanical reinforcement and reduce thermal stresses on indium bumps, all these for avoiding fatigue and crack growth during temperature cycles. When the temperature of 8×8 InSb IRFPA drops from 370K to 77K, Von Mises stress distribution in underfill is shown in Fig. 5. On the whole region under InSb chip, the stress distribution is uniform, and its stress value is about 120MPa, but around indium bump octahedral shell, the stress is apparently enlarged with maximal value 165MPa, and its minimum appears on the intersect region of convex triangular prisms, which is made of underfill locating in the troughs etching in InSb chip for isolating the neighboring detector cells. At the four corners of underfill top surface, Von Mises stress is small and no more than 20MPa, here the underfill can shrink freely, as for the four corners of underfill bottom surface, Von Mises stress is

correspondingly enlarged for underfill is glued with Si ROIC and do not shrink freely. On the whole, the stress on underfill bottom surface is larger than that on its top surface, which comes from the larger thermal mismatch existing between underfill and Si ROIC. Compared with indium bump array, apparently the underfill bears most thermal strain, for its stress is almost tenfold as large as stress in indium bump array.

Von Mises stress distribution in Si ROIC is almost concentrated strongly on the contacting areas between indium bumps and Si ROIC, around the contacting areas, the Von Mises is so small that it is ignorable, besides, on the quadrilateral borders of Si ROIC top surface, there are several non-continuous spots where Von Mises stress are the largest, especially near the corner of Si ROIC top surface, just as shown in Fig. 6. This is distinctly different from the stress distribution in the structure without underfill, where the stress distribution on the quadrilateral borders of Si ROIC top surface is ignorable [13].

Conclusion

Crack appearing in the InSb chip limited the InSb IRFPA final yield. Basing on finite element analysis, impacts on Von Mises stress and its distribution in the InSb IRFPA from the structure parameters, including indium bump diameters, heights and InSb chip thicknesses, are completely discussed in this manuscript. Simulation results show that as the indium diameter, standoff height and InSb thickness are set to 32 μ m, 15 μ m and 12 μ m, respectively, the maximal Von Mises value existing in InSb chip reaches minimal values 628MPa, and its stress distribution is uniform at all the contacting areas. These are favorable to reduce the crack happening in InSb chip, and improve the yield rate.

References

- [1] Gau Y. T., Dai L. K., Yang S. P., Weng P. K., Huang K. S. et al: Proceedings of The International Society for Optical Engineering, Vol. 4078 (2003), p. 467
- [2] Parrish W. J., Blackwell J. D., Kincaid G. T. and Paulson R. C.: Proceedings of the International Society for Optical Engineering, Vol. 1540 (1991), p. 274
- [3] J. H. L. Pang and D.Y.R. Chong: IEEE Transactions on Advanced Packaging, Vol. 24(4) (2001), p. 499
- [4] Z. Zhang and C. P. Wong: IEEE Transactions on Advanced Packaging, Vol. 27(3) (2004), p. 515
- [5] R. W. Chang and F. Patrick Mccluskey: Journal of Electronic Materials, Vol. 38(9) (2009), p.1855
- [6] L. G. Sun, C. Meng and Q. D. Meng: Journal of Advanced Materials Research (2011), in press.
- [7] S. Kim and H. Ledbetter: Materials Science and Engineering A, Vol. 252 (1998), p.139
- [8] E. B. Hermida, D. G. Melo, J. C. Aguiar and D. E. Lopez: Journal of Alloys and Compounds, Vol. 310(1) (2000), p. 91
- [9] R. P. Reed, C.N. McCowan and R. P. Walsh: Materials Science and Engineering, Vol. 102(2) (1988), p.227
- [10] G. Z. Wang, Z. N. Cheng, K. Becker and J. Wilde: Journal of Electronic Packaging, Vol. 123(3) (2001), p.247
- [11] Wilde J., Becker K., Thoben M., Blum W., Jupitz T., Wang G. and Cheng Z. N.: IEEE Transactions on Advanced Packaging, Vol. 23(3) (2000), p.408
- [12] Antoni Rogalski: Progress in Quantum Electronics Vol. 27 (2003), p.59
- [13] Q. D. Meng, X. L. Zhang, X. L. Zhang and W. G. Sun: Applied Mechanics and Materials Vol. 33-34 (2010), p.207

Research on 3D Reconstruction of the Facial Surface Reverse Engineering

Jie Yang^{1,2, a}, Lei Zhao^{1, b}

¹Mechanical and Electronic Information Faculty, China University of Geosciences,
Wuhan, 430074, China

²School of Engineering, The University of California, Merced, California, 95343, U.S

^aflyyangj@163.com, ^b flea0816@163.com

Keywords: 3D Facial Reconstruction; Reverse Engineering; Laser Digitizing Technology

Abstract: According to the surface integration of laser technology and computer-aided design and computer-aided manufacturing technology (CAD & CAM), a method that is rebuilt surface of three-dimensional facial reconstruction has been explored. A laser scanning system is used to collect the 3D discrete point data of the facial model, which will be cut up by their characteristics and curvature in order to make a 3D face reconstruction. The maximum reconstructive error is 0.2174mm. Application results indicate that the proposed method is quite satisfactory for facial reconstructive surgery, rehabilitation design and plastic surgery.

Introduction

With the scientific and technological development, more and more advanced manufacturing technology participate in the medical technology field, such as reverse engineering, rapid prototyping technology and laser digitizing technology. Laser digitizing technology brings a particularly wide range of applications, which can provide modeling support for the medical industry. At present, 3D surface reconstruction of the face for many researchers has become the challenging subject [1]. The model can be used to simulate oral and maxillofacial surgery plastic surgery. Using rapid prototyping technology to create the complex surface models of human face, the communication between doctors and physicians, or doctors and patients, can not only be finished by the computer virtual technology, but also the 3D simulated surgery.

In this paper, based on the research of 3D Data acquisition method, a feasibility plan has been proposed that the point cloud is divided according to the characteristics of facial features and curvature. This method is fully different from the traditional way constructing patches from mesh lines and blending [2]. After analyzing the error between the original data and the reconstruction model, the results show that the method proposed in this paper can meet the clinical medicine requirements of Oral and Maxillofacial Surgery, facial plastic surgery on the precision and error.

Data Acquisition

System Composition and Working Principle. The 3D surface reconstruction system mainly consists of two parts: A, data acquisition section. JS654N-type coordinate measuring instrument, with the Japanese origin of pairs of CCD, the U.S. imported laser generator, measurement accuracy is 0.02mm, working distance is 150mm, resolution is 768 × 576PAL, and scanning speed is 1500 points / sec. B, the data processing section. Computer ASUS (Intel Duo T6400, Memory 2G, Hard disk 320G), Windows XP OS, reverse engineering software (installing *Scan Manager* and *Imagerware V12.0*).

Fig. 1 shows the use of triangulation to obtain the basic principles of three-dimensional coordinates [3, 4]. The light issued by the laser passes through the amplitude grating components paralleling like the equidistant straight lines or interferometer, and forms a linear interference fringes projected onto the object. Because the changes of surface curvature or depth bring stripe deformation, the use of CCD (Charge Coupled device image sensor) camera could get the picture of this deformed fringe images. The data, such as measured point distance or location coordinates, can be obtained by the triangular geometric relations according to the laser beam's angle and imaging position in the CCD.

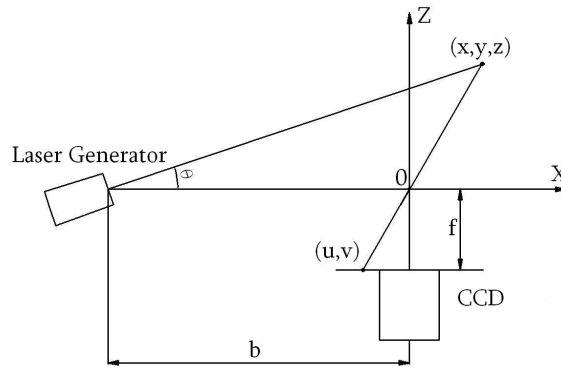


Fig. 1 Principle of 3D coordinate measurement

The figure above, the origin of measurement coordinate system is the center point of CCD camera lens, (x, y, z) is an arbitrary point on the surface, (u, v) is imaging point of (x, y, z) in the CCD camera, f is the camera focal length, b is the distance between laser projection center (light source) and the camera center, θ is the angle between the X-axis and a straight line which is formed by the measured point and the light source center. b, f, θ are the system parameters which are obtained through the calibration, u and v are the coordinate figures of image points on the sensitive surface of the CCD camera.

In the X-0-Z plane:

$$\frac{f}{u} = \frac{z}{x}, \quad \frac{b+x}{z} = \cot \theta \quad (1)$$

In the Y-0-Z plane:

$$\frac{f}{v} = \frac{z}{y}, \quad \frac{x}{y} = \frac{u}{v} \quad (2)$$

Therefore, 3D coordinates (x, y, z) of the measured points can be obtained:

$$(x, y, z) = \frac{b}{f \cot \theta - u} (u, v, f) \quad (3)$$

Facial Three-Dimensional Data Acquisition. Because the existing laser scanning range is limited, a facial surface model by 1:3 scaled down becomes the object of data acquisition in this paper. The scan parameters, the scan range and accuracy of the images acquisition can be set up according to clinical needs. Being selected the front of the face model as the main scanning direction, the mainly scan range is between the two ears and between chin and forehead. The scanning result is shown in Fig. 2 which is formed by 49954 points, and the file format is " *.asc ". The process of 3D surface reconstruction is shown in Fig. 3.

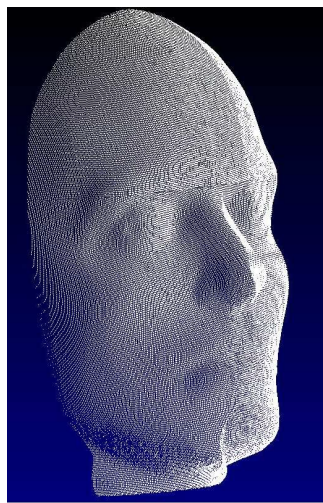


Fig. 2 Point cloud of facial 3D coordinate

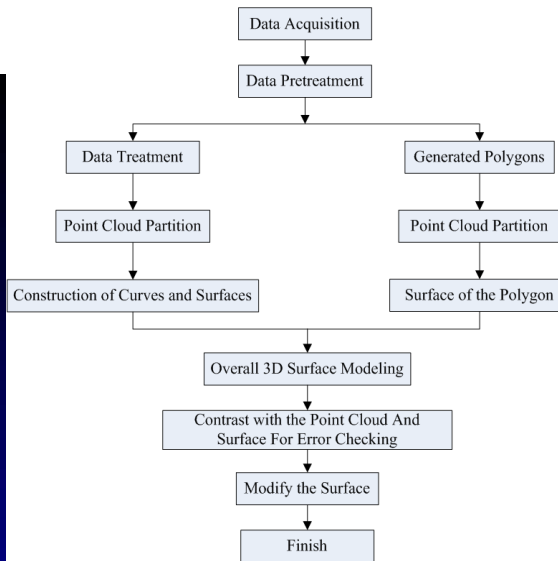


Fig. 3 Process of 3D surface reconstruction

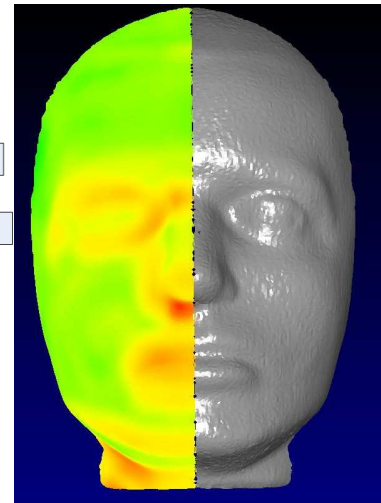


Fig. 4 Result of curvature analysis of point cloud

Facial Surface Reconstruction and Error Analysis

In this paper, reverse engineering software *Imageware* is used to carry out data processing and analysis. Throughout the measurement process, there are some random factors in addition to the accuracy of machine itself, such as some miscellaneous points. Therefore, before restoring into the CAD 3D model, it's necessary to process the point cloud, such as cutting, filtering, simplification, sorting and noise reduction. After processing, the curvature analysis of point cloud is shown in Fig.4, the left shows curvature changes and the right is original points which are shown as the polygonize cloud.

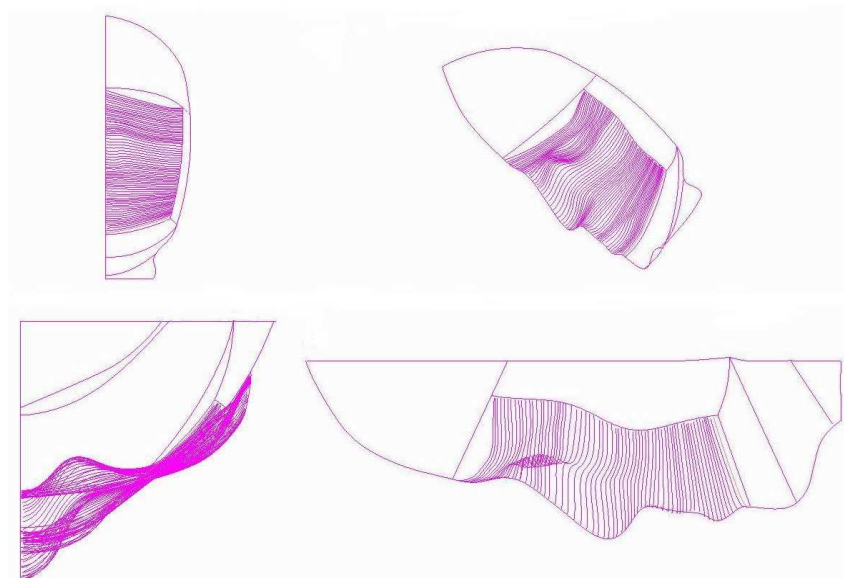


Fig. 5 Divided curves of facial point cloud according to characteristics of facial features

On account of the facial surface being a symmetrical model, only half of the point cloud need to process on the process of cutting and 3D reconstruction, and the whole 3D model can be reconstructed with the image method. According to the curvature difference, point cloud is classified into one group whose curvature changes smoothly, such as the head, forehead, cheeks and chin. In this way, it will be a great increase of accuracy, because the eyes, nose and mouth have

rapid changes in curvature, and then lofting to process is used. Fig. 5 shows the divided curves of facial point cloud.

In the fitting process, the image method is used to complete the 3D model reconstruction which is shown in Fig. 6. The method of rectifying the number and distribution of control points can be used to increase fitting accuracy or obtain different requirements of 3D surface model.

Comparing the dimensional precision of model size, the results are shown in Fig.7. Results explore that the deviation between the original point cloud and model is -0.2174 to $+0.1416$ mm, and the error is mainly caused by the number and distribution of control points. The more the number of control points is got, the more reasonable the position is obtained. The smaller the error is shown, and the 3D model reconstruction is closer to the realistic shape.

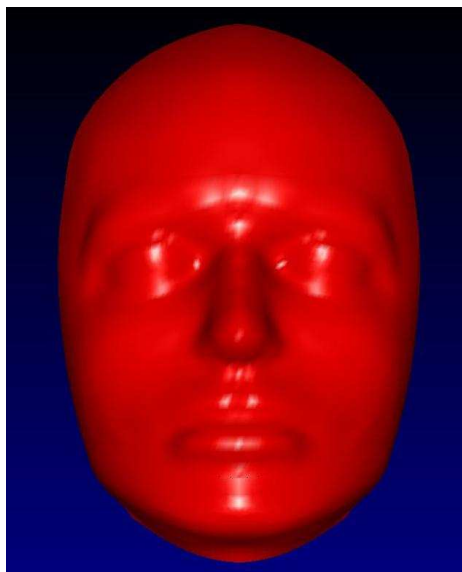


Fig. 6 Facial 3D model reconstruction

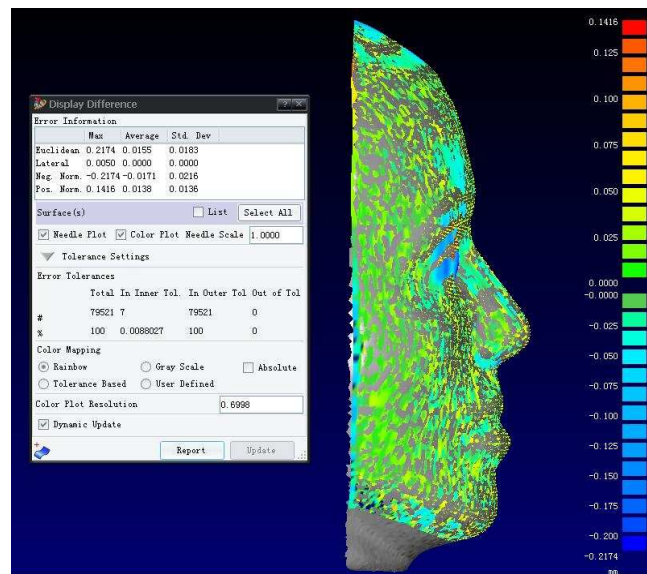


Fig. 7 Error analysis of 3D face model

Conclusions

In this paper, laser digitizing technology is used to reconstruct a complex 3D surface model. In order to pick up the more reasonable points, the point cloud is divided according to the characteristics of facial features and curvature. With the use of analysis tools which are provided by reverse engineering software, the location and continuity of the surface can be measured to evaluate the quality of reconstructed surface. There are more practical value of the reconstructed surface through rectifying the number and distribution of control points. This method is quickly and easy, the reconstructed surface has high precision. Fully integrated modern technology and medical technology, this method can provide technical support to the production of artificial implants, such as human organs, prostheses and artificial joints. There are broad application prospects.

References

- [1] C.H. Xu, Y.H. Wang, T.N. Tan: Journal of Image and Graphics. Vol. 9 (2004), p. 893-902.
- [2] S.Y. Wang, X.S. Qian, B. Ge, Y. Zhou: Journal of University of Shanghai for Science and Technology. Vol. 30 (2008), p. 64-66.
- [3] Z.Q. Xu: *3D Reverse Engineering* (China Metrology Publishing House, Beijing, China 2000).
- [4] B. Xu, Y. Huang, W. Yu, et al: Journal of Textile and Apparel, Technology and Management. Vol. 2 (2002), p. 1-11.

A Digital Near Net Shape Manufacturing Propeller with Complex Surface

Zhongfei Jiao^a, Shan Yao^b, Shuming Zhao^c, Feng Zeng, Di Wu

School of materials science and Engineering, Dalian University of Technology, Ling gong Road,
 DaLian, China

^axx2000jzf@163.com, ^byaoshan@dlut.edu.cn, ^cscorpion2.0@163.com

Keywords: Digital Manufacturing; Laser Rapid Prototyping; Marine Propeller; Pattern-Less Casting

Abstract. An integrated digital routine is applied in the near net shape manufacturing of marine propeller. Firstly, the 3D CAD file of propeller is created by parametric modeling. Secondly, the propeller casting process is simulated using CAE software, through which an optimized casting scheme is obtained. Thirdly, fabricates the mold using laser rapid prototyping and cast the metal propeller. Finally, evaluate the casting precision performance. CAD, CAE and CAM are integrated in this process. The dimensional accuracy of the final piece is controlled within 1mm and its surface roughness achieves Ra 6.3μm. The result shows that the pattern-less casting of propeller can be achieved by this method, reducing cost and performing high accuracy.

Introduction

Propeller with complex surface is one of the most important components for the ship dynamic system, which works in poor conditions with high speed and wears easily[1]. The performance of the whole system is directly affected by the design and manufacturing standards of propeller. The blades of propeller are spiral-shaped and their thickness is uneven, which makes the propeller a typical complex casting[2].

The propeller mold is manually made with scrapers in traditional method due to its complex geometry. The ultimate propeller is obtained through manual grinding or numerical control machining after cast blank. In the actual production, from propeller design to making mold, the whole process is done by workers, which is a hard work and will lead apparent errors.

Propeller is made using a fully digital process. Parametric modeling, simulation on propeller casting and process optimization, digital manufacturing of mold, and digital evaluation of casting are integrated to realize pattern-less casting of propeller.

The 3D parametric modeling of propeller

There are two parts in propeller, the hub and the blades. The hub is a standard axisymmetric piece and is defined by 5 parameters, the inside and outside diameters of bottom surface, the inside and outside diameters of top surface, and the height of the hub. The surface shape of the propeller blades are defined by a series of data points in the expanded blade surface and some related parameters which include the radius of the profile circle r , pitch p , pitch angle ϕ , and data point locations to the reference point (1,h). The coordinates of data points in the expanded blade surface has to be transformed though Eq.1 before building 3D mold, for their coordinate system is different from Cartesian coordinates. Figure 1 is the schematic diagram of coordinate transformation (Let the coordinate of any point in blade back of propeller (X,Y,Z), b' is the corresponding point in the unfolded surface, d' is the projection of the point in horizontal plane, the corresponding circumferential angle of d' is θ , d is the corresponding point of d' in the expanded surface, O is the datum point). All kind 3D CAD models can be built according to Eq.2, which is the definition formula of NURBS surface (P_{ij} is the control point columns of feature mesh in rectangular domain, W_{ij} is the weight factor of the corresponding control points, $N_{i,k}(u)$ and $N_{j,l}(v)$ which are defined in

knot vectors are k th power and l th power of B-spline function). Figure 2 is the 3D models for 4 blades propeller and 5 blades propeller.

$$\begin{aligned} X &= r \cos\left(\frac{(1-h \tan \phi) \cos \phi}{r}\right) \\ Y &= r \sin\left(\frac{(1-h \tan \phi) \cos \phi}{r}\right) \end{aligned} \quad (1)$$

$$Z = \frac{P\theta}{2\pi} + h \cos \phi - r \tan \phi$$

$$S(u, v) = \frac{\sum_{i=0}^m \sum_{j=0}^n W_{ij} p_{ij} N_{i,k}(u) N_{j,l}(v)}{\sum_{i=0}^m \sum_{j=0}^n W_{ij} N_{i,k}(u) N_{j,l}(v)} \quad u, v \in [0, 1] \quad (2)$$

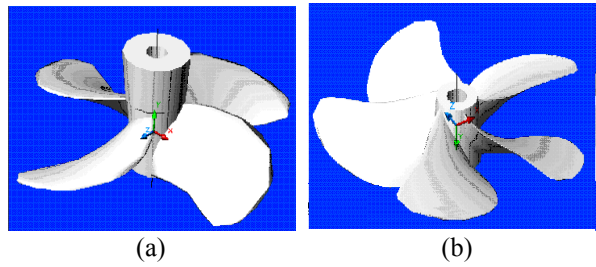
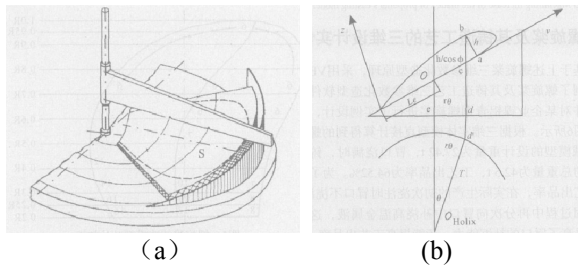


Figure 1. Coordinate transformation for propeller data point (a) schematic diagram of the propeller blades, (b) schematic diagram of unfolded blades

Figure 2. Propeller models (a) 4 blades propeller, (b) 5 blades propeller

Numerical simulation of propeller casting and process optimization

After getting the 3D propeller model, it can be imported to CAE software to simulate the propeller casting process. PROCAST is used in this paper to calculate the temperature field and solidification process of propeller casting. The casting defects are forecasted according to the simulation results and optimized casting scheme is proposed to ensure the quality of propeller casting.

A propeller with 4 blades is shown as an example to analyze the simulation results. In 55s-1846s, the temperature field and solidification process of the center section are respectively shown in figure 3 and figure 4. As shown in the simulation results, hot spot is formed in the hub of propeller. So casting defects such as shrinkage porosity and shrinkage cavity are easily to be produced here.

Based on the analysis results above, riser and chill can be used respectively in the top and bottom of propeller hub. Then liquid metal can solidify from the bottom up to avoid casting defects.

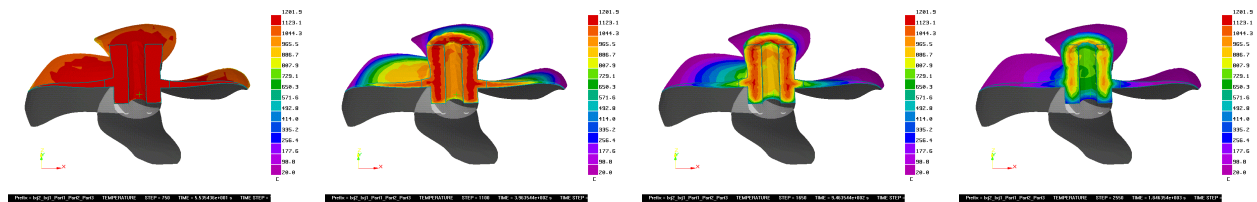


Figure 3. The temperature field of the center cross section

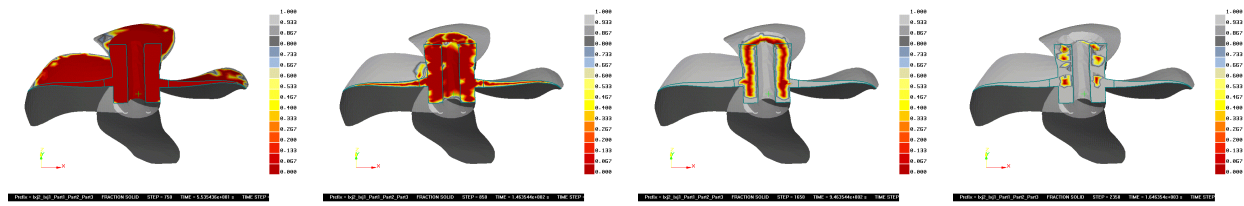


Figure 4. Solidification process of the center cross section

Digital manufacturing principles of propeller mold

After determining the casting program, the propeller mold can be produced with coated sand though laser rapid prototyping method, which is driven by the 3D CAD model of propeller.

The laser rapid prototyping method used in this paper is called profile invalidation rapid prototyping (PIRP) [3]. During the manufacturing, coated sand is scanned by laser along a fixed track. When the power is large enough, the scanned coated sand will be invalidated and couldn't be cured, which will form a dividing surface between the extraneous materials and the objective part. The coated sand which is not scanned by laser can bond together sintered in the oven. After consolidation, the coated sand mold can be finally got by removing the extraneous materials out of the dividing surface. Figure 5 is the flow chart of PIRP.

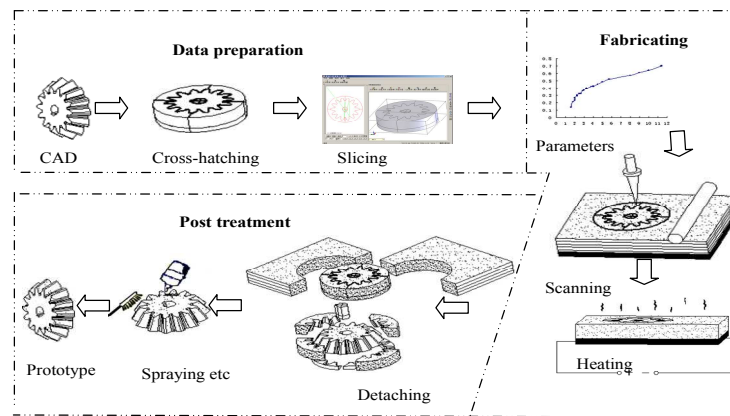


Figure 5. The flow chart of PIRP

PIRP is proposed based on SLS method and LOM method, but it overcomes their shortcomings and forms the following distinct advantages:

- 1) Processing time is saved. Only the profile is scanned for each slice in PIRP, but the whole area is swept by laser in SLS method for every layer. So the processing time of PIRP is much less than that of SLS for a same part.
- 2) Processing way is flexible. The material used in PIRP is powder. The layer thickness of every layer is non-uniform. The accuracy and efficiency could be greatly improved, for the layer thickness is adjustable according to the shape of part.
- 3) Various materials are available for PIRP. In theory, any thermosetting powder is suitable for this method.

Digital pattern-less near net shape casting for propeller

The mold of propeller is made into 4 modules though PIRP method for the complex surface shape and interference characteristic of propeller. Then the 4 parts can be combined into a complete propeller mold. Figure 6 is the propeller mold.

A 0.2-0.25mm foundry coating is sprayed on the mold to improve the surface quality of casting before pouring. Then the propeller casting can be got using the casting process proposed above. Figure 7 is the 4 blades propeller casting.

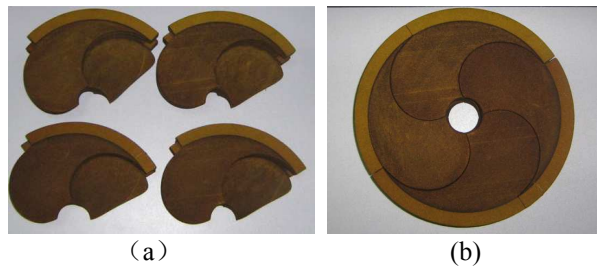


Figure 6. Propeller mold (a)modules of propeller mold, (b) complete propeller mold



Figure 7. Propeller casting (a) casting with riser, (b) riser removed

Digital assessment for the accuracy of propeller casting

The three-dimensional coordinates of each point on the propeller casting, especially on the blades, are measured using 3D profiler after getting the casting. Then these measured data are compared with the CAD model and the differences are calculated to evaluate the precision of castings. The figure 8(a) is the 25000 point cloud data collected by 3D profiler. The figure 8(b) shows the point cloud data fitted with the propeller model. The statistics for the differences between point cloud data and the designed model are got and shown by different colors in figure 8(c). The analysis results are that the absolute errors of propeller can be controlled within 1mm except for the blades edge where the collected signals are instable. And the relative errors are less than 0.3%. The surface roughness can achieve Ra 6.3 μ m.

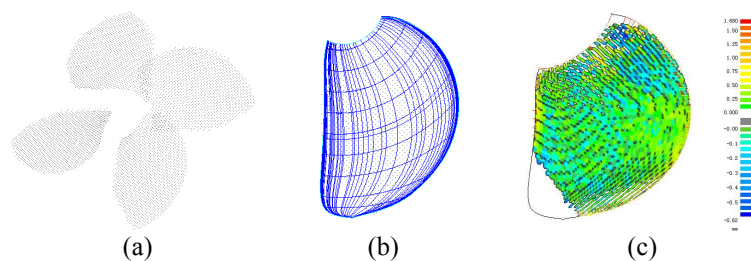


Figure 8. Assessment for the propeller accuracy (a) point cloud data, (b) point cloud data fitted with propeller model, (c) error distribution of propeller blade

Conclusions

To overcome the deficiency of traditional process, digital method is used to carry out the pattern-less near net shape casting for propeller. All processing steps are auto completed by computer and the integration of CAD/CAE/CAM is realized. The production error is greatly restrained. Manufacturing propeller by this method can greatly reduce costs and improve accuracy, and the cycle from design to casting could be shorten.

Reference

- [1] Gao Tongbing, Yang Xiangwei: Ship & Ocean Engineering Vol. 2 (2002), p 11-15
- [2] YAO Shan, MA Chun-ying, XU Yan-li: Foundry Vol. 55 (2006), p 1004-1006
- [3] Yang Tong, Yao Shan, Zeng Feng: Rapid Prototyping Journal Vol 16 (2010), p 146-155.

Finite Element Analysis for Analog Modes of SCS Series Truck Scale with Different Loads

Taowei Shi^a, Jian Li^b Jun He^c

Department of mechanical engineering, Guangxi University of Technology, Liuzhou, Guangxi,
545006 ,China

^a shixi8509@163.com, ^b gxlzlj@tom.com, ^c hejun004201@163.com

Keywords: Truck Scale; ANSYS; Finite Element Analysis; Load Mode.

Abstract. The weighing platform of the truck scale is a load-bearer, which is used for bearing a load. Its structure has many forms, in this paper, the finite element analysis of a structure with u-beam which is currently the most widely used for different loading modes, the traditional method of structural analysis of truck scale is to simplify the platform as a simply supported beam. As the model is too simplified, the result of this method will be unreliable and it cannot make part analysis about stress and strain. In this research, ANSYS was used to model, and loaded analysis. Through different loading, get the structure of weighing platform stress distribution and deformation. By analysing, we give reasonable proposals and provide valuable reference for the design and production of truck scale.

Introduction

Truck scale, also known as loadometer, is the mainly a weigh equipment which is used for bulk cargo. It is widely used in industrial and mining enterprises, transport, ports, warehouses and other departments, with the rapidly economic development, vehicle load capacity is increasing, weighing platform structure design is more important.

In request of an enterprise, finite element analysis software was used to check the strength of the weighing platform structure by different loading. According to material mechanics, the truck scale is to simplify the platform as a simply supported beam to analysis, this is the traditional method, mechanical model of this method is too simple, but we use ANSYS to build a more realistic model, and obtain a result. Through analysis, we give reasonable proposals, for the truck scale design and production provide a valuable reference [1].

Weighing Platform Structure Dimension, Check Indicators, Load Mode

Analogical Modes of SCS Series Truck Scale Platform Structure Dimension. The parameters of this paper were provided by an enterprise drawing, the series is SCS—120 which compose of four truck scales. The main technical parameters are following:

- 1) Maximum weighing (t): 120;
- 2) Weighing Mode: Measurement of the static vehicle;
- 3) Size of the overall structure of truck scales: 16m×3m×0.01m;
- 4) Sensor quantity: 10 [2].

For analysing the main problem, one weighing platform was taken, structure dimension is 4m×3m×0.01m, It has seven U-beams which welded a nickelclad panel in the above, welding ribs between U-beams, both ends of the covered nickelalad, the diagram shown in Figure 1:

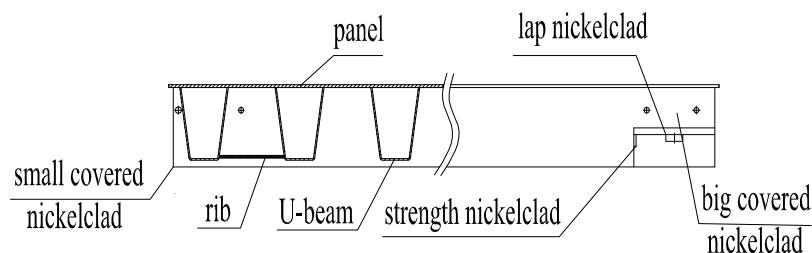


Fig 1 Schematic diagram of the weighing platform

Check Indicators . Weighing platform structure designed to meet the intended use. According to the provisions of GB-1589, at present, normal use in our country, maximum weighing 30t to 150t for the large truck scale of load-bearer. Its relative deformation are requirements of the following table. Table 1 [3]:

Table 1 The relative deformation of weighing platform

Maximum weighing(t)	Test load(t)	Loading area(m)	The maximum relative deformation of weighing platform	
			First testing After installation	Subsequent testing in use
30~40	15	1	$\leq 1/800$	$\leq 1/600$
50~60	26	1.8	$\leq 1/800$	$\leq 1/600$
80~100	40	2.6	$\leq 1/800$	$\leq 1/600$
120~150	50	3	$\leq 1/800$	$\leq 1/600$

In actual production, every weighing platform under the maximum rated load, allowable bending portrait length scale platform shall not exceed $1/800$ to $1/1000$. From a security point of view here, we taken the portrait length scale body $1/1000$ of the deformation of the stiffness index as a check indicator. The length of Scale body table is 4 m, so the deformation can not exceed 4 mm.

Load Mode. In this paper, after reference to other papers , taken another load mode, as following:

- 1) The first loading way :Loaded by the national standard, this paper analyzes the SCS-120 truck scale, which composed of four truck scales, the largest weighing is 120 tons, so each section is the largest weighing between 30 to 40 tons. By the check indicators, in the scale's finite element model, 1.5 m portrait left and right middle area to load, horizontal width of the table for the scale is 3 m, $1\text{ m} \times 3\text{ m}$ is the rectangular area load testing load of 15 tons.
- 2) The second loading way :Consider the case of overloading based on 1), that is loaded with the biggest weighing 40 tons.
- 3) The third loading way : In the national standard requirements, we taken into account the vehicle wheels and truck access to the actual situation, so we divided the loading into two equal portions to load, 7.5 tons of loading above the truck tire contact area, we simplified to a rectangular area (two rectangular axle spacing of 1.8m), it is $0.4\text{ m} \times 0.3\text{ m}$ at the middle of 1 m region.
- 4) The fourth loading way :Consider the case of partial load based on 3), for instance, one side is 5 tons, another is 10 tons.

The following two pictuers (Fig 2, Fig 3) are used to indicate the location of load:

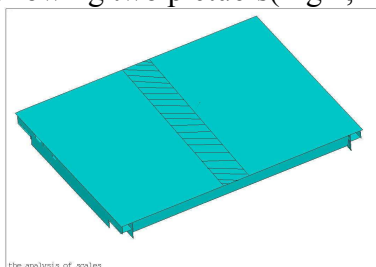


Fig 2 Location of the first and second loading way



Fig 3 Location of the third and fourth loading way

The Finite Element Model for The Truck Scale Platform Establishment

Materials and Properties. Truck scale's materials: Q235 , Elasticity modulus: $2.1 \times 10^{11} Pa$, Poisson's ratio: 0.27 , Material density: $7.9 \times 10^3 kg/m^3$, Long measure: m [4].

Modeling and Meshing. In order to analyze the problem of convenience, we omitted corner and small hole in the modeling process, also eliminated U-beam at the center, the main purpose is to consider in the worst condition, whether deformation of the structure of the weighing platform is also to meet the requirements or not. For this reason, structure of the scale platform can be optimized. Modeling using shell elements, select unit type shell163 [5].

Quadrilateral mesh, free meshing.

Loading and Constraints. Loading: Loading surface in accordance with the requirements stated in the previous spoken, at this point, we used the finite element software to extract the number of nodes, and loaded the average surface force on the node.

Constraints: Weighing devices installed on the sensor, the UX, UY, UZ direction constraints.

Solution. In this research, we taken into account the complex structure of the weighing platform, not used solid modeling to analysis, directly reduced to surface, ultimately built out of the model, submitted directly to the finite element solver, and quickly calculate the results.

Post-processing Results and Analysis. The first above loading way. The results shown in Figure 4:

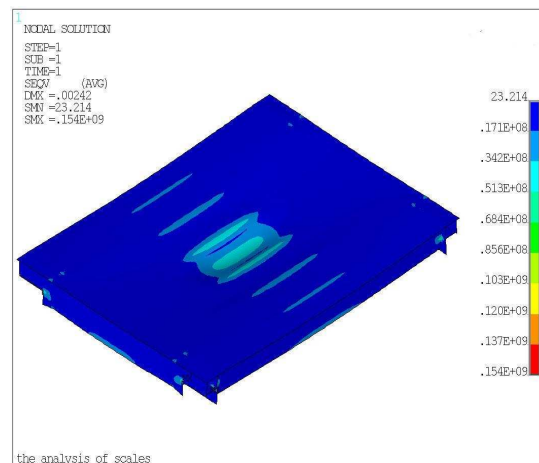


Fig4 loading 1) deformation results

Analysis: Deformation is 2.42 mm, maximum stress is 154 MPa, both meet the requirements. The second above loading way. The results shown in Figure 5:

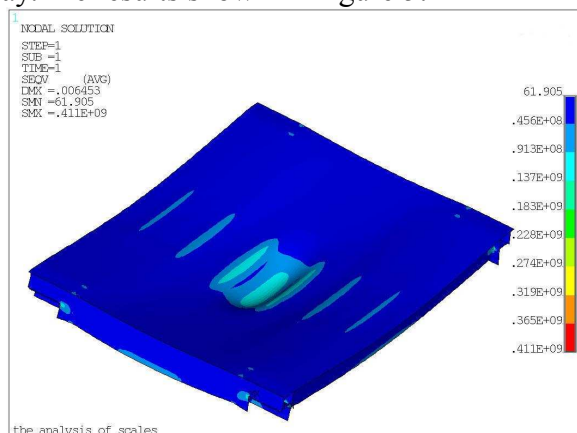


Fig5 loading 2) deformation results

Analysis: Deformation is 6.453 mm, maximum stress is 411 MPa, if the national standard in accordance with the requirements, deformation in this range, but the stress exceeds the material yield strength.

The third above loading way. The results shown in Figure 6:

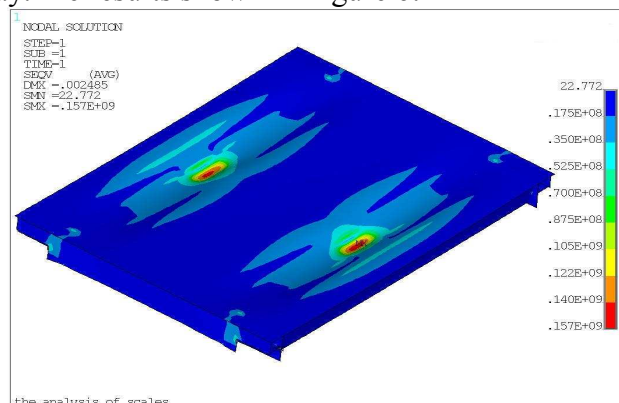


Fig6 loading 3) deformation results

Analysis: Deformation is 2.485 mm, maximum stress is 157 MPa, both meet the requirements. The fourth above loading way. The results shown in Figure 7:

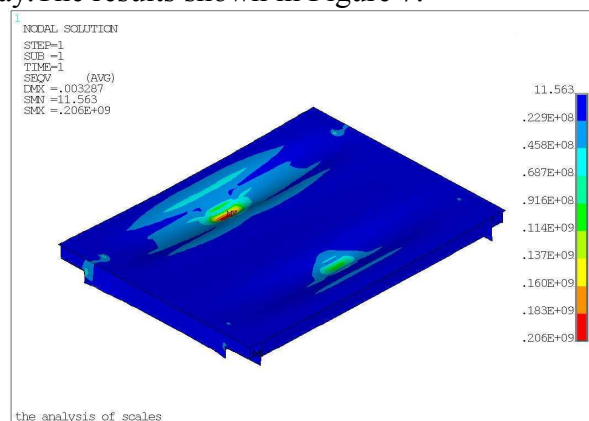


Fig7 loading4) deformation results

Analysis: Deformation is 3.287 mm, Maximum stress is 206 MPa, both meet the requirements[6,7].

Conclusion

Figure 4, Figure 6, Figure 7 shown the results of finite element analysis, which meet the requirements. Owing to, this enterprises manufacture products by experience, material size are very conservative. As a private enterprises, ANSYS shows its advantages, which can be used to simulate and test the strength and stiffnes of weighing platform.

Figure 5 shown, the results do not meet the requirements. We taken into account the cost and structure has become rational, in actual use, should not to overload use.

Figure 4, Figure 5 shown, we found the maximum stress occurring at strength steel board and welding covered board. So to do well here process.

Figure 4, Figure 5 was according to national standard to load, Figure 6, Figure 7, the author loaded on the platform according to wheel position and consider the partial load conditions, therefore, optimization of the structure size for the weighing platform provide a reference.

Acknowledgment

This paper is sponsored by Liu Zhou Te Li Machinery Co.,Ltd, analysis is based on technical data provided by this enterprise, the author analysed according to their practical problems, obtained the feasibility results. The authors gratefully acknowledge the support agency.

References

- [1] Zhenrong Wang: Discuss Electronic Truck Scale Platform of The Structure and Stiffness Calculation(1997), in Chinese.
- [2] Mei Liu, Peisi Zhong, Zhaoyang Sun, Xiaojun Meng, Shuhui Ding: Finite Element Analysis for Modular Platform of SCS Series Truck Scale with Multi-Block (2004),in Chinese.
- [3] GB / T 7723-2008, Fixed Electronic Weighing, in Chinese.
- [4] Hui ZU Shan: Material Mechanics, Higher Education Press(1999), in Chinese.
- [5] Nukulchai W K. A Simple and Efficient Finite Element for General Shell Analysis. Int . J. Num. Meth.Eng . ,1979, 14: 179~200
- [6] Surana K S. Transition Finite Elements for Three-Dimensional Stress Analysis. Int.J.Num.Meth.Eng. , 1980, 15: 991~1020
- [7] Shuguang Gong: ANSYS Analysis Based Applications and Examples, Machine Press(2003), in Chinese.

Finite Element Analysis of Blanking Process by Superimposing Ultrasonic Vibrations

Weiching Yeh^{1, a}, Tsuhsiao Chu^{1, b}, Shiuansheng Wang^{2, c},
 Kuanghua Fuh^{3, d} and Kuanhun Chen¹

¹ Department of Mechanical Engineering, National Central University, Chungli 32054, Taiwan

² Department of Mechanical Engineering, De-Lin Institute of Technology, Taipei 23656,

³ Department of Mechanical Engineering and Mechatronic, National Taiwan Ocean University, Keelung 20224, Taiwan

^awcyeh@cc.ncu.edu.tw, ^b963403011@cc.ncu.edu.tw, ^cwangss@dlit.edu.tw,
^da0065@mail.ntou.edu.tw

Keywords: Ultrasonic Vibrations; Blanking; Finite Element.

Abstract. The application of ultrasonic vibrations superimposed on wire drawing, deep drawing, upsetting and rolling has been developed in the literature. No attempts have ever been made to develop the application of the ultrasonic vibration to blanking process. This paper reports an investigation into the effects of the superimposed ultrasonic vibrations of the die during the blanking process by finite element software DEFORM-2D. The results are compared with the conventional blanking experiment by Hatanaka and Yamaguchi [7] and the simulations are analyzed with various vibration directions, amplitudes and frequencies. The effects of the ultrasonic vibration on the punch load, flow stress and edge profile are systematically studied. The results show ultrasonic vibration can decrease the punch load and improve the quality of edge profile by increasing the vibration amplitudes and frequencies.

Introduction

Blanking is one of the most frequently used processes in metal forming process. The shearing process develops between a punch and a die and leads to the total rupture of the sheet. The quality of the blanking product is affected not only by the mechanical properties but also by the ductile fracture process in shearing band between the punch and the die. The choice of process parameters for blanking is determined by an iterative procedure involving a large number of tests. In recent years, with the increase of computational capabilities, numerical simulations of the shearing process of sheet metals have been performed to better understand the mechanics based on the finite element method (FEM) [1,2]. Different strategies, such as the node separation method [3] and coupled thermo-mechanical method [4] have also been proposed to simulate the crack propagation in blanking process.

Few experimental and numerical analyses have been reported in the literatures by superimposing ultrasonic vibrations on the wire drawing, deep drawing, upsetting and rolling processes. It is well known that the forming force, the flow stress and the friction between the die and the sheet could be reduced by the applications of ultrasonic vibration [5,6].

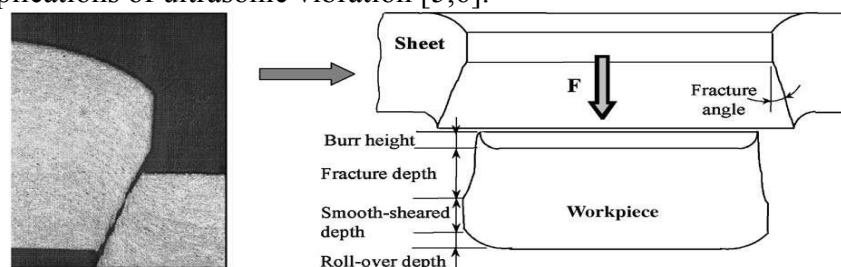


Fig. 1. Characteristic features of edge profile.[10]

In this report, blanking process by superimposing ultrasonic vibrations is studied by using a commercial finite element code, DEFORM-2D. The objective of the proposed study is to analyze, in the case of thin SPCC sheets, the influence of parameters such as various vibration directions, amplitudes and frequencies on the characteristic features of the punch load and edge profile, as illustrated in Fig. 1.

Simulation of Blanking Process Using the Finite Element Method

The simulation of conventional blanking process was performed firstly. To validate the simulation results, a comparison is made between the numerical results and the experiment results of Hatanaka and Yamaguchi [7]. Due to symmetry, an axial-symmetric modeling was performed, as illustrated in Fig. 2. The Table 1 and Table 2 show the blanking conditions and material properties used in the analysis. The Power law elastic-plastic equation, $\bar{\sigma} = F(0.002 + \bar{\epsilon}_p)^n$, is used to describe the behavior of sheets and the Cockcroft and Latham [8] expression is used as the ductile fracture criterion.

Table 1. Blanking conditions

	Experiment	Simulation
Blanking speed, V_p (mm/min)	1	1
Blank holding force, F_h (kN)	4.0	4.0
Diameter of die, D_d (mm)	30.0	30.0
Diameter of punch, D_p (mm)	29.4(0.10t)	29.4(0.10t)
, D_p (mm) (clearance)	29.7(0.05t)	29.7(0.05t)
Punch and die edge radii, R (mm)	—	0.064
Coefficient of friction, μ	—	0.2
Sheet thickness, t (mm)	3	3

Table 2. Material properties

Young's modulus(GPa)	210
Yield strength(MPa)	218
Ultimate tensile strength(MPa)	495
Strength coefficient, F (MPa)	831
Work hardening exponent, n	0.21
Poisson's ratio, ν	5
	0.29

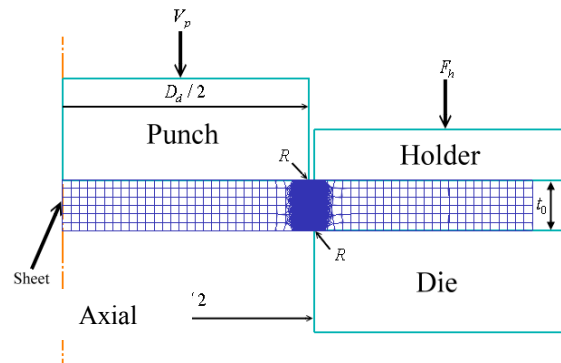


Fig. 2 Model of FE mesh.

Fig. 3 shows the diagram of blanking force versus punch stroke for different clearances between the punch and the die. Fig. 4 shows the depth of roll-over(r/t), smooth-sheared(s/t), fracture(f/t) and burr depth (b/t). The results show a good agreement between the numerical and the experimental results.

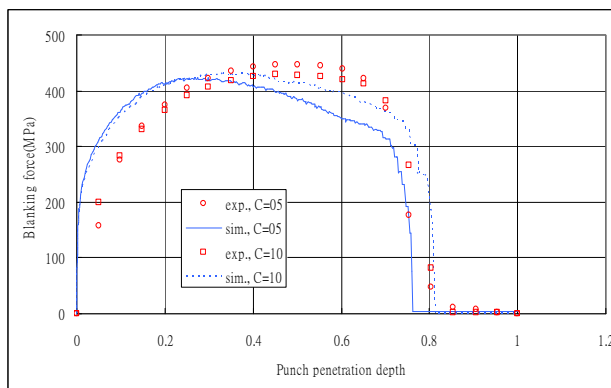


Fig. 3 Blanking force with punch stroke

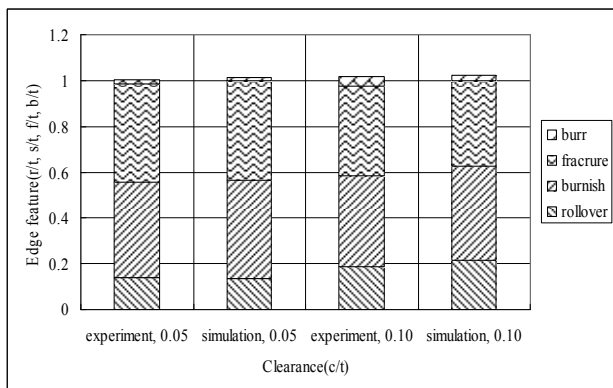


Fig. 4 The depth of blanking profiles

Results and Discussion

Since the simulations of the conventional blanking process are validated, simulation of blanking was performed by superposing sinusoidal axial and radial vibrations on the die, respectively. The amplitude (a) and frequency (f) of vibrations used are ranged from $a=5$ to $20\text{ }\mu\text{m}$ and $f=5$ to 20 kHz . The simulations of conventional blanking process and ultrasonic vibrations blanking are similar. The only difference is the application of the ultrasonic vibration on the die additionally required in the ultrasonic vibration blanking process. It is not necessary that the ultrasonic vibration be applied throughout the forming process and is preferable that the vibration be stopped after the maximum punch load [9]. To allow for manageable computational time while ensuring that the effects of the change in interface friction can be evaluated, the ultrasonic vibration was applied for extensively short intervals in the FEM models. Ultrasonic vibration was applied at two period of time in the simulations, one was before the maximum punch load, and the other was before the fracture of sheet. The former is mainly discussed the variety of punch load and the latter is mainly discussed the quality of edge profile. To exert the most influence of ultrasonic vibration, the blanking speed was considered less than the maximum vibration critical speed ($V_{cr} = 2\pi af$) [5].

Effects of Ultrasonic Vibration on Punch Load

Fig. 5 (axial) and Fig. 6 (radial) show the diagram of blanking force versus punch stroke with superimposing one-dimensional ultrasonic vibrations having $a=20\text{ }\mu\text{m}$ and $f=20\text{ kHz}$, respectively; both are presented at the time intervals of 0.001 s before approaching the maximum load. During the period of ultrasonic vibration, the maximum blanking load decreases 10% and 20% and the mean blanking load decreases 50% and 23% for axial and radial vibration, respectively. The fluctuation period of blanking load obtained is $50\text{ }\mu\text{s}$ which is similar to vibration period of time ($T=1/f=50\text{ }\mu\text{s}$). The reduction of blanking load is due to continuously alternate contact and separation by superimposing ultrasonic vibrations, considerably resulted in the decrease of friction condition between the die and the sheet.

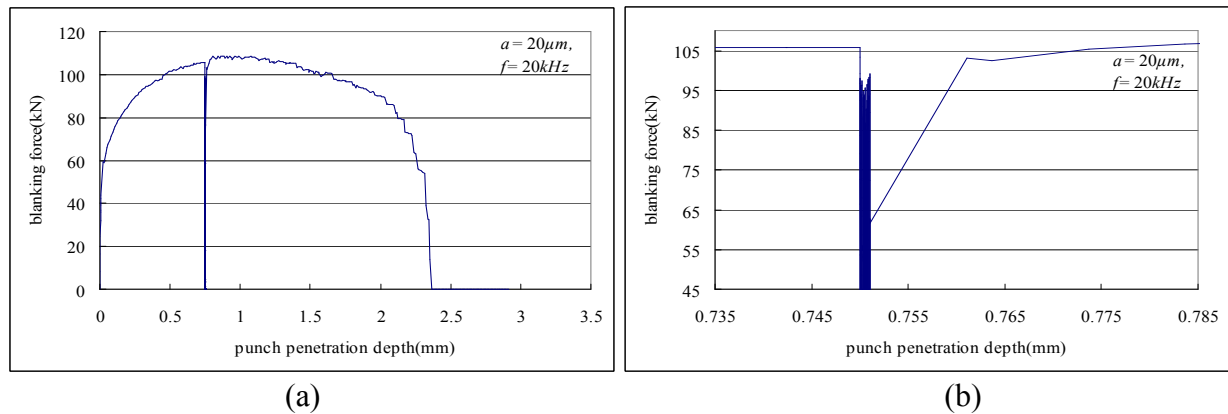


Fig. 5 (a) The diagram of blanking force versus punch stroke with superimposing the axial vibration only. (b) Expanded oscillatory force.

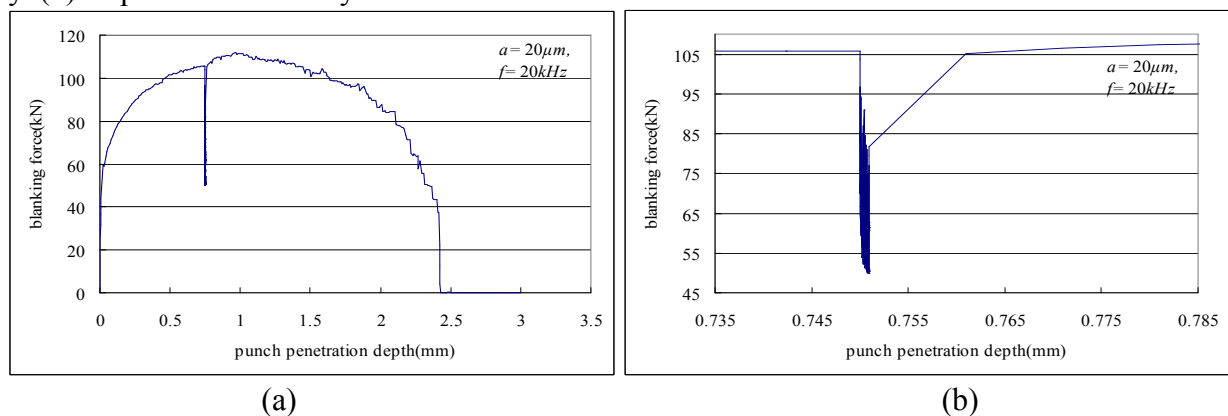


Fig. 6 (a) The diagram of blanking force versus punch stroke with superimposing the radial vibration only. (b) Expanded oscillatory force.

Effects of Axial Vibration on Edge Profile

From practical point of view, the size of the smooth-sheared depth and burr height are often the most important quality parameters. For this reason, this report only discusses the characteristics of these two zones. In simulating the blanking process, the ultrasonic vibration was only superimposed axially. Fig. 7 and Fig. 8 show the ratio of smooth-sheared depth and burr height under different combinations of vibration frequency and amplitude. When the frequency (amplitude) remains unchanged, along with the increase of amplitudes (frequencies) the size of smooth-sheared depth increases whereas the size of burr height decreases drastically. Fig. 9 shows the comparison of the distribution flow stress between conventional and ultrasonic vibration blanking processes. When the punch is separated from the die, the maximum stress decreases substantially by 58.3% as shown in Fig. 9(c). The edge profile after blanking process with and without the axial ultrasonic vibration superimposed is showed in Fig. 10 for comparison. Because of the reduction of the mean flow stress, the fracture appeared later and more slowly during application of the axial ultrasonic vibration, as showed in Fig. 11(a). It not only increases the plasticity of the sheet but also extends the shear zone. These factors show that the reduction in mean flow stress results from the separation of the die from the sheet, and have positive effect on the quality of edge profile.

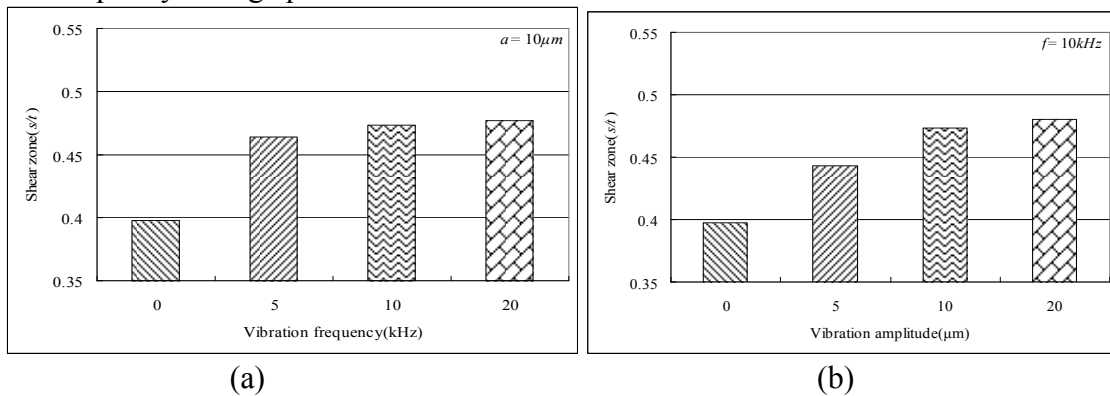


Fig. 7 Smooth-sheared depth under (a) different frequencies. (b) different amplitudes.

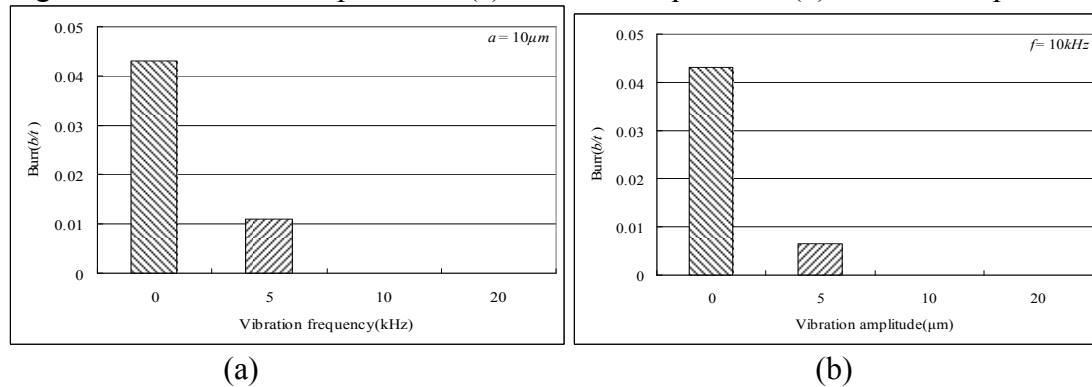


Fig. 8 Burr height under (a) different frequencies. (b) different amplitudes.

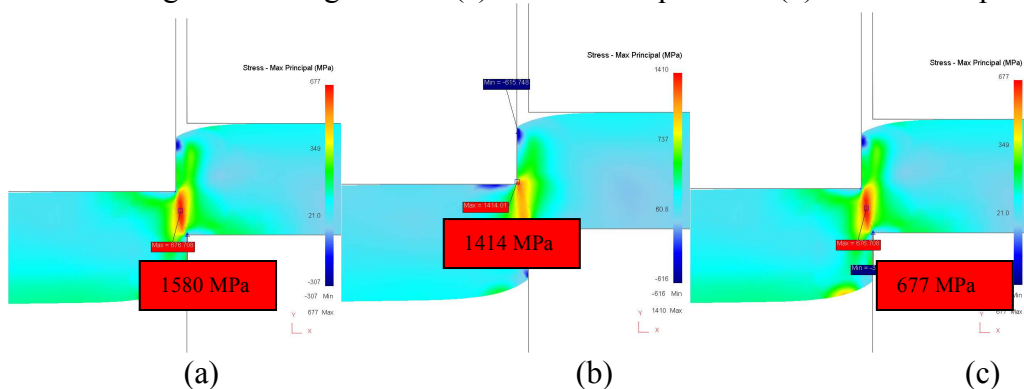


Fig. 9 Stress distribution for : (a) the conventional blanking process. (b) the die and sheet under the contact condition. (c) the die and the sheet under the separation condition.

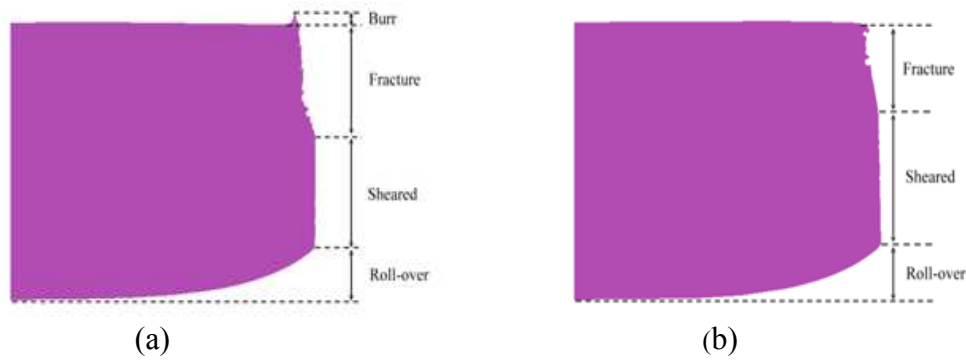


Fig. 10 The edge profile after blanking process, (a) without ultrasonic vibration ; (b) with axial superimposed.

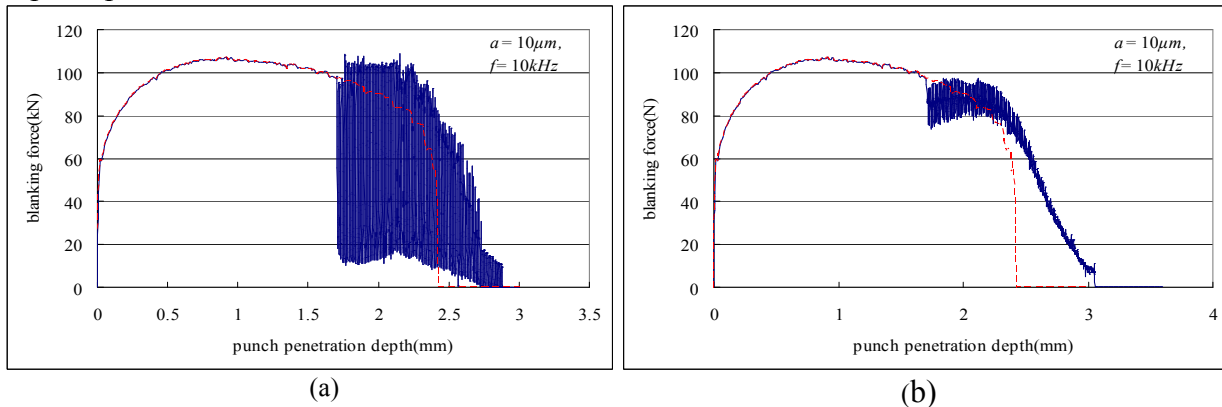


Fig. 11 The diagram of blanking force vs. punch stroke under (a) an axial vibration superimposed, and (b) a radial vibration superimposed.

Effect of Radial Vibration on Edge Profile

Similar simulation conditions are executed in the radial vibration. In simulating the blanking process, the ultrasonic vibration was superimposed in the radial direction only. Fig. 12 and Fig. 13 show the ratio of smooth-sheared depth and burr height under different combinations of vibration frequency and amplitude. The size of smooth-sheared depth increases with the increase of either frequency or amplitude whereas that of corresponding burr depth decreases drastically. Fig. 14 shows the comparison of the distribution flow stress between conventional blanking and ultrasonic vibration blanking processes. While the punch is separated from the die, the maximum stress decreases substantially by 19.3%, as shown in Fig. 14(b). The edge profile after blanking process with and without the radial ultrasonic vibration superimposed is shown in Fig. 15 for comparison. Burr-free condition and the greater smooth-sheared depth are both clearly observed due to the effect of the radial vibration. Because of the reduction of the mean flow stress, the fracture appeared later and more slowly during application of the radial ultrasonic vibration, as showed in Fig. 11(b). It not only increases the plasticity of the sheet but also extends the shear zone. Burr always forms at the beginning of the rupture and is elongated during the final blanking process. By numerous vibrations between the die and the sheet, burr forms later and reduces the damage evolution in the neck zone. By this way, the elongation of burr is limited by superimposing the radial ultrasonic vibrations, which also show positive effect on the mean flow stress and the quality of edge profile. The quality of rupture profile after additionally superimposing radial vibration is therefore much improved compared with that produced by conventional blanking process.

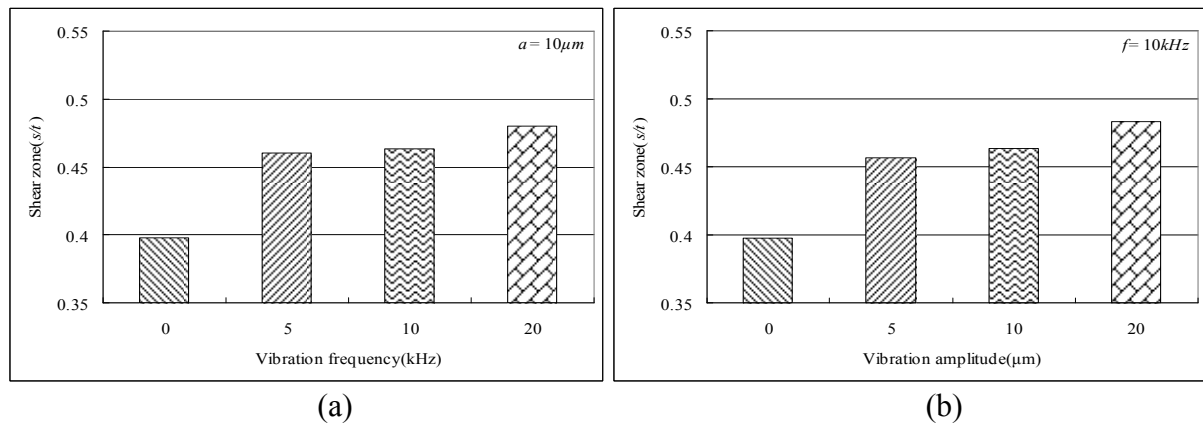


Fig. 12 Smooth-sheared depth under (a) different frequencies. (b) different amplitudes.

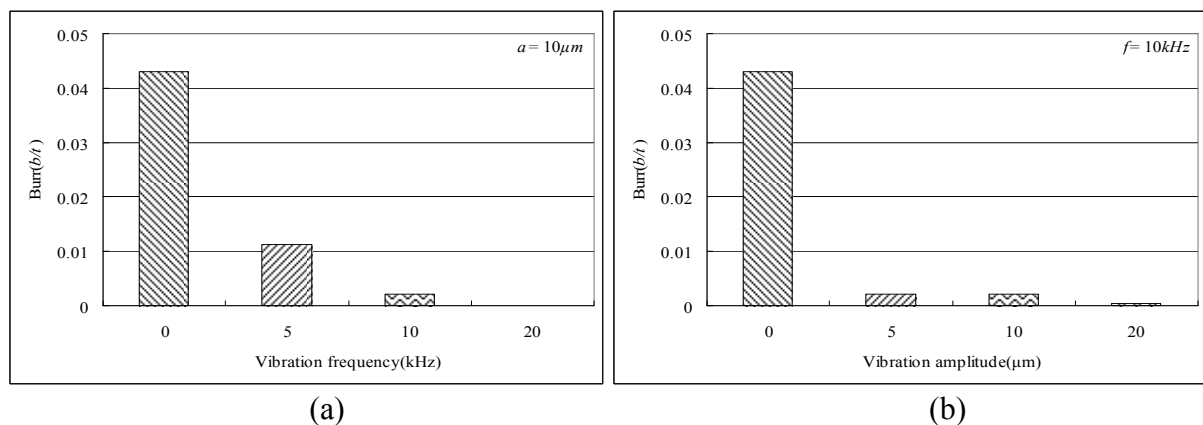


Fig. 13 Burr height under (a) different frequencies. (b) different amplitudes.

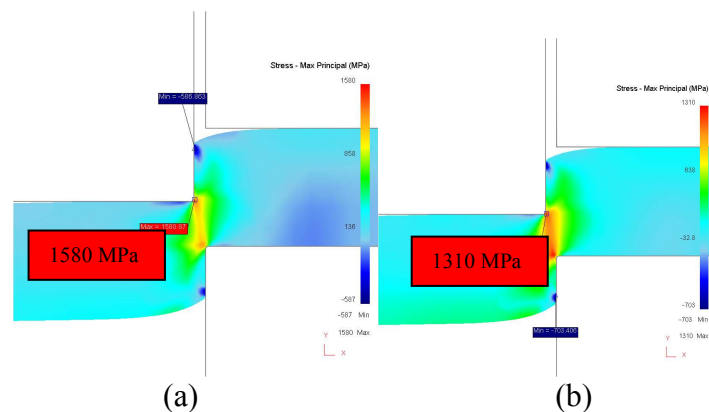


Fig. 14 Stress distribution for : (a) the die and sheet under the contact condition. (b) the die and the sheet under the separation condition.

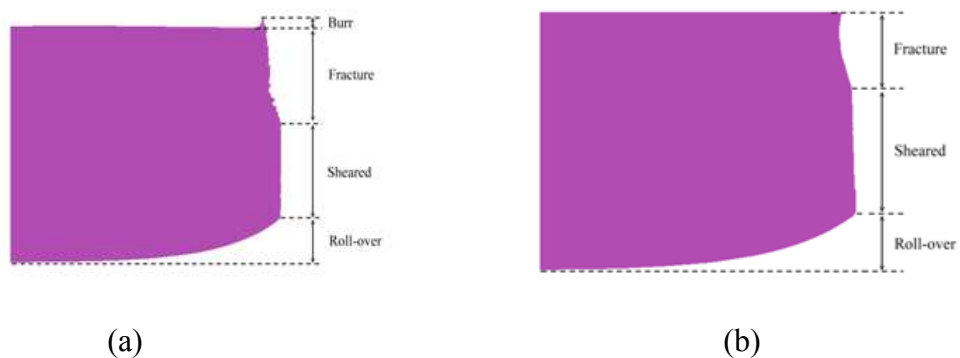


Fig. 15 The edge profile after blanking process, (a) without ultrasonic vibration ; (b) with radial superimposed.

Conclusions

In the FE simulation of blanking process superimposed ultrasonic vibration, the following results are obtained:

1. The maximum and mean punch load can be reduced by superimposed ultrasonic vibration either in axial or radial vibration. The radial vibrations are more effective in the decreasing of maximum load required, and thus can extend the punch life.
2. The size of shear zone increases with the increase of either frequency or amplitude of the ultrasonic vibration whereas that of corresponding burr height decreases drastically.
3. The radial vibration is more effective than the axial vibration in reducing the size of burr height; at the given condition being discussed, it could almost reach the burr-free level.
4. The results reveal that ultrasonic vibrations not only have positive effect on decreasing the punch load required, but also improve the quality of edge profile by increasing the vibration amplitudes and frequencies.

References

- [1] S. Yu, X. Xie, J. Zhang, and Z. Zhao: Journal of Materials Processing Technology, Vol 187–188(2007), pp.169
- [2] C. Husson, J.P.M. Correia, L. Daridon and S. Ahzi: Journal of Material Processing Technology, Vol 199(2008), pp.74
- [3] N. Hatanaka and K. Yamaguchi: Journal of Materials Processing Technology, Vol 139(2003), pp. 64
- [4] A. Rafsanjani, S. Abbasion, A. Farshidianfar, N. Irani: The International Journal of Advanced Manufacturing Technology, Vol 45(2009), pp.459
- [5] S.A.A.A. Mousavi, H. Feizi, and R. Madoliat: Journal of Materials Processing Technology, Vol 187-188(2007), pp. 657
- [6] V.C. Kumar and I.M. Hutchings: Tribology International, 37(2004), pp.833
- [7] N. Hatanaka, K. Yamaguchi: Journal of Materials Processing Technology, Vol 139(2003), pp.64
- [8] S.I. Oh, C.C. Chen, and S. Kobayashi: ASME Journal of Engineering for Industry, Vol 101(1979), pp.36–44
- [9] T. Jimma, Y. Kasuga, N. Iwaki, O. Miyazawa, E. Mori, K. Ito and H. Hatano: Journal of Materials Processing Technology, Vol 80-81(1998), pp.406
- [10] R. Hambli : International journal of Mechanical Sciences, 44(2002), pp.2089

Special Purpose Five-Axis Machine Tool for Manufacturing a Precision Cam

Chen-Hua She^a, Kai-Sheng Li^b and Zhi-Hao Zheng^c

Department of Mechanical and Computer Aided Engineering, National Formosa University

64 Wen-Hua Road, Huwei, Yunlin 632, TAIWAN

^achshe@nfu.edu.tw, ^bplay760119@hotmail.com, ^c19851132@gm.nfu.edu.tw

Keywords: Five-Axis Machining; Postprocessor; Nonorthogonal Linear Axis

Abstract. Five-axis machining, an important processes in precision manufacturing, has been used in defense, aerospace and consumer product industries. Many combinations can be synthesized to generate various five-axis machine tool configurations, in which the linear and rotary axes are normally orthogonal. Since five-axis NC data can only be applied to a specific configuration, the portability of the NC data is inevitably limited. A special purpose five-axis machine with a nonorthogonal linear axis configuration is investigated in this research. The complete analytical equations for NC data are obtained using the homogeneous coordinate transformation matrix and inverse kinematics. A window-based postprocessor system written by Borland C++ Builder was developed according to the proposed algorithm. A roller gear cam was adopted as an example to generate the NC code using the proposed postprocessor system. A trail-cut experiment conducted with this special purpose machine tool confirms the effectiveness of the proposed methodology.

Introduction

Five-axis machining, an advanced technology developed to meet the industrial demands for geometric variety and high precision, can provide two additional rotational degrees of freedom and a line cutting mode with flank milling by tilting the cutting tool axis. Compared with the point cutting mode, the line cutting mode increases the cutting efficiency markedly and is extremely important in manufacturing processes. Therefore, it has many industrial applications, such as in automotive, aeronautic, and naval industries, manufacturing wooden furniture and laser-beam machining [1-2].

Many combinations can be synthesized to generate various five-axis machine tool configurations in which the linear and rotary axes are normally orthogonal. A five-axis machine with a nonorthogonal linear axes configuration is investigated in this research. This configuration is a special purpose five-axis machine tool which is used to manufacture precision mechanical components such as index tables and roller gear indexing drives. A special purpose five-axis machine tool facilitates the convenient and rapid mass production of products with specific functions, even though the machining center is only dedicated to a particular product.

Programming multi-axis machining is more difficult than that for three-axis machining because of the varying orientation of the cutter relative to the workpiece during machining. To generate the five-axis NC program, the interface, known as the postprocessor capable of converting the cutter location (CL) data created by CAM systems into the machine control data, should be utilized. Postprocessors are machine dependent since different machine tools may have different controllers and configurations. Consequently, a manufacturing system with various machine tools requires several postprocessors. Notably, a postprocessor can be developed using the graphical method [3], homogeneous coordinate transformation matrix [4], or numerical method [5]. However, recent studies apply postprocessor schemes for five-axis machine tools with orthogonal linear or rotary axes. Relatively fewer studies [6] have addressed the nonorthogonal linear axis configuration.

In this work, a postprocessor system dedicated to the proposed special configuration is developed to transform the CL data into machine control data through homogeneous coordinate transformation

matrix and inverse kinematics. A spatial cam called the roller gear cam for an automatic tool change mechanism is selected as a machining example. A trial-cut experiment, performed with model material, demonstrates practical application of the developed method.

Postprocessor for the Machine Tool

Determination of form-shaping function matrix by forward kinematics. One rotary movement (the A -axis) occurs on the workpiece and the other (B -axis) is on the spindle (Fig. 1). The linear Z -axis is nonorthogonal to the machine base coordinate system while the B -axis rotates. Five-axis machine tools can be considered as a mechanism with serially connected links with revolute or prismatic joints. Forward kinematic equations must be established to describe cutting tool motion mathematically relative to the workpiece. The fundamental coordinate transformation matrices, including the translation matrix **Trans** and the rotation matrix **Rot** [7] are introduced.

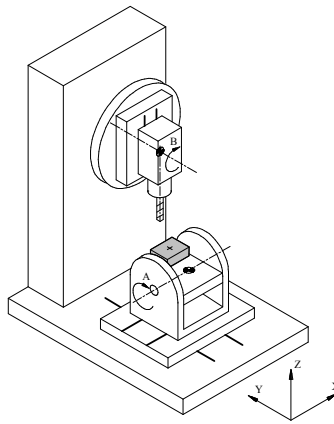


Fig. 1 Five-axis machine tool with nonorthogonal linear axis configuration

Figure 2 shows relevant coordinate systems for this configuration. The coordinate system for the workpiece is $O_W X_W Y_W Z_W$ while the system $O_t X_t Y_t Z_t$ is attached to the cutting tool. The offset vector $L_x \mathbf{i} + L_y \mathbf{j} + L_z \mathbf{k}$ is determined from the origin, O_W , to the pivot point RA. The term d_{AB} is the distance between A -axis and B -axis. Effective tool length, L_t , represents the distance between the pivot point RB and the cutter tip centre.

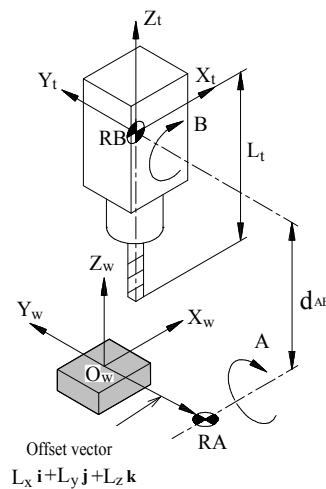


Fig. 2 Coordinate systems of the five-axis machine tool

The structural elements of the machine tool are an A rotary table, machine bed, X linear table, Y linear table, B rotary axis, Z linear table, and cutting tool. The relative position and orientation of the cutting tool with respect to the workpiece can be determined sequentially starting from the workpiece and ending at the cutting tool and is referred to as the form-shaping function [8]. The form-shaping function of this machine tool can be expressed mathematically in the following matrix form:

$$\text{Trans}(L_x, L_y, L_z) \text{Rot}(x, -\phi_x) \text{Trans}(P_x, P_y, d_{AB}) \text{Rot}(y, \phi_y) \text{Trans}(0, 0, P_z) \begin{bmatrix} 0 & 0 \\ 0 & 0 \\ 1 & -L_t \\ 0 & 1 \end{bmatrix} \quad (1)$$

where P_x , P_y and P_z denote the relative translation distances of the X , Y and Z linear tables, respectively; and ϕ_x and ϕ_y are the rotation angles for the A -axis and the B -axis, respectively. Positive rotation is in the direction of an advancing right-hand screw about the $+A$ and $+B$ axes. Equation (1) specifies the form-shaping function matrix of this machine tool, and joint parameters P_x , P_y , P_z , ϕ_x and ϕ_y should be determined by inverse kinematics.

Determination of NC data by inverse kinematics. When CL data including the position of the centre of the tool tip $Q_x \mathbf{i} + Q_y \mathbf{j} + Q_z \mathbf{k}$ and the tool orientation $K_x \mathbf{i} + K_y \mathbf{j} + K_z \mathbf{k}$ are known, the CL data can be expressed in the following matrix form:

$$\begin{bmatrix} \mathbf{K} & \mathbf{Q} \\ 0 & 1 \end{bmatrix} = \begin{bmatrix} K_x & Q_x \\ K_y & Q_y \\ K_z & Q_z \\ 0 & 1 \end{bmatrix} \quad (2)$$

Since Eqs. (1) and (2) represent the same relationship between the cutting tool and the workpiece, the desired joint parameters can be determined by equating these two matrices. By equating the CL data matrix and the form-shaping function matrix, and taking the corresponding elements of the two matrices yield the following equations:

$$\begin{bmatrix} K_x & Q_x \\ K_y & Q_y \\ K_z & Q_z \\ 0 & 1 \end{bmatrix} = \begin{bmatrix} S\phi_y & L_x + P_x + (P_z - L_t)S\phi_y \\ C\phi_y S\phi_x & L_y + d_{AB}S\phi_x + P_y C\phi_x + (P_z - L_t)C\phi_y S\phi_x \\ C\phi_y C\phi_x & L_z + d_{AB}C\phi_x - P_y S\phi_x + (P_z - L_t)C\phi_y C\phi_x \\ 0 & 1 \end{bmatrix} \quad (3)$$

where "C" and "S" refer to cosine and sine functions, respectively.

In this study, the NC program coordinate system is assumed to coincide with the workpiece coordinate system and Z -axis reference zero is set when the distance between pivot point RB and tool tip is L_t . The desired X , Y , Z , A and B values for NC data can be solved by Eq. (3) and expressed as follows:

$$B = \phi_y = \arcsin(K_x) \quad -\pi/2 \leq \phi_y \leq \pi/2 \quad (4)$$

$$A = \phi_x = \arctan2(K_y, K_z) \quad -\pi \leq \phi_x \leq \pi \quad (5)$$

$$X = L_x + P_x = Q_x - [(Q_y - L_y)S\phi_x + (Q_z - L_z)C\phi_x - d_{AB}] \tan\phi_y \quad (6)$$

$$Y = L_y + P_y = (Q_y - L_y)C\phi_x - (Q_z - L_z)S\phi_x + L_y \quad (7)$$

$$Z = P_z = L_t + [(Q_y - L_y)S\phi_x + (Q_z - L_z)C\phi_x - d_{AB}]/C\phi_y \quad (8)$$

where $\arctan2(y, x)$ is the function that returns angles in the range of $-\pi \leq \theta \leq \pi$ by examining the signs of both y and x [7].

Implementation and Verification

To confirm the feasibility of the proposed methodology, a window-based postprocessor system was developed under the Windows-XP environment in Borland C++ Builder programming language. When parameters : $\alpha=30^\circ$, $a=140$ mm, $r=12.5$ mm, $\ell=12$ mm, $\delta=41$ mm and the timing chart for the globoidal cam ϕ_2 versus turret ϕ_3 are known, the CL data can be acquired by Eq. (9). Therefore, the NC data for machining roller gear cam can be generated by the developed postprocessor system and CL data. The generated five-axis NC data are further verified by performing an experimental trial-cut with the special purpose five-axis machine tool. Figure 5 shows the finished roller gear cam with model material, indicating that the proposed scheme can be applied for practical five-axis machining.



Fig. 5 Machined roller gear cam model

Conclusions

A postprocessor methodology for the five-axis machine tool with nonorthogonal linear axis configuration was developed. The complete analytical equations of NC data were determined by the homogeneous coordinate transformation matrix, and the forward and inverse kinematics. Although the proposed machine tool is a special purpose configuration, the proposed postprocessor system can convert the CL data generated by various commercial CAD/CAM systems into NC data. Therefore, the dedicated machine tool can manufacture various products flexibly, and create considerable added value, and enhance industrial competitiveness.

Acknowledgements

The financial support of the National Science Council of the Republic of China and Fei Jih Company under grant NSC 99-2622-E-150 -015 -CC3 is gratefully acknowledged.

References

- [1] F. Mason: Am. Machinist (1991), p. 37
- [2] G. Connolly: Mech. Eng. (1994), p. 64
- [3] O.R. Fauvel, J. Vaidyanathan and D.H. Norrie: J. Manuf. Syst. Vol. 9 (1990), p. 353
- [4] R.S. Lee and C.H. She: Int. J. Adv. Manuf. Technol. Vol. 13 (1997), p. 658
- [5] K.J. Mei: *Studies on Virtual Multi-Axis Milling Machine Construction and Postprocessor Program Integration* (Master Thesis, National Cheng-Kung University, Taiwan 2009).
- [6] C.H. She and C.W. Hung: Proc. Inst. Mech. Eng. Part B-J. Eng. Manuf. Vol. 222 (2008), p. 741
- [7] R.P. Paul: *Robot Manipulators: Mathematics, Programming and Control* (MIT press, Cambridge, Mass. 1981)
- [8] D.N. Reshetov and V.T. Portman: *Accuracy of Machine Tools* (ASME press, New York 1988)
- [9] R.S. Lee and C.H. She: Int. J. Mach. Tools Manuf. Vol. 38 (1998), p. 277

Accurate Prediction of Die Face Coloring Rate for Short-Period Manufacturing of Automotive Drawing Dies

Qiang Yu^{1,a}, Dehua Miao^{1,b}, Yujun Cai^{2,3,c}, and Changfeng Men^{1,d}

¹Tianjin Key Laboratory of High Speed Cutting and Precision Machining, Tianjin University of Technology and Education, Tianjin 300222, P.R.China

²School of Mechanical Engineering, Tianjin University, Tianjin 300072, P.R.China

³Tianjin Motor Dies Company Limited, Tianjin 300308, P.R.China

^ayuqiang95@yeah.net, ^bmiaodh@126.com, ^ccyjal@126.com, ^dmenzi6210@sohu.com

Keywords: Automotive Die; Coloring Rate; Die Structure Simulation; Surface Compensation

Abstract: In this paper, the thinning rate and die elastic deformation under large forming force are investigated by finite element simulation with experimental validation focused on the problem of coloring rate between die and panel in automotive die manufacturing. The study suggests that when the panel is formed, the thinning rate of panel has little influence on the coloring rate and the die elastic deformation under large forming force is the main influence factor. The definition of high contact pressure area is proposed by the comparison between the simulation and industrial experiment results. The definition greatly benefits the predication of die face coloring rate. The method that die face is compensated reasonably is also proposed. It can reduce the die polishing workloads obviously compared to the traditional method of die face equivalent offset. This paper has a guide for comprehensive understanding the influence factors of coloring rate and greatly reducing the die tryout period.

Introduction

It is known that a crucial part in the automotive production is the development of high quality dies. The problem analysed in this paper is the coloring rate of automotive die, which is very important to the die performance and the panel accuracy [1]. In order to develop the stamping dies with the equivalent offset die face by CAM software in traditional way, the trial-and-error method is still prevalent by the die makers. One of the main reasons why the trial-and-error method can not vanish in die making industries may be consideration of blank thinning and die deformation under press loads required to shape the blank [2]. The polishing method by die makers can not meet the short-period and high quality requirements in die manufacturing. For shorting the cycle and reducing the die makers' workloads, the factors of influencing die face coloring rate must be studied. Further more, modifications of the main geometry of drawing die face with computer aided methods rather than polishing by die-maker is an effective way aiming an efficient die tryout [3].

In order to get the influence factors of die face coloring rate, this paper takes a panel as an example. Through the analysis of drawing thinning rate and the die elastic deformation under large force with Ls-Dyna software, the die face compensation are carried out. The coloring rates between the results of simulation and die tryout are compared.

Surface contact analysis between panel and die

Theoretically, the blank and die uniformly fit with each other as the die reaches the lowest point of the travel distance. The blank is formed to be a panel by the interaction of the die and punch. Traditionally, the die face is equivalently offset by CAM software. The die face machined with equivalent offset face must be uniformly fit with the panel (see Fig. 1).

The contact pressure distribution between die and panel must be uniform when the die contacts panel evenly. However, the die contacts panel unevenly in practice and the gap between them will be appeared (see Fig. 2) because of the blank thinning and elastic deformation of die under large force in

forming process. The elastic deformation of die is not uniform because of uneven forming force distribution. As a result, the contact pressure and the coloring rate between die and panel are not uniform. Thus the panel thinning rate and the die elastic deformation must be studied at the same time to improve the coloring rate [4].

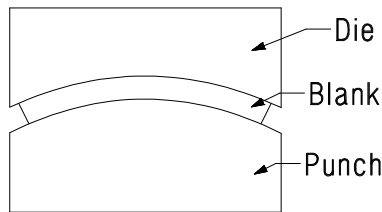


Fig. 1 The ideal surface contact state between die and panel

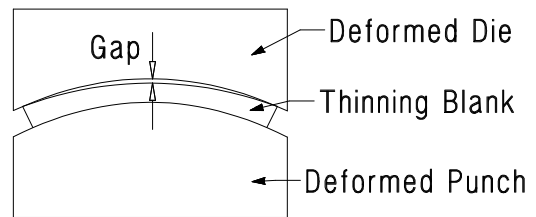


Fig. 2 The real surface contact state between deformed die and thinning blank

The analysis of panel thinning rate

An automotive panel is studied as an object in this paper. Fig. 3 shows the drawing geometry surface of the panel. In the simulation model the blank and drawing tool are shell elements. It has about 1.5×10^4 elements in total. The main material parameters are Yield stress 0.370 GPa, Tensile strength 0.457 GPa, thickness 0.9 mm. In single drawing process simulation, the binder force is 5.5×10^2 KN. Because the panel is symmetrical, the simulation model is half model hereinafter. Fig. 4 shows the simulation result of thinning rate.

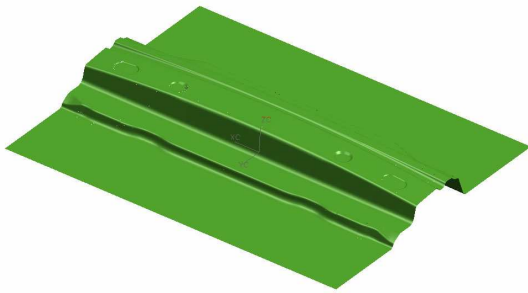


Fig. 3 Drawing geometry surface of a panel

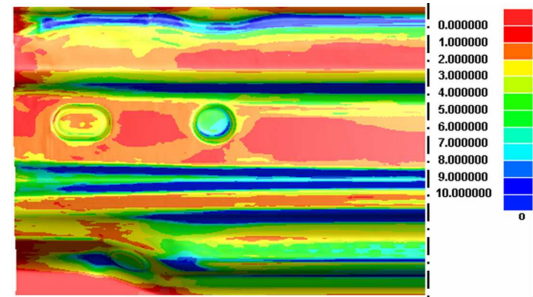


Fig. 4 The thinning rate of the panel (%)

The thinning rate is in the range of 0~2% with the thickness changed from 0mm to 0.018mm in the panel main surface except some radius areas. The thickness changes so few that has little influence on the coloring rate of die face. So in this study, the influence of thickness change on the coloring rate can be ignored. We will focus on the die elastic deformation in the following text.

The analysis of die deformation with original drawing surface

Fig. 5 shows the die structure FEM model. The mesh type is tetrahedron 4-nodes solid element. It has about 1.14×10^6 elements in total. The die casting material is HT300. The force on the press slider is 5×10^3 KN. The thinning rate of panel main face is small and can be ignored for studying the coloring rate of die face from the analysis in 2.1. Thus the punch and the uniform thickness panel are treated as one part that still called punch hereinafter for the analysis of die elastic deformation. The punch, die and binder are flexible tools. The press slider and cushion pad are rigid tools. In the industrial applications, the coloring rate mainly depends on the contact states between die and panel when the die reaches the lowest position. So the contact pressure can be used to express the coloring rate. The die face in the simulation model is the original drawing surface generated by product surface of panel. The gap between die and punch is uniform. The simulation result of contact pressure distribution on the punch is shown in Fig. 6. From the figure, the die face contact pressure is in the range of 0~0.02 GPa. The pressure value near punch edge, about one-sixth of the distance from punch edge to center, is in the range of 0.007~0.020 GPa. This area is defined as high pressure area. The face coloring rate is good in this area. In other areas the die face contact pressure is in the range of 0~0.002 GPa. These areas are defined as low pressure areas. The face coloring rate will not be good in these areas. The distribution of the contact pressure in Fig. 6 also shows that the pressure value is increasing from center to the edge. The closer to the punch edge the contact pressure value is much higher. The

reason is that the casting material in the center of die is continuous and the support force to the die face is strong. On the contrary, there is no casting material out of the punch edge. Thus, the support force to the die face is much lower than center and the punch face is easily deformed. These deformations lead to the high contact pressure on the die face near the punch edge. The die face coloring rate is lower than 30%. It will take the die makers lots of time and workloads to polish the die face to improve the coloring rate to reach 90%.

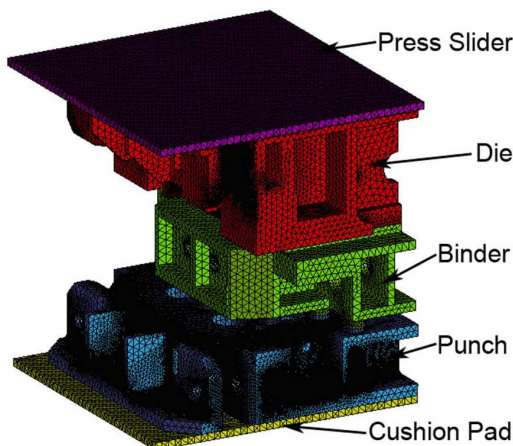


Fig. 5 Die structure analysis FEM model
(Half model of die)

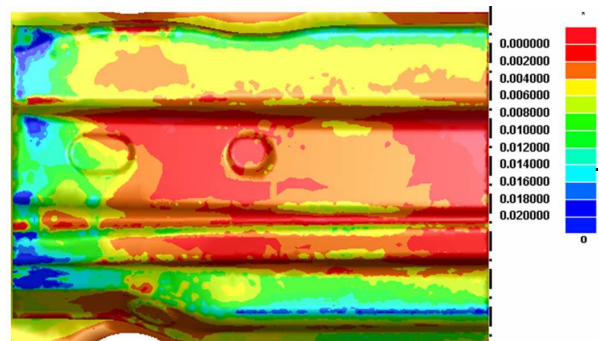


Fig. 6 The punch contact pressure simulation
result with original draw surface (GPa)

Die face compensation

In order to decrease the workloads and time of improving the coloring rate, the die and punch face can be reasonably compensated with CAD software before the die casting machined by NC tool. As the panel is formed by punch face, the face compensation is usually designed on the die surface for not to influence the panel precision. In the industrial application, if the coloring rate near the punch edge is better than the center, the die face is polished gradually from punch edge to the center aiming to improve the entire coloring rate. But it is difficult and takes a long time because the polishing area is not convergent. The polishing reference is hard to control for the die makers. On the contrary, if the coloring rate of center die face is better, the polishing work is easier because of convergent polishing area and easily controlled polishing reference. Thus the coloring rate will be increased with few workloads.

Based on the above analysis and consideration for the simulation errors, the die face compensation value must be a little bigger than normal. According to the contact pressure distribution in Fig. 6 that the center pressure is lower than around, 0.4mm bump is designed on the die geometry drawing surface in an ellipse area (see Fig. 7). With the surface compensation, the gap between die and punch will be smaller and smaller from punch edge area to the center. The max gap change is 0.4mm.

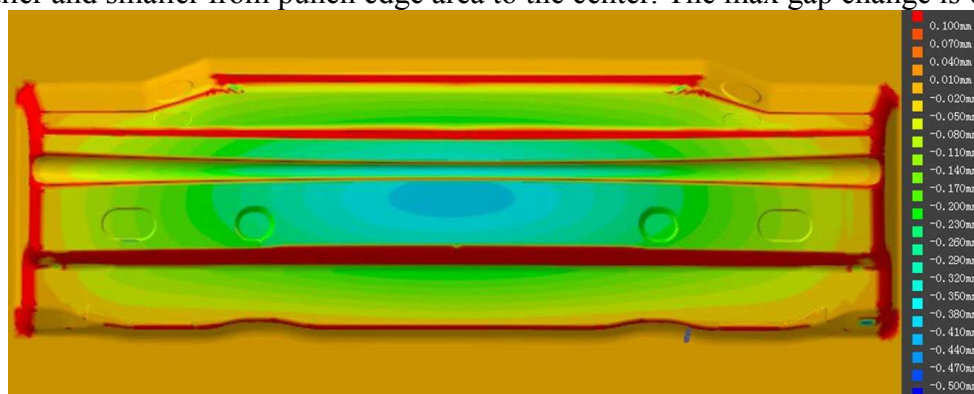


Fig. 7 The compensated region of die surface.
The values are differences between compensated and original surface.

The analysis of die deformation with compensated drawing surface

The elastic deformation of die is simulated again with the compensated die face. Fig. 8 shows simulation result of the punch contact pressure. The contact pressure distribution between die and punch changes obviously. The pressure in the range of 0.007~0.02GPa is in 10% area from center to punch edge. It is high pressure area. Other 90% area is low pressure area where the contact pressure distribution is low and uniform. Thus it will take less time to polish the die face to get a high coloring rate.

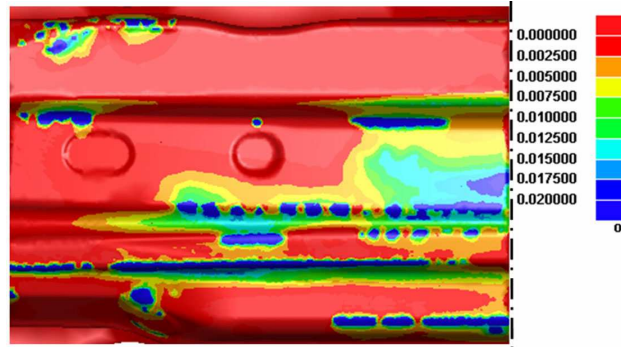


Fig. 8 The simulation result of punch contact pressure with compensated drawing surface (GPa)

Industrial application

Fig. 9 shows the coloring verification results of panel with blue oil in industrial application. The die face is machined by compensated face. The coloring distribution of blue oil is very close to the high contact pressure area shown in Fig. 8. The comparison shows the simulation results are useful and accurate to predict the die face coloring rate in industrial application. The result also shows that the high contact pressure area definition that the pressure distribution in the range of 0.007~0.02GPa is accurate and close to the real blue oil color distribution. Fig. 10 shows the panel in a high coloring rate in main face after simple polishing. The uniform distribution of blue oil means the contact pressure is uniform. With the die face compensated method, the tryout process can be more accurate and short-period than traditional process.



Fig. 9 The contact color of die surface with compensated die face



Fig. 10 The panel contact color after simple polishing

Conclusions

In this study, the thinning rate analysis of the panel and the die elastic deformation under large force in forming process are discussed. The die face compensation is carried out. The simulation result and die tryout result of the coloring rate are compared. Through this research, the followings are summarized and point out.

(1) For the panel in this paper, the die elastic deformation under large forming force is the main influence factor for coloring rate. The thinning rate has little influence on coloring rate.

(2) The high contact pressure definition is proposed. It is very close to the die tryout results. The definition greatly benefits the predication of the coloring rate.

(3) The die face is reasonably compensated before the die casting machined by NC tool. Through comparison between simulation and industrial application, the compensated method for coloring rate of die face are accurate and decrease the workloads and tryout period.

Acknowledgments

The authors would like to thank Tianjin Motor Dies Company Limited for industrial application. This work was supported by the Tianjin Colleges and Universities Double Five Science Research Foundation Tianjin, China, and the Science Research and Development Foundation of Tianjin University of Technology and Education Tianjin, China, under Grant SWPY20080003 and KJ10-10 respectively.

References

- [1] M.Firat: Materials and Design, Apr 2007, Vol. 28(4), P1311-1320
- [2] Y. T. Keum, I. H. Ahn, I. K. Lee, M. H. Song, S. O. Kwon, J. S. Park: AIP Conference Proceedings, 2005, Vol. 778(1), P90-95
- [3] Del Pozo D, de Lacalle LNL, Lopez JM: International Journal of Advanced Manufacturing Technology, Jun 1, 2008, Vol. 37, P649-656
- [4] Zhang Gui-bao, Chen Jun, Wang Amber: Journal of Shanghai Jiaotong University, 2008, 13(6), P727-733

Automation of Design and Analysis in Simulation System for Rough Rolling Process of H-Beam

Chuanyu Li^a, Qinhe Zhang^b, Rupo Ma^c and Baotian Dong^d

School of Mechanical Engineering, Shandong University, Jinan, Shandong, 250061, China

^alichuanyu@mail.sdu.edu.cn, ^b zhangqh@sdu.edu.cn, ^c marp2005@163.com,

^ddbt_002@yahoo.com.cn

Keywords: Simulation System; Rough Rolling; H-Beam

Abstract. In view of present problems that interior information of H-beam in multi-pass hot rolling process is not clear enough, an integrated simulation system with automatic design and analysis is developed based on ABAQUS Scripting Interface. Architecture of simulation system is designed according to the process of rough rolling, and several key problems are illustrated in the paper. The reliability of the system is verified through the forming simulation of H-beam H250x125. The system is very helpful for experienced mill designers who are unfamiliar with finite element analysis to test new section designs through virtual hot rolling trials.

Introduction

Rough rolling is an essential industrial process in the production of H-beam. Rough rolling, which involves multiple back-and-forth movements, will need a large amount of work in simulation for the process. Many researches have been carried on for rough rolling both at home and abroad [1,2]. However, common finite element software like Deform, ANSYS and ABAQUS, are generally used, and on account of their universality, it is difficult to handle one type of software for analysis in the short term. For experienced mill designers who are unfamiliar with finite element analysis, it is indispensable to create a simulation system exclusively for rough rolling, which includes robust modeling, fast and automotive meshing, analysis job submittal, visualization, and report documentation. Process automation enables engineers to focus on particular tasks, like achieving an optimal design of the H-beam, and less-frequent users could take advantage of the predictive benefits of analysis.

ABAQUS can effectively simulate and analyze the rough rolling processes with its nonlinear finite element analysis function [3]. In this paper, an integrated simulation system is built based on ABAQUS solver for multi-pass rolling with the way of customized applications.

ABAQUS Scripting Interface

When you use the ABAQUS/CAE graphical user interface (GUI) to create a model and to visualize the results, commands are issued internally by ABAQUS/CAE after every operation. These commands reflect the geometry you created along with the options and settings you selected from each dialog box. The GUI generates commands in an object-oriented programming language called Python. The commands issued by the GUI are sent to the ABAQUS/CAE kernel. The kernel interprets the commands and uses the options and settings to create an internal representation of your model. The kernel is the brain behind ABAQUS/CAE. The GUI is the interface between the user and the kernel [4].

System design

Requirements on the simulation system. Rolling data can be calculated accurately by the solver; Automatic modeling, assembling, boundary condition setting and meshing in pre-processing can be implemented automatically; Information, involving node temperature, stress, contact force and so on, can be extracted conveniently; Main window should be created with particular menu, toolbar, and toolbox for the process of hot rolling specially.

Architecture of the simulation system. Transient rolling process involves drastic plastic deformation, which leads to mesh distortion for work-piece in simulation [5]. It is necessary to re-mesh the work-piece after every pass, and transmit important parameters like temperature and equivalent plastic strain to the subsequent pass.

In the simulation system, the first pass is different from others, mainly because in this pass, dimensions for the work-piece are input by users via GUI according to procedure manuals, while in subsequent passes, dimensions for the work-piece inherit the former automatically. Fig. 1 presents the architecture of simulation system.

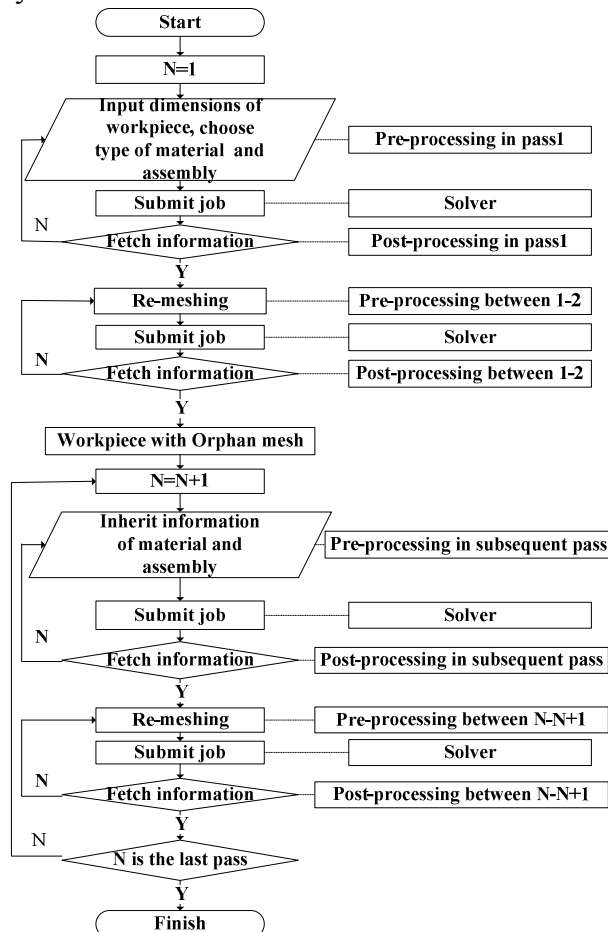


Fig. 1 Flow chart of simulation system for rough rolling

Customized application. There are two ways you can make use of the ABAQUS GUI Toolkit—through the use of the plug-in architecture or by creating a custom application [6]. Pre-processing and post-processing of each pass and inter-pass can be constructed through customized applications, while job submittal can be inserted in pre-processing. Customized applications consist of several components, and connections among them are introduced in the Fig. 2.

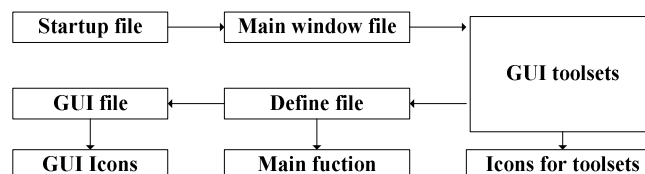


Fig. 2 Connections among components in one customized application

Information inheritance of material and assembly. When the users select the material for the work-piece in the pre-processing of the first pass, there is no doubt that the material used in subsequent passes should be the same. For example, if Q235B is selected in the first pass, the second and the subsequent passes should be operated with Q235B without selection.

Assembly is another type of vital feature for pre-processing. Every pass corresponds to its own assembly relationship between work-piece and rollers, parameters of which can be input by the GUI. Assembly information in each pass is not the same as material properties, because change of location for work-piece is based on the position of the former pass rather than the first one.

In order to solve the problems of information inheritance, *File* operation of python can be used. Information of material and assembly can be written to a text file, which is used to record the information input for every pass. Information of material can be inherited by means of reading parameters from text file for the first pass, while information of assembly from text file for the former pass.

System verification

In present rough rolling process, H400x200 has eleven passes, while H250x125 has seven. In the simulation system, process design is according to type of H400x200, while H250x125 can be used to verify. Considering the differences between the first pass and subsequent ones, the pre-processing and the post-processing of the first pass and any pass of the subsequent of H250x125 can be illustrated to display the validity.

Fig. 3 illustrates the GUI of pre-processing for the first pass in rough rolling of H250x125, and the job will be submitted after clicking *OK*. Fig. 4 shows the assembly including rollers and work-piece after being solved. Fig. 5 illustrates the GUI of pre-processing for the fifth pass in rough rolling of H250x125, and Fig. 6 shows the GUI of post-processing for this pass. Assembly can be obtained as indicated in Fig. 7 with different location according to the parameters for this pass. Fig. 8 shows the stress contour of the fifth pass.

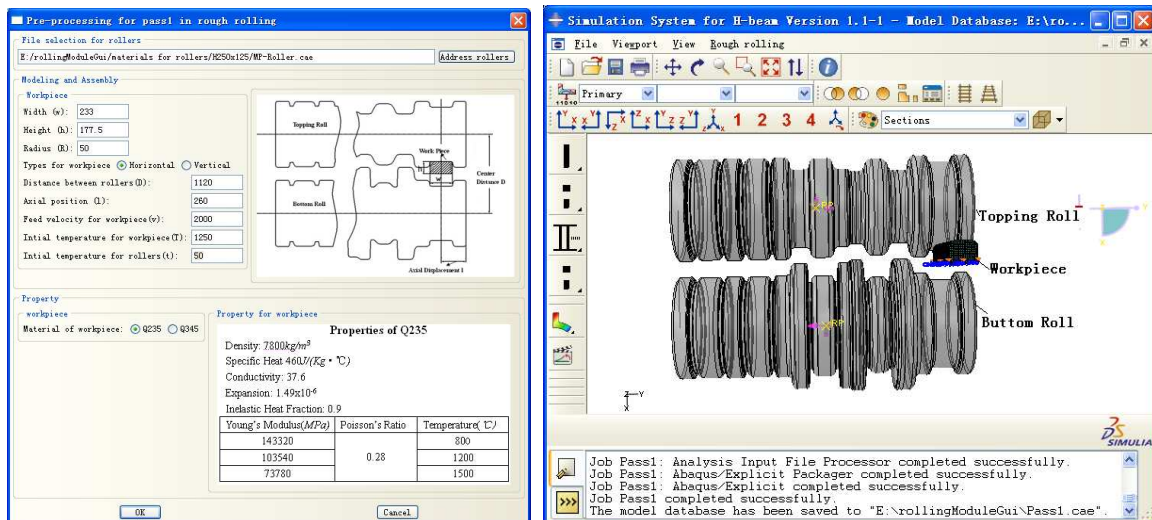


Fig. 3 GUI of pre-processing for the first pass Fig. 4 Assembly after being solved for the first pass

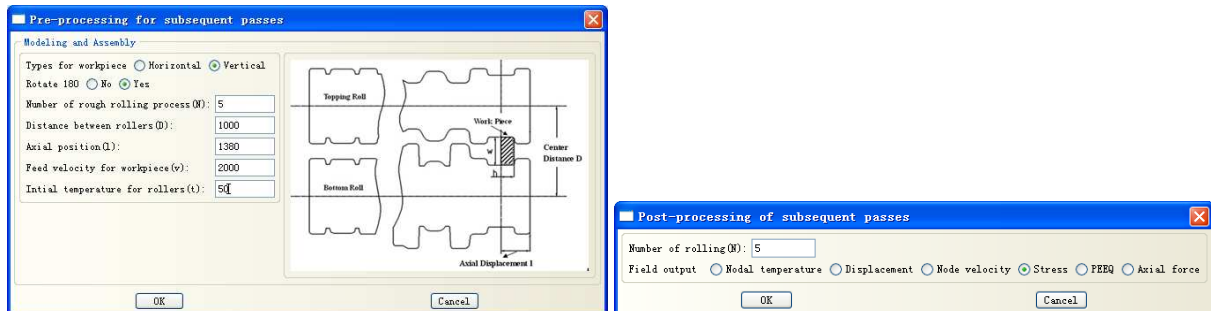


Fig. 5 GUI of pre-processing for the fifth pass Fig. 6 GUI of post-processing for the fifth pass

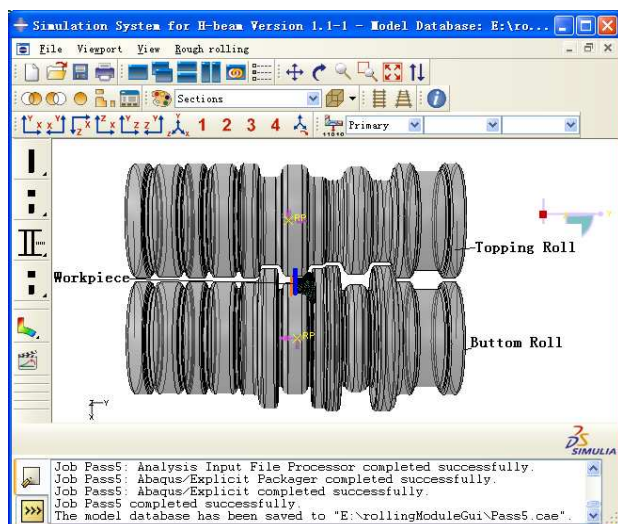


Fig. 7 Assembly after being solved for the fifth pass

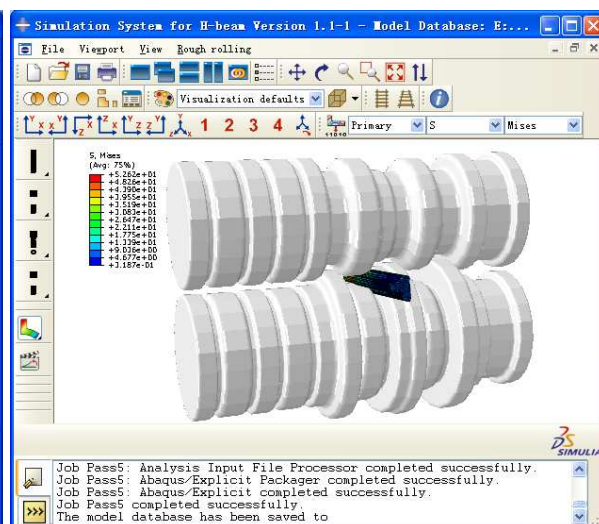


Fig. 8 Stress contour of the fifth pass

Conclusions

Simulation system with automatic design and analysis for rough rolling process has been built based on ABAQUS Scripting Interface. The way of custom applications can be used to design pre-processing or post-processing in every pass or inter-pass. Furthermore, information of material properties and assembly can be inherited accurately in subsequent passes. Problems to previous simulation systems, which include complexity in pre-processing, difficulty in re-meshing of inter-pass, and inconvenience of information extraction in post-processing, have been solved effectively with the system.

Acknowledgements

The work is supported by Science and Technology Development Program of Shandong (Grant No. 2010GGX10421) and Program for New Century Excellent Talents in University (2007).

References

- [1] M.P.Phaniraj, B.B. Behera and A.K.Lahiri: Journal of Materials Processing Technology Vol. 170 (2005), p. 323
- [2] G.H.Herling and H.C.Bryant: Nuclear Instruments and Methods in Physics Research Section A Vol. 598 (2009), p. 667
- [3] Q.Q.He, Q.H.Zhang, K.Q.Liu, J.H.Chen: International Technology and Innovation Conference(2006)
- [4] Abaqus 6.9 HTML Documentation/Abaqus Scripting User's Manual/ How does the Abaqus Scripting Interface interact with Abaqus/CAE(2009)
- [5] E.T.Ooi, S.Rajendran, J.H.Yeo and B.R.Zhang: Finite Elements in Analysis and Design Vol. 43 (2007), p.771.
- [6] Abaqus 6.9 HTML Documentation/Abaqus GUI Toolkit User's Manual/ Plug-ins and customized applications(2009)

A Fuzzy C-Means Clustering Method Based for 3D Mechanical Models Retrieval

Hui Jing^{1,a}, Cong Li^{2,b}, Bing Kuang^{1,c}, Meifa Huang^{1,d}, Fuyun Liu¹

¹ School of Mechanical and Electrical Engineering, Guilin University of Electronic Technology, Guilin 541004, China

² Department of Mechanical Engineering, Guilin College of Aerospace Technology, Guilin 541004, China

^aJinghui@guet.edu.cn, ^blicong@glcat.edu.cn, ^ckuangbing@guet.edu.cn, ^dhmhmf@guet.edu.cn

Keywords: Fuzzy C-Means Clustering; Shape Distribution

Abstract. To accelerate the development of new product, one important method is to use the information of the existed products. In this paper, Fuzzy C-Means clustering method (FCM) is proposed to retrieve the desired model in the given model database. In the retrieval process, first, the shape distribution histograms of the model are established and transformed into the proper format of FCM. Then, the shape distribution histograms of the model are served as inputs of FCM and classified into several groups by this algorithm. Last, all the models that belong to the classification of the query model are returned as the retrieval results. To validate the proposed method, a case study is presented. The results show that the result of proposed method is better than that of Shape Distribution. Thus, this method is suitable for 3D mechanical models retrieval.

Introduction

With the great progress of computer hardware and software, the speed of product design has been accelerated rapidly. To accelerate the development of new product, one important method is to use the information of the existed products. By retrieving the given CAD design repository, the desired models can be extracted and then can be used to design the new model. Therefore the design work can be reduced and the efficiency can be improved. Therefore, how to retrieve the models in the repository with huge amounts of CAD models and then to reuse the design and manufacturing information, however, become focus for both industry and academy. To meet these requirements, various methods have been proposed that enable the efficient querying of the required 3D models from the given repositories [1-2].

Recently, some simple and fast 3D retrieval approaches are proposed to retrieve models by evaluating the shape histogram as the feature vectors to map the shape properties. Osada.R. et al. proposed a novel method for 3D models named Shape Distribution (3DSD) [3-4]. 3DSD method employs the shape distribution histograms as its shape descriptor to represent the characteristics of a model. The advantages of this method are that it uses simple calculation without concern about the location and posture of model. However, it also has drawbacks: the histograms of the same model will undergo a local change whenever they are drawn because of the characteristic of the random point sampling [3].

To improve the retrieval efficiency, Fuzzy C-Means clustering method (FCM) is proposed in this paper. In the retrieval process, first, the shape distribution histograms of the model are established and transformed into the proper format of FCM. Then, the shape distribution histograms of the model are served as inputs of FCM and classified into several groups by this algorithm. Last, all the models that belong to the classification of the query model are returned as the retrieval results. To validate the proposed method, an experiment is presented. The database of the experiment is based on the Engineering Shape Benchmark (ESB) [5]. This paper chooses the *solid of revaluation* datasets of ESB and tests the retrieval efficiency of proposed method.

The paper is structured as follows: Section 2 gives the algorithm of 3DSD. Section 3 shows the retrieval process of FCM. Section 4 presents a case study to validate the proposed. Section 5 concludes the study.

Shape Distribution

Osada.R. et al. proposed a novel method for 3D models named Shape Distribution (3DSD). This method employs the shape distribution histograms as its shape descriptor to represent the characteristics of a model [3]. In the matching process, 3DSD method firstly samples a number of points on the model's surface and calculates Euclidean distances for each pair of points, and then draws shape distribution histograms with those distances. The shape distribution histograms show the typical trends according to the overall shape of the model. Once we have established the shape distribution histograms of the models, the similarity between the models can be evaluated using any measure that reflects the distance between models histograms, possibly with a normalization step for matching scales. Here, D2 shape function (shown in Fig.1) is employed to establish the shape distribution histograms. The main steps of 3DSD are as follows [3-4].

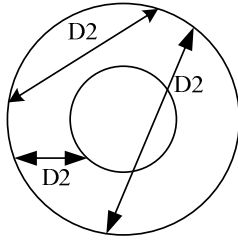


Fig.1. D2 shape function

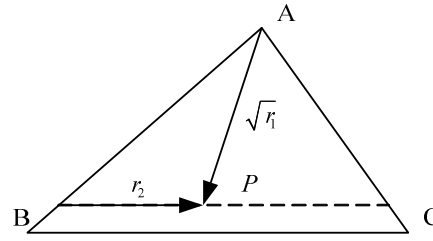


Fig. 2. Sampling a random point in a triangle

The main process of constructing shape distribution histograms is shown as follows [3]:

Step1. Sampling on the model surface

In order to obtain shape distribution histograms, the sampled point on the surface of the retrieved model should be carried out. The main process of sampling on the surface of the retrieved model is as follows. Let the model surface is composed of a number of polygons. First, all polygons of the 3D model are iterated and split into triangles, such as the specific triangle with vertices A , B , and C in Fig.2. Then, all the triangles $T=(t_1, t_2, \dots, t_k, \dots, t_N)$ are stored in the memory, where $k=1, 2, \dots, N$ is the number of triangles, N is total number of the triangles, and t_k is the k^{th} triangles. For the given triangle with vertices A , B , and C , the area $A(t_i)$ is computed by Herlon formula:

$$A(t_i) = \sqrt{s(s - \|AB\|)(s - \|BC\|)(s - \|CA\|)} \quad (1)$$

where s is the triangle perimeter, $\|AB\|$, $\|BC\|$ and $\|CA\|$ are the length of edge AB , BC and CA , respectively.

Each triangle area is stored in an array (TA), along with the cumulative area array (TA_k) of triangles visited so far. Next, the triangle are selected by generating the random number $i_{rand} \in [0, TA_k]$, and by performing a binary search on the array of cumulative areas. If $0 < i_{rand} \leq TA_j$, then the triangle t_j is chosen. For each selected triangle with vertices (A , B , C), the position of point P in the triangle is established by Eq. (2):

$$P = (1 - \sqrt{r_1})A + \sqrt{r_1}(1 - r_2)B + \sqrt{r_1}r_2C \quad (2)$$

where r_1 and r_2 are two random numbers, $0 < r_1, r_2 < 1$. Intuitively $\sqrt{r_1}$ sets the percentage from vertex A to the opposing edge, while r_2 represents the percentage along that edge (see Fig. 2).

Step2. Constructing shape distribution histograms

Once the sampled points are chosen, the shape distribution histograms of 3D models can be constructed by computing the distances between all the sampled points. Here the Euclidean distances are employed to compute the distances D between pairs of randomly selected points on the surface of a 3D model:

$$D = \sqrt{(x_1 - x_2)^2 + (y_1 - y_2)^2 + (z_1 - z_2)^2} \quad (3)$$

where x_1 , y_1 , and z_1 are the coordinate components of point P_1 in one triangle in axis X , Y , and Z , respectively. And x_2 , y_2 , and z_2 are the coordinate components of another point P_2 in another triangle in axis X , Y , and Z , respectively.

The shape distribution histogram can be established after all the distances are obtained. For certain shape functions, we must add a normalization step to the comparison process for differences in scale. In this paper the mean distance value is chosen to normalize the shape distribution histogram [3]. Fig.3 shows the model and its histogram.

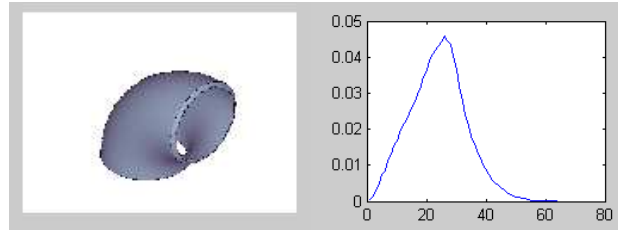


Fig. 3. The model and its histogram

Step3. Comparing Shape Distributions

There are many standard ways of comparing two shape distribution histograms including the Minkowski distance, Kolmogorov-Smirnov distance, and Kullback-Leibler divergence distance. In this paper, Euclidean distance is chosen to measure the similarity. The Euclidean distance is just as follows.

$$L_2(x, y) = \left[\sum_{i=0}^N |x_i - y_i|^2 \right]^{1/2} \quad (4)$$

Then, all the distances between the histograms of query model and the model in the given database are calculated and stored in an ascending order. The smaller the distances they are the higher similarity they have.

The Retrieval Process of FCM

Fuzzy C-Means clustering method. Fuzzy C-Means clustering method is a conventional clustering algorithm. This method is a widely used partitional clustering algorithm because of its high computational efficiency and low memory space requirement. In order to obtain a partition of the dataset, the FCM algorithm attempts to minimize an objective function. This function can be written as sum of distances of the patterns from the prototypes of the clusters [6-7]:

$$\begin{aligned} \min J_m &= \sum_{i=1}^c \sum_{k=1}^n (u_{ik})^m \|X_k - V_i\|^2 \\ S.T. & \begin{cases} \sum_{i=1}^c u_{ik} = 1, k \in [1, n] \\ 0 \leq u_{ik} \leq 1, 1 \leq i \leq c, 1 \leq k \leq n \\ 0 < \sum_{k=1}^n u_{ik} < n, i \in [1, c] \end{cases} \end{aligned} \quad (5)$$

where, $x_k, k=1, 2, \dots, n$ are the patterns in R^n , c is the number of clusters, v_1, v_2, \dots, v_c are the prototypes of the clusters, m is a parameter that control the fuzziness of the clusters and $U = [u_{ik}]$ is the partition matrix. The minimization of the object function is performed with respect to the partition matrix U and the prototypes of the clusters [7].

Retrieval process of FCM. In this section, the retrieval process of FCM is proposed. This method makes use of both the shape information and the surface information of the models. In the retrieval process, the shape histograms of models are extracted, respectively. Then these histograms are transformed into the proper format of FCM. The shape distribution histograms of the model are served as inputs of FCM and classified into several groups by this algorithm. Last, all the models that belong to the classification of the query model are returned as the retrieval results.

Retrieval Experiment

In this section, a case study is given to validate the proposed method. This case study chooses database of *Engineering Shape Benchmark* (ESB) [5] as the given database. Based on the database of ESB, this paper chooses appropriate amount of the different models that belong to the *Solid of Revaluation* datasets. There are 367 models including *Bearing like parts*, *Bolt like parts*, *Simple pipes* and *Gear like parts*, etc.

For the query model being a simple pipe shown in the top-left one in Fig.4, the retrieval results are presented in Fig.4. In Fig.4 (a), there are 12 unrelated models in the top 15 retrieved results by 3DSD. In Fig.4 (b), we can find that only 8 unrelated models in the top 15 retrieved results. Therefore, the retrieval performance of FCM is better than that of 3DSD method. Thus, this method is suitable for 3D mechanical models retrieval.

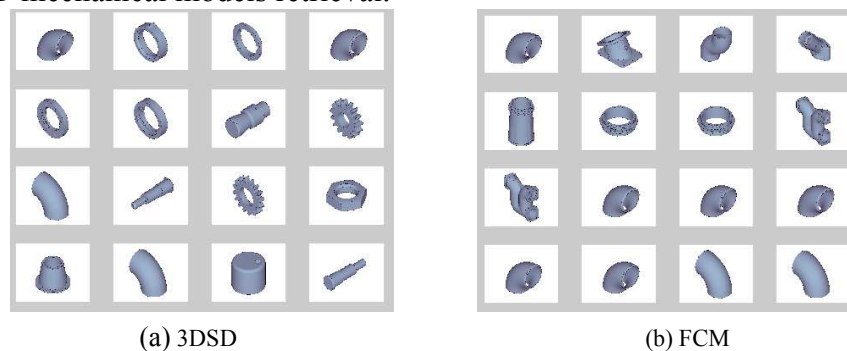


Fig.4. The retrieval results

Conclusion

In engineering domain, to accelerate the development of new product, it is very important to present reliable retrieval methods for product design and manufacturing. In this paper, FCM method is proposed to retrieve 3D mechanical models. Also, a case study is given to validate the proposed method. The result shows that the method we present has advantages in mechanical model retrieval.

Acknowledgements: This research is supported by the Natural Science Foundation of China (NSFC, Grant No. 50865003 and 50865002) to Prof. Meifa Huang and Fuyun Liu, respectively.

References

- [1] Michael. M. Kazhdan: Doctor Thesis of Princeton University, Princeton, U.S. (2004).
- [2] Iyer N, et al. Computer-Aided Design, 37(5):509-30(2005).
- [3] Osada. R. et al: ACM Transaction on Graphics, Vol.21 (2002), p.807-832.
- [4] Meifa Huang and Hui Jing: Virtual and Physical Prototyping, Vol.2 (2009), p.105-112.
- [5] Subramaniam Jayanti. et al: Computer-Aided Design, Vol.38(2006), p.939-953.
- [6] Hui Jing, Meifa Huang, Yanru Zhong: Proc. of SPIE, Vol 6788(2007), pp. 678823.1-678823.6.
- [7] Alberto Amato, Vincenzo Di Lecce. Image vision computing. Vol 26 (2008), p.1466-1480.

Tolerance Synthesis Modeling Based on Degree of Freedom of Geometric Variations of Features

Bensheng Xu^{1,a}, Can Wang¹ and Meifa Huang^{2,b}

¹ Department of Mechanical Engineering, Guilin College of Aerospace Technology, China

² School of Mechanical & Electric Engineering, Guilin University of Electronic Technology, China

^axuxh1980@163.com, ^bhmhmf@guet.edu.cn

Keywords: Tolerance Synthesis; Tolerance Zone; Geometric Variations; Degree of Freedom (DOF); Functional Requirement of Assembly

Abstract. A tolerance synthesis model is established based on degree of freedom of geometric variations of features in this paper. The method allows a designer to analyze the relationship between geometric variations of features of a part and functional requirement of assembly (FRA). Firstly, tolerance is modeled with DOFs of geometric variations of features and the tolerance zone is expressed with six kinematic DOFs in three-dimensional (3D) space. Secondly, the stack-up of geometric variations of features is formulated as explicit tolerance analysis equations using kinematical coordinate systems associated with each feature. To express mathematically the relationship between given FRA values and the corresponding DOFs of geometric variations of features, the reverse synthesis equations are obtained using a matrix inversion scheme of the tolerance analysis equations. Finally, a case study is used to illustrate the proposed method.

Introduction

Tolerance synthesis plays a key role in reducing production costs and the number of assembly/part defects. In tolerance synthesis, it is critical to establish the function to interpret the assigning a set of tolerances. Most of the published papers use the cost-tolerance models to establish the function [1]. Due to the complexity of the models, most of these methods are concerned with only the dimensional tolerances. When we deal with the 3D tolerance, however, the dimensional and geometric tolerances should be considered simultaneously. Liu et al. [2] proposed a hierarchical tolerance model based on feature-based topologically and technologically related surfaces (FTTRS) to represent the tolerance in CAD system. Hu et al. [3] studied the dimensional and geometric tolerance design based on constraints. Tolerance is represented by 3D feature variations, and the variation specified by tolerance. Those models bear many similarities to DOF models which treat geometric features (the ideal surfaces of parts) as rigid bodies with degrees of freedom and represented tolerance zone with the six screws in DOF [4,5].

On the basis of tolerance representation of DOF model, this paper uses the homogeneous matrix transforms to acquire the nonlinear 3D relationship between the geometric variations of features of a part and functional requirement of assembly. The model can be described as $\delta_{FRA} = f(\delta_1; \delta_2; \dots; \delta_n)$, where δ_{FRA} is the FRA expressed in the global frame. δ_i ($i=1,2,\dots, n$) and n is the number of mating features of DOFs of geometric variations of the features in an assembly. The f is the function presented to be established in the mechanical assembly.

Theory of geometric variations of features

Expression of tolerance zone. Tolerances are specified to relax slightly the nominal dimensions, ideal shapes, and positions of geometric features of a real part. In the view of manufacturing and measuring process, geometric features of a real part are essentially variational. In 3D space, tolerance zone can be considered as the region of minute variations of geometric feature. Without regarding of surface roughness and distortion by force, the variations of geometric features can be resolved into six

kinematic DOFs in 3D space. In the given coordination system, those kinematic degrees of freedom are divided into three translational degrees of freedom (TDOFs) along the X, Y, and Z axis and three rotational degrees of freedom (RDOFs) around the X, Y, and Z axis. As shown in Fig.1, plane P draw with heavy line is the ideal surface. Since manufacturing error exists, the real plane P' is variational and can be represented by the rectangular with fine line frames. As an acceptable part, the real plane (obtained by measurement) must be in the rectangular solid with imaginary frames. The rectangular solid is the tolerance zone of the real plane P' and association tolerance types specified may be flatness, parallelism, or perpendicular error. The relationship between tolerance t and variations of DOFs of plane P is: $-t/2 \leq \omega \leq t/2$, $-t/L_2 \leq \alpha \leq t/L_2$ and $-t/L_1 \leq \beta \leq t/L_1$.

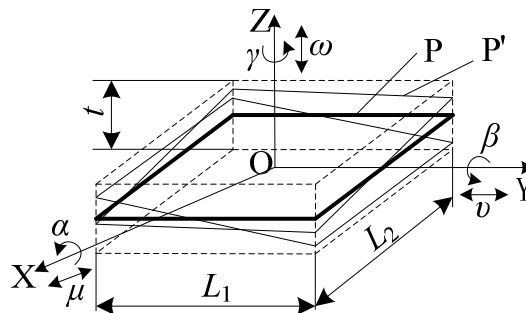


Fig.1 Plane-P' tolerance zone and variations in DOFs

Because of shape and symmetry of a geometric feature, it may be translational invariant in some TDOFs and rotationally invariant in some RDOFs, i.e. it does not change the shape, size, or location when it is displaced in these DOFs. For example, in Fig.1, it does not change the size, shape, or location when the nominal plane P is displaced along the X, Y, and around the Z axis. The variations of plane P named as μ , ν , and γ , are denoted as 0. Thus minute variations of the real plane P' are expressed as: $[0, 0, \omega, \alpha, \beta, 0]$ in tolerance zone.

Basic Elements of geometric variations of features. There are three major basic elements involved in geometric variations of features, i.e. geometric features, coordinate system, and variations in DOFs, as shown in Fig.2. In a feature-based CAD system, the geometric features are the ideal surfaces on a nominal geometric model of a part. Geometric features can be classified into 7 classes: spherical, cylindrical, planar, helical, revolute, prismatic, and complex. The coordinate system is the datum frame of geometric variations. It determines the orientations of the six kinematic DOFs in 3D space. The six kinematic DOFs, including three RDOFs (denoted as α , β , γ) and three TDOFs (denoted as μ , ν , ω) are related to tolerance value.

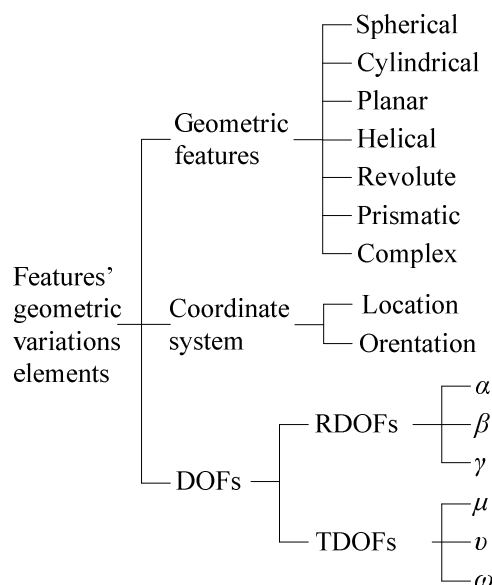


Fig.2 Elements of geometric variations of features

Tolerance synthesis modeling

Stack-up of geometric variations of features. The assembly process is nothing but the mating process of geometric features which consist of the parts. Using variations on the six kinematic degrees of freedom associated with each mating feature, the position and orientation variability of features can be established and propagated from part to part in an assembly, as shown in Fig.3. With the coordinate transform algorithms used in robotic applications, tolerances so represented can be analyzed rapidly in 3D space.

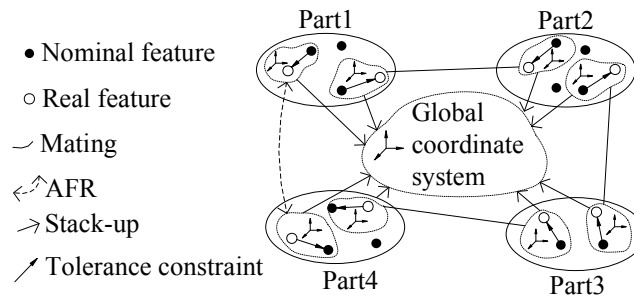


Fig.3 Stack-up of geometric variations of features in a four-part assembly

In Fig.3, a four-part assembly is given. Local and global coordinate systems are concerned. The geometric variation occurs in the local coordinate system and accumulates in the global coordinate system. Since two or more parts consist of a mechanical assembly, there are n ($n \geq 2$) mating features around a desired functional requirement. Let $[\mu_i, v_i, \omega_i, \alpha_i, \beta_i, \gamma_i]$ and $[\mu_{FRA_i}, v_{FRA_i}, \omega_{FRA_i}, \alpha_{FRA_i}, \beta_{FRA_i}, \gamma_{FRA_i}]$ to be used to express the i th geometric variations of features in local coordinate system $O_i-X_i-Y_i-Z_i$ and accumulations in global coordinate system $O-X-Y-Z$, respectively. The equations of translational and rotational stack-up are formulated as follows.

Rotational stack-up is:

$$\alpha_{FRA_i} = \alpha_i, \beta_{FRA_i} = \beta_i, \gamma_{FRA_i} = \gamma_i \quad (1)$$

Transitional stack-up is:

$$\vec{V}_i^O = \vec{V}_i^{Oi} + {}^O R_i \vec{V}_{Oi}^O \quad (2)$$

Where

$$\vec{V}_i^O = [\mu_{FRA_i}, v_{FRA_i}, \omega_{FRA_i}], \vec{V}_i^{Oi} = [\mu_i, v_i, \omega_i], \text{ and}$$

$${}^O R_i = \begin{bmatrix} \cos \beta_i \cos \gamma_i & \sin \alpha_i \sin \beta_i \cos \gamma_i - \cos \alpha_i \sin \gamma_i & \cos \alpha_i \sin \beta_i \cos \gamma_i + \sin \alpha_i \sin \gamma_i \\ \cos \beta_i \sin \gamma_i & \sin \alpha_i \sin \beta_i \sin \gamma_i + \cos \alpha_i \cos \gamma_i & \cos \alpha_i \sin \beta_i \sin \gamma_i - \sin \alpha_i \cos \gamma_i \\ -\sin \beta_i & \sin \alpha_i \cos \beta_i & \cos \alpha_i \cos \beta_i \end{bmatrix}$$

As the rotational variation is very small, $\sin \alpha_i \approx \alpha_i$, $\cos \alpha_i \approx 1$. Then

$${}^O R_i = \begin{bmatrix} 1 & -\gamma_i & \beta_i \\ \gamma_i & 1 & -\alpha_i \\ -\beta_i & \alpha_i & 1 \end{bmatrix}$$

$\vec{V}_{Oi}^0 = [X_i, Y_i, Z_i]$. $[X_i, Y_i, Z_i]$ is the coordinate component of the local coordinate system in the global coordinate system. Eq.2 can be formulated as follows.

$$\mu_{FRA_i} = \mu_i - Y_i\gamma_i + Z_i\beta_i, \quad v_{FRA_i} = v_i + X_i\gamma_i - Z_i\alpha_i, \quad \omega_{FRA_i} = \omega_i - X_i\beta_i + Y_i\alpha_i \quad (3)$$

Tolerance synthesis model. The translational and rotational stack-up of geometric variations of the i th feature can be expressed in matrix form shown in Eq.4.

$$\begin{bmatrix} \mu_{FRA_i} \\ v_{FRA_i} \\ \omega_{FRA_i} \\ \alpha_{FRA_i} \\ \beta_{FRA_i} \\ \gamma_{FRA_i} \end{bmatrix} = \begin{bmatrix} 1 & 0 & 0 & 0 & Z_i & -Y_i \\ 0 & 1 & 0 & -Z_i & 0 & X_i \\ 0 & 0 & 1 & Y_i & -X_i & 0 \\ 0 & 0 & 0 & 1 & 0 & 0 \\ 0 & 0 & 0 & 0 & 1 & 0 \\ 0 & 0 & 0 & 0 & 0 & 1 \end{bmatrix} \begin{bmatrix} \mu_i \\ v_i \\ \omega_i \\ \alpha_i \\ \beta_i \\ \gamma_i \end{bmatrix} \quad (4)$$

Let $\delta_{FRA_i} = [\mu_{FRA_i}, v_{FRA_i}, \omega_{FRA_i}, \alpha_{FRA_i}, \beta_{FRA_i}, \gamma_{FRA_i}]^T$, $\delta_i = [\mu_i, v_i, \omega_i, \alpha_i, \beta_i, \gamma_i]$, and

$$J = \begin{bmatrix} 1 & 0 & 0 & 0 & Z_i & -Y_i \\ 0 & 1 & 0 & -Z_i & 0 & X_i \\ 0 & 0 & 1 & Y_i & -X_i & 0 \\ 0 & 0 & 0 & 1 & 0 & 0 \\ 0 & 0 & 0 & 0 & 1 & 0 \\ 0 & 0 & 0 & 0 & 0 & 1 \end{bmatrix}$$

Furthermore, the assembly functional requirement can be expressed as: $\delta_{FRA} = [\mu_{FRA}, v_{FRA}, \omega_{FRA}, \alpha_{FRA}, \beta_{FRA}, \gamma_{FRA}]^T$. Then the following equation can be obtained.

$$\delta_{FRA} = \sum_{i=1}^n \delta_{FRA_i} = [J_1, J_2, \dots, J_n][\delta_1, \delta_2, \dots, \delta_n]^T \quad (5)$$

Let $J = [J_1, J_2, \dots, J_n]$, then $\delta_{FRA} = J[\delta_1, \delta_2, \dots, \delta_n]^T$. To establish the synthesis model, the inverse of matrix J needs to be calculated. As matrix J is not square (it is $6 \times 6n$ where n is the number of the mating features), a method that computes an approximation of the inverse is used as follows [6]:

$$J^+ = J^T (JJ^T)^{-1} \quad (6)$$

Where

J^+ is the approximation of the inverse of the matrix J ;

J^T is the transposed of the matrix J .

The mathematical representation of synthesis model simply becomes:

$$[\delta_1, \delta_2, \dots, \delta_n]^T = J^T (JJ^T)^{-1} \delta_{FRA} \quad (7)$$

Case study

The example assembly of gear wheel pump is shown in Fig.4a. This assembly consists of pump box, drive gear wheel axis, and driven gear wheel axis [7]. In Fig. 4, we illustrate the process how to

The geometric variations in DOFs of each mating feature can be calculated with the tolerance synthesis model shown in Eq.7. Take involute flanks A1 as example, the result is obtained as follows.

$$\left\{ \begin{array}{l} \nu_1 = \frac{3\nu_{FRA} + 2b\gamma_{FRA}}{2(9 + 3r^2 + 2b^2)} \\ \omega_1 = \frac{3\omega_{FRA} - 2b\beta_{FRA}}{2(2b^2 + 9)} \end{array} \right\}, \text{ and } \left\{ \begin{array}{l} \alpha_1 = \frac{\alpha_{FRA}}{2} - \frac{3\omega_{FRA} + 2br^2\gamma_{FRA}}{2r(9 + 3r^2 + 2b^2)} \\ \beta_1 = \frac{(2b^2 + 3)\beta_{FRA} - 2b\gamma_{FRA}}{2(2b^2 + 9)} \\ \gamma_1 = \frac{2b\nu_{FRA} + (3 + r^2 + 2b^2)\gamma_{FRA}}{2(9 + 3r^2 + 2b^2)} \end{array} \right.$$

Conclusions

The paper proposes a method to establish the tolerance synthesis model based on geometric variations in DOFs of features. Six kinematic DOFs in three-dimensional space are used to express the geometric variations of mating features in the tolerance zone. The stack-up functions of geometric variations are formulated as explicit tolerance analysis equations with the coordinate transform algorithms used in robotic applications, and the mathematical model of tolerance synthesis problem is obtained using a simple matrix inversion scheme. The relationship between given FRA values and the corresponding DOFs of geometric variations of features can be expressed as tolerance synthesis equations with the proposed method. In a true synthesis environment, the result obtained with the proposed method is related to two significant points: determination of geometric variations of the mating features in a 3D tolerance chain influence the desired FRA, and acquisition of stack-up functions of geometric variations. Both have been tested extensively with the example assembly.

Acknowledgement

Research was supported by the National Natural Science Foundation of China (Grant No. 50865003).

References

- [1] Y. S. Hong, T. C. Chang, "A Comprehensive Review of Tolerancing Research", International Journal of Production Research, Vol.40, No.11, 521-527, 2002.
- [2] Liu Yusheng, Gao Shuming, Wu Zhaotong, Yang jiangxin, "Hierarchical representation model and its realization of tolerance based on feature", Chinese Journal of Mechanical Engineering, Vol.39, No.3, 1-7, 2003.
- [3] Hu Jie and Xiong Guangleng, "Dimensional and Geometric Tolerance Design Based on Constraints". Int J Adv Manuf Technol, Vol.26, 1099-1108, 2004.
- [4] T. M. Kethara Pasupathy, Edward P. Morse and Robert G. Wilhelm, "A survey of mathematical methods for the construction of geometric tolerance zones", Journal of Computing and Information Science in Engineering, Vol.3, 65-75, 2003.
- [5] Desrochers, A., Riviere, A., "A matrix approach to the representation of tolerance zones and clearances", International Journal of Advanced Manufacturing Technology, Vol.13, 630-636, 1997.
- [6] Luc Laperriere and Tassere Kabore, "Monte Carlo Simulation of Tolerance Synthesis Equations". International Journal of Production Research, Vol.39, No.11, 2395-2406, 2001.
- [7] Hu Jie and Xiong Guangleng, "Concurrent design of a geometric parameter and tolerance for assembly and cost", International Journal of Production Research, Vol.43, No.2, 267-293, 2005.

Development of CAD/CAE Software System for Raw-Soil Structure

Zhihao Zhou^a, Jia Hu^b and Qilin Zhang^c

College of civil engineering, Tongji University, Shanghai RPC 200092

^ahobbylofty@gmail.com, ^b2008iviehj@tongji.edu.cn, ^czhangqilin@tongji.edu.cn

Keywords: Raw-Soil Structure; CAD/CAE; BIM; Software Development

Abstract. With the good ecological functions, the raw-soil structures attract attention of the people all over the world recently. According to surveys, more than 30 million farmers in China still choose to build their house using raw-soil. Since the advent of CAD/CAE technology, it became easier for engineers to design better buildings. However, for lack of adequate research on raw-soil structure, existing domestic and overseas softwares are incapable of solving the detailing work of this structure. In this paper, characteristics of the raw-soil structure and software function requirements are analyzed; the framework, data structure kernel are designed for a specialized detailing CAD information system based on BIM (Building Information Modeling). Finally the raw-soil software is developed with Object ARX technology and AutoCAD graphics platform, and an example is introduced to show the main functions.

Introduction

Raw-soil structure house is made up of raw-soil and timber. According to surveys [1], there are over 30 million farmers in the countryside who still live in raw-soil structure houses. However, these houses are built by the farmers themselves mainly based on the experience handed down from age to age. In many cases, the raw-soil structure houses are designed and constructed in low level.

Raw-soil structure houses in China can be divided into three categories: adobe house, rammed earth wall house and cave. The structural system of adobe house and rammed earth wall house are similar. In recent years experimental studies on shear properties and compressive properties of raw-soil material which is raw-soil structure house's major building materials have been performed [2,3]. In this paper, the raw-soil structure refers to adobe house and rammed earth house, not including cave.

Fig. 1 presents a typical method to pull the raw-soil wall effectively. In this way, the shear strength and compression strength can be improved obviously. Fig. 2 shows a type of rafter joint. Those measures are crucial to improve the behavior of the structure. In our raw-soil structure software, the characteristics and difficulties of these kinds of joints are analysed. These kinds of joints can be implemented automatically in our software system.

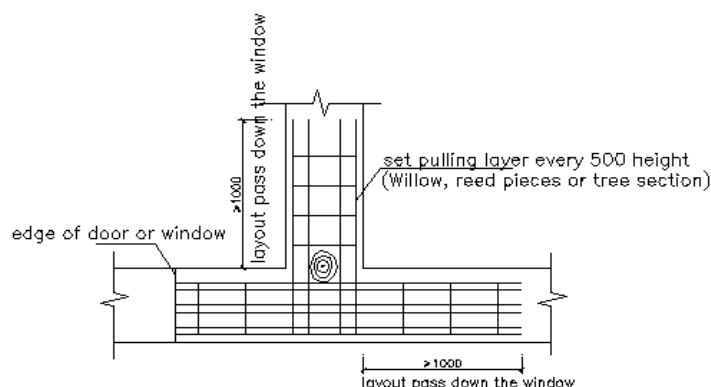


Fig. 1 One type of raw-soil wall joints

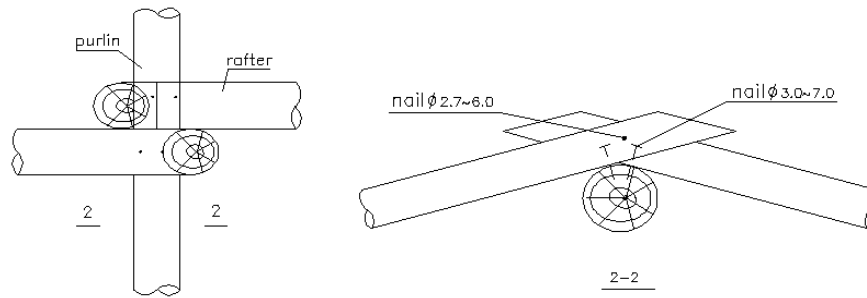


Fig. 2 One type of rafter joints

As is known to all of us, the computer aid design (CAD) software system [4] has played an important role in improving building design level. However, for the lack of adequate research on raw-soil structure, existing domestic and oversea CAD software system is incapable of solving the detailing work of this structure.

Today, “Building Information Modeling (BIM)” has been presented recently as a demarcation of the next generation of Information Technologies (IT) and Computer-Aided Design (CAD) for buildings which focus on the production of drawings [5]. BIM is the process of generating, storing, managing, exchanging, and sharing building information in an interoperable and reusable way.

In this paper, we consider the raw-soil structure building as an information system. Our object is to propose a method and tools which make it possible to build a 3D information model and solve the detailing work of this type of structure. First, characteristics and function requirements of the raw-soil structure are analyzed. Secondly, the software system architecture and core data structure is described. Thirdly, an example is presented to show the functions of the software system. Finally, in the conclusions we discuss the advantage and disadvantage of the CAD system and propose method to improve the system.

Functional Analysis

The raw-soil structure BIM software builds digital constructed models containing all information of the real houses. Any change made to the 3D information can automatically update the drawings needed printed for construction. The software has the following characteristics:

- (1) The 3D solid raw-soil structure can be constructed automatically by the Solid Model Construction module. The parametric model can be modified through editing the values of the parameters.
- (2) The structural model can be exported and imported into the finite element analysis software such as SAP and ANSYS. So an interface for data exchange should be developed.
- (3) After calculation, check the structural design to make sure the structural designs meet the rules of the code. Thus, the automatic interactive design, edit and check of the members of raw-soil structure can be implemented.
- (4) Based on the 3D information model, graphic and text query functions can be implemented easily. Calculation sheet can be exported automatically according to standard format.
- (5) According to the analysis results, the members and joints can be designed automatically after the types are chosen, the assembly of complex joints can be implemented easily, and the detailing can be drawn automatically, which can reduce the workload of the designer's drawing effectively.
- (6) The processing map, material list, project cost, and so on can be generated for users.

Software system architecture

Based on the common AutoCAD 3D graphics platform, the specialized CAD/CAM software system is developed in visual C++ programming language by using the SDK of AutoCAD [6]. AutoCAD is a very sophisticated graphics system, and is widely used in China for many years. The detailed designers who can use AutoCAD are able to completely master the software in a very short period of time. The software development platform and runtime environment of the hierarchical structure [7] are shown in Fig. 3.

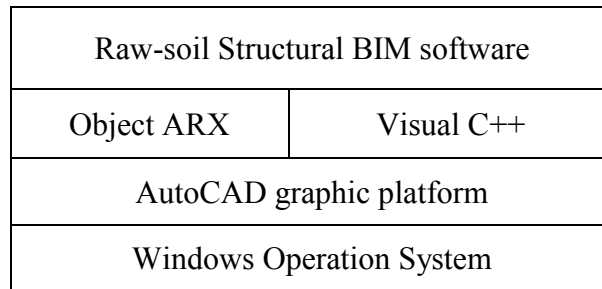


Fig. 3 Development platform& running environment

The main function module organizations [8] of the Software system is shown in Fig. 4, "3D solid model of Raw-soil structure" is the core of the system database and according to commands and necessary control parameters, each function module is named.

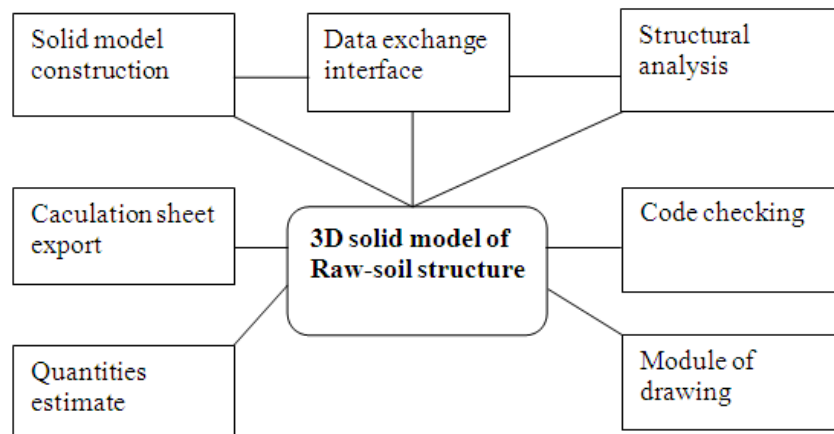


Fig. 4 Components & frame of primary functional module

Core Data Structure

The core technology of BIM is the central database consisting of the 3D solid model. The 3D solid model of the structure is mainly composed of several kinds of foundation custom entities such as plates, holes and bars. Subclasses used to decibel various structural components are derived from the foundation classes. The derived relationship of the typical classes is showed in Fig. 5.

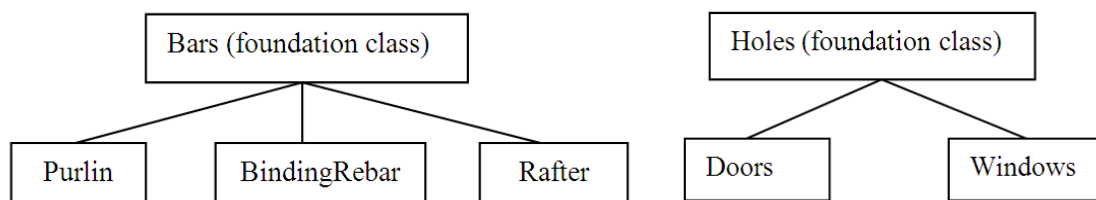


Fig. 5 Derived relationship of entity classes

By using object oriented design which is included in C++ language, class wall, class holes and class rafter are designed to describe raw-soil wall, windows and doors and rafters respectively. The custom entity, which records the geometrical and structural information of building parts, and overloads virtual functions such as 'viewport draw', 'Boolean operate', is derived from the ObjectARX [9] foundation class AcDb3dSolid to extend the 3D solid functions of AutoCAD. The data contained in custom entity, for example, a number of ordered control points, are used to label detailed drawing.

Engineering application

In this developed CAD/CAE system, the complete process of designing a raw-soil structural building is showed as follows. Fig. 6 presents a 3D solid model of raw-soil structure constructed. By changing the values of the parameters, the model can be edited easily. The finite element analysis results can be read into the model to revise the properties of the structural members. Once the types of joint are selected, the joints can be implemented automatically. Hence, the drawings can be implemented automatically. Fig. 7 show the drawing dialog box, different types of drawings can be selected from the list on the left.

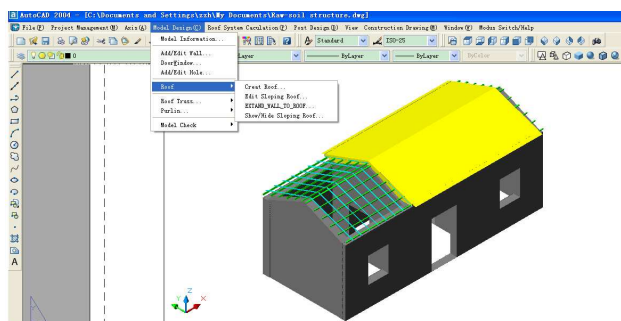


Fig. 6 3D solid model of Raw-soil house

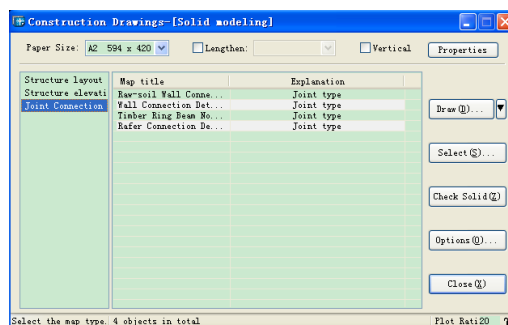


Fig. 7 Scene of drawings dialog

Fig. 8 shows the sence of Elevation, plan and section of the Raw-soil house drawn automatically based the 3D solid model. Fig. 9 is the details of the house which is also atuomatically implemented.

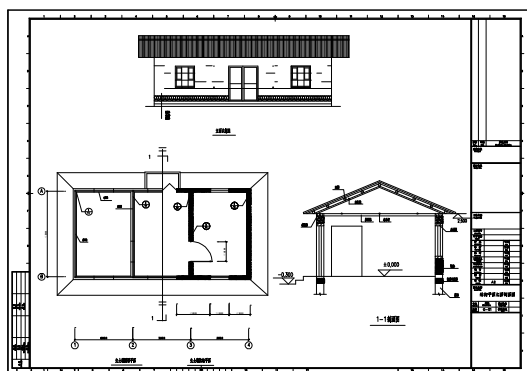


Fig. 8 Elevation, plan and section of the house

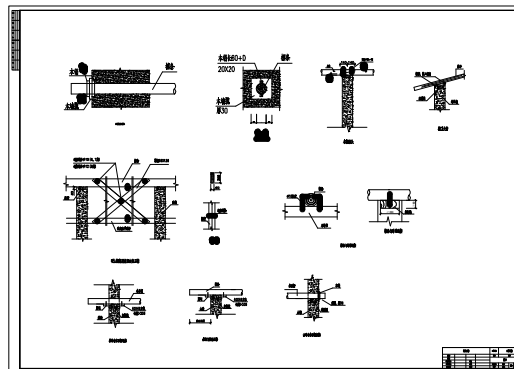


Fig. 9 Details of the Raw-soil house

Conclusions

Considering existing computer aided design systems are incapable of raw-soil structure which is still a common type of village building, it is feasible and necessary to develop specialized software for the designers. The raw-soil structure CAD/CAE system makes it easy to design raw-soil structures and draw detailing drawings.

(1) The 3D solid model based on BIM ensures that when a change is made in the design, it will be implemented throughout the entire project and will, thus, provide a security concerning the quality of information coming from the design.

(2) The BIM model can be exported for structural analysis. After finite element analysis, the code checking module can check and revise the design parameters automatically according to national codes. Members can be edited easily to meet the rules of the codes.

(3) The 3D digital model with high precision to ensure the accuracy of detailing drawings; all the detailing drawings are drawn automatically according to the solid model, hence, manual work or modification is reduced to the least level, and the detailed design work is very efficient.

Acknowledgements

The research is supported by National Technology Support Project: Research on Rural Residential Planning, Design and Construction Standard, and the subject is Structure and construction technology of residential design and software development (2008BAJ08B06).

References

- [1] L.P. TONG, X.P. ZHANG: Constr. Tech. Vol. 36 (2007), p. 90, in Chinese.
- [2] Y.H. WANG, D.J. SU, B.Q. LIU, et al: J. Xi'an Univ. of Archit. & Tech. Vol. 39 (2007), p. 451, in Chinese.
- [3] Y.H. WANG, C.Y. WANG, X.S. LI, et al: J. Xi'an Univ. of Sci. and Tech. Vol. 26 (2006), p. 469, in Chinese.
- [4] Y.Q. Fan, X.J. Feng, J.H. Zhou: *Design of CAD Software* (Beihang university press, Beijing 1996), in Chinese.
- [5] R. Vanlande, C. Nicolle, and C. Cruz: Aut. Constr. 18: 70-78 (2008), p.70.
- [6] B. Chen, N. Wang, J.F. Guo: *AutoCAD2000 application software development with ObjectARX* (Post & Telecom press, Beijing 2000), in Chinese.
- [7] W.M. Yang, W.M. Wu: *Data Structure* (Tsinghua university press, Beijing 1992), in Chinese.
- [8] J. Tian, G.P. Yuan, and S.X. Wen: *Computer aided 2D drawing and 3D modeling* (Electronics press, Beijing 1994), in Chinese.
- [9] C. McAuley, translated by S.G. Li, et al: *AutoCAD 2000 ObjectARX program guide* (Mechanical press, Beijing 2000), in Chinese.

The HSM Intelligent Database System Based On Neural Networks

Lijuan Liu^{1, 2, a}, Ming Lv^{1, b} Wenge Wu^{2, c}

¹ College of Mechanical Engineering, Taiyuan University of Technology, Taiyuan, Shanxi, 030024, China

² College of Mechanical Engineering and Automatization, North University of China, Taiyuan, Shanxi, 030051, China

^acy30mk@sina.com, ^blvming@tyut.edu.cn, ^cwuwenge@nuc.edu.cn

Keywords: HSM; INeural Network; Intelligent Database.

Abstract. High speed cutting (HSM) is one of the main trends of cutting machinery. In our country, the relevant research of HSM starts later, the actual machining and experiment on the machining technology and the machining parameters of HSM are few, the reasonable machining parameters selection scheme and the appropriate cutter choice method are lack. The paper established the HSM cutters management system based on BP artificial neural networks to facilitate optimized database system and to improve cutting efficiency. The result shows the system is very helpful to select cutting parameters and the value of prediction fits with the test very well.

Introduction

High speed cutting is one of the most important technologies in the 21st century. It has been widely used in different fields. The research of process and equipment on the high speed cutting start later in our country. As compared with developed countries, it lags fairly far behind. To determine HSM cutting parameters is very important and it immediately influences the quality of products, productivity, processing cost. But the machining parameters were usually determined by the cutting handbooks, the production practices or the cutting tests in the field of high speed cutting. The machining parameters are difficult to select because that the tool samples are not integrity and the identical data is variant from different tool manufacture factory. In order to meet the requirements of advanced manufacturing and technical personnel of the HSM enterprises, we develop the HSM intelligent database to provide valuable HSM cutting parameters, to select the suitable cutting tools and the optimal tool-path planning.

Structure and Function of the HSM Intelligent Database System

Based on neural networks, the intelligent database system integrates recommended values of the machining data, tool selection (including planning of cutters, procurement and budgeting, inventory management, tool sharpening, maintenance and repairing of tools, the optimization of tools, cost control), fault diagnosis, trademark and ingredient of the work-piece and tool materials, performance parameters and types of the machine models, and graph and regression formula of the experimental technique of metal cutting. With the web, users can get processing data corresponding by ways of inputting the basic parameters (such as processing materials, feed, tools, and so on) in the system.

The system contains five modules, and it provides a comprehensive management system on HSM. The system's structure diagram is shown in Fig 1.

The System of Cutting Dosage Selection. To determine HSM cutting parameters is very important in formulating the machine parts processing craft and it immediately influences the quality of products, productivity, processing cost. There are many factors that affect the choice. To determine the best cutting parameters is a difficult thing because these factors are mutually restrictive^[3]. The right choice of cutting parameters is a very difficult assurance in the actual processing. Generally, it should be determined by consulting cutting handbook, according to the processing properties, the

processing request, the work piece's material, the cutting tool's size and material performance, and other aspect, and it relays on the rich experience. This module aims at the question which meets in the traditional selective of cutting parameters, realizes the intelligent selective to determine HSM cutting parameters by using the computer. This module is the main part of the system. It incorporates summarizing and analyzing more than 40 process examples from different enterprises, classifying and compiling each kind of data, empirical datum and cutting handbook, and summarizes the optimized HSM process. The module gives the optimization HSM cutting parameters, tool-path planning and craft automatically according to the different processing material, feed and cutting tool, and simulates high-speed milling to determine the cutting craft way.

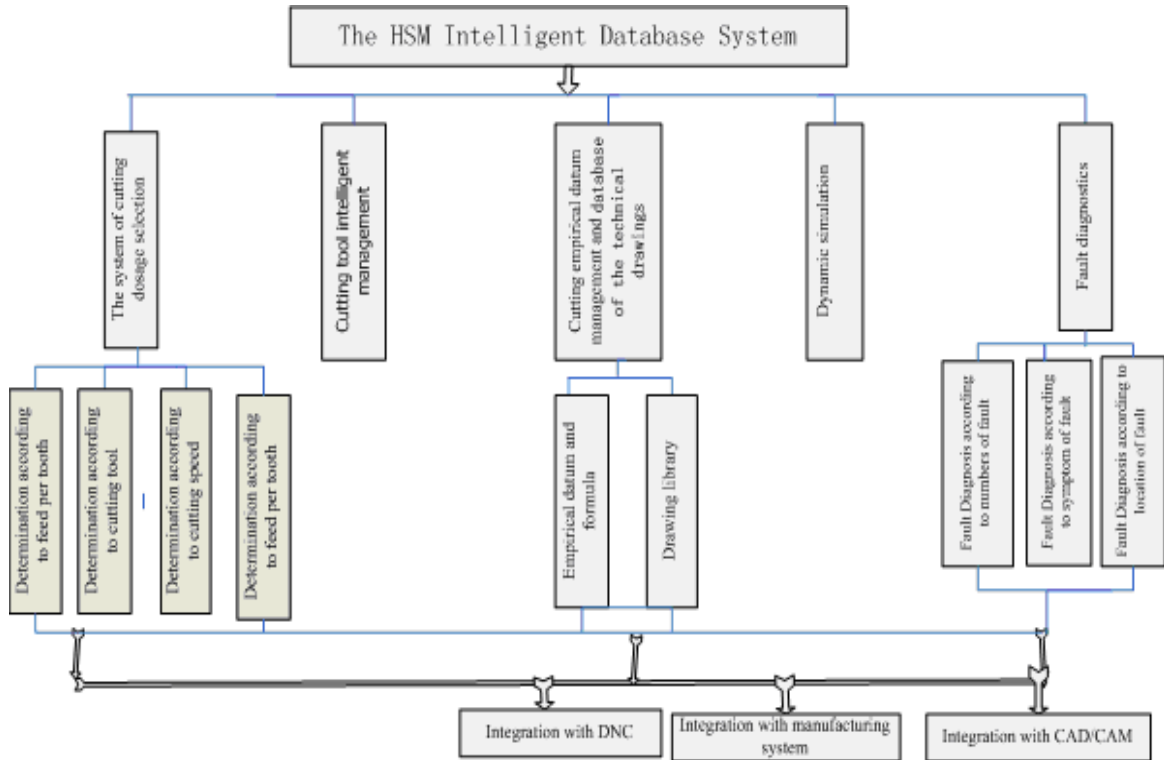


Fig.1 Intelligent Database System Total Diagram

Cutting Tool Intelligent Management. It is a major issue in present cutting tool management that the operators need to spend much time on searching cutting tool because the cutting tool is lacking or the cutting tool stock is not under control. Nowadays HSM cutting tool intelligent management doesn't get suitable development for HSM in the simultaneousness which develops quickly. A prominent module of cutting tool intelligent management based on HSM may reduce initial investment, staff and stock fund as well as the purchase managed cost.

This module is another main module of the system. And it can trace and collect cutting tool's concrete information in processing, and can process the information timely and effectively. The users may directly manage the cutting tool detailed information (variety, specification, quantity, etc.) from processing workshop, tool setting chamber, cutting tool storehouse, daily maintenance and repairing department and other cutting tool circulation department, may realize the online cutting tool selection, may realize the total life cycle tracing and management to the cutting tool, may produce the cutting tool cost evaluation detailed list and cutting tool use situation statistical table, optimizes the cutting tool use cost and frequency, reduces the production cost.

Cutting Empirical Datum Management and Technical Drawings Database. The module consists of two sub-modules Cutting empirical datum management and database of the technical drawings. Cutting empirical datum management has experimental data and experiential formulae such as the cutting tool effective diameter, the relations of the cutting tool effective diameter and the oblique angle, effective linear velocity of the ball end mill, feed and speed of cutter spindle, and so on.

Making the connection with the module of cutting dosage selection, the system will realize the intellectual selection of the cutting parameters.

Dynamic Simulation. It can provides dynamic simulation with the data generated by the application of the system, such as cutting dosage (federate, cutting deep, cutting width), tools and machines, etc .Through simulation, users can check the validity of the selected data. We collected dozens of experimental instances and provided animation and video of the typical process. Here is proof of the superiority of dictatorship high speed cutting.

Fault Diagnostics .The system can realize monitor various tools and machines on-line , orientate the breakdown and deal with faults quickly, respond to the abnormal situations ,such as tool wear, breaking down, and so on. Users input codes or the symptoms of the fault and the system can connect to the fault diagnostics module which summarized for hundreds of common malfunctions from a great many sets of machine tools.

Key Technologies

Establish the Database. The database of backstage supporter of system adopts SQL Server. It integrates with Windows servers tightly. Windows servers has the stronger safety and do not allow an unauthorized user to access your data. SQL Server meets requirements for security and remote because that user can query data stored in SQL Server database with web browser. Each database can create as many as 20 million data sheet which is limited by hard disk space of the server only. The system has four sub-databases sub-database of cutting dosage sub-database of cutting tool management sub-database of fault diagnostics and sub-database of technical drawings. I shall illustrate with sub-database of cutting dosage.

Create a database named HSC .We store every data field in one sheet in which key words connect every sheet. The database includes data collection, Appraisal and Disposal; establishment and optimization of cutting parameters; output and information service. There are 9 sections in the sheets: Feed per tooth, grouping of material, milling flute, spiral / milling angled surfaces / milling flat, side milling rough machining, side milling precision work, profiling milling rough machining, profiling milling precision work. Then Set site and connect to the database. Connect with web by way of related functions of MYSQL or ODBC. The default address of the database is local host. Input <http://localhost> (if the port is 8080, we can input <http://localhost:8080>) in address column of IE explorer. And it means that the configuration is correct if the host interface is appeared.

Dream weaver. Dream weaver is a special editor which could create web sites and applications. It integrates visual distribution tools, application development and code editor into a powerful IDE. It supports multifarious server technology (such as CFML, ASP.NET, ASP, JSP, and PHP) by which could create a web application supported by dynamic database. With the Dream waver, we select Windows XP as the network operating system and use the Internet Information Server as the Web server. We use the homepage to design the static homepage that the users can inquire the corresponding content by inputting the corresponding address. There are vast amounts of data in the system. We use the module of cutting dosage parameters as the example to illustrate it.

We build the dynamic inquiry homepage named HSC.asp and link it with determination high-speed milling parameter according to feed per tooth. We establish dynamic homepage named inquiry.asp whose function is to display correspond result with the inquiry order. The pages linked each other by the key words and the page inquiry.asp displays results according to filtration conditions. Input <http://localhost> in the IE browser's address fields and the main interface of the system will appear.

We apply neural network technology. We establish intelligent high-speed cutting database system based on BP neural network with neural network theory. BP neural network algorithm is a learning algorithm with teachers. The network connection weights after learning and training is distributed storage and expression of Knowledge .Placing input on the network trained, we will get the Corresponding output. Modify the threshold and weights and error function will decline in gradient

direction. A typical BP neural network is usually comprised by three layers of units (nodal points) or artificial neurons. The first layer is input layer consisting of a group of processing units which are responsible for acceptance of data imported to the network. BP nerve network model is shown in Fig.2.

The network of the system has 36 input layer neurons and 6 output layer neurons. Hidden layer neurons will reach 73 approximately. Numbers of neurons in the hidden layer are not fixed and need adjust according to the practical training constantly. In the study, we use high speed cutting process parameters from experiments (changing the feed rate per tooth, cutting speed, tool materials) to train the network. It requires that the training samples contain as much as possible the full range of input data (maximum and minimum of parameter values). We want enough to make the network can get the high precision and wide application scope.

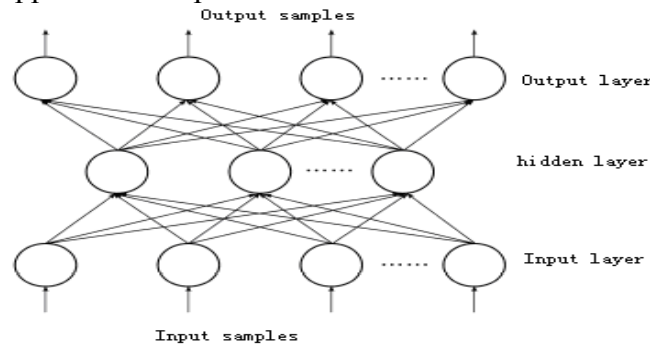


Fig. 2 BP nerve network model

In the HSM intelligent database system based on neural networks, we select BP neural network algorithm to get the process decision knowledge according to learning from Process Data, and achieve knowledge reasoning of the expert system with the predictive function of the neural network. It can provide guidance of the technology decision for specific high-speed machining and test its effects by means of experimental data.

The Realization of the HSM Intelligent Database System Based on Neural Networks.

Users can determine the parameters of high-speed cutting according to different materials, feed per tooth, etc, as shown in the Fig. 3. According to the users' requirement, we can select the tool shanks, cutter holders, cutter bits, grippers and cutter materials, and can realize cutters' automatic assembling. Users can open drawings Library System with AutoCAD or Solid Works and can view or modify 2D and 3D drawings of products and tools , as shown in the Fig.4. User can monitor operational states of tools and the machines online and can diagnose and deal with faults.

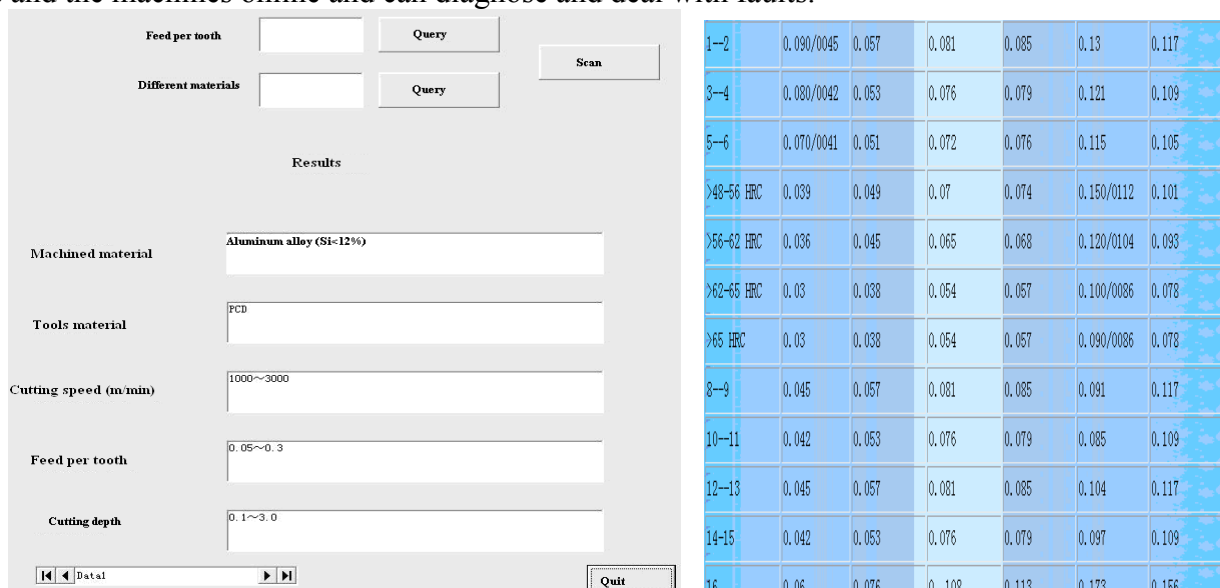


Fig. 3 Determination HSM cutting dosage according to different inquiry way

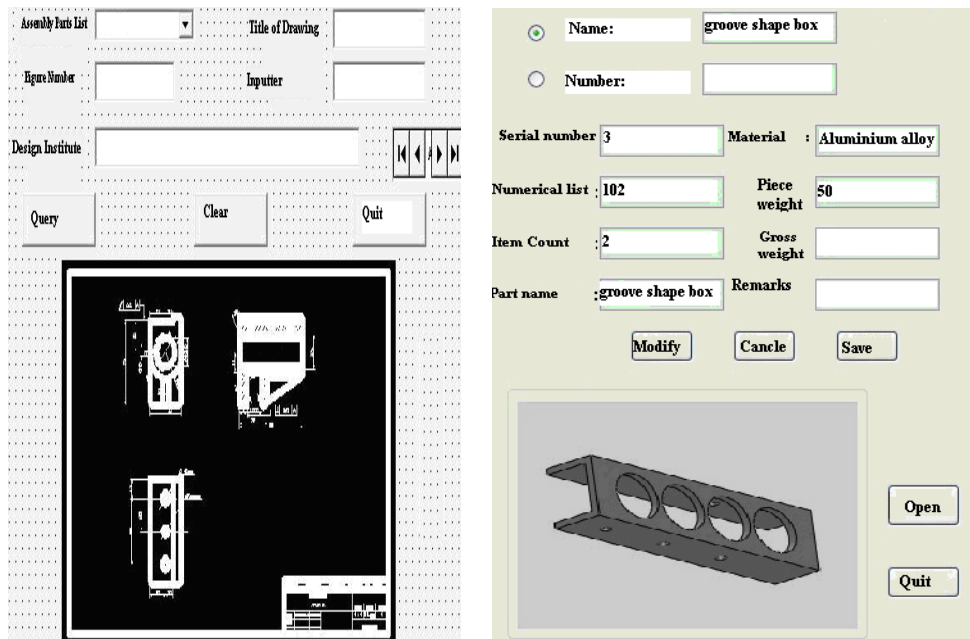


Fig. 4opening drawings library system with AutoCAD or Solid Works

Conclusions

We use neural networks as a means to build the HSM intelligent database system in the study. It selects browser/server software construction and database technology to realize accurate index and management for the HSM information. The system provides the beneficial guidance and reference for users in the HSM production whole life cycle, including the selection of cutting dosage, tool management, calling drawing library and fault diagnosis.

The system works stably and secure; the pattern is popular; the manipulation is simple and the maintenance is convenient.

Acknowledgments

Financial support from the Shanxi province nature science foundation (Grant No.:2008011056), key lab for advanced manufacturing technology of Shanxi province open foundation (Grant No.:2007031007) and the Shanxi province higher education youth discipline leader foundation. The author is acknowledged with gratitude.

References

- [1] M.V.Ribeiro, N.L.Coppini: *An applied database system for the optimization of cutting conditions and tool selection*. Journal of Materials Processing Technology, 2002,92-93:p.371
- [2] W. Liangde, Z. Jun and G. Shengguang: *High speed NC processes on earphone die*. Modern Manufacturing Engineering, (2004): p.18
- [3] B.Mursec,F.Cus: *Integral model of selection of optimal cutting conditions from different database of tool makers*. Journal of Materials Processing Technology, 2003,133:158
- [4] Yang Yin: *Network environment, the development of metal cutting database system*. Tool Engineering, 2002

Study on Meshing Characteristic and CAM Technology of Limacon Type Gears

Yongping Liu, Pengfei Meng

School of Mechanical & Electronical Engineering, Lanzhou University of Technology, Lanzhou ,
 730050 China

cameliu@163.com

Keywords: Limacon; Noncircular Gear; Pitch Curve; Meshing Characteristic; Computer-Aided Manufacturing.

Abstract. According to the meshing principle of non-circular gears, the meshing characteristic and digital manufacturing technology of Limacon type gears is studied. Based on analyzing the parameterized modeling of pitch curve, transmission characteristics and convexity-concavity analysis on Limacon type gears, the transmission feasibility of this type gear is proved. Through tooth shape design, CAM calculation and analysis with example, and processing simulation, the validity and manufacturability of theoretical design method on this type gear is proved. The research results can provide more systemic theory basis for the design, manufacture, measure and application of Limacon type gears.

Introduction

Limacon is a conchoidal curve, usually used as a cam contour curve for specific situations. According to the above application background, Yongping LIU [1] proposed a new type noncircular gear, named Limacon type gears, it used Limacon as the gears' pitch curve equation. According to the research result of document [1], Limacon type gears can realize variational transmission ratio.

Based on the related domestic and international literature in recent years [2-3], the meshing characteristic and CAM technology of Limacon type gears will be researched in this article, which can provide more systemic theoretical basis for design, manufacture, measure and application of Limacon type gears.

The definition and characteristic of Limacon

The definition of Limacon is shown in Fig.1. There is a defined circle in polar coordinates system, which radius is $b/2$, the centre point is $(b/2, 0)$. When the radius vector distance between moving point and any point of defined circle is l , the trajectory of moving point is called Limacon. The mathematical equations of Limacon can be expressed in polar coordinates by $r = b\cos\theta + l$, where b is the diameter of defined circle, l is fixed length. When b and l are different, the shape of Limacon are also different. There are mainly including four kind of cases as follows, its shape as shown in Fig. 2.

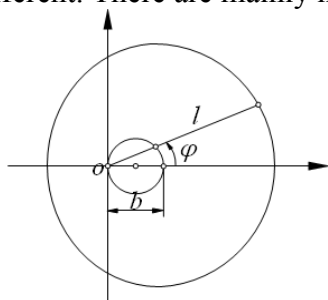


Fig. 1 Diagram of Limacon

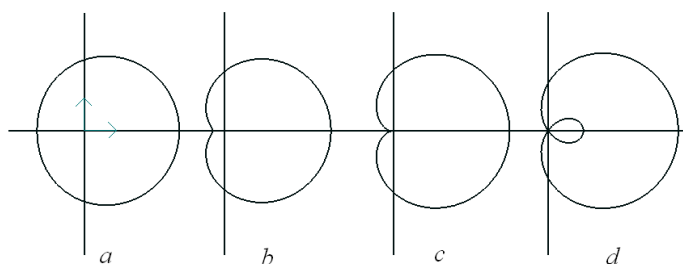


Fig. 2 Four cases of Limacon

- (1) while $l \geq 2b$, Limacon is a whole convex closed pitch curve as shown in Fig. 2(a).
- (2) while $b < l < 2b$, Limacon is a uncrimping concave pitch curve as shown in Fig. 2(b).

(3) while $l=b$, Limacon is a cardioid diagram as shown in Fig. 2(c).

(4) while $l<b$, Limacon is a self-crimping concave curve as shown in Fig. 2(d).

The pitch curve of Limacon type gears

The pitch curve equation of Limacon type gear pairs. If the pitch curve of driving gear 1 is a Limacon, the pitch curve equation of driving gear can be expressed by the following equation [4]:

$$r_1 = b \cos \theta_1 + l \quad (1)$$

According to differential geometry, the curvature radius at any pitch point of the pitch curve can be represented as follows:

$$\rho_1 = \frac{[l^2 + b^2 + 2lb \cos \theta_1]^{\frac{3}{2}}}{l^2 + 3lb \cos \theta_1 + 2b^2} \quad (2)$$

If the order of conjugating driven gear 2 is n_2 , the close condition of pitch curve for gear 2 can be obtained as follows:

$$\frac{2\pi}{n_2} = \int_0^{2\pi} \frac{a}{a - (b \cos \theta_1 + l)} d\theta_1 - 2\pi \quad (3)$$

The center distance a of gear pairs can be expressed as follows:

$$a = \frac{(n_2 + 1)\sqrt{(2n_2 + 1)b^2 + l^2 n_2^2 + l(n_2 + 1)^2}}{2n_2 + 1} \quad (4)$$

So the pitch curve equation of driven gear 2 can be expressed as follows:

$$\begin{cases} r_2 = a - (b \cos \theta_1 + l) \\ \theta_2 = \int_0^{\theta_1} \frac{(b \cos \theta_1 + l)}{a - (b \cos \theta_1 + l)} d\theta_1 \end{cases} \quad (5)$$

The transmission ratio of external meshing noncircular gear pairs can be obtained as

$$i_{12} = \frac{a - (b \cos \theta_1 + l)}{b \cos \theta_1 + l} \quad (6)$$

The pitch curve arc length of driving gear 1 can be obtained as

$$S = \int_0^{2\pi} \sqrt{b^2 + l^2 + 2bl \cos \theta_1} d\theta_1 \quad (7)$$

Assuming there are $L=l+b$, $S_a=l-b$, $k=S_a/L$, where L is called long axis, S_a is called minor axis, k is called the ratio between minor axis and long axis. So the diameter of defined circle and fixed length can be expressed respectively by $l=(L+S_a)/2$, $b=(L-S_a)/2$, the arc length can be expressed in the rectangular coordinate system by the following equation:

$$S = 4L \int_0^{2\pi} \sqrt{1 - \left(\sqrt{1-k^2}\right)^2 \sin^2 \theta_1} d\theta_1 \quad (8)$$

In addition, according to the closure property of pitch curve and uniform distribution characteristic of gear tooth around pitch curve, the arc length of pitch curve also must meet the condition as follows [5-8]:

$$S = \pi m z \quad (9)$$

Therefore, if the teeth number z_1 and module m of driving gear, the ratio k between minor axis and long axis are defined when design this kind of gears, the long axis parameter L and the pitch curve equation of driving gear can be obtained according formula (8) and (9), then the pitch curve equation of driven gear can also be obtained according formula (5).

The transmission ratio of Limacon type gears. If the basic parameters of Limacon gears are given as follows: $n_2=1$, $k=0, 0.2, 1/3, 2/3, 1, 1.5$ and 2 , the transmission ratio can be calculated according formula (5) and (6), the transmission ratio curve can also be drew by the calculation results, as shown in Fig.3(a).

The whole pitch curve convex condition of Limacon is $k \geq 1/3$. The Limacon is cardioid curve when $k=0$, the pitch curve has partly concave. The transmission ratio amplitude Ai_{12} become smaller as the ratio k gets larger when $1 < k < 0$. The transmission ratio is a constant when $k=1$, the pitch curve become a circle. The transmission ratio amplitude Ai_{12} become larger as the ratio k gets larger when $k > 1$.

If the basic parameters of Limacon gears are given as follows: $k=2/3$, $n_2=1, 2, 3, 4$ and 5 , the transmission ratio of gear pairs are shown in Fig.3(b). The transmission ratio amplitude Ai_{12} become smaller as the variable n_2 gets larger when the ratio k is a constant value, namely Ai_{12} is inversely proportional to i_{12} .

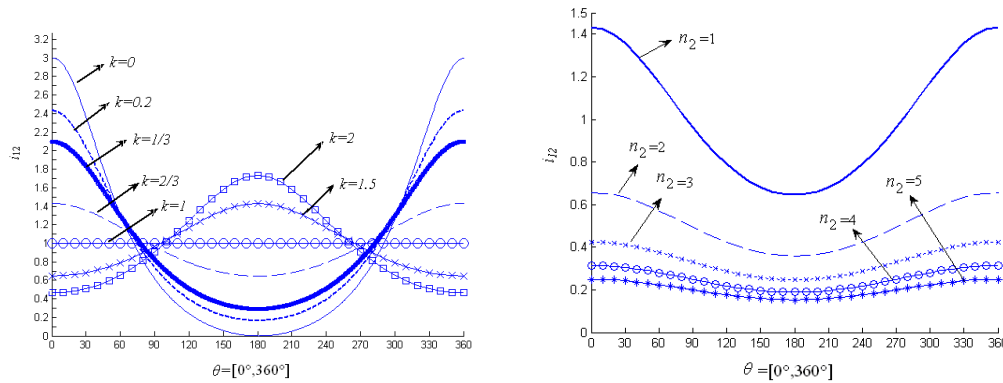


Fig. 3 (a) Transmission ratio curve of Limacon gear pairs with different value k , (b) Transmission ratio curve of Limacon gear pairs with different order n_2

Convexity-concavity property of Limacon type gears. The convexity-concavity property of the driven gears which meshed with Limacon gears will be discussed as follows.

There are necessary to introduce a new symbol d which called the relative center distance.

$$d = \frac{a}{l} \quad (10)$$

Assuming ε is the eccentricity, its computing formula can be expressed as follows:

$$\varepsilon = \frac{1-k}{1+k} \quad (11)$$

So the relative center distance can be obtained as

$$d = \frac{(n_2 + 1)\sqrt{(2n_2 + 1)\varepsilon^2 + n_2^2} + (n_2 + 1)^2}{2n_2 + 1} \quad (12)$$

According to the document [1], the curvature radius of driven gears can be expressed as follows:

$$\rho_2 = \frac{(a - r_1)(r_1^2 + b^2 \sin^2 \theta_1)^{\frac{3}{2}}}{r_1^3 + (2r_1 b^2 - ab^2) \sin^2 \theta_1 + (r_1^2 b - ar_1 b) \cos \theta_1} \quad (13)$$

There because of $a > r_1$, the numerator in equation (13) is always a positive value. So if the denominator in equation (13) is a positive value, the pitch curve of driven gears which meshed with Limacon gears is a convex curve. It must satisfy following equation:

$$r_1^3 + (2r_1 b^2 - ab^2) \sin^2 \theta_1 + (r_1^2 b - ar_1 b) \cos \theta_1 \geq 0 \quad (14)$$

The minimum value of equation (14) is determined by derivation, which can be obtained while $\theta_1=0$ and $r_1=l+b$. Substituting the extremum conditions into equation (14) gives:

$$l^2 + 3lb + 2b^2 - ab \geq 0$$

$$\text{or } 2\varepsilon^2 + (3-d)\varepsilon + 1 \geq 0 \quad (15)$$

According to equation (12) and (15), if $n_2=1, 2, 3$ and 4 , the pitch curve of driven gears which meshed with Limacon gears is a whole convex curve when $k \geq 1/3$.

CAM analysis with an example for Limacon type gears

Assuming the initial parameters are given as follows: $b=20$, $l=34$, $m=3$, $z_1=25$, $n_1=1$, $n_2=2$. Since $l \leq 2b$, the pitch curve of driving gear is not a whole convex curve, there is some concave curve, the pitch curve, addendum curve and dedendum curve of driving gear, the curvature radius ρ and converting teeth number Z_A at each divide point can be calculated.

The each gear tooth profile of driving gear can be generated using CAXA software as shown in Fig. 4(a), the three-dimension simulation graphics is shown in Fig. 4(b).

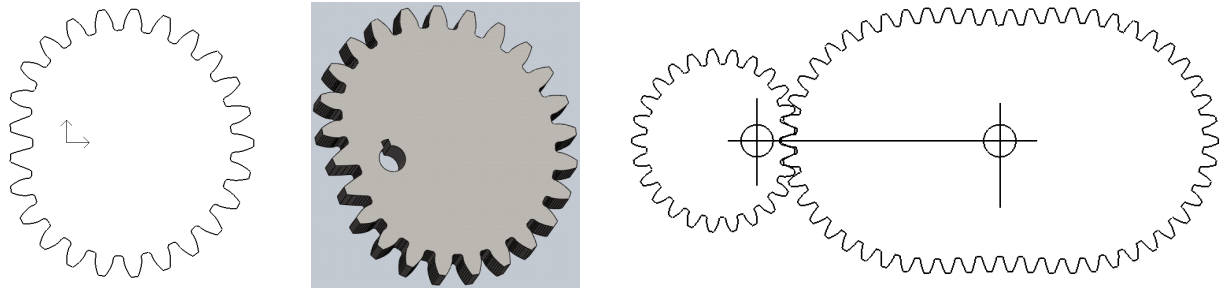


Fig. 4 (a) Tooth profile of Limacon type gears, (b) 3D simulation graphics of Limacon gears, (c) Tooth profile graphics of conjugate Limacon gear pairs

Similarly, the tooth profile of driven gears engaged with Limacon gears can also be calculated and generated, the teeth number of driven gears $z_2=54$, the center distance of conjugate gear pairs $a=110.031$, the meshing state and tooth profile graphics of conjugate gear pairs is shown in Fig. 4(c), the driven gears is also a noncircular gear.

Conclusions

According to the meshing principle of noncircular gears, the meshing characteristic and digital manufacturing technology of Limacon gears is studied in this article, including the parametric design of pitch curve, analysis of the transmission characteristics, the design of tooth profile, CAM and machining simulation analysis. The feasibility of transmission and machinability of this kind of gears is also be verified. The research results should be helpful in the design, production and practical application of high-precision Limacon gears.

References

- [1] Yongping Liu, Xutang Wu, Heqi Li: Transactions of the Chinese Society for Agricultural Machinery (In Chinese), Vol. 38, No. 6 (2007), p. 143-146
- [2] Wei Liao, Yun Zhao, Minghui Fang: Journal of Zhejiang Institute of Science and Technology (In Chinese), Vol. 26, No. 3 (2009), p. 547-551
- [3] Tingzhi Ren, Aiming Cheng, Fengru Jing: Chinese Journal of Mechanical Engineering (In Chinese), Vol. 42, No. 9 (2006), p. 71-75
- [4] 《Math Handbook》 writers: *Math Handbook* (Higher Education Press, Beijing, 1998, In Chinese)
- [5] Xutang Wu, Guihai Wang: *Elliptical gears and non-uniformity velocity ratio transmission* (Mechanical Industry Press, Beijing, 1997, In Chinese)
- [6] S. H. Tong, C. H. Yang: Transactions of the ASME, Journal of Mechanical Design, Vol. 120, No. 2 (1998), p. 337-341
- [7] B. W. Bair: Transactions of the ASME, Journal of Mechanical Design, Vol. 124, No. 6 (2002), p. 787-793
- [8] H. C. Huang, C. C. Tsai, S. C. Lin: Journal of Intelligent and Robotic Systems, Vol. 55, No. 6 (2010), p. 101-122

Theoretical Model of Wall Heat Transfer in Turbulent Flow

Wei-zheng Zhang^a, Xiao Liu^b, Chang-hu Xiang^c

School of Mechanical Engineering, Beijing Institute of Technology, Beijing 100081, China

^azhangwz@bit.edu.cn, ^bliuxiao0923@bit.edu.cn, ^cxch2004@bit.edu.cn

Keywords: Turbulent Flow; Wall Heat Transfer; Theoretical Model.

Abstract. The turbulent flow in the near-wall region affects the wall heat transfer dominantly. The farther it is from the wall, the less effect it has. So a two-step mechanism of the turbulent wall heat transfer is released: first, the energy is transferred to the outside of the viscous sub-layer by the rolling of the micro-eddy; secondly, the energy gets to the wall by conduction. Then, a theoretical model of wall heat transfer is developed with this concept. The constant in the model is confirmed by experiment and simulation of the transient turbulent heat transfer in pipe flow. Finally, the model is used to predict the local heat flux under different conditions, and the results agree well with the experimental results as well as the simulation results.

Introduction

The typical method of thermal analysis in engineering is using formulas of Nusselt number [1]. These empirical or semi-empirical formulas are usually derived from dimensionless analysis and show the relationship between the average value of parameters of flow field and the global heat transfer [2-3]. But the average value of flow field parameters can't tell the detail of turbulent flow. And there is large difference between global heat transfer and the local one. Fortunately, theory of boundary layer overcomes these limitations [4] and makes it possible to accurately predict the wall heat flux in free shear flow. However, theory of boundary layer isn't suitable to be used in some special flows because of some of its assumptions. For example, because of the complex flow field and intense chemical reaction, the assumption that the normal gradient of wall is much bigger than tangent gradient in theory of boundary layer can't be met in small space, such as the combustion chamber of reciprocating internal combustion engine. Theory of boundary layer shows that the wall heat transfer is affected by turbulent flow in the near-wall region dominantly [5-6]. So the wall heat transfer model based on the analysis of turbulent flow in near-wall region can reveal the direct relationship of turbulent flow and wall heat transfer.

Mechanism and Mathematical Physical Model

The turbulent flow can be divided into turbulent core and near-wall region by flow behavior. The near-wall region can be divided into logarithmic law region, buffer region and viscous sub-layer [5]. In near-wall region, the eddy has layered distribution along the normal direction. The nearer away from the wall, the smaller the velocity and the size of the eddy are [5-6], therefore, the biggest eddy has the longest distance from the wall. The different sizes of eddies in normal direction of the wall induce the energy transport. Energy is transported from the big eddies in the turbulent core far from the wall to the small ones near the wall. Then part of the energy is transported to smaller ones next while the rest energy is dissipating at the same time.

In the region outside the viscous sub-layer, energy is transferred to wall through the transport of eddies; in the viscous sub-layer, it is transferred to wall through heat conduction because the transport is weak [7]. So the wall heat transfer in turbulent flow can be divided into two steps: first, energy is transferred from outside of near-wall region to outside of viscous sub-layer by eddies; secondly, energy is transferred from viscous sub-layer to the wall by heat conduction.

The energy transported by eddies in the first step should satisfy the equation:

$$Q_n \propto m_n c_p (T_n - T_v). \quad (1)$$

Where m_n is the mass, c_p is the specific heat, T_n and T_v are the temperature of outside of near-wall region and viscous sub-layer, respectively.

In near-wall region, velocity scale is represented by turbulent intensity. Then the time of energy transport is

$$t_n \propto L_n / u'. \quad (2)$$

Where L_n is the length of near-wall region, u' is turbulent intensity.

According to the geometric relationship, the circulation area of energy transport is

$$A_n = \frac{m_n}{\rho L_n}. \quad (3)$$

Where ρ is density.

The energy flux density is defined as

$$q_n = \frac{Q_n}{A_n t_n}. \quad (4)$$

In the viscous sub-layer, energy is transferred by heat conduction. According to Fourier's law, the heat flux is

$$q_v = k(T_v - T_w) / L_s. \quad (5)$$

Where k is thermal conductivity, L_s is the thickness of viscous sub-layer, T_w is the wall temperature.

According the equation (1)-(5) and the law of thermal resistance, the convective heat transfer coefficient is

$$\frac{1}{h_c} = \frac{1}{C \rho c_p u'} + \frac{1}{k / L_s}. \quad (6)$$

Where C is constant.

According to turbulent theory [5], there is a simple relationship between turbulent intensity and turbulent kinetic energy:

$$u' = \sqrt{\frac{2k_t}{3}}. \quad (7)$$

Where k_t is turbulent kinetic energy.

The range of viscous sub-layer is determined from the dimensionless distance:

$$y^+ < 5. \quad (8)$$

Which is defined as

$$y^+ = y u^* / \nu. \quad (9)$$

Friction velocity satisfies [5]

$$u^* = c_D^{1/4} k_t^{1/2}. \quad (10)$$

The value of the factor c_D is of different opinions between 0.055 and 0.09. It is known that c_D is the reciprocal of turbulent Reynolds number from the derivation process of k - ε model [6]:

$$c_D = \nu_t \varepsilon_t / k_t^2. \quad (11)$$

Where ν_t and ε_t are turbulent viscosity and turbulent dissipation rate, respectively.

It is shown that c_D changes significantly in the near-wall region, approaches to 0.09 only far from the wall, and couldn't be treated as constant by the simulation results of Kim et al [5]. So the equation (11) should be used in the equation (10) to calculate the fraction velocity, instead of constant c_D .

According to the equations (6)-(11) and taking into account the heat diffusivity coefficient $a = k / (\rho c_p)$, Prandtl number $Pr = \nu / a$, the total convective heat transfer coefficient is derived:

$$h_c = \frac{\rho c_p k_t^{0.5}}{c + 5 Pr Re_t^{0.25}}. \quad (12)$$

Where c is constant.

Mathematical physical model parameters and validation

Because the turbulent heat transfer in pipe flow is fully validated, constant c in equation (12) is determined by pipe flow experiments. The relevant turbulent parameters (such as turbulent kinetic energy and turbulent dissipation etc.) are difficult to be measured in experiments. So they are obtained by simulation of pipe flow.

The data of pipe flow comes from the transient turbulent pipe flow experiments of Barker et al [8]. The diameter of pipe is 38mm, the temperature of pipe wall is fixed to 353K and the working fluid is air in the experiments. The inlet velocity is set to step-type and impulse-type. The local transient heat flux is measured 1.5m away from the entrance.

Fluent is used in the pipe flow simulations with the setting of the experiments above. Two-dimensional symmetric model of pipe is adopted. In order to decrease the effect of outlet boundary on flow simulation, the length of pipe in simulative model is 0.3m longer than the distance from heat flux testing points to entrance in experiments. The mesh is fined in entrance section and near-wall region according to reference [9], in order to accurately compute the turbulent flow in near-wall region. The smallest axial length of mesh in entrance section is 0.05mm, the proportion of length to width is 1.05, and the maximum axial length is 1.6mm. The smallest radial length of mesh in near-wall region is 0.01mm, the proportion of length to width is 1.2, and the maximum radial length is 1mm. The Reynolds stress turbulent model which has five equations is used, and enhanced wall treatment model is used in near-wall region. Because there are no data for turbulent flow in experiments, the turbulent intensity is specified to 4% and length scale is 30% of pipe diameter, and the physical character of air is supposed to be constant in reference [9]. After several testing calculations, it is found that the boundary condition is not appropriate. Because the change of heat flux under experimental conditions is small, and the change of turbulent parameters with the velocity will lead to big change relatively. So the turbulent kinetic energy and turbulent dissipation rate are computed from the turbulent parameters in entrance by the empirical formula in the document of Fluent. The physical performance of air is specified according to the thermal physical properties table [10]. Before transient simulation, a steady state analysis is carried out first to make the flow stable.

The inlet boundary for simulation is shown in Fig.1. The velocity changes faster in the simulation of Benim et al [9] while the time at which velocity changed is also delayed than experiments. But the velocity diverges obviously in the steady process. The inlet velocity specified in this paper is the same as experiments. At the moment of valve opening (controlling inlet velocity), complex fluctuation of inlet velocity is occurred, which is also simulated in detail in this paper.

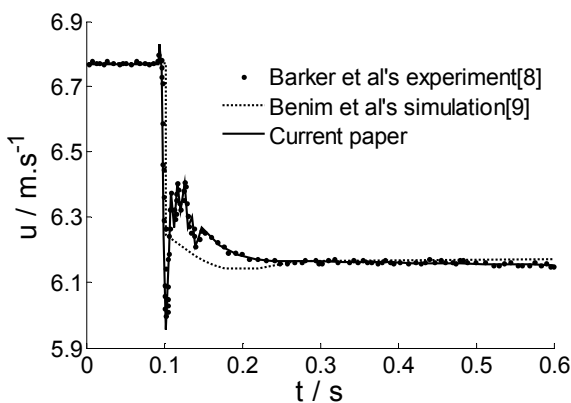


Fig.1 Step-type inlet velocity

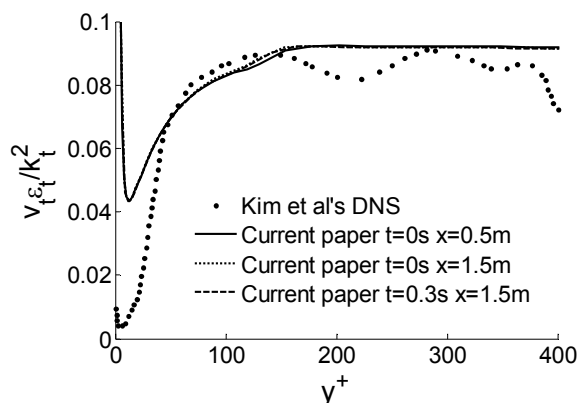


Fig.2 Distribution of turbulent Reynolds number along the wall normal direction

Fig.2 shows the distribution of the reciprocal of turbulent Reynolds number (in equation (11)) along the normal direction of wall at different times and positions. The t in figure refers to the time after simulation starting and x is the distance away from entrance. It indicates that the results of

turbulent parameters have the similar trend as the direct numerical simulation results of Kim et al [5], only different values in buffer layer. It is also shown that c_D is constant 0.09 approximately outside the near-wall region.

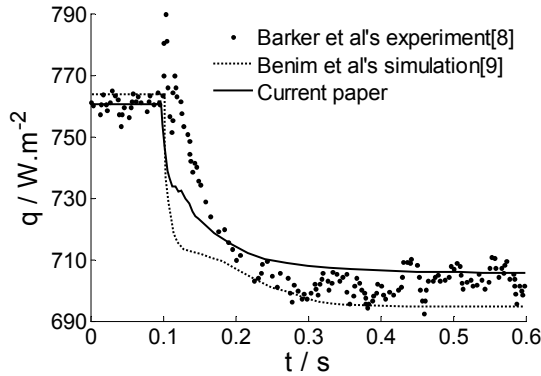


Fig.3 Transient local heat flux 1.5m away from the entrance

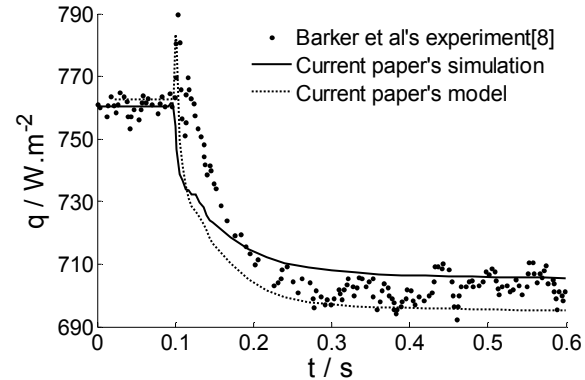


Fig.4 Local heat flux with step-type velocity

The transient heat flux distribution 1.5m away from inlet in pipe wall is shown as Fig.3. It shows that the wall heat flux in simulation of Benim et al [9] is close to the upper value of experimental data before inlet velocity changes. When the inlet velocity is slow down, the turbulence induced by velocity fluctuation affects the instantaneous amplitude of wall heat flux obviously. Just as Benim et al [9] mentioned, the transient simulation can't obtain the delay of heat flux variety to velocity variety accurately.

The wall heat flux of simulation in this paper is the average value of the experimental data before inlet velocity changing. Because velocity changes at the same time as experiments, the former phase of velocity variety is earlier than Benim et al [9], but the wall heat flux is close to the experimental results gradually at the later phase, and agrees well with the experimental results at the steady phase finally after velocity changing.

The prediction of transient wall heat flux 1.5m away from the entrance by equation (12) is shown as the dashed line in Fig.4. Because the local turbulent parameters in near-wall region, but not the average parameters of entire flow field is used to analyze the heat transfer in the equation (12), the prediction of local transient heat flux agrees well with the experimental data. The heat flux variety induced by the turbulent pulsation is also predicted when velocity is changing.

According to simulations, the constant in equation (12) is:

$$c=13.05. \quad (13)$$

The pulse-type inlet velocity time is shown in Fig.5.

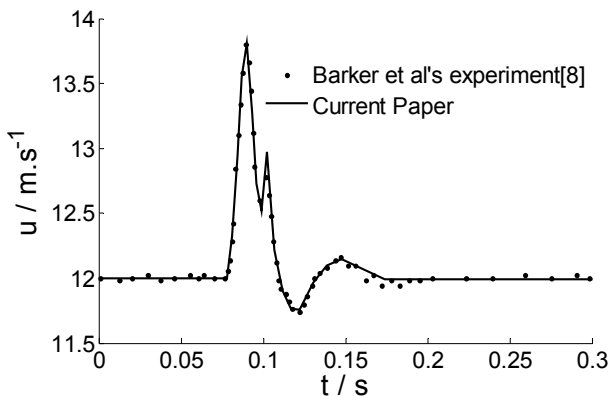


Fig.5 Pulse type inlet velocity

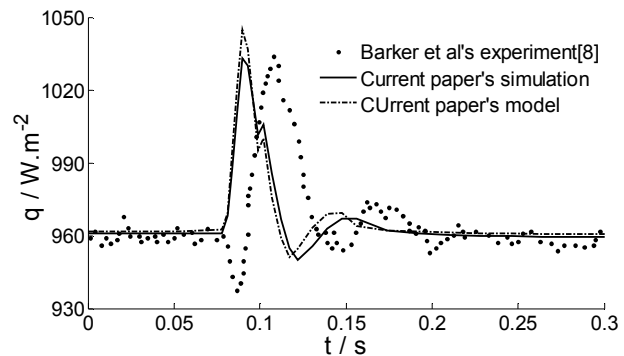


Fig.6 Local heat flux of pulse-type inlet velocity

The local transient heat flux of experiments, simulation result, prediction of equation (12) and equation (13) with pulse-type inlet velocity are shown in Fig.6. It indicates that the variety trend and amplitude of local heat flux agree well with the experimental results except the delay of heat transfer.

Conclusions

Some conclusions can be obtained from the work in this paper:

(1) The convective heat transfer is affected by the flow in near-wall region dominantly in turbulent flow, so the local turbulent parameters in near-wall region are the key factor for turbulent convective heat transfer.

(2) Turbulent heat transfer can be divided into two steps: the energy is transferred to outside of viscous sub-layer by eddies first, and then transferred to wall by conduction.

(3) Based on the two-step energy transport mechanism, turbulent characteristics and fundamental principles of heat transfer etc., the theoretical model of turbulent convective heat transfer is presented.

(4) According to the transient simulation results which are validated by experiments, the constant of the theoretical model are determined and the wall heat transfer in turbulent flow is obtained:

$$h_c = \frac{\rho c_p k_t^{0.5}}{13.05 + 5 \text{Pr} \text{Re}_t^{0.25}}$$

(5) The local transient heat flux predicted by the theoretical model in this paper agrees well with the experimental results.

References

- [1] Chen X D. A mechanistic insight of convective heat transfer in turbulent flow in smooth round pipe with a turbulent 'scoops' concept. *Trans I Chem E, Part A, Chemical Engineering Research and Design*, 2007, 85(4): 465–472
- [2] Arpaci V S, Larsen P S. *Convection Heat Transfer*. Translated by Gu Chuan-bao, Luo Di-an, Li Xin-gui. Beijing: Higher Education Press, 1992
- [3] Finol C A, Robinson K. Thermal modelling of modern engines: a review of empirical correlations to estimate the in-cylinder heat transfer coefficient. *Proc I Mech E Part D: J. Automobile Engineering*, 2006, 220: 1765-1781
- [4] Schlichting H. *Boundary-layer theory*. Kestin J translated. New York: McGraw-Hill Inc, 1979
- [5] Pope S B. *Turbulent flows*. London: Cambridge University Press, 2000
- [6] Piquet J. *Turbulent flows: Models and physics*. Berlin, German: Springer- Verlag, 1999
- [7] Takashi Suzuki, Yasufumi Oguri, Masatake Yoshida, Heat transfer in the internal combustion engines. SAE2000-01-0300
- [8] Barker A R, Williams J E. Transient measurements of the heat transfer coefficient in unsteady turbulent pipe flow. *Internat. J. Heat Mass Transfer*, 2000, 43: 3197–3207
- [9] Benim A C, Cagan M, Gunes D. Computational analysis of transient heat transfer in turbulent pipe flow. *International Journal of Thermal Sciences*, 2004, 43 : 725–732
- [10] Tao Wen-quan. *Heat transfer*. Xi'an: Northwestern Polytechnical University Press, 2006 (in Chinese)

Local Gouge Detection Algorithm for 5-Axis Sculptured Surface Machining Using the Toroidal Cutter

Wengang Fan^a, Jianyong Li^b, Yonglin Cai^c and Zehua Huang^d

School of Mechanical and Electronic Control Engineering, Beijing Jiaotong University,
Beijing 100044, P.R.China

^awgfan.alan@gmail.com, ^bjyli@bjtu.edu.cn, ^cylcai@bjtu.edu.cn, ^d06116264@bjtu.edu.cn

Keywords: 5-Axis; Gouge Detection; Sculptured Surface

Abstract. Based on the geometrical property of the toroidal cutter, an improved local gouge detection method for 5-axis sculptured surface machining was presented here. By alternately taking full advantage of point projection principles on curve and surface, the minimum distance between the circular curve of the toroidal cutter and the design surface was firstly calculated. Then the local gouge detection was accomplished through comparing the minimum distance with the corner radius of the toroidal cutter. The maximum interference quantity required for correction was also gotten. Results of an example showed the new method was correct and stable.

Introduction

The 5-axis numerically controlled (NC) milling technology is widely applied in the area of sculptured surface machining. These sculptured surfaces are common in industries such as automobile, aircraft, watercraft, and especially in molds and dies. The local gouge detection and the global interference detection are always the main concern for 5-axis surface machining. To solve the tool interference problem, many algorithms have been developed. Lee and Chang [1] proposed two different methods to detect potential interference using the convex hull of the control mesh of the sculptured surface. The correction method was also developed. Gao et al. [2] and Xu et al. [3] presented similar interference checking algorithms based on the property of convex hull. Zhang et al. [4] first made the design surface and the cutter surface scattered into a sequence of triangles, and then checked the interference through the intersection judgement between these two sets of triangles. Gray et al. [5] developed the rolling ball method to generate the gouge-free tool positions. A ball surface with a variable radius was firstly used to approximate a small region of the design surface, and then the cutter was located in this ball. Finally, the local gouge can be effectively avoided. Yan et al. [6] proposed a method for interference checking and avoidance by the intersection between the cutter movement envelope surface and the design surface. The method can realize the interference checking and avoidance for the whole movement path. In addition, Cai et al. [7] solved the global interference detection and correction problem by the proposed method of calculating the minimum distance from the axis of the cutter to the surface. Chen et al. [8] proposed a simple method to obtain the gouge-free tool positions for 5-axis surface machining using non-ball cutter. The local gouge checking was realized by calculating the minimum distance between the cutter's curve and the design surface. But this efficient geometric iterative algorithm was not stable and would be sometimes diverging because of the complicated expression of the cutter's curve and the design surface. Based on this, an improved geometric iterative algorithm to calculate the minimum distance for local gouge checking of 5-axis sculptured surface machining using the toroidal cutter was presented here. The theory of this new algorithm and a computing example are shown in the rest of this paper.

Theory of the improved local gouge detection algorithm

The cutting surface of the toroidal cutter is a torus. The parameters R and r respectively represent the torus radius and corner radius of the cutter, as shown in Fig. 1. Suppose l_{\min} represents the minimum distance between the circular curve K of tool and the design surface S . According to the geometrical symmetry of the torus, the local gouge will occur when the minimum distance l_{\min} is less than the corner radius r . The maximum interference quantity d_{\max} between the toroidal cutter and the surface S can be easily given by

$$d_{\max} = r - l_{\min} . \quad (1)$$

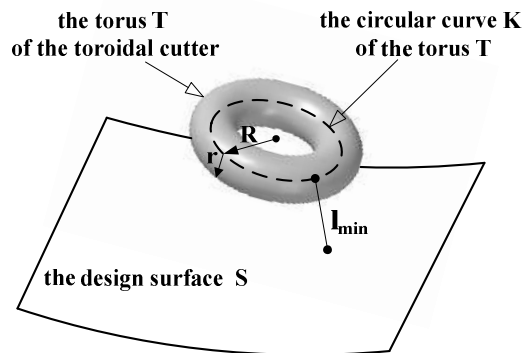


Fig. 1. The local gouge checking principle for the toroidal cutter

As a result, the problem of local gouge checking is translated into that of calculating the minimum distance l_{\min} . In Fig. 2, points P_0 , P_1 , P_2 and P_{\min} on the design surface S are correspondingly projective points of Q_0 , Q_1 , Q_2 and Q_{\min} on the circular curve K of tool. Points P_0 , Q_0 are the initial iterative points, and P_{\min} , Q_{\min} are the final iterative points for the minimum distance. The tangential vectors of Q_0 , Q_1 , Q_2 and Q_{\min} on the circular curve K of tool are relatively expressed as t_0 , t_1 , t_2 and t . And Δt is defined as the increment of parameter t .

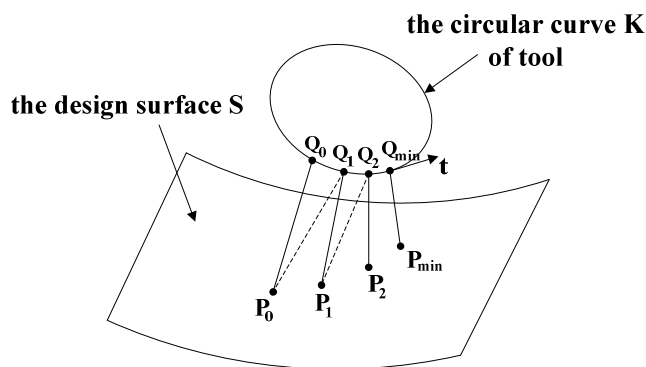


Fig. 2. The improved algorithm for calculating the minimum distance

The procedure of the improved geometric iterative algorithm is shown as follows.

(1) Compute the initial iterative information. By the point projection principle for surface, the minimum distance between the twenty-four iso-parametric points of the circular curve K of tool and the design surface S can be separately obtained. Then the geometric information of points on curve and surface making the distance least is defined as the initial iterative information: Q_0 , P_0 , t_0 and t_0 .

(2) Consider the problem to be that projecting point P_0 onto the circular curve K of tool in this step. At this time, point Q_0 is thought to be initial iterative point, and point Q_1 is thought to be the next iterative point on the circular curve K of tool. So the increment Δt of parameter t of the circular curve K of tool can be given by

$$\Delta t = -\frac{\mathbf{P}_0 \mathbf{Q}_0 \cdot \mathbf{t}_0}{|\mathbf{t}_0 \cdot \mathbf{t}_0|}. \quad (2)$$

(3) As the new parameter t can be given by equation $t = t_0 + \Delta t$, the point Q_1 and the corresponding tangential vector \mathbf{t}_1 can be easily gotten. By using the point projection principle for surface, point P_1 is obtained.

(4) Consider the problem to be that projecting point P_1 onto the circular curve K of tool again. Point Q_1 is thought to be initial iterative point, and point Q_2 is thought to be the next iterative point. Repeat step (2) and (3) and we can get the new iterative information: Q_2 , P_2 , \mathbf{t}_2 and the new parameter t .

The procedure of this improved geometric iterative algorithm is repeated again, until the desired accuracy criteria, $|\Delta t| < 10^{-6}$, is met. Finally, the iterative point on the circular curve K of tool converges to point Q_{\min} , and vector $\mathbf{P}_{\min} \mathbf{Q}_{\min}$ is perpendicular to the tangential vector \mathbf{t} . At the same time, point P_{\min} is also the projection of point Q_{\min} . So $|\mathbf{P}_{\min} \mathbf{Q}_{\min}|$ represents the minimum distance l_{\min} between the circular curve K of tool and the design surface S . By alternately taking full advantage of point projection principle for curve and surface, the improved algorithm to calculate the minimum distance for the local gouge checking is convergent and robust. Then the maximum interference quantity d_{\max} can be eliminated by adjusting the tool orientation.

Example and analysis

The proposed algorithm for local gouge detection is verified by the design surface S described by

$$\begin{cases} S_x = -94.4 + 88.9v + 5.6v^2 \\ S_y = -131.3u + 28.1u^2 \\ S_z = 5.9(u^2v^2 + u^2v) - 3.9uv^2 + 76.2u^2 + 6.7v^2 - 27.3uv - 50.8u + 25v + 12.1 \end{cases}. \quad (3)$$

The parameters of the toroidal cutter are chosen: $R = 8 \text{ mm}$, $r = 5 \text{ mm}$. The parametric equation of the circular curve K of tool can be deduced since the tool positioning strategy is determined. This is not discussed here. At the cutter contact point determined by parameters of surface $u = v = 0.5$, the minimum distance l_{\min} between the circular curve K of tool and the design surface S would be easily calculated by the new algorithm. The final results are shown in Table 1.

Table 1 The calculation results of the example

	X (mm)	Y (mm)	Z (mm)
Q_{\min}	-54.253061	-64.011944	18.817982
P_{\min}	-53.401079	-65.261318	14.158354
l_{\min}		4.898871	

The results in Table 1 show the corresponding points, Q_{\min} and P_{\min} , on the circular curve K of tool and the design surface S making the minimum distance. And the minimum distance l_{\min} is obviously less than the corner radius r . So the local gouge has occurred and needs to be eliminated. Fig. 3 shows the real relative position of all elements in this example. The new algorithm to calculate the minimum distance is quite efficient for local gouge detection.

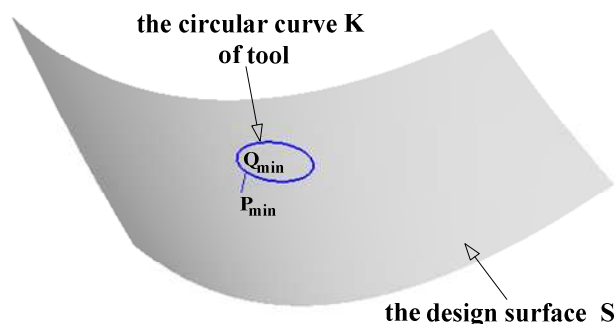


Fig. 3. Illustration of the example

Conclusions

By taking full advantage of the geometric property of 5-axis surface machining using the toroidal cutter, a new method for local gouge detection was proposed here. An algorithm to compute the minimum distance between the circular curve of the toroidal cutter and the design surface was the core of this method. An example showed this new algorithm was stable and easier to obtain the optimal solution.

Acknowledgement

This work was financially supported by Research and Development Program of China Railway Ministry (KMD10003531).

References

- [1] Y.S. Lee and T.C. Chang. Computer-Aided Design 27 (10) (1995), pp. 715-729.
- [2] F. Gao, J.J. Wu, T.Y. Wang and J. Zhou. Journal of Computer Aided Design and Computer Graphics 12 (6) (2000), pp. 435-440. (In Chinese)
- [3] X.G. Xu. Aviation Precision Manufacturing Technology 44 (6) (2008), pp. 28-32. (In Chinese)
- [4] H.M. Zhang, Y.Y. Zhang and G.L. Xiong. Journal of Tsinghua University 38 (2) (1998), pp. 65-68. (In Chinese)
- [5] P. Gray, S. Bedi and F. Ismail. Computer-Aided Design 35 (4) (2003), pp. 347-357.
- [6] S.J. Yan, Y.F. Zhou, X.D. Chen and X.D. Lai. Chinese Mechanical Engineering 17 (17) (2006), pp. 1822-1825. (In Chinese)
- [7] Y.L. Cai, G. Xi, H.Z. Fan and S.J. Wang. Chinese Journal of Mechanical Engineering 38 (9) (2002), pp. 131-135. (In Chinese)
- [8] L.P. Chen, Y. Chen and D.J. Hu. Journal of Shanghai Jiaotong University 38 (7) (2004), pp. 1130-1133. (In Chinese)

Virtual Processing Research on Auto Control Valve Cylinder Mold

Ping Xu^a, Kunpeng Ma^b and Shaofeng Wang^c

Liaoning Technical University, Fuxin, Liaoning, 123000, China

^axupingliaoning@163.com, ^bmkp2006lh@163.com, ^cailing@gmail.com

Keywords: Virtual Machine; NC Simulation; Post Processing; Pro/e; Vericut.

Abstract. Especially from the perspective of geometric simulation, through the combination of CAD/CAM software Pro/e with professional numerical control machine tool simulation software Vericut, achieve the virtual processing of cylinder mold. Numerical control programs will be transferred to the virtual machine tool, producing products meet the requirements. Proving the combination of Pro/e and Vericut for the research of virtual machine technology is a possible method.

Introduction

Through access to relevant information, found Pro/e applied to the study of virtual machine technology is rarely reported. Research based on Pro/e virtual machine technology is imminent. The Vericut software has advantages in machine tool simulation and optimization of tool path. Therefore, the combination of Pro/e and Vericut for the research of virtual machine technology is a new method. The significance can not be ignored.

Study and Processing Objects

In this paper, auto control valve is taken as the research object. The structure of the specimen dimensions is shown in Fig.1 and the geometry shown in Fig.2. Application of Pro/e mold design function design rough cylinder, selecting the generated cavity mold as the processing object which is shown in Fig.3. The material of cavity mold is rectangular blanks of aluminum (190mm×85mm×55mm) .

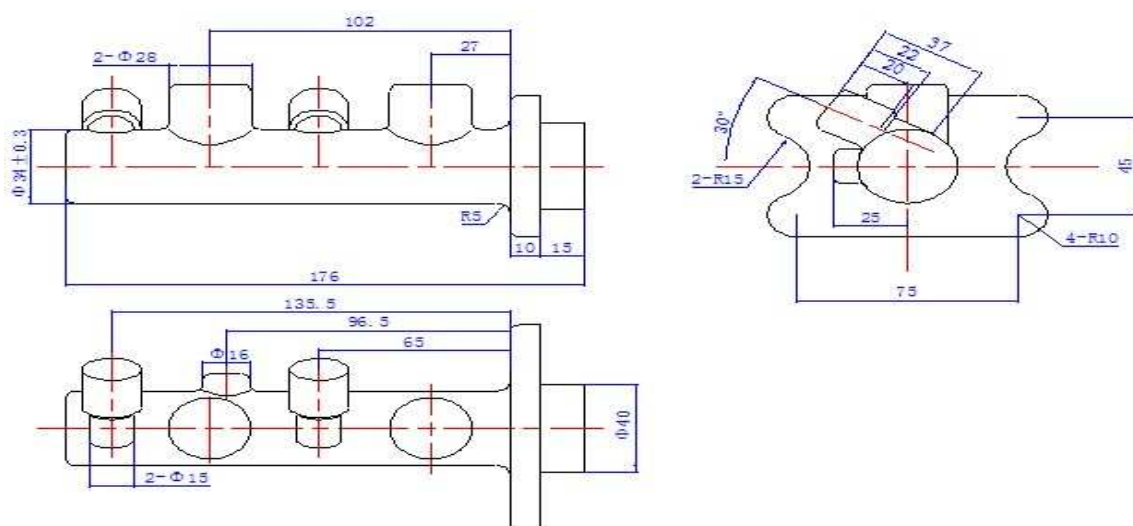


Fig.1 The dimensions of the specimen



Fig.2 Cylinder valve

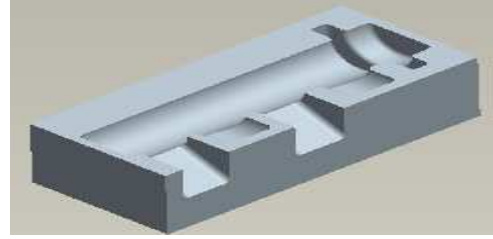


Fig.3 Cavity mold

NC Programming and Post Processing

Process analysis of the cavity mold. The surface of the cavity mold is relatively complex and not continuous so that rational planning tool path is more difficult. The try cut process can easily happen tool collision and other dangerous interference. The surface of the cavity mold requires relatively high quality. According to the structural characteristics of the cylinder cavity mold, preliminary planning the process as follows: rough finish milling, semi finish milling, finish milling. Select spherical milling cutter R4 of high speed steel, the whole process without tool change.

Determination of processing programs and generation of tool path. Into the Pro/e NC machining environment, set machine tools, coordinate system, blanks, cutters, processing parameters. The processing flow chat is shown in Fig.4 [1].

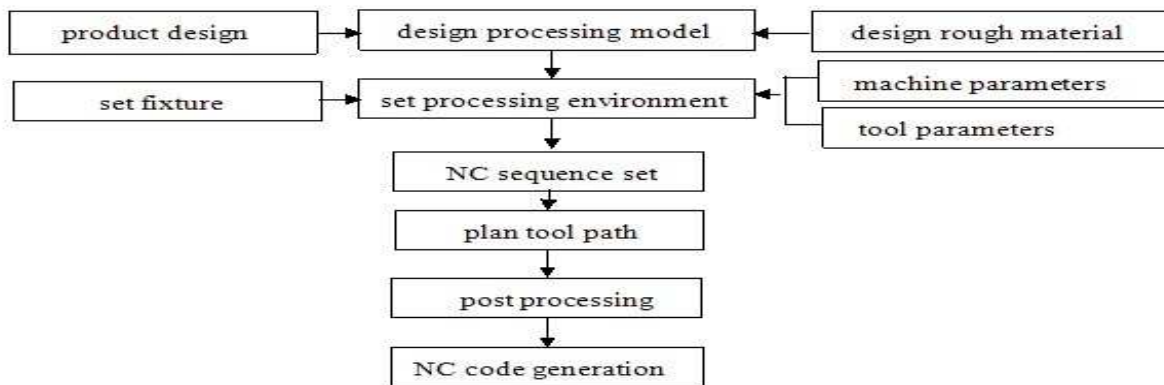


Fig.4 The processing flow chart in Pro/e environment

Tab.1 summarizes the machining scheme of cavity mold. Through the implementation of the programs, get rough finish, semi finish and finish tool path, and finally obtain the CL documentation for each procedure. This document can not be identified by NC machine which must be post processed to generate NC codes that machine tools can be identified.

Tab.1 Machining scheme of cavity mold

processing methods	cutters	spindle speed (r/min)	feed rate (mmpm)	feed per knife (mm)	span (mm)
rough finish	spherical milling cutter R4	1000	200	3	3
semi finish		1200	300	0.5	0.6
finish		1400	600	0.1	0.3

Siemens 802S post processor development. Post processing is a process that tool path is calculated by automatic programming, which can transform the generated cutter location data files into NC programs that can be performed by a specific NC machine. In this paper takes the XKN713 milling machine in our school practice base as the processing platform. XKN713 NC machine tool applies Siemens 802S control system, while Pro/e post-processing module does not have 802S NC post processor. This requires us to develop [2]. To meet the requirements of the control system of Siemens 802S, through the Pro/e NC Post programs post processing procedures. Application of Siemens 802S post processor process the above cutter location files, generating the NC programs that can be identified by machine tool. The rough machining NC program file is shown in Fig5.


```

rough - NoteXpad
File Edit View Help
N0010 T01
N0020 S1000 M03
N0030 G00 X-80.5 Y-45.5
N0040 Z20.
N0050 Z5.
N0060 G01 Z-3. F200.
N0070 X-60.5
N0080 Z20.
N0090 G00 X-12.292
N0100 Z5.
N0110 G01 Z-3.
N0120 X9.708
N0130 Z20.
N0140 G00 X-80.5 Y-42.528
N0150 Z5.
N0160 G01 Z-3.
N0170 X-60.5
N0180 Z20.

```

Fig.5 The rough machining NC program

Modeling of Virtual Machine

Create virtual machine components and assemble. Use Pro/e software to create solid geometry models of each component of machine tool, and convert into IGES format that Vericut software can identify. The 3D models of virtual machine are shown in Fig.6.

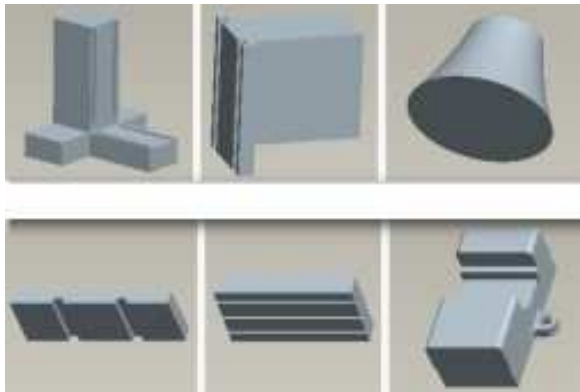


Fig.6 3D model of virtual machine

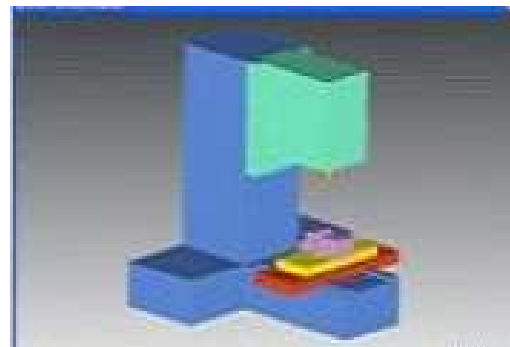


Fig.7 Virtual machine model

The component models will be added to the virtual machine Vericut component tree, application of the relationship of mate, insert, align, etc. to determine the location. Fig.7 shows the virtual machine model [3, 4].

The control system set. After setting the virtual machine model, the machine must be initialized including interference checking, machine trip set and distribution of motion axes. And configure digital control system to the machine so that the machine has the interpretation of numerical codes, interpolation calculation, simulation and other basic functions.

Vericut control system does not have the required control system documents. We can open a close control file of system to find out the difference, after appropriate modifications can be used. Through access to relevant literature, there is a little difference between the company FANUC 0M FANUC control system with the control system of Siemens 802S. There are only different definitions for some G or M function codes, making appropriate modifications can be used for Siemens 802S. Summarize by need to modify or delete G or M function codes and their meanings are shown in Tab.2.

Tab.2 The codes that need to revise or delete

FANUC 0M	code meaning	modify or delete
G20	inch size	G70
G21	metric size	G71
G80	drilling cycle	delete
G81	cancel drill cycle	delete
G28	back to reference point	G74
G43	tool length compensation	delete
G49	cancel tool length compensation	delete
M6	tool change	delete
M30	end of program	M2

The establishment of tool library. Vericut tool library includes cutting tool part, arbor and tool holding part and other information, such information is stored as ".tls" format in the tool library. This paper defines a spherical milling cutter diameter of 8mm, blade length of 60mm, clamping point of 115mm as. The cutter is shown in Fig.8.



Fig.8 Define tool

Virtual machine has 3D models, control systems and cutting tools, which is similar to the actual machine. Then NC programs can be transferred to the simulation tools [5].

Cavity Mold Simulation

Transfer the NC program. Vericut can simulate single or multiple tool path files and can simulate various types of tool path files. So when transferred to tool paths, firstly select the appropriate tool path type. The above post processing generates G code tool path files, so use tool path files G code format.

Virtual machining simulation. When the mold cavity NC programs transferred to virtual machine, you can simulate the work piece in a virtual machine. Through state bar observes the data changes. Fig.9 is a moment chat of rough finish simulation.

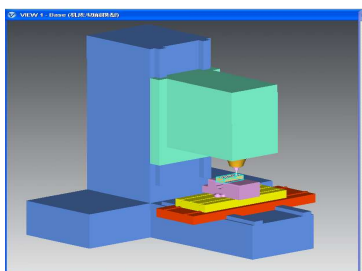


Fig.9 The chat of rough finish simulation

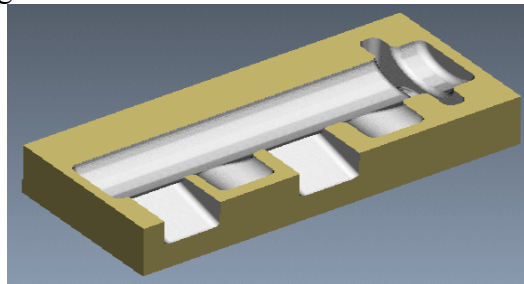


Fig.10 Mold of simulate machining

After virtual machine executes all of the processing procedure, the resulting simulation model is shown in Fig.10. After virtual machining simulation, Vericut will automatically generate a log of ASCII format (.Log) files. Log file contains the simulation errors, warnings and other information.

Test Cutting Experiment

In order to verify the correctness of the work above, we need to have test cutting to the cavity mold. Input the NC programs generated by the virtual machining to XKN713 type CNC milling machine, observe real processing finding that the process does not appear tool collision. The results obtained by the measurement of the shape of the mold cavity and surface quality meet the requirements. To sum up, verify the correctness of simulation of the mold cavity mold. The result of processing experiment is shown in Fig.11.



Fig.11 The result of processing experiment

Conclusion

Through the combination of Pro/e and Vericut software to create a virtual machine model, and transferred numerical control programs into the virtual machine, we realized the simulation process of cavity mold. We also had test cut experiments. Proving the combination of Pro/e and Vericut for the research of virtual machine technology is a possible method.

References

- [1] Jianghong Sui, Xiaolong Huang: Pro/ENGINEER Wildfire CNC Machining Tutorial, edited by Tsinghua University Press (2005)
- [2] Weibing Wang, Jinsheng Wang: Pro/ENGINEER Wildfire Chinese Practical CNC Programming Tutorial, edited by Tsinghua University Press (2003)
- [3] Junfeng Li, Jian Li, Ping Xi: NC Machining Simulation Technique and Application. Computer Simulation Vol. 74(2009), p. 93
- [4] Jian Li: Five-axis NC Machining Simulation(2003)
- [5] Xiang Chen: Research on Modeling and Simulation of Manufacturing System in Virtual Environment. Journal of ZongZhong University (2004), p. 118

Boom System Kinematic Simulation of Truck-Mounted Concrete Pump

Xinxiang Zhou¹, Nannan Ren², Shujun Guo³, Yanling tang⁴, Rongliang Tian⁵

School of Mechanical Engineering and Automation, Liaoning University of Science and
Technology, Anshan, China

E-mail:zhouxxas@163.com

Keywords: Truck-Mounted Concrete Pump; Boom System; Kinematic Simulation

Abstract. In this paper, we study the boom of truck-mounted concrete pump from a company. After analyzing, we determine that the four booms extending horizontally is the most dangerous working conditions. We use the software Solid Works to design three-dimensional entity. With the help of Cosmos Motion which is a part of Solid Works, realizing the kinematic simulation. This paper study and analyze the problems during the simulation process, and collect a series of curves of kinematic simulation, mainly including the place-time curve, velocity-time curve and force-time curve, and analyze these curves detailedly.

Introduction

Concrete pump is especially suitable for vertical transportation in concrete situations, such as high-rise buildings, elevated highways, bridges, dams and underground works such as concrete pouring^[1]. They are mobile and flexible, casting speed, to keep the job site clean, reducing the disadvantages of working strength of workers. Concrete pump (concrete pumps) and the pump has become an indispensable construction equipment. Concrete Pump Truck arm boom is an important component in satisfying the conditions of its features, requiring a simple structure, light weight, to meet strength, stiffness, stability design, and a good dynamic character. Force in the boom for strength and stability of the basic analysis and calculation, people are more concerned about the motion characteristics of the boom.

kinematics Simulation of the Boom System

Through the simulation of Arm movement, you can visually understand the dynamic character of the system is a convenient movement of each member and deputy sports analysis. This article uses Solid Works software plug-ins for mechanical equipment Cosmos Motion Simulation of the motion state.

Concrete pump in practical work, according to site requirements, there are so many conditions because of different kinds of arm stretching way. Select this article, the most dangerous working conditions - all four levels, extended arm, the fourth, the second, and the first arm movements in order to do back when the kinematics simulation.

Based on Solid Works model of concrete pump boom and interference checking

Solid Works basic method of model

The methods using Solid Works to create parts with three-dimensional model are very flexible, the basic creating means include stretch, rotate, scan, and setting. In this paper the main character used in this way is stretch and rotation. After completing the three-dimensional modeling of parts, you assemble all the parts together to form a complete mechanical equipment, machinery and equipment for the motion simulation. In this article, we use Solid Works 2007 software to complete the virtual assembly work of the accessories^[2,3].

Virtual assembly is a link between uses of the computer parts to create a virtual assembly model arm. In the paper, the assembly adopted a bottom-up approach. Figure1 shows the total assembly.

After generating the boom assembly, you check whether there is interference in the boom situation or not. Interference checking is divided into static interference checking and dynamic interference checking. Static interference checking is done here first. Figure2. After inspecting the arm, there is no interference in the boom of the modeling and assembly process is reasonable. Using Solid Works software to boom the motion simulation, you firstly select the appropriate movement accessories for the machinery.



Fig.1 The assembled-drawing of the boom system
Interference Check boom



Fig.2 The manger of the examine intervene
and the examined assembled-drawing

Cosmos Motion mode set to enter the turntable is stationary parts, the rest are moving parts, fuel tanks added to the mobile vice constraints. Figure 3 is a sketch map bounded to add fuel tank numbered 4. Figure 4 is a sketch map after adding constraints. Other steel tank is set in the same way. After adding the corresponding constraint, the boom is imposed the movement. According to campaign requirements, cylinder 4, cylinder 3, cylinder 2, you apply a moving pair of time on each movement with function STEP (TIME, x0, h0, x1, h1), and the expression of the STEP function after its parameters defined is as follows^[4,5].



Fig.3 The sketch map of the appended
restriction for the forth oilcan

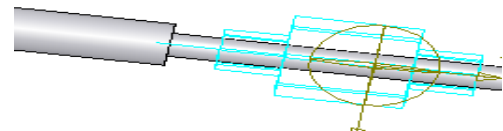


Fig.4 The sketch map of the forth oilcan with
moving restriction

Drive mechanism can be set after a successful motion simulation, which is a key part of this paper. In the course of the simulation, the data used in this paper is all the international system of units, and impose gravity to the machinery. Set the simulation time 200 seconds, 200 frames, and start the simulation. At the same time, animation check box is generating with the emulation mode opened.

After the simulation, the process to prevent the movement interference occurs between components is done to exercise on the movement interference checking. As shown in Figure5, There is no interference in the examination during the campaign. After the motion simulation, the results of the motion simulation need to be acquired in order to further analysis of the mechanical equipment and improvements as well as the results can be saved. In this section, through the plug Cosmos Motion for the second and third arm center of mass, the location of the end of the fourth quarter boom - time curve, the speed - time curve, and accordingly the simulation results are analyzed.



Fig.5 Before the examine intervene

Section II boom position and velocity curves is shown in Figure6,7.

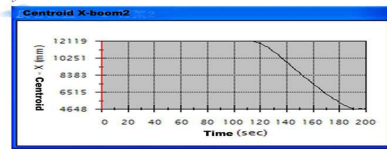


Fig.6 The place-time curve of the center of mass of the second boom

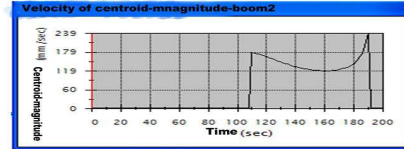


Fig.7 The velocity-time curve of the center of mass of the second boom

It can be seen from the figure, the centric of the boom section II is gradually smaller, and the change is smooth. The speed of the center of mass movement is relatively large at the beginning and end of movement, then it becomes intermediate small and the change smoothly.

Section III arm position and velocity curves is shown in Figure 8,9.

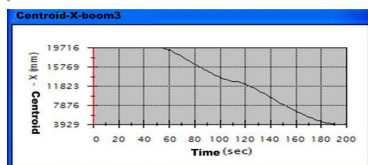


Fig.8 The place-time curve of the center of mass of the third boom

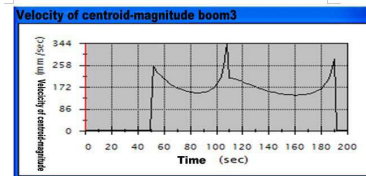


Fig.9 The velocity-time curve of the center of mass of the third boom

It can be seen from the figure, the centric of the third quarter boom is gradually reduced. Center of mass velocity of the boom in the second quarter begins to exercise a great deal, and the speed is the maximum at end of their movement.

IV arm position and velocity curves is shown in Figure 10,11.

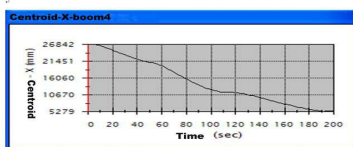


Fig.10 The place-time curve of the center of mass of the forth boom

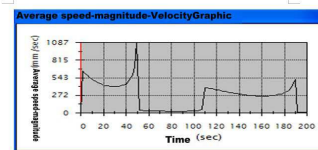


Fig.11 The velocity-time curve of the center of mass of the forth boom

Section IV can be seen from the figure. The centric of the boom gradually decreased in the second and third carriage which begins to exercise a smaller float, but the transition is smooth. Generally speaking, the change is relatively stable. The speed of the end of the fourth arm, arm themselves does back in the fourth quarter action, it is the curve; in the movements of the third arm, it almost changes to a linear change; in the movements of the second quarter arm, also it is into the curve. After analysis, a linear change in velocity is because the fourth quarter. After recovery boom, booms near the end of the third quarter when the boom is for movement is around the back of the rotation axis. Therefore, a speed change tends to be line. And the boom has a peak speed of movement in the third quarter. The results of the first, the second, the third the fourth-arm force

simulation are shown in Figure 12-18 (omission). From the figure we can see, the force linked by the boom numbered 1 and the turntable and the force linked by the arm strength and the cylinder numbered 1 are at the beginning of exercise to be a maximum value and then gradually decreased. At the end of the boom in the fourth quarter and III sports movement, there is a smaller float. And the transition is smooth.

It can be seen from the figure, with the crank arm 1 junction force decreases to an upright position II which the arm movement is set, and then has a smaller fluctuations. Also it can be seen from the figure, the arm strength of both the boom 1 and tank 2 connected, and arm 1 and arm 2 is the largest movement at the beginning and then gradually reduces to a minimum when the arm moves to the Section vertical position. Section II of the boom is up and then gradually increases to full time combination. From the above chart shows, the force and the connection with both the boom 2, 3 and arm 3, 4 are a maximum value at the beginning. In summary, the forces is related to the boom cylinder's the velocity and acceleration of the start and stop. Greater acceleration is, the greater the force arm is; when all the forces of the boom is at the beginning that is all four level arms are extended, there is the maximum. In this paper, the pace for the fuel tank is set $18.2m/s$ in the simulation process. This study also carries out finite element arm strength and fatigue analysis.

Conclusion

1. I build a concrete pump platforms boom system model on the basis of Solid Works, and examine the movement of the boom system and the interference. In the assembly model based on the realization of the boom of the computer simulation, an objective description of the arm frame motion is done, and provide a reference for the actual improvement device.

2. To Use plug-Solid Works Cosmos motion in kinematics simulation of the boom system, we access to the center of mass of each arm speed, position, curve and force curves, and prove the actual device design is reasonable, and make sure of the static analysis position.

3, virtual prototyping technology is based on digital computer simulation system model. To substitute the virtual prototype of the system of physical prototype, innovative design, testing, evaluation, system design is carried out in order to solve the various problems and virtual prototyping technology provides a powerful means of solution.

4. In the simulation process, this is the use of STEP function to control fuel tank to simulate the movement of tanks, but the stopped state of the fuel tank can not simulate the real motion, and the cylinder pressure and other parameters can not be simulated. If the actual parameter can be used to control the fuel tank in the hydraulic part, we get more accurately statistic reflected the movement of the boom, and improve simulation accuracy.

References

- [1] Wu Xuesong . Domestic concrete pump car development. [J] building survey Mechanization Vol (3),(2004), p.9-10
- [2] Yin L.Young and Michael R. Motley. Three-Dimensional Numerical Modeling of the Transient Fluid-Structural Interaction Response of Tidal Turbines[J]. Offshore Mech. Arct. Eng. (2010), 132, 12
- [3] Pierre Leroy, Nouredine Atalla, and Alain Berry. Three dimensional finite element modeling of smart foam[J]. Acoust. Soc. Am. (2009), 126, 2873-2885
- [4] Zheng changSong, Guo Jun. Solid Works 2006 Chinese Mechanical Design - Advanced Application [M]. Beijing: China Machine Press, (2006).200 ~ 209,215 ~ 232
- [5] Zhang Jinxi, Guo Xueqin. Solid Works and Cosmos Motion Machine Simulation Design [M]. Beijing: Tsinghua University Press, (2007).10 ~ 14

Research on Assembly Variant Design Based on Complex Network

Kun Xu^a, Fuyun Liu^b and Guang Li^c

School of Mechanical & Electrical Engineering, Guilin University of Electronic Technology, Guilin, 541004, P.R. China

^axukun0608@163.com, ^bliufuyun310@yahoo.com.cn, ^c286123275@qq.com

Keywords: Mass-Customization; Assembly Variant Design; Standard Component; Complex Network.

Abstract. To realize the variant design of assembly containing standard component, both type characteristics and parameter characteristics of standard component are studied. With complex network theory, the parameters of assembly are analyzed. A method of assembly variant design is presented. UG (Unigraphics) is re-developed with VC++ and UG/Open. A variant design module is developed, and assembly variant design is realized.

Introduction

With the development of individual requirement, MC (Mass Customization) technology has already become a main current production model of enterprises. And variant design is one of the key technologies of MC. Because it is difficult to analyze the dimension relationships between the components contained by assembly, the assembly variant design technology developed slowly. Because the dimension values of standard component are usually discrete, it is more difficult to realize variant design of assembly containing standard component. In this paper, we will discuss the variant design of assembly containing standard component.

Analysis on Product Parameter Correlative Relationship Network

A network is a set of items, which we will call node or sometimes nodes, with connections between them, called edges. Systems taking the form of networks abound in the world. Examples include the Internet, the World Wide Web, science collaboration network, movie actor collaboration network, metabolic networks, neural network, etc. There are many kinds of network in mechanical manufacturing field, such as part relation network of product family, supply chain network, etc. Extensive attentions have been paid in the studies of network, and some achievements were obtained [1-5]. In this paper, we apply the complex network to variant design field, and parameter correlative relationship network of product is built. In a parameter correlative relationship network, each edge has its relevant weight, and the weight represents the scaling from the start point to the end point. For example, $A=B+C*0.7$, it shows that the weight from A to B is 1, and the weight from C to A is 0.7 [6]. The parameter correlative relationship network of part and assembly are analyzed as follows.

Dimension parameters of standard component. Taking bearing as an example, the dimension parameters of inside and outside rings of bearing are analyzed as shown in Fig. 1. The left of Fig. 1 is the dimension parameters analyzing result of inside ring of bearing. And the right of Fig. 1 is the dimension parameters analyzing result of outside ring of bearing.

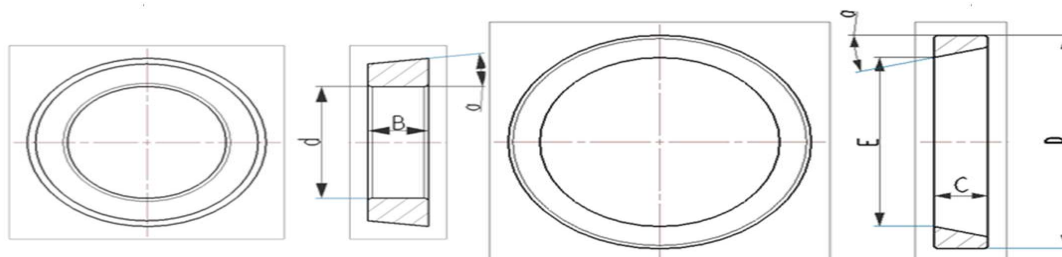


Fig. 1. Dimension parameters of inside and outside ring of a bearing

POSI (Parameters of standard interface) is defined as follow: In an assembly, if two components have dimension parameters to match each other, the assembly dimension parameters will be assigned the same name. Both POSI of the inside ring model and outside ring model as shown in Fig. 1 are set equal to 7211, and parameters are assigned as follows.

(1) Inside ring(named *zc_nt*) parameters analyzing, type parameters:

$B = \text{if}(\text{POSI}=7211)(21)\text{Else}(\text{if}(\text{POSI}=7213)(23)\text{else}(24)); a = \text{if}(\text{POSI}=7211)(15.106/2)\text{else}(\text{if}(\text{POSI}=7213)(15.106/2);\text{else}(15.642)); d = \text{if}(\text{POSI}=7211)(55)\text{else}(\text{if}(\text{POSI}=7213)(65)\text{else}(70)); E = \text{if}(\text{POSI}=7211)(84.197)\text{else}(\text{if}(\text{POSI}=7213)(101.934)\text{else}(105.748)); T = \text{if}(\text{POSI}=7211)(22.75)\text{else}(\text{if}(\text{POSI}=7213)(24.75)\text{else}(26.25)). L = T - B.$

(2) Outside ring(named *zc_wt*) parameters analyzing, type parameters:

$C = \text{if}(\text{POSI}=7211)(18)\text{else}(\text{if}(\text{POSI}=7213)(20)\text{else}(21)); a = \text{if}(\text{POSI}=7211)(15.106)\text{else}(\text{if}(\text{POSI}=7213)(15.106)\text{else}(15.64)); D = \text{if}(\text{POSI}=7211)(100)\text{else}(\text{if}(\text{POSI}=7213)(120)\text{else}(125)); E = \text{if}(\text{POSI}=7211)(84.197)\text{else}(\text{if}(\text{POSI}=7213)(101.934)\text{else}(105.748)).$

(3) Assembly parameters (named *ZC*) parameters analyzing.

$\text{POSI}=7211, zc_wt::\text{POSI} = ZC::\text{POSI}, zc_nt::\text{POSI} = ZC::\text{POSI}$. Both correlative relationship of types and parameters of the bearing are described in the network as shown in Fig. 2.

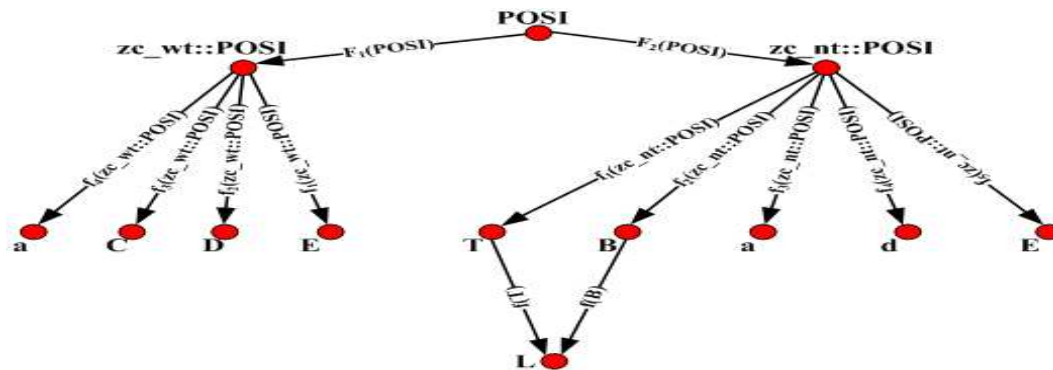


Fig. 2. Correlative relationship network of types and parameters of bearing

In Fig. 2, when a edge starts from a type node, its weight will be determined through a function, and the value of this function will be determined through conditional execution, i.e. a set of optional types are included in this function, such as: if $\text{POSI}=7211$, $dc=58$; and if $\text{POSI}=7213$, $dc=68$; else $dc=73$, so this function contains three values: 0.008043267, 0.009427422 and a variable value.

Type correlative relationship network of assembly. Fig. 3 is a description of a slow-speed-shaft of a gear box.

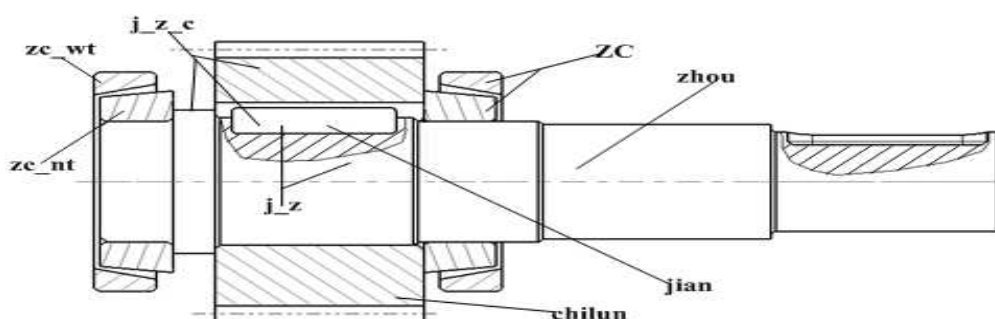


Fig. 3. Slow-speed-shaft of a gear box

The meanings of symbols in Fig. 3 are as follows: *zc_nt*—the inside ring of bearing; *zc_wt*—the outside ring of bearing; *ZC*— bearing, it is assembled by *zc_nt* and *zc_wt*; *j_z_c*— it is a component assembled by shaft, key and gear; *j_z* — it is a component assembled by key and shaft; *zhou*— shaft; *jian* — key; *chilun*— gear.

The correlative relationship network of the slow-speed-shaft is built, it is shown in Fig.4.

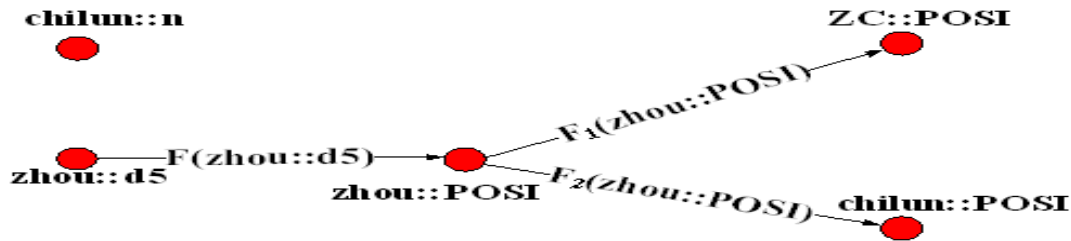


Fig. 4. Correlative relationship network of slow-speed-shaft of a gear box

As shown in Fig. 4, there are two parameters such as chilun::n and zhou::d5 can be considered as variable parameter in this assembly. To realize variant design, the variable parameter can be modified flexibly according to the request of customer. And the parameters such as zhou::POSI and chilun::POSI can be considered as derived parameter. The value of derived parameter can be derived from the variable parameter. For example, we can obtain the derived parameter zhou::POSI through the following rule. $POSI = \text{if}(d5 > 40 \& \& d5 \leq 45)(7211) \text{else}(\text{if}(d5 > 50 \& \& d5 \leq 55)(7213) \text{else}(7214))$.

The parameter ZC::POSI and chilun::POSI can be derived from zhou::POSI. So ZC::POSI and chilun::POSI can be derived from zhou::d5.

Parameters Transferring and Calculating Methods Based on Network Statistics

The meanings of network statistics. Product parameters correlative relationship network is a directed loop-free network, so the number of edges pointing to the same node can be defined as in-degree of this node, and edges starting from the same node can be defined as out-degree. When the in-degree of one node equals to its out-degree, this node can be defined as a single node, if there is a complete network can be divided into two or more individual networks once one of the nodes in it was removed, this node can be defined as a cut node. If there is a complete network can be made up just by a single edge between two sub-networks, this edge can be defined as a bridge. In order to ensure the completeness of a network, cut nodes and bridges are key parts, especially when messages are being transferred, for the smoothness of transferring is determined by them. Type parameters of standard components are cut nodes here. The most meaningful purposes of network statistics are to make analyzing of key nodes more conveniently and to realize product variant design more effectively [2].

Transferring and calculating methods of type and dimension parameters. In master model of standard component constructed in UG NX, many dimension parameters can be derived from its related type parameters, and all of these nodes have in-degree. The parameters of nodes with in-degree can not be modified directly, their value can only derived from variable nodes having out-degree edge connected to this node. In assembly variant design, it is needed to determine the values of dimension parameters and assemblage parameters. In variant design, it is critical to calculate the main dimension parameters of product from the type parameter or variable parameter of product. Eq. 1 is proposed in reference [7], which can be used to determine the transferring way of dimension parameters in assembly variant design.

$$D = d \prod_{j=1}^k w_{j,(j+1)} \quad (1)$$

Where D represents the derived dimension, d represents the variable dimension, k represents the number of nodes linking d and D; $w_{j,(j+1)}$ represents the weight from node j to node j+1. Based on Eq. 1 and the type parameter of standard component, a dimension transferring equation is presented in this paper, and it is shown as Eq. 2.

$$D = [P \times f(P)] \prod_{j=1}^k w_{(j+1),(j+2)} \quad (2)$$

In Eq. 2, D represents the dimension will be derived, p represents the type value of part; k represents the number of nodes linking p and D; $f(P)$ represents the weight from the second node

to p , which is the set of variant weighted values; $w_{(j+1),(j+2)}$ represents the weight from $j+1$ to $j+2$. To obtain the transferring way of type parameters, Eq. 3 is proposed in this paper, which is based on Eq. 2.

$$P_c = P_p \prod_{j=1}^k f_{j,(j+1)}(P) \quad (3)$$

In Eq. 3, P_c represents the type value of c , and c is a component; P_p represents the prime type value of product; k represents the number of nodes linking P_p and P_c ; $f_{j,(j+1)}(P)$ represents the weight from node j to node $j+1$.

In the process of variant design, sometimes there are parameters must be derived from two or more parameters, for example: P_1 must be derived from P_2 and P_3 . In order to deal with this situation, Eq. 4 is proposed in the reference [6]:

$$D = \sum_{i=1}^l \left(\prod_{j=1}^k w_{j,(j+1)} \right) d_i \quad (4)$$

In Eq. 4, l represents the number of dimension parameters which affecting the value of the specified derived dimension parameter. Every other parameter has the same meaning as described in Eq. 1. But Eq. 4 can only be applied to just one situation, and in this situation, one parameter can only be derived from other two or more parameters. On the contrary, Eq. 4 is not fit for the situation when a type derived from a few types. The reason is that to derive a type from other types, it can not be derived through arithmetical operation, but only be obtained through conditional execution. For example:

$P4::POSI = \text{if}(P1::POSI=7211 \&\& P2::POSI=7213 \&\& P3::POSI=6201)(7211) \text{else}(7212).$

As it is shown in this expression, only when P_1 , P_2 and P_3 get the values as required at the same time, can the type value P_4 be changed from 7212 to 7211, type value 7212 is its original type value. In order to deal with this problem, a mathematical expression is given here, and it can be used to calculate transferring types in this situation.

$$\left. \begin{array}{l} f(P_1) \\ \dots\dots\dots \\ f(P_n) \end{array} \right\} \Rightarrow f(P_m) \quad \left. \begin{array}{l} \dots\dots\dots \\ f(P_i) \\ \dots\dots\dots \\ f(P_x) \\ \dots\dots\dots \\ f(P_k) \end{array} \right\} \Rightarrow f(P_x) \quad \left. \begin{array}{l} \dots\dots\dots \\ \dots\dots\dots \\ \dots\dots\dots \end{array} \right\} \Rightarrow P_c \quad (5)$$

In Eq. 5, all of the edges start from the node P_n , and $f(P_n)$ are the weight function of edges start from node P_n , P_c represents the type will be derived.

Steps of assembly variant design. The steps of assembly variant design are as follows: (1) To build parametric model of parts with CAD software and to analyze dimension parameter and assembly parameter of the model. Then the packaged and the unpackaged parameters can be obtained; (2) To assemble the parts together and obtain parametric model of assembly and to analyze the parameters of assembly. The packaged parameters can be packaged into the type of standard component according to conditional expression; (3) To construct correlative relationship network of product types. The transferring way between product types in the correlative relationship network can be analyzed; (4) To analyze customer's requirements and the correlative relationship network, and to determine the value of every variable parameters; (5) With the variant design module, to modify the value of variable parameters according to step (4), and then to rebuild the model of assembly. The assembly variant design is realized.

Conclusions

In this paper, we can obtain some conclusions as follows:

(1) Other parameters of the standard component can be derived according to the type parameter of the standard component. And assembly variant design can be realized with the discrete value of the type parameter of standard component.

(2) The complex network theory is introduced into the parameter analyzing field, and the efficiency of parameter analyzing is improved.

(3) An assembly variant design module is developed by programming, and the assembly variant design is successfully realized.

Acknowledgments

This work is supported by National Natural Science Foundation of China (50865002), Guangxi Key Laboratory of Manufacturing System & Advanced Manufacturing Technology (07109008_017_Z, 09-007-05_008) and Guangxi Education Department Foundation (0815). The authors would like to acknowledge the many helpful suggestions of anonymous reviewers of this paper.

References

- [1] Albert R, Barabasi A L: submitted to Journal of Review of Modern Physics, Vol. 74(1):47-97 (2002)
- [2] Hong-an Che, Ji-fa Gu: submitted to Journal of System Engineering Theory and Practice. (2004)
- [3] NEWMAN M E J: SIAM Review SIAM Review. (2003)
- [4] Jin-shan Wu,Zeng-ru Di: submitted to Journal of Progress in Physics. (2004)
- [5] Buckley,F. Lewinter,M. (translated by Hui-ba Li, Feng-qin Wang) in: *A Friendly Introduction to Graph Theory*[M]. Beijing: Tsinghua University Press,2005.
- [6] Xiao-lin Deng. in: *Part Variant Design Methods Based on Parametric Technology*[D]. Guangxi: Guilin: Guilin University of Electronic Technology, 2008.
- [7] Fu-yun Liu, Guo-ning Qi, Qing-hai Yang: submitted to Journal of Chinese Journal of Mechanical Engineering. (2006)

Line Segment Nearest Neighbor Query of Spatial Database Based on R*S-Tree

Dianzhu Sun^a, Yongwei Sun^b, Xincai Kang^c, and Yanrui Li^d

School of Mechanical Engineering, Shandong University of Technology, Zibo 255091, China

^adianzhus@sdut.edu.cn, ^bsunyongwei2004@126.com, ^ckangxincal@126.com,
^dliyanrui@gmail.com

Keywords: Spatial Database; K-Nearest Neighbor; R*S-Tree; Dynamic Spatial Indexing Structure; The Hollow Ball, Sorting

Abstract. An algorithm for nearest neighbor query of Line Segment based on the R*S-tree is proposed. The dynamic spatial indexing structure for spatial line segments was constructed based on the R*S-tree, and the k -nearest neighbor of the target line segment were obtained by the hollow ball. The distance between the target line segment and the neighbor line segments was computed, and the neighbor line segments were sorted by the distance. The result shows that the algorithm can obtain nearest neighbor line segment accurately and effectively and has the strong adaptability of data type.

Introduction

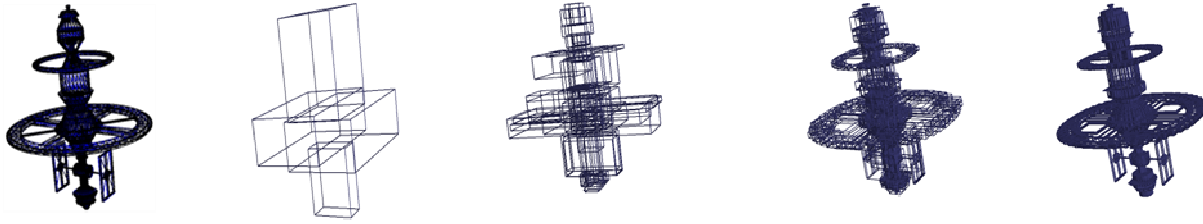
Nearest neighbor query is one of the core technology of the spatial database, and can effectively solve some problems abstract as points or line segments in space, and has important practical value, and attention by technical staff of the computer aided design and manufacturing, geographic information system, multimedia system and digital earth etc.

According to the abstract degree, nearest neighbor query has three main categories: nearest neighbor query between point and point, nearest neighbor query between point and line segment, and nearest neighbor query between line segment and line segment. At present, the former two nearest neighbor queries have received more research, and have formed a number of sophisticated algorithm^[1-3]. Nearest neighbor queries for line segment with less study, article [4] nearest neighbor query by the relationship of the plane point and plane line segment, the algorithm can solve same problems which can't abstract as points in the two-dimensional, such as the nearest freeway on both sides of the object, the nearest farm or factory on both sides of the river, etc, but can't solve the problems in three-dimensional space.

To solve these problems, an algorithm for nearest neighbor query of Line Segment based on the R*S-tree is proposed. The dynamic spatial indexing structure for spatial line segments was constructed based on the R*S-tree, and the k -nearest neighbor of the target line segment were obtained by expand hollow ball. The distance between the target line segment and the neighbor line segments was computed, and the neighbor line segments were sorted by the distance. The result shows that the algorithm can obtain nearest neighbor line segment accurately and effectively and has the strong adaptability of data type.

The Construction of R*S-tree for line segments. R*S-tree^[5-8] is a kind of spatial balanced tree and improved from R*S-tree, which use the node MBR (Minimum Bounding Rectangle) to organize the neighborhood relations between data objects, with good clustering properties^[8] for the multi-dimensional data. Spatial line segment is usually formed from a large number of discrete lines. If the R*S-tree is established for spatial line segments, the quick acquisition of the intersection line segments, can be realized, and thereby efficiency is improved effectively.

As the triangular mesh model contains a large amount of line segments, which component triangles. Take the line segments of mesh as the data nodes, as shown in Fig.1(a), using dynamic index construction method in article[5], the R*S-tree of line segments is established easily.



(a) Mesh model of satellite (b) The root node (c) The second layer inner nodes (d) The third layer inner nodes (e) The data nodes

Fig.1. The spatial index structure of satellite model

Fig. 1(a) shows the mesh model of satellite, Fig. 1(b)-(e) shows the R*S-tree dynamic spatial index structure for line segments. Fig. 1(b) shows the root node of R*S-tree, Fig. 1(c) and Fig. 1(d) show the inner nodes, Fig. 1(e) shows the data nodes of R*S-tree, each data node contains a line setment.

Calculate the distance between the line segments.

The distance between the point and line segment. For any point P and any line segment L in the three-dimensional space, make the vertical line of the line segment L through the point P , the pedal is O . If the pedal O is located on the L , the minimum distance between the point P and line segment L is the distance between the point P and point O ; if the point O in the extension line of L , computing the distance between P and the two endpoints of L , whichever is less as the minimum distance between the point P and the line segment L .

The distance between the line segments. Make the vertical plane P_A and P_B through the endpoint of target line segment L . According to position relationship between the target line segment and others, as shown in Fig.2, the calculations of minimum distance between line segments can be divided into the following situations:

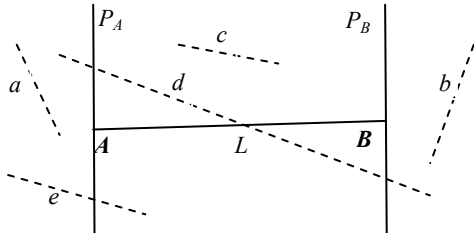


Fig.2. The position relationship between the line segments

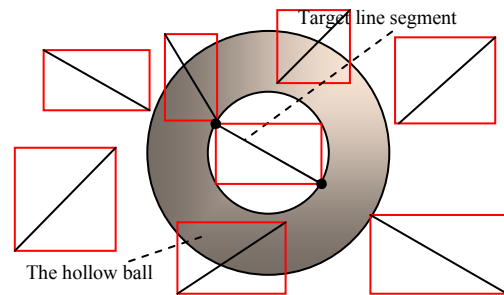


Fig.3. The expand hollow ball

1) If the line L_1 in the left side of P_A or right side of P_B , such as the line segment a and b , the minimum distance between L and L_1 is the distance between endpoint A or B and the line segment L_1 ;

2) If the line L_1 between the P_A and P_B , such as line segment c , projects L_1 onto the P_A , and calculate the minimum distance between endpoint A and the projection line, as the minimum distance between L and L_1 ;

3) If L_1 through the P_A or P_B , or both through P_A and P_B , such as line segment d and e , projection the part of line segment between the P_A and P_B onto the P_A , computing the minimum distance between endpoint A and the projection line, and calculate the distance between the endpoint A or B and the line outside of the plane P_A or P_B , whichever is less, as the minimum distance between L and L_1 .

Access the neighbor Line Segments. According to the spatial neighbor relationship between nodes of the R*S-tree, accessing the k -nearest neighbor line segments of the target line segment based on the expand hollow ball, and computing the minimum distance by the relationship between the neighbor line segment and the target line segment, and sorting for neighbor line segments by the minimum distance. Finally, accesses the nearest neighbor segment.

The expand hollow ball. In the process of accessing the k -nearest neighbor based on the expand hollow ball, needs to use the area of hollow ball, as shown in Fig.3, let point P to any point in space, the center of the hollow ball is c , outer diameter is r_2 , diameter is r_1 , and the area of hollow ball definitions:

$$S(c, r_1, r_2) = \{p | r_1 \leq \|p - c\| \leq r_2\} \quad 1)$$

Nearest neighbor query of Line Segment. Accessing the k -nearest neighbor of target line segment based on the expand hollow ball, as shown in Fig.3, taking the initial center of the hollow ball is the bounding box center of the target line segment, $r_1=0$, and $r_2 = r_1 \sqrt{\frac{k}{M}}$, where M is the number of the largest sub-nodes of R*S-tree, specific steps are as follows:

- 1) Initialize auxiliary sequence V ;
- 2) Input the root of the R*S-tree;
- 3) If the input node is a leaf node, for its each data node, added into the sequence V ;
- 4) If the input node is the root or internal node, computing the minimum distance d between the node's bounding box and the point c , if $d < r_2$, then cycle access the current node's child nodes, recursively, if $d > r_2$, return;
- 5) If the number of line segments in the sequence V is more than k , sorting for the line segments by the distance from the target line segment;

6) If the number of line segments in the sequence V is less than k , then order $r_1=r_2$, $r_2 = r_2 \sqrt{\frac{k-N}{N}}$, where N is the number of line segments in the sequence V , return 2).

Above steps use the algorithm of the expand hollow ball to access the k -nearest neighbor of target line segment, and sorting for the neighbor line segments by the distance between the neighbor line segment and target line segment. The first data of the sequence V is the nearest line segment from the target line segment, and the last data is the furthest neighbor line segment from the target line segment. The sequence V can use for effective solution the nearest neighbor query abstract for the line segment in the two-dimensional or three-dimensional space.

Time complexity analysis. The number of line segments in the spatial database is n , using this article algorithm for nearest neighbor queries for all line segments, the time complexity analysis is as follows:

1) Let the number of the largest sub-nodes of R*S-tree node is M , and tree's layer $L = \frac{\lg n}{\lg M} + 1$, and the time complexity of construction the dynamic spatial index structure of R*S-tree is $nM(L - 1) = n \frac{M \lg n}{\lg M} = O(n \lg n)$;

2) The time complexity of nearest neighbor query based on the extended hollow ball is $O(\delta M^{L-1})$, where δ is the number of range queries for target line segment bounding box, the time complexity of sorting for neighbor line segments is $O(\delta^2)$, where $\delta \ll n$.

Therefore, the time complexity of this article is $O(n \lg n) + O(\delta M^{L-1}) + O(\delta^2) \approx O(n \lg n)$

Examples of Application. To validate the applicability for spatial data of this article, extraction the edges information of mesh to form the space line segment sequence, as shown in Fig.4, construction of dynamic spatial index structure based on the R*S-tree for line segments, and query the k -nearest neighbor for the target line segment, where $k=26$. As shown in Fig.4, the red line segment is the target line segment, and the green line segments are neighbor line segments. As the time of a single nearest neighbor query is very short, nearest neighbor query for all line segments of the model, a total of 5986 line segments, the running time is 0.63s, the algorithm of article 4 for line segments nearest neighbor query based on the distance between the point and line segment in the plane, can't query neighbor line segments in the three-dimensional.

Nearest neighbor query for a set of collection of line segments, the trend of the query time increases with the number of line segments as shown in Fig.5. From the figure we can know, nearest neighbor query for line segments from the same model, the running time of this article is less than article 4, and the more the number of line segments, the higher the relative efficiency of this article.

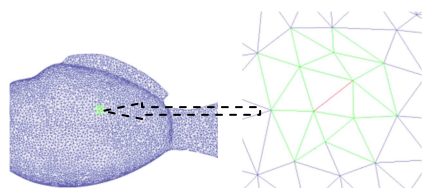


Fig.4. Nearest neighbor query line segment

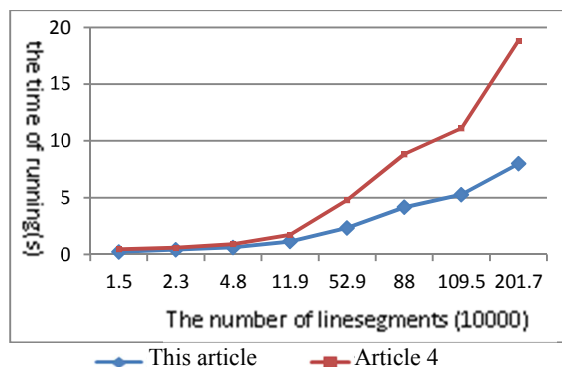


Fig.5. The running time of this article and article 4

Conclusions

Contrasted with other related algorithms, this algorithm has several characteristics as follows:

- 1)The neighbor line segments query based on neighbor relations of R*S-tree nodes, which can effectively deal with the spatial databases line segment data, adaptable;
- 2)Neighbor query by the expand hollow ball, effectively reduce the search range of data, and improve the efficiency of nearest neighbor query of line segments;
- 3)Computing the minimum distance between line segments by the position relationship between the neighbor line segment and the vertical plane of target line segment, computation is fast, and easy to implement.

Acknowledgements

National Natural Science Foundation-funded project (51075247).

References

- [1].Bespamyatnikh S, Snoeyink J. Queries with segments in voronoi diagrams[C]. Proc of the 10th Annual ACM-SIAM Symp on Discrete Algorithms. Baltimore: ACM/SIAM, 1999: 1222129
- [2].Y.F. TAO, Dimitris P, Qiongmao S. Continuous nearest neighbor search[C]. Proc of the 28th VLDB Conference. San Francisco: Morgan Kaufmann, 2002: 2872298
- [3].H.B. HU, Dik Lun L. Range nearest neighbor query[J]. IEEE Trans on Knowledge and Data Engineering, 2006, 18(1): 78291
- [4].Z.X. Hao, Y.D. Wang, Y.B. He. Line Segment Nearest Neighbor Query of Spatial Database[J]. Journal of Computer Research and Development, 2008, 45(9): 1539-1545. In Chinese
- [5].D.Z. Sun, Y.R. Li, C.Z. Zhu, et al. Node splitting algorithm for R*-tree based on united expression of all geometry objects[J]. Journal of Huazhong University of Science and Technology(Nature Science Edition), 2010, 38(2): 55-58. In Chinese
- [6].D.Z. Sun, Z.X. Zhu, Y.R. Li, et al. Research and application of surface feature analysis for scatter data points[J]. Chinese Journal of Mechanical Engineering, 2007, 43(6): 133-136. In Chinese
- [7].Q. Zhu, J. Gong, Y.T. Zhang. An efficient 3D R-tree spatial index method for virtual geographic environments[J]. ISPRS Journal of Photogrammetry and Remote Sensing, 2007, 62(3): 217-224
- [8].D.Z. Sun, C.Z. Zhu, Y.R. Li, et al. Algorithm of Local Model Reference Data Querying for Scattered Points[J]. Transactions of the Chinese Society for Agricultural Machinery, 2009, 5: 218-221. In Chinese

Study on the Optimum Choice of Cutting-Tools in NC Machining Based on the Polychromatic Sets Theory

Enfu Liu ^{1, a}, Xiaoyang Liu ^{1, b}, Yixiang Fang ^{1, c} and Zongbin Li ^{2, d}

¹ College of Mechanical and Electronic Engineering Hebei University of Science and Technology
Shijiazhuang, Hebei Province, China 050023

² State Key laboratory for Manufacturing System Engineering Xi'an Jiaotong University Xi'an,
Shanxi Province, China 710049

^aliuef_60@yahoo.com.cn, ^blxy_841211@163.com, ^cfang_yixiang@163.com,

^dlzb9910@mail.xjtu.edu.cn

Keywords: The Choice of Cutting-Tools; Polychromatic Sets; Box-Type Parts; Fuzzy Optimization

Abstract. Based on the polychromatic sets theory, a relational model of cutting-tool choice was established, which was shown with a contour Boolean matrix. Through the coloring logical operation, the cutting-tools candidate set was calculated to meet machining conditions. With the candidate cutting-tools set, the fuzzy optimization was made for every part feature. And with considering the effects of the time of cutting-tool exchange, processing sequence and other relevant information for the selection of cutting-tool, the choice of cutting-tools is optimized as a whole during machining.

Introduction

Tools selection is one function of CAPP system. It is a key step of machining process, and it is directly related to the surface quality and machining cost.

Optimizing selection of cutting-tool is to choose "optimal" cutting-tool from the tool data base, but it doesn't consider the influence of the whole processing for tools. Due to the machining scope of the tool is often overlapping, so the machining scope of cutting tools which are chosen as the "optimal" principle is usually a small part of machining scope. Almost every face is corresponding with a different tool, which leads to a great many cutting-tools when machining box parts. For the time of cutting tool exchange is much longer than the time of the workbench turning, and to improve the efficiency, the purpose of optimizing selection of cutting-tools is trying to turn the workbench instead of exchanging the cutting tools to reduce the number of cutting-tool. In a word, with the effects of the time of cutting tool exchange, processing sequence and other relevant information, the choice of cutting-tools is optimized as a whole during machining.

Establishing relational model

Polychromatic sets theory (TPS) [1,2] is proposed by Pavlov V.V. who is a Russian professor in 1995, and is a new information processing tools.

Optimizing selection of cutting-tool is hierarchical process, which is progressively realized based on the relational model established information according to part feature information to find the reasonable cutting-tool contains attributes (tools type, material, etc.), as shown in Fig 1. Line segment is used to connect layers, while " \wedge " shown "close" relationship. Based on polychromatic sets, the tools attributes named as elements have unified color and individual color, and elements and sets themselves can be described by coloring, which can describe well the relationship between layers. Thus we can use the polychromatic sets as a set of reasoning mechanism of tools attribute choice to select the reasonable tools[3].

Through using polychromatic sets, the relationship model of machining parts, parts type, and production, the relationship model of common tools material and machining parts material, the relationship model of machining parts and the processing scope of cutting-tools, as well as the relationship model of machining parts type and tools type are expressed clearly in the form of

Boolean matrix, as shown in Fig. 2, 3, 4, 5. In the figures, "●" shows the logic value is "1" in this place. With the parts characteristic information regarding as the polychromatic sets design elements, the tool feature attribute information regarding as the polychromatic sets unified color and feature information regarding as individual color, a network mathematical model of optimizing selection of cutting-tools is established.

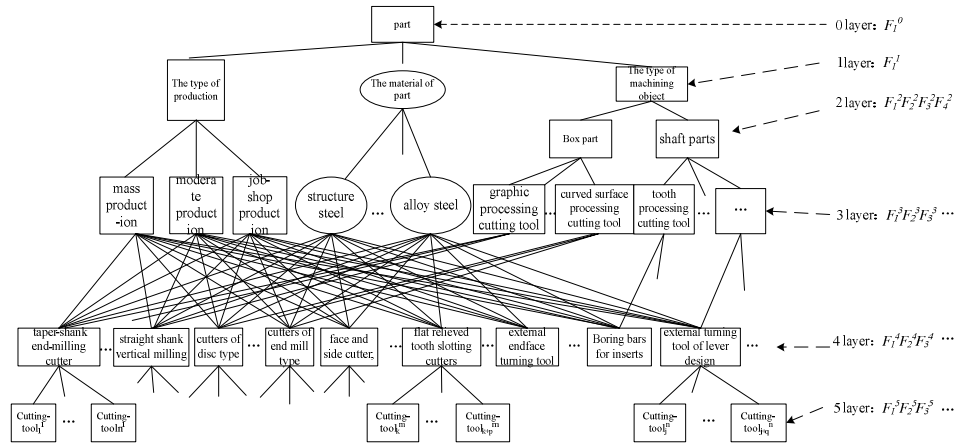


Fig. 1 The tree graph of tools selection method

The contour matrix	machining parts type		production type		
	F_1^2	F_2^2	F_1^3	F_2^3	F_3^3
F_1^0		●		●	

Fig. 2 The contour matrix 1

The contour matrix			Common material of part				
			F_1^1	F_2^1	F_3^1	...	F_9^1
High speed steel		F_1^3	●	●	●	...	●
hard metal	P	F_2^3	●	●		...	
	M	F_3^3	●	●	●	...	●
	K	F_4^3			●	...	●
coated carbides		F_5^3	●	●	●	...	●
superhard material	ceramics	F_6^3	●	●	●	...	
	diamond	F_7^3				...	●
	borazon	F_8^3				...	

Fig. 3 The contour matrix 2

The contour matrix		The classification of box parts cutting-tools					The classification of shaft parts cutting-tool	
		F_1^3	F_2^3	F_3^3	F_4^3	...	F_{11}^3	F_{12}^3
parts type	F_1^2					...	●	●
	F_2^2	●	●	●	●	...		

Fig. 4 The contour matrix 3

	F_1^4	F_2^4	...	F_i^4	F_{i+1}^4	...
F_1^3	●					...
F_2^3		●				...
\vdots	\vdots	\vdots	\vdots	\vdots	\vdots	\ddots
F_7^3				●		...
F_8^3					●	...
\vdots	\vdots	\vdots	\vdots	\vdots	\vdots	\ddots

Fig. 5 The contour matrix 4

In Fig. 2, 3, 4, 5, F_1^0 —machining parts, F_1^1 —structure steel,, F_9^1 —non-metal, F_1^2 —box part, F_2^2 —axisymmetrical part, F_1^3 —mass production, F_2^3 —moderate production, F_3^3 —job-shop production, F_1^4 —face processing cutting tool, F_2^4 —curved surface processing cutting tool,, F_{12}^4 —tooth processing cutting tool, F_1^5 —straight shank vertical milling, F_2^5 —spherical cutter,, F_i^5 —straight shank twist drill, F_{i+1}^5 —composite screw tap

Optimizing selection of cutting-tool

Determining the candidate cutting-tools set. Based on relationship models in Fig. 2, 3, 4, 5, the candidate cutting-tool set is determined using the polychromatic sets.

The choice of machining parts type is shown as Formula (1):

$$F_i^2 = \begin{cases} 1 & \text{If choosing this type of part} \\ 0 & \text{On the contrary} \end{cases} \quad (1)$$

$i=1$ shows that the choice is box part, and $i=2$ shows that the choice is shaft part.

Similarly, the choice of production type, tool material, the processing scope of cutting-tool and tool type are shown as Formula (2), (3), (4), (5):

$$F_s^3 = \begin{cases} 1 & \text{If choosing this type of production} \\ 0 & \text{On the contrary} \end{cases} \quad (2)$$

$s=1$ shows that production type is mass production, and $s=2$ shows that production type is moderate production, and $s=3$ shows that production type is job-shop production.

$$F_c^3 = \begin{cases} 1 & \text{If the material of cutting-tool can process this part. } (c=1, 2, 3, \dots, 9) \\ 0 & \text{On the contrary} \end{cases} \quad (3)$$

$$F_l^3 = \begin{cases} 1 & \text{If choosing the machining scope of cutting-tool} \\ 0 & \text{On the contrary} \end{cases} \quad (4)$$

$1 \leq l \leq 5$ shows that the choice is the cutting-tool of machining box part, and $6 \leq l \leq 12$ shows that the choice is the cutting-tool of machining shaft part.

$$F_n^4 = \begin{cases} 1 & \text{If choosing this type of cutting-tool} \\ 0 & \text{On the contrary} \end{cases} \quad (5)$$

The cutting-tool F_m^5 which meets the requirements need the existing of F_i^2 , F_s^3 , F_c^3 , F_l^3 , F_n^4 at the same time, as described by the following formula:

$$\begin{cases} \text{if} & F_m^5 = F_i^2 \wedge F_s^3 \wedge F_c^3 \wedge F_l^3 \wedge F_n^4 = 1 \\ \text{then} & F_m^5 = 1 \end{cases} \quad (6)$$

Through the step 1, 2, 3, 4, 5, the types of machining parts, production type, tools material, tools type, tools name are determined, as well as the candidate cutting-tool set $F_m^5[n] = (F_m^5[1] F_m^5[2], \dots, F_m^5[n])$ $n \geq 1$.

Optimizing selection of single cutting-tool. First of optimizing selection of cutting-tools is to choose "optimal" the cutting-tool, which provides basic dates for the whole optimization of cutting-tools. The candidate cutting-tool set is $F_m^5[n]$.

When the target for optimizing selection of cutting-tools is machining quality, the three factors (size, surface roughness, material affecting tools selection) are used to evaluate the candidates tools, shown as the following evaluation matrix[4](7):

$$R_z = \begin{bmatrix} R_{1z} \\ R_{2z} \\ R_{3z} \end{bmatrix} = \begin{bmatrix} r_{11z} & r_{12z} & \cdots & r_{1nz} \\ r_{21z} & r_{22z} & \cdots & r_{2nz} \\ r_{31z} & r_{32z} & \cdots & r_{3nz} \end{bmatrix} \quad (7)$$

For the balance of the relative importance of each affecting factor, the weight of each factor[5] can be established through the analytic hierarchy process, shown as: $W_z = (w_{1z}, w_{2z}, w_{3z})$.

When the target for optimizing selection of cutting-tools is machining quality, the score set of the candidate cutting-tool set is: $S_z = W_z \cdot R_z = (s_{1z}, s_{2z}, \cdots, s_{nz})$.

Similarly, when the targets for optimizing selection of cutting-tool are separately efficiency and cost, the score sets of the candidate cutting-tool set are: $S_x = (s_{1x}, s_{2x}, \cdots, s_{nx})$, $S_c = (s_{1c}, s_{2c}, \cdots, s_{cx})$.

Total score set of the candidate cutting-tool set is:

$$S = (w_z, w_x, w_c) \begin{bmatrix} s_{1z} & s_{2z} & \cdots & s_{nz} \\ s_{1x} & s_{2x} & \cdots & s_{nx} \\ s_{1c} & s_{2c} & \cdots & s_{nc} \end{bmatrix} = (s_1, s_2, \cdots, s_n) \quad (8)$$

In the formula, $W = (w_z, w_x, w_c)$ is weight distribution set for balancing the relative importance of three affecting factors, which is produced by the analytic hierarchy process.

To make overall evaluation to elements in the score sets, the cutting-tool $F_m^5[k]$ is the selected tool in the candidate cutting-tool set when

$$s_k = \max_{1 \leq i \leq n} S_i \quad (9)$$

Optimizing of the whole cutting-tool. The principle of the whole optimization tool is: under the premise of determining the sequence of processing and meeting processing requirements, the number of tool changing is the least. If there are m tool sets, and m tool sets are corresponding to m machining steps. After optimizing selection of single cutting-tool and choosing the tool set $F_m[n]$ which meet processing requirements for single feature, $F_m[n] = (F_1^5, F_2^5, \cdots, F_n^5)$ $n \geq 1$, the tools optimization is dealt with:

Step 1: If the initial machining step $o=1$, optimize the selection $F_1^5[n]$ to get the optimal tool $F_1^5[k]$ and $o+1$. If $o < m$, go on optimizing. while if $o=m$, selecting cutting-tool is over.

Step 2: When $o=2$, judge whether $o=2$ contains the same feature type as $o=1$. If same, judge on whether the candidate tool set $F_2^5[n]$ contains cutting-tool $F_1^5[k]$. If it contains cutting-tool $F_1^5[k]$, select cutting-tool $F_1^5[k]$. If not, select optimizing cutting-tool $F_2^5[k]$. If not same, select cutting-tool $F_2^5[k]$ too and $o+1$. If $o < m$, go on optimizing, and if $o=m$, selecting cutting-tool is over.

⋮

Step i: When $o=i$, find out the cutting-tool whose feature is the same as feature type which corresponds with $o=i$, composing set $F^5[a]$. And judge whether tool set $F_i^5[n]$ contains the same cutting-tool in $F^5[a]$. If it contains the same one, select the cutting-tool whose evaluation set is the highest. If not same, select cutting-tool $F_i^5[k]$ and $o+1$. If $o < m$, go on optimizing. If $o=m$, selecting cutting-tool is over.

⋮

Based on the optimal selection of single cutting-tool shown as the above, the selection of the whole cutting-tools is optimized using the characteristic that machining scope of the tool is often overlapping.

Example

In Fig.6, a simple box part of 3d model is shown, and the material of part is HT200, and production type is moderate production. The back, left, front, right and top sides of the part in Fig.6 are named orientation 1, 2, 3, 4 and 5 respectively.

Taking orientation 3 as an example, the semi-finish boring and finish boring and drilling and tapping the holes in the front face are accomplished in a machining center. Optimizing selection of cutting-tool is shown in Table 1:

Through the whole optimization selection of cutting-tools, all faces are finished machining with one or two milling cutters. For example: a boring cutter finishes the same size of holes in one change, reducing the time of cutting-tools exchange.



Fig. 6 The 3D model of parts

Table 1 The result of optimal selection cutting-tool

Product name and code: ***		The name of part: ***		Part drawing number: ***
Order number	Tool code	Cutting-tool specifications and name /mm	number	Processing surface(mm)
1.	T01	Boring cutter Ø 100 2.	1.	Rough boring hole Ø 110H7.
2.	T02	Boring cutter Ø 94 2.	1.	Rough boring Ø 95 hole H7.
3.	T03	Boring cutter Ø 61 2.	1.	Rough boring hole Ø 62 J7.
4.	T05	Boring cutter Ø 51 2.	1.	Rough boring hole Ø 52J7.
5.	T06	Special boring 124-24.	1.	The end face of hole 12-M8, and the end face of 8-M10, and the end face of 3-Ø16.
6.	T08	Centre drill 134-4.	1.	Drilling centre hole of hole 12-M8, and drilling hole 8-M10 and 3-Ø16.
7.	T10	Taper shank twist drill Ø15.	1.	Drilling hole 3-Ø16.

Conclusion

The cutting-tool selection in the machining center is optimized, and the part is clamped only once. Using methods tree and the polychromatic sets to establish relation model, and through the logic operation of coloring, the candidate cutting-tool set is found out which meets processing conditions. Using the fuzzy algorithm, the "optimal" cutting-tool is selected, and the whole optimization for all cutting-tools is finished, which reduces the type of needed cutting-tools, improves processing efficiency and decreases cost.

Acknowledgements

This work was financially supported by the Natural Science Foundation of Hebei Province, China (under grants No.E2008000687).

References

- [1] Pavlov VV: Polychromatic sets and graphs for CALS in Machine Building. Moscow, 2002
- [2] Zongbin Li, Lida Xu: Computers & Operations Research, 2003, 30 (6): 851-860
- [3] Zongbin Li: Polychromatic sets theory research and application in the advanced manufacturing. Bei Jing: China Water Conservancy and Hydropower Press, 2005, In Chinese.
- [4] Dan Wu, Xiankui Wang: Modular Machine Tool & Automatic Manufacturing Technique, 1998, (1): 9-15, In Chinese.
- [5] Jin Lu: Practical Fuzzy Mathematics. Bei Jing: Science and Technology Literature Press, 1989, 10, In Chinese.

Analysis and Simulation of the Shear Deformation for Woven Cloth

Liang Chen^{1, a}, Shuguang Zhao^{1, b}, Lijuan Zhang^{1, c}, Liqiang Zhang^{2, d} and Wenbing Zhang^{1, e}

¹College of Information Science and Technology, Donghua University, Shanghai 201620 P.R. China

²School of Mechanical Engineering, Jiangsu University, Zhenjiang 212013 P.R. China

^alawrence.cl@hotmail.com, ^bsgzhao@dhu.edu.cn,

^czljmx@mail.dhu.edu.cn, ^dzhangliqiang010@sina.com, ^ezwb850506@126.com

Keywords: Woven Fabrics; Shearing; Physical-Based Model; Cloth Animation

Abstract. Woven fabrics are used in a wide variety of products, and they are prized for their flexibility, formability, and high specific strength. However, modeling woven cloth is difficult due, in particular, to complex mechanical properties. In this paper, the shear behavior of plain woven fabric is studied. Through the analysis, a mechanical model is proposed which take the shearing properties into account. It uses physical-based model for animating cloth objects. Furthermore, we demonstrate the efficiency of this method with examples related to accurate cloth simulation from experimental shear curve measured on actual materials.

Introduction

There exist a wide range of applications for woven fabrics. Despite the widespread use of woven fabrics, there is no comprehensive, universally accepted computational model for the deformation of woven fabrics. Since the mechanical properties of cloth materials are highly anisotropic and nonlinear, significant challenges have been created when it comes to generating a simulation system for the appearance and motion of cloth objects efficiently. In cloth simulation particle systems models, tensile stiffness is fairly easy to simulation, as it involves computing deformations and forces within mesh elements. On the other hand, the simulation of shearing and bending stiffness is more complicated, as several adjacent mesh elements have to be considered simultaneously. Therefore, the accurate reproduction of the mechanical behavior of cloth has always been a key issue.

In this paper, we develop a robust physical-based model, which is specially designed to rapidly and easily simulate deformation surface motion in any situation. Our main goal of this paper is to show the influence of the shear stiffness in the deformation of woven fabrics. It is shown that the wrinkles of deformation woven cloth, to some extent, accommodated by relative yarn rotation, also known as in-plane shear. The shear behavior of woven fabric is studied first. And then describe the simplified shearing model, which is beneficial to real-time response. Finally, give the simulation results with our model.

Background and Motivation

Cloth simulation and fabric measurement are tightly linked areas of research. Over the last decade, a great deal of research [1, 2, 4, 8, 9] has been dedicated to simulating cloth motion. For the purpose of obtaining high quality animations of cloth model, it is essential to evaluate the mechanical properties of the simulated cloth. The mechanical properties of cloth materials are highly anisotropic and nonlinear. And this anisotropic and nonlinear create significant challenges when it comes to modeling a cloth simulation system.

In virtual simulations, the main imitated mechanical properties of fabric are tensile elasticity, bending, shear, density and friction. Tensile stiffness is the most important and best studied aspect of fabric. It is usually described in terms of stain-stress relations, and is fairly easy to simulation.

However, the simulation of bending stiffness is more complicated. Several solutions have been proposed in the literature [10, 11].

Furthermore, shearing of fabrics is a major deformation model during draping [13]. So a thorough understanding of the shearing behavior is also very important for designing model to simulate fabrics. For the simulation of draping fabrics, an approach named fishnet algorithm has been developed [12]. The Advantages of this approach is fast and simplicity. Nevertheless, this method does not take into account the mechanical behavior of fabric and boundary conditions. So an alternative to this method is the use of finite element approaches [14]. The woven fabric can be approximated as a continuum, the mechanical behavior is considered to model the cloth. Finite elements methods express the mechanical equations according to the deformation state the surface within well-defined elements. Unfortunately, most implementations focus on the accurate reproduction of mechanical properties of fabrics but restrict the application field to the simulation of simple garment samples, mostly because of the huge computational requirements. This leads us to consider efficiently techniques for modeling improved particle system, as well as accurately techniques which deal with and correct any deformation result from shearing of cloth.

Experimental Analysis

The mechanical behavior of woven fabric is special due to the motions between each yarn. Experimental investigation is to determine relationship between mechanical behavior and woven architectures. For study of fabric shear deformation, there are many experimental methods. Three principal methods are uses: KES-F test, the FAST test and the picture frame test (Fig. 1).

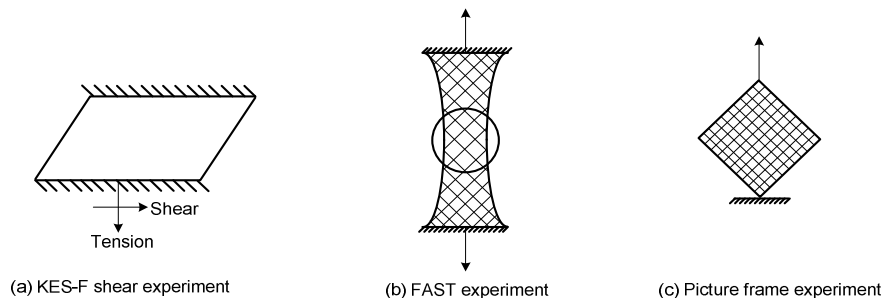


Fig. 1 Shear experiment methods

The KES-F test is usually used in the early experimental of shear behavior. The second type of shear tests is the bias test. The disadvantage of it is, in the boundary of specimen, many yarns would slip each other obviously. Another famous experimental device of shearing is picture frame apparatus. In this section, we use the third technique to describe the shear behavior of woven fabrics.

The picture frame experiment. The picture frame test is one of common methods used in research on the shear deformation. Several studies have show that the apparatus is very satisfactory to characterize the shear properties of fabrics. The shear frame apparatus which is essentially a square four-bar linkage. The base of equipment is fixed, and a removable brace is designed to allow transport and loading of the apparatus. The frame is installed on an electronic tensile machine named INSTRON 5569, which stretching rate at 10 mm/min.

The specimen under test is one of plain fabrics. The fabric test size is 250mm×250mm, minus a 20mm side length square cut from each corner. This square is required so that rotation of the hinges can occur freely. The test material is placed into the fixture via a clamping arrangement located along each bar linkage. It is essential to make sure that the weft and warp tows are positioned parallel to the frame.

Test results. The shear behavior of deformation fabrics has obviously stages which are directly related to micro-scale of cloth. Before deformation, warp and weft yarns are orthogonal to each other. When the shear deformation happen in the specimen, the pores between yarns turn shrink because of the yarns become in contact with their neighbors and are laterally compressed.

Grosberg and Park [7] demonstrated that the trends for fabric shearing typically consist of three stages: the initial region, the mid-region and the last region. Through the experiment, we can obtain the load-displacement curves of plain fabric. The curve can be divided into three zones corresponding to the above mentioned stages. In the first part, the shear angle is small (0° - 2°). There is no shearing inside the yarns and the shear rigidity is very weak. The fabric can be idealized to be in a state of pure shear. In the second phase, the shear angle increases with rotation of the yarns between the cross-over points. The friction due to rotation between the warp and weft yarns is opposed to the distortion. As the yarns are compressed with their neighbors, the shear rigidity increases gradually. The transition to the zone 2 corresponds to the “shear locking angle”. After this angle, in the third zone, the yarns are subjected to side contacts with other yarns completely. The space between yarns disappears shows that the yarn is in lateral compression and this compression is more important as the shear increases. The experiment explains the relationship between increase of the shearing force and the transformation of yarns.

Woven Fabric Model

To model the plain woven fabrics, previous works approximate cloth as a continuum [5, 6]. They employ finite elements method to simulate the sheet forming of woven. The FEM has been practically and broadly applied to the field of structural-mechanical analysis. However, cloth is not a homogeneous continuum, and the FEM has several potential drawbacks. So, on the other hand, other works simulate fabric with particle system [4]. They approximate a cloth with a quadrilateral mesh of particles. The particles connect with each other in specific type. The model is relatively straightforward to implement. Either an implicit or explicit methods for solving the nonlinear ODEs would be acceptable. However, the mechanical behavior of cloth is not performance fully.

In this section, to take into account the shear behavior of fabric, we propose an improvement system of particles that are better efficient for simulating the deformation. We first define the fabric architecture, and then describe the in-plane shear. Subsequently, the shear behavior and its implementation are presented.

Definition of fabric architecture. To model the property of plain woven fabrics, an idealized deformation of a section of discrete yarns is depicted in Fig. 2. Our model is an efficient particle system, since the simulation process is quite different from FEM. With the analysis the microstructure of woven fabrics, we have developed particle system for representing the macroscopic deformation of the fabric.

In determining the fabric deformation characteristics, the model is assumed to be the repeating, symmetrical cell section. The unit cell of the plain woven fabric consists of two crossing sections of yarn. The warp and weft yarns are each approximated as pin-jointed. On the other hand, to implement the model, we treat a cloth with an idealized truss network with lumped mass nodes. The model of initially fabric sheet is comprised of undeformed two-dimensional network of yarns. The yarns are joined at the nodes, in other words, they are sutured together at those locations to form a network. The nodes are placed at the every cross of warp and weft yarns.

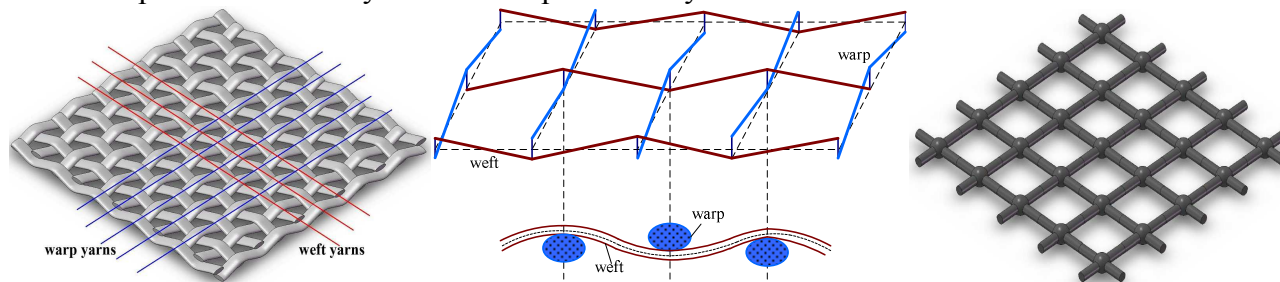


Fig. 2 (Left) Geometry of warp and weft yarns. (Right) Truss network with lumped mass nodes.

In-plane shear. Large deformations of woven fabrics may be accommodated by relative yarn slip and yarn rotation at the cross-over points. As a large frictional resistance to slip between warp and weft yarns, yarns slippage at intersection will be incorporated into particles system in a future

publication. In this paper, we only concentrate on the relative yarn rotation, also known as trellising or in-plane shear.

The observations made in the shear experiments on the woven fabrics, explain that the cloth deformation is the result of a relative rotation between the warp and weft yarns. As we know, there are some spaces between yarns when the cloth is in unloaded status. Once shear loading is added, the yarns are rotated so as to the spaces turn small. Then the warp and weft yarns compress with their neighbors so that it shows resistance to prevent rotation, i.e. shearing deformation.

The relative rotations of the warp and weft yarns lead to a force applied at the yarn intersections. The value of this shear resistance for a shear angle is well experimentally given by the shear-frame test. To find the value of the resistance, the fibers were assumed to remain straight during the experiment. Consequently, all the angles between weft and warp, and all the force at the intersections are equal over the frame. The power gained by the intersections and the power provided by the tensile machine are supposed to be equal.

Using the notations of Fig. 3, shear angle γ is given by

$$\gamma = \pi/2 - 2\theta \quad (1)$$

$$\cos \theta = \delta/2L + \cos(\pi/4) \quad (2)$$

According to the torque equilibrium between friction and resistance at the yarn intersections, from the picture frame experiment, we can get the relationship between loads and shear angle in the initial shear stage of plain woven carbon fabrics, see [3].

$$P = \frac{4096\mu EI h L W \cos \gamma}{57 P_y^4 S^2 \sin\left(\frac{\pi}{4} - \frac{\gamma}{2}\right)} \int_0^{\pi/2} \frac{d\varphi}{\cos^3(\theta - \varphi)} \quad (3)$$

Where the model parameters of shear loads P , shear angle γ , angle between bar and tensile direction θ , friction coefficient between warp and weft μ , bending rigidity EI , deflection of the yarn h , yarn length L , yarn width W . Fig. 4 shows the loads according to the shear angle. The load value is small at the beginning and then becomes important after yarn rotation at the intersections.

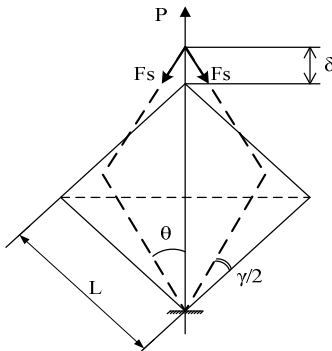


Fig. 3 Parameters of the picture frame test

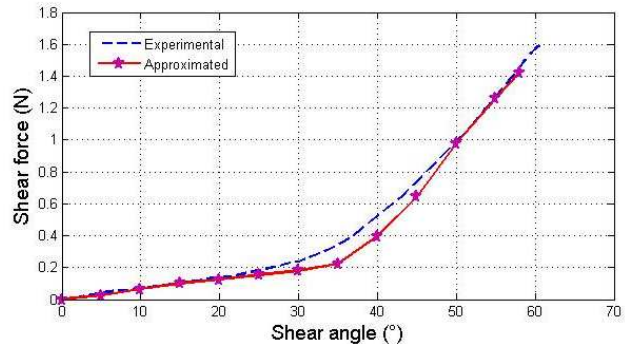


Fig. 4. Shear load versus shear angle

Implementation of shearing on particle system. General speaking, it would produce a complex strain when a shear stress implement into the fabrics. Simple shear can be generated by the diagonal stretching. When you pull the fabric in diagonal direction, it stretches along the direction of external loading; on the other hand, the cloth shrinks in the direction perpendicular to the stretch. The loading is related to the size of the shear angle γ between the warp and weft. The recording of this relationship is usually in the form of stress-strain curve.

If a shear force is applied in diagonal direction, at beginning very little shear occurs, the cloth is considered to be in a state of pure shear. As shear force increase, the shear angle is increase with rotation of the yarns between the cross-over points, the shear load is mainly due to friction between the weft and warp yarns. The shear response of fabric is shown in Fig. 5. The picture frame test explains the relationship between the shearing force and the shear angle. Therefore, we can propose an idealized particle system which improve mass-spring model.

The conventional mass-spring model is a mesh of virtual masses, each mass being linked to its neighbors by massless springs. The linkage in-between neighbor is achieved in three different ways: structural springs, shear springs and bending springs. Indeed, under pure shear stress, the shear springs of stretch direction are elongated in each grid to prevent excessive deformation of cloth. Although mass-spring model used widely, there are some drawbacks such as the simulation of fabric shear. The Provot model is consistent to the solid mechanics theory, which can be used to simulate continuous elastic solids. Another famous model is the immediate buckling model which is based on the assumption that the fabrics are very soft. However, in this model, no in-plane compression is allowed. In short, the shear buckling is can not simulate.

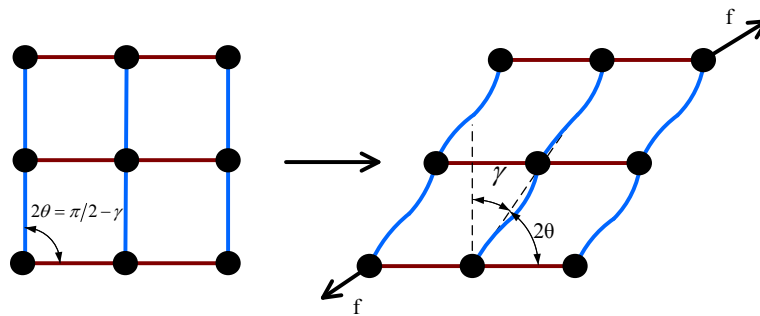


Fig. 5 Rotation of structure under simple shear loading

From the picture frame experiment and previous mass-spring model, we will give an improvement mechanical model, which take the shearing properties of microstructure fabric into account. In conventional mass-spring model, shear springs working to prevent stretches or shrinks according to distance of the two masses. Our model based on the mass-spring system, keep the functions of structural and bending springs, and focus on refine the function of shear springs. In order to increase the simulation accuracy of shear deformation, the shear angle between warp and weft is considered in the system. When the diagonal stretching loadings on the fabric, the simple shear deformation occurs, and each particles in the system update their relative position in every time-steps. The model obtains the force direction of particles according to their position, and determines the size of force based on the angle of adjacent particles. In short, computing the shear force applied on each particle used its shear angle and force direction instead of shear spring to simulate the shear deformation.

Results and Simulation

The first test is that observe the changes of a real square fabric place in the table with the diagonal stretching load. Fig. 6 shows that the fabric stretches along the direction of external loading, and shrinks in the direction perpendicular to the stretch. As the increase of the shear force, one phenomenon of fabric different from other elastic objects is occur, it is wrinkles or shear buckling.



Fig. 6 The test on real fabric Fig. 7 Simple shear deformation test and virtual drape of fabric

The second test is the performance of the physical model under simple shear loading. In order to verify the accuracy of the model, a simple shear loading is tested, the diagonal shear with 45° angle to the direction of warp and weft. This test has been implemented in a cloth simulation system which uses an accurate particle scheme, integrated with Implicit Euler using C++ language and OpenGL. Fig. 7 shows that the simulation of fabric with 34×34 grids. Before any loading, the fabric has no deformation. However, with the diagonal shear loadings, the wrinkle generated by simple shear along

the diagonal direction of cloth. Another simulation is the virtual drape of a piece of fabric. The snapshot of cloth collides with a sphere indicate the robust collision detection and response of system.

Conclusion

The objective of this paper is to analyze and show the influence of the shear behavior on the simulation of deformation fabric. Through the experimental study of shearing with picture frame, it has been obtained that shear deformation of the cloth is accommodated by the relative rotation between the weft yarns and warp ones. Consequently, we found the force applied at the weft and warp yarn intersections varying according to the shear angle. The evolution of the shear force according to the shear angle has been deduced. After the analysis of the diagonal stretching of the fabric, we introduce the method about how to implement our particles model in a modified mass-spring system. This approach gives better results and can capture the mechanical property of cloth more accuracy. For the future, one of our main goals will be to research the influence of bending stiffness in particle systems.

Acknowledgements

This project is supported by National Natural Science Foundation of China (Grant no: 60973072) and “211” Key Discipline Program of Donghua University.

References

- [1] D. Baraff and A. Witkin: Computer Graphics. Vol. 32 (1998), p. 43
- [2] D.E. Breen, D.H. House and M.J. Wozny: Computer Graphics. Vol. 32 (1994), p. 365
- [3] LIIN Guochang, WAN Zhimin and DU Xingwen: Acta Aeronautica et Astronautica Sinica. Vol. 28 (2007), p. 1005
- [4] K. Choi and H. Ko: ACM Transactions on Graphics. Vol. 11 (2002), p. 604
- [5] Powell D and Zohdi Ti: Composites: Part B. Vol. 40 (2009), p. 451
- [6] Ethan M. Parsons, Tusit Weerasooriya: Journal of the Mechanics and Physics of Solids, In Press, Corrected Proof, Available online 8 June 2010
- [7] Grosberg P, Park BJ: Textile Res J. Vol. 36 (1966), p. 420
- [8] Provot, X.: Proceedings of Graphics Interface'95. (1995), p. 147
- [9] Volino, P., Courchesne, M. and Magnenat-Thalmann, N.: Comput. Graph. Vol. 29 (1995), p. 137
- [10] B. Thomaszewski and M. Wacker: WSCG Short Communication Proceedings. Vol. 9 (2006)
- [11] Volino, P., Magnenat-Thalmann, N., and Faure, F: ACM Trans. Graph. Vol. 28 (2009)
- [12] Van Der Ween F: Int J Numer Meth Eng. Vol.31 (1991), p.1414
- [13] Potter KD. Composites. Vol.10(1979), p. 161.
- [14] Boisse P. Finite element analysis of composite forming. In: Long AC, editor. Composite forming technologies. Woodhead Publishing. 2007. p. 46

Molding CAE Technology and Its Application Research

Yanfeng Wang^a

Department of Mechanical Design, Manufacture and Their Automation, HuaiHai Institute of Technology, Lianyungang, Jiangsu Province, 222005, China

^aemail:wangyanfeng1968@sina.cn

Keywords: Injection Molding; CAE; Numerical Simulation; Mold Design

Abstract. In this paper, the study of numerical simulation method used in jet molding CAE major technology is carried out, including simulation of filling flow process, keeping the stress process, cooling process, warping deformation and molecular orientation and so on; also makes a system induced study on injection molding CAE successfully applied in the injection mold design.

Introduction

Plastic injection molding is a very complicated physical process. Driven by the injection pressure, high temperature melt plastic flows to the mold cavity through the pouring system; then melt rapidly solidifies due to cooling system in the mold; at the same time, melt is accompanied by shear heat, volume contraction, molecular orientation and crystallization process. Molding CAE technology carries out numerical simulation to the process of injection molding flowing, keeping pressure, cooling and so on, which can simulate the practical molding process directly on the computer screen before mould manufacturing by applying basic theory such as polymer processing rheology, heat transfer, computational mechanics and computer graphics and so on. It can forecast the effect of the mould design and molding conditions on the products, find potential defects, provide scientific basis for judging whether the mould design and processing conditions is reasonable or not, which makes plastic processing molding become an applied science from a practical technology.

The Contents of Molding CAE Technology

Filling Flow Process Simulation. The process of filling mould in injection molding belongs to non-newtonian fluid, non-isothermal and unsteady flow and heat transfer process, which meets the basic equations of viscosity fluid mechanics, but this equation is too complex. Only introduces appropriate and necessary assumption, and simplifies it, and combines specific boundary conditions, can it be solved with numerical method. Basic equations of molding process includes generalized Newton's law, conservation of mass, momentum conservation, the first law of thermodynamics. According to the characteristics of injection molding, may introduce certain simplifying and assumptions, mainly is the laminar flow hypothesis, non-compressible fluid hypothesis, etc. Using the above assumptions and simplifying, derives control equations of the plastic melt flowing when filling mold through the basic equations of the viscosity fluid mechanics as follows:

$$\frac{\partial}{\partial x}(b\bar{u}) + \frac{\partial}{\partial y}(b\bar{v}) = 0 \quad (1)$$

$$\frac{\partial}{\partial z} \left(\eta \frac{\partial u}{\partial z} \right) - \frac{\partial P}{\partial x} = 0 \quad (2)$$

$$\frac{\partial}{\partial z} \left(\eta \frac{\partial u}{\partial z} \right) - \frac{\partial P}{\partial y} = 0 \quad (3)$$

$$\rho C_p \left(\frac{\partial T}{\partial t} + u \frac{\partial T}{\partial x} + \frac{\partial T}{\partial y} \right) = k \frac{\partial^2 T}{\partial z^2} + \eta \dot{\gamma}^2 \quad (4)$$

Where η is dynamic viscosity coefficient of the fluid; ρ is density; C_p is specific heat; k is fluid thermal conductivity; t is time;

T is fluid temperature; P is hydrostatic pressure; γ is shear rate; u, v are the velocity along X and Y directions;

\bar{u} , \bar{v} are the average flow velocity of X and Y directions; b is cavity thickness in half.

In the control equations, equation (1) is the continuity equation, its meaning is the quality of fluid remains constant in the process of flowing; equation (2) is the equations of motion, its meaning is that the time rate of the fluid momentum equals to the sum of exert external force; equation (3) is energy equation, its meaning is increase of internal energy of the system is equal to the sum of the power consumed in the system and the energy exerted to the system. These four equations are basic equations of filling simulation. Based on the equations, simulation to melt flowing can be carried out by computer.

Simulation of Pressure Maintaining Process. The essence of the simulation of the pressure maintaining is to solve the problems such as compressible, non-isothermal flowing problem of non-newtonian fluid flow and so on. Its principle of analysis is similar to the flowing simulation, but there are several differences:

In filling mold flow stage, change of the melt density is small, and assumes melt can not be compressed during simulation. While in the simulations of pressure maintaining, change of the melt density is relatively bigger, and this hypothesis can not be used. In essence, the process of pressure maintaining do make useful the compressibility of the melt to add new plastic. Therefore, density change of the melt must be considered in the simulation of the pressure maintaining.

Due to the increase of the density parameters, the state equations(relationship among P - V - T) must be introduced to solve the equations during the simulation of pressure maintaining.

In the process of pressure maintaining, temperature change range of the melt is larger, so viscosity model that is suitable to a wider range must be adopted, and the melt heat, thermal conductivity changes with the temperatures should be considered.

When simulating filling mold flow, the melt flow is known, pressure is to be solved, and the inlet pressure is set keeping pressure during the pressure maintaining, it is needful to solve the melt flow, and their boundary conditions is different.

Similar to the derivation in the filling mold flow simulation, considering the changes of density of the melt, specific heat and heat conductivity, deduced the control equations of pressure maintaining process are:

$$\frac{\partial \rho}{\partial t} + \frac{\partial}{\partial x}(\rho u) + \frac{\partial}{\partial y}(\rho v) + \frac{\partial}{\partial z}(\rho w) = 0; \quad \frac{\partial P}{\partial x} + \frac{\partial}{\partial z} \left(\eta \frac{\partial u}{\partial z} \right) = 0; \quad \frac{\partial P}{\partial y} + \frac{\partial}{\partial z} \left(\eta \frac{\partial v}{\partial z} \right) = 0$$

$$\rho C_p \left(\frac{\partial T}{\partial t} + u \frac{\partial T}{\partial x} + v \frac{\partial T}{\partial y} \right) = \frac{\partial}{\partial z} \left[K(T) \frac{\partial T}{\partial z} \right] + \eta \left[\left(\frac{\partial u}{\partial z} \right)^2 + \left(\frac{\partial v}{\partial z} \right)^2 \right]$$

Where w is velocity component of the direction z ; other parameters are the same as that in filling mold flow simulation. After derivation that is similar with the simulation of filling mold flow, can obtain below pressure control equations:

$$G \frac{\partial P}{\partial t} - \frac{\partial}{\partial x} \left(\bar{S} \frac{\partial P}{\partial x} \right) - \frac{\partial}{\partial y} \left(\bar{S} \frac{\partial P}{\partial y} \right) = -F$$

$$\bar{S} = \int_0^b \rho \left[- \int_0^z \frac{\bar{z}}{\eta} dz \right] dz; \quad G = \int_0^z \left(\frac{\partial \rho_s}{\partial T} \right)_T dz + \int_0^z \left(\frac{\partial \rho_l}{\partial p} \right)_T dz;$$

$$F = \int_0^z \left(\frac{\partial \rho_s}{\partial T} \right)_p \frac{\partial T}{\partial t} dz + \int_0^b \left(\frac{\partial \rho_l}{\partial T} \right)_p \frac{\partial T}{\partial t} dz + (\rho_s - \rho_l) z = \hat{z} \frac{\partial z}{\partial t}$$

Where ρ_1, ρ_2 are density of liquid and solid; \hat{z} is the liquid-solid interface position.

The empirical formula provided by Tait is usually used to express the relationship among P - V - T during pressure maintain process:

$$V(P, T) = V_0(T) \left[1 - 0.0894 \ln \left(1 + \frac{P}{B(T)} \right) \right] - V_t(T, P)$$

$$V_0(T) = \begin{cases} b_{1,1} + b_{2,1}(T - b_5) & T \geq T_g \\ b_{1,s} + b_{2,s}(T - b_5) & T < T_g \end{cases};$$

$$B(T) = \begin{cases} b_{3,1} e^{-b_{4,1}(T - b_5)} & T \geq T_g \\ b_{3,s} e^{-b_{4,1}(T - b_5)} & T < T_g \end{cases}; \quad V_t(T, P) = \begin{cases} 0 & T \geq T_g \\ b_7 e^{-b_8(T - b_5) - b_9 P} & T < T_g \end{cases}$$

Where T_g is the glass transition temperature (for nonlinear materials) or the crystallization temperature (for crystalline materials). T_g may be thought linear function of the pressure: $T_g(P) = b_5 + b_6 P$. In the above equations, $b_{1,1} \sim b_9$ are material constants.

The Simulation of Cooling Process. The Factors of Influencing Temperature Field During Cooling and the Method for Determining:

The Cooling Time. The cooling time has relationship with the temperature of ejecting product, temperature of the cavity, and the length of cooling pipe etc. Starting from the temperature field, the iteration method can be used to determine reasonable cooling time after simulation model of cooling process being established.

The Cavity Temperature. The temperature of the cavity is controlled by the temperature of cooling medium, flow velocity and the heat transfer area of cooling pipe. After selecting material, forming and determining of technology conditions, Numerical analysis method can be used to solve the temperature distribution in the cavity in the process of cooling, and according to the numerical analysis method, further optimizes cooling pipes and its parameters.

Cooling Pipes and Its Parameters. Including the diameter, length, distribution of the pipe and the temperature and velocity of the cooling medium. The diameter, length and distribution of the cooling pipe are determined by geometric modeling. The initial temperature and flow velocity of the cooling medium are set by the way of the interaction before solving temperature field.

Mathematical Modeling and Analysis of the Boundary Condition. After high temperature plastic melt being filled in the mold cavity, its heat transfer phenomenon is very complex in the cooling process, including three ways such as thermal radiation, heat convection and heat conduction. When establishing the mathematical model of temperature field in the process of cooling, simplifying should be done as follows:

Ignores the gap thermal resistance between cavity with plastic melt, and takes heat-conducting properties of the mould materials as isotropic.

In the cooling process of melt, assuming the thermal physical parameters (including specific heat, thermal conductivity and density) do not change with temperatures.

The total quantity of heat lost through radiation on outside surface of the mould is less than 5%, so the heat loss is only approximate estimated, and mainly considers the heat conducting and heat convection among mold, cooling medium and the melt.

The cooling process of injection mould has non stability. Measured temperature at some point in the mould cyclic changes in a cyclical injection process, but this kind of transient temperature fluctuation is smaller, and the main performance is in the surface area of the cavity, so may ignore the cyclical change of the temperature, think the temperature field is stable.

Using Laplace's equation to describe three-dimensional steady temperature field:

$$\nabla^2 T(x, y, z) = \frac{\partial^2 T}{\partial x^2} + \frac{\partial^2 T}{\partial y^2} + \frac{\partial^2 T}{\partial z^2} = 0$$

If not given boundary conditions, there will be countless solution for the heat conduction differential equation used to describe the problem of temperature field. , The temperature or heat flux density on the border area is described by boundary conditions, and there are three boundary conditions.

The first kind of boundary is called Dirichlet condition, which gives the temperature value of each point on the boundary of the heat conduction object, has the following form:

$$T = T_0 \quad x \in \Gamma_1$$

The second boundary condition is called Neuman conditions, Given normal differential coefficient of the temperature at the different points of object boundary, the boundary conditions is equivalent to the given heat flux density on the boundary, expressed as the following:

$$q = \frac{\partial T}{\partial n} = q_0 \quad x \in \Gamma_2$$

Where n is outer normal on the boundary.

The third kind of boundary condition is called Robin condition, which gives differential coefficient relationship between the temperature at the points of the object boundary and temperature along normal direction, namely

$$-\lambda \frac{\partial T}{\partial n} = h(T - T_0) \quad x \in \Gamma_3 \quad (5)$$

Where λ is thermal conductivity of the mould material; h is heat transfer coefficient on the boundary.

On the problem of cooling the injection, the part of mould contacting with air can be considered as Γ_1 . At this time, simply think that the temperature of mould outside wall is constant, and equal to room temperature. If don't think the temperature of the mould outside wall is constant, must consider heat transfer of the mould and outside air, and use the boundary condition Γ_3 . At this time, in equation (5), h is coefficient of heat transfer between mould and air (room temperature T_0). Boundary condition Γ_2 often is used in cavity boundary, takes the heat flow on contact surface of the plastic part and mold as boundary conditions. Boundary condition Γ_3 is corresponding to the border of the mold and cooling pipes, at this time, in the equation (5), h is heat transfer coefficient of pipe wall and boundary of cooling water pipe, T_0 is the temperature of cooling water.

The simulation of inner stress and warpage deformation. Plasticizing of plastic in the feed barrel is uneven, melt in filling molding flow suffers the effects such as shear force and orientation, non-uniform cooling, plastic melt crystallization and adverse stripping of the products, all are possible to produce inner stress. On the basis of the reasons, inner stress will be divided into current stress, orientation stress, cooling stress, crystallization stress and stripping stress. Producing inner stress within the plastic part will likely make it produce warping deformation, which is a common defect to the plastic parts. While the purpose of the simulating warping deformation is to forecast plastic parts' appearance quality, geometric dimensioning, stress distribution and mechanical performance after stripping model under given process conditions, which helps designers to correct plastic part and design scheme of injection, further predict using performance of the plastic parts.

The warpage deformation of the plastic parts not only relate with the internal stress, but also relate with contraction of the part. In injection molding process, in stage of molten plastic injecting filling into molding, due to the polymer molecules arrange along the direction of flowing, make plastic's shrinkage in the direction of flowing is larger than that in the vertical direction. The difference between the plastic shrinkage is the main reason that produces warping deformation. General uniform shrinkage only causes the change of the volume of plastic. Only the uneven contraction will cause warping deformation. Crystalline plastic's shrinkage rate difference between in flow direction and in vertical direction is larger than that of amorphous plastic, and its shrinkage rate is also larger than that of the amorphous plastic. The composition of larger crystalline plastic shrinkage and anisotropic contraction, which causes the tendency of warping deformation of crystalline plastic much more than that of amorphous plastic. The basic shapes warping deformation are arched and saddle form. The reason of vaulted plastic deformation is for the contraction in the middle of the plastic smaller than that of surrounding edge. The saddle form deformation is caused for shrinkage around the edges of plastic part being less than that of the middle. Actually seen plastic deformation is usually combination of arched and saddle distortion.

In addition, the mould structure will produce different degree of effects on the warping deformation of the product such as the inappropriate runner gate position, the structure of the plastic, unreasonable shape design; and the thermal properties of plastic material and the conditions

and parameters in injection molding process such as temperature, pressure, flow rate and time of keeping pressure, etc. Therefore, when studying warping deformation mechanism of plastic products, must comprehensively consider whole forming process and the factors of structure and material properties of plastic

The Simulation of Molecular Orientation. There are many atoms on polymer molecular chain, which makes the molecules chain long and asymmetric. It will be parallel arrangement along the direction of external force under the effect of external force. This process called "orientation".

The purpose of molecular orientation simulations is to simulate experienced physical process of the melt when it is shaping, determine the microstructure of the plastic part, To predict the physical properties of the plastic part and molding quality. Its microstructure includes crystallinity, orientation angle, shear modulus variation, double refractive index, state of orientation distribution and the stress form orientation etc. The orientation simulation plays an important role to filling mold flow, drafting of molding process conditions and the forecast to the quality of plastic parts.

Applications of Molding CAE

The analysis to injection molding process flow has important significance for improving the quality of plastic parts. The flow analysis can show various causes of the defects from the principle, overall deal with the problems in injection molding, which can obtain high quality plastic products. Currently, the injection molding CAE has been successfully applied in the following aspects.

The cavity design. (1) Understands the flow state of melt in different stages of filling process and the leading peak position of flow, and determine if can full of cavity. (2) Understands whether produces air-pocket in the melt in the process of flowing and determine the position of the air-pocket, If there are air-pockets, may set the exhaust position. (3) Understands the weld lines position that melt generated when it flowing in the cavity, and judge whether its position would affect the appearance and intensity of plastic parts.

The design of flowing passageway. (1) Observes the flow changes of a mold with a few of cavities and a plastic part with some runners in different passageways and time interval, and achieves casting balance by changing the cross-sectional area of the passageway or the position of the gate.(2) The sectional area and length of the passageway directly affects flow resistance of the melt, and the CAE can be used to more reasonably determine the shapes and sizes of the passageway.

The design of gate. (1) The cross-sectional area of all gates is smaller, and flow resistance is very big, slightly different, there is a great influence to the filling state of the melt, and the use of CAE can more reasonably select the types of gates. (2)Inappropriate position of sprue easy cause phenomenona of viscous flow, jet flow, which influences appearance of the plastic parts, and CAE can be used to correctly choose gate location. (3)It can be used to select opening and closing time of the gate more reasonably in the molding process, which plays its role effectively.

Forecast to deformation. (1) Reasonable holding pressure and pressure-keeping time can be determined, which makes the volume change of the melt decrease, and minimize distortion. (2) Unreasonable shape design and mold design of the plastic parts make it deform easily, the CAE can be used to get reasonable geometry shape and mould structure of the plastic parts, and make deformation tends of the plastic parts be the smallest.

The design of cooling system. (1) Analyzes the design scheme of cooling system, making it possible to the temperature on the cavity surface as far as possible even. (2) Calculates and analyzes heat efficiency of injection mold, which make the thermal efficiency of the mold is the best and energy saving.

Conclusions

Injection molding CAE technology can be used to meticulously, precisely describe various physical phenomena in injection molding process. It already gradually becomes extremely important constituent on injection mold CAD/CAM/CAE system. It can provide scientific basis for design of

plastic parts, mold design, process formulation of injection molding and control to injection molding process by research on material properties of plastic and simulation and analysis to the injection process. It has been successful applied in different links of the mould design such as in the cavity design, flow design, the gate design, the deformation forecast and cooling system design. Along with the developing and perfecting of injection molding CAE technology, its application prospect is very promising.

References

- [1] Liu Xifen, Huang Jianguang, Study on Integration Technology of Injection Mould CAD/ CAE/ CAM [J]. journal of electric processing and mould, 2008 (6) : 47-49.
- [2] Wang Limin, Ji Xiaobei, Study on Application of CAD/CAE/CAM technology in Mould Design Manufacture [J], Modern manufacture technology and equipment, 2008 (4) : 72-74.
- [3] Lan Fang, Qin Bo, CAE Technology Application in Injection Products [J], journal of Chinese manufacturing's informatization, 2009 (9) : 54-57.

Research and Development of UG-Based CAD/ CAM System for Turbine Blade

Fangjie Ren^{1, a}, Shiquan Zhou^{1, b}, Jian Li¹, Zhiqian Wan², Yi Zhao¹, Yi Liu¹

¹ Huazhong University of Science and Technology, Wuhan 430074, China

² Technology Department, China Chang Jiang Energy Corp. (Group),
 Wuhan 430074, China

^aRFJHUST@foxmail.com, ^bzhoushiquan@foxmail.com

Keywords: Turbine Blade; Secondary Development of UG; Four-Axis CNC Machining Center; CAD / CAM; Database; Management System

Abstract. A CAD/ CAM system has been developed for turbine blade's manufacturing based on the software of UG in accordance with a type of static blade of China Chang Jiang Energy Corp. (Group) in this paper. According to a few parameters input by users, the system automatically generate three-dimensional geometric model of the blade, and through its CAM module, it automatically generates the CNC track for four-axis CNC machining center. A management system has been developed by using UG / Open API, MFC, and database technology so as to improving the design efficiency in the UG.

Introduction

Turbine blade surface is a complex curved surface, of which the materials are 1Cr13 and other stainless steel materials. These materials are high strength, toughness, good thermal rigid and the most difficult part of processing in turbine Engine Group. It accounts for about 40% of all the engine processing workload[1]. Before, blade surface was manufactured by using triaxial CNC machines, and it was need to fix twice, so the accuracy can not be guaranteed. Now five-axis CNC machines are used for the large-scale turbine blade surface processing (except for hand-grinding the leaves) domestic and abroad. The process can be achieved in a single setup, including the processing of type surface, boss, blade crown, tail and other closed curves. But the five-axis CNC machines are very expensive. Therefore it is generally used for large or important blade processing, such as water turbine blades, aircraft engine turbine blade. In contrast, four-axis CNC machines is a more economical machine in processing small and medium blades[2,3].

China Chang Jiang Energy Corp. (Group) equips some four-axis CNC machining centers, and uses them to improve efficiency in turbine blades design and processing. A CAD/ CAM system was developed based on UG combined with a type of static blades of China Chang Jiang Energy Corp. (Group).

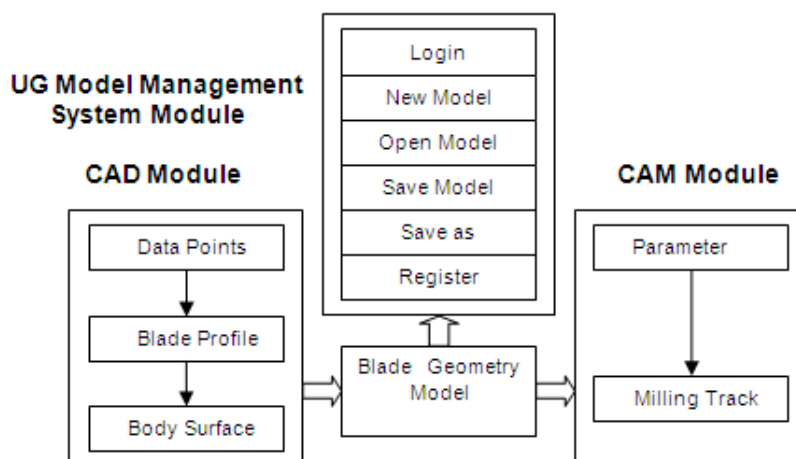


Fig. 1. Functional diagram

The Development OF Turbine Blade CAD / CAM System

The system includes three main modules: CAD module, CAM module and UG model management system module as shown in Fig. 1.

Environment and Tools of System Development

This paper use UG / OPEN Manuscript to develop system menus, use the UG / OPEN UIStyler and MFC in VC + +6.0 application platform to develop system interface, use UG / OPEN GRIP language to realize CAD / CAM function. And the UG model management system is based on the database technology.

Achievement of CAD Module

In engineering applications, the spline curves are not uniquely identified only by data points. Although put in the same data, different splines are generated using different algorithms. Especially in the secondary development, only consistent with the algorithm of development platform that you use, reconstruction errors can be avoided[6]. In paper 6, the de Boor recursive algorithm is used for seeking the reverse derivation of the control points. In this way, node parameters and data points determine the control points. And it gives a recursive algorithm consistent with UG, CAXA and some other commercial CAD softwares.

$$\begin{bmatrix} 2 & -1 & & & \\ a_4 & b_4 & c_4 & & \\ & a_5 & b_5 & c_5 & \\ \dots & \dots & & & \\ & & a_{n+1} & b_{n+1} & c_{n+1} \\ & & & a_{n+2} & b_{n+2} & c_{n+2} \\ & & & & -1 & 2 \end{bmatrix} \begin{bmatrix} d_1 \\ d_2 \\ d_3 \\ \vdots \\ \vdots \\ d_n \\ d_{n+1} \end{bmatrix} = \begin{bmatrix} Q_3 \\ Q_4 \\ Q_5 \\ \vdots \\ \vdots \\ Q_{n+2} \\ Q_{n+3} \end{bmatrix}$$

Of which, d stands for control points vector and Q is the data points vector.

$$a_i = (1 - \alpha_{i-2}^1)(1 - \alpha_{i-1}^2) \quad i = 3, 4, \dots, n+2 \quad b_i = (1 - \alpha_{i-1}^2)\alpha_{i-2}^1 + (1 - \alpha_{i-1}^1)\alpha_{i-1}^2 \quad i = 3, 4, \dots, n+2$$

$$c_i = \alpha_{i-1}^1 \alpha_{i-1}^2 \quad i = 3, 4, \dots, n+2 \quad \alpha_j^l = \frac{u - u_j}{u_{j+k+1-l} - u_j} \quad (u \text{ is a parameter value.})$$

Curve Fitting of Cross-Section Profile. First of all, the fitting of each cross section profile will be completed according to the user parameters. The steps are as follows.

①The GRIP read file function: READ / 1, X (I), Y (I), Z (I)

Through the read statement, coordinate data file can be established by the read data, and then data points are generated.

②The GRIP spline and arc spline generation function: obj = SPLINE / [closed,] point [, VECT, dx, dy, dz [TANTO, curve | angle], obj = CIRCLE / point1, point2, point3

③The GRIP rounding function: obj = FILLET/line1, line2, CENTER, center, RADIUS, r

In this step, the inlet and outlet arcs are fitted. The connection direction needs to pay attention to. The default is round clockwise defined in GRIP language.

④The GRIP curve approximation function: obj = SPLINE / APPROX, [, BLANK | DELETE [, TOLER, t,] objlist

In this step, blade basin /back curves, inlet side arc and outlet side arc form a closed smooth blade section profile.

Generation OF Blade Body Type Face. Through above steps, all the needed section profiles have been generated by the existing cross-section of blade type lines. Then the required body surface can be established by using the GRIP function:

obj = BSURF / CURVE, objlist1 [, ENDOF, |, objlist2 |, numlist] [, DEGREE, num [, CLOSED]][, IFERR, label:]

Of which: “objlist1” stands for the array of section profiles; “num” is the rank of the type face.

Blade Crown AND Blade Tail Generation. We can use the GRIP stretching function to get the simplified blade crown and tail.

The GRIP stretching function: obj = SOLEXT/line1, line2, line3, line4, HEIGHT, h, AXIS, i, j, k
Of which: i, j, k defines the tensile direction.

Verification

The results showed that: the model generated by this module meets the design requirements about the smoothness as shown in Fig. 2.

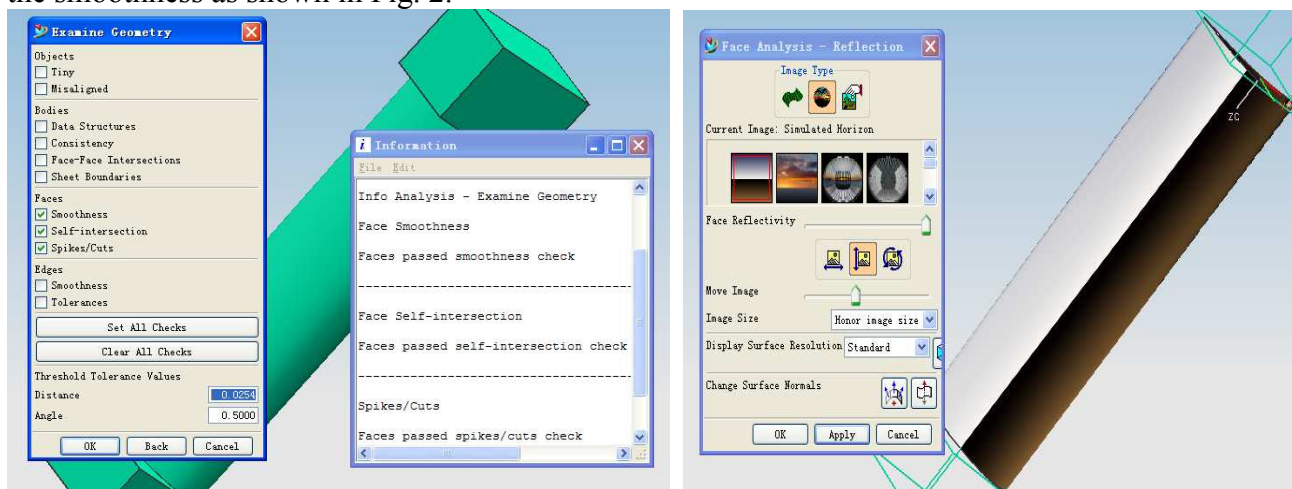


Fig.2. Verification

Cam Module

Equipment. There are two Daewoo XK5040 CNC four-coordinate vertical machining centers in China Chang Jiang Energy Corp. (Group) .

The Choice of Processing Routes and Methods. As shown in Table 1, processing routes can be set based on existing four-axis CNC machine features and the situation of blade stock, and then a rational processing mode is chosen according to the process routes.

Table 1 Processing methods

Step	Processing Method	Cut Area	Cutter
1	Rough and Finish	Blade inside and outside radial surface and tail	Ø80 face milling cutter and Ø10 end milling cutter
2	Rough Semi-finishing	Blade inlet and outlet side	Ø18 carbide ball end cutter
3	Finish	Blade inlet and outlet side	Ø16 and Ø8 carbide ball end cutter

Achievement of Cam Module. This system’s target is to process blade type surface which is free surface. The simifinished product is forging. It needs semi-finishing and finishing. The two processes in general is the same, only set on a different process parameters in the UG platform

To get blade in right size, the milling area can not be the whole blade body. No less than the radius of the milling tool must be left out in using when the first cutting and the last cutting.

Programming is described as follows for the finishing part of the blade :

- ① Initialization of processing module and set UG processing environment[4]

& MODULE = & MACH (Initialize processing module of UG)

& OPTSET = '\ mydir \ template_set \ mill_multi-axis.opt' (initialize multi-axis machining environment)

OPER / NEW, OPNAME, 'NAME', 'mill_multi-axis', 'VARIABLE_CONTOUR' (UG provides the variable multi-axis contour in milling surface mode)

② Definition of milling cutter and process-driven method

PARAM / 'Define tool', 'diameter', D ..., resp (the definition of tool parameters)

OPGEOM / GLIST, DRIVE (drive mode is surface driven)

OPGEOM / GITEM, surface (add the blade surface to the driver program)

③ Select the type of tool axis

CHOOSE / 'define tool axis type', 'Normal to Part', ...,resp

④ Define technology parameters

The technology parameters in the system involve surface stock allowance, internal / external milling tolerances, the maximum scallop and the cutting speed, using GRIP function as follow:

PARAM / 'Define parameters', 'surface stock', n1, 'outol', n2, 'intol', n3, 'scallop', n4, 'cut speed', n5, resp

⑤ Define cutting area and the generation of processing path

PARAM/'define surface%', 'firtcut start', fl...resp

& GENPTH = & YES (confirm the track)

OPER / SAVE (save the track)

Then users can use UG post-processing tools to generate NC codes for the manufacturing.

Ug Model Management System

Users may daily use dozens, or even more UG models. Finding the right model in the operating system will be time-consuming, and accuracy can not be guaranteed. To solve this problem, we develop the model management system embedded in the UG platform. It can enable users to manage their own UG models to improve the design efficiency. The system is based on Microsoft Office Access 2003 database.

The database contains the user name, password, post, department and other basic information. We use the tool of UG / Open API and MFC to achieve access to the database, the key code as follows:

```
CDatabase *m_pdatabase;
```

```
CRecordset *m_pset;
```

```
...
```

```
sSQL="delete * from prt where Username='"+seNUM+"' and Modelname='"+sPrtName+"' and Path='"+sPrtDir+"'";
```

```
m_pdatabase->ExecuteSQL(sSQL);// read the database, implementation of relevant action
```

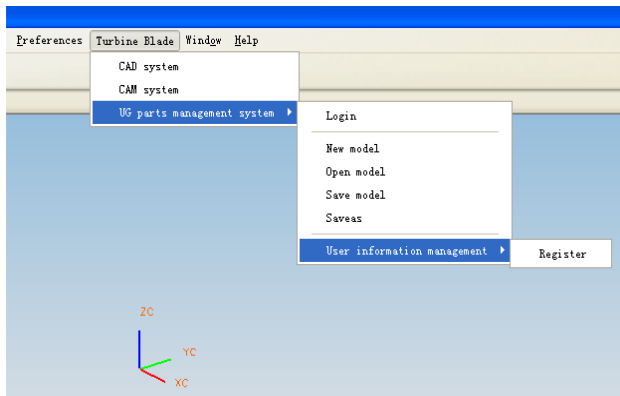


Fig. 3. System interface

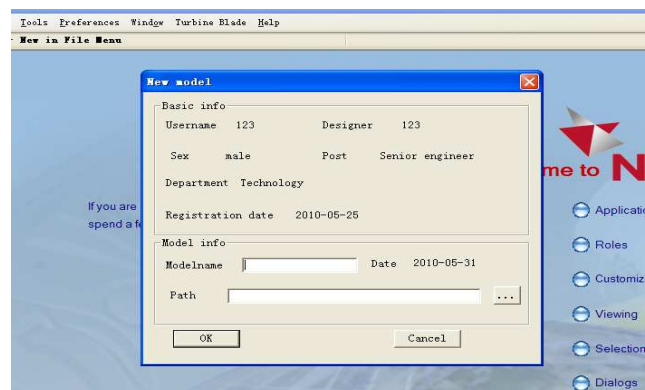


Fig. 4. System interface after login

Completemnet

After completing the above steps, we get the entire related implemented file. The system interface will be generated in the UG platform .When you start UG, you must login first. The functions are the same with UG such as creating new models, opening models and so on. These buttons are put integrated together in the system. System interface is showed in Fig. 3 and Fig. 4.

Conclusions

This system is four-axis NC machining for turbine blade type surface and design and processing efficiency are significantly improved. It reduces manufacturing costs, shorten the operation time and have a good prospect for industrial application.

Because of the four-axis NC machining process limitations, large-scale enterprises domestic and abroad have adopted five-axis machining center to process the whole blade. The future direction of secondary development of CAD/CAM systems is based on five-axis and more than five-axis manufacturing. Besides, the development of processing expert systems is our important research direction.

Acknowledgments

The authors acknowledge the support from Engineering Training Center of Huazhong University of Science and Technology and China Chang Jiang Energy Corp. (Group).

References

- [1] Y.Y.JI, L.T. WANG, W.M. QIAN and Y. J. XIANG:Manufacture Information Engineering of China.23, 40(2007)
- [2] C.Y. HUANG:MACHINETOOL & HYDRAULICS.10, 66(2005)
- [3] ALIM, ROBERTH: Proceedings of the ASME Turbo Expo 2003, (2003) June 16-19;Atlanta, USA.
- [4] Y.HUANG,B.L.ZHANG,Y.F. XUE:Publishing House of Electronics Industry,Beijing(2008)
- [5] N.KOINIG,S.S. SARAKINOS, I.K. NIKOLOS:The International Conference on Computer as a Tool,(2005)NOV.21-24;Belgrade, Serbia &Montenegro.
- [6] LV Yan-ming: Reconstructing B-Spline for Turbo Blade Section, TURBINE TECHNOLOGY, 5,48(2006)

Kinematics Analysis and Simulation of a New Type of Mechanical Excavator with Controllable Mechanism

Ganwei Cai^a, Zhuan Zhang^b, Yuchen Pan^c, Duchao Wu and Xiyong Xu

College of Mechanical Engineering, Guangxi University, Nanning 530004, China

^acaiganwei@163.com, ^bzhangzhuan-198511@163.com, ^cgxu_panyuchen@163.com

Keywords: Excavator; Screw Theory; Controllable Mechanism; Inverse Kinematics

Abstract. A new type of excavator is introduced in this paper aiming at solving the problems the hydraulic excavator and traditional mechanical excavator (also called Electric Shovel) have respectively, which are hydraulic leaks and high maintenance cost of the former one and the lack of flexibility of the latter one. The analysis of the proposed novel excavator is carried out including: Degree-of-Freedom (DOF) of the new mechanism by constraint screw theory, inverse kinematics using the method of constraint equations, velocities and acceleration. A simulation study is proposed based on the analysis above. Results show that: the new type of mechanical excavator has the ability to achieve flexible trajectory output within its workspace.

Introduction

The traditional excavators are divided into two categories: hydraulic ones and mechanical ones. The former has a simple structure, light weight, can achieve various trajectories, etc. Therefore the hydraulic excavators are widely used in surface mining, construction, and geotechnical operations [1]. But the hydraulic system of hydraulic excavator uses hydraulic fluid for the operating media, while containing a large number of hydraulic components. Without proper plumbing procedures, correct materials, and preventive maintenance, the hydraulic leaks are inevitable. With the increasing complexity of the hydraulic system, the faults have become even more sudden and concealment [2]. While the traditional mechanical excavators are huge and complex. And there is not enough flexibility and tracks for work. Even if only for the mining problems are often encountered [3], such as: Dipper teeth can not produce enough force in mining higher mesa ; Unloading height is small when unloading to the loading car, etc.

Based on the lack of traditional hydraulic excavators and mechanical excavators, we design a new type of mechanical excavator [4], which can avoid the deficiency of traditional excavator, and can realize a number of trajectories within the workspace by combining with the controlling technique.

The Mechanism Configuration and the Calculation of DOF

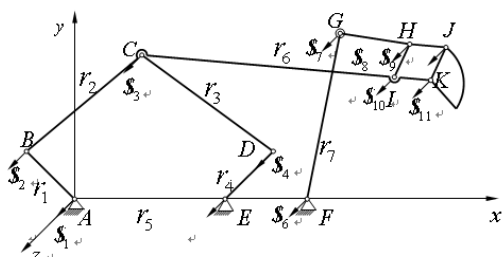


Fig. 1 Screw system of the novel excavator

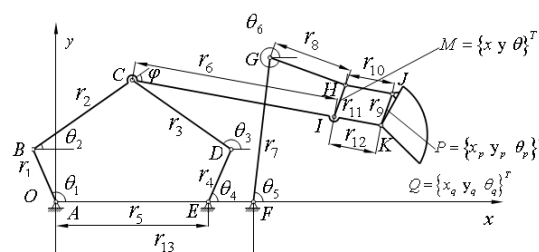


Figure. 2 Coordinates

Screw system of the novel excavator is shown in Fig. 1. This mechanism consists of a five-bar mechanism and a branched-chain. Through controlling of the five-bar's two drive links (r_1 r_4) it's able to drive the movement of the arm (r_2 r_6), so as to realize various actions of the bucket. By control the

movement of the branched chain (r_7) matching up with the movement of arm, it can realize the control of the bucket's position and posture, and realize a series of actions: digging, lifting and unloading.

Established coordinate system shown in Fig. 1, accounting excavator DOF based on screw theory [5]. 12 revolute joints can be described as screw, whose screw system can be shown as follows:

$$\begin{aligned} \mathcal{S}_1 &: (0 \ 0 \ 1; 0 \ 0 \ 0) & \mathcal{S}_2 &: (0 \ 0 \ 1; a_2 \ b_2 \ 0) & \mathcal{S}_3 &: (0 \ 0 \ 1; a_3 \ b_3 \ 0) & \mathcal{S}_4 &: (0 \ 0 \ 1; a_4 \ b_4 \ 0) \\ \mathcal{S}_5 &: (0 \ 0 \ 1; 0 \ b_5 \ 0) & \mathcal{S}_6 &: (0 \ 0 \ 1; 0 \ b_6 \ 0) & \mathcal{S}_7 &: (0 \ 0 \ 1; a_7 \ b_7 \ 0) & \mathcal{S}_8 &: (0 \ 0 \ 1; a_8 \ b_8 \ 0) \\ \mathcal{S}_9 &: (0 \ 0 \ 1; a_9 \ b_9 \ 0) & \mathcal{S}_{10} &: (0 \ 0 \ 1; a_{10} \ b_{10} \ 0) & \mathcal{S}_{11} &: (0 \ 0 \ 1; a_{11} \ b_{11} \ 0) & \mathcal{S}_{12} &: (0 \ 0 \ 1; a_{12} \ b_{12} \ 0) \end{aligned}$$

in which a_i, b_i are different constant, and during the movement process change only the value of a_i, b_i . Because the first, second and six elements of 12 *Plücker* coordinates are all zero, which is nothing to do with the changes of configuration, three reverse screws can be determined by the method of observation: $\mathcal{S}_1^r: (0 \ 0 \ 1; 0 \ 0 \ 0)$, $\mathcal{S}_2^r: (0 \ 0 \ 0; 1 \ 0 \ 0)$, $\mathcal{S}_3^r: (0 \ 0 \ 0; 0 \ 1 \ 0)$. Because there are 3 reverse screws, the mechanism has three general constraints ($\lambda = 3$), and the order is six ($d = 6 - 3 = 3$). Besides, the redundant constraint (ν) and the passive degree of freedom (ζ) are both zero. So the DOF of the excavator can be gained as follow:

$$M = d(n - g - 1) + \sum_{i=1}^g f_i + \nu - \zeta = 3 \times (10 - 12 - 1) + 12 + 0 - 0 = 3 \quad (1)$$

$$\text{in which, } d = 3, n = 10, g = 12, \sum_{i=1}^g f_i = 12, \nu = \zeta = 0$$

The DOF of the mechanism is 3 what means that it can accomplish the translation of two directions and a rotating in-plane.

Inverse kinematics

As to inverse kinematics of the five-bar, many scholars have done research [6]. In this paper, analysis of branched-chain (two-link mechanism) is added based on five-bar mechanism. Eventually, inverse kinematics of the planar excavating mechanism has been drawn.

A reference coordinate system is attached to the fixed link 5 with its original point A as shown in Fig. 2. r_1, r_4 and r_7 are the drive bars. Point Q ($\{x_q \ y_q \ \theta_q\}^T$) is tip of the bucket. M ($M = \{x \ y \ \theta\}^T$) and P ($P = \{x_p \ y_p \ \theta_p\}^T$) are the middle points of the bar r_{11} and r_9 , respectively. Points *JKIH* form a parallelogram. Then we have

$$\begin{cases} (y - y_p)^2 + (x - x_p)^2 = r_{10}^2 \\ \frac{y - y_p}{x - x_p} = \frac{y_I - y_c}{x_I - x_c} \end{cases} \quad (2)$$

Point M can be defined by the position of H and I, so

$$\begin{cases} x_I = x - \frac{r_{11}}{2} \cos \theta \\ y_I = y - \frac{r_{11}}{2} \sin \theta \end{cases} \quad \begin{cases} x_H = x + \frac{r_{11}}{2} \cos \theta \\ y_H = y + \frac{r_{11}}{2} \sin \theta \end{cases} \quad (3)$$

Because P is the midpoint of r_9 as well as the dot of the bucket, the movement of the point P can reflect the bucket's movement. And joints *JKIH* form a parallelogram, while point M is the midpoint of r_9 opposite side, so point M has the same form of movement with P . Therefore, movement of the output can be expressed with the movement of $M = \{x \ y \ \theta\}^T$.

Constraint equations can be obtained, say

$$\begin{cases} (x_c - r_1 \cos \theta_1)^2 + (y_c - r_1 \sin \theta_1)^2 = r_2^2 \\ (x_c - r_4 \cos \theta_4 - r_5)^2 + (y_c - r_4 \sin \theta_4)^2 = r_3^2 \\ (x_H - r_{13} - r_7 \cos \theta_5)^2 + (y_H - r_7 \sin \theta_5)^2 = r_8^2 \end{cases} \quad (4)$$

Let $r_1 = r_4$, $r_2 = r_3$, $\theta_i = 2 \arctan t_i$ ($i = 1, 4, 5$), $\sin \theta_i = \frac{2t_i}{1+t_i^2}$, $\cos \theta_i = \frac{1-t_i^2}{1+t_i^2}$, yields

$$a_i t_i^2 + b_i t_i + c_i = 0 \quad (i = 1, 4, 5) \quad (5)$$

Then we have $t_i = \frac{-b_i \pm \sqrt{b_i^2 - 4a_i c_i}}{2a_i}$ ($i = 1, 4, 5$), so

$$\theta_i = 2 \arctan t_i \quad (i = 1, 4, 5) \quad (6)$$

Analysis of velocity and acceleration

Differentiating Eq. 4 with respect to time, we get

$$\begin{cases} (x_c - r_1 \cos \theta_1) x_c + (y_c - r_1 \sin \theta_1) y_c + (x_c r_1 \sin \theta_1 - y_c r_1 \cos \theta_1) \theta_1 = 0 \\ (x_c - r_4 \cos \theta_4 - r_5) x_c + (y_c - r_4 \sin \theta_4) y_c + [(x_c - r_5) \sin \theta_4 - y_c \cos \theta_4] \theta_4 = 0 \\ (x_H - r_7 \cos \theta_5 - r_{13}) x_H + (y_H - r_7 \sin \theta_5) y_H + [(x_H - r_{13}) r_7 \sin \theta_5 - y_H r_7 \cos \theta_5] \theta_5 = 0 \end{cases} \quad (7)$$

Substituting each parameter into Eq. 7, yields:

$$\begin{cases} B_{11}x + B_{12}y + B_{13}\theta = N\theta_1 \\ B_{21}x + B_{22}y + B_{23}\theta = P\theta_1 + Q\theta_4 \\ B_{31}x + B_{32}y + B_{33}\theta = R\theta_5 \end{cases} \quad (8)$$

Eq. 8 can be written into matrix form, we can get the relationship between input and output:

$$A(\dot{\theta}_1 \dot{\theta}_4 \dot{\theta}_5)^T = B(\dot{x} \dot{y} \dot{\theta})^T \quad (9)$$

in which,

$$A = \begin{bmatrix} N & 0 & 0 \\ P & Q & 0 \\ 0 & 0 & R \end{bmatrix} \quad B = \begin{bmatrix} B_{11} & B_{12} & B_{13} \\ B_{21} & B_{22} & B_{23} \\ B_{31} & B_{32} & B_{33} \end{bmatrix}$$

Differentiating the velocity (Eq. 9) with respect to time, we can get the relationship of acceleration,

$$\dot{A}(\ddot{\theta}_1 \ddot{\theta}_4 \ddot{\theta}_5)^T = \dot{B}(\ddot{x} \ddot{y} \ddot{\theta})^T. \quad (10)$$

Simulation Study

Structure parameters are shown in the table1:

Table 1 Structure parameters (in mm)

r_1	r_4	r_2	r_3	r_5	r_6	r_7	r_8	r_9	r_{10}	r_{11}	r_{12}	r_{13}
300		600			800	700		150				300

Initial position of the excavator: the angle between r_1 and x -axis positive is θ_1 ($\theta_1=135^\circ$); the angle of r_4 and x -axis positive is θ_4 ($\theta_4=45^\circ$); the angle of r_7 and x -axis positive is θ_5 ($\theta_5=80^\circ$).

In order to illustrate the fact that the new excavator can accomplish given trajectories within the workspace, simulation of inverse kinematics is carried out. Two trajectories are given as follows:

Case I. The excavator can be used for leveling soil, so the horizontal movement is necessary for the new excavator. The trajectory of horizontal direction is given as shown in Fig. 5:

For this specific output trajectory, the angular velocities and angular acceleration of the input variables (link 1, link 4, link 7) can be obtained, shown in Figs. 3-4.

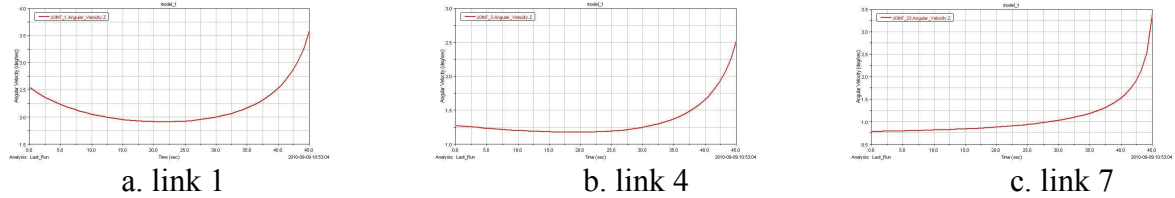


Fig. 3 Angular velocities of drive links

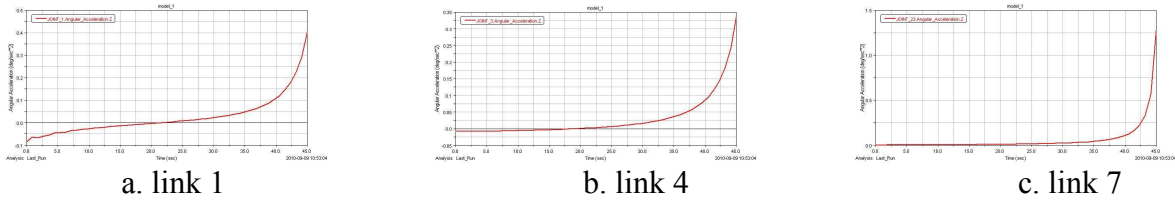


Fig. 4 Angular acceleration of drive links

When the output of the new mechanism is horizontal straightness, the angular velocity and acceleration of the active components are relatively stable within 0~30s, while there is a mutation after 30s. One can get the results from Figs. 3-4 as above.

Case II. High unloading is a task of excavator, which is used to finish mining and loading task. So the trajectory as shown in Fig. 6 is given, it can finish the task which is similar to hydraulic excavator's mining and loading when Bucket tips move along the given trajectory.

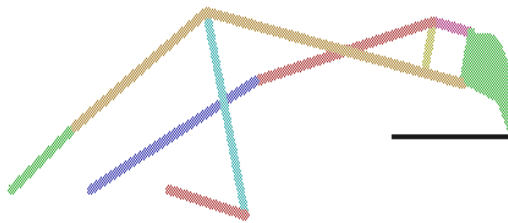


Fig. 5 Case I

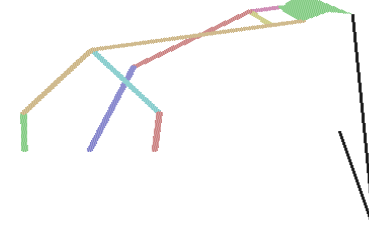


Fig. 6 Case II

When Bucket tips move along the given trajectory, the angular velocity and angular acceleration of the input variables (links 1, link 4, link 7) can be obtained, shown in Figs. 7-8

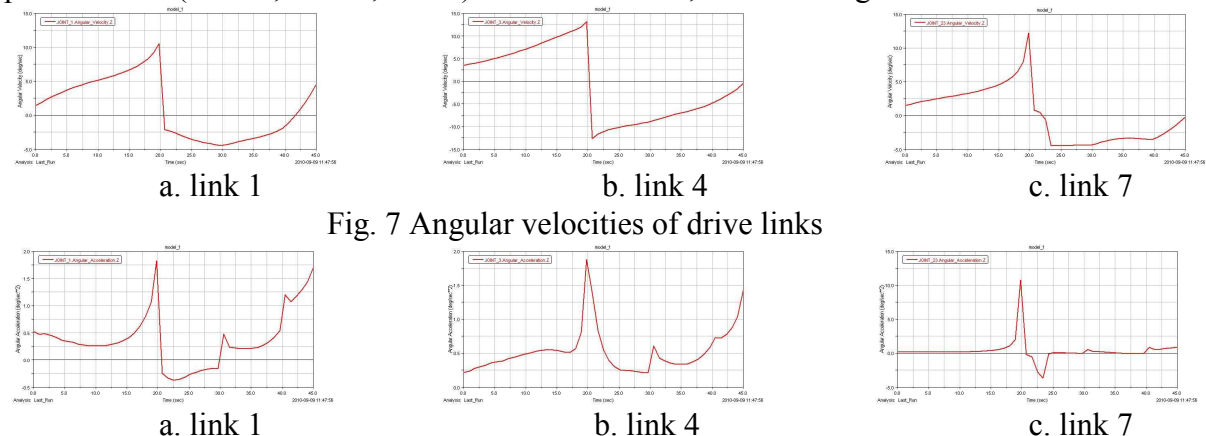


Fig. 7 Angular velocities of drive links

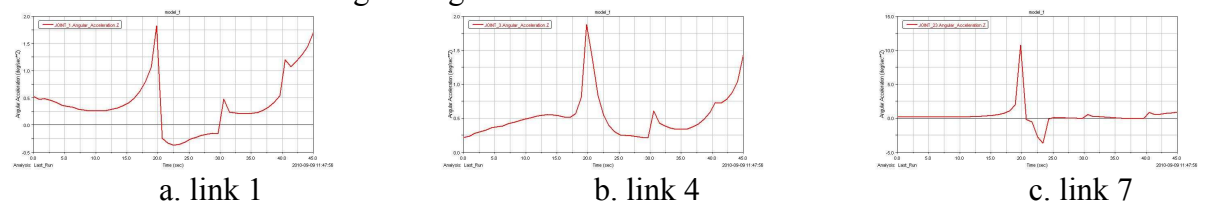


Fig. 8 Angular acceleration of drive links

From the simulation process and the simulation output one can see that during 0-20s mechanism completes the task of bucket down and digging, after 20s Bucket from the downstream to upstream, then handling the material to the design position, finally completing the uninstall action. From the Figs. 7-8 can also be seen the acceleration of drive links are very fluctuation when the mechanism moves in accordance with the given trajectory. Therefore, in the follow-up work one needs to couple with control technique, carry out real-time control about the input of drive links, thereby it can realize the purpose of reducing the impact.

Conclusions

(1) A new type of mechanical excavator was introduced in this paper as well as the calculation of the DOF based on constraint screw theory.

(2) Kinematics analysis of the proposed excavator was investigated including constraint equations, inverse kinematics, angular velocities and acceleration.

(3) Computer simulations were then carried out based on the kinematics analysis above. Results show that the new type of excavator has the ability to accomplish complex trajectories just like a flexible hydraulic excavator by the joint motions of the three driving bars while over problems such as hydraulic leaks and high cost of maintenance.

Acknowledgement

The research work is jointly sponsored by the National Natural Science Foundation of China (No. 51075077), Guangxi Key Laboratory of Manufacturing System & Advanced Manufacturing Technology Projects (No. 07109008_00 9_Z, 09-007-05S013) and Teams for Innovation in the Construction of Talent Highlands in Guangxi Institutions of Higher Learning.

References

- [1] J. Maciejewski, A. Jarzgbowski, W . Trampczyriski: Journal of Terramechanics, Vol.40(2004), p. 221.
- [2] Samuel Frimpong, Ying Li.: Engineering Failure Analysis, Vol. 14 (2007), p. 702.
- [3] Shu-wen Yan. Mechanical Excavator Design [M].Beijing: China Machine Press, 1996. (In Chinese)
- [4] Ganwei Cai, Yuchen Pan. A Type of Planar 3-DOF Controllable Excavating Mechanism, 200910114447.0[P]. 2010-03-10.
- [5] Zhen Huang, Yongsheng Zhao, Tieshi Zhao. Advanced Spatial Mechanism [M] . Beijing: HEP 2005. (In Chinese)
- [6] Yuan Jian-feng Zhang Xian-min: Journal of South China University of Technology (Natural Science Edition), Vol. 35 (2007), p. 39. (In Chinese)

3D Laser Inner Engraving Path Generation and Simulation for Crystal Glass

Hu Zhu^a, Nan Li^b and Zhijun Liu^c

College of Mechanical and Electrical Engineering, Shenyang Aerospace University, Shenyang, Liaoning 110136, China

azhuhu100@yahoo.com.cn, blinanxiujiao@163.com, cdongfangshenglong1@163.com

Keywords: Laser Inner Engraving; Crystal Glass; Engraving Path; Simulation

Abstract: The method of laser inner engraving path generation and simulation for crystal glass is presented based on STL(Stereo Lithography) model. To generate the laser exposure points that are adaptive to the surface of model, the contour lines are obtained by cutting the STL model with unequal distance using a series of plans that are perpendicular to Z-axis. Then the contour lines are offset and scattered, and then the path is generated by sorting and connecting each discrete point in order. Simultaneously, simulation method of laser inner engraving for crystal glass is also proposed. The case studies show that the method can primely realize the engraving path generation and the simulation for the laser inner engraving of crystal glass, and that the system runs stably and reliably.

Introduction

The laser engraving technology of crystal glass can generate a pretty image on the inner of crystal glass, and is widely used in making artware. In this technology, the engraving path generation is one of the most important problems because it influences the engraving quality and time. However, the researches on engraving path generation have not been fully conducted. Most existing papers are related to the engraving machine system design and control[1-3], but the papers on the engraving path generation are not many, especially on the engraving path for 3D image. Wang[4] studied real-time slicing algorithm for 3D laser carving system. Fu[5] researched on the optimization of the engraving order, but not mentioned on the methods of overall engraving path generation. In this paper, a method of laser inner engraving path generation and simulation for crystal glass is proposed based on the STL model by using variant slicing approach.

Laser Inner Engraving Path Generation

The contour lines are obtained by slicing 3D model with a series of plans that are perpendicular to Z-axis. According to the accuracy of 3D graphics to be generated, contour lines are offset inward on the same cutting plane. Then the contour lines and the offset contour lines are scattered in a certain distance so that the position of laser exposure points are acquired. Finally the exposure points are linked in a certain order to generate the laser inner engraving path.

3D Model Slicing and the Contour Lines Calculating. To make the laser exposure points adaptively distributed on the surface along the Z-axis, this paper proposes a non-equidistant slicing method for controlling the distance between exposure points according to the adaptive slicing approach[6], and the key of the method is the determination of slicing distance. As shown in Fig. 1, the layer distance $H_{i,j}$ of j th triangle between i th and $i+1$ th layer can be calculated as follows:

$$H_{i,j} = L \cdot \sin \alpha_{i,j} \quad (1)$$

Where L is the control distance between two exposure points on the surface along Z-axis and determined by user, $\alpha_{i,j}$ is the angle between triangular facet and cutting plane that can be calculated by using the normal vector of triangle facet. The minimum value of $H_{i,j}$, namely $h_i = \min\{H_{i,j}\}$, is taken as the cutting distance.

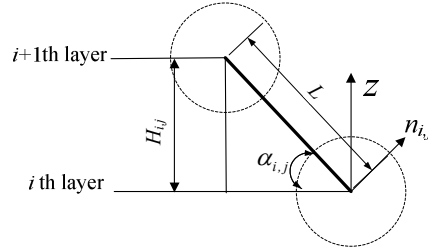


Fig. 1 Cutting model

The key of the contour lines determination is to calculate the intersection points of triangular facet and cutting plane. As shown in Fig. 2 $Q_{ik}(x_{ik}, y_{ik}, z_{ik})$ stands for the k th intersection point of the i th cutting plane and the edge $P_{j1}(x_{j1}, y_{j1}, z_{j1})P_{j2}(x_{j2}, y_{j2}, z_{j2})$ of triangular facet, Z_{\min} is the minimum value of z coordinate of the points on the model, and the coordinate of $Q_{ik}(x_{ik}, y_{ik}, z_{ik})$ can be calculated by using equation(2) and (3). The i th cutting contour line is acquired by connecting the Q_{ik} in order. In the same way, all the cutting contour lines can be obtained by cutting the model at interval of h_i .

$$\frac{x_{ik} - x_{j1}}{x_{j2} - x_{j1}} = \frac{y_{ik} - y_{j1}}{y_{j2} - y_{j1}} = \frac{z_{ik} - z_{j1}}{z_{j2} - z_{j1}} = t \quad (0 \leq t \leq 1) \quad (2)$$

$$\begin{cases} x_{ik} = \frac{z_{ik} - z_{j1}}{z_{j2} - z_{j1}}(x_{j2} - x_{j1}) + x_{j1} \\ y_{ik} = \frac{z_{ik} - z_{j1}}{z_{j2} - z_{j1}}(y_{j2} - y_{j1}) + y_{j1} \\ z_{ik} = Z_{\min} + \sum_{i=1}^m h_i \end{cases} \quad (3)$$

Contour Lines Offset and Scattering. Each line segment of the contour lines is offset along the direction vertical to the line segment on the cutting plane by a distance of I that is determined by the user according to the engraving precision. Then the intersection points of the offset line segments are calculated and the offset contour lines are obtained by linking the intersection points.

Exposure points are acquired by scattering the contour lines and the offset contour lines by a distance of L_1 which is determined by the user according to the engraving precision. Fig. 3 shows that the exposure point C is gained by scattering the segment AB at interval L_1 . The scattering process will end if the length of CB is smaller than L_1 , otherwise it will not terminate until the length of CB is smaller than L_1 . Finally the exposure points are arranged in order and connected to be engraving path.

Simulation of Laser Engraving

The simulation environment of laser inner engraving is built by using VC++ and OpenGL as shown in Fig. 4, where the colorless transparent cube represents crystal glass(workpiece), the cone of 2:5 taper with a small cylindrical represents laser beam head, the small black points represent exposure points. The galvanometer scanner type laser engraving machine is taken as the studying platform, and the fixed crystal glass is carved by means of laser beam movement in this paper.

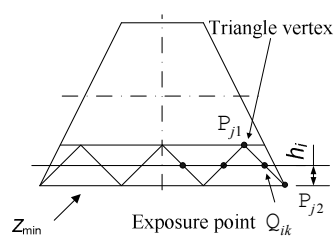


Fig. 2 Exposure points calculation

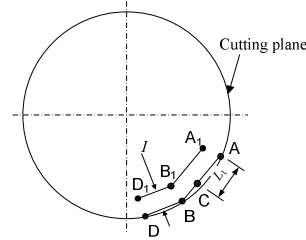


Fig. 3 Offset points calculation

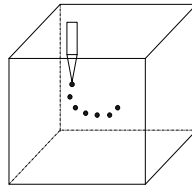


Fig. 4 Simulation

The simulation process of laser inner engraving is accomplished by OnTimer(), SetTimer() function in MFC and glTranslate() function of OpenGL. First, set a timer by using SetTimer() function in OnInitialUpdate() function, which sends a movement signal to its information processing function OnTimer() at a certain time interval. Then add cube, cone, cylinder image output function mentioned above and glTranslatef() function in OnTimer() function, the spatial location of laser beam is translated by changing x, y, z parameters value of the glTranslate() function. Finally, add InvalidateRect() function to refurbish image synchronously, which shows animated simulation.

Case Studies

The described algorithm has been implemented using VC++ and OpenGL. Fig. 5 shows the user interface of the developed software and the test STL model. Fig. 6a shows the cutting contour lines, which are obtained by adaptively cutting the STL model at unequal intervals. In the example the control distance L between two exposure points is set as 1.5 mm, the radius of exposure point is set as 2 mm. As shown in Fig. 6a, the cutting contour lines obtained by the proposed method are evenly distributed on the model surface compared with the one obtained by cutting the model with equal distance of 1.5mm shown as Fig. 6b.

Fig. 7 shows the offset contour lines which are obtained by offsetting the cutting contour lines inward 1.5 mm. Fig. 8 shows the discrete points that are obtained by scattering each contour line at the interval of 1.5mm. Fig. 9 shows the simulation process of laser inner engraving for crystal glass.

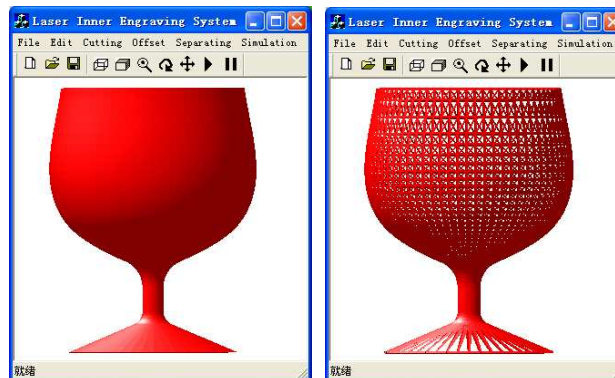


Fig. 5 The test model

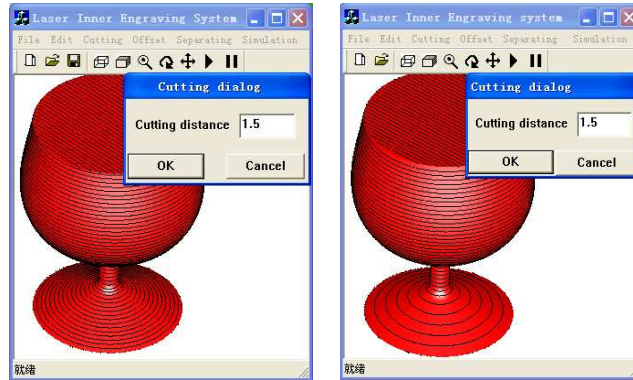


Fig. 6 (a) Contour cutting-1 (b) Contour cutting-2

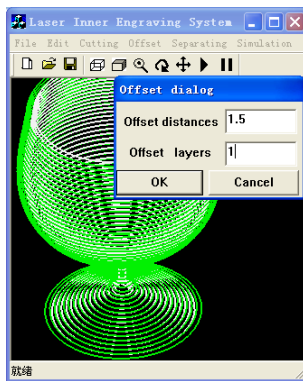


Fig. 7 Contour offset

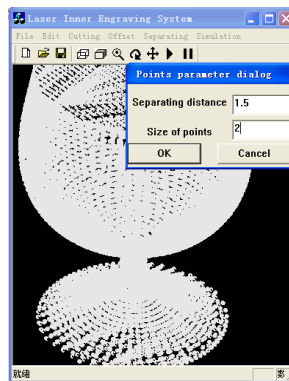


Fig. 8 Scattered points

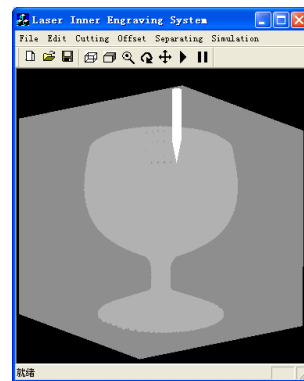


Fig. 9 Simulation process

Conclusions

The proposed method can automatically control the density of laser exposure points according to the complexity of the model surface, and improve the engraving efficiency on the premise of ensuring the accuracy. In addition, the engraving path verification, engraving effect forecasting, defect diagnosing and engraving parameters optimizing can be completed by the simulation function of the software. The developed software system runs stably and reliably, and it not only can be applied to laser inner engraving for crystal glass, but also can be used in the other areas of laser machining.

References

- [1] W.H. Jiang and X.L. Wen: Electrical Automation Vol. 30(2008), p. 14.(In Chinese)
- [2] W.H. Jiang: Electric Drive Vol. 34(2004), p. 25.(In Chinese)
- [3] S.D. Ma, Z.Q. Yin and F. Xue: Machine Tool & Hydraulics Vol. 32(2004), p. 59.(In Chinese)
- [4] C. Wang, X. Y. Zeng: Journal of Engineering Graphics Vol. 29(2008), p.13.(In Chinese)
- [5] X.D. Fu, P.J. Wang, X.Q. Tang and J.H. Chen: China Mechanical Engineering Vol. 19(2008), p. 598.(In Chinese)
- [6] A. Dolenc, I. Makela: Computer Aided Design Vol. 1(1994), p. 4.

Visualized Equivalent Variational Modeling in Tolerance Analysis of 3D Mechanical Assemblies

Dongya Yang^a, Jun Gong^b

College of Mechano- Electronic Engineering, Lanzhou Univ. of Tech., Lanzhou 730050, China

^aeastasiayang@163.com, ^bgongjjdxy@sohu.com

Keywords: Tolerance Analysis; Equivalent Variational Modeling; EVJ; EVM.

Abstract. This paper introduces a new, visualized approach for including all the geometric feature variations in the tolerance analysis of mechanical assemblies. It focuses on how to characterize geometric feature variations in vector-loop-based assembly tolerance models. The characterization will be used to help combine the effects of all variations within an assembly in order to perform tolerance analysis of mechanical assemblies by employing commercial 3D kinematic software (e.g. ADAMS). Equivalent variational modeling, based on TAKS method, has been developed for modeling variations in 3D mechanical assemblies. Create a library of Equivalent Variational Joints (EVJs) to allow inclusion all kinds of variations in analysis, and allow the kinematic model to include both geometric and dimensional variation in a velocity analysis. EVJ, for use in tolerance analysis, was developed for commonly used 3D kinematic joint types, and was implemented with examples to explain their use to form Equivalent Variational Mechanisms (EVMs).

Introduction

Tolerance is imperative for seamless integration of CAD/CAM and influences greatly the quality, process planning, measurement, cost and assembly of the product. Many researches have been conducted on tolerance [1,2]. Most of these researches are focused on numerical analysis and synthesis. Unfortunately, tolerance analysis generally involves complex and tedious calculations which are time-consuming and prone to error. Furthermore, in those researches tolerance information has already been correspondingly used with entity element. However there are still some issues. The tolerances are just analyzed numerically in most of those modules, such as statistical tolerance analysis and worst-case tolerance analysis.

In an attempt to solve this problem, efforts are being made to simplify the tolerance modeling and automate tolerance analysis as much as possible. Fortunately, the TAKS method (Tolerance Analysis Using Kinematically-Derived Sensitivities) [3] leads a road to create a tolerance model from a kinematic mechanism using equivalent variational mechanisms (EVMs) [4]. With the increasing use of CAD/CAM/CAE systems for mechanical design, it is desirable to use a visualized model of the assembly to perform the tolerance analysis at the design stage.

In this study, three sources of variation in 3D mechanical assemblies are fully studied and equivalently replaced. A library of equivalent variational joints is created to allow inclusion all kinds of variations in analysis. The objectives of this work are: (1) Simplifying tolerance analysis of 3D assembly system and avoiding complex and tedious calculations; (2) Image model rather than digital model, enhances the perception of tolerancing; (3) Performing tolerance analysis by means of kinematic analysis software (e.g. ADAMS).

Equivalent Variational Modeling

Three sources of variation. There are three main sources of variation which must be accounted for in mechanical assemblies: (1) Dimensional variations (lengths and angles); (2) Geometric form and feature variations (flatness, roundness, angularity, etc.); (3) Kinematic variations (small adjustments between mating parts). Dimensional and form variations are the result of variations in the manufacturing processes or raw materials used in production. Kinematic variations occur at

assembly time, whenever small adjustments between mating parts are required to accommodate dimensional or form variations.

The two-component assembly shown in Fig. 1 and 2 demonstrates the relationship between dimensional and form variations in an assembly and the small kinematic adjustments which occur at assembly time. The parts are assembled by inserting the cylinder into the groove until it makes contact on the two sides of the groove. For each set of parts, the distance U will adjust to accommodate the current value of dimensions A , R and θ . The assembly resultant U_1 represents the nominal position of the cylinder, while U_2 represents the position of the cylinder when the variations A , R and θ are present. This adjustability of the assembly describes a kinematic constraint, or a closure constraint on the assembly.

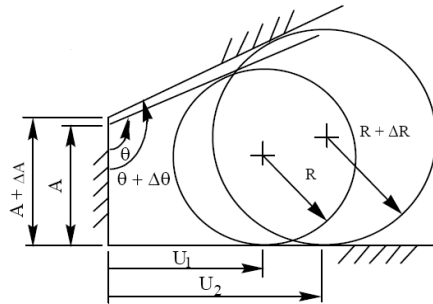


Fig.1 Kinematic adjustment due to component dimensional variations

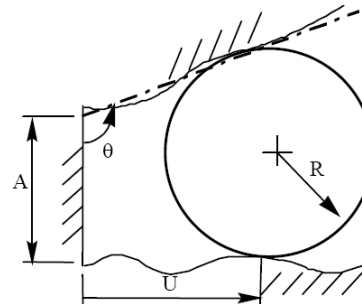


Fig. 2. Adjustment due to component dimensional variations and geometric shape variations

It is important to distinguish between component and assembly dimensions in Fig. 1. Whereas A , R and θ are component dimensions, subject to random process variations, distance U is not a component dimension, it is a resultant assembly dimension. U is not a manufacturing process variable, it is a kinematic assembly variable. Variations in U can only be measured after the parts are assembled. U is a dependent variable. A , R and θ are the independent random variables in this assembly.

Fig. 2 illustrates the same assembly with exaggerated geometric feature variations. For production parts, the contact surfaces are not really flat and the cylinder is not perfectly round. The pattern of surface waviness will differ from one part to the next. In this assembly, the cylinder makes contact on a peak of the lower contact surface, while the next assembly may make contact in a valley. Similarly, the lower surface is in contact with a lobe of the cylinder, while the next assembly may make contact between lobes.

Local surface variations such as these can propagate through an assembly and accumulate just as size variations do. Thus, in a complete assembly model all three sources of variation must be accounted for to assure realistic and accurate results.

KDF. The kinematic degrees of freedom (KDF) which describe the small adjustments between mating parts may be added to a vector assembly model by inserting kinematic joints into the vector loops. Fig. 3 shows 12 common kinematic joints used to represent mating surfaces in assemblies. The arrows and numbers indicate the degrees of freedom in each case.

Vector models have been widely used to represent the rigid body kinematics of mechanisms. They may also be used to model static assemblies. The major differences between a kinematic model of a mechanism and a kinematic model of a static assembly are the inputs and outputs. For mechanism analysis, the inputs are large motions of one or more of the members; the outputs are the rigid body displacements, velocities, etc. of the members. For static assemblies, the inputs are small variations in the dimensions or form of the members; the outputs are the small rigid body displacements and geometric variations that occur due to production variations. For a mechanism model, the solution describes the motion of a single mechanism with time. For a static assembly, a statistical solution gives the variation of all assemblies compared to the nominal assembly.

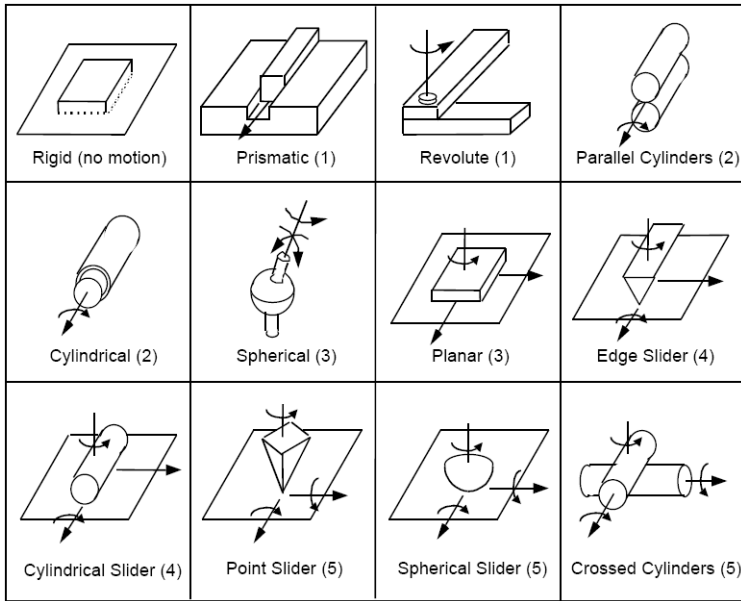


Fig. 3 Kinematic joint types in 3D

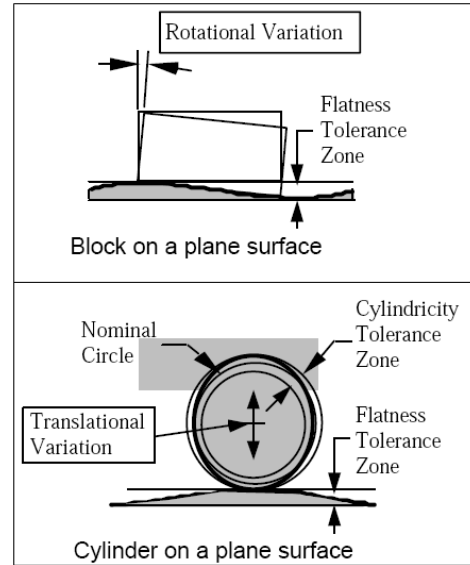


Fig. 4 3D effects of geometric feature tolerance

Geometric Variations. The third source of variation to be included in a vector assembly model is due to geometric variations of form, orientation and location. Such variations can only introduce variation into an assembly where two parts make mating contact. The manner in which geometric variation propagates across mating surfaces depends on the nature of the contact.

Fig. 4 illustrates this concept. Consider a cylinder on a plane, both of which are subject to surface waviness, represented by a tolerance zone. As the two parts are brought together to be assembled, the cylinder could be on the top of a hill or down in a valley of a surface wave. Thus, for this case, the center of the cylinder will exhibit translational variation from assembly-to-assembly in a direction normal to the surface. Similarly, the cylinder could be lobed, as shown in the figure, resulting in an additional vertical translation, depending on whether the part rests on a lobe or in between.

In contrast to the cylinder/plane joint, the block on a plane showed in Fig. 4 exhibits rotational variation. In the extreme case, one corner of the block could rest on a waviness peak, while the opposite corner could be at the bottom of the valley. The magnitude of rotation would vary from assembly-to-assembly. Waviness on the surface of the block would have a similar effect.

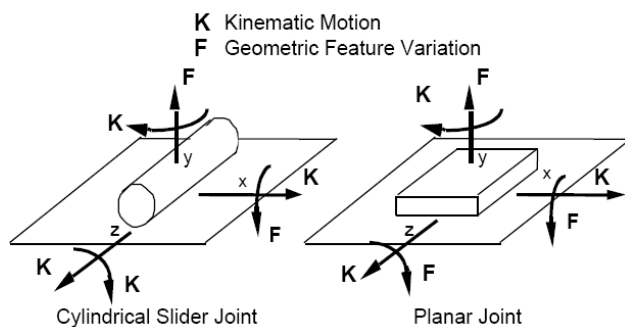


Fig. 5 Degrees of freedom for kinematic motions and geometric feature variations

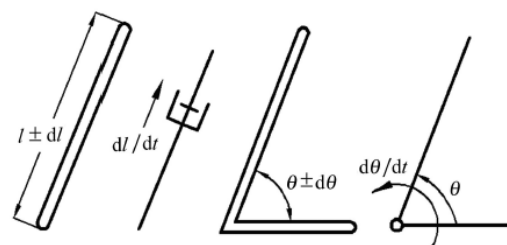


Fig. 6 Equivalent Variational Sources

In general, for two mating surfaces, we would have two independent surface variations which introduce variation into the assembly. How it propagates depends on the nature of the contact, that is, the type of kinematic joint. Fig. 5 shows two 3D joints subject to surface variation. The arrows marked by an F indicate the direction of form variation propagation. The arrows marked with a K indicate the kinematic degrees of freedom in the joint.

Equivalent Variational Sources. The variations are modeled by including equivalent variational elements in the EVM. Independent linear variations are modeled by splitting a link in the vector model into two sublinks and joining them with a translational joint and applying a unit linear velocity. Independent angular variations are modeled by creating a pin joint at the point of variation, and applying a unit angular velocity. As velocity is analogous to variation, a specified velocity must be included in the assembly for every dimension with specified variation. The equivalent elements allow for dimensional variation to be introduced using traditional kinematic elements. Fig. 6 shows representations of these equivalent elements for independent linear and angular variation.

EVJ. The equivalent variational joint (EVJ) simulates a type of contact in a 3D mechanical assembly by replicating its degrees of freedom with an equivalent skeleton model joint. The skeleton model permits inclusion of varying length and angular dimensions in the joints. The purpose of the EVJ is to allow a kinematic model of a mechanical joint to include dimensional variation that might occur in the joint. An additional reason to have an EVJ for some joints is the possibility that a kinematic modeler may not include a specific joint type in its joint library. ADAMS does not include a parallel cylinders joint, or an edge slider, or any of the other kinematic joint types that have been represented by EVJs in this research. Thus, it is required to model these joints with equivalent joints, even though perhaps no dimensional variation is generated within the joint, as is the case with the edge slider. This results in equivalent variational joints, which are used to form equivalent variational mechanisms are summarized in Fig. 7.

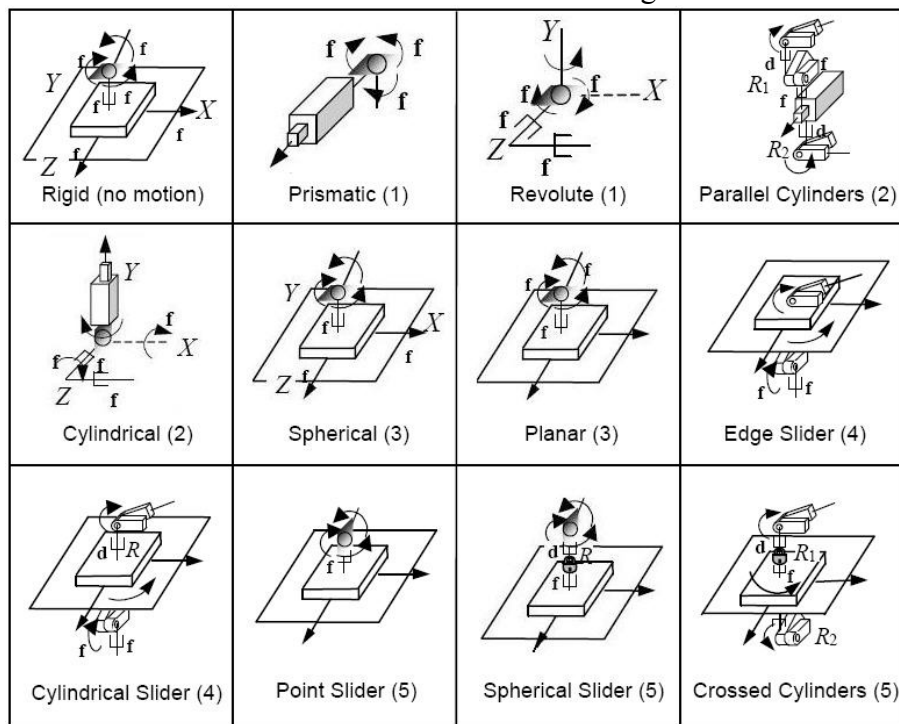


Fig. 7 3D Equivalent Variational Joints (EVJs)

EVM. An equivalent variational mechanism (EVM) is a modified mechanism that is theoretically and analytically equivalent to the original mechanism. It has been modified to allow all the variations to be introduced into the model, and to facilitate the modeling of the mechanism in kinematic software. When the dimension chain has been incorporated with the equivalent variational components and joints, a complete EVM can be constructed.

The EVJs can be generated automatically by customization. Each EVJ was modeled by software language and imbedded in the well-known CAD/CAE software (e.g. ADAMS) as a built-in function button [5, 6]. The method above simplifies the modeling of EVM. When the dimension chain has been incorporated with the equivalent variational components and joints, a complete EVM is constructed.

Visualized 3D Example

The crank slider shows in Fig. 8, along with its vector loop. In this figure, the independent and dependent variables are also illustrated. Next, modifications are made to the vector loop to allow the inclusion of dimensional variation. According to the equivalent variational elements shown in Fig. 6, schematic EVJs for variation are inserted into the vector loop model. Fig. 9 displays the EVM for the 3D crank slider, with the dimension chain and all equivalent variational components and joints.

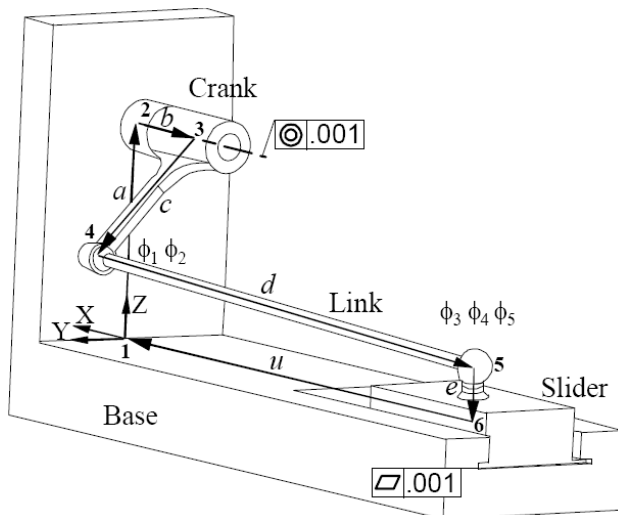


Fig. 8 Crank slider with vector loop

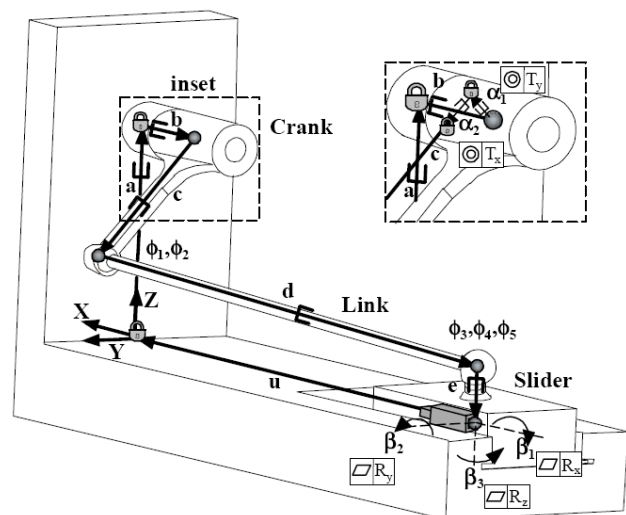


Fig. 9 EVM for 3D crank slider

Conclusions

A visualized equivalent variational modeling method has been presented for characterizing geometric feature tolerances in vector-loop-based assembly tolerance models and including such tolerances in the estimation of variations and assembly rejects 3D mechanical assemblies.

Create a library of 3D equivalent kinematic joints for use in tolerance analysis. A library of new Equivalent Variational Joints was developed for commonly used 3D kinematic joint types, and was implemented with examples to explain their use to form Equivalent Variational Mechanisms (EVMs).

Create a library of equivalent joints to allow inclusion all kinds of variations in analysis. Equivalent Variational Joints (EVJs), which allow the kinematic model to include both geometric and dimensional variation in a velocity analysis.

Demonstrate the kinematic analogy by employing commercial 3D kinematic software to perform tolerance analysis of both static assemblies and mechanisms. The EVM of the example can be modeled using the commercial kinematic modeler ADAMS, demonstrating the viability of the equivalent mechanism approach.

References

- [1] Y.L. Cao, Y.S. Liu, J. Mao and J.X. Yang: Journal of Zhejiang University SCIENCE A, Vol. 7 (2006) No.11, pp.1180-1188.
- [2] D.B. Parkinson: ASME J. Mech. Des., Vol. 22 (2000), pp.149-154.
- [3] P.J. Faerber: *Tolerance Analysis of Assemblies Using Kinematically-Derived Sensitivities* (MS., Brigham Young University, USA 1999), pp.7-30.
- [4] K. W. Chase, J. Gao, and etc.: IIE Transactions, Vol. 28 (1996), pp.795-807.
- [5] D.Y. Yang and J. Gong: Advanced Materials Research, Vol. 139-141 (2010), pp.1289-1293.
- [6] D.Y. Yang and J. Gong: ICPR21 (Shanghai, China, August 2-6, 2009). Vol. 1, pp.63.

Computer Simulation of Uniform Corrosion Process for Carbon Steel

Wu Anqi^{1,2,a}, Yu Hongying^{2,b}, Sun Dongbai^{1,2,c}

¹National Center for Materials Service Safety,

University of Science and Technology Beijing, Beijing 100083, China

² Laboratory for Corrosion-Erosion and Surface Technology, Corrosion and Protection Center,

University of Science and Technology Beijing, Beijing 100083, China

^awuanqi-2002@163.com, ^bhyyu@ustb.edu.cn, ^cdbsun@mater.ustb.edu.cn

Keywords: Simulation, Carbon Steel; Uniform Corrosion; Cellular Automata, Model

Abstract. Computer simulation is a new research approach for corrosion science. A simple model is proposed to describe uniform corrosion process which is a common corrosion failure type for carbon steel. As a lot of chemical and physical processes take place during corrosion reaction with complexity and random, we have to simplify the complex process to establish a math model which is suitable for a simulation calculation. The computational model based on cellular automata (CA) approach uses local rules to govern the electrochemical reactions, and simulate the corrosion system as a discrete dynamical system. As a result the simulation computational solution is compared with experimental data in this work, both of which show the same characteristics of data distribution. The results presented the feasibility of the cellular automata approach to simulate the corrosion process and to describe change of surface topography in company with the increase of corrosion quantity.

Introduction

Computer simulation for corrosion process, which is developed based on original experimental methods, is an accurate and fast method to evaluate corrosion damage. The results of computer simulation can be used to predict and evaluate corrosion behavior and long term damage degree of material. The research on computer simulation is composed of two processes, mathematical modeling and simulation computation. Mathematical modeling is the basis and core of simulation computation. Nowadays the process of computer simulation for corrosion process normally includes three steps. First, the corrosion phenomenon is abstracted and hypothesized based on the feature process of corrosion reaction. Second, proper mathematical modeling is setting up based on the corrosion effect or influence defined by experimental measures or fixed parameters. Third, simulation computation is processed. Cellular Automata, finite element method, probabilistic method, image method and geometric method are the common methods used for mathematical modeling.

Corrosion reaction of material includes electron transfer, mass transfer and diffusion of ion and many other complicate physical-chemical processes. Due to the randomness of material structure and chemical reaction process, it is not possible to set up a determined mathematical model to

describe the whole process of corrosion. Therefore, computer simulation research for the corrosion process has to start from the simple corrosion process such as the uniform corrosion, and abstracting and hypothesizing corrosion reaction is needed, factors that extracted corrosion reaction and random or probabilistic method are used to set up mathematical model which is able to describe corrosion process efficiently within a definite error.

J.Saunier and A. Chauss used a cellular automata model to simulate computation in diffusion process of corrosion products and growing process of film. In this work, they simulated the changing of interfaces between material surface and film[1]. A. Jivkon and N. Stevens built a finite element model based on the influence functions of loads in corrosion reaction, stress intensity factor and strain value were calculated for susceptible boundaries in a crack tip, and crack extension process of intergranular corrosion is described[2]. J. R. Ankar and N. R. Iyer abstracted the oval geometric features of pitting, mathematical model was settled based on the probabilistic growing features of pitting in aluminum, they focused on the growing process of pitting influenced by electrochemistry and fatigue load[3]. A. Turnbull set up a model based on the determined equation of distribution statistics according to input parameters, which described the evolutionary process of pitting depth distribution in different exposure stages and possibility of the transformation from pitting to Stress Corrosion Cracking[4].

Those works show that the research on simulation of corrosion process is focused on settling mathematical models from different computational requirements and aspects. Cellular Automata and finite element method are able to simulate corrosion reaction process in a micro scale based on the mathematical model, which is defined by characteristic and interaction relationships in units. Thus the model is efficient and effective. However, the research on simulation of corrosion process is still in the initial stage. There is no model that is widely accepted and meets the requirements in simulation results. In this paper, a cellular automata approach based on kinetics of corrosion will be explored throwing light on the perspective of material micro scale and corrosion theory.

Simplification and Hypothesis of Corrosion Process

Uniform corrosion on the whole surface of material, which is going to bring on decrease of the thickness and weight loss of material, is a common corrosion type for carbon steel. Comparing with localized corrosion, uniform corrosion is a simple and uncomplicated electrochemistry process, in addition, corrosion damage is easy to be measured. Corrosion reaction of carbon steel in 3.5%NaCl solution was selected as the research object. The anodic reaction is dissolution of Fe expressed by equation (1), and the cathodic reaction is depolarization of oxygen expressed by equation (2).



Microstructure of carbon steel is composed of ferrite and pearlite, which is the mixture of cementite and ferrite, so there are more energy fluctuations inside of the pearlite grain. Results of Fang Zhi indicated that corrosion potential of pearlite grain is lower than that of ferrite, and corrosion current density of the former is larger than the latter[5]. In this case, a corrosion micro-cell with the effect of galvanic corrosion occurs in microstructure. Pearlite is corroded firstly as the anode, as well as ferrite becomes to be the cathode at where depolarization of oxygen carries

out. However, there is no evidence to explain the exact area of anode and cathode in this kind of corrosion micro-cell. To sum up, simplification and hypothesis of corrosion process are formed as follows:

(a) Microstructure of carbon steel is composed of ferrite phase and pearlite grain, impurities and second-phase particles are not considered.

(b) We assume that the surface of carbon steel is smooth and flat before it is corroded.

(c) In this paper we suppose that any pearlite grains in microstructure will be involved in a corrosion micro-cell with its nearest ferrite grain, corrosion reaction will take place at pearlite region firstly.

(d) We consider a ferrite grain without pearlite grains surrounding as an “isolated” grain, and corrosion reaction, which is disconnected with pearlite, will take place at its region since random atom arrangement and atom defect.

(e) Diffusion of oxygen dissolved in solution and influence of corrosion products are thoughtless.

Cellular Automata Modeling

Cellular automata(CA) has been successfully used in the field of surface kinetics. It can be used to describe the discrete space and evolution of systems by applying local deterministic or probabilistic transformation rules. Based on the local rules, all cells are updated synchronously[6]. CA model has good controllability, operability and scalability. B. Malki and B. Baroux's CA model calculated the initiation of pitting on the surface of aluminum alloy[7]. R. Pidaparti, F. Long and M. Palakal established a CA mathematical model to describe initiation and propagation of pitting[8,9]. CA model was adopted by Q. Chen and D. Li to describe the corrosion cracking of material under the action of particle erosion[10].

In this work, computing model used for simulation is based on CA, so there are some important information for the CA model as follows:

(a) The computing space is called cellular space denoted by Ω . Space Ω is a 3D cellular space with a definite size corresponding to real material, and is dispersed into many cubes with same shape and size, called cells.

(b) Cells without upper neighbors are reputed as “exposed” cells. During computation, surface composed of “exposed” cells is called Ψ surface, and only the cells involved in Ψ may be corroded.

(c) Each cell in Ω is taken as the research object, denoted by X , in a computing time one by one.

(d) A state function $S(X)$ is used to denote the grain type of a cell, X . And a function $C(X)$ is used to denote the corrosion damage at X site in Ω , if X is corroded, value of $C(X)$ changes.

(e) Dissolution probability p ranged from 0 to 1 is used to decide the transformation of $C(X)$.

(f) Von Neumann neighbors of X are considered in our model as shown in Fig.1.

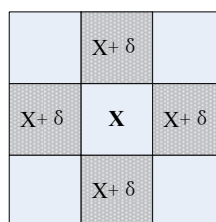


Fig.1 Von Neumann neighbor configuration of cell X , neighbors of X are $X + \delta$

Microstructure Model. Microstructure simulation of material is taken as the initial condition for corrosion model in order to compute the evolution process of carbon steel corrosion loss at small scale. The results of metallographic experiment show that the microstructure of carbon steel includes ferrite phase and pearlite phase. Hereby, the microstructure model is defined as follows:

(1) The size of simulated specimen, Ω , is $300 \times 300 \times 500$, that means there are $300 \times 300 \times 500$ cells in Ω . Side length of a cell represents $2\mu\text{m}$ corresponding to actual size. Distribution of grains is uniform in simulated specimens, diameter of which is about $10\mu\text{m}$. We assume there are about 4500 grains in Ω .

(2) The initial value of $S(X)$ is 0, and at the beginning of computing time, some cells are picked up randomly in the first instance, $S(X)$ values of these cells are assigned an integral value from 1 to 4500. A part of them denotes ferrite cells and others denote pearlite cells.

(3) Within computing time, if $S(X)$ of a cell is 0, and at least one $S(X+\delta)$ of its Von Neumann neighbor cells is not 0, $S(X)$ transforms to $S(X+\delta)$ randomly.

(4) Once $S(X)$ changes, total number of cells whose $S(X)$ values are same should be calculated to make sure that size of a grain is not too big.

(5) For all the cells that the values of $S(X)$ are 0, step 3 and step 4 are carried out repeatedly until $S(X)$ value of all cells are not 0.

The computing result of microstructure model is a three-dimensional distribution for ferrite and pearlite grains in the space of Ω .

Corrosion Computing Model. In this paper, a corrosion computing model which takes the results of the microstructure model as the initial condition is developed to simulate the corrosion damage process. Details of the proposed model are given as below.

(1) According to the results of microstructure model, for all cells in Ω , that kind of cells whose upper cells does not exist, are considered as the “exposed” cells on Ψ surface.

(2) We define that many corrosion micro-cells (CMC) are existed on Ψ surface. In a CMC loop, the micro anode region (MA) is a pearlite grain made up by “exposed” pearlite cells on Ψ ; the micro cathode regions (MC) is a proximate “exposed” ferrite grain to MA on Ψ with cathodic reaction of oxygen depolarization happened.

(3) The effect of IR drop is considered in model. It is true that in real system the potential distribution is complicated, thereby, we only focus on the influence of solution resistance for the simplicity of calculations.

(4) If a cell is a pearlite cell in CMC as above, $C(X)$ changes depending on instantaneous velocity at its site in a computation time. In a smaller range of scale, corrosion rate—current density is different at every single cell site of MA in corrosion loop as the solution resistance R_s has a linear relationship with l , the distance between a pearlite cell to MC. R_s at the cell X is formulated by (3):

$$R_s(X) = \left. \frac{dR_s}{dx} \right|_{x=l(X)} \quad (3)$$

Where $l(X)$ is the distance between a pearlite cell, X , to its nearest MC. According to the Ohm's law, current density i at X site in corrosion loop is expressed via (4).

$$i|_X = \frac{\Delta E}{R_s(X)} \cdot \frac{1}{s} \quad (4)$$

Where ΔE is the polarization potential in CMC, s is the area of cell which is same in corrosion loop. For a pearlite cell, the probability p as above is picked up in a computing time, if $p \leq i|_x$, X becomes a vacancy site (dissolution).

(5) If a cell is a ferrite cell belongs to MC, the ferrite cell could be corroded till all pearlite cells of its Von Neumann neighbors are dissolved. Dissolution probability of the cell is determined as next item.

(6) If a ferrite cell is either the “isolated” grain ferrite cell or the cell at the situation of step (5), corrosion reaction will take place in grain region. A cell is corroded depending on probability of p . If $p \leq P_0$, where P_0 is the volume fraction of O_2 in solution (3.5% NaCl), the cell dissolves.

(7) All cells on Ψ is traversed, and the value of $C(X)$ changes according as (2) to (6) during the computation time.

Results

The computational simulation program is based on the models presented in the previous sections, and implemented in MATLAB environment. The simulation program run with various times to correctly simulate the initiation and growth process of uniform corrosion damage.

Description of corrosion damage on surface of carbon steel is figured by grey images. Fig. 2 is the image showing the corrosion initiation and growth on the Ψ surface. At the time of step 1, the color degree of the picture is light, this means that there is less corrosion damage degree on the surface as shown in Fig.2(a). At time of step 12, color turns to be deeper, which means there are more corrosion damage on the surface as shown in Fig.2(b). At the time step of 30, a lot of serious corrosion can be seen at large range on the surface which is showed in Fig.2(c).

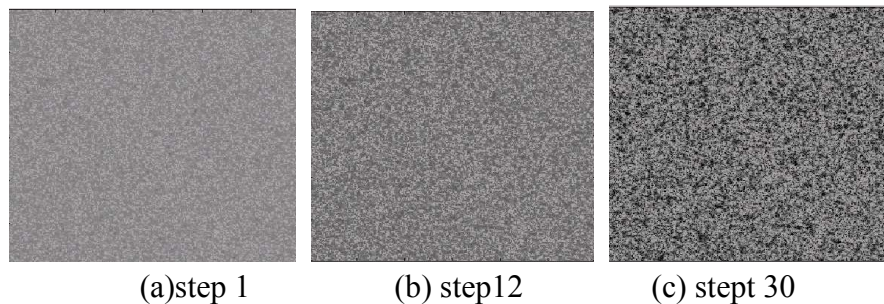


Fig.2 Corrosion damage image of 20 steel from simulation results

In order to identify the corrosion model is effective and practicable, weight loss is computed by model via calculating the thickness reduction at every cell site of the simulated sample. Simulating data of weight loss are compared with experimental data obtained in 3.5%NaCl as shown in Fig.3. According to the results, these two group data have the same distribution characteristics. Both of them show an increasing development tendency during the whole corrosion process. Moreover, the increasing tendency slows down in the later period, especially the increasing rate of experimental data. Simulating data is very close to experimental data at the first point, however, it diverges from the experimental data with the elapse of time, this kind of difference continues and becomes more and more serious during the later three weeks.

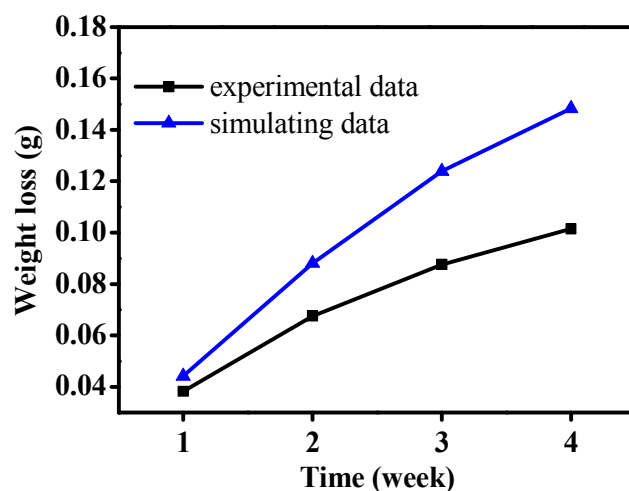


Fig.3 Comparison of weight loss between experimental data and simulation data for 4 weeks of carbon steel

The phenomenon of data distribution is investigated from the theories used in modeling and the real corrosion process. The corrosion products will form a layer on the surface of carbon steel in 3.5% NaCl solution in fact, which is ignored in our model. There are different structure characteristics between product layer and matrix metal, as well as solution, and this difference will change the surface condition where the corrosion reaction takes place. Diffusion of mass is affected, especially the oxygen which is the main factor for corrosion rate. In real corrosion system, product layer will adhere to the surface of material, and decrease the oxygen concentration on the metal surface because of the lower diffusion coefficient of oxygen, as well the corrosion rate is smaller than the situation without a layer on the surface. This is the main reason for the experimental data increases slowly comparing with simulating data. In addition, oxygen depolarization of cathodic reaction contains is a complicated process and intermediate products may affect whole corrosion rate, as a result a more complex probability model has to be introduced into the model to this for further work.

Conclusions

A highly simplified model based on Cellular Automata(CA) is used to understand basic facts on a corroding carbon steel, and to study the uniform corrosion damage. There are several conclusions gained for this work: (1)Working on a mesoscopic scale, three main influencing factors are mainly considered in the model: material microstructure, solution properties and corrosion potential. (2)Model is a simple description and calculation for corrosion process between different phase grains caused by corrosion micro-cell in microstructure. (3)Moreover, effect of solution resistance and solubility of oxygen in solution are considered in the model as the dissolved criterion for a cell. (4)Corrosion damage on the surface of carbon steel can be expressed by gray image and weight loss simulating data. (5)Computational results show that surface topography on carbon steel is uniformity with the increasing of weight loss, and there is no notable local corrosion on the simulated surface. (6)Calculation of corrosion damage is a relative local work in microstructure scale, whereas, as a result the simulation computational solution is compared with test data in this work.

Computation outcome indicates that there is certain similarity with experimental data and

simulation and test data represent same characteristics of data distribution. The results presents that this model is simple and practical, and illustrates the feasibility of the cellular automata approach to simulate the corrosion process and to describe change of surface topography as well as the increase of corrosion quantity.

Acknowledgements

This work was financially supported by National Science and Technology Ministry (2007BAB27B06).

References

- [1] J. Saunier, M. Dymitrowska, A. Chausse, J. Stafiej and J. P. Badiali. Journal of Electroanalytical Chemistry: Vol. 582(2005), p.267
- [2] A. Jivkov, N. Stevens, T. Marrow. Acta Materialia: Vol. 54 (2006), p.3493
- [3] J. Rajasankar, N. Iyer. Engineering Fracture Mechanics: Vol.73(2006), p.553
- [4] A. Turnbull, L. McCartney, S. Zhou. Corrosion Science: Vol.48(2006), p.2084
- [5] F. Zhi, H. Jianfeng, Z. Lin, Y. Wu. Corrosion Science and Technonogy, Vol.8(1996), p.195
- [6] B. Chopard, M. Droz: *Cellular Automata Modeling of Physical Systems* (Trans by X. Zhu, X. Zhao, Beijing 2003)
- [7] B. Malki, B. Baroux. Corrosion Science: Vol.45 (2005), p.171
- [8] R. Pidaparti, F. Long, M. Palakal. Computational Materials Science: Vol. 41(2008), p.255
- [9] R. Pidaparti, M. Palakal, F. Long. International Journal of Artificial Intelligence Tools Vol.14 (2005), p.361
- [10] Q. Li. Materials Science and Engineering. A, Structural Materials: Vol. 369(2004), p.284

The Analysis in the Difficulty of Carrying on the Innovation Based on the TRIZ Theory

Keshe Wang^a, Huanli Liu^b AND Yuxiang Xu^c

Mechanical Design Dept. School of Electromechanical Engineering,
Beijing Information Science and Technology University,
Beijing, 100192 P.R.China

^awangkesh@126.com, ^bliuhuanli123@126.com, ^cyuxiang_xu@hotmail.com,

Keywords: TRIZ; Innovation Theory; Innovative Software; Application Difficulties

Abstract. Although TRIZ has obvious advantages over other current known innovative ways in the following aspects: high-efficiency, high degree of controllability, the design staff still has difficulties in using the TRIZ tools, such as matrix technology to solve conflicts, TRIZ algorithm, or even combining the Inventiontool 2.0 Technology Innovative software to design creative programmers, value innovative programmers. This paper, on the basis of introducing the TRIZ theory, analyzes the characteristics of TRIZ theory, introduces the use and application of the process about a computer-aided software product of innovation --Inventiontool2.0, then point out the difficulties in the theoretical innovation based on TRIZ and bring forward the direction of amelioration.

Introduction

In the process of product design, the design method based on the innovation of knowledge innovation and the application of product design is the key to success. At present, the combination of TRIZ theory with computer aided innovation TRIZ combination technology innovation and product innovation has become the focus of research at home and abroad. However, after learning in the beginner, TRIZ theory does not provide a clear TRIZ formula to lead us to the theory of TRIZ models use in the process of innovation in theory. Of course, the theory of TRIZ is qualitative rather than quantitative, which may not make a definite mathematics model to guide the practice in the theory of the proposed algorithm for solving technical system TRIZ the contradiction that is strong guidance. However, the researchers who familiar with TRIZ theory understand that many TRIZ function module is difficult to define and less and less persons are very easy to use in the process of practical application. Although product innovation with computer aided innovation can help designers in solving technical problems and using effectively TRIZ tools, knowledge and technology system evolution mode in the process of product development, and the problem is difficult to describe accurately parameter. Therefore that need to have defined TRIZ theory applied principle, further simplified and defined TRIZ algorithm and specific technical parameters to adapt to specific requirements in different field, more deep connotation of 40 innovation principles corresponded to the new principle of science and technology development and then to strengthen the application of TRIZ theory to improve our scientific and technological innovation ability[1,2,3].

Introduction of TRIZ Theory

TRIZ theory(Invention of solving problem) --former Soviet excellence inventor G.S. Altshuler spent many years working hard to research product innovation. G.S. Altshuler and his staff took 1500 person•years researching 2.5 million patents to put forward this creative problem-solving theory since 1946. It is a tough problem in engineering field systematic solution method, which is based on the analysis of the existing achievements in different fields, to summarize the experiences of general significance. This theory puts forward a series of methods and tools that can help designer effectively for new product, new technology development.

TRIZ theory based on the knowledge is an invented problem solving systematic methodology of orientation of people. TRIZ is the heuristic method knowledge of inventing and solving problem, which is abstracted from patent from worldwide and it is only employed by a few products based on the objective trend of evolutionary heuristic method. Meanwhile the natural sciences and the engineering knowledge are included and utilized in the problem domain knowledge. In addition, this knowledge includes technology itself, or contrary technology or similar process, environment, development and evolution. The theory of TRIZ system itself is decomposed into subsystem, useful and practical, these harmful function, and environmental problems depends on environment which itself is random. Computer software which has only supportive function cannot completely replace designers who are needed to provide methods and tools to deal with the stochastic problem. TRIZ inventing and solving problem theory innovation is needed to solve the design conflict, but some steps to solve the conflict is not know. The unknown solution can be often instead of imaginary ideal which is usually obtained the ideal solution through the environment or resources system itself. The ideal solution can usually be deduced through the known system evolution tendency.

TRIZ theories include the following aspects: (1) the product evolution theory: TRIZ product evolution theory divide product evolution process into four stages: infancy, growth, maturity and retreat. In the first two stages, the enterprise should increase investment in order to make it into mature enterprises to obtain maximum benefit as soon as possible. The enterprise should study the alternative technologies for product in the period of the maturity, which made new alternative technologies in response to the future market competition. In the period of the retreat, because profit fell sharply, the product should be eliminated as soon as possible. These can provide product planning and scientific support for the enterprise. Products evolutionary theory also study product evolutionary mode, evolution laws and evolving route of products. With application of mode, law and route, designers can be determined rapidly innovative design of original design conception and make a breakthrough. (2) Conflict resolution principle: principle is the solution of the conflict, which should follow the general rules. Main research of TRIZ is technique and physical conflict. Technical conflict refers to compromise of the traditional design because one of the system itself needed do not reach the state. Physical conflict refers to contrary of demand. TRIZ guides designers to choose a principle which can solve the conflict with premise that determine conflict according to the standard engineering parameters. There are 39 standards conflict and 40 principles for application. (3) matter - field analysis standard solution: one of G.S. Altshuler's contributions in inventing and solving problem theory is that he put forward description method and model of matter-field. Its principle is: all the function can be decomposed into two which are matter and a kind of field, which means that a function is included two kinds of matter and a kind of field. The product is a kind of function, therefore material - field can analyze function of products in which this method is one of the tools of TRIZ. The model is shown in fig. 1.

In the figure, the S1 and S2 stand for matter, F for field. Matter S1 can be controlled particles, materials, objects or process, while matter S2 is tools or object of controlling S1 with field F which is energy of interaction between S1 and S2 such as mechanical, hydraulic, electromagnetic energy etc. Figure 1 can be interpreted that energy F uses for S2 which transforms to S1. According to this model, Altshuller put forward 76 kinds of standard solution which

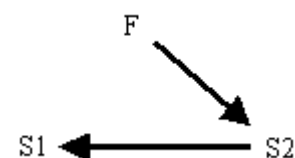


Fig. 1 Model of Matter-Field

divided into 5 types: ① the existing system does not change or a little: 13 kinds of standard solution; ② the existing system has been changed: 23 kinds of standard solution; ③ transformation of system: 6 kinds of standard solution; ④ measuring and inspection: 17 kinds of standard solution; ⑤ simplified and improved strategies: 17 kinds of standard solution. The standard solution is transferred into specific solutions for new concept by specific issues of the existing system. (4) effect: refers to the use of the field and relevant laws in other fields, especially to solve problems in design. For example, the principle of mathematics, chemical, biological, and electronic fields are utilized to solve problems in mechanical design innovation. (5) TRIZ (inventing and solving problem algorithm) considers that the degree of difficulty in solving problem depends on method of description and

stylization for the problem, more clearly it is described, more easily the solution is found. TRIZ invention of problem solving process is described and stylized constantly. Through this process, the initial problems by the fundamental conflict are exposed and clear whether that is solved. There is solution if the existing knowledge can be used for this problem; there is no solution if the existing knowledge can't solve this problem. That waits for further development of natural science or technology. This process is realized by TRIZ algorithm. TRIZ is called inventing and solving problem algorithm, which is one of the main tools of TRIZ and complete inventing and solving problem algorithm. This method adapts a logical process to stylize initial problems gradually. This algorithm specially emphasizes on stylization of conflict and ideal solution. On the one hand, the technical system evolve toward direction of the ideal solution; on the other hand, if a technical problem is needed to overcome, this problem becomes an innovate issue. The elimination of conflict in TRIZ has powerful support of effect knowledge. Effect knowledge includes physical, chemical, and geometry, etc. As a rule, there is still no solution through analysis and the application of effect, initial problem is incorrect and needs more general definition. Before the key to successful application of TRIZ is not understand the essence of problem, the problem is needed to refine constantly until physical conflict is determined. This process and solution of physical conflict has software support[4,5,6,7,8,9,10].

The computer aided innovation design software InventionTool 2.0

The computer aided innovation design software system InventionTool2.0 (invented tools) which is tracking and adapt the research achievements of the theory of TRIZ (inventing and solving problem theory) is independent research and development of domestic computer aided innovation design software which includes three modules: technical evolution module, the effect module, conflict resolution module, corresponding to solution principle of evolution, effect, and conflict respectively in TRIZ theory. It is innovative tool based on knowledge and examples and suitable for product innovation, technology innovation in all kinds of engineering field, which can help enterprise and engineering and technical personnel solve the key problems of product development in the stage of conceptual design, put forward scheme of the feasible design and guide the correct direction. At the same time it can help users to predict law of technology evolution, design future product, solve the conflict in design and avoid compromise design. There is function that expands user's knowledge field and provide various solution. In addition, it also has the S curve guide operation, automatic generation of analysis report and a lot of engineering examples and animation.

The general process of using innovative software: firstly, the product waited for design is expressed issue of TRIZ; secondly, the tool of TRIZ is utilized to solve general solution of TRIZ, for example, invention theory, effect; lastly, designer transforms this solution to undetermined solution. Recommend process: technical evolution theory predicts product development direction; conflict module help overcome conflict of product evolution; Effect module help determine function principle of system. Eventually a new product concept is integrated and formed.

In conclusion, when using the computer aided innovation design software proceeds product innovation, TRIZ theory is needed to understand and grasp. If problem is not correctly described or analyzed, the proposal principle of innovative software can't be utilized or no product innovation.

The Cause of Difficulty in Applying TRIZ

Firstly, TRIZ theory is a kind of abstract generalizations, which provide a general solution and summarize general questions through the standard model and is not theory of specific problems for each user. Because the TRIZ theoretical system itself propose many application skills which is difficult to grasp and complicated to decide that it is not very easy to understand. It also becomes quite difficult to apply TRIZ theory to solve concrete problem. Therefore, it is necessary to simplify method of researching and analyzing problem in TRIZ theory to define simple and effective route of solving common problem.

Secondly, it is not definite that how about contradictions of the technique system describe abstractly. The main problem puzzles that TRIZ theory provide for accurate application of TRIZ 39 engineering technical parameters which divide into system parameters and physical parameters to deepen our understanding of the parameters. However, it is not enough objective with assistance of overcoming the difficulties obviously practical application.

Thirdly, we should use the general theory of TRIZ to get common solution as study of specific solutions, but specific process is not easy for most people. Only 40 innovation principles almost cover the whole technical field in which technical persons concretize TRIZ general theory into professional innovation. It is believed that the degree of difficulty is obvious if there are not solid professional knowledge and skilled application of the TRIZ theory. Therefore, it is a problem that needs to think about how to manage 40 innovation principles of TRIZ theory in accordance with the professional field and make them easy apply.

Finally, TRIZ theory is founded based on the statistical theory. Then, TRIZ theory provide the tool model for studying comparison in accordance with the application of the different characteristics of the professional technology domain, aiming at the different technology to use statistical analysis method for summarizing and guiding practical application. This also need think about.

The author holds that simplification of functional modules of TRIZ theory is inevitable Based on these, and professional should be the main direction of research.

Simplification of the Major Technical Parameters

TRIZ covers the domains of machinery, chemical engineering, material, construction, agriculture and so on. The extensive applicability of engineering technical parameters determines that it is a kind of abstract representation in which this will increase the difficulty of describing the standard professional parameters of professional and make TRIZ theory easy to promote and difficult to apply. However, this process is the key of applying TRIZ theory. So it is how to deal with aiming at this problem. The author thinks that specific features of engineering parameters should be clear. TRIZ theory can be better application because specific features of the parameters are clear. From the perspective of professional technology domain, TRIZ theory involves engineering technical parameters which also will have different ways of expression in different professional field. If statistical principle can be applied to solve problems for professional description of engineering technical parameters in this field according to the law of professional engineering, professional and technical person understand more clearly every project technical parameters of the specific meaning represented and reduce difficulty of their theoretical application to strengthen the practicability of TRIZ theory and improve the efficiency of innovation.

Of course, because 39 engineering technology parameters apply inordinately in various professional fields, engineering parameters can be considered to simplify. Engineering parameters which apply frequently make statistical analysis in a certain field. Engineering parameters are summarized to apply in this technological field widely, which engineering parameters are prior to the professional technology person in the application of TRIZ theory for solution of innovation. This allows us to believe that the problem has more pertinence and save unnecessary time.

Professionalization of Innovation Principle

The idea of combining engineering technical parameters which can be described in this field with 40 new innovation principles could be simplified to realize description of TRIZ theory in professional field. The most frequent innovation principles are summered through study of 40 innovation principles with which professional features combine in various field. Then designers might be more inclined to choose the common innovation principles to solve the professional problem, which make sense pertinence and improve the efficiency of innovation.

Of course, it does not mean that other innovation principles are not application in this field but they are less application through analysis and statistic study. New innovation principles are refined for more frequent application in the field and more coincidence with innovation features in this field.

Therefore this professional technical innovation might be prior to choose and be made to simplify TRIZ theory.

Another is that 40 innovation principles were summered by Altshuller et al in 1970s in the former Soviet union, which will be omissions and errors comparing with current scientific development in certain degree. Therefore we should accumulate experience in the process of solution of the professional technique to sort out some new innovation principle suitable for China's condition corresponding to law of professional and technical development to guide application of TRIZ theory, which become an important task to think in future.

The Application of Simplified TRIZ Algorithm

In no other effective existing ways of thinking and method, TRIZ theory is a unique and strong solution tool. However, the whole process of applying TRIZ to solve is not better estimated for users and still in a state of chaos. Therefore, how to simplified algorithm also becomes a consideration of the problems.

The earliest TRIZ algorithm is put forward in 1956-1961. In that time the structure is divided into 3 stages, 15 steps, 19 models. In 1971, TRIZ algorithm is divided into 6 stages, 36 steps, 25 methods, 34 comments. In 1977, TRIZ algorithm defined 7 stages, 30 steps, 90, 34 comments. Until 1985, TRIZ gradually formed current algorithm when TRIZ structure has been divided into 9 phase, 40 steps, 200 method, 82 comments. From then, because the degree of the difficulty in TRIZ application algorithm is more and more high, it causes that a beginner can't learn to solve practical problems of TRIZ applications in a short time. However, through comparison of several generations of TRIZ algorithm, TRIZ structure put forward in 1956 and 1961 by Altshuller et al is clear and accepted easily by users. Nonetheless, a new TRIZ algorithm request in the development of systematic science into a new level of today in which we hope to simplify the operation process as far as possible, make TRIZ algorithm more easily and ensure greater efficiency. Therefore, we hope to improve from the beginning of the structure because TRIZ structure is the most simple understandable TRIZ at this time. Consequently, for the development of current TRIZ theory, the development of the theory of TRIZ, META - TRIZ structure put forward by professor Orloff largely cater to our current requirements, which is known to summarize and simplify the structure of TRIZ based on the traditional algorithm. TRIZ algorithm is divided into four steps: 1) TREND: problem analysis state of diagnosis, at this stage the development of technology system is predicted to find the conflicts working area and working time and define the reasons of generating problems and the purpose of perfection. 2)REDUCING: establish of problem models, the problems are transformed into technical conflict and physical conflict to define ideal model for direction and goal of solving technical systematic problem. 3) INVENTING: adoption of solving model, at this stage, by the assumption, the application of conflict matrix and physic conflict of four separating laws conflict are transformed into innovation principle to guide the scheme of conflict solution and form invention. 4)ZOOMING: scheme of analysis solution, it aims at zooming scheme of invention in which the effect of invention is viewed in different aspect and level. The above is the META-TRIZ algorithm basic structure design which makes the META - TRIZ meet requirement of short-cut tools regardless of whether the methodology of TRIZ research or solution of the concrete practical problem. It is known that TRIZ structure is useful. It is indicated that the direction of TRIZ theory is efficiency and simplified practice.

Conclusion

TRIZ theory applies to technological and even unskilled field with deep intension, but easy application and even using computer aided innovation software is also unrewarding, especially for undergraduates to be difficult to apply. Therefore, it is necessary to simplify the functional modules in professional fields. For TRIZ algorithm structure, simplified version META - TRIZ structures should be in-depth study. The way of Simplified application is useful to spread and popularize and

enhance efficiency of technology innovation and play the strong function of TRIZ and give full play to the innovation of the software. It is further to promote innovation ability in mechanical industry.

References

- [1] Zihui Wei, Huiqiang Yan, Runhua Tan. Research and Application of TRIZ Algorithm in TRIZ Theory [J]. Mechanical Design. 2008 (4)
- [2] Zhiping Liao. Systematic Research of Product Innovation Design Based on TRIZ [D] Zhejiang university of Technology. 2006.
- [3] Runhua Tan, Caiyun Yuan, Ruigong Zhang, Dongxing Cao. Study of Process of Product Design Based on the Technology Evolution [J]; Journal of Mechanical Engineering. 2002 Vol:12.
- [4] Lianying Sun, Dezheng Zhang, Wenliang Niu. Innovation Theory and its Extension Application [J]. Journal of Beijing Union University. 2005 Vol:02
- [5] Yigui Dai, Fengzhang Pan, Xiubing Jing. Based on the Computer Aided TRIZ Innovative Design of Mechanical Products [J]; Mechanical design and manufacturing. 2004 Vol:03
- [6] Chuan He, Zhiyuan Zhang, Peng Zhang. Application of TRIZ theory to Solve the Conflict of New Product Development. [C]; Manufacturing and the Future of China - 2002, Proceedings of the Chinese Mechanical Engineering Society Conference
- [7] SiPing Liu, ShuWu Liu. Methodology of Innovation [J]. Harbin Institute of Technology Press. 1998.4
- [8] Lingzi Meng. Research on How to Apply TRIZ to Solve Problems of Innovation; Heilongjiang Productivity Promotion Centre; Harbin 150001
- [9] Runhua Tan. Innovative design—TRIZ: Invention of problem solving [M]. Beijing: Mechanical industry press. 2002
- [10] Runhua Tan. Invention of problem solving [M]. The Science Publishing Company, 2004

A Nonlinear Tolerance Analysis Method Using Worst-Case and Matlab

Meiqiong Yu^a, Yan Yan^b, Jia Hao^c, Guoxin Wang^d

School of Mechanical Engineering, Beijing Institute of Technology, Beijing, China, 100081

^aymq0427@126.com, ^byanyan331@bit.edu.cn, ^chaojia632@gmail.com, ^dwangguoxin@bit.edu.cn

Keywords: Nonlinear Tolerance Analysis; Worst-Case; Dimension Chain; Matlab

Abstract. The tolerance analysis methods are usually used to test the result of product design and assembly; moreover the tolerance analysis also is a fundamental technique in precision design process. So far, there are two kinds of tolerance analysis methods: statistical tolerance analysis and worst-case analysis; they have their own characteristics and drawbacks. In this paper, it presents a nonlinear tolerance analysis method which uses Matlab tool to construct the nonlinear tolerance analysis mathematical formulation and calculate the result of nonlinear tolerance analysis based on the principle of worst-case tolerance analysis. All the processes are dealt with and tested by computer. The engineers only enter some basic parameters through the standardized interface, and then the result can be obtained without artificial intervention. In addition, the accuracy of calculation result meets the production requirement. The system of the nonlinear tolerance analysis is easier for engineers to use.

Introduction

As the technology improves and performance requirements continually tighten, the cost and the required precision of assemblies increase as well. Interest in tolerance analysis is rapidly increasing in industry. The quest for quality has focused attention on the effects of variation on cost and performance of manufactured products. Higher cost or poor performance will gradually lose the market share. Precision design is one main factor which determinate the quality of a product and product cost. So, how to design and analysis the tolerance of a part or assembly product is very important for the manufacturing enterprise. At the same time, traditional precision design can't meet the requirement in the digital manufacturing process. Therefore, the researchers now are researching a way with computer to design the tolerance limits on each dimension of part or assembly. Also the way can properly integrate the design and manufacturing process.

Precision design contains two parts: tolerance analysis and tolerance allocation. This paper is about the research of tolerance analysis. There are two kinds of tolerance analysis methods: statistical tolerance analysis and worst-case tolerance analysis. Hong YS and Chang T-C [1] reviewed on various tolerance issues in design and manufacturing and tried to draw the potential research directions in the future. Dantan and Qureshi [2] presented a mathematical formulation of tolerance analysis to simulate the influences of geometrical deviations on the geometrical behavior of the mechanism. A nonlinear kinematic tolerance analysis algorithm for planar mechanical systems comprised of higher kinematic pairs is presented [3].the papers [4] discussed the application of different statistical analysis method. GAO Jinsong [5] presented the tolerance analysis method based on the Monte Carlo simulation which was suit for nonlinear tolerance analysis. As observed, these two kinds of tolerance analysis methods can cause different tolerance limits on each dimension, product cost and the successful rate of assembly, they have their own characteristics and drawbacks. So far, the linear tolerance analysis methods are very mature in engineering. The nonlinear analysis methods based on Monte Carlo simulation could resolve the obstacle in nonlinear tolerance analysis by computer, which is used in tolerance analysis widely. But these tolerance analysis methods lack of intelligence and need too much manual intervention.

It is the purpose of this research to realize automatic calculation process of nonlinear tolerance analysis. And the article adopts worst-case analysis method and Matlab tool to reach the purpose.

The rest of this study is organized as follow: Section 2 presents the construction of the nonlinear tolerance analysis mathematical formulation and the calculation process. Section 3 presents the solution of the tolerance analysis method using Matlab tool. An illustrative and computational example is discussed in Section 4.

The nonlinear tolerance analysis method based on worst-case

In this section, the nonlinear tolerance analysis method is discussed. The nonlinear tolerance analysis is expressed by a nonlinear mathematical formulation. First, how to construct a nonlinear tolerance analysis mathematical formulation is discussed. Then, the calculation process of the method is presented.

(1) The construction of the nonlinear tolerance analysis mathematical formulation

Usually, a product is assembled by some subassemblies or parts. The result (characteristics such as gap or functional characteristic) of assembly is determined by the characteristic (such as situation deviations or/and intrinsic deviations). How to build the relation between these factors (such as situation deviations or/and intrinsic deviations) and the performance of assembly was really a big problem for tolerance analysis. According to previous studies, the aim of tolerance analysis is to simulate the influences of deviations on the geometrical behavior of mechanism. Usually, the tolerance analysis uses a relationship of the form:

$$Y = f(X_1, X_2, \dots, X_n) \quad (1)$$

Where Y is the response of the performance of assembly and $X = \{X_1, X_2, \dots, X_n\}$ are the values of some characteristic of the individual parts or subassemblies making up the assembly. The Eq.1 is also called tolerance analysis mathematical formulation.

The value of Eq.1 is determined by the input parameter X_i . The input parameter X_i includes two main factors: the mutative dimension and the mutative angle. The tolerance analysis should take into account not only the mutative dimension, but also the mutative angle. Therefore, if the angle is change, then it is considered a variation $X_j (1 \leq j \leq n)$ which can influence the result of assembly. For example, angle α in Fig. 1.

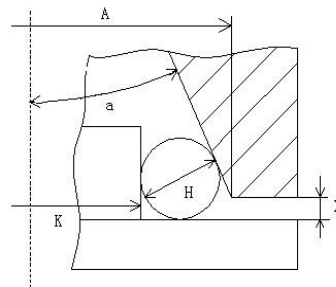


Fig 1 a production assembly drawing

According to the dimension chain principle, the factors which impacted the final characteristic should be extracted from the assembly model to form a dimension chain. A coordinate system is built in proper position to quantify the dimension and angle. In the coordinate system, three equations can be deduced based on relation between the dimension chain and X, Y, Z axis:

$$\begin{cases} f_x(X) = X_1 \cos \alpha_1 + X_2 \cos \alpha_2 + \dots + X_n \cos \alpha_n + X_0 \cos \alpha_0 \\ f_y(X) = X_1 \cos \beta_1 + X_2 \cos \beta_2 + \dots + X_n \cos \beta_n + X_0 \cos \beta_0 \\ f_z(X) = X_1 \cos \gamma_1 + X_2 \cos \gamma_2 + \dots + X_n \cos \gamma_n + X_0 \cos \gamma_0 \end{cases} \quad (2)$$

Which $\{X_1, X_2, \dots, X_n\}$ is the dimensions which can impact the final characteristic, $\{\alpha_i, \beta_i, \gamma_i\}$ is the angles between the dimension i and X, Y, Z axis. If the final assembly characteristic is a dimension, then X_0 is the functional characteristic, $\{\alpha_0, \beta_0, \gamma_0\}$ is the angles between functional characteristic X_0 and X, Y, Z axis. On the other hand, if the final assembly characteristic is an angle, then one of the angles $\{\alpha_0, \beta_0, \gamma_0\}$ will be the functional characteristic, the rest angles $\{\alpha_0, \beta_0, \gamma_0\}$ and X_0 will be the normal input parameters.

If the dimension chain is described in 1D, only the equation $f_x(X)$ should be constructed. Then, If the dimension chain is described in 2D, the equations $f_x(X), f_y(X)$ should be constructed. The third, if the dimension chain is described in 3D, then all equations should be constructed. At last, the nonlinear tolerance analysis mathematical formulation can be deduced from upper three situations.

The procedure of constructing the tolerance analysis mathematical formulation as follows:

- (i) make sure the final characteristic (such as the functional characteristic) which needs to calculate;
- (ii) Search for the factors impacted the final characteristic and construct the dimension chain based on these factors;
- (iii) Establish the coordinate system in proper position to quantify the dimension and angle;
- (iv) Establish the three equations $f_x(X), f_y(X), f_z(X)$ according to type of dimension chain;
- (v) Deduce the final tolerance analysis mathematical formulation.

(2)the characteristic judgment of input parameters

The input parameters usually are independent and different each other. The value of nonlinear tolerance analysis mathematical formulation usually is a mutative value. In order to get the change interval of the Eq.1, the relation between change trend of input parameter X_i and change trend of equation value is very important. According to the mathematical principle, the partial derivatives of Y with respect to X_i can response the relation. At the same time, the partial derivative of Y with respect to X_i represents the sensitivity of tolerance limits between functional characteristic and input variations X_i . If the value of the partial derivatives of Y with respect to X_i is greater than zero, the equation value will increase as the component X_i value increasing. Otherwise, if the value of the partial derivatives of Y with respect to X_i is less than zero, the equation value will decline as the component X_i value increasing. All the partial derivative values will be used for the tolerance limit calculation of Eq.1.

(3)The tolerance limit calculation of functional characteristic

As the increased level of processing, the part processing is not a main constraint problem. The successful rate of assembly is more important for enterprise. Based on this view, this paper adopts the worst-case model to analysis tolerance. The worst-case (WC) model assumes all the component dimensions occur at their worst limit simultaneously. It is used by designers to assure that all assemblies will meet the specified assembly limit.

The value of gap or functional characteristic of assembly usually locates in a mutative interval. Therefore, according to change trend between input parameters and the value of Eq.1 and the value of each partial derivatives X_i , the max value of Eq.1 can be expressed as follow:

$$Y_{\max} = f(X_{1\max}, X_{2\max}, \dots, X_{(i)\max}, X_{(i+1)\min}, \dots, X_{(n)\min}) \quad (3)$$

Similarly, the min value of Eq.1 also can be expressed as follow:

$$Y_{\min} = f(X_{1\min}, X_{2\min}, \dots, X_{(i)\min}, X_{(i+1)\max}, \dots, X_{(n)\max}) \quad (4)$$

Where Y_{\min}, Y_{\max} are the max and min value of Eq.1, X_1, X_2, \dots, X_i are the input parameters for which their partial derivatives values are greater than zero, X_{i+1}, \dots, X_n are the input parameters for which their partial derivatives values are less than zero.

At last, the tolerance of assembly will equal to the value of follow expression:

$$\text{Upper allowance limit: } T_u = Y_{\max} - Y \quad (5)$$

$$\text{Lower allowance limit: } T_d = Y_{\min} - Y \quad (6)$$

$$\text{Tolerance of assembly: } T_a = Y_{\max} - Y_{\min} \quad (7)$$

The solution of the nonlinear tolerance analysis using Matlab tool

Based on upper description of worst-case model, this section presents the solution of nonlinear tolerance using Matlab tool.

(1) The definition of input parameters

The value of Eq. 1 is determined by the input parameters which are the mutative dimensions and angles. In order to realization easily, This nonlinear tolerance analysis system uses $A_1, A_2 \dots A_{20}$ to denote the mutative dimensions or angles, and uses X and U_1, U_2 to denote the functional gap or characteristic and the unknown dimensions or angles. At the same time, because the way of tolerance analysis is expressed by the mathematical formulation, so there is a requirement to build a coordinate system to quantify the range of mutative dimensions and angles. If there are the same intrinsic dimensions and angles in the dimension chain, such as the radius or the parallel edges in a rectangle etc, they use the same symbol A_i ($1 \leq i \leq 20$) in the input parameters. All the data will be stored in the text file.

E.g. Fig. 2 is the local drawing of a product assembly and the corresponding dimension chain; the factors impacted the final functional characteristic are listed in Table 1. The X-angle, Y-angle and Z-angle in the Table 1 are the angles between the dimension and the X, Y, Z axis. The system uses A_1 instead the all symbols $H/2$ in the dimension chain, uses U_1, X, A_4 instead the unknown dimension, functional characteristic and the mutative angle α . If the angles (the X-angle, Y-angle, Z-angle) are relative with angle α , then the system use A_4 instead the angle α , like the expression of X-angle, Y-angle in Table 1.

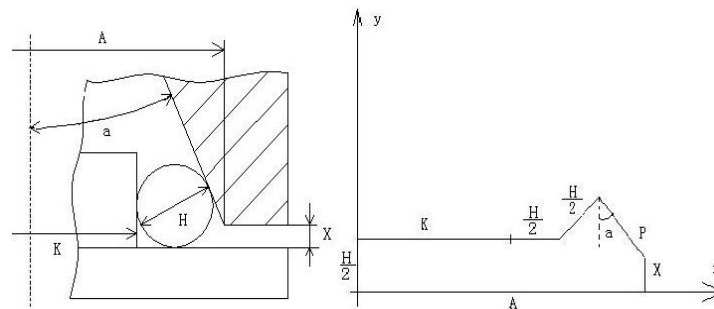


Fig 2 a product assembly and the dimension chain

Table 1 the input parameter definition

Serial number	The original symbol	The new symbol	X-angle [°]	Y-angle [°]	Z-angle [°]
1	H/2	A_1	$\pi/2$	0	NULL
2	K	A_2	0	$3\pi/2$	NULL
3	H/2	A_1	0	$3\pi/2$	NULL
4	H/2	A_1	A_4	$3\pi/2 + A_4$	NULL
5	P	U_1	$3\pi/2 + A_4$	$\pi + A_4$	NULL
6	X	X	$3\pi/2$	π	NULL
7	A	A_3	π	$\pi/2$	NULL
8	α	A_4	NULL	NULL	NULL

(2) The procedure of the solution

The Matlab software of Mathworks Ltd. is commercial mathematical software. Matlab can be used for algorithm development, data analysis and numerical calculation etc. This solution mainly uses the function of some basic functions, such as SOLVE, DIFF, SUBS etc.

The Eq. 1 usually is derived by engineers in the previous methods of tolerance analysis, which is not convenient to use. In order to get the Eq. 1 with computer automatically, there is a requirement to convert human calculation to calculation in computer. However, Matlab software offers a 'SOLVE' function which is symbolic solution of algebraic equations. It can solve the equations.

The system first constructs Eq. 2 according the type of dimension chain. When the equations are constructing in the system, they are considered as character strings. Then, before they are used for

'SOLVE' function, these character strings are converted into symbolic expression. At last, the system calls for the 'SOLVE' function to deduce the final nonlinear tolerance analysis mathematical formulation.

After getting the expression of mathematical formulation, the partial derivatives are too intractable to compute for human, but it becomes very easy in Matlab. There is a "DIFF" function in Matlab software which is the difference and approximate derivative solution of equation. The system calls for DIFF function to deduce each input parameter X_i expression of partial derivatives and calculate the partial derivative value through SUBS function.

At last, the system calculates the nominal size and deviation of functional characteristic according to the Eq. 3, 4, 5, 6, 7 and stores the results of calculation into the output text file. The all functions of steps can be achieved by programming the M files of Matlab.

Based above description, the procedure of the solution as follow in Fig.3:

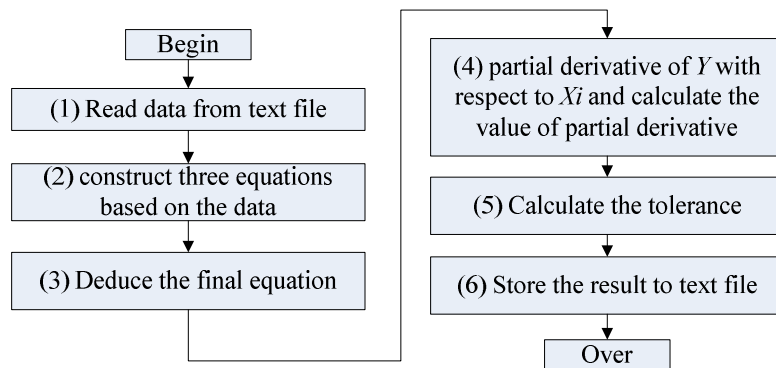


Fig 3 the procedure of nonlinear tolerance analysis

Example

In this section, the example of an assembly product has been taken to illustrate the proposed way. The object of functional characteristic needed to calculate is a gap or dimension. Following are the details:

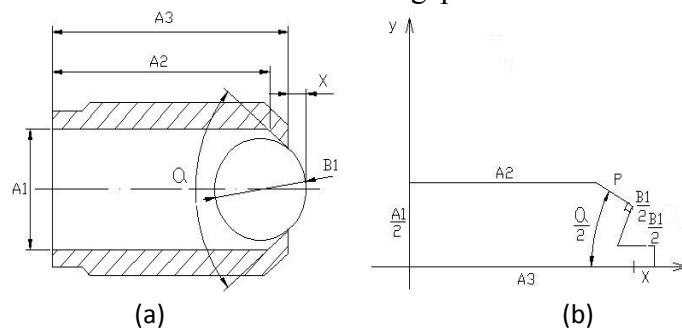


Fig 4 a product assembly and dimension chain

No.	Code	Type	BaseVal	UpperVal	LowerVal	X-Angle	Y-Angle	Z-Angle
1	A1	Angle	60	0.5	-0.5	NULL	NULL	NULL
2	A2	Dimension	4.1	0.1	0	90	0	NULL
3	A3	Dimension	15.8	0.24	0	0	270	NULL
4	U1	Unknown-Dim	NULL	NULL	NULL	360-A1	270-A1	NULL
5	A4	Dimension	4	0	-0.25	270-A1	180-A1	NULL
6	A4	Dimension	4	0	-0.25	0	270	NULL
7	X	Fun-Dim	NULL	NULL	NULL	180	90	NULL
8	A5	Dimension	17.7	0	-0.12	180	90	NULL

Output

BaseVal: 1.201408

UpperVal: 0.584748

LowerVal: -0.022167

Fig 5 the input window of nonlinear tolerance analysis system

There is a ball bearing and a sleeve in Fig. 4 (a). they assemble together to form a subassembly. Now there is a requirement for engineers to compute the length of outstretch of ball bearing (the length of functional characteristic X). Meanwhile, The length of the other dimension as follow: $A_1 = \phi 8.2^{+0.2}_0$ mm, $A_2 = 15.8^{+0.24}_0$ mm, $A_3 = 17.7^{0}_{-0.12}$ mm, $\alpha = 60^\circ \pm 30'$, $B_1 = \phi 8^{0}_{-0.05}$ mm.

The dimension chain can be constructed based on the subassembly in Fig. 4 (b). Fig. 5 displays the input window of nonlinear tolerance analysis system and the result of upper example. The parameters of input area in Fig. 5 are formatted according to the format of Table 1. These variations are the input parameters in the system.

The nonlinear tolerance analysis system is achieved based on C# program language and Matlab. It divides into three models: input model, process model, output model. The process model is achieved by customized M files of Matlab. These files are called by the system to realize the function of nonlinear tolerance analysis.

The operational result of upper example is $1.20^{+0.58}_{-0.02}$ mm. However, the result of manual calculation of the functional characteristic is $1.19^{+0.58}_{-0.02}$ mm. Compare the results of operation and manual calculation, the calculation error is less than five per cent, and the nonlinear tolerance analysis system has high accuracy. So, the system can be utilized in the engineering.

Conclusions

In this article, the automatic calculation of nonlinear tolerance analysis based on worst-case has been realized by the Matlab tool. It allows the engineers to input some basic parameter, such as the value and deviation of dimensions, the angles between dimensions and axis etc, which it is easy for engineers to use.

The nonlinear tolerance analysis method is achieved by programming M files of Matlab. The model uses the interface to read and write the input and output parameters, which is easy for invoking by other program. The system can be used in the tolerance analysis of the different types of dimension chain, such as 1D, 2D, 3D. The result of tolerance analysis has very high accuracy and can meet the requirement of product design and assembly analysis etc. It can be prove to be very useful for precision design and assembly analysis.

Acknowledgements

This work was financially supported by the support of National Defense Research Foundation, China (No.B2220090014).

References

- [1] Hong YS, Chang T-C: International Journal of Production Research, Vol. 40 (2002), p. 2425-2459.
- [2] Jean-Yves Dantan, Ahmed-Jawad Qureshi: Computer-Aided Design, Vol. 41(2009), p. 1-12.
- [3] Kyung MH, Sacks E : Computer Aided Design, Vol.35 (2003), p.901-911.
- [4] Swami D Nigam, Joshua U Turner: Computer-Aided Design, Vol. 27(1995), p.6-15.
- [5] Gao Jinsong, Chase Kenneth W. Magleby Spencer P. Comparison of assembly tolerance analysis by Direct Linearization and modified Monte Carlo simulation method, 21st Annual Design Automation Conference ,Vol.82 (1995), p.353~360

Theoretical and Finite Element Analysis of Crosshead of Quintuple Cylinders Fracturing Pump

Zhipeng Lv^a, Sizhu Zhou^b, Xiuhua Ma^c

School of Mechanical Engineering, Yangtze University, Jingzhou, Hubei, 434023, China

^axhaihq@126.com, ^blzpgs10502@126.com, ^chqix@sina.com,

Keywords: Crosshead; Finite Element Analysis; Stress.

Abstract. According to the plunger pump movement principle, this paper analyzed the two kind of typical force situation of the crosshead, and obtained the theoretical maximum force. Established the finite element model of the crosshead, gave an analysis to the load handling and boundary condition. The last results of the node stress and displacement show that the crosshead can work safely.

Introduction

As one of the main moving parts of the Quintuple Cylinders fracturing pump, crosshead's function is to achieve the movement expendable conversion. From linkage to plunger the crosshead endures complicated loads, it is one of the vulnerable part of the plunger pump. This paper will analyze the motion and force of the crosshead, and use the finite element method to analyze the stress and displacement of the crosshead.

Motion and force analysis

The kinematic mechanism of the Quintuple Cylinders fracturing pump consists of crank shaft, linkage and plunger, it can be simplified as a crank-slider mechanism. The motion analysis is shown in Fig.1. From which we can find that the center line of the cylinder is horizontal and passes through the rotation center (O) of crank shaft, OB is the length of the crank; point B is the center of crankpin; Point A is the center of the small-end of linkage, or crosshead pin.

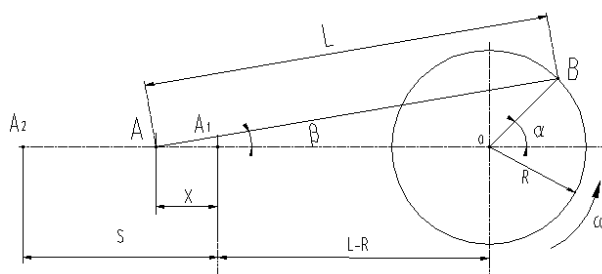


Fig.1 Motion analysis

When the pump is in operation, crosshead moves back and forth along the X axis, driving the plunger to move. While the plunger is in discharge stroke, it is under the force caused by high pressure fluid. Also, there are inertia and friction force acting on the plunger. Fig.2(a) and Fig.2(b) show the force status of crosshead when the plunger is in discharge and suction stroke.

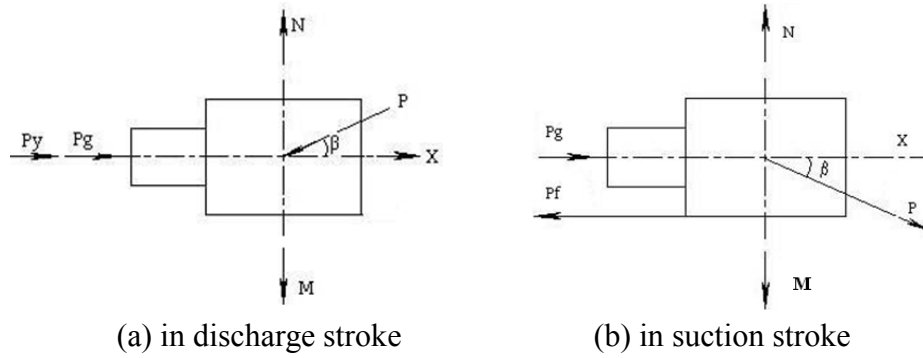


Fig.2 Force status of crosshead while the plunger is in discharge and suction stroke

According to the principle of balance, using the equation of force balance in X direction, we can obtain that

In discharge stroke:

$$P = \frac{P_l + fmg + ma}{\cos \beta - f \sin \beta} \quad (1)$$

In suction stroke:

$$P = \frac{fmg - ma}{\cos \beta - f \sin \beta} \quad (2)$$

Where, P is the linkage force; P_s is the inertia force caused by “ m ”; P_l is the pressure force exerted by fluid; P_f is the friction force acted on “ m ”; m is the total mass of plunger rod, crosshead and 27% of linkage mass; f is the friction coefficient between the crosshead and guide sleeve, $f=0.1$.

At last we can obtain that the maximum crosshead force $P=1033757\text{N}$ when the angle between linkage and horizontal line is 11.25° .

Finite Element Analysis of the crosshead

Material Properties and Finite element model. Material : ZG40CrNiMoA; Yield Strength: $\sigma_s \geq 900\text{Mpa}$; Elasticity modulus: $E=211\text{Gpa}$; Poisson ratio: $\mu=0.3$.

The model of element is produced and analyzed in ANSYS. The number of the elements is 88281, and the number of the nodes is 22291. The meshed model is shown in Fig.3.

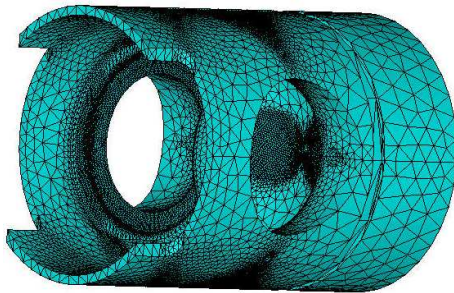


Fig.3 meshed model of the crosshead

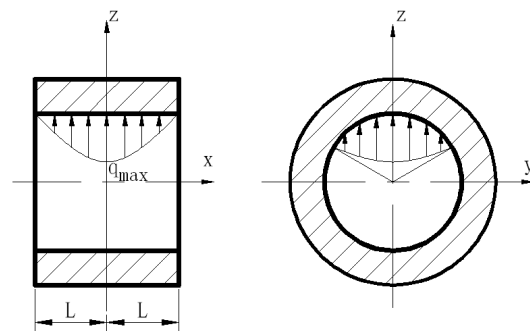


Fig.4 Load distribution on the inner surface of the pin hole

Load analysis. Based on the conventional theory and stress distribution regularities of oil membrane of the limited-width axis diameter, the influence of the peck stress at the oil hole is ignored. Fig.4 shows that q_x is described as a “parabolic” pattern distribution along axis-direction,

and described as the “cosine” pattern distribution along direction within the scope of 120° .

According to the References [1], the equation of the load distribution on the inner surface of the pin hole can be obtained as Eq.3.

$$q_{x\theta} = \frac{9Q_c}{16RL} \left[1 - \frac{x^2}{L^2} \right] \cos\left(\frac{3\theta}{2}\right) \quad (3)$$

Where, Q_c is the total load acting on the inner surface; R is the radius of the inner surface of the pin hole; $x=-L \sim L$; $\theta=-60^\circ \sim 60^\circ$.

In this model, $R=0.064125\text{m}$, $L=0.01295\text{m}$.

Because the small end of the linkage is linked with the two pin holes of the crosshead, and the maximal force acting on the pin rod by linkage is $P=1033757\text{N}$, The force P is equably distributed in the two pin rods, and the force acting on one pin hole is $Q_c=516878.5\text{N}$.

According to the above formula, and the load according to the method of formula in ANSYS was applied, shown in Fig.4, the equivalent node force can be derived.

Boundary conditions. According to the working condition, the radial UX direction displacement was fixed imposed on the upside and downside round surface which contacts with the guide. And the UY and UZ direction on the annular slot which contacts with the gasket were fixed, shown in Fig.5.

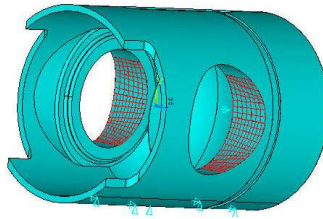


Fig.5 load and boundary conditions.

Results. The maximal stress 483.115MP is located at the pin hole, shown in Fig.6, which is less than the allowable stress, and the safety factor is,

$$s = \frac{\sigma_s}{\sigma_{\max}} = \frac{900}{483.115} \approx 1.86. \quad (4)$$

The maximal displacement is 0.045208mm , shown in Fig.7, belongs to the small deformation range. So, the crosshead is safe.

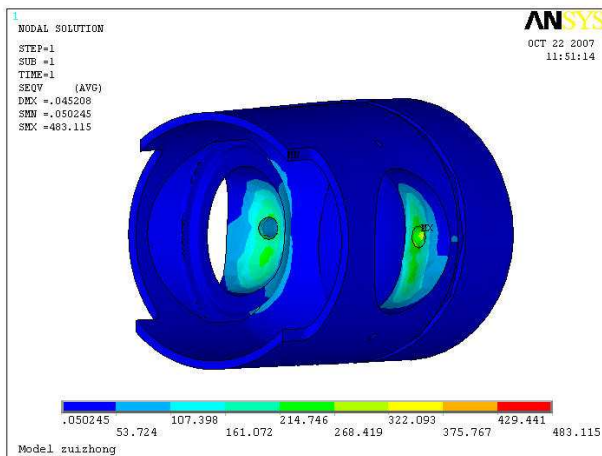


Fig.6 The maximal node stress

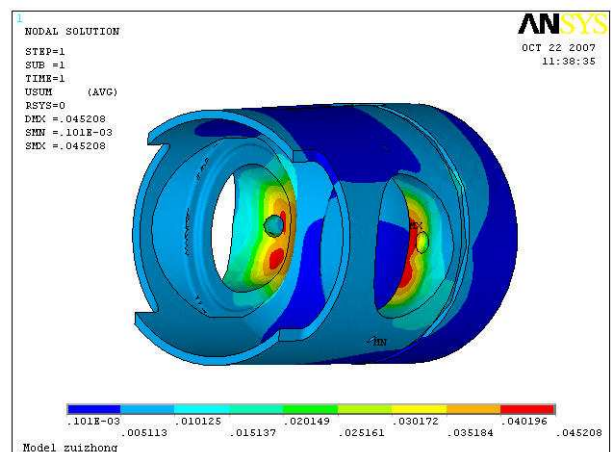


Fig.7 The maximal displacement

Conclusion

The crosshead has a complicated load and structure, is one of vulnerable parts in plunger pump. According to the plunger pump movement principle, this paper analyzed the two kind of typical force situation of the crosshead, and obtained the theoretical maximum force. Established the finite element model of the crosshead, gave an analysis to the load handling and boundary condition. The last results of the node stress and displacement show that the crosshead can work safely.

References

- [1] Chunlei Yu, Shuli Jiang: Finite Element Analysis and Optimal Design of SL4105ZDiesel Engine's Crankshaft[J]. Tractor & Farm transporter, 2005, 32 (1): 37~40.
“In Chinese”

A Lamp Coating Temperature Field Calculation Method

Kang Lin^a

Taizhou Vocational and Technical College, College of Mechanical and Electrical Engineering,
 Zhe Jiang, China, 318000

^alink1227@163.com

Keywords: Temperature Field; Lamp; Aluminized Coating

Abstract: Surface of the lamp reflector are plated a layer of aluminum. It is hard to accurately establish calculate model when use finite element software to analysis the temperature field. For this reason, a new temperature field calculate model of aluminum layer is presented. And it apply to calculate the temperature field of front fog(084). Finally use temperature field experiment to verify that the calculate model of aluminum layer is correct.

Introduction

Surface of the lamp reflector are plated a layer thickness of 500 to 2000 Å. This layer of aluminum play a major role that is reflects light and heat. And it greater impact on the temperature field of lamp. Also, because the thickness of aluminum is only 500 to 2000 Å. Finite element software is difficult to accurately simulate this layer of aluminum. Both simplified to the surface model to calculate^{[1][2]}, found by studying it also caused large error in the temperature field calculating. Therefore, establish a suitable aluminum layer model is important to accurately calculate the temperature field of lamp.

Aluminum layer model processing

According to theory of composite laminates^{[3][4]}, the structure of the reflector as shown in Figure 1. Thickness h and length and width L ratio is very small. First assume that the temperature along the thickness direction (Z direction) linear distribution.

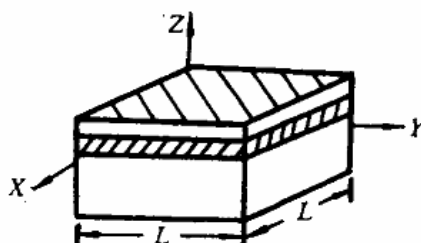


Fig1. structure of reflector

$$T(x, y, z, t) = T_0(x, y, t) + T'_z(x, y, t) \cdot z \quad (1)$$

Where $T_0(x, y, t)$ ——under the surface temperature; $T'_z(x, y, t)$ ——temperature gradient of Z direction.

Proposed the “generalized heat” Q of thermal laminated theory by Use the theory of composite laminates and define:

$$\{Q\} = - \int_h [s]^T [k][s] \bullet dz \bullet \{\sigma\} \quad (2)$$

The structure of lamp reflector is isotropic ply. For isotropic ply, can be seen as the special orthogonal symmetric. According to isotropic laminate theory derive the finite element equation.

Take plane quadrilateral element. Assuming temperature is linear temperature distribution in the cell. Using the same bilinear interpolation function $N(x, y)$. Interpolation function is exactly same to the general finite element method.

$$[N] = [N^1, N^2, N^3, N^4]$$

$$\{\delta\} = \{T_0^1, T_z^1, T_0^2, T_z^2, T_0^3, T_z^3, T_0^4, T_z^4\}^T \quad (3)$$

Where

$$[N^i] = \begin{bmatrix} 0 & 0 & 0 & N^i & N_x^i & N_y^i \\ N^i & N_x^i & N_y^i & 0 & 0 & 0 \end{bmatrix} \quad (4)$$

So

$$\{\bar{\delta}\} = [N]\{\delta\} \quad (5)$$

$$[C]_1 \{\delta\} + [\bar{K}]_1 \{\delta\} = \{P\} \quad (6)$$

Where the heat capacity matrix $[C]_1$:

$$[C]_1 = \int_v \rho c [N]^T [R]^T [R][N] \bullet dv \quad (7)$$

$$[\bar{K}]_1 = [K_1] + [K_2] \quad (8)$$

$$[K_1] = \int_v [N]^T [k_q][N] \bullet dv \quad (9)$$

$$[K_2] = \int_{\Gamma_3} \alpha [N]^T [R]^T [R][N] \bullet ds \quad (10)$$

$$\{P\} = \{P_1\} + \{P_2\} \quad (11)$$

$$\{P_1\} = \int_{\Gamma_2} \bar{q} [N]^T [R]^T \bullet ds \quad (12)$$

$$\{P_2\} = \int_{\Gamma_3} \alpha \bullet T_\infty \bullet [N]^T [R]^T \bullet ds \quad (13)$$

Element stiffness matrix formed by use different integration strategies. That $[K_1]$ and $[K_2]$ division two layer integral. And it enable the same integral precision of the layers by different layers of the integral strategy. Assembled the (6)~(13) units by the whole finite element assembly rules, than obtained the finite element equation.

When using finite element software to calculate the temperature field of lamp, according to centralized parameter method^[5], When the heat conduction thermal resistance of solid internal is

less than the surface's. Any time the temperature inside the solid is same. So that the temperature of the whole solid are same in the moment. Then the required solution temperature is only a function of time, and nothing to do with the space coordinates. Like the original continuous distribution of the solid mass and heat capacity aggregated to the point, and as like only one temperature value.

Thermal conductivity of aluminum reflector is $203 \text{ W/(m}^\circ\text{C)}$. The thickness is small, that the temperature of the aluminum is same in the thickness direction. In this assumption the thickness of coating can be amplified. And the thermal conductivity is also equivalent amplified.

Calculate the temperature field of front fog lamp named 084

(1) Simplified geometric model

According to the theory of model which is lamp under the lights 30 minutes^[6]. Don't consider the fluid in a period of lamp under lights. Only study the part of fog which composed of mask, hood, light bulbs, reflector. In order to facilitate the mesh to reduce the computational, simplified the small structure which is in little effect on temperature field analysis. Such as smooth the corrugated surface which is around inner surface of the mask, remove the part which the mask in contact with the lamp body, etc. The simplified model shown in Figure 2.

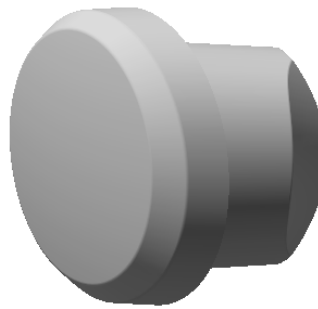


Fig. 2 simplified model

(2) Establish the finite element model

Before the division of unit must be done the structural analysis to determine the type of unit. According to the results of previous study, bulbs use a layer of hexahedral unit, reflector and the hood is divided into two layers of hexahedral element, and given different materials. Mask is divided into two layers of hexahedral element to meet the requirements of different boundary conditions. The equivalent physical parameters of parts of the material shown in Table 1.

Table 1 The equivalent physical parameters of parts of the material

part	material	Thermal conductivity ($\text{W/m}^\circ\text{C}$)	Heat capacity ($\text{W}\cdot\text{S/kg}\cdot^\circ\text{C}$)	density (kg/m^3)
mask	PC	0.2	880	1180
Aluminum plat	aluminum	203	900	2700
hood	iron	46.4	450	7800
reflector	BMC	0.0635	443	1900
bulbs	glass	0.8	840	2400

Select solid 70 in the ANSYS element library which is three-dimensional eight-node hexahedral element. Solid 70 units is only one degree of freedom per node which is temperature, and it is suitable for three-dimensional steady-state or transient thermal analysis. Construction of the finite element model shown in Figure 3.

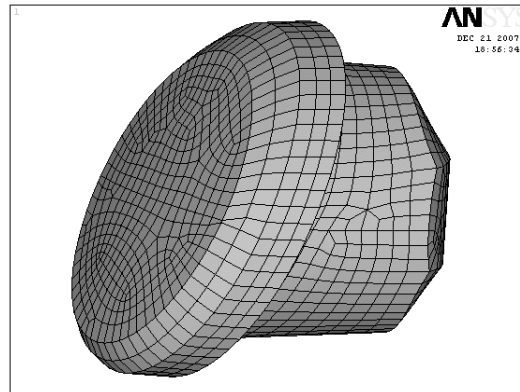


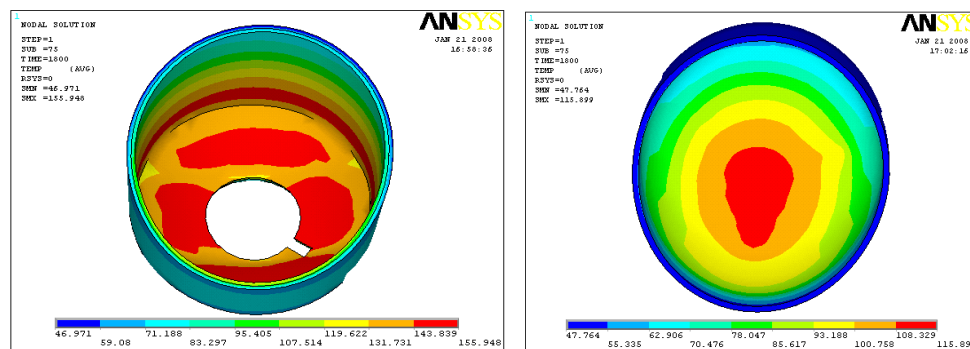
Fig.3 the finite element model

(3) Boundary conditions and loads^{[7][8]}

Before the analysis we must determine the correct boundary conditions and loads. Lamp at work, between its various components to heat transfer by radiation. Loading radiation boundary conditions in all parts. The bulb wall as heat source, and loading heat flux. The total power of the lamp system is 55W, and the heat efficiency is 85%.

(4) Numerical results

Calculated by ANSYS software, the results of temperature distribution in the lamp as shown in Figure 4.



a. reflector temperature distribution

b. mask temperature distribution

Fig. 4 FEA results

Figure 4 shows that the reflector exist local high temperature which located on the back of the bulb. In the mask, due to the reflection reflector convergence of the role of energy, the middle part of the mask at high temperature.

Experimental study

(1) Experimental platform

The experimental method use the thermocouple to measure temperature distribution^[9]. Experiment carry out at room temperature is 25°C, relative humidity 68%RH. Experimental system use a total of four data acquisition channels. Data acquisition instrument have timer. And set 30s interrupted once, that a data collection 30s. Experimental platform shown in Figure 5.



Fig. 5 Experimental platform

(2) Distribution of measuring points

According to the results of finite element analysis, in the mask, reflector and lamp body to select several feature points are labeled thermocouple hole. And to determine the coordinates of identify points in the coordinate system. Location of each point shown in Figure 6.

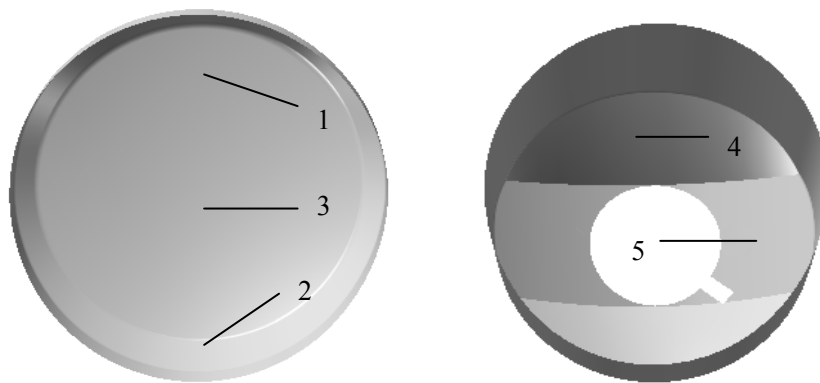


Fig. 6 The measurement points on the mask and the reflector

(3) Comparison of experimental data and numerical calculation results

This paper experiment the front fog lamp(084). The temperature response curve of the experimental measuring points shown in Figure 7-9.

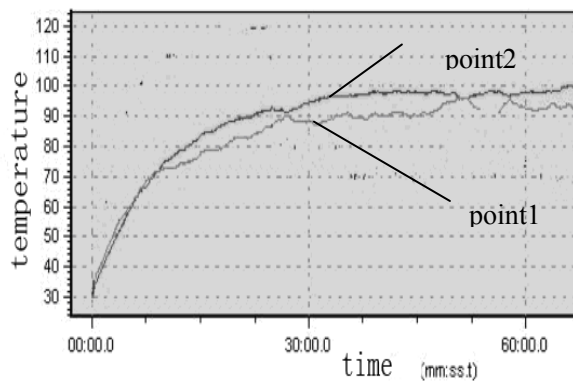


Fig. 7 The temperature response curve of the point 1,2 on the mask

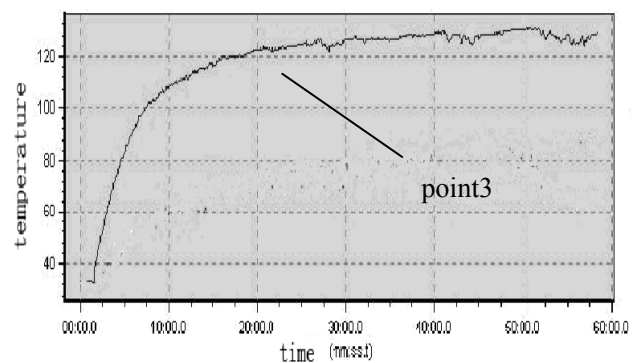


Fig. 8 The temperature response curve of the point 3 on the mask

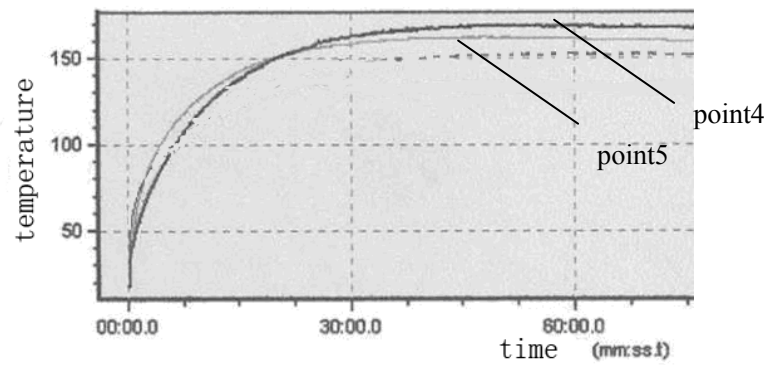


Fig. 9 The temperature response curve of the point 3 on the reflector

Table 2 is the comparison of experimental date and calculated values of temperature of 5 points on the mask and reflector for on the light 30 minutes. Overall, the actual temperature distribution trend of lamp mask is consistent with the calculated results.

Table 2 Test results and calculation results

Measuring point	1	2	3	4	5
Experimental date	88.5	98.5	129.5	161.9	157
Calculated value	78.9	99.5	111	150.8	156

Conclusion

When calculate temperature field of lamp, as the structure like the aluminum plating layer of reflector, this paper presents a new model. Been to compared by experiment, validate this new finite element model is feasible.

References

- [1] Zhao Liang, Zhou Binhai. Machinery, 45(509):12-15,2007.
- [2] Hao Jingyang, Zhang Jian, Gu yuqin, et.al. Automobile Technology, 12:7-11,2003.
- [3] Chang Xiaoquan, Zheng Gangtie. Chinese Journal Of Applied Mechanics, 22(4):633-637,2005.
- [4] Yang Zichun. Journal Of Naval University Of Engineering, 5:9-13,2000.
- [5] Zhang Tiansun, in: *Heat Transfer*, edited by china electric power press, china, BJ(2006), in press.
- [6] Hong Liu, Jinguo Li, Yongtian Wang. Key Engineering Material.364-366:783-788,2008.
- [7] William I. Moore, Eric S. Donovan, Christopher R. Powers. Computers and Structures 72:17-30,1999.
- [8] Yoshihiro Okada, Takahide Nouzawa, Takaki Nakamura. JSAE Review 23:95-100,2002
- [9] J.M.M. Sousa, J.Vogado, M.Costa, H.Bensler, C.Freek, D.Heath. International Journal of Heat and Fluid Flow 26:709-721,2005.

Numerical Simulation of the Two-Phase Flow in a New type Cyclone

Ningning Xing^{1a}, Weilin Zhao^b

School of Material Science and Engineering, University of Jinan, Jinan, Shandong, 250022, China
^aningning8997@163.com, ^bmse_zhaowl@ujn.edu.cn

Keywords: Cyclone Preheater; Numerical Simulation; k- ϵ Model; Discrete Random Walk Model; FLUENT Software.

Abstract. A new type cyclone with oblique top, transitional volute chamber, eccentric inner cylinders and sloping outlet were designed and manufactured by numerical analysis, which had been applied to the five-stage preheater in the cement plant with the capacity of 5000t/d. To simulate the gas flow field and particle trajectory in cyclone, the Fluent software was used, and the RNG k- ϵ model and discrete random walk model were proposed. The flow characteristics of gas-solid two-phase were analyzed. It is found that the strongly swirling flow occurs in the new type cyclone, and the particles of raw meal can be more efficiently separated from the gas.

Introduction

Cyclone preheater is one of the most crucial equipments in rotary cement kiln system with a new type of suspension preheater. Its main function is to disperse uniformly the particle of raw meal, rapidly preheat the raw meal with the hot gas of kiln and calciner, and efficiently separate the particle of the raw meal from the hot gas flow [1, 2]. The separation process of raw meal is extremely complex in cyclone preheater. It includes three-dimensional turbulent and two-phase flow. In order to improve the separation efficiency of cyclone preheater, it is necessary to investigate the gas flow field and particle trajectory. The some work has been reported [3-5]. In this paper, a new type cyclone was proposed. It is the intention to provide reference to the structure design and engineering applications of cyclone preheater.

Geometrical model and generating grid

The design of the new type cyclone is for the five-stage preheater in the cement plant with capacity of 5000t/d. The Entity structure of the new type cyclone is given in Fig.1. It is composed of pentagonal inlet, transitional volute chamber, eccentric inner cylinders and sloping feed outlet. The corresponding size is shown in Fig. 2. The total height is 16.75 m and the cylinder diameter is 7m. To simulation numerically, tetrahedral mesh is generated by Gambit software (preprocessor of Fluent software), as shown in Fig. 3.

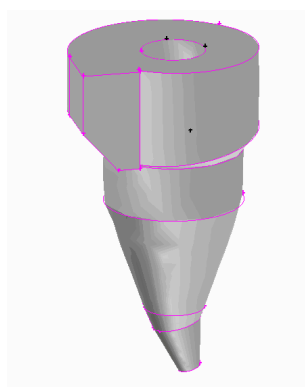


Fig. 1 Entity structure of cyclone

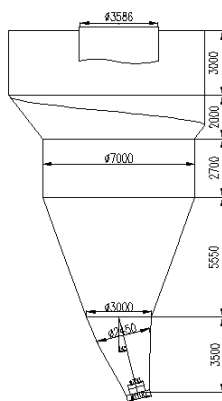


Fig. 2 Size of cyclone

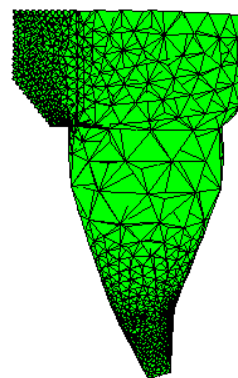


Fig. 3 Grid figure of cyclone

Mathematical model

Turbulence model. The gas flow is assumed incompressible steady turbulent flow. The three-dimensional flow control equation can be written as follows:

$$\frac{\partial}{\partial x}(\rho u \varphi) + \frac{\partial}{\partial y}(\rho v \varphi) + \frac{\partial}{\partial z}(\rho w \varphi) = \frac{\partial}{\partial x}(\Gamma_{\varphi} \frac{\partial \varphi}{\partial x}) + \frac{\partial}{\partial y}(\Gamma_{\varphi} \frac{\partial \varphi}{\partial y}) + \frac{\partial}{\partial z}(\Gamma_{\varphi} \frac{\partial \varphi}{\partial z}) + S_{\varphi} \quad (1)$$

The symbol Φ in equation represents the rate of u , v , w , turbulent kinetic energy k , turbulent dissipation rate ε respectively. S_{Φ} is the source term as shown in table 1.

Table 1 Control equations of the gas flow

φ	Γ_{φ}	S_{φ}
1	0	0
u	μ_{eff}	$-\frac{\partial p}{\partial x} + \frac{\partial}{\partial x}(\mu_{eff} \frac{\partial u}{\partial x}) + \frac{\partial}{\partial y}(\mu_{eff} \frac{\partial v}{\partial x}) + \frac{\partial}{\partial z}(\mu_{eff} \frac{\partial w}{\partial x})$
v	μ_{eff}	$-\frac{\partial p}{\partial y} + \frac{\partial}{\partial x}(\mu_{eff} \frac{\partial u}{\partial y}) + \frac{\partial}{\partial y}(\mu_{eff} \frac{\partial v}{\partial y}) + \frac{\partial}{\partial z}(\mu_{eff} \frac{\partial w}{\partial y})$
w	μ_{eff}	$-\frac{\partial p}{\partial z} + \frac{\partial}{\partial x}(\mu_{eff} \frac{\partial u}{\partial z}) + \frac{\partial}{\partial y}(\mu_{eff} \frac{\partial v}{\partial z}) + \frac{\partial}{\partial z}(\mu_{eff} \frac{\partial w}{\partial z})$
K	$\alpha_k \mu_{eff}$	$G_k + \rho \varepsilon$
ε	$\alpha_{\varepsilon} \mu_{eff}$	$\frac{C_{1\varepsilon}^* \varepsilon}{K} G_k - C_{2\varepsilon} \rho \frac{\varepsilon}{K}$

$$G_k = \mu_{eff} \left\{ 2 \left[\left(\frac{\partial u}{\partial x} \right)^2 + \left(\frac{\partial v}{\partial y} \right)^2 + \left(\frac{\partial w}{\partial z} \right)^2 \right] + \left(\frac{\partial u}{\partial y} + \frac{\partial v}{\partial x} \right)^2 + \left(\frac{\partial w}{\partial x} + \frac{\partial u}{\partial z} \right)^2 + \left(\frac{\partial v}{\partial z} + \frac{\partial w}{\partial y} \right)^2 \right\}$$

$$\mu_{eff} = \mu + \mu_t, \mu_t = C_{\mu} \rho K^2 / \varepsilon, C_{\mu} = 0.0845, \alpha_k = \alpha_{\varepsilon} = 1.39, C_{1\varepsilon}^* = C_{1\varepsilon} - \frac{\eta(1 - \eta / \eta_0)}{1 + \beta \eta^3}$$

$$C_{1\varepsilon} = 1.42, C_{2\varepsilon} = 1.68, \eta = (2E_{ij} \cdot E_{ij})^{1/2} \frac{K}{\varepsilon}, E_{ij} = \frac{1}{2} \left(\frac{\partial u_i}{\partial u_j} + \frac{\partial u_j}{\partial u_i} \right), \eta_0 = 4.377, \beta = 0.012$$

Particle trajectory model. Particle trajectories are calculated by discrete random walk model. The external force that influence solid particles in flow field mainly includes: fluid drag, gravity, buoyancy, pressure gradient force, false mass force, Basset force, Mangus lift and samffman lift and so on [6]. Since the particle size is small and concentration is low in cyclone, ignoring the interaction between the gas phase and particles, only considering the fluid drag force. Therefore, the force equilibrium equations of particles are:

$$\begin{aligned} \frac{du_p}{dt} &= F_D(u - u_p) + \frac{g_x(\rho_p - \rho)}{\rho_p} + F_x \\ \frac{dv_p}{dt} &= F_D(v - v_p) + \frac{g_y(\rho_p - \rho)}{\rho_p} + F_y \\ \frac{dw_p}{dt} &= F_D(w - w_p) + \frac{g_z(\rho_p - \rho)}{\rho_p} + F_z \end{aligned} \quad (2)$$

where u , u_p , v , v_p , w , w_p are the velocity component of gas and particles at x , y , z directions respectively. ρ_p , ρ are particle density and gas density. F_x , F_y , F_z are additional mass force and g_x , g_y , g_z are acceleration of gravity at x , y , z directions respectively. F_D is defined as follows:

$$F_D = \frac{18\mu}{\rho_p d_p^2} \frac{C_D R}{24} \quad (3)$$

Where d_p is the particle diameter. μ is the viscosity coefficient of gas molecules. C_D is the drag coefficient, and it takes the following functional form: